frontiers | Research Topics

Sediment dynamics and geohazards in estuaries and deltas

Edited by
Xiaolei Liu, Paul Liu and Ya Ping Wang

Published in
Frontiers in Earth Science

ISSN 1664-8714
ISBN 978-2-83251-491-7
DOI 10.3389/978-2-83251-491-7

About Frontiers

Frontiers is more than just an open access publisher of scholarly articles: it is a pioneering approach to the world of academia, radically improving the way scholarly research is managed. The grand vision of Frontiers is a world where all people have an equal opportunity to seek, share and generate knowledge. Frontiers provides immediate and permanent online open access to all its publications, but this alone is not enough to realize our grand goals.

Frontiers journal series

The Frontiers journal series is a multi-tier and interdisciplinary set of open-access, online journals, promising a paradigm shift from the current review, selection and dissemination processes in academic publishing. All Frontiers journals are driven by researchers for researchers; therefore, they constitute a service to the scholarly community. At the same time, the *Frontiers journal series* operates on a revolutionary invention, the tiered publishing system, initially addressing specific communities of scholars, and gradually climbing up to broader public understanding, thus serving the interests of the lay society, too.

Dedication to quality

Each Frontiers article is a landmark of the highest quality, thanks to genuinely collaborative interactions between authors and review editors, who include some of the world's best academicians. Research must be certified by peers before entering a stream of knowledge that may eventually reach the public - and shape society; therefore, Frontiers only applies the most rigorous and unbiased reviews. Frontiers revolutionizes research publishing by freely delivering the most outstanding research, evaluated with no bias from both the academic and social point of view. By applying the most advanced information technologies, Frontiers is catapulting scholarly publishing into a new generation.

What are Frontiers Research Topics?

Frontiers Research Topics are very popular trademarks of the *Frontiers journals series*: they are collections of at least ten articles, all centered on a particular subject. With their unique mix of varied contributions from Original Research to Review Articles, Frontiers Research Topics unify the most influential researchers, the latest key findings and historical advances in a hot research area.

Find out more on how to host your own Frontiers Research Topic or contribute to one as an author by contacting the Frontiers editorial office: frontiersin.org/about/contact

Sediment dynamics and geohazards in estuaries and deltas

Topic editors

Xiaolei Liu — Ocean University of China, China

Paul Liu — North Carolina State University, United States

Ya Ping Wang — East China Normal University, China

Citation

Liu, X., Liu, P., Wang, Y. P., eds. (2023). *Sediment dynamics and geohazards in estuaries and deltas*. Lausanne: Frontiers Media SA.

doi: 10.3389/978-2-83251-491-7

Table of contents

frontiers | Frontiers in Earth Science

TYPE Editorial
PUBLISHED 16 January 2023
DOI 10.3389/feart.2022.1079804

OPEN ACCESS

EDITED AND REVIEWED BY
Chunyan Li,
Louisiana State University, United States

*CORRESPONDENCE
Xiaolei Liu,
xiaolei@ouc.edu.cn

SPECIALTY SECTION
This article was submitted to Geohazards and Georisks, a section of the journal Frontiers in Earth Science

RECEIVED 25 October 2022
ACCEPTED 08 November 2022
PUBLISHED 16 January 2023

CITATION
Liu X, Liu J and Wang YP (2023), Editorial: Sediment dynamics and geohazards in estuaries and deltas. *Front. Earth Sci.* 10:1079804. doi: 10.3389/feart.2022.1079804

Editorial: Sediment dynamics and geohazards in estuaries and deltas

Xiaolei Liu[1]*, J. Paul Liu[2] and Ya Ping Wang[3]

[1]Shandong Provincial Key Laboratory of Marine Environment and Geological Engineering, Ocean University of China, Qingdao, China, [2]Department of Marine, Earth and Atmospheric Sciences, North Carolina State University, Raleigh, NC, United States, [3]State Key Laboratory of Estuarine and Coastal Research, School of Marine Sciences, East China Normal University, Shanghai, China

KEYWORDS

sediment dynamics, geotechnical and engineering characteristics, transport of suspended sediment, marine geohazards, estuaries and deltas

Editorial on the Research Topic
Sediment dynamics and geohazards in estuaries and deltas

Estuaries and deltas are the most complex areas of the earth's dynamic system, where frequent interactions and transformation of energy and materials occur (Gao et al., 2014; Yang et al., 2020, Yang et al.). Human exploitation and utilization of the ocean are relatively concentrated in these areas because of the extremely fertile lands with abundant water and diverse vegetation. More than 600 million people live on or near estuaries and deltas, who occupy only 1% of the world's land mass, and the productive intersection of river and ocean has allowed port cities to flourish (Syvitski and Saito, 2007; Higgins, 2016). Therefore, estuaries and deltas have both important ecological and environmental values and socio-economic significance (Giosan et al., 2014).

However, most of the world's estuaries and deltas are deteriorating at an accelerated rate (Syvitski et al., 2009; Bergillos et al., 2016). Under the combined effects of hydrodynamics, human activities and climate change, the sediments undergo a series of dynamic changes, such as consolidation, liquefaction, erosion, resuspension, and transportation, as well as the dynamic changes of sediment composition, structure, physical, chemical, and geotechnical engineering properties (Morton and Sallenger, 2003; Liu et al., 2017; Burchard et al., 2018; Xiong et al., 2018; Albatal et al., 2019; Yang et al., 2019; Čelić et al., 2019; Glover et al., 2021). These sediment dynamic changes would induce the morphological evolution of estuaries and deltas and a series of geological disasters, such as coastal erosion, submarine landslides, gravity flow, which seriously threaten the marine engineering activities (Liu et al.; Maloney et al., 2020; Wang et al., 2020). Generally speaking, sediment dynamics in estuaries and deltas and its derivative disasters are important aspects of marine geology and engineering studies and is one of the foci of international interest.

In this Research Topic, we have gathered contributions from scientists working in diverse disciplines, from the geotechnical and engineering characteristics of sediments,

distribution and transport of suspended sediment, observation of geomorphic feature and geohazards in estuaries and deltas. We have got a varied group of authors to contribute. In total, 13 papers have been included, with a mixture of 12 original research articles and 1 review.

The geotechnical and engineering characteristics of sediments are important parameters in design of marine engineering such as offshore oil platforms, submarine pipelines, and offshore wind power foundations (Al-Bared and Marto, 2017). In this Research Topic, the evolution of strength and microstructure of clay were discussed, which emphasized the change in the cementation degree between clay particles and pore distribution is the fundamental reason for the strength of clay in the thixotropic process (Tang et al.). Liu et al. summarized the strength and deformation characteristics of gassy soil and its constitutive models which have been used in the current simulation of geological disasters.

In estuaries and deltas areas, the distribution and transport of suspended sediments play an important role in morphodynamics, and will affect the development and utilization of coastal resources and the economic development (Talke et al., 2009; Normandin et al., 2019; Yu and Mantravadi, 2019). In this Research topic, Li et al. and Li et al. studied Hangzhou Bay, established and validated a three-dimensional wave–current–sediment coupled numerical model, to quantify the effect of wave-current coupling mechanism on suspended sediment characteristics during normal weather and typhoons. Results show that there are two high-SSC areas in Hangzhou Bay, inducing the siltation at the mouth and center of the bay. Wave-current combined bottom stress can affect sediment resuspension process and thus the characteristics of SSC, especially in shallow water or during typhoon. In this process, the bottom drag coefficient (C_d) is one of the most important parameters to define the bottom friction and influence the velocity profile and turbulence. Qi et al. took the muddy deposit of Shandong Peninsula as an example, examined the variability of C_d, revealed the significant tidal asymmetry characteristics, and further determined the critical bottom wave orbital velocity $U_b \approx 0.1$ m/s. Xie et al. pointed out that advection and tidal pumping are the key control factors in determining suspended sediment, while the water column stratification inhibit the effective vertical diffusion. Li et al. analyzed the past 60 years' SSC data for the Nanliu River and pointed out that the SSC of Nanliu River shows a downward trend year by year under the influence of climate change and human activity.

The dynamic changes of sediment can result in serious geological disasters such as erosion, landslide, gravity flow and so on, and then affect the changes of coastline and seabed topography (Herman et al., 2001; Chen et al., 2020; Wang et al., 2020). It is of great significance for the construction and development of estuaries and deltas region to observe these hazard processes and reveal their evolutionary mechanism. In this research topic, using the remote sensing images and corresponding hydrodynamic data, Lu et al. analyzed the relationship between the supply of terrestrial and marine sediments and the dynamic changes of the coastline in the Yangtze River Delta, and discussed the internal and external driving factors and interactions between the long-term evolution of the coastline and human activities in the past 40 years. Zhu et al. described the distribution and morphological characteristics of hummocky patches in an accretional intertidal zone of Jiangsu Province, China, and pointed out that the key factor in controlling the formation of hummocky patches is erosivity variability caused by the difference in sediment properties. Yang et al. investigated and analyzed the distribution, morphological characteristics and migration direction of sand waves in Taiwan shoal, northern South China Sea, which laid the foundation for the study of sediment transport and marine engineering site selection in this area. Xue and Shan carried out the long-term *in situ* observation on the typically inclined seabed slope in the southwest of Zhujiajian Island in Zhoushan, China based on the independently developed observation system with the results showing that the Zhujiajian landslide creep accelerates under the action of waves. Fluid mud is widely developed in estuaries, including natural mud and fluid mud formed by sediment erosion, resuspension and liquefaction forced by waves and/or currents. Wang et al. investigated the rheological characteristics of natural mud and explained its "two-step" yielding process in detail, which laid a foundation for the study of its movement characteristics and morphology evolution. Taking the silty sediment from the subaqueous Yellow River Delta as the experimental seabed in a flume, Yu et al. reproduced the formation, movement, and deposition processes of wave-induced liquefied sediment gravity flow (WILSGF). The results clearly revealed that under the combined action of pore water seepage and environmental water entrainment, a coarsened seabed is finally formed along the transport path of WILSGF with the fine particles suspended into seawater.

This Research Topic presents some original research papers and review on sediment dynamics and geohazards. These studies lay the theoretical foundation for the establishment of sediment transport models, geomorphic evolution studies, water and sediment regulation and engineering construction in estuaries and deltas, and provide valuable reference for the development and ecological protection in these areas.

Author contributions

The Research Topic "*Sediment Dynamics and Geohazards in Estuaries and Deltas*" is edited by XL, PL and YW. XL wrote the manuscript with support from PL and YW.

Conflict of interest

The authors declare that the research was conducted in the absence of any commercial or financial relationships that could be construed as a potential conflict of interest.

Publisher's note

References

Albatal, A., Wadman, H., Stark, N., Bilici, C., and McNinch, J. (2019). Investigation of spatial and short-term temporal nearshore sandy sediment strength using a portable free fall penetrometer. *Coast. Eng.* 143, 21–37. doi:10.1016/j.coastaleng.2018.10.013

Bergillos, R. J., López-Ruiz, A., Ortega-Sánchez, M., Masselink, G., and Losada, M. A. (2016). Implications of delta retreat on wave propagation and longshore sediment transport - guadalfeo case study (southern Spain). *Mar. Geol.* 382, 1–16. doi:10.1016/j.margeo.2016.09.011

Burchard, H., Schuttelaars, H. M., and Ralston, D. K. (2018). Sediment trapping in estuaries. *Annu. Rev. Mar. Sci.* 10, 371–395. doi:10.1146/annurev-marine-010816-060535

Čelić, M., Gros, M., Farré, M., Barceló, D., and Petrović, M. (2019). Pharmaceuticals as chemical markers of wastewater contamination in the vulnerable area of the ebro delta (Spain). *Sci. Total Environ.* 652, 952–963. doi:10.1016/j.scitotenv.2018.10.290

Chen, D., Li, M., Zhang, Y., Zhang, L., Tang, J., and Wu, H., (2020). Effects of diatoms on erosion and accretion processes in saltmarsh inferred from field observations of hydrodynamic and sedimentary processes. *Ecohydrology*. 13(8), 2246. doi:10.1002/eco.2246

Gao, G. D., Wang, X. H., and Bao, X. W. (2014). Land reclamation and its impact on tidal dynamics in jiaozhou bay, qingdao, China. *Estuar. Coast. Shelf Sci.* 151, 285–294. doi:10.1016/j.ecss.2014.07.017

Giosan, L., Syvitski, J., Constantinescu, S., and Day, J. (2014). Climate change: Protect the world's deltas. *Nature* 516 (516), 31–33. doi:10.1038/516031a

Glover, H. E., Ogston, A. S., Fricke, A. T., Nittrouer, C. A., Aung, C., Naing, T., et al. (2021). Connecting sediment retention to distributary-channel hydrodynamics and sediment dynamics in a tide-dominated delta: The ayeyarwady delta, Myanmar. *JGR. Earth Surf.* 126 (3). doi:10.1029/2020JF005882

Herman, P. M. J., Middelburg, J. J., and Heip, C. H. R. (2001). Benthic community structure and sediment processes on an intertidal flat: Results from the ecoflat project. *Cont. Shelf Res.* 21 (18), 2055–2071. doi:10.1016/S0278-4343(01)00042-5

Higgins, S. A. (2016). Review: Advances in delta-subsidence research using satellite methods. *Hydrogeol. J.* 24 (3), 587–600. doi:10.1007/s10040-015-1330-6

Liu, X., Zhang, M., Zhang, H., Jia, Y., Zhu, C., and Shan, H. (2017). Physical and mechanical properties of loess discharged from the Yellow River into the bohai Sea, China. *Eng. Geol.* 227, 4–11. doi:10.1016/j.enggeo.2017.04.019

Maloney, J. M., Bentley, S. J., Xu, K., Obelcz, J., Georgiou, I. Y., and Jafari, N. H., (2020). Mass wasting on the Mississippi River subaqueous delta. *Earth. Sci. Rev.* 200, 103001. doi:10.1016/j.earscirev.2019.103001

Mohammed Al-Bared, M., and Marto, A. (2017). A review on the geotechnical and engineering characteristics of marine clay and the modern methods of improvements. *Mal. J. Fund. Appl. Sci.* 13, 825–831. doi:10.11113/mjfas.v13n4.921

Morton, R. A., and Sallenger, A. H. (2003). Morphological impacts of extreme storms on sandy beaches and barriers. *J. Coast. Res.* 19 (3), 560–573. doi:10.2307/4299198

Normandin, C., Lubac, B., Sottolichio, A., Frappart, F., Ygorra, B., and Marieu, V. (2019). Analysis of suspended sediment variability in a large highly turbid estuary using a 5-year-long remotely sensed data archive at high resolution. *J. Geophys. Res. Oceans* 124 (11), 7661–7682. doi:10.1029/2019JC015417

Syvitski, J. P. M., Kettner, A. J., Overeem, I., Hutton, E. W. H., Hannon, M. T., and Brakenridge, G. R., (2009). Sinking deltas due to human activities. *Nat. Geosci* 2 (10), 681–686. doi:10.1038/ngeo629

Syvitski, J. P. M., and Saito, Y. (2007). Morphodynamics of deltas under the influence of humans. *Glob. Planet. Change* 57 (3-4), 261–282. doi:10.1016/j.gloplacha.2006.12.001

Talke, S. A., de Swart, H. E., and Schuttelaars, H. M. (2009). Feedback between residual circulations and sediment distribution in highly turbid estuaries: An analytical model. *Cont. Shelf Res.* 29 (1), 119–135. doi:10.1016/j.csr.2007.09.002

Wang, Z., Sun, Y., Jia, Y., Shan, Z., Shan, H., and Zhang, S., (2020). Wave-induced seafloor instabilities in the subaqueous Yellow River delta—Initiation and process of sediment failure. *Landslides* 17 (8), 1849–1862. doi:10.1007/s10346-020-01399-2

Xiong, H., Huang, G., Fu, S., and Qian, P. (2018). Progress in the study of coastal storm deposits. *Ocean. Sci. J.* 53 (2), 149–164. doi:10.1007/s12601-018-0019-x

Yang, G., Wang, X. H., Zhong, Y., Cheng, Z., and Andutta, F. P. (2020). Wave effects on sediment dynamics in a macro-tidal estuary: Darwin harbour, Australia during the monsoon season. *Estuar. Coast. Shelf Sci.* 244, 106931. doi:10.1016/j.ecss.2020.106931

Yang, M., Lu, K., Batzer, D. P., and Wu, H. (2019). Freshwater release into estuarine wetlands changes the structure of benthic invertebrate assemblages: A case study from the Yellow River delta. *Sci. Total Environ.* 687, 752–758. doi:10.1016/j.scitotenv.2019.06.154

Yu, S., and Mantravadi, V. S. (2019). Study on distribution characteristics of suspended sediment in yellow river estuary based on remote sensing. *J. Indian Soc. Remote Sens.* 47 (9), 1507–1513. doi:10.1007/s12524-019-00985-9

frontiers | Frontiers in Earth Science

ORIGINAL RESEARCH
published: 02 May 2022
doi: 10.3389/feart.2022.909605

Characteristics of the Sediment Gravity Flow Triggered by Wave-Induced Liquefaction on a Sloping Silty Seabed: An Experimental Investigation

Heyu Yu [1,2], Xiaolei Liu [1,2,3], Yang Lu [1,2], Weijia Li [1,2], Han Gao [1,2], Ruoyu Wu [1,2] and Xingyu Li [1,2]*

[1]Shandong Provincial Key Laboratory of Marine Environment and Geological Engineering, Ocean University of China, Qingdao, China, [2]Key Laboratory of Marine Environment and Ecology, Ministry of Education, Qingdao, China, [3]Laboratory for Marine Geology, Qingdao National Laboratory for Marine Science and Technology, Qingdao, China

The sloping silty sediments in estuarine deltas are frequently affected by extreme storms, and they are prone to liquefaction instability. The unstable liquefied sediments of the slopes can subsequently form a sediment gravity flow (SGF), which can seriously endanger offshore engineering facilities. To better understand the characteristics and mechanism of wave-induced liquefied sediment gravity flow (WILSGF), a flume experiment was conducted to reproduce the formation, movement, and deposition processes of the WILSGF and analyze their controlling factors using natural silty sediment samples collected from the Yellow River Delta in China. The results show that the mass of the WILSGF comes from the sediment in the liquefied layer, and the movement of the WILSGF in these experiments was significantly affected by the wave orbital velocity and the relative outflow position. At the initial stage of the formation of the WILSGF, the phase and amplitude of the WILSGF were the same as those of waves, and the maximum velocity of the WILSGF reached 2.39 cm/s. The velocity of the WILSGF decreased continuously with the downward evolution of the liquefaction interface. When the liquefaction depth reached its maximum value, there was no WILSGF. We also found that the median particle size of the WILSGF was greater than that of the original seabed due to wave-induced seabed coarsening and the intrusion of ambient water. This study has guiding significance for in-depth understanding and prediction of the geological hazards caused by WILSGF.

Keywords: wave-induced liquefaction, sediment gravity flow, movement characteristics, depositional characteristics, sloping seabed

OPEN ACCESS

Edited by:
Chong Xu,
Ministry of Emergency Management, China

Reviewed by:
Aiguo Xing,
Shanghai Jiao Tong University, China
Siyuan Ma,
China Earthquake Administration, China

***Correspondence:**
Xiaolei Liu
xiaolei@ouc.edu.cn

Specialty section:
This article was submitted to Geohazards and Georisks, a section of the journal Frontiers in Earth Science

Received: *31 March 2022*
Accepted: *19 April 2022*
Published: *02 May 2022*

Citation:
Yu H, Liu X, Lu Y, Li W, Gao H, Wu R and Li X (2022) Characteristics of the Sediment Gravity Flow Triggered by Wave-Induced Liquefaction on a Sloping Silty Seabed: An Experimental Investigation. Front. Earth Sci. 10:909605. doi: 10.3389/feart.2022.909605

INTRODUCTION

Sediment gravity flow (SGF) is a flow type of sediments or sediment-fluid mixtures under the action of gravity (Middleton and Hampton, 1973). As one of the main dynamic processes of the seaward transport of sediment, the SGF has a profound impact on the morphological evolution of continental shelves (Traykovski et al., 2000; Wright et al., 2001; Jaramillo et al., 2009; Macquaker et al., 2010; Plint, 2014; Harazim and Mcilroy, 2015), and it has led to great threats to marine engineering facilities (e.g., platforms, oil and gas pipelines, power and telecommunications cables) (Carter et al.,

2014; Guo et al., 2022). The dynamic characteristics (propagation, velocity, distance, etc.) of different types of gravity flow vary considerably, as do their depositional characteristics, making this topic a complex and cutting-edge problem of multidisciplinary interests.

The triggering factors of SGF are complex, and they include earthquakes, storm waves, rapid accumulation of sediment, and submarine volcanoes (Heezen and Ewing 1952; Ma et al., 2010; Prior et al., 1989; Bailey et al., 2021; Anfinson et al., 2016). Among these factors, storm-wave-induced liquefaction could be a special trigger mechanism for the formation of SGF, especially in shallow shelf areas. During frequent extreme storm events, slope sediments are prone to bottom cyclic pressures during the passage of surface waves (Maa and Mehta, 1987), resulting in the formation of excess pore-water pressure inside the seabed sediments (Foda and Tzang, 1994); the effective stress of the sediment will decrease with the increasing excess pore-water pressure (Atigh and Byrne, 2004). When the excess pore-water pressure exceeds the effective stress of the sediment, it will liquefy (Sumer et al., 2006). Such liquefied sediments lose their original strength (Kessel and Kranenburg, 1998), and the liquefied sediments may slide or move under the action of gravity to form SGF (Puig et al., 2004; Piper and Normark, 2009; Wang et al., 2020).

SGF formed by wave-induced liquefaction of slope sediments has been preliminarily recognized in previous studies. For instance, Prior et al. (1989) first observed the phenomenon of submarine landslides during extreme storms on the slope of the subaqueous Yellow River Delta. Through analysis of pore-water pressure data, these submarine landslides were found to be related to wave-induced liquefaction. Kessel et al. (1997) studied the problem of wave-induced liquefaction of sloping seabed sediments through laboratory experiments and measured the rheological properties of the liquefied mud using independent rheological experiments. They considered that if the fluid mud layer produced by liquefaction flowed under the influence of a net force, there would be a very high sediment transportation rate in a short time. Subsequently, using experiments and mathematical flow-model calculations, Kessel and Kranenburg (1998) revealed that the sediment on the slope begins to flow under combined wave and gravity action after liquefaction and that the velocity could reach the cm/s order of magnitude. Xu et al. (2016) studied the formation process of silty bed liquefaction and the subsequent wave-induced liquefied SGF (WILSGF) using physical model experiments, pointing out that such a WILSGF moves along the slope by bed-load transport. In these studies, the formation mechanisms and outflow characteristics of WILSGF have mostly been explained from the perspective of geotechnics. However, the hydrodynamic effects during WILSGF have not been considered, leading to a lack of comprehensive description of their movement processes.

Noticeably, wave action not only causes the liquefaction of a sloping seabed to form SGF but also affects the movement and depositional characteristics of the SGF. It has been demonstrated that cyclic oscillatory currents generated by surface waves determine the movement behavior of highly concentrated SGF (Ng and Fu, 2002). Such cyclic wave oscillations increase the transport and erosion capacity of SGF (Musumeci et al., 2017). The amplitude and phase of SGF are also related to the wave orbital velocity (Robinson et al., 2013). These studies have quantified the effect of wave action on SGF movement from a hydrodynamic perspective. However, the nature of the liquefied sediments that form an SGF (e.g., the dynamics of pore pressure accumulation and dissipation) have been ignored. Evidently, the physical properties of the sources that form the SGF directly influence the movement and depositional characteristics of that SGF. In addition, due to the WILSGF process involving complex physical mechanisms such as seabed sediment phase transformation and large deformation, the numerical simulation method based on soil or fluid constitutive model is difficult to accurately describe the complete WILSGF movement behavior (Wang et al., 2015; Yue et al., 2020). In contrast, the flume experiment has become an effective method to study the WILSGF problem because it can better reproduce the interaction process between real sediments and hydrodynamic forces.

This study aimed to reveal the movement and depositional characteristics of WILSGF by integrating the effects of the properties of the liquefied sediment and wave-generated cyclic oscillatory currents on WILSGF movement and deposition. The whole processes of slope sediment liquefaction, outflow, movement, and deposition were simulated and observed using flume experiments. The relationship between wave orbital velocity and WILSGF velocity, the movement characteristics of the WIFSGF, and the physical properties of the deposits of WILSGF were examined.

MATERIALS AND METHODS

Experimental Setup and Procedure

The experiments were conducted in a wave flume with a length of 4 m, a width of 0.4 m, and a height of 1 m. Regular waves were generated by a piston-type wave maker at one end of the flume and a wave-dissipating slope was placed at the opposite end (**Figure 1**). Regular waves with different frequencies and wave heights were obtained by changing the amplitude and frequency of the piston. In the experiments, the wave height was 0.12 m and the wave frequency was 0.5 Hz. A model sediment slop was established in the middle of the flume. This was 1.2 m long, 0.4 m wide, 0.5 m high at the top, and 0.3 m high near the toe. The slope gradient was approximately 9°. The sediment used in the experiments was sampled from the subaqueous Yellow River Delta. The median size (d_{50}) of sediment was 34 μm, and it contained 87.4% silt, and 12.6% clay. This type of sediment, which is composed of a high silt content and a low clay content, is more prone to liquefaction (Kirca et al., 2014; Liu et al., 2017). The water content of the sediment was 25.0%.

To reproduce the water content and homogeneity of the field-derived sediments of the Yellow River Delta, the obtained sediments were firstly air-dried. Secondly, the sediment clusters were pulverized into individual particles and sieved to remove the larger gravels. The dry sediments were mixed with water according to a constant weight proportion of 3:1 to prepare a slurry with a saturated water content of 25.0%. Thirdly, this

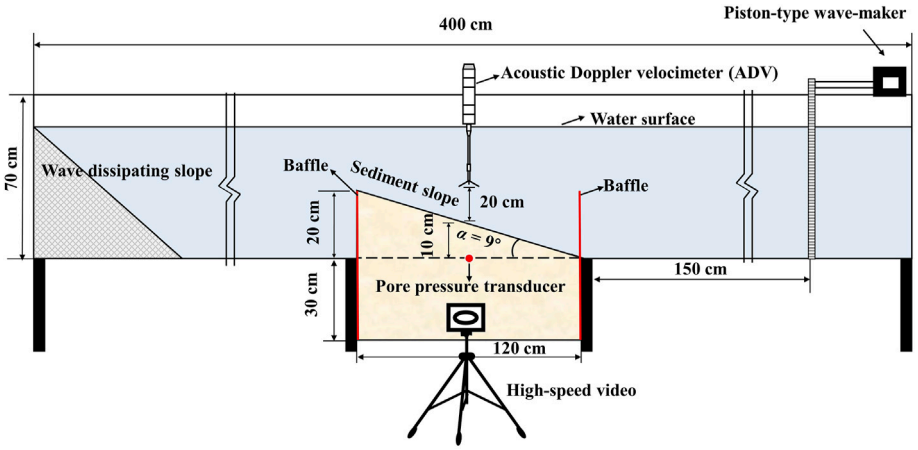

FIGURE 1 | Schematic of the experimental setup.

slurry was then slowly poured along the flume walls into the soil tank up to about 50 cm thick (**Figure 1**). As the mud settled during natural consolidation, it was necessary to replenish it after 24 h of consolidation to bring the sediment height to a predetermined level. After the consolidation process, the right-hand baffle of the flume was removed, and the sediment was trimmed to a slope of 9° using a geotechnical knife. Subsequently, water was gradually added to the wave flume to a depth of 45 cm above the soil surface. The flume test was started after 24 h of soil bed consolidation under hydrostatic pressure. A small-amplitude wave was applied to the seabed sediment for 5 min to expel any gas that may be present within the sediment and to stabilize the sloping seabed. Finally, wave-making experiments were carried out.

Instrumentation and Measurements

As shown in **Figure 1**, a pore-water pressure transducer (CYY4, Xi'an Weizheng Electronic Technology Co. Xi'an) was deployed at 10 cm below the sediment surface and along the central axis of the soil tank, with a collection frequency of 5 Hz. The measuring range of the pore water pressure sensor is ±50 kPa, the resolution is 0.02% FS, the diameter is 5 mm and the height is 12 mm, which can minimize the disturbance of the pore water pressure sensor to the seabed. Before the pore pressure transducers were embedded in the soil bed, they were soaked in water for 24 h with continuous shaking to ensure gas removal. To obtain the variation of pore-water pressure within the sloping seabed sediment under wave action, the measured pore-water pressure data were low-pass filtered using the fast Fourier transform to remove the pressure-variation values generated by waves and wave reflections. Velocity was measured using a down-looking 6 MHz acoustic Doppler velocimeter (ADV). This ADV was placed 20 cm above the sediment bed (the blanking distance was 15 cm) to measure the three-dimensional velocities and to calculate the wave orbital velocity (**Figure 1**), and the collection frequency was 16 Hz. Doppler signal aliasing, Doppler noising, and boundary layer interference can lead to the presence of spikes, which can affect the quality of the data obtained by the ADV (Voulgaris and Trowbridge, 1998; Nikora and Goring, 1998). The modified phase-space threshold method proposed by Parsheh et al. (2010) was used for quality control of the ADV data, while a polynomial fit interpolation, also proposed by Parsheh et al. (2010), was used for spikes substitution.

A high-speed video camera was placed along the sidewall of the flume to record the formation of the slope-sediment liquefaction interface and its evolution, and this was also used to characterize the movement of the WILSGF and the morphological changes in the sloping seabed (**Figure 1**). The high-speed video camera has previously been successfully used for particle tracking of sand grains (Ilstad et al., 2004), and to describe the flow behavior of subaqueous debris flow. At the end of the experiment, the water column inside the flume was removed, and some photographs were taken from above and through one sidewall to characterize the structure of the WILSGF deposit. In addition, water-content tests and particle-size analyses of the deposits were carried out on samples from different areas of the sloping seabed. The median particle sizes of the deposits were measured using a Beckman Coulter laser particle sizer from (model LS-12-320).

Flow Dynamics Calculation

In this study, the ADV data was influenced by the flume size and slope topography, and its direct measurement results included velocity components such as wave orbital velocity and turbulent fluctuations. To accurately obtain the wave orbital velocity (u_{orb}) and study its influence on the WILSGF velocity, the empirical mode decomposition (EMD) method proposed by Huang and Coauthors (1998) was used. The accuracy of the EMD method for calculating the wave orbital velocity has been verified (Bian et al., 2020). The value of u_{orb} can be obtained using:

$$u_{\mathrm{orb}} = u' + u'_{\mathrm{tur}} \tag{1}$$

where u'_{tur} is the turbulent fluctuation, $u' = u - \bar{u}$ is the residual velocity, u is the horizontal flow velocity measured by ADV, and $\bar{u}$ is the 10-min-averaged velocity.

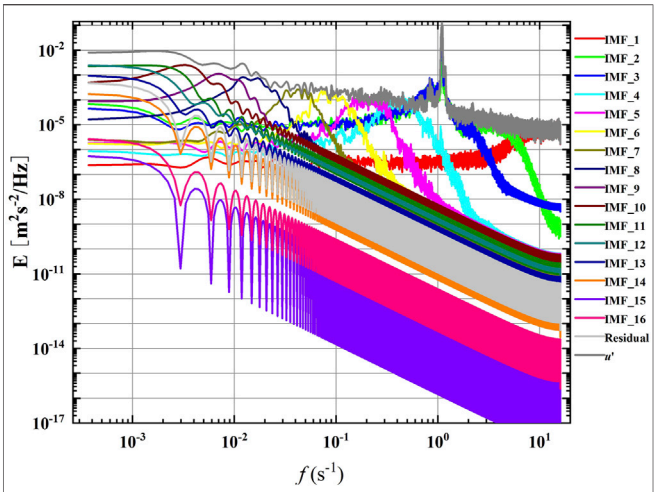

FIGURE 2 | Power spectra of velocity fluctuation u', its decomposed IMFs, and residual velocity.

The EMD method was used to decompose the observed u' value into several intrinsic mode functions (IMFs) and a residual velocity:

$$u' = u'_{\mathrm{IMF\_1}} + u'_{\mathrm{IMF\_2}} + u'_{\mathrm{IMF\_3}} + \cdots + u'_{\mathrm{IMF\_}n} + u'_{\mathrm{Residual}} \quad (2)$$

Each IMF represents a stationary stochastic process. Through spectral analysis of the IMF components (**Figure 2**), if the peak frequency of an IMF is within the range of the wave frequency, the IMF is classified as a wave component:

$$u' = u'_{IMF\_N1} + u'_{\mathrm{IMF\_N2}} + u'_{\mathrm{IMF\_N3}} + \cdots + u'_{\mathrm{IMF\_NN}} \quad (3)$$

where $u'_{\mathrm{IMF\_N1}}, u'_{\mathrm{IMF\_N2}}, u'_{\mathrm{IMF\_N3}}, \ldots, u'_{\mathrm{IMF\_NN}}$ are the residual velocity components of the peak frequency in the wave frequency range.

RESULTS

Pore Pressure Response of Seabed

We filtered the data measured by the pore-water pressure transducer at 10 cm below the seabed surface and obtained the periodic-average pore-water pressure change within 70 min (**Figure 3**). Then, the experimental process was divided into three stages ("A", "C", and "E" in **Figure 3**) and two critical points ("B" and "D" in **Figure 3**) according to the change in the pore-water pressure. To understand the changes of these stages and critical points more intuitively, we extracted the changes in the seabed surface and liquefaction interface at 0, 34, 42, and 70 min from the high-speed video camera (**Figure 4**). In the "A" stage, the pore pressure remains stable in the initial period under wave action, and then a sharp increase is observed after a certain number of wave cycles; the excess pore pressure then begins to build up, and the seabed surface of the sediment is lower than the initial seabed surface due to wave compaction (**Figure 4A**). At critical point "B" in **Figure 3**, the pore-water pressure reaches a peak of 5.64 kPa, and the excess pore pressure (Δu) reaches its maximum value. The maximum value of the excess pore-water pressure can be determined by the maximum value measured by the pore-water pressure transducer at the depth of 10 cm and the hydrostatic pressure value at 10 cm (Liu et al., 2020):

$$\Delta u_{\max} = u_{\max} - \gamma_{\omega}(h_1 + h_2) \quad (4)$$

where: $u_{\max}$ represents the maximum value of the pore-water pressure measured by the pore-water pressure transducer; γ_{ω} is the unit weight of water (10.00 kN/m); h_1 and h_2 are the distance from the surface of the seabed to the surface of the water and the buried depth of the pore water pressure transducer (where h_1 is 44 cm and h_2 is 10 cm), respectively.

According to the criteria proposed by Jia et al. (2014), the sediment liquefaction index at 10 cm depth is approximately 45.6%, which is less than the liquefaction threshold (100%). This indicates that the sediment at 10 cm is not liquefied, but the sediment above it is partially liquefied. After the peak value of pore pressure is reached, it then gradually decreases ("C" in **Figure 3**). At this stage, the liquefaction interface continues to evolve downward (**Figures 4B,C**), and the liquefaction depth continues to increase. At critical point "D" in **Figure 3**, the liquefaction interface extends downward to the deepest position, the sediment begins to be compressed, and the maximum liquefaction depth can reach 4.5 cm (**Figure 4C**). Compared with the results of Jia et al. (2014), which were conducted under similar experimental conditions, this lower liquefaction depth is caused by the loss of sediment flow in the liquefaction layer. These lost liquefied sediments are

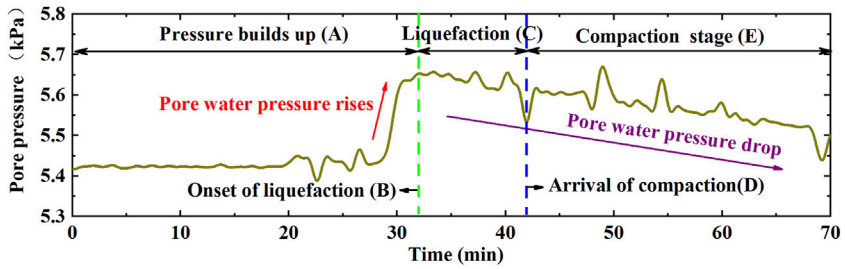

FIGURE 3 | Variation of periodic-average pore-water pressure with time at 10 cm depth.

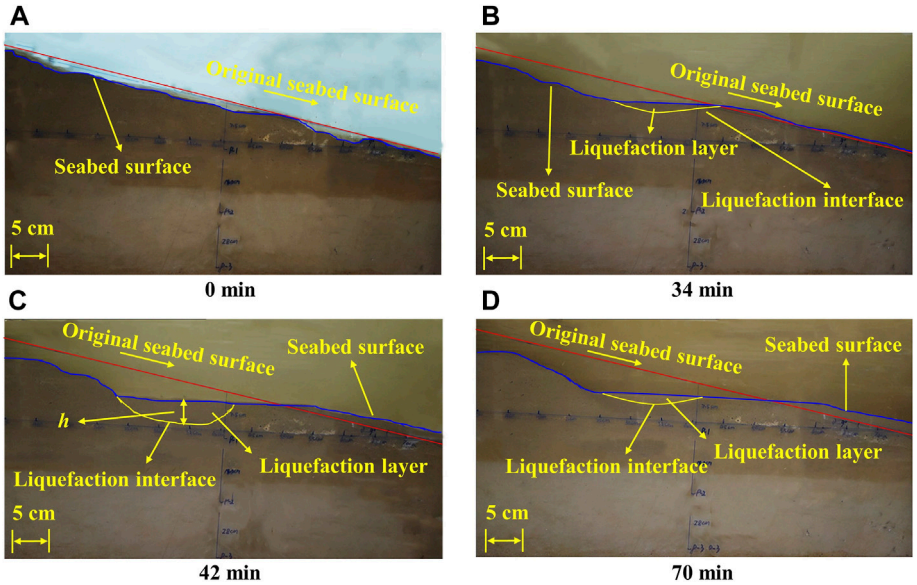

FIGURE 4 | Changes of seabed surface and evolution of liquefaction interface at different times. **(A-D)** are the positions of seabed surface and liquefaction interface at 0, 34, 42 and 70 min, respectively, where h is the liquefaction depth.

moved to the bottom of the sloping seabed by gravity flow, and some are suspended in the ambient water by the shear action of waves, resulting in high turbidity in the water column (**Figures 4A–D**). As the wave load continues to be applied, the pore-water pressure continues to decrease steadily and the sediment is gradually compressed ("E" in **Figure 3**, and **Figures 4C,D**). The liquefaction interface then begins to move upward until it reaches the sediment surface.

Wave Orbital Velocity and WILSGF Velocity

The decomposition results of the flow fluctuations by the EMD method demonstrated that the peak frequencies of IMF_2 and IMF_3 are within the wave frequency range (**Figure 2**), from which the root mean square (RMS) wave orbital velocity is calculated (**Figure 5A**). During the period 0–5 min of the experiment, the RMS wave orbital velocity is small and fluctuates due to the small wave load compacting the slope sediment. After 5 min, the RMS orbital velocity becomes more stable, with an average RMS orbital velocity of 5.67 cm/s.

The WILSGF is mainly formed in the "C" stage in **Figure 3**; this moves slowly downward in the form of a laminar flow (**Figure 6**). The thickness of the head of the WILSGF is small, and its body is thick. Deposition along the sloping seabed will occur during the movement of WILSGF along the slope. Due to the "paving" effect of WILSGF, the original uneven sloping seabed becomes smooth. A plot of the velocity of the WILSGF is shown in **Figure 5B**, in the incipient stage, the velocity is high, reaching a peak of 2.39 cm/s. With the downward evolution of the liquefaction interface, the liquefaction depth (h) of the sediments continuously increases (**Figure 4C**), while the WILSGF velocity decreases rapidly.

To better study the movement characteristics of the WILSGF at the initial stage of its formation, the velocity data of the first 20 s and the wave orbital velocity data after the formation of WILSGF were extracted (as shown in **Figures 5C,D**. During the first 7 s of the formation of the WILSGF, its velocity is affected by wave orbital velocity, and the direction of the wave orbital velocity determines the WILSGF velocity. When the direction of the wave orbital velocity is the same as that of the WILSGF, the wave orbital velocity will promote the movement of the WILSGF. The fluctuation of the phase and amplitude of the WILSGF is the same as that of the cyclic oscillating flow generated by the waves.

Particle Size, Water Content, and Bedforms

To study the depositional characteristics of the WILSGF, the experiment was artificially stopped when the liquefaction interface evolved upward and came near to the sloping seabed surface. The ambient water was slowly drained from the tank, and the different types of deposits on the sloping seabed were then divided into four zones (**Figure 7A**). Zone Ⅰ is the central deposition zone of the WILSGF, which was formed by the accumulation of sediments deposited on the sloping seabed after the movement of the WILSGF along the slope. Zone Ⅱ is the WILSGF head deposition zone, which consists of sediment deposited after the head of the WILSGF had stopped moving. Zone Ⅲ is the liquefaction zone and zone Ⅳ is the non-liquefaction zone.

The variation of the water content in the four zones is presented in **Figure 8**. It can be seen that the water content of the sediments in the deposition area of the WILSGF head deposition zone was the greatest (28.01%), while that in the liquefaction zone was low (23.90%). The median particle sizes

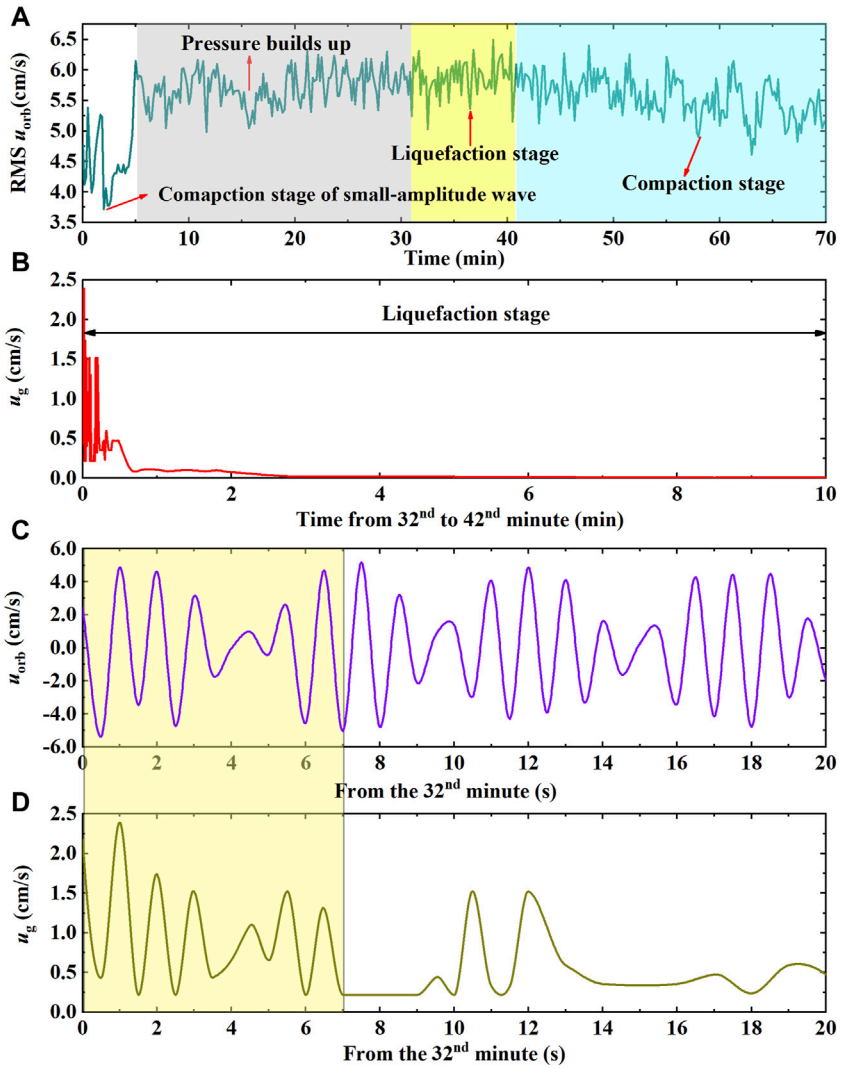

FIGURE 5 | Time series records of wave orbital velocity and the WILSGF velocity. **(A)** RMS wave orbital velocity (RMS u_{orb}) of the experiment. The white region indicates the small-amplitude-wave compaction stage, the gray region indicates represents the pore water pressure establishment stage, the yellow region indicates the liquefaction stage, and the light blue scale represents the compaction stage. **(B)** Plot of the velocity of the WILSGF (u_g), from the 32nd min to the 42nd min. **(C)** Instantaneous wave orbital velocity in the 20 s, period from the 32nd min. **(D)** WILSGF velocity u_g in the 20 s, period from the 32nd min.

of the sediments in the four regions were quite different from that of the original seabed sediments. Zone I and II showed a coarsening phenomenon, and the median particle size of sediments in these two zones was approximately 50% higher than that of the original seabed. Grain refinement occurred in the sediments in zone III and IV.

The formation and movement of the WILSGF changed the sloping bedform. **Figure 9** shows the seabed outlines (taken from photographs) at 0, 28, 32, 42, and 70 min. The intersection of the outline at 0 min with the subsequent seabed-surface outline obtained at each time point was defined as the critical erosion boundary. The sediments in the seabed area on the left-hand side of the critical erosion boundary are eroded by waves, and sediment deposition mainly occurs on the right-hand side of the critical erosion boundary. In the "A" stage, the sloping bedform changes little. The phenomenon of slope-sediment erosion is not obvious, and the slope sediment settles due to wave compaction. After liquefaction of the slope sediments, the position of the critical erosion point shifts to the right until the end of the experiment, by which point the original sloping seabed had changed into a stepped topography due to sediment liquefaction and deposition by the WILSGF (**Figures 7A,B**).

The angle of the step trailing edge changed with the position of the liquefaction interface. This angle also reached its maximum near the deepest position of the liquefaction interface. The angle of the trailing edge of the step decreased slowly in the compaction stage, and it reached 31° (α_1) at the 70th minute (**Figure 7C**). The angle of the

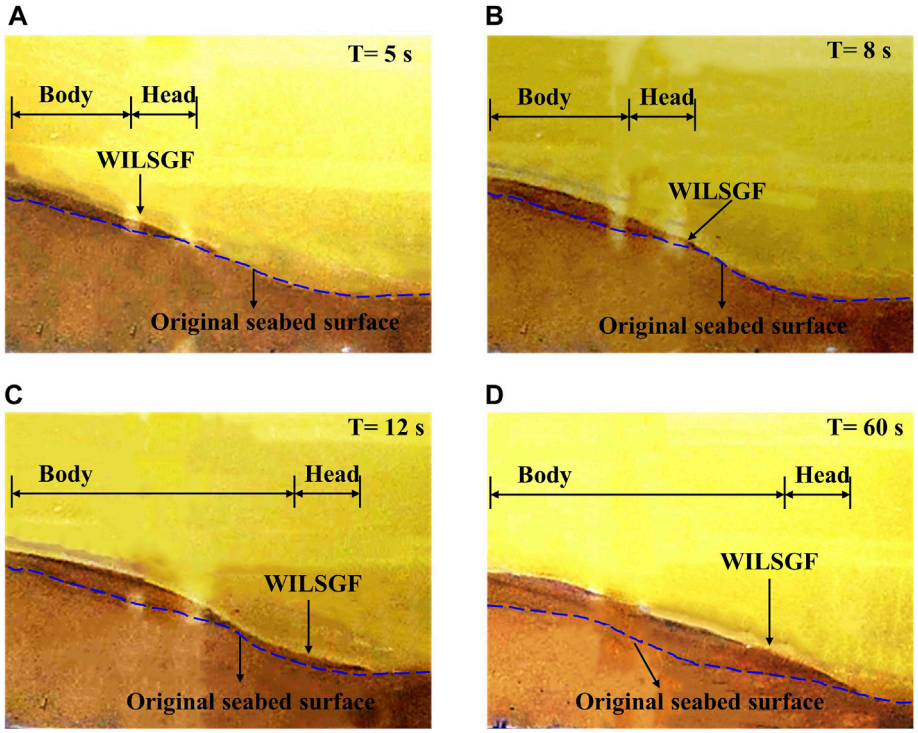

FIGURE 6 | Ongoing process of the WILSGF and the resulting morphological changes at 5, 8, 12, and 60 s in panels **(A–D)**, respectively.

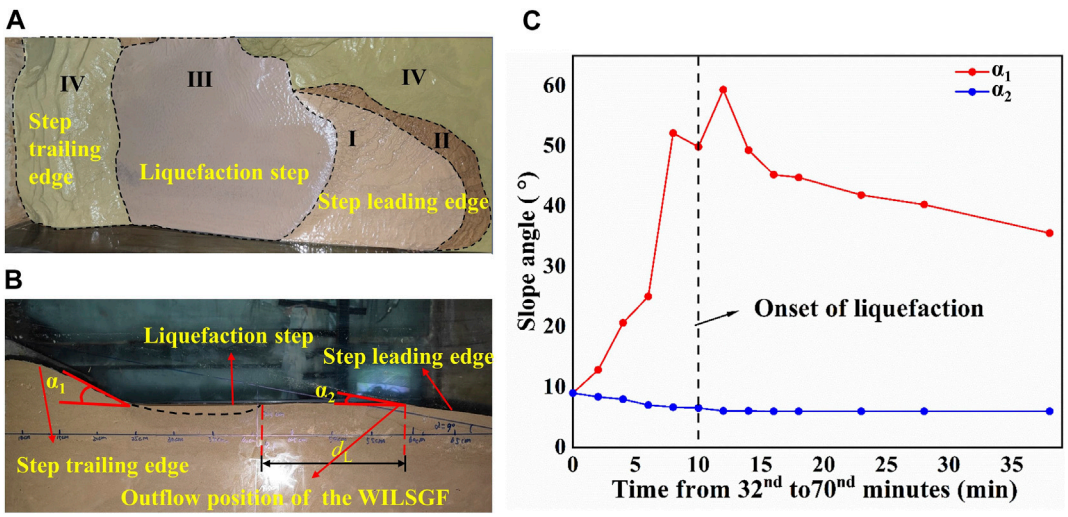

FIGURE 7 | Seabed morphological changes. **(A)** Top view of the sloping seabed. **(B)** Side view of the sloping seabed, where dL is the distance between the rightmost end of the liquefaction interface and the outflow location of the WILSGF, and α1 and α2 are the slope angle of the step trailing edge and step leading edge, respectively. **(C)** Slope change at the step trailing edge (α1) and step leading edge (α2).

leading edge of the step decreased continuously in the liquefaction stage. However, after the liquefaction interface had reached its deepest position, the angle of the step leading edge was almost unchanged, forming a gentle slope of 6° (α_2).

DISCUSSION

This study found that the velocity of the WILSGF was highest in the first 7 s after its formation, reaching 2.39 cm/s, which is

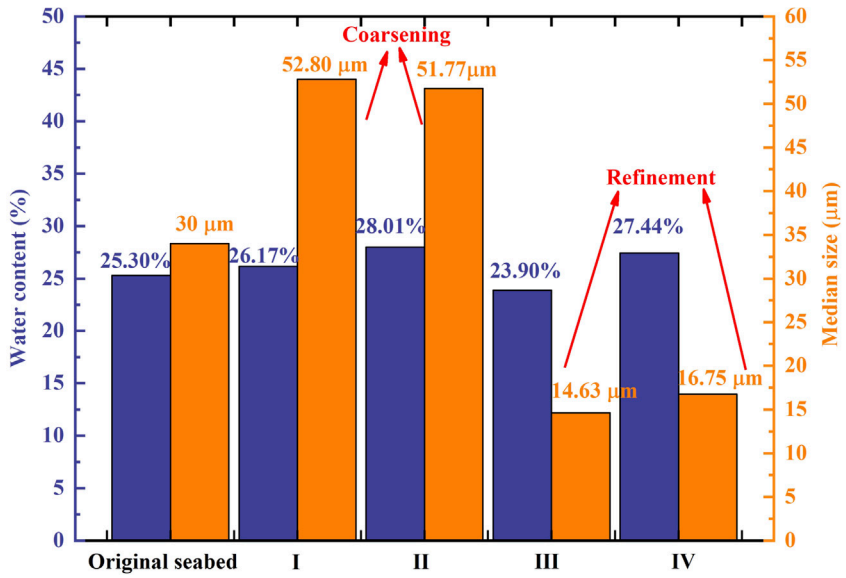

FIGURE 8 | Water content (bluish violet) and median particle size (orange) of sediments in the four areas as compared to their original values. Zone I and II present the particle coarsening, and zone III and IV present the particle refinement.

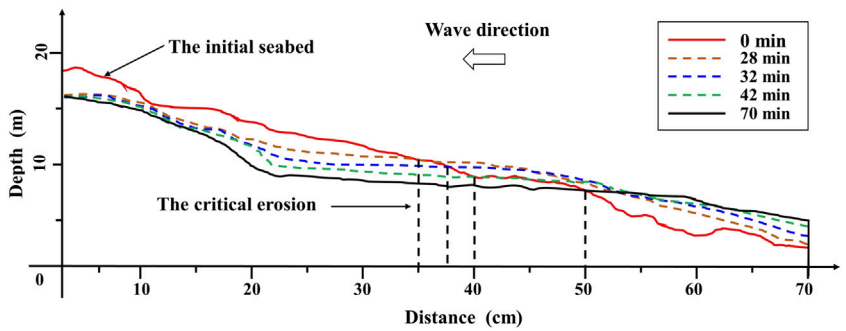

FIGURE 9 | Evolution of the surface morphology of the sediment seabed with time.

similar to the findings of Kessel and Kranenburg (1998). However, the velocity of the WILSGF decreased rapidly with the downward evolution of the liquefaction interface. This rapid decrease can be attributed to the expansion rate of the liquefaction layer being less than the evolution speed of the outflow position along the slope.

Figure 10 shows the variation of the distance (d_L, as shown in **Figure 7B**) between the rightmost end of the liquefaction layer and the outflow position of the WILSGF with time. It can be seen that d_L increased continuously with the downward evolution of the liquefaction interface, and the liquefaction layer area moved farther from the sediment outflow position of the WILSGF. The increase of d_L led to the liquefied sediment particles not being able to move directly along the slope to form a WILSGF. During wave entrainment, these sediment particles could be transported to the outflow position of the WILSGF, and they could then form a WILSGF under the

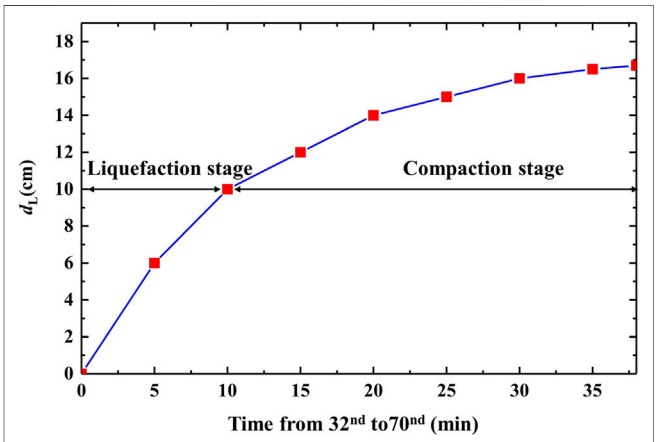

FIGURE 10 | Distance between the rightmost end of the liquefaction interface and the outflow location of the WILSGF.

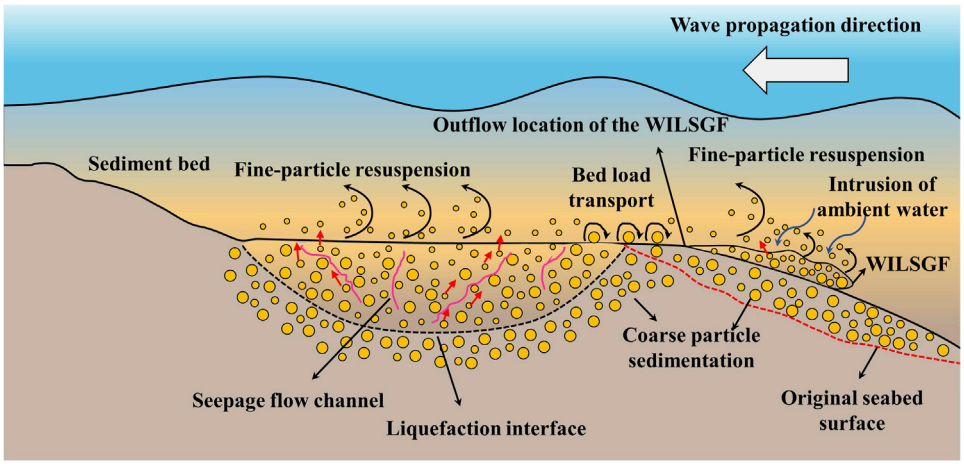

FIGURE 11 | Mechanism of WILSGF forming coarse-grained depositional characteristics.

action of gravity. However, during the movement of these sediment particles to the outflow position, the fine particles were resuspended under the action of waves; only a few particles could reach the outflow position of the WILSGF, resulting in the decrease of the mass source of the WILSGF and the decrease of its WILSGF velocity.

The rapid decrease of the WILSGF velocity was also due to the decrease of the step leading edge slope (α_2) and the consequent decrease of the gravity component of the WILSGF. When the liquefaction reached its maximum depth, the WILSGF could no longer form. Evidently, this is related to the area in which the liquefaction layer expanded. Xu et al. (2016) suggested that the sediments on the slope will be eroded by the expansion of the liquefaction layer area and evolve downward along the slope direction to form a WILSGF. Subsequently, due to the change of physical properties of the sediments, the liquefaction interface evolved upward, and the liquefied sediments no longer formed a WILSGF.

The cyclic oscillatory currents generated by the wave had a significant impact on the movement of the WILSGF that was initially formed (**Figures 5C,D**). The velocity of a WILSGF is related to the direction of the wave orbital velocity. In a wave period, when the direction of the wave orbital velocity is the same as that of the WILSGF, the waves will promote the movement of the WILSGF. When the direction of the wave orbital velocity is opposite to that of the WILSGF, the waves will hinder the movement of the WILSGF. Musumeci et al. (2017) and Smith et al. (2019) both found that cyclic oscillatory currents have a significant impact on the movement of an SGF. Similarly, Smith et al. (2019) also found that the transport and erosivity of an SGF were enhanced due to wave front oscillation. However, the WILSGF in this study was a type of high concentration sediment flow, which can reach hundreds of kg/m^3, similar to that in the research of Kessel and Kranenburg (1998). This type of extremely high concentration WILSGF moves downward at a low speed and in the form of a laminar flow on the sloping seabed surface. Unlike the high Reynolds number SGF studied by Smith et al. (2019), the WILSGF is not supported by turbulence and has a short moving distance. Observations on the prodelta have revealed that SGF of high -concentration mud suspensions could be supported by wave-induced turbulence during cross-shelf transport (Traykovski et al., 2007). This wave-supported gravity flow (WSGF) is also related to the liquefaction of sloping sediments (Jaramillo et al., 2009). Additional modeling work to examine the exchange of matter and energy between WILSGF and WSGF would be interesting to investigate the dynamics and kinematics of SGF under actual storm waves.

Wave action not only affects the movement behavior of a WILSGF but also changes the physical properties of WILSGF deposits. Among the four regions, it can be seen that the water content and median particle sizes of sediments in zones Ⅰ and Ⅱ are higher than those in zone Ⅲ and the initial sediments (**Figure 7**); the water content and median particle size of sediments in zone Ⅲ are also lower than those in the other three zones and the initial sediments. The decrease of the water content in the sediment liquefaction area and the refinement of sediment particles are due to compaction under liquefaction (Sumer et al., 2006) and particle classification (Liu et al., 2013).

There are two possible reasons for the coarsening of sediment particles in zone Ⅰ and Ⅱ (**Figure 11**). The first of these is coarsening of the mass source of the WILSGF. Liquefied sediment is the source of the WILSGF's mass. Under the action of a pressure gradient, some fine particles are carried out from the solid skeleton of the soil by seepage. These migrate upward along the seepage flow channel in the liquefied sediment and are resuspended by wave shear (Liu et al., 2013). With the loss of fine-grained sediments in the liquefied sediment layer, the sediments in the liquefaction layer are gradually coarsened (**Figure 11**), that is, the mass source of the WILSGF is coarsened. The second reason is that ambient water intrusion exists in the process of the movement of the WILSGF. In this

experiment, the velocity of the WILSGF was low. When a WILSGF moves downward along the slope, it will be strongly affected by wave shear. This shear action will carry the fine particles in the WILSGF into the ambient water (**Figure 11**), further amplifying the coarsening phenomenon of the WILSGF deposited particles.

CONCLUSION

In this study, we reproduced the formation, movement, and deposition of an SGF influenced by wave-induced liquefaction using flume experiments. In this paper, we examined and discussed the movement and deposition characteristics of the WILSGF. The conclusions can be summarized as follows.

1) At the initial stage of WILSGF formation in our experiments, the peak velocity of the WILSGF reached 2.39 cm/s. This velocity is affected by the slope angle of the step leading edge and the relative outflow position. With the downward evolution of the liquefaction interface, the slope angle of the step leading edge decreases and d_L increases, and the velocity of the WILSGF decreases rapidly. When the liquefaction depth reached its maximum value of 4.5 cm, the WILSGF did not continue.
2) In the incipient stage, 7 s after the formation of the WILSGF, the direction of the wave orbital velocity significantly affected the WILSGF velocity. The direction of the wave orbital velocity was the same as that of the WILSGF, and the waves promoted the movement of the WILSGF. The phase and amplitude fluctuations of the WILSGF were the same as those of the wave orbital velocity.
3) The particles of the WILSGF deposits were coarsened due to wave-induced seabed coarsening and the intrusion of ambient water. The median particle size of the WILSGF deposits was approximately 50% greater than that of the original seabed. The water content of WILSGF deposits was higher than that of the original seabed and liquefaction zone (Pyles et al., 2013; Clare et al., 2016; Gan et al., 2020).

DATA AVAILABILITY STATEMENT

The raw data supporting the conclusion of this article will be made available by the authors, without undue reservation.

AUTHOR CONTRIBUTIONS

HY: Methodology, Experiments, Writing- Original draft preparation. XaL: Supervision, Writing- Reviewing and Editing, Guidance. YL: Experiments, Visualization. WL: Experiments, Editing, Validation. HG: Experiments, Writing- Reviewing and Editing. RW: Experiments, Editing. XnL: Experiments, Writing- Reviewing.

FUNDING

This study was financially supported by funding from the National Natural Science Foundation of China (Grants 42022052 and 41877221), the Shandong Provincial Natural Science Foundation (ZR2020YQ29) and the Laboratory for Marine Geology, Qingdao National Laboratory for Marine Science and Technology (No. MGQNLM-TD201808).

ACKNOWLEDGMENTS

The authors would like to thank Shuyu Zhang, Junkai Sun, Xiaotian Xie,Yueying Wang, and Yujun Tian for their technical support during the experimental process. The authors are also grateful to Xingsen Guo for his review and help in the writing and presentation of the manuscript.

REFERENCES

Anfinson, O. A., Malusà, M. G., Ottria, G., Dafov, L. N., and Stockli, D. F. (2016). Tracking Coarse-Grained Gravity Flows by LASS-ICP-MS Depth-Profiling of Detrital Zircon (Aveto Formation, Adriatic Foredeep, Italy). *Mar. Petroleum Geol.* 77, 1163–1176. doi:10.1016/j.marpetgeo.2016.07.014

Atigh, E., and Byrne, P. M. (2004). Liquefaction Flow of Submarine Slopes under Partially Undrained Conditions: an Effective Stress Approach. *Can. Geotech. J.* 41, 154–165. doi:10.1139/t03-079

Bailey, L. P., Clare, M. A., Rosenberger, K. J., Cartigny, M. J. B., Talling, P. J., Paull, C. K., et al. (2021). Preconditioning by Sediment Accumulation Can Produce Powerful Turbidity Currents without Major External Triggers. *Earth Planet. Sci. Lett.* 562, 116845. doi:10.1016/j.epsl.2021.116845

Bian, C., Liu, X., Zhou, Z., Chen, Z., Wang, T., and Gu, Y. (2020). Calculation of Winds Induced Bottom Wave Orbital Velocity Using the Empirical Mode Decomposition Method. *J. Atmos. Ocean. Technol.* 37 (5), 889–900. doi:10.1175/JTECH-D-19-0185.1

Carter, L., Gavey, R., Talling, P., and Liu, J. (2014). Insights into Submarine Geohazards from Breaks in Subsea Telecommunication Cables. *oceanog* 27, 58–67. doi:10.5670/oceanog.2014.40

Clare, M. A., Hughes Clarke, J. E., Talling, P. J., Cartigny, M. J. B., and Pratomo, D. G. (2016). Preconditioning and Triggering of Offshore Slope Failures and Turbidity Currents Revealed by Most Detailed Monitoring yet at a Fjord-Head Delta. *Earth Planet. Sci. Lett.* 450, 208–220. doi:10.1016/j.epsl.2016.06.021

Foda, M. A., and Tzang, S.-Y. (1994). Resonant Fluidization of Silty Soil by Water Waves. *J. Geophys. Res.* 99 (C10), 20463–20475. doi:10.1029/94JC02040

Gan, Y., Steel, R. J., Olariu, C., and De Almeida, F. (2020). Facies and Architectural Variability of Sub-seismic Slope-channel Fills in Prograding Clinoforms, Mid-Jurassic Neuquén Basin, Argentina. *Basin Res.* 32, 348–362. doi:10.1111/bre.12409

Guo, X. S., Stoesser, T., Nian, T. K., Jia, Y. G., and Liu, X. L. (2022). Effect of Pipeline Surface Roughness on Peak Impact Forces Caused by Submarine Mudflow. *Ocean. Eng.* 243, 110184. doi:10.1016/j.oceaneng.2021.110184

Guy Plint, A. (2014). Mud Dispersal across a Cretaceous Prodelta: Storm-Generated, Wave-Enhanced Sediment Gravity Flows Inferred from Mudstone Microtexture and Microfacies. *Sedimentology* 61 (3), 609–647. doi:10.1111/sed.12068

Harazim, D., and Mcilroy, D. (2015). Mud-Rich Density-Driven Flows along an Early Ordovician Storm-Dominated Shoreline: Implications for Shallow-Marine Facies Models. *J. Sediment. Res.* 85 (5), 509–528. doi:10.2110/jsr.2015.38

Heezen, B. C., and Ewing, W. M. (1952). Turbidity Currents and Submarine Slumps, and the 1929 Grand Banks [Newfoundland] Earthquake. *Am. J. Sci.* 250 (12), 849–873. doi:10.2475/ajs.250.12.849

Huang, N. E., Shen, Z., Long, S. R., Wu, M. C., Shih, H. H., Zheng, Q., et al. (1998). The Empirical Mode Decomposition and the Hilbert Spectrum for Nonlinear and Non-stationary Time Series Analysis. *Proc. R. Soc. Lond. A* 454, 903–995. doi:10.1098/rspa.1998.0193

Ilstad, T., Elverhøi, A., Issler, D., and Marr, J. G. (2004). Subaqueous Debris Flow Behaviour and its Dependence on the Sand/clay Ratio: a Laboratory Study Using Particle Tracking. *Mar. Geol.* 213, 415–438. doi:10.1016/j.margeo.2004.10.017

Jaramillo, S., Sheremet, A., Allison, M. A., Reed, A. H., and Holland, K. T. (2009). Wave-mud Interactions over the Muddy Atchafalaya Subaqueous Clinoform, Louisiana, United States: Wave-supported Sediment Transport. *J. Geophys. Res.* 114, C04002. doi:10.1029/2008JC004821

Jia, Y., Zhang, L., Zheng, J., Liu, X., Jeng, D.-S., and Shan, H. (2014). Effects of Wave-Induced Seabed Liquefaction on Sediment Re-suspension in the Yellow River Delta. *Ocean. Eng.* 89, 146–156. doi:10.1016/j.oceaneng.2014.08.004

Kessel, T., and Kranenburg, C. (1998). Wave-induced Liquefaction and Flow of Subaqueous Mud Layers. *Coast. Eng.* 34, 109–127. doi:10.1016/S0378-3839(98)00016-7

Kessel, T. V., Kranenburg, C., and Battjes, J. A. (1997). "Transport of Fluid Mud Generated by Waves on Inclined Beds," in Proceeding of the 25th International Conference on Coastal Engineering, Orlando, September 1997, 3337–3348. doi:10.1061/9780784402429.258

Kirca, V. S. O., Sumer, B. M., and Fredsøe, J. (2014). Influence of Clay Content on Wave-Induced Liquefaction. *J. Waterw. Port. Coast. Ocean. Eng.* 140 (6), 04014024. doi:10.1061/(asce)ww.1943-5460.0000249

Liu, X.-L., Jia, Y.-G., Zheng, J.-W., Hou, W., Zhang, L., Zhang, L.-P., et al. (2013). Experimental Evidence of Wave-Induced Inhomogeneity in the Strength of Silty Seabed Sediments: Yellow River Delta, China. *Ocean. Eng.* 59, 120–128. doi:10.1016/j.oceaneng.2012.12.003

Liu, X., Jia, Y., Zheng, J., Wen, M., and Shan, H. (2017). An Experimental Investigation of Wave-Induced Sediment Responses in a Natural Silty Seabed: New Insights into Seabed Stratification. *Sedimentology* 64, 508–529. doi:10.1111/sed.12312

Liu, X., Zhang, H., Zheng, J., Guo, L., Jia, Y., Bian, C., et al. (2020). Critical Role of Wave-Seabed Interactions in the Extensive Erosion of Yellow River Estuarine Sediments. *Mar. Geol.* 426, 106208. doi:10.1016/j.margeo.2020.106208

Ma, Y., Friedrichs, C. T., Harris, C. K., and Wright, L. D. (2010). Deposition by Seasonal Wave- and Current-Supported Sediment Gravity Flows Interacting with Spatially Varying Bathymetry: Waiapu Shelf, New Zealand. *Mar. Geol.* 275, 199–211. doi:10.1016/j.margeo.2010.06.001

Maa, P.-Y., and Mehta, A. J. (1987). Mud Erosion by Waves: a Laboratory Study. *Cont. Shelf Res.* 7, 1269–1284. doi:10.1016/0278-4343(87)90030-6

Macquaker, J. H. S., Bentley, S. J., and Bohacs, K. M. (2010). Wave-enhanced Sediment-Gravity Flows and Mud Dispersal across Continental Shelves: Reappraising Sediment Transport Processes Operating in Ancient Mudstone Successions. *Geology* 38 (10), 947–950. doi:10.1130/G31093.1

Middleton, G. V., and Hampton, M. A. (1973). "Sediment Gravity Flows: Mechanics of Flow and Deposition," in *Turbidites and Deep-Water Sedimentation. Soc. Econ. Paleont. Miner. (Pacific Sect.) Short Course Lect. Notes*, 1–38.

Musumeci, R. E., Viviano, A., and Foti, E. (2017). Influence of Regular Surface Waves on the Propagation of Gravity Currents: Experimental and Numerical Modeling. *J. Hydraul. Eng.* 143 (8), 04017022. doi:10.1061/(asce)HY.1943-7900.0001308

Mutlu Sumer, B., Hatipoglu, F., Fredsøe, J., and Kaan Sumer, S. (2006). The Sequence of Sediment Behaviour during Wave-Induced Liquefaction. *Sedimentology* 53 (3), 611–629. doi:10.1111/j.1365-3091.2006.00763.x

Ng, C.-O., and Fu, S.-C. (2002). On the Propagation of a Two-Dimensional Viscous Density Current under Surface Waves. *Phys. Fluids* 14 (3), 970–984. doi:10.1063/1.1448348

Nikora, V. I., and Goring, D. G. (1998). ADV Measurements of Turbulence: Can We Improve Their Interpretation? *J. Hydraulic Eng.* 124 (6), 630–634. doi:10.1061/(asce)0733-9429(1998)124:6(630)

Parsheh, M., Sotiropoulos, F., and Porté-Agel, F. (2010). Estimation of Power Spectra of Acoustic-Doppler Velocimetry Data Contaminated with Intermittent Spikes. *J. Hydraul. Eng.* 136 (6), 368–378. doi:10.1061/(ASCE)HY.1943-7900.0000202

Piper, D. J. W., and Normark, W. R. (2009). Processes that Initiate Turbidity Currents and Their Influence on Turbidites: a Marine Geology Perspective. *J. Sediment. Res.* 79 (6), 347–362. doi:10.2110/jsr.2009.046

Prior, D. B., Suhayda, J. N., Lu, N.-Z., Bornhold, B. D., Keller, G. H., Wiseman, W. J., et al. (1989). Storm Wave Reactivation of a Submarine Landslide. *Nature* 341 (6237), 47–50. doi:10.1038/341047a0

Puig, P., Ogston, A. S., Mullenbach, B. L., Nittrouer, C. A., Parsons, J. D., and Sternberg, R. W. (2004). Storm-induced Sediment Gravity Flows at the Head of the Eel Submarine Canyon, Northern California Margin. *J. Geophys. Res.* 109, C03019. doi:10.1029/2003JC001918

Pyles, D. R., Straub, K. M., and Stammer, J. G. (2013). Spatial Variations in the Composition of Turbidites Due to Hydrodynamic Fractionation. *Geophys. Res. Lett.* 40, 3919–3923. doi:10.1002/grl.50767

Robinson, T. O., Eames, I., and Simons, R. (2013). Dense Gravity Currents Moving beneath Progressive Free-Surface Water Waves. *J. Fluid Mech.* 725, 588–610. doi:10.1017/jfm.2013.112

Smith, E., Daniller-Varghese, M. S., Myrow, P. M., and Mohrig, D. (2019). Experimental Investigations of Combined Flow Sediment Transport. *J. Sediment. Res.* 89 (8), 808–814. doi:10.2110/jsr.2019.43

Traykovski, P., Geyer, W. R., Irish, J. D., and Lynch, J. F. (2000). The Role of Wave-Induced Density-Driven Fluid Mud Flows for Cross-Shelf Transport on the Eel River Continental Shelf. *Cont. Shelf Res.* 20, 2113–2140. doi:10.1016/S0278-4343(00)00071-6

Traykovski, P., Wiberg, P. L., and Geyer, W. R. (2007). Observations and Modeling of Wave-Supported Sediment Gravity Flows on the Po Prodelta and Comparison to Prior Observations from the Eel Shelf. *Cont. Shelf Res.* 27 (3), 375–399. doi:10.1016/j.csr.2005.07.008

Voulgaris, G., and Trowbridge, J. H. (1998). Evaluation of the Acoustic Doppler Velocimeter (ADV) for Turbulence Measurements*. *J. Atmos. Ocean. Technol.* 15 (1), 272–289. doi:10.1175/1520-0426(1998)015<0272:eotadv>2.0.co;2

Wang, L. M., Ye, J. H., and Zhu, C. Q. (2015). Investigation on the Wave-Induced Progressive Liquefaction of Offshore Loosely Deposited Sandy Seabed. *Rock Soil Mech.* 36 (12), 3583–3588. doi:10.16285/j.rsm.2015.12.031

Wang, Z., Sun, Y., Jia, Y., Shan, Z., Shan, H., Zhang, S., et al. (2020). Wave-induced Seafloor Instabilities in the Subaqueous Yellow River Delta-initiation and Process of Sediment Failure. *Landslides* 17, 1849–1862. doi:10.1007/s10346-020-01399-2

Wright, L. D., Friedrichs, C. T., Kim, S. C., and Scully, M. E. (2001). Effects of Ambient Currents and Waves on Gravity-Driven Sediment Transport on Continental Shelves. *Mar. Geol.* 175, 25–45. doi:10.1016/S0025-3227(01)00140-2

Xu, G. H., Wang, G., Lv, C. X., and Sun, Z. H. (2016). Experimental Study on the Motion Froms of Outflowed Sediments from Wave-Induced Liquefied Seabed. *Periodical Ocean Univ. China* 46 (10), 98–105.

Yue, L., Cheng, Z., and Hsu, T. J. (2020). A Turbulence-Resolving Numerical Investigation of Wave-Supported Gravity Flows. *J. Geophys. Res. Oceans* 125 (2), e2019JC015220. doi:10.1029/2019jc015220

Conflict of Interest: The authors declare that the research was conducted in the absence of any commercial or financial relationships that could be construed as a potential conflict of interest.

Publisher's Note: All claims expressed in this article are solely those of the authors and do not necessarily represent those of their affiliated organizations, or those of the publisher, the editors and the reviewers. Any product that may be evaluated in this article, or claim that may be made by its manufacturer, is not guaranteed or endorsed by the publisher.

frontiers | Frontiers in Earth Science

REVIEW
published: 13 June 2022
doi: 10.3389/feart.2022.915735

A Review of Gassy Sediments: Mechanical Property, Disaster Simulation and *In-Situ* Test

Tao Liu[1,2,3], *Xiaotong Yang*[1] *and Yan Zhang*[1]*

[1]College of Environmental Science and Engineering, Ocean University of China, Qingdao, China, [2]Shandong Provincial Key Laboratory of Marine Environment and Geological Engineering, Ocean University of China, Qingdao, China, [3]Laboratory for Marine Geology, Pilot National Laboratory for Marine Science and Technology, Qingdao, China

Gassy sediments are an important cause of engineering disasters such as large-area coastal submarine landslides, excessive tilting of marine foundations, and excessive deformation of tunnels. Under different stress paths, the gassy soil exhibits different microstructure changes and mechanical responses. This paper introduces the current research status regarding the mechanical responses, numerical simulation and the *in-situ* test methods of gassy sediment. In terms of mechanical responses, it summarized the strength and deformation characteristics of gassy soil under different stress paths, tracking the study on constitutive model. The disaster simulation work using constitutive model of gassy sediment is introduced. It also analyzes the advantages and limitations of various methods in the *in-situ* test. It can provide theoretical support for further study on disaster prevention and geological risk assessment of gassy sediments.

Keywords: gassy sediments, mechanical responses, constitutive model, *in-situ* methods, disaster simulation

OPEN ACCESS

Edited by:
Ya Ping Wang,
East China Normal University, China

Reviewed by:
Lizhong Wang,
Zhejiang University, China
Zhongnian Yang,
Qingdao University of Technology, China

***Correspondence:**
Yan Zhang
zhangyan4850@ouc.edu.cn

Specialty section:
This article was submitted to Geohazards and Georisks, a section of the journal Frontiers in Earth Science

Received: *08 April 2022*
Accepted: *23 May 2022*
Published: *13 June 2022*

Citation:
Liu T, Yang X and Zhang Y (2022) A Review of Gassy Sediments: Mechanical Property, Disaster Simulation and In-Situ Test. Front. Earth Sci. 10:915735. doi: 10.3389/feart.2022.915735

INTRODUCTION

Gassy sediments are widely distributed in the coastal areas of all the world's continents (**Figure 1**) (P et al., 2001). The gases are usually formed by microbial degradation of organic matter under anaerobic conditions, thermogenic methanogenesis, or volcanic eruptions. Their main components include methane, carbon dioxide, and nitrogen (**Figure 2**). The gases mostly exist in the pores as dissolved or discrete bubbles (Wheeler, 1986; Grozic et al., 2000; Sánchez et al., 2017).

Unlike unsaturated soil, the saturation of gassy soil is usually in the range of 85–90%, and the gas phase usually exists in the form of discrete bubbles while the water phase is in a connected state. The size of the soil particles determines the microstructure of gassy soils, and gassy soils are mainly divided into two categories according to the size of the air bubbles (Wheeler, 1988b; Sills and Wheeler, 1992). In one category, the air bubbles are smaller than the soil particles and pore size. The air bubbles are discrete in the soil pores, which only changes the compressibility of the pore fluid and does not affect the soil structure (Wang et al., 2018; Hong et al., 2021b; Xu et al., 2022). In the other category, the air bubbles are much larger than the soil particles and pore size. The bubbles rearrange the soil particles and thus affect the soil structure (Hong et al., 2020a; Gao et al., 2020). This microstructure often exists in fine-grained air-bearing soils, as shown in **Figure 3**. Hong et al. (2017) and Guo et al. (2021) observed the microstructure of typical fine-grained gassy soil by scanning electron microscopy and computed tomography. The results are shown in **Figure 4**. The undissolved gas exists as large discrete bubbles in the saturated matrix, and the bubbles are much larger than the soil particles and pores.

Due to the structural characteristics of gassy soil, the mechanical properties are considerably different from those of saturated soils and unsaturated soils. Kaminski et al. (2020) summarized the

FIGURE 1 | Distribution of marine gassy sediments in the five continents (Fleischer et al., 2001).

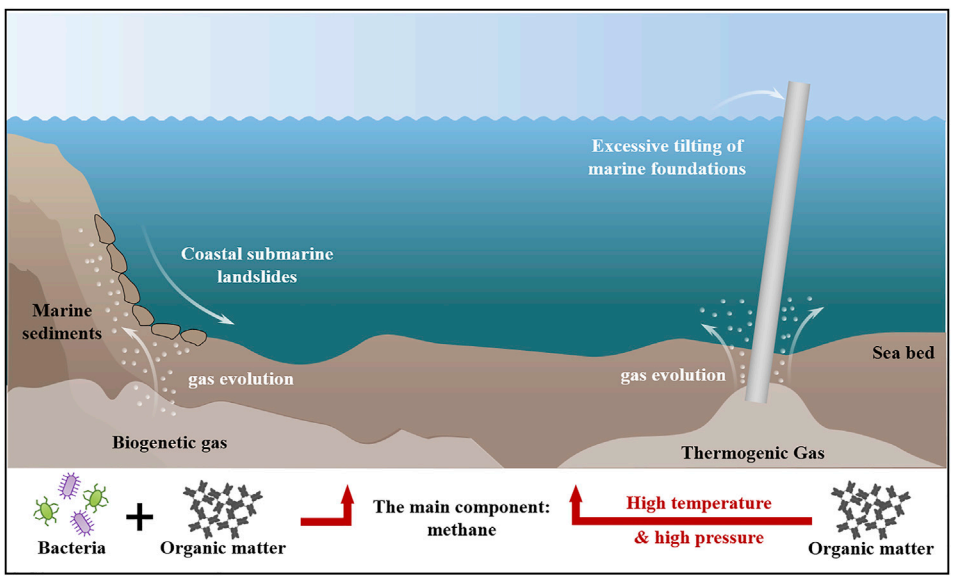

FIGURE 2 | Gassy source and geological disasters.

undrained shear strength of gassy soils under different conditions. The mechanical properties of gassy soils under different conditions change the engineering characteristics of the corresponding soil layers. During construction engineering, geological disasters have often been induced by the presence of shallow gas, and some major engineering accidents have occurred, causing serious economic losses (Sobkowicz and Morgenstern, 1984; Rad et al., 1994; Rowe et al., 2002; Kortekaas and Peuchen, 2008; Sultan et al., 2012; Xu et al., 2017; Rowe and Mabrouk, 2018; Jommi et al., 2019).

EXPERIMENTAL TESTING

In the gas-bearing soil test, due to the release of pressure caused by deep-water sampling, the gas in the soil is dissolved and

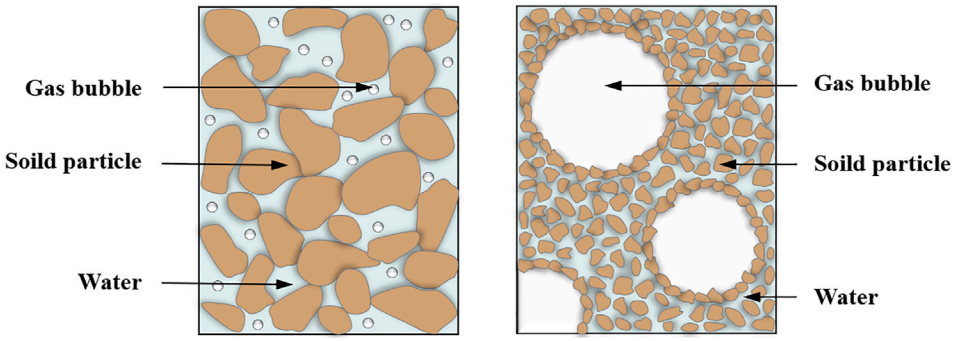

FIGURE 3 | Types of soil containing air bubbles (Wheeler, 1988b).

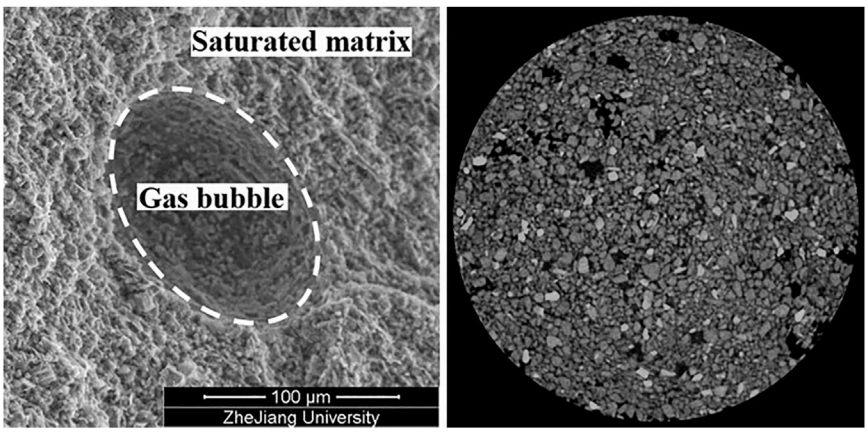

FIGURE 4 | Microscopic scan of a typical gassy soil (Hong et al., 2017; Guo et al., 2021).

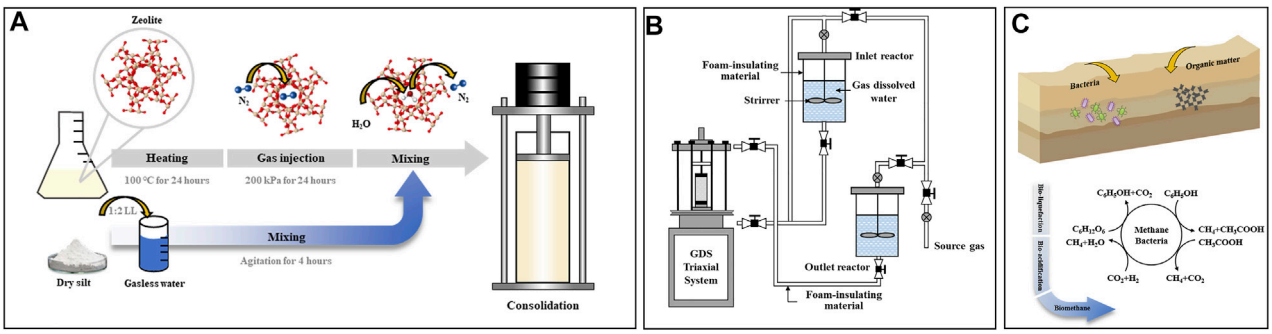

FIGURE 5 | Gassy specimen preparation methods: **(A)** the zeolite molecular sieve technique; **(B)** the axis-translation technique; **(C)** the biological anaerobic fermentation method.

expanded, which causes changes in the soil structure and even cracks (Zhang and Lunne, 2003; Sultan et al., 2012). It is therefore difficult to obtain undisturbed gassy soil samples under *in-situ* conditions. Previous experiments have mainly used remolded gassy soil samples. There are three main preparation methods: the zeolite molecular sieve technique (Sills et al., 1991; Hong et al., 2017; Hong et al., 2020b) the axis-translation technique (Sultan et al., 2012; Wang et al., 2018; Blouin et al., 2019), and the biological anaerobic fermentation technique (Sills and Gonzalez, 2001; Hu, 2010).

The zeolite molecular sieve technique replaces the adsorbed gas by adding the zeolite-absorbing gas into the slurry. This

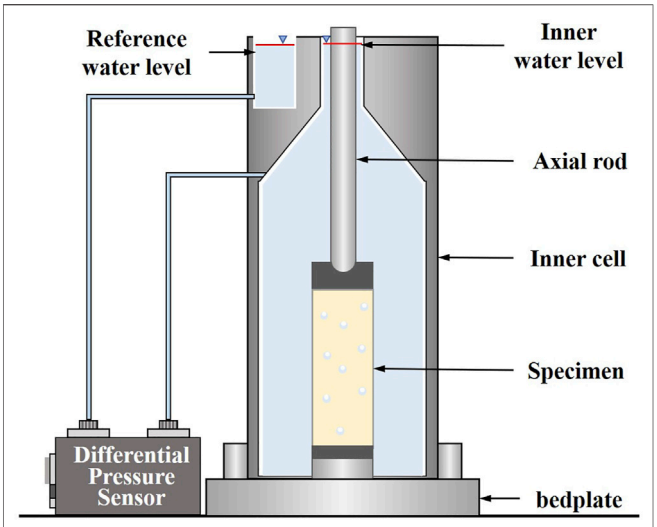

FIGURE 6 | Double-cell system.

method is simple and effective while the stress history is known. In this method, the samples can be prepared in batches with similar physical properties under *in-situ* conditions. The main principle is shown in **Figure 5A**. The gas content of the prepared samples cannot be accurately controlled, but the bubble distribution is relatively uniform.

The axis-translation technique involves replacing the internal pore water by circulating the dissolved gas water through the saturated sample and releasing the gas by unloading to form the gassy soil sample. The test system is shown in **Figure 5B**. This method is mainly applicable to coarse-grained soil, and the gas-charging effect of fine-grained soil is poor.

The principle of the biological anaerobic fermentation technique is that organic matter is decomposed by anaerobic bacteria to release methane and carbon dioxide, as shown in **Figure 5C**. Its mechanism is closest to the formation process of bubbles in the marine environment. The preparation process, however, requires certain values for temperature, pH, redox potential, and other parameters. Only by satisfying these biological requirements will the fermentation cycle be short and the gas production suitable.

Both zeolite molecular sieve technique and axis-translation technique can prepare uniform samples for triaxial test. zeolite molecular sieve technique is used for fine-grained gassy soil, which can mimic the natural formation process of free bubbles in soil. Axis-translation technique is used to prepare coarse-grained gassy soil, which can mimic the process of gas exsolution due to stress release. Although the bubble formation process of the biological anaerobic fermentation technique is the closest in the marine environment, its sample preparation method is complex and immature, so it cannot be used for triaxial test to determine the mechanical properties. It can be used for model box test, and it needs further research. The zeolite molecular sieve technique and axis-translation technique can produce specimens containing a uniform distribution of gas bubbles, but the gas saturation of gassy soil cannot be measured specifically. Therefore, the double-cell system can be installed in triaxial apparatus to measure the change of gas saturation. The accuracy of the volumetric system can reach 31.4 mm^3 (equivalent to 0.04% volumetric strain of the soil sample with a diameter of 38 mm and a height of 76 mm) (Ng et al., 2002). **Figure 6** shows the structural diagram.

MECHANICAL BEHAVIOR OF GASSY SOIL

On the basis of the soil microstructure, many researchers have analyzed the mechanical properties and discussed the relationship between those properties and the microscopic mechanism (Nageswaran, 1983; Thomas, 1987; Wheeler, 1988a; Gardner and Goringe, 1988; Sills et al., 1991; Sham, 1992; Hong et al., 2017; Bai, 2018). The bubble-water-soil skeleton microstructure interaction in fine-grained gassy soil includes two mechanisms: bubble flooding and gas intrusion into the saturated matrix (Wheeler, 1988b). The existence of bubbles make the effective stress and void ratio in the saturated matrix unevenly distributed (Sham, 1992). The bubble-water-soil skeleton interaction is affected by the initial pore water pressure (Hong et al., 2017). When the initial pore water pressure is low, the bubbles in the soil are large and the radius of the meniscus at the water–gas interface is large, which means that the water inflow value of the bubble cavity is relatively small. During the undrained shear process, with the increase of the pore water pressure, bubble flooding may occur (the water in the saturated matrix enters the bubble cavity, and partial drainage occurs), resulting in a reduction of the excess pore pressure and an increase in strength, as shown in **Figure 7A**. When the initial pore water pressure is high, the gas pressure in the soil is also relatively high, which produces micro-cracks in the surrounding saturated matrix. In the process of undrained shear, the micro-cracks may collapse, resulting in reduced strength and increased excess pore pressure, as shown in **Figure 7B**.

Bubbles in gassy soil change the compression characteristics of the pore fluid and the structure of the soil, which affects the mechanical properties, such as compression, and the static and dynamic characteristics. A large number of compression, monotonic, and cyclic shear tests of gassy fine-grained soil and gassy sand have been carried out, and the key influencing factors of the modulus, monotonic, and cyclic shear strength of gassy soil have been determined. The results show a clear influence of air content on the elastic shear modulus and shear strength of gassy soil (Duffy et al., 1994; Pietruszczak and Pande, 1996; Mathiroban, 2004; Vega-Posada et al., 2014; Hong et al., 2017). The drainage shear test of sand shows strain hardening, and the strain law of undrained shear is related to the initial state of gassy sand (Amaratunga and Grozic, 2009; Vega-Posada et al., 2014). Under dynamic load, the cyclic stress of gassy sand is linearly related to liquefied vibration times and the increase of the gas content delays the liquefaction of gassy sand (Guan, 2017). The greater the gas content, the slower the pore pressure dissipation and the smaller the amplitude of excess pore water pressure (Han, 2020). The change in the cyclic stiffness of gassy fine-grained soil is related to the initial pore

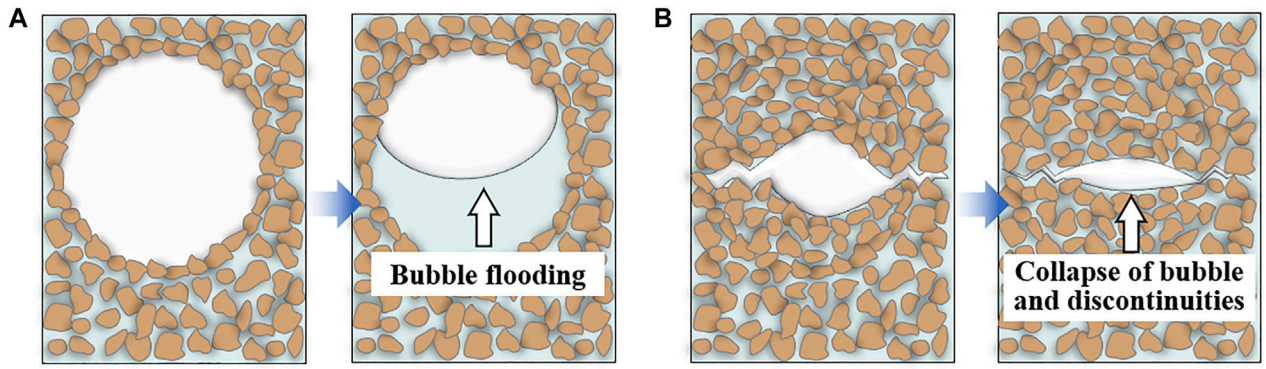

FIGURE 7 | Schematic diagrams showing fine-grained gassy soil under different back pressures (Hong et al., 2017): **(A)** Relatively low initial back pressure; **(B)** Relatively high initial back pressure.

pressure. The high pressure enhances show the stiffness enhancement and the low pressure weakens the stiffness (Hong et al., 2021a). Research into various stress-path problems in actual projects has shown that the deformation of the soil can be reduced by gradual deflation (Wang, 2009). The change direction of the confining pressure is closely related to the stress–strain characteristics of the sample. The increase of the confining pressure induces strain hardening of the sample, and the decrease induces strain softening (Zhong, 2007). The gas evolution and bubble expansion caused by pressure unloading enhances the compressibility of gassy soil, reduces the pre-consolidation pressure and the undrained shear strength. The structural change caused by gas evolution influences the effective stress path (Sultan et al., 2012). The rapid accumulation of gas leads to a rapid increase of the pore water pressure and a reduction of the effective stress of the soil, triggering the liquefaction of gassy soil (Liu, 2018; Kong et al., 2019). The change of temperature and pressure of gassy soil also affects the compressibility and permeability. After the dissipation of excess pore pressure, the consolidation time is prolonged, resulting in long-term settlement and showing a complex consolidation creep process. The lower the saturation is, the more obvious the phenomenon is (Wang, 2021; Zhu et al., 2021).

Researchers have proposed mechanical models for engineering calculations. The fine-grained gassy soil mechanical model is an improvement on the Cambridge model, while the coarse-grained gassy soil mechanical model is used to construct the mechanical analysis model by describing the compressibility of the "bubble-water" mixture. Wheeler and Gardner (1989) regarded soil containing large bubbles as a composite material containing spherical filler. They derived the calculation formulas of the shear modulus and bulk modulus of soil containing large bubbles under drainage and undrained conditions. Grozic J. L. H. et al. (2005) quantitatively simulated the enhancement effect of bubbles on the undrained shear strength of fine-grained gassy soil, but their model cannot describe the strength attenuation caused by bubbles. Hong et al. (2021b) proposed a critical-state model that takes into account both hardening and softening by defining the ratio of the deviatoric stress increment to the plastic shear strain increment. Pietruszczak and Pande (1996) introduced "gas–water interfacial tension" into the pore pressure expression and established the rotational hardening model of gassy sand. The change of pressure in gassy sand causes gas dissolution, and so Grozic J. L. et al. (2005) considered the compressibility and solubility of gas at the same time using Henry's law and Boyle's law. By introducing a volume dissolution coefficient h, they deduced the expression of pore pressure:

$$\triangle \bar{u}_g = \left\{ \frac{\triangle n}{[(1 - S_0)n_o + hS_0n_0 - \triangle n]} \right\} \triangle \bar{u}_{g0} \tag{1}$$

This model can accurately predict the strain softening but not the strain hardening.

Gao et al. (2020) established a critical-state model that takes into account the influence of the initial pore water pressure and initial air content on the yield and dilatancy characteristics of gassy soil. However, it is unable to predict the undrained unloading response. Sultan et al. (2012) explored the influence of gas evolution on soil in undrained unloading stress paths through triaxial tests. They also introduced the gas-phase damage parameter d (related to gas content) and proposed the following relationship between gassing volume and soil pre-consolidation pressure:

$$\frac{p'_c}{p'_0} = \exp(-\delta d) \tag{2}$$

Smith et al. (2022) proposed a model that takes into account the bubble damage effect. The anisotropic yield surface function is defined as

$$q = \frac{2}{3}p'\frac{q_0}{p'_0} \pm \sqrt{M^2\left(p'p'_0 - p'^2 + \frac{1}{9}\frac{p'}{p'_c}q_0^2\right)} \tag{3}$$

Using the non-associated flow rule, this model can simulate the strength reduction of gassy soil caused by gas evolution.

TABLE 1 | Stress–dilatancy relations assumed in the existing models for fine-grained gassy soil.

References	Dilatancy
Pietruszczak and Pande (1996)	$D = \frac{d\varepsilon_v^p}{d\varepsilon_q^p} = M\ln(\frac{p'}{p'_c}) + M$
Grozic et al. (2005b)	$D = \frac{d\varepsilon_v^p}{d\varepsilon_q^p} = \frac{M^2-\eta^2}{2\eta}$
Sultan et al. (2012)	$D = \frac{d\varepsilon_v^p}{d\varepsilon_q^p} = \mu(M-\eta)(\frac{\alpha M}{\eta}+1)$
Hong et al. (2019)	$D = \frac{d\varepsilon_v^p}{d\varepsilon_q^p} = [1+\xi\frac{u_{w0}-u_{w0\_ref}}{p'_0}\exp(-\frac{\chi}{\psi_0})]\ \frac{M^2-\eta^2}{2\eta}$

Note: $d\varepsilon_v^p$ denotes increments of plastic volumetric strain; $d\varepsilon_q^p$ denotes increments of plastic deviatoric strain; M denotes the stress ratio at the critical state; η denotes the stress ratio (i.e., $\eta = q/p$); and ξ and χ are two material constants.

At present, however, the mechanical models of gassy soil mainly focus on the description of static loading characteristics; the gas-phase damage under static unloading conditions has only been partially considered.

The theory of granular solid hydrodynamics are combined with the temperature motion equation of soil particles (Yang and Bai, 2020):

$$d_t\left(T_{gg}\right) = c_2c_5\frac{d_te_{ij}d_te_{ij}}{\rho^S} + c_3c_5\frac{d_t\varepsilon_v d_t\varepsilon_v}{\rho^S} + c_4\frac{\Gamma d_tT}{\rho^S} - c_5\frac{T_{gg}}{\rho^S} \tag{4}$$

Yang and Bai (2020) established a thermodynamic model describing the mechanical properties and temperature effect of fine-grained soil containing gas. The results show that the increase of temperature under drainage conditions increases the compression coefficient and the thermal shrinkage coefficient, and the pore water pressure under undrained conditions also increases. The influence of temperature on the undrained shear characteristics depends on the initial conditions.

Vanoudheusden et al. (2003) established a numerical model to describe the mechanical properties of unsaturated expansive soil based on the elastic-plastic model. Under undrained conditions, its characteristics are controlled by the drainage curve of gassy soil (the relationship between saturation and capillary pressure) and the solubility of the gas.

Dilatancy is an important property of the mechanical responses of gassy soil. For coarse-grained gassy soil, bubbles only change the compressibility of the pore fluid, and so the effective stress principle is still applicable to this type of soil (Pietruszczak and Pande, 1996; Grozic J. L. et al., 2005). The study of dilatancy function, plastic modulus, and related material parameters of saturated sand is still relevant for gassy sand (Yin and Chang, 2013; Xiao et al., 2015; Kong et al., 2016; Xiao et al., 2019).

However, there are few studies on the dilatancy of fine-grained gassy soil. The dilatancy function used in the existing constitutive model of gassy soil is mostly the same as that of saturated soil (Pietruszczak and Pande, 1996) and they cannot consider the potential effect of gas bubbles on dilatancy. While the dilatancy function proposed by Hong et al. (2019) introduces the initial pore water pressure and gas volume fraction on the basis of Grozic J. L. et al. (2005). To characterize the influence of gas content on the dilatancy, the relevant material parameters need to be calibrated. The Stress–dilatancy relations assumed in the existing models for fine-grained gassy soil is shown in **Table 1**.

NUMERICAL SIMULATION

The existence of gas in the soil layer affects the mechanical properties of the stratum. Thus, in the design of offshore foundations, offshore drilling, and slope stability analysis, a constitutive model that can uniformly describe the response of the gassy soil under different conditions is needed. Current research on fine-grained gassy soil mainly focuses on the unit response in the triaxial test. Few studies have been conducted on practical engineering issues and the constitutive model needs further development (Grozic J. L. H. et al., 2005; Sultan et al., 2012; Hong et al., 2017; Sánchez et al., 2017; Goao and Hong, 2019; Hong et al., 2019; Hong et al., 2020a; Gao et al., 2020). The constitutive model of coarse-grained soil is relatively mature, but the analysis is mostly base on liquefaction and landslide (Grozic, 2003; Atigh and Byrne, 2004; Mabrouk and Rowe, 2011; Hong and Xu, 2020; Thomas, 2021a; Hong et al., 2021b; Thomas, 2021b).

Grozic (2003) introduced the concept of flow potential and proposed a method to evaluate the liquefaction potential of loose sand, which can judge the potential liquefaction area according to the flow potential. The zone of potential liquefaction is shown in **Figure 8**.

Atigh and Byrne (2004) proposed a liquefied sand flow model to analyze the liquefaction-sliding flow of loose gassy sand caused by tidal changes. Dense sand slopes are more common in real environments, however. Hong et al. (2021b) established a model of coarse-grained gassy soil, quantified the influence of such soil under different initial conditions, and used the model to analyze the stability of submarine slopes under undrained conditions. For loose gassy sand, gas has an enhancing effect on the stability of submarine slopes; for dense gassy sand, it has a weakening effect, as shown in **Figure 9**.

Hong and Xu (2020) simulated the undrained shear of gassy sand using the discrete element method. They analyzed the influence of different gas solubilities, and this method can be used to effectively simulate the gas dissolution in the process of undrained unloading (**Figure 10**).

For fine-grained gassy soil, Thomas (2021a, 2021b) proposed the governing equation of porous elastic gas-bearing soil based on the modified Biot theory to simulate the changes of stress, displacement, and pore water pressure of a gassy seabed with buried pipelines under wave pressure loading. In the buried pipelines, the stress and pore pressure are concentrated, which may lead to local liquefaction.

IN-SITU INVESTIGATION

In-situ sampling of gassy sediments inevitably causes disturbances. Although temperature-preserving and pressure-

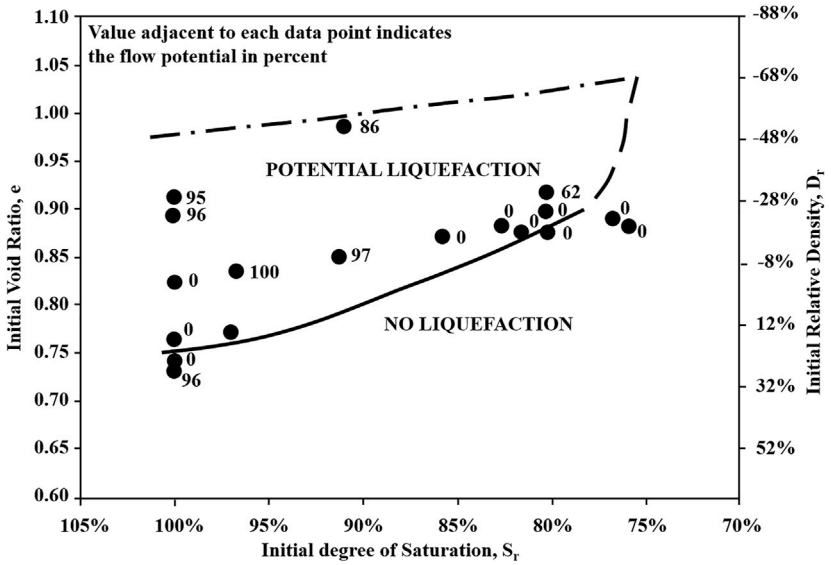

FIGURE 8 | The zone of potential liquefaction (Grozic, 2003).

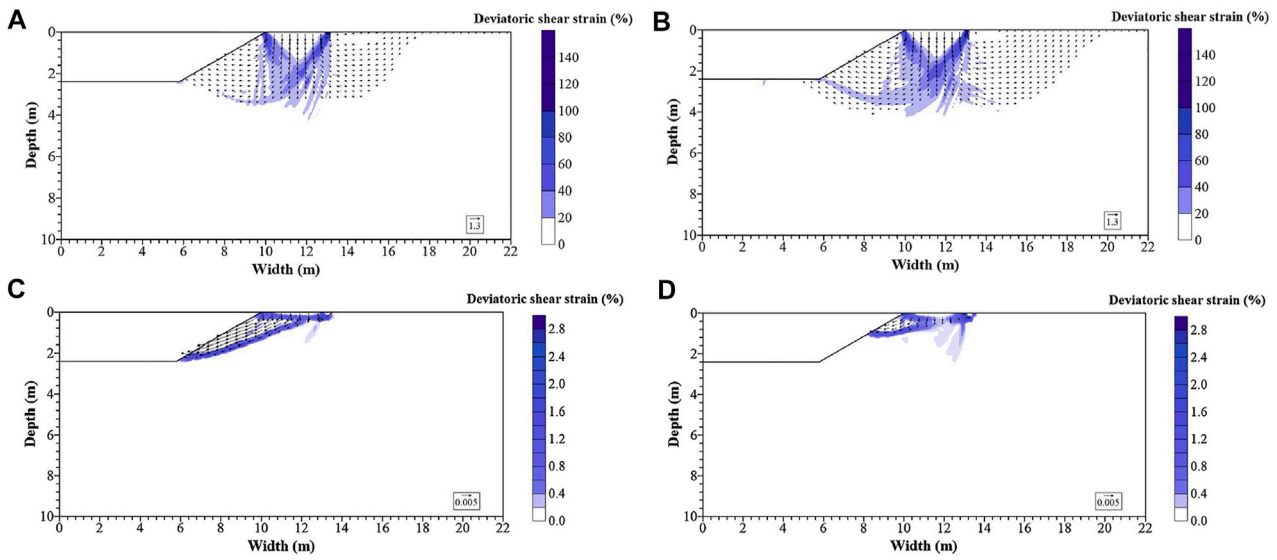

FIGURE 9 | Contours of the shear strain and displacement vectors for gassy sand (Hong et al., 2021b): **(A)** Saturated dense sand; **(B)** Gassy dense sand; **(C)** Saturated loose sand; **(D)** Gassy loose sand.

holding sampling technology can be used to obtain *in-situ* gassy sediment samples, the sampling cost is high (Bai and Li, 2010; Zhu et al., 2011; Wu et al., 2022; Zhu et al., 2022). Experiments have therefore mainly been carried out using laboratory gassy soil samples. Moreover, the current sample preparation method for gassy soil cannot effectively reproduce the gas-production process of microbial bacteria in the coastal soft soil layer under *in-situ* conditions. It is also difficult to realize the batch of gassy soil sample preparation and the quantitative introduction of gas. It is therefore essential to study the *in-situ* test equipment that can quantitatively detect the gas content in the soil. Accidents involving uncontrolled gas leaks caused by drilling in marine engineering can be avoided by researching the *in-situ* testing technology of gassy soil. The simulation parameters can be accurately established for numerical calculation.

Rad and Lunne (1994) developed a new type of offshore *in-situ* testing device, the BAT probe, which is pushed to the required depth to obtain water-air samples in the gassy soil layer. Its structure is shown in **Figure 11**. After the recovery of the device, the samples are analyzed using a gas chromatograph for gas

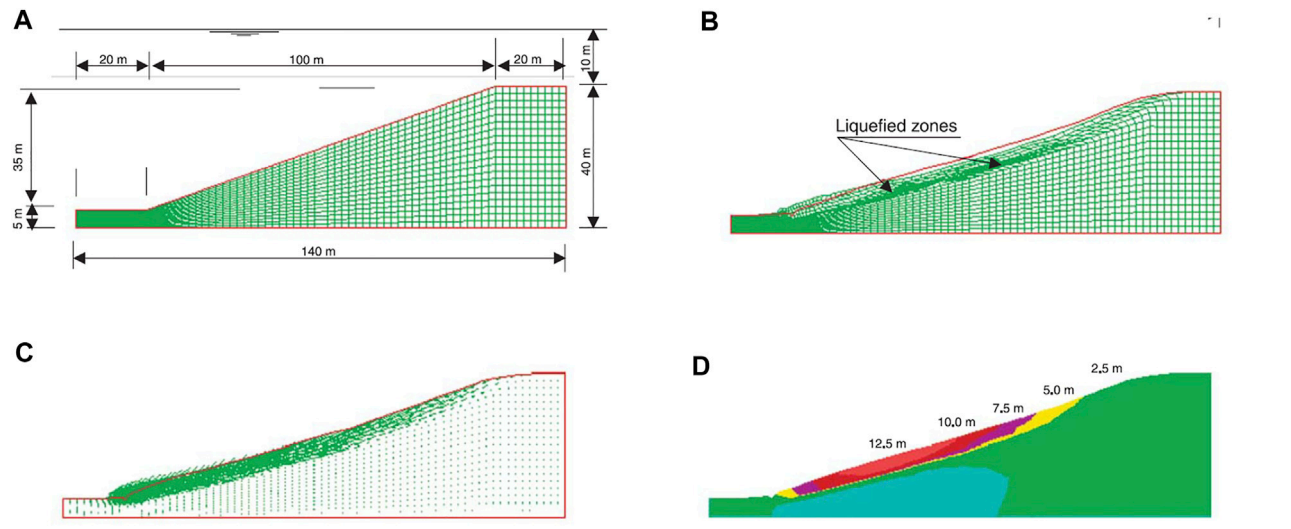

FIGURE 10 | Submarine slope of gassy soil (Hong and Xu, 2020): **(A)** grid used in analysis; **(B)** deformed mesh during low tide; **(C)** displacement vectors; **(D)** horizontal displacement contours (in m).

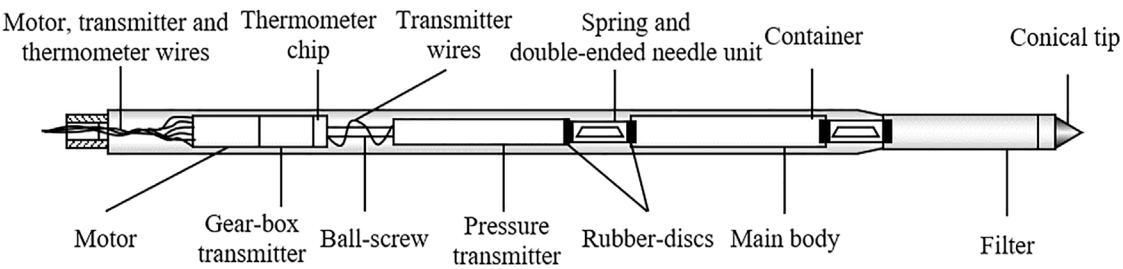

FIGURE 11 | BAT probe (Rad and Lunne, 1994).

composition and gas saturation in pore water to assess the possibility of a shallow air bladder in the soil. Hong et al. (2018) also developed a new type of device. After penetration, the device takes horizontal samples, performs *in-situ* sonic testing, and determines the gas content by *in-situ* compression to minimize the influence of sampling disturbance.

Since the BAT probe can only be used for *in-situ* water-gas sample testing and has a single function, recent research has mainly used the geophysical prospecting measurements to detect the source layer, reservoir and burial depth of gassy soil (**Figure 12A**). The gassy soil can be identified as shown in **Figure 12B**. The shear wave seismic section can delineate the boundary of the gassy sand layer (Wood et al., 2000; Pruessmann et al., 2004; Reeves, 2005; Lin et al., 2006; Zheng et al., 2006; Li et al., 2009). In addition, the change of resistivity can be used to judge the gassy layer by the electromagnetic exploration method, allowing the distribution range to be delineated (Lee and Collett, 2006; Li et al., 2007; Pezard et al., 2015). The irregular and robust reflection interface of the gassy formation can be formed by the shallow stratum cross-section method using sound-wave propagation and scattering (Mustafa et al., 2002; Wang et al., 2013; Tóth et al., 2014; Janiewicz et al., 2019).

The cone penetration test (CPT) can be used to carry out a variety of test methods, and as the scope of the investigation is extensive, CPT can be used to identify the gassy layer (Wang et al., 2019). Guo et al. (2007) found that CPT can also preliminarily determine whether biogas is present in sand. When the tip resistance increases, the friction–resistance ratio decreases, the fluctuation amplitude of the pore water pressure remains small, and there is no negative excess pore water pressure during the penetration process. It can thus be determined preliminarily that there may be shallow biogas in the sand layer.

Li et al. (2009) improved the CPT and separated the probe and probe rod to realize gas sampling and pressure measurement. Lai et al. (2016) invented a Membrane Interface Probe and Cone Penetration Technology that decomposes and passes organic matter by adding a MIP film. It uses gas chromatography to determine the organic matter's phase state and content.

CPT with different probes can be used to detect different physical properties of sediments, such as gas occurrence,

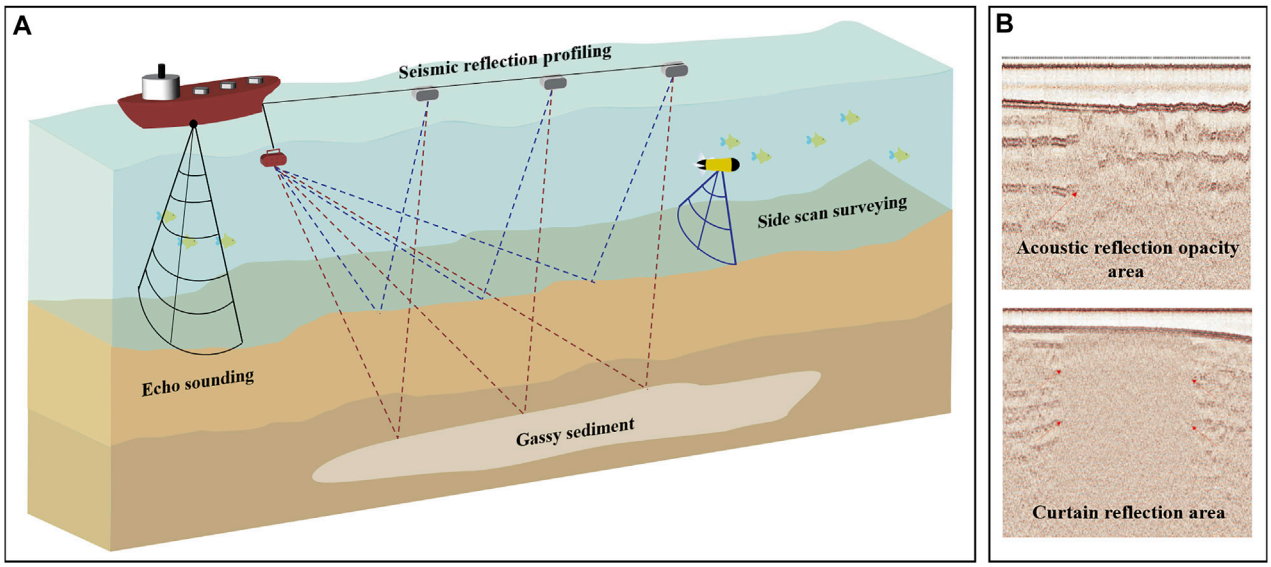

FIGURE 12 | Geophysical prospecting: **(A)** methods; **(B)** Sub-bottom profile of gassy sediment (Xing et al., 2017).

temperature gradient, acoustic characteristics, and chemical anomalies. Detecting these characteristics can improve the current conventional *in-situ* measurements in terms of the identification accuracy of gassy soils. Thus, CPT has a wide application prospect in gassy soil exploration.

RESEARCH PROSPECTS

Due to its mechanical properties, gassy sedments are an important cause of engineering disasters. The researches mainly focus on the mechanical response and development of constitutive model. From this summary of the current research, the author believes that future research on gassy soils should explore the following aspects:

1) Mechanical responses of gassy soils with different stress paths. Combined with the actual engineering or disaster, based on the soil stress path under the actual conditions of gassy soil shield, waves, landslides etc., research could be conducted into mechanics and deformation mechanism to achieve accurate prediction;
2) The constitutive model of fine-grained gassy soil. The numerical simulation of coarse-grained gassy soil is relatively mature, whereas the simulation of fine-grained gassy soil has mainly focused on the unit scale, and there is no mature constitutive model for practical engineering problems;
3) The bubble-migration mechanism in gassy soil. Under real conditions, due to soil faults and cracks, discrete bubbles may migrate, accumulate, and be released. The relationship between the triggering conditions of bubble migration and gassy soil mechanical behaviour needs to be furthur research.
4) Effect of microstructure of bubbles in gassy soil. The change of bubbles in the mechanical test can be observed by means of microscopic scanning device to clarify microcosmic mechanism.
5) Risk assessment of geological disasters such as liquefaction, landslides, and the settlement of gassy soil. Based on the research into the deformation mechanism of gassy soil under different conditions, engineers should carry out site risk assessments and implement disaster-prevention and mitigation measures;
6) *In-situ* measurements of gassy soil. At present, the *in-situ* measurements for gassy soils are mainly the gassy soil distribution range detection. It is necessary to improve the accuracy of the *in-situ* parameters of gassy soils to improve the accuracy of research into constitutive models.

AUTHOR CONTRIBUTIONS

TL, XY, and YZ contributed to conception and design of the study. TL wrote the first draft of the manuscript. XY and YZ wrote sections of the manuscript. All authors contributed to manuscript revision, read, and approved the submitted version".

FUNDING

The study is supported by the National Natural Science Foundation of China (No. U2006213) and the Fundamental Research Funds for the Central Universities (201962011).

REFERENCES

Amaratunga, A., and Grozic, J. L. H. (2009). On the Undrained Unloading Behaviour of Gassy Sands. *Can. Geotech. J.* 46, 1267–1276. doi:10.1139/t09-056

Atigh, E., and Byrne, P. M. (2004). Liquefaction Flow of Submarine Slopes under Partially Undrained Conditions: an Effective Stress Approach. *Can. Geotech. J.* 41, 154–165. doi:10.1139/t03-079

Bai, C. (2018). *Evaluation of Uniformity and Preliminary Mechanical Properties of Simulated Samples of Soft Soil Containing Bubbles*. Tianjiaan, Huainan, Anhui, China: AnHui University of Science and Technology.

Bai, Y., and Li, Q. (2010). Progress on Natural Gas Hydrate Sampling Techniques and Tools. *Pet. Drill. Tech.* 038, 116. doi:10.3969/j.issn.1001-0890.2010.06.026

Blouin, A., Sultan, N., Callot, J-P., and Imbertb, P. (2019). Sediment Damage Caused by Gas Exsolution: A Key Mechanism for Mud Volcano Formation. *Eng. Geol.* 263, 105313. doi:10.1016/j.enggeo.2019.105313

Duffy, S. M., Wheeler, S. J., and Bennell, J. D. (1994). Shear Modulus of Kaolin Containing Methane Bubbles. *J. Geotech. Engrg.* 120, 781–796. doi:10.1061/(asce)0733-9410(1994)120:5(781)

Fleischer, P., Orsi, T., Richardson, M., and Anderson, A. (2001). Distribution of Free Gas in Marine Sediments: a Global Overview. *Geo-Marine Lett.* 21, 103–122. doi:10.1007/s003670100072

Gao, Z., and Hong, Y. (2019). Constitutive Modelling of Gassy Clay. *E3S Web Conf.* 92, 15005. doi:10.1051/e3sconf/20199215005

Gao, Z., Hong, Y., and Wang, L. (2020). Constitutive Modelling of Fine-grained Gassy Soil: A Composite Approach. *Int. J. Numer. Anal. Methods Geomech.* 44, 1350–1368. doi:10.1002/nag.3065

Gardner, T. N., and Goringe, M. J. (1988). The Measurement of Gas Bubble Size Distributions in a Three Phase Laboratory Gassy Soil. *Geotechnical Test. J.* 11, 49–55.

Grozic, J. L. H. (2003). "Liquefaction Potential of Gassy Marine Sands," in *Submarine Mass Movements and Their Consequences* (Dordrecht, Netherlands: Springer), 37–45. doi:10.1007/978-94-010-0093-2_5

Grozic, J. L. H., Nadim, F., and Kvalstad, T. J. (2005b). On the Undrained Shear Strength of Gassy Clays. *Comput. Geotechnics* 32, 483–490. doi:10.1016/j.compgeo.2005.10.002

Grozic, J. L., Imam, S. M., Robertson, P. K., and Morgenstern, N. R. (2005a). Constitutive Modeling of Gassy Sand Behaviour. *Can. Geotech. J.* 42, 812–829. doi:10.1139/t05-015

Grozic, J. L., Robertson, P. K., and Morgenstern, N. R. (2000). Cyclic Liquefaction of Loose Gassy Sand. *Can. Geotech. J.* 37, 843–856. doi:10.1139/t00-008

Guan, X. (2017). *Experimental Research on Liquefaction Characteristics of Seabed Gassy Sand under Cyclic Loading*. Huainan, Anhui, China: AnHui University of Science and Technology.

Guo, A., Kong, L., Chen, J., and Zhong, F-J. (2007). On Engineering Characteristics of Sallow Biogenetic Gassy Sand by Piezocone Test. *Rock Soil Mech.* 28, 1539. doi:10.3969/j.issn.1000-7598.2007.08.003

Guo, Z., Liu, T., Wu, C., Su, X., and Li, S. (2021). Characterization and Reconstruction of Meso-Structure of Gas-Bearing Soils at Different Storage Pressures. *Haiyang Xuebao* 43, 96–104. doi:10.12284/hyxb2021154

Han, Z. (2020). *Study on the Dynamic Response of Gas-Bearing Sandy Seabed Induced by Wave Loadings [M]*. Guilin, Guangxi, China: Guilin University of Technology.

Hong, J., and Xu, M. (2020). DEM Study on the Undrained Mechanical Behavior of Gassy Sand. *Acta Geotech.* 15, 2179–2193. doi:10.1007/s11440-019-00910-x

Hong, Y., Chen, X. Y., Wang, L. Z., and Bin, Y. (2021a). Distinct Undrained Cyclic Behavior of Fine-Grained Gassy Soil at Various Initial Pore Water Pressures. *J. geotechnical geoenvironmental Eng.* 147, 06020027. doi:10.1061/(asce)gt.1943-5606.0002419

Hong, Y., Wang, L., and Yang, B. (2018). *A Device for* In-Situ *Measurement of Gas Content in Submarine Gassy Soil and Measurement Method.*

Hong, Y., Wang, L., Yang, B., and Zhang, J. (2019). Stress-dilatancy Behaviour of Bubbled Fine-Grained Sediments. *Eng. Geol.(C)* 260, 105196. doi:10.1016/j.enggeo.2019.105196

Hong, Y., Wang, L., Zhang, J., and Gao, Z. (2020a). 3D Elastoplastic Model for Fine-Grained Gassy Soil Considering the Gas-Dependent Yield Surface Shape and Stress-Dilatancy. *J. Eng. Mech. [J]* 146, 04020037. doi:10.1061/(ASCE)EM.1943-7889.0001760

Hong, Y., Wang, X., Wang, L., and Gao, Z. (2021b). A State-dependent Constitutive Model for Coarse-Grained Gassy Soil and its Application in Slope Instability Modelling. *Comput. Geotechnics* 129, 103847. doi:10.1016/j.compgeo.2020.103847

Hong, Y., Wang, L. Z., Ng, C. W. W., and Yang, B. (2017). Effect of Initial Pore Pressure on Undrained Shear Behaviour of Fine-Grained Gassy Soil. *Can. Geotech. J.* 54, 1592–1600. doi:10.1139/cgj-2017-0015

Hong, Y., Zhang, J. F., Wang, L. Z., and Liu, T. (2020b). On Evolving Size and Shape of Gas Bubble in Marine Clay under Multi-Stage Loadings: Microcomputed Tomography (μCT) Characterization and Cavity Contraction Analysis. *Can. Geotech. J.* 57, 1072–1091. doi:10.1139/cgj-2019-0076

Hu, G. (2010). *Identification of Submarine Landslides along the Continental Slope of the East China Sea and Analysisi of Factors Causing Submarine Landslides*. Qingdao: Ocean University of China.

Janiewicz, D., Klusek, Z., Brodecka-Goluch, A., and Jerzy, B. (2019). Acoustic Investigations of Shallow Gas in the Southern Baltic Sea (Polish Exclusive Economic Zone): a Review. *Geo-Marine Lett.* 39, 1–17. doi:10.1007/s00367-018-0555-5

Jommi, C., Muraro, S., Trivellato, E., and Zwanenburg, C. (2019). Experimental Results on the Influence of Gas on the Mechanical Response of Peats. *Géotechnique* 69, 753–766. doi:10.1680/jgeot.17.p.148

Kaminski, P., Urlaub, M., Grabe, J., and Berndt, C. (2020). Geomechanical Behaviour of Gassy Soils and Implications for Submarine Slope Stability: a Literature Analysis. *Geol. Soc. Lond. Spec. Publ.* 500, 277–288. doi:10.1144/sp500-2019-149

Kong, L., Liu, W., Yuan, Q., and Dong, T. (2019). Triaxial Test on Gassy Sandy Soil under Constant Shear Stress Paths. *Rock Soil Mech.* 40, 3319–3326. doi:10.16285/j.rsm.2018.1863

Kong, X., Liu, J., Zou, D., and Liu, H. (2016). Stress-dilatancy Relationship of Zipingpu Gravel under Cyclic Loading in Triaxial Stress States. *Int. J. Geomech.* 16, 04016001. doi:10.1061/(asce)gm.1943-5622.0000584

Kortekaas, S., and Peuchen, J. (2008). "Measured Swabbing Pressures and Implications for Shallow Gas Blow-Out," in Offshore Technology Conference, Houston, Texas. OnePetro.

Lai, X., Chen, Z., and Gou, Z. (2016). *Seabed Shallow-Layer Gas Detection Method Based on MIP-CPT Technology*.

Lee, M. W., and Collett, T. S. (2006). A Method of Shaly Sand Correction for Estimating Gas Hydrate Saturations Using Downhole Electrical Resistivity Log Data. Scientific Investigations Report2006-5121. Available at: https://pubs.er.usgs.gov/publication/sir20065121.

Li, L., Zhao, Y., and Yu, L. (2009). Exploration for Quaternary Shallow Biogenic Gas by Sealed Core Drilling and Modified CPT. *Coal. Geol. Explor.* 37, 72–76.

Li, Y., Lin, C., and Yu, J. (2007). Application of Stratagem EH4 Electromagnetic Imaging System in the Late Quaternary Strata in the Hangzhou Bay Area. *Geol. Rev.* 53, 413–420. doi:10.16509/j.georeview.2007.03.016

Lin, C., Li, G., and Li, Y. (2006). The Exploration Method of Late Quaternary Shallow Biogenic Gas Reservoirs in Hangzhou Bay Area. *Geophys. Prospect. Petroleum.* 45 (2), 202.

Liu, W. (2018). *Triaxial Testing Study on Gassy Sand Soil under Constant Shear Stress Paths*. Qingdao, China: Qingdao University of Technology.

Mabrouk, A., and Rowe, R. K. (2011). Effect of Gassy Sand Lenses on a Deep Excavation in a Clayey Soil. *Eng. Geol.* 122, 292–302. doi:10.1016/j.enggeo.2011.06.009

Mathiroban, S. (2004).*A Model to Predict the Undrained Response of Loose Gassy Sand*. (Unpublished master's thesis).Calgary, AB: University of Calgary.

Mustafa, E., Derman, D., and Günay, Ç. (2002). Acoustic Evidence for Shallow Gas Accumulations in the Sediments of the Eastern Black Sea. *Terra nova.* 14, 313–320. doi:10.1046/j.1365-3121.2002.00434.x

Nageswaran, S. (1983).*Effect of Gas Bubbles on the Sea Bed Behaviour*. Thesis (Ph.D.), United Kingdom: University of Oxford.

Ng, C. W. W., Zhan, L. T., and Cui, Y. J. (2002). A New Simple System for Measuring Volume Changes in Unsaturated Soils. *Can. Geotech. J.* 39, 757–764. doi:10.1139/t02-015

Pezard, P. A., Abdoulghafour, H., Denchik, N., Perroud, H., Lofi, J., Brondolo, F., et al. (2015). On Baseline Determination and Gas Saturation Derivation from Downhole Electrical Monitoring of Shallow Biogenic Gas Production. *Energy Procedia* 76, 555–564. doi:10.1016/j.egypro.2015.07.910

Pietruszczak, S., and Pande, G. N. (1996). Constitutive Relations for Partially Saturated Soils Containing Gas Inclusions. *J. geotechnical Eng.* 122, 50–59. doi:10.1061/(asce)0733-9410(1996)122:1(50)

Pruessmann, J., Coman, R., Endres, H., and Trappe, H. (2004). Improved Imaging and AVO Analysis of a Shallow Gas Reservoir by CRS. *Lead. Edge* 23, 915–918. doi:10.1190/1.1803503

Rad, N. S., and Lunne, T. (1994). Gas in Soil. I: Detection and η-Profiling. *J. Geotech. Engrg.* 120, 697–715. doi:10.1061/(asce)0733-9410(1994)120:4(697)

Rad, N. S., Vianna, A. J. D., and Berre, T. (1994). Gas in Soils. II: Effect of Gas on Undrained Static and Cyclic Strength of Sand. *J. Geotech. Engrg.* 120, 716–736. doi:10.1061/(asce)0733-9410(1994)120:4(716)

Reeves, J. J. (2005). "An Integrated 3D-Seismic Exploration Method for Fractured Reservoirs in Tight Gas Sands," in SPE Latin American and Caribbean Petroleum Engineering Conference. *OnePetro*.

Rowe, R., Goveas, L., and Dittrich, J. (2002). *Briefing: Excavations in Gassy Soils*. United Kingdom: Thomas Telford Ltd.

Rowe, R. K., and Mabrouk, A. (2018). Three-dimensional Analysis of Unanticipated Behavior of a Deep Excavation. *Can. Geotechnical J.* 55, 1647–1656. doi:10.1139/cgj-2017-0511

Sánchez, M., Gai, X., and Santamarina, J. C. (2017). A Constitutive Mechanical Model for Gas Hydrate Bearing Sediments Incorporating Inelastic Mechanisms. *Comput. Geotechnics* 84, 28–46. doi:10.1016/j.compgeo.2016.11.012

Sham, W. K. (1992). The Undrained Shear Strength of Soils Containing Large Gas Bubbles. *Géotechnique* 38, 399

Sills, G. C., and Gonzalez, R. (2001). Consolidation of Naturally Gassy Soft Soil. *Géotechnique* 51, 629–639. doi:10.1680/geot.2001.51.7.629

Sills, G. C., and Wheeler, S. J. (1992). The Significance of Gas for Offshore Operations. *Cont. Shelf Res.* 12, 1239–1250. doi:10.1016/0278-4343(92)90083-v

Sills, G. C., Wheeler, S. J., Thomas, S. D., and Gardner, T. N. (1991). Behaviour of Offshore Soils Containing Gas Bubbles. *Géotechnique* 41, 227–241. doi:10.1680/geot.1991.41.2.227

Sobkowicz, J. C., and Morgenstern, N. R. (1984). The Undrained Equilibrium Behaviour of Gassy Sediments. *Can. Geotech. J.* 21, 439–448. doi:10.1139/t84-048

Sultan, N., De Gennaro, V., and Puech, A. (2012). Mechanical Behaviour of Gas-Charged Marine Plastic Sediments. *Géotechnique* 62, 751–766. doi:10.1680/geot.12.og.002

Sultan, N., and Garziglia, S. (2014). Mechanical Behaviour of Gas-Charged Fine Sediments: Model Formulation and Calibration. *Geotechnique* 64, 851–864. doi:10.1680/geot.13.P.125

Thomas, S. D. (1987). *The Consolidation Behaviour of Gassy Soil*. United Kingdom: University of Oxford.

Thomas, S. D. (2021a). "Finite Element Model of Wave Loading on a Soil Seabed Part I: Multi-Layered Anisotropic Gassy Soil Conditions," in *Vietnam Symposium on Advances in Offshore Engineering*. Editors D. V. K Huynh, A. M. Tang, D. H. Doan, and P. Watson (Singapore: Springer), 105

Thomas, S. D. (2021b). "Finite Element Model of Wave Loading on a Soil Seabed Part II: Heterogeneous Gassy Soil Conditions," in *Vietnam Symposium on Advances in Offshore Engineering*. Editors D. V. K. Huynh, A. M. Tang, D. H. Doan, and P. Watson (Singapore: Springer), 114

Tóth, Z., Spieß, V., and Jensen, J. (2014). Seismo-acoustic Signatures of Shallow Free Gas in the Bornholm Basin, Baltic Sea. *Cont. Shelf Res.* 88, 228–239. doi:10.1016/j.csr.2014.08.007

Vanoudheusden, E., Sultan, N., and Cochonat, P. (2003). "Hydro-mechanical Behaviour of Gassy Soils," in *Submarine Mass Movements and Their Consequences*. Editors J. Locat, J. Mienert, and L. Boisvert (Dordrecht: Springer), 145–153. doi:10.1007/978-94-010-0093-2_17

Vega-Posada, C. A., Finno, R. J., and Zapata-Medina, D. G. (2014). Effect of Gas on the Mechanical Behavior of Medium-Dense Sands. *J. Geotech. Geoenviron. Eng.* 140, 04014063. doi:10.1061/(asce)gt.1943-5606.0001163

Wang, J., Qin, C., Luo, X., Wang, S., and Yang, N. (2019). Application Prospect of in Gas Hydrate Exploration. *Mar. Geol. Front.* 35, 52–59. doi:10.16028/j.1009-2722.2019.11008

Wang, L. (2021). On the Consolidation and Creep Behaviour of Layered Viscoelastic Gassy Sediments. *Eng. Geol.* 293, 106298. doi:10.1016/j.enggeo.2021.106298

Wang, Y. (2009). *Study on Evolution Characteristics of Engineering Effects and the Disaster Mechanism for Shallow Gassy Sand*. Beijing, China: Institute of Rock & Soil Mechanics, Chinese Accdemy of Sciences.

Wang, Y., Wang, Z., and Liu, W. (2013). Measurement of Shallow Stratigraphic Sections for Seabed Gas Exploration in Northern Hangzhou Bay. *Shanghai Land & Resour.* 34, 59

Wang, Y., Kong, L., Wang, Y., Wang, M., and Wang, M. (2018). Liquefaction Response of Loose Gassy Marine Sand Sediments under Cyclic Loading. *Bull. Eng. Geol. Environ.* 77, 963–976. doi:10.1007/s10064-017-1164-7

Wheeler, S. J. (1986).*The Stress-Strain Behaviour of Soils Containing Gas Bubbles*. MPLSthesis.United Kingdom: University of Oxford.

Wheeler, S. J. (1988a). A Conceptual Model for Soils Containing Large Gas Bubbles. *Géotechnique* 38, 389–397. doi:10.1680/geot.1988.38.3.389

Wheeler, S. J., and Gardner, T. N. (1989). Elastic Moduli of Soils Containing Large Gas Bubbles. *Géotechnique* 39, 333–342. doi:10.1680/geot.1989.39.2.333

Wheeler, S. J. (1988b). The Undrained Shear Strength of Soils Containing Large Gas Bubbles. *Géotechnique* 38, 399–413. doi:10.1680/geot.1988.38.3.399

Wood, W. T., Holbrook, W. S., and Hoskins, H. (2000).27 Situ Measurements of P-Wave Attenuation in the Methane Hydrate–and Gas-Bearing Sediments of the Blake Ridge1," in Proceedings of the Ocean Drilling Program. Scientific Results, Ocean Drilling Program, 265

Wu, S-J., Wang, X., wang, S., Zhang, B., Yang, C-J., and Zhi, H. (2022). Active Temperature-Preserving Deep-Sea Water Sampler Configured with a Pressure-Adaptive Thermoelectric Cooler Module. *Oceanogr. Res. Pap.* 181, 103701. doi:10.1016/j.dsr.2022.103701

Xiao, Y., Liu, H., Sun, Y., Liu, H., and Chen, Y. (2015). Stress-dilatancy Behaviors of Coarse Granular Soils in Three-Dimensional Stress Space. *Eng. Geol.* 195, 104–110. doi:10.1016/j.enggeo.2015.05.029

Xiao, Y., Long, L., Matthew Evans, T., Zhou, H., Liu, H., and Stuedlein, A. W. (2019). Effect of Particle Shape on Stress-Dilatancy Responses of Medium-Dense Sands. *J. Geotech. Geoenviron. Eng.* 145, 04018105. doi:10.1061/(asce)gt.1943-5606.0001994

Xing, L., Jiao, J., and Liu, X. (2017). Distribution and Seismic Reflection Characteristics of Shallow Gas in Bohai Sea. *Periodical Ocean Univ. China* 47, 9. doi:10.16441/j.cnki.hdxb.20160354

Xu, D.-S., Su, Z.-Q., Lalit, B., and Qin, Y. (2022). A Hybrid FBG-Based Load and Vibration Transducer with a 3D Fused Deposition Modelling Approach. *Meas. Sci. Technol.* 33, 065106. doi:10.1088/1361-6501/ac5a9b

Xu, Y.-S., Wu, H.-N., Shen, J. S., and Zhang, N. (2017). Risk and Impacts on the Environment of Free-phase Biogas in Quaternary Deposits along the Coastal Region of Shanghai. *Ocean. Eng.* 137, 129–137. doi:10.1016/j.oceaneng.2017.03.051

Yang, G., and Bai, B. (2020). A Thermodynamic Model to Simulate the Thermo-Mechanical Behavior of Fine-Grained Gassy Soil. *Bull. Eng. Geol. Environ.* 79, 2325–2339. doi:10.1007/s10064-019-01694-w

Yin, Z.-Y., and Chang, C. S. (2013). Stress-dilatancy Behavior for Sand under Loading and Unloading Conditions. *Int. J. Numer. Anal. Meth. Geomech.* 37, 855–870. doi:10.1002/nag.1125

Zhang, R., and Lunne, T. (2003). Deepwater Sample Disturbance Due to Stress Relief. *Chin. Jounal Geotechnical Eng.* 25, 356. doi:10.3321/j.issn:1000-4548.2003.03.023

Zheng, H., Jiang, W., and Zhang, T. (2006). Using AVO Technique to Detect Quaternary Shallow Biogas in Hangzhou Bay Area. *Oil Geophys. Prospect.* 21-24, 142

Zhong, F. (2007). *Research on Pressure Characteristics of Gas Reservoir and Mechanical Effect of Stress Path for Shallow Gassy Sand*. Beijing, China: Institute of Rock & Soil Mechanics, Chinese Academy of Sciences.

Zhu, B., Huang, J., Wang, L., and Ye, Z. (2021). Precise Numerical Study on the Behaviour of Gassy Marine Soils Subjected to Thermal and Mechanical Loadings. *Comput. Geotechnics* 137, 104269. doi:10.1016/j.compgeo.2021.104269

Zhu, H., Chen, J.-w., Ren, Z.-q., Zhang, P.-h., Gao, Q.-l., Le, X.-l., et al. (2022). A New Technique for High-Fidelity Cutting Technology for Hydrate Samples. *J. Zhejiang Univ. Sci. A* 23, 40–54. doi:10.1631/jzus.a2100188

Zhu, H., Liu, Q., Deng, J., Wang, G., Xiao, X., Jiang, Z., et al. (2011). Pressure and Temperature Preservation Techniques for Gas-Hydrate-Bearing Sediments Sampling. *Energy* 36, 4542–4551. doi:10.1016/j.energy.2011.03.053

Conflict of Interest: The authors declare that the research was conducted in the absence of any commercial or financial relationships that could be construed as a potential conflict of interest.

Publisher's Note: All claims expressed in this article are solely those of the authors and do not necessarily represent those of their affiliated organizations, or those of the publisher, the editors and the reviewers. Any product that may be evaluated in this article, or claim that may be made by its manufacturer, is not guaranteed or endorsed by the publisher.

frontiers | Frontiers in Earth Science

ORIGINAL RESEARCH
published: 23 June 2022
doi: 10.3389/feart.2022.908351

The Hummocky Patches and Associated Sediment Dynamics Over an Accretional Intertidal Flat

Shibing Zhu[1], Yining Chen[2], Weibing Yan[3], Fei Xing[4], Renzhi Li[4], Mingliang Li[1], Benwei Shi[4] and Ya Ping Wang[1,4]**

[1]Ministry of Education Key Laboratory for Coast and Island Development, School of Geographic and Oceanographic Sciences, Nanjing University, Nanjing, China, [2]Second Institute of Oceanography, Ministry of Natural Resources, Hangzhou, China, [3]Geological Exploration Technology Institute of Jiangsu Province, Nanjing, China, [4]State Key Laboratory of Estuarine and Coastal Research, School of Marine Sciences, East China Normal University, Shanghai, China*

Tidal flat system is composed of multiple sub-scale geomorphological units. We found a new mesoscale geomorphological unit on sand-mud mixed intertidal zone along China coast, which was defined as hummocky patches. Hummock patches are most developed in middle tidal flat, with horizontal magnitude of 10–20 m and vertical magnitude of ~15 cm. Hummocky patches significantly influence local sediment transport, thus affect morphological evolution of tidal flats. In order to understand the formation and development mechanisms of hummocky patches, we collected hydrodynamics, topography, sediment properties, and substrate erosion thresholds data through an *in-situ* field observation covering a spring-neap tidal cycle over an accretional intertidal flat in Jiangsu, China. We found that sediment characteristics including sorting coefficient (σ: measuring the uniformity of sediment particles) and silt/clay/organic matter/water content are essentially different between hummocky patches and nearby seabed, which leads to spatially varied substrate erosion resistance. The measured erosion thresholds for patches are two times higher comparing to surrounding seabed sediment, which provides foundation for the formation of hummocky patches. Under the impact of periodical tidal currents and waves, surrounding seabed experiences considerably more erosion than patch area, which finally develops to hummocky patches. Therefore, hydrodynamic forces drive the formation and development of patches. The erosion resistance of patches decreases vertically from seabed surface to sublayer, causing initial erosion in the lower sublayer, followed by a mass collapse of the seabed surface layer. Hummocky patches are commonly found in middle tidal zone and their sizes decrease to the shore as tidal currents and waves attenuate with shoreward propagation. Hummocky patches have distinct seasonal variations, which only appear in summer and autumn when wind waves are comparatively lower than winter and spring. We infer the reason is that the strong hydrodynamics caused by winter storms cause larger bottom shear stress than the erosion threshold of hummocky patches, leading to destruction of hummocky patches and a smooth tidal flat surface. This study shed new insight on the knowledge of mesoscale geomorphological units and their formation and development in intertidal flats, which provides crucial information for developing more realistic tidal flat sediment transport and morphological models.

OPEN ACCESS

Edited by:
Chong Xu,
Ministry of Emergency Management, China

Reviewed by:
Qi Yao,
China Earthquake Administration, China
Pei Xin,
Hohai University, China

***Correspondence:**
Fei Xing
fxing@sklec.ecnu.edu.cn
Ya Ping Wang
ypwang@nju.edu.cn

Specialty section:
This article was submitted to Geohazards and Georisks, a section of the journal Frontiers in Earth Science

Received: *30 March 2022*
Accepted: *30 May 2022*
Published: *23 June 2022*

Citation:
Zhu S, Chen Y, Yan W, Xing F, Li R, Li M, Shi B and Wang YP (2022) The Hummocky Patches and Associated Sediment Dynamics Over an Accretional Intertidal Flat. Front. Earth Sci. 10:908351. doi: 10.3389/feart.2022.908351

Keywords: intertidal, geomorphological units, hummocky patches, morphodynamic, critical erosion threshold, wave-current interactions, sedimentation characteristics

1 INTRODUCTION

Tidal flats form in coastal areas with strong tidal forces and abundant supply of fine-grained sediments. It is an important buffer against typhoons, storm surges, and other natural disasters in coastal areas, and an essential reserve land resource (Wang et al., 2012; Kirwan and Megonigal, 2013; Walstra et al., 2015). However, tidal flats all over the world are experiencing decreased accretion rate or even changing from accretion to erosion due to human activities, sea-level rise, and decrease in riverine sediment supply in recent decades (Syvitski et al., 2005). Tidal flat protection has become an important aspect in making sustainable regional development strategy, which requires further understanding of tidal flat evolution and their controlling factors (Tessler et al., 2015).

Various geomorphological units with different spatial scales constitute tidal flat geomorphological features (**Figure 1A**). The characteristics of these geomorphological units are the most intuitive expression of tidal flat morphology, which provides critical clues to understand tidal flat evolution (Wang et al., 2006). The geomorphologic units of tidal flats can be classified as macroscale, mesoscale, and microscale units, according to their magnitudes. Macroscale geomorphological units of tidal flats indicate morphological patterns controlling the entire flat system, such as profile geometry, e.g., convex and concave profile morphology (Gao, 2009; Zhou et al., 2016), and zonation of flat sediments (Roberts et al., 2000; Zhang et al., 2018). Mesoscale geomorphological units refer to those features with the length of 1–10 m, including scarps occurring at the boundaries between flat and vegetation (salt marsh plants and mangroves), ridges (Weill et al., 2010; Weill et al., 2012), sand waves (Allen, 1980; Besio et al., 2006), and waterways (Weimer et al., 1982; Pieterse et al., 2016), as well as tidal creeks (Blanton et al., 2002). Microscale geomorphological units, which generally

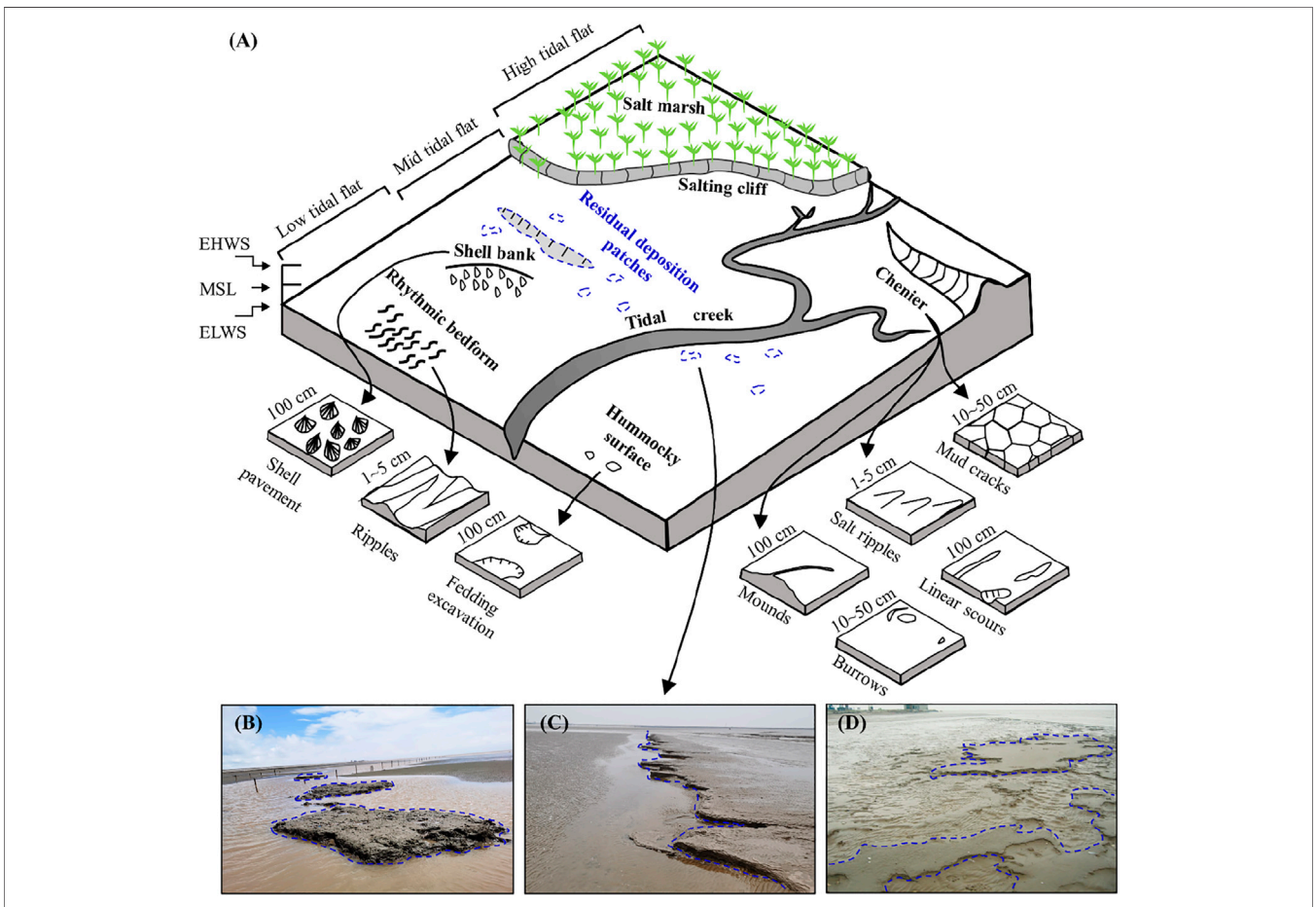

FIGURE 1 | Generalized geomorphology of tidal flats. **(A)** Macroscale geomorphology of tidal flat and morphological characteristics of mesoscale and microscale geomorphology units. **(B–D)** Photos of intertidal hummocky patches taken in three major tidal flat areas in China: **(B)** The tidal flat in the Yangtze River Delta, photographed in August 2021; **(C)** Tidal flat in Dafeng along Jiangsu coast, photographed in May 2021; **(D)** Tidal flat in the Yellow River Delta, photographed in July 2008.

less than 1 m, include flat surface cracks (Gardel et al., 2009), sand grains (Harms, 1969), linear scour pits (Sumer et al., 2001), biological holes (Takeuchi and Tamaki, 2014), and flat surface uplift caused by fish or large burrowing, which usually located in the low tidal zone (Dott and Bourgeois, 1982). Mechanisms controlling the genesis and development of these geomorphological units have been well studied (Gao, 2019).

Other than these features, we discovered a new mesoscale geomorphological unit, which is defined as hummocky patches, mostly occurring in intertidal zone with diverse sediment composition (**Figure 1**). Generally, hummocks refer to undulating relief with alternating convex and concave topography, which have distinctive spatial distribution patterns: vary from transversely or radially aligned ridges, ripples or hummocks, to almost uniformly, tightly packed hummocks (Robinson et al., 2015). Hummocky landform is seen on most sub-aerial and sub-marine environments on Earth and other planets, whose formation are mainly controlled by the following factors: accumulation of organic matter (Hughes and Barber, 2004), differential erosion by flowing water (Dawkins, 1939), frost heave (Grab, 1997), etc. The patches that we found on tidal flats have similar characteristics as other hummocky landforms, so we defined them as hummocky patches.

Hummocky patches with varying sizes and irregular shapes have been observed in several tidal flat systems along China coast (**Figures 1B–D**), shown as elevated mounds and ridges which typically less than 1 m in height and more than 10 m in length, composed of chaotic assemblages of hillocks and depressions of variable sizes and shapes in the intertidal zones. On tidal flats, where topography is usually featured with very gentle slope and uniform surface, the presence of such patches is very distinctive and significantly influence the morphological and ecological evolution of tidal flats and correlated wetland systems. However, studies of these hummocks are still rare as they are not as widely distributed as other geomorphological units. There are some studies mentioned similar patches, but these patches are usually limited in both distribution area and magnitude comparing to hummocky patches. These small patches are stated to form by biological effects, or spatial variations of sediment substrate, without accounting for the importance of dynamics in their formation processes. From the biological point of view, former studies show that microphytobenthos such as diatoms can stabilize sediment by secreting extracellular polymeric substances (EPS) during locomotion (Edgar, 1982; Hoagland et al., 1993understanding of the geomorphological), which act to increase the strength of interparticle bonding (Chenu and Guerif, 1991; Perkins et al., 2004; Gerbersdorf et al., 2008). These temporally and spatially heterogeneous diatom biofilms can form hummocky shaped diatom mats on intertidal flats (Boer, 1981; Grant et al., 1986; Underwood and Paterson, 1993). The magnitude of these diatom mats is usually limited to be 1–50 cm in magnitude and 0.5–3 cm in depth. From sediment substrate point of view, former studies show that sediment with different physical and chemical properties, such as water content, organic matter content, sand-silt proportion, significantly influence soil erosion resistance and thus play a dominant role in shaping geomorphology of tidal flats (Tolhurst et al., 2000b; Defew et al., 2002; Amos et al., 2004). But these studies did not explain how the spatial variations of substrate properties interact with understanding of the geomorphological geomorphology. As a specific tidal flat geomorphological features, hummocky patches are formed under the interactions of base sediment type, wave and tidal forces, biogenic activities and sediment supply (Meckel, 1975; Semeniuk, 1981). Therefore, in this study, we try to study the properties and formation mechanism of hummocky patches from a dynamic point of view based on long-term field measurement data.

A systematic understanding of the geomorphological behaviors of tidal flats requires better knowledge about physical processes involved, performance of geomorphological modelling techniques, interactions between substrate stability and geomorphology, and biological influences on bed composition in the different geomorphic units (French et al., 2016). At present, most sediment transport models ignore the spatial and temporal variabilities of sediment properties by applying empirical values (Black et al., 2002; Lundkvist et al., 2007), which may cause significant uncertainty on modeled sediment transport flux and predicted morphology (Murray et al., 2008). The most important reason to exclude mesoscale and microscale sediment properties in model is that there is very few information on the high-resolution soil erosion threshold data on tidal flats.

In this work, we study hummocky patches in tidal flat systems from the perspective of sediment dynamics with long-term measurement data. The main objective is to investigate the formation, distribution, and development mechanisms of patches in intertidal flats and the influence of biological activities on morphological evolution, based on 16 days of observation throughout a neap-spring tide cycle, including records of hydrodynamics, sediment transport, and morphology. Our analyses based on these detailed and systematic long-term data not only broadens our knowledge on the geomorphology of tidal flat systems, but also provides crucial clues for the development of more realistic models that can highly improve the predictive accuracy of sediment transport and morphological changes on tidal flats.

2 STUDY AREA

The study area is located along Jiangsu coast, China, on the west of the South Yellow Sea, and the north of the radial sand ridge system, between the Yangtze River Delta and the Abandoned Yellow River Delta (**Figure 2A**). Abundant sediment from the sand ridge system, Yangtze and Yellow River deltas, and strong tidal forces formed wide tidal flats along the Jiangsu coast with a fast progradation rate (Wang et al., 2012). The strata are composed of Tertiary and Quaternary sediments. Hydrodynamics in this area is mainly controlled by the interactions of the advancing tidal waves from the East China Sea and the rotating tidal waves from the Yellow Sea, and their shallow-water tidal components, forming semidiurnal tides with an average tidal range of 3.68 m, which belongs to mesotidal

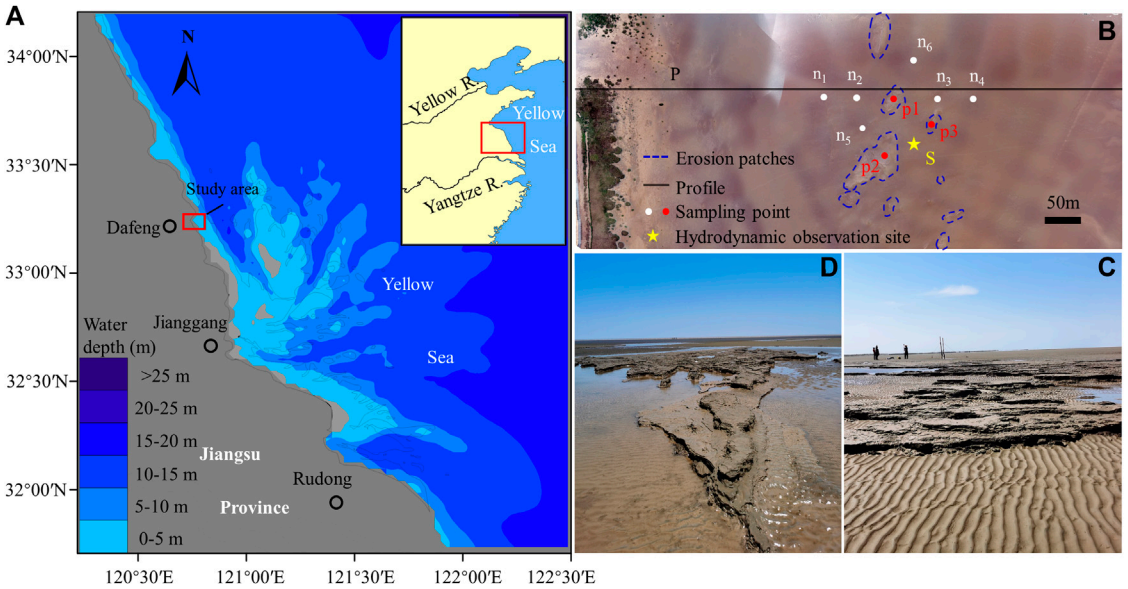

FIGURE 2 | Location of the study area and observation sites (red box). **(A)** Maps showing the study area located at Dafeng, Jiangsu, China. **(B)** Topographic map of the tidal flat taken by unmanned aerial vehicles, showing hummocky patches (bright color circled by a blue dash line), measuring profile P, sampling points n1–n6 (white dots on the tidal flat surfaces), p1–p3 (red filled dots on patches) and hydrodynamic observation site (S). A sediment core with a length of 30 cm was taken at sampling point p1. **(C)** and **(D)** show the morphological characteristics of hummocky patches (bright color circled by a blue dash line) distributed in the intertidal zone.

conditions (Li et al., 2007). The average wind speed is 4–5 m/s throughout the year, and the wind direction is dominated by NNE and ENE. Sheltered by the radial sand ridge system (**Figure 2A**), the maximum significant wave height in the study area is less than 2 m, and 85% of waves are less than 1 m (Jia et al., 2005).

The intertidal flat in our study area is a muddy flat with wide and smooth surface. Tidal creeks are less developed in this area. The intertidal flat is divided into three zones from land to sea based on elevation: 1) High tidal flat, located between mean high-level neap tide to mean high-level spring tide, where bed surface sediment is composed of silt and clayey silt, and seabed surface is covered by horizontal laminae; 2) Middle tidal flat, located between mean low-level neap tide and mean high-level neap tide, where bed surface sediment is composed of silt and fine sand. 3) Low tidal flat, located between mean low-level neap tide to mean low-level spring tide, where bed surface sediment is mainly composed of fine sand (Ke, 1993). Hummocky patches are distributed in high tidal zone and middle tidal zone (**Figure 2B**), and the magnitude of patches decreases landward. Our statistical analysis shows that patches in middle tidal flat usually present in the form of banded ridges and irregularly hummocky surfaces. The length of ridges exceeds 50 m and the height is about 25 cm. Hummocky patches is characterized by vertical laminae surfaces, whose horizontal scale is between 1–20 m and vertical scale is about 20 cm (**Figures 2C,D**). Patches in high tidal flat are less noticeable with horizontal scale of less than 5 cm, and vertical scale of less than 10 m. These patches have distinctive seasonal evolution pattern: they occur in summer and autumn but disappear in spring and winter (according to previous long-term field surveys in the study area and consultations with local fishermen).

3 MATERIALS AND METHODS

3.1 Field Measurements

We organized a field trip from 9th May to 26th May 2021 in the study area to investigate the mechanisms of formation and development of hummocky patches in tidal flat systems. The observation platform (S) was installed among patches to obtain hydrodynamic and sediment dynamic data (**Figure 3A**): water depth, wave height, and wave period were measured using an SBE 26 plus SEAGAUGE (Sea-Bird Electronics, United States; Washington, United States), and the instrument was set to collect 1,024 samples per burst, with a frequency of 4 Hz over a 256 s period. Three-dimensional turbulent velocity at 15 cm above seabed was monitored using a Vector Acoustic Doppler (ADVs, 6 MHz vector current meter, Nortek AS, Norway) with a burst interval of 5 min in autonomous deployment mode for 256 s at a frequency of 16 Hz. Turbidity at 15 cm above seabed was measured every 5 min using optical backscatter sensors of OBS-3A (D&A Instrument Company, United States) (**Figure 3B**). A bucket with volume of 50 L was set close to the platform to collect water samples for instrument calibration. At the same time, an anemometer was set up near the shore to record wind speed and direction.

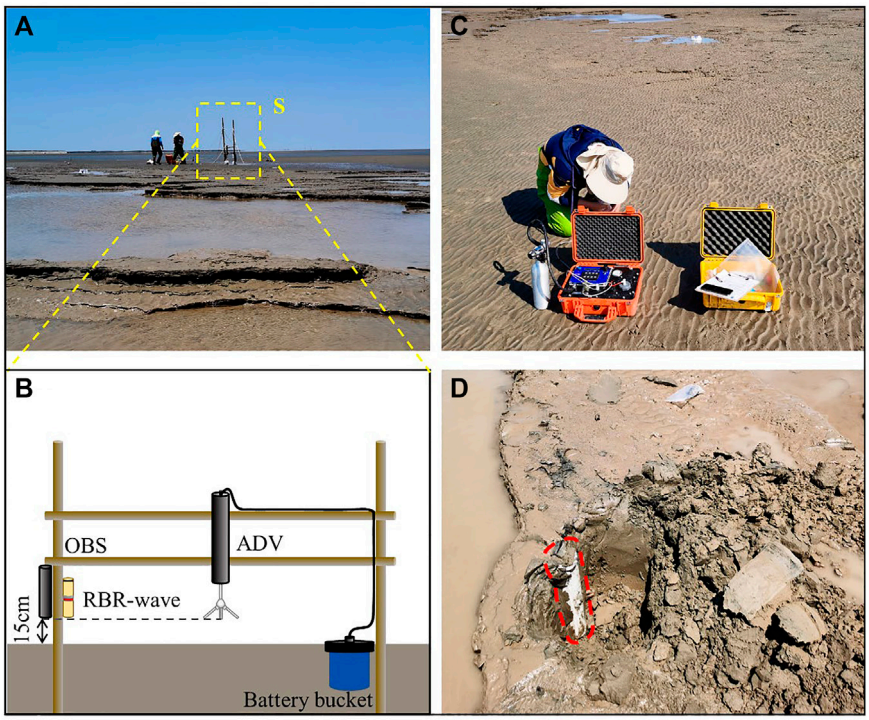

FIGURE 3 | Schematic and photograph of the observation platform and instruments deployed during field measurements. **(A)** Schematic diagram of the observation platform; **(B)** Photo of the instrument installation, all instrument sensors are deployed at 15 cm above the seabed; **(C)** Coherent strength meter (CSM) used to estimate seabed critical erosion shear stress; **(D)** Sediment core collected on a hummocky patch.

An RTK-GPS (Real Time Kinematic, STONEX Company, China) with a benchmark of mean sea level was used to measure elevation along the tidal flat from dyke to the lowest water level of the maximum spring tide, and the distance between neighboring points was approximately 5 m. Denser measurements (every 1 m) were carried out where surface topography changes sharply to obtain more detailed information on tidal flat profile. In addition, different sedimentary zones and boundaries of hummocky patches were recorded to better depict the geomorphological characteristics of tidal flats in the study area.

Sediment samples were collected and erosion thresholds were measured on hummocky patches and their surrounding flat surfaces. We collected three samples on patches (p1, p2, and p3) and six samples on the surrounding flat, which includes two landward samples (n1 and n2), two seaward samples (n3 and n4), one southwestward sample (n5) and one northeastward sample (n6). The distance between two adjacent points is approximately 30 m. The intensive sample points ensured we can depict changes of sediment properties in hummocky patch area. Surface sediment samples were collected at the nine points, and the critical erosion thresholds (kPa) of sediment were measured by a coherent strength meter (CSM, Partrac Ltd., UK) (**Figure 3C**), which was then converted into critical erosion shear stress (N/m^2). At the same time, a 30 cm sediment core was collected at p1 to analyze sediment properties along the vertical profile of a hummocky patch (**Figure 3D**).

3.2 Laboratory Analysis

The sediment core collected at station p1 was cut along a vertical profile using a core cutter made by GeoTek Company of the United Kingdom, and then sediment samples were taken with a 2 cm interval along the core (e.g., 0–2 cm, 2–4 cm, and 28–30 cm). In total, 15 samples were taken from the core, and nine sediment samples were collected at surrounding hummocky patch surface and smooth flat surface. All sediment samples were analyzed in the laboratory.

3.2.1 Sediment Grain Size

Particle size of 24 sediment samples was analyzed using a Mastersizer 2000 laser granulometer (Malvern Instruments Ltd.; measuring range of 0.02–2,000 μm; particle size resolution of 0.01 φ, reproducibility error of <3%). Sand (medium grain size (d_{50}) > 64 μm), silt (d_{50}: 4–64 μm), and clay (d_{50} < 4 μm) proportion were calculated based on the grain size analysis. Sorting coefficient of sediment (σ) was calculated by the Collias moment method with statistical significance (Zhu et al., 2019).

3.2.2 Water Content

Sediment samples were weighed and then dried at 50°C for 48 h in oven until their weights were stable. Water content (W) was determined as the ratio of wet mass minus dry mass to the total mass of sediment samples (Taki, 2000).

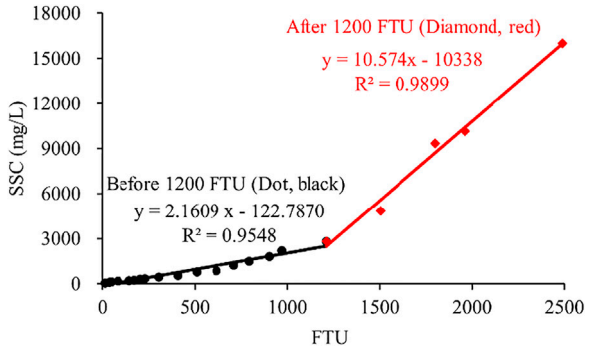

FIGURE 4 | Calibration curves used to convert optical turbidity (FTU, recorded by OBS) to suspended sediment concentration (SSC, mg/L). The trend varies significantly from low to high turbidity, according, we classify the data into two groups: the black line shows the calibration curve below 1,250 FTU, and the red line shows the calibration curve above 1,250 FTU.

3.2.3 Total Organic Carbon

Total Organic Carbon (TOC) of sediment samples were measured with an NCsoil element analyzer (Thermo scientific, United States). Inorganic carbon was first removed by adding HCl to sediment samples, and then these samples were sonicated, dried, freeze-dried, ground, packaged, and tested on the machine (Li et al., 2021).

3.2.4 Suspended Sediment Concentration Calibration

Water samples collected in field were used in the laboratory to reconstruct suspended sediment concentrations (SSCs, mgL^{-1}) with turbidity data (FTUs). As suspended sediment concentration (FTUs > 1,000) increases, more scattered light is absorbed by sediment before reaching the sensor of instrument. This leads to an increased slope in retrieving SSCs from FTUs (Liu et al., 2006), Therefore, we reconstructed SSCs from FTUs with two separate lines based on FTU values to better represent their relationship (**Figure 4**).

3.3 Data Analyses

3.3.1 Hydrodynamic Parameters Under Combined Wave-Current Conditions

Tides and waves are the main forces on tidal flats, which control hydrodynamics and sediment transport in tidal flat systems. In our study, wave- and current-induced bed shear stress are calculated separately, and the bed shear stress caused by current-wave interactions are then calculated with a wave-current interaction model.

The wave-induced shear stress is calculated as (Tucker and Pitt, 2001; Green and Coco, 2007):

$$\tau_w = \frac{1}{2}\rho_w f_w \hat{U}_\delta^2 \tag{1}$$

where ρ_w is density of seawater (kg/m^3), f_w is wave friction coefficient (related to the wave Reynolds number), and $\hat{U}_\delta$ is the peak orbital velocity (m/s).

Wave friction coefficient (f_w) is calculated as:

$$f_w = \begin{cases} 2Re_w^{-0.5}, & Re_w \le 10^5 \text{ (laminar)} \\ 0.0521Re_w^{-0.187}, & Re_w > 10^5 \text{ (smooth turbulent)} \\ 0.237r^{-0.52}, & \text{(rough turbulent)} \end{cases} \tag{2}$$

where Re_w [= $(\hat{U}_\delta \hat{A}_\delta)/\nu$] is wave Reynolds number (-), r (= $\hat{A}_\delta/ks$) is relative roughness (-), ks is Nicholas roughness coefficient (-), and ν is viscosity coefficient of seawater (m^2/s).

The peak value of wave orbital velocity ($\hat{U}_\delta$, m/s,)

$$\hat{U}_\delta = \omega \hat{A}_\delta = \frac{\pi \hat{A}_\delta}{T} \tag{3}$$

where ω (=π/T) is angular velocity (s^{-1}), $\hat{A}_\delta$ {=H/[2 sin (kh)]} is the peak value of the orbital excursion (-), and $\hat{U}_\delta$ is wave orbital velocity (m/s). H is significant wave height (m), h is water depth (m), k (=2π/L) is wave number (m^{-1}), L [=($gt^2/2\pi$) tanh (kh)] is wave length (m) and T is wave period (s).

Velocity data are processed by spectral analysis to eliminate the influence of waves on current. The Reynolds stress method is used for calculation (Tucker and Pitt, 2001; Green and Coco, 2007), and the expression is as follows:

$$\tau_c = \rho \overline{u'w'} \tag{4}$$

where ρ is seawater density (kg/m^3), based on Reynolds decomposition, $u = \bar{u} + u'$, u is horizontal velocity (m/s), $\bar{u}$ is average horizontal velocity (m/s) during the measurement period, representing the expectation value of u, and u' is fluctuations of velocity in horizontal direction (m/s); w' is fluctuations of velocity in vertical direction (m/s). $w = \bar{w} + w'$, w is vertical flow velocity (m/s), and $\bar{w}$ is average vertical flow velocity (m/s) during the measurement period.

The shear stress due to combined wave-current interactions is calculated by the Soulsby model (Soulsby and Clarke, 2005). First, the average bed shear stress (τ_m, N/m^2) is calculated under combined wave-current interactions:

$$\tau_m = \tau_c \left[1 + 1.2\left(\frac{\tau_w}{\tau_c + \tau_w} \right)^{3.2} \right] \tag{5}$$

Bottom shear stress under combined wave-current interaction ($\tau_{cw}, N/m2$) is calculated as:

$$\tau_{cw} = \sqrt{\left(\tau_m + \tau_w \left|\cos \varphi_{cw}\right|\right)^2 + \left(\tau_w \left|\sin \varphi_{cw}\right|\right)^2} \tag{6}$$

where φ is the angle between wave and tidal current directions (degree).

3.3.2 Critical Shear Stress for Erosion Measured by Coherent Strength Meter

Critical shear stress for erosion (τ_{ce}) is an important parameter that determines sediment movement. It is also an important input parameter in numerical modeling of sediment transport because it controls cohesive sediment entrainment (Tolhurst et al., 2000a; Black et al., 2001). Due to environmental complexity and interactions of multiple factors that control sediment erosion (e.g., grain size, clay content, TOC content, and water content), especially for areas with biological activities, the erosion threshold of cohesive sediment cannot be accurately calculated by existing

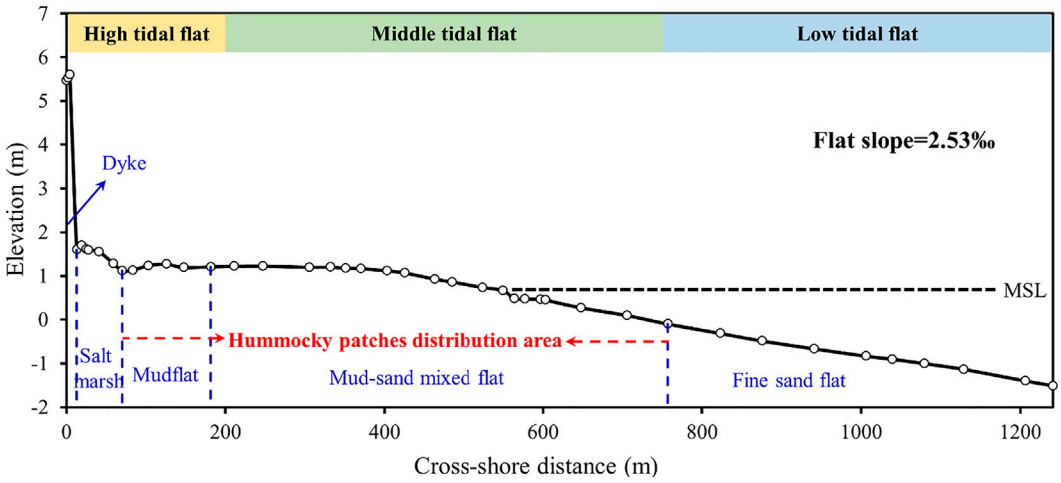

FIGURE 5 | Tidal flat cross-section elevation profile and slope based on measurement of RTK-GPS, showing four different sedimentary zones (blue font). Locations of hummocky patches are shown in red font. MSL, mean sea level.

formula. CSM is the state of art instrument to measure critical shear stress for erosion (Vardy et al., 2007).

The operation principle of CSM is that water is driven by air pressure to produce jet flow vertical to bed surface with increasing intensity. Bottom shear stress caused by water flow drives sediments to be eroded and suspended, changing the transmittance in the cabin. Therefore, rapid decline in transmittance indicates that external shear stress generated by the instrument is about the same magnitude of the erosion threshold of sediments at a certain depth (Parchure and Mehta, 1985; Tolhurst et al., 1999). This study defines a decrease in transmittance >5% as the threshold that critical shear stress for erosion is reached (Chen et al., 2012). CSM measurement data are recorded as a series of transmittance percentages and vertical flow jet pressures. The flow jet pressure (P, kPa) corresponding to the sudden change in transmittance is then transformed by a calibration function to obtain the critical erosion shear stress (τ_{ce}, N/m^2) of sediment at the field station.

4 RESULTS

4.1 Geomorphological Features of Intertidal Flat

The length of intertidal zone in our study area is approximately 1,250 m (the width of the tidal flat has significantly decreased due to land reclamation in recent years), and the general slope of the tidal flat is 2.53‰. The tidal flat has a sedimentological zonation pattern (**Figure 5**): the high flat has a length of ~170 m (10–180 m from dyke), where benthic animals, such as crabs and worms, are very active. The high flat consists of two different zones. The landward high flat (10–70 m) is occupied with a large number of *Spartina alterniflora* and the seaward flat (70–180 m) is bare mudflat. Because of the long exposure time, hexagonal cracks are often developed in this zone. The middle tidal flat is mainly mud-sand mixed bare flat located 180–760 m from the dyke, characterized by rapid morphological changes and rough surface. The low tide flat is a fine sand flat (of a distance of 760–1,250 m) located from the low tide level to the high tide level. Sediment is mainly composed of fine sand, with various flow marks and wavelet marks on the surface and staggered bedding development. The majorities of hummocky patches are distributed in the mud-sand mixed flat and mudflat. In the transition zone between middle and low tidal flat (580–680 m from the dyke), hummocky patches are well developed with horizontal magnitude of ~50 m and vertical magnitude of about 20 cm.

4.2 Hydrodynamic Settings

Our hydrodynamic observations among hummocky patches covered 31 tidal cycles in May 2021 (**Figures 6A-E**). Velocity data from ADV were missing from 15th to 16th May due to instrument fault (**Figure 6D**). During the observational period, the study area was dominated by northeastern and southeastern winds, with wind speed ranged from 0.1 to 13.1 m/s and mean wind speed of 4.0 m/s (temporal resolution of wind data was 1 min) (**Figure 6A**). Strong winds were observed from 16 to 17 May, with gust wind higher than 10 m/s. Our observation covered a spring and neap tide cycle, and water depth varied significantly, with tide ranges of approximately 1 m during neap and 1.6 m during spring. The maximum water depths of spring tide and neap tide were 1.66 and 0.94 m, respectively. Strong winds significantly influenced hydrodynamics on the tidal flat, during which the tidal range increased to 1.5 m for one neap tide.

The near bottom hydrodynamics control sediment resuspension, deposition, and seabed shaping. Near-bottom flow velocities measured by ADV (**Figure 6D**) showed significant fluctuations over time, consistent with tidal phase. Flow velocities during spring tides ranged from 0.05 to 0.25 m/s, which was much larger than that during neap tides (0.03–0.15 m/s, **Figure 6D**). Strong winds considerably increased current

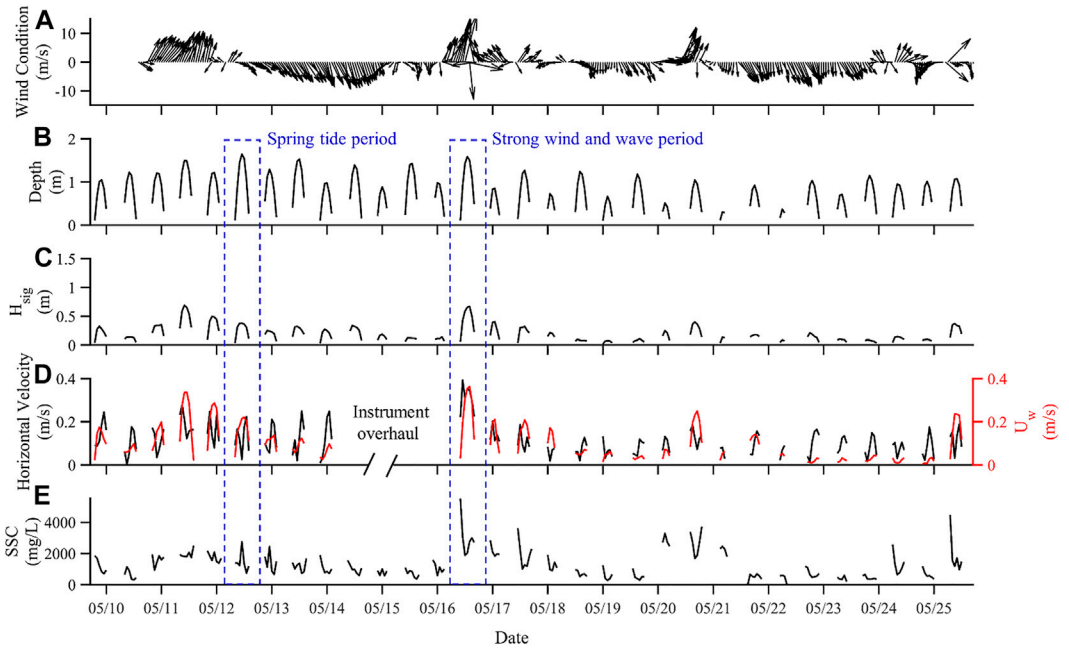

FIGURE 6 | Time series of hydrodynamics and suspended sediment concentrations in the study area: **(A)** wind speed and direction; **(B)** water depth; **(C)** significant wave height; **(D)** current velocity at 15 cm above the bottom (data on 15th May are lacking due to instrument overhaul); **(E)** suspended sediment concentration (SSC) at the observation site during 10–25 May 2021.

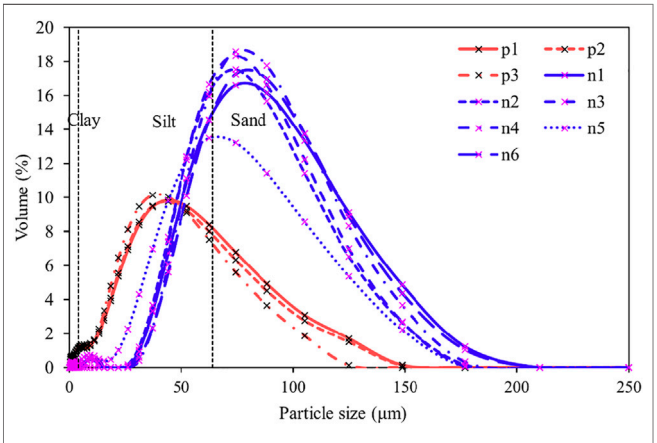

FIGURE 7 | Grain size distribution curve of sediment on erosion patterns (red lines) and surrounding tidal flat (blue lines).

velocity, and the maximum flow velocities (0.38 m/s) observed during the high wind event concurrently with neap tidal condition were larger than the maximum velocity of the spring tide (0.25 m/s).

Our study area is located in coastal shallow water zone, where waves are dominated by wind waves. In addition to wind, depth is another major limit for wave development on tidal flats, so observed waves were higher during spring tides with larger water depth than that during neap tides. During spring tidal condition, significant wave height was about 0.05–0.45 m. Significant wave height gradually decreased from spring tide to neap tide. During the strong wind period, the maximum significant wave height was close to 0.8 m (16th May) (**Figure 6C**). Wave orbital velocity (U_w) followed the same trend as significant wave height that decreased from spring to neap tides (**Figure 6D**).

4.3 Regional Sedimentary Characteristics of Hummocky Patches

Sediment properties of hummocky patches are quite different from that on surrounding tidal flat (**Figure 7**). Mud content of sediment on hummocky patches is higher than that on surrounding flat, and grain size (p1–p3) of sediment on hummocky patches [the median grain size of the samples (d50) is 49 μm] is generally smaller than that of the sediment on surrounding tidal flat (n1–n6, the median grain size of these samples is approximately 96 μm). Although all samples have a similar single-peak pattern of grain size distribution, the grain size curves of samples collected from hummocky patches are lower and flatter (the peak is located at 43 μm) than that collected from surrounding flat, which means the composition of sediment on hummocky patches is more diverse than surrounding flat (**Figure 7**).

The collected nine samples among hummocky patch area are mainly composed of sand (>64 μm) and silt (4–64 μm), the total content of which exceeds 90% (**Figure 7**). Significant differences are observed between hummocky patches and the surrounding flat. Sediment from hummocky patches is finer, with 81.71 ± 8.32% of silt and 10.05 ± 1.58% of clay. On the other hand,

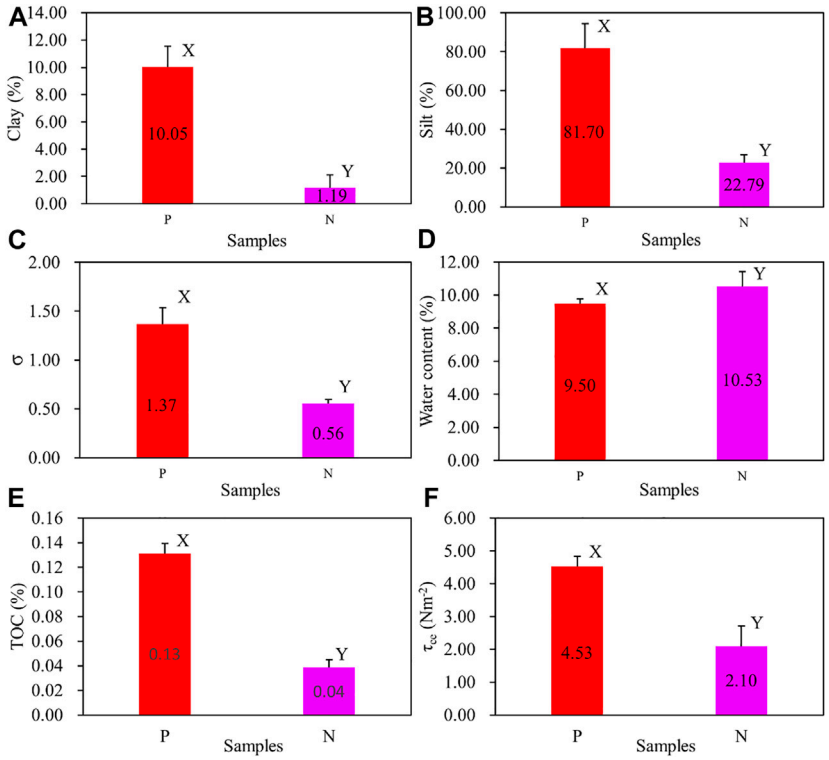

FIGURE 8 | Comparison of sediment properties between hummocky patches and surrounding areas. P represents the hummocky patches (red stripes), and N represents the surrounding flat (purple stripes). Error bars show the standard deviation of the EPS content. Letter (X or Y) on top of the bars denotes the results of the tests, indicating that there is a significant difference between sediment from hummocky patches and nearby seabed ($p < 0.001$).

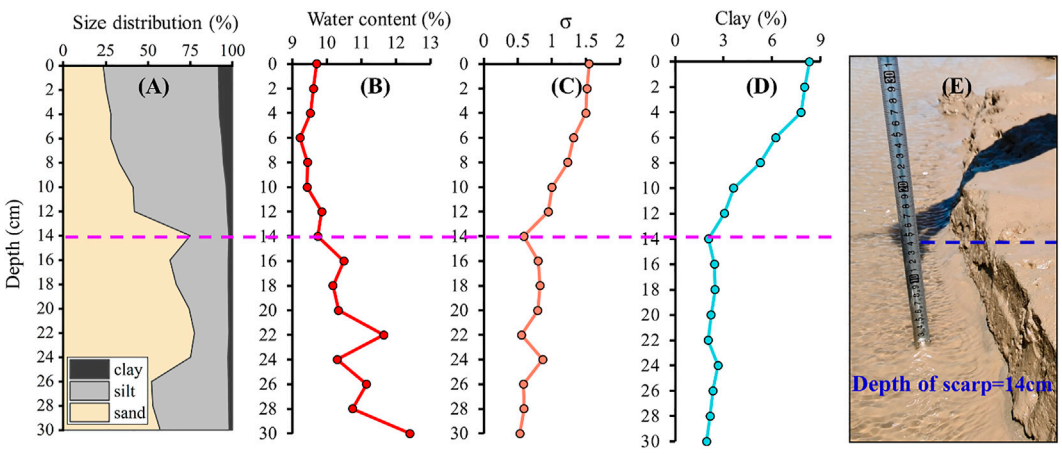

FIGURE 9 | Vertical profiles of sediment characteristics on hummocky patches, **(A)** grain size distribution of sediments, **(B)** water content, **(C)** sorting coefficient, **(D)** clay content, **(E)** field photo of hummocky patches, photographed on 15th May, showing the depth of erosion patch is around 14 cm (blue dash line). The purple dash line shows the boundary between upper and lower layers with remarkable differences in sediment properties.

sediment from the surrounding flat has 22.79 ± 3.15% of silt and 1.19 ± 0.65% of clay (**Figures 8A,B**). Sorting coefficient (σ) of hummocky patches sediment is about 2.5 times higher than that of smooth flat sediment (**Figure 8C**). Water contents of sediment samples from hummocky patches (9.5 ± 0.25%) are slightly lower than that from surrounding flat (10.53 ± 1.04%) (**Figure 8D**). Organic matter content and sorting coefficient of sediments from hummocky patches are significantly higher than those from the surrounding flat (approximately 3 times) (**Figure 8E**). Correspondingly, the erosion threshold of hummocky patches

TABLE 1 | Relevant research on factors affecting sediment erosion resistance.

Factor	Related parameters	Mechanism	Representative achievements
Physical factors	Particle size distribution	Uniform deposit is more easily eroded than the non uniform deposit.	Wiberg et al. (2015)
	Component content	When the seabed is dominated by muddy sediments (particle size ≤ 63.5 μm), the surface charge of sediments particles causes cohesive force between particles, thus making the substrate more stable.	Taki, (2000)
	Clay content	When the clay content =7%, it is defined whether the sediments mixture is viscous, that is, when the clay content >7%, the sediments have viscous and the substrate is more stable.	Van Ledden et al. (2004)
	Water content	For the newly formed muddy sediments layer, the lower the water content, the harder it is for the substrate deposit to erode.	Grabowski et al. (2011)
Biological factors	Organic matter	Sediments with organic matter content of less than 2% are most likely to be eroded. When the content of organic matter range 0%–10%, the erodibility of substrate deposit is negatively correlated with the content of organic matter.	Morgan, (2009)
	EPS	Extracellular polymeric substances (EPS) are an important component of sediments and their inner biofilm, which has a biological solidification effect on substrate sediments.	Grabowski et al. (2011)

is approximately 2.5 times higher than that of the surrounding flat (**Figure 8F**).

Sediment properties from the sediment core vary significantly in vertical profile, with 14 cm as a clear boundary between upper and lower layers. The hummocky patches are mainly composed of sand and silt (**Figures 9A,D**). Sand content tends to decrease from seabed surface to bottom sublayer, while silt content shows the opposite trend. Although clay content is comparatively low throughout the core, it is comparatively higher in the surface layer than that in the sublayer (**Figure 9D**). The water content of sediments at 0–14 cm from the surface remains relatively stable, which gradually increases and shows more fluctuation from 14 to 30 cm (**Figure 9B**). Sorting coefficient (σ) describes the extent of variance in particle size distribution in the way that the smaller the coefficient, the lower variance of the particle size, and it acts as a measure of the filling density between the sediments (Le Roux and Rojas, 2007), σ of sediment samples gradually decreases downward from 0 to 14 cm and becomes relatively stable from 14 to 30 cm (**Figure 9C**). Accordingly, we define the depth of the erosion patch to be ~14 cm (**Figure 9E**).

5 DISCUSSION

5.1 Formation Mechanism of Hummocky Patches

5.1.1 Erodibility of Substrate Sediments

Erosion and deposition of substrate sediment directly determine sediment transport and is a crucial factor in the formation of tidal flat geomorphological features (Brand et al., 2010). The erodibility of sediment determines whether and when seabed sediment will be suspended. It is controlled by multiple factors with complex interactions that are still poorly understood (Teisson et al., 1993).

In recent decades, a lot of research has been conducted on the influencing factors of substrate sediment erodibility (**Table 1**). In accordance with previous research, this study analyzes the spatial distribution of sediment erodibility from the perspective of physical processes and biological effects.

Our analysis shows that silt accounts for around 80% of sediments on hummocky patches, while clay accounts for around 10% (>7%, **Figures 8A,B**). According to previous research (Van Ledden et al., 2004), high content of cohesive sediment on hummocky patches can largely increase the stability of seabed. The sorting coefficient of sediment on hummocky patches is much larger than that on the surrounding flat (approximately 3 times), which indicates that the particle grain size distribution of sediment on hummocky patches is less uniform compared to the surrounding flat. Under this condition, fine sediment particles are filled in the gaps between coarse particles, resulting in a denser sediment mixture and a more stable surface (Rogers and Head, 1961). It has been reported that water content directly affects the mechanical properties of cohesive sediments in the way that water reduces the erosion threshold of sediment (Shi et al., 2018). Water content of sediment samples from hummocky patches is slightly lower than that from nearby seabed sediment, in favor to increase erosion threshold of substrate sediment. Analysis of physical properties of substrate sediment shows that hummocky patches should be more difficult to erode than surrounding areas, consistent with our result from CSM measurement.

Biological impacts on erosion resistance of substrate sediment mainly refer to biological disturbance and biological solidification. Biological disturbance causes a slight change in surface roughness, but its impact on erosion resistance is insignificant. Biological solidification is caused by the extracellular polymeric substances (EPS) secreted by organisms which can largely solidify sediments. Winterwep and Van Kesteren (2004) claimed that biological activity brings to the substrate an abundance of organic matter (quantified by the value of TOC), and many components of organic matter are bio-adhesive. Besides, biological activities also produce a variety of organic debris and organic colloids (EPS) through biological

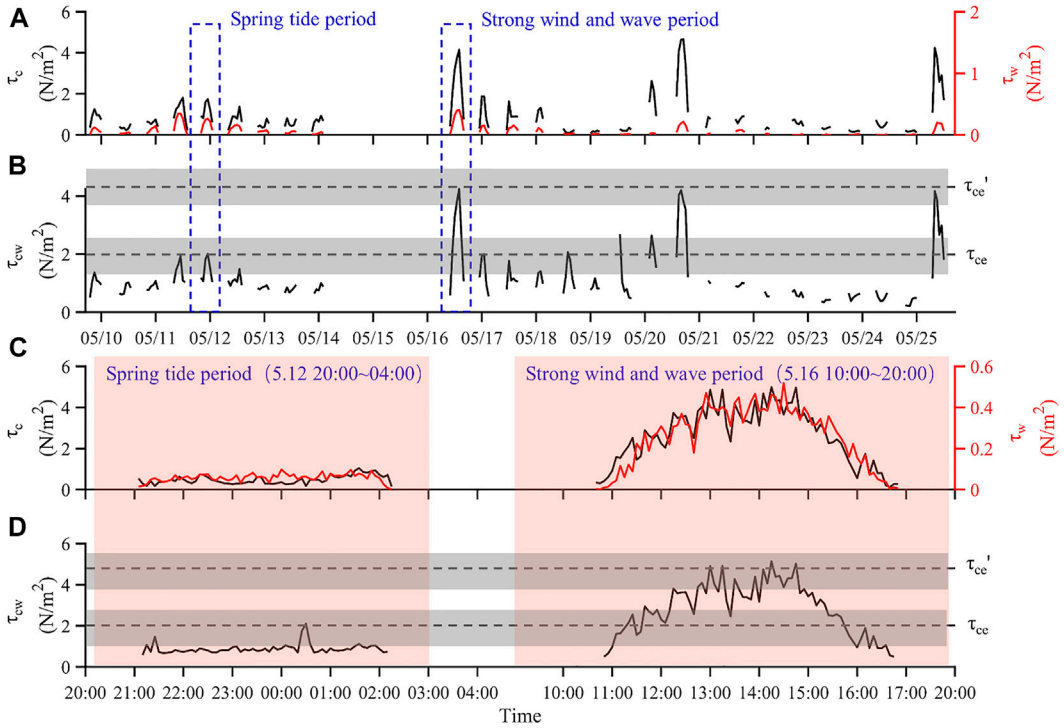

FIGURE 10 | Time series of bed shear stress and critical erosion shear stress of substrate. **(A)** and **(B)** show the time series of wave-induced shear stress τ_w, current-induced shear stress τ_c, and wave-current combined shear stress τ_{cw} throughout the whole observation period, **(C)** and **(D)** show the time series of wave-induced shear stress τ_w, current-induced shear stress τ_c, and wave-current combined shear stress τ_{cw} during the spring tides and strong winds, respectively. τ_{ce} and τ_{ce}' are the average values of the critical erosion shear stresses of the smooth flat and hummocky patches, and the gray strips are the range of τ_{ce} and τ_{ce}'.

metabolism, which makes sediments more difficult to be eroded. EPS can be secreted by many kinds of organisms which is difficult to quantify, therefore, organic matter content is used to illustrate the influence of biological activities on sediment erodibility (Winterwerp and Van Kesteren, 2004). The TOC content of the substrate sediment from hummocky patches is remarkably higher than that of the surrounding flat (approximately 3 times), which largely increases the erosion threshold of hummocky patches.

The physical characteristics and the influences of biological activities both favor to increase the erosion threshold of sediment on hummocky patches. Under periodical hydrodynamics, sediment that are susceptible to erosion are removed, while sediment that are more resistant to erodibility are kept, which eventually leads to the formation of hummocky patches. Hence, the spatial variations in erosion resistance of substrate sediments provide the fundamental condition for the formation of hummocky patches.

5.1.2 Hydrodynamics

Waves, currents, and their interactions are the dominant forces shaping tidal flat topography. Wave-induced shear stress (τ_w), flow-induced shear stress (τ_c), and wave-current combined shear stress (τ_{cw}) are used to evaluate the importances of different forces. The shear resistance of sediment shows the susceptibility of sediment to erosion (Shi et al., 2014), which is usually represented by erosion threshold or critical shear stress for erosion (τ_{ce}). When bed shear stress is lower than this threshold ($\tau_{cw} < \tau_{ce}$), no erosion or little erosion occurs, but once it exceeds this value, the amount of erosion increases significantly (Panagiotopoulos et al., 1997; Zhu et al., 2014). Because the duration of *in-situ* observations is relatively long (16 days), we calculated shear stress caused by currents, waves, and current-wave interactions by averaging shear stress every 12 bursts (1 h) to show the temporal changes of bed shear stress over time. The temporal variations of bed shear stress showed a clear trend with spring-neap tidal cycle, indicating the dominance of bed shear stress by tidal currents. Several peaks appeared over time, in response to storm events (16th May, 20th May, and 25th May). However, the relationship between τ_{ce}' (the critical erosion shear stresses of hummocky patches) and τ_{cw} was unclear during strong wind periods as the bed shear stress data were averaged hourly (**Figures 10A,B**). Therefore, we chose two representative time periods (**Figures 10C,D**), one during a spring tide with low winds and the other during a neap tide but dominated by strong winds and waves, to analyze the detailed hydrodynamics and morphodynamics with burst-averaged shear stress (every 5 min).

During our observation period, wave-induced shear stress ranged from 0.1 to 0.8 N/m^2, and current-induced shear stress ranged from 0.2 to 4.3 N/m^2 (**Figure 10C**). Wave-current combined shear stress τ_{cw} ranged from 0.3 to 4.6 N/m^2, and the critical shear stresses for erosion of smooth tidal flat (τ_{ce}) and

TABLE 2 | Substrate erosion thresholds calculated using two different equations based on physical properties of the sediment, compared to that measured with CSM on other tidal flats around the world.

	Formula calculation		CSM field measurements		
Method	**Formula 1** Chen et al. (2018)	**Formula 2** Guo (2020)	Skeffling mudflat, (UK)	Westerschelde Estuary (Netherlands)	Yellow River Delta (Germany)
Critical erosion shear stress (N/m^2)	0.8 (smooth seabed) 1.7 (patches)	0.4 (smooth seabed) 1.1 (patches)	0.5–2.8 Paterson et al. (2000)	1.2–8.2 Houwing (1999)	0.1–5.8 Meng et al. (2012)

erosion patches (τ_{ce}') are 0.9–2.7 N/m^2 and 3.8–5.1 N/m^2 (**Figure 10D**), respectively. Based on our calculation of near-bed shear stress and erosion threshold of bed sediment, three situations occur: 1) $\tau_{cw} < \tau_{ce}$, seabed sediment are not eroded. 2) $\tau_{ce} < \tau_{cw} < \tau_{ce}'$, high near-bed shear stress causes erosion of tidal flat, but hummocky patches remain steady. It is an important step for the formation of hummocky patches. 3) $\tau_{cw} > \tau_{ce}'$, under this condition, both hummocky patches and surrounding flat are eroded, and hummocky patches start to die out. The durations of condition two and three determine the development extent of hummocky patches.

During our 16 days observation, the near-bed shear stress caused by current and waves was less than the erosion threshold of hummocky patches ($\tau_{cw} < \tau_{ce}'$) for most of the time (12 days) (**Figure 10B**), therefore, the geomorphological features of hummocky patches were basically unchanged (the geomorphological changes caused by seabed scouring and siltation in a short period of time can be ignored). Our study shows that tides alone cannot form hummocky patches. Even in the spring tide stage, the near-bed critical shear stress caused by tidal current is less than the erosion threshold of seabed sediment on hummocky patches. During the three strong wind events (16th May, 20th May, and 25th May), the critical shear stress caused by wave-current interactions is high enough to erode sediment from smooth tidal flat surface, but unable to erode sediment from hummocky patches, in favor to the formation of hummocky patches (**Figure 10B**). The height of hummocky patches is determined by the duration of high shear stress, and soil erodibility of surrounding tidal flat (Amos et al., 1997; Sanford, 2008). Due to the spatial variations in surface sediment erosion resistance, the place where sediment have a smaller erosion threshold are removed during strong wind events. As soil strength increases downward due to soil consolidation, erosion declines downward and stops at a depth where $\tau_{cw} = \tau_{ce}$, which determines the height of residual hummocky patches. The maximum height of hummocky patches observed in our study area was approximately 20 cm. Even during the strongest wind event (16th May), the duration when bed shear stress caused by wave-current interactions was larger than the erosion threshold for hummocky patches lasted for less than 2 h (**Figure 10D**), so no evident elevation changes occurred on hummocky patches. Therefore, we infer that hummocky patches can be preserved under conventional hydrodynamics. In summary, the formation and preservation of patches are highly related to hydrodynamic intensity and duration, which explains the seasonal evolution of patches in tidal flats. Winter time is characterized by frequent high-energy storm events (Chang et al., 2006), which cause resuspension of deposited muds and patches break-up. Hence, hummocky patches on intertidal flat tend to appear under weak dynamic conditions in summer and autumn.

Tidal flat substrate erosion resistance is controlled by multiple factors (e.g., biological effects, sediment properties, chemical factors, etc.) and their interactions, while their importances on determining soil erosion threshold are still unknown (Tolhurst et al., 2002). At present, there is no direct way to calculate critical erosion stress of cohesive sediments with one or more measured parameters. CSM serves as an excellent tool to estimate the erosion thresholds of sediment influenced by complex factors *in-situ* as it is easy to operate and produces reliable results to estimate critical shear stress for soil erosion. However, as CSM utilizes a water jet vertical to sediment surface to estimate the critical shear stress of sediment layers, it has been argued that CSM cannot measure the realistic horizontal shear stress of soil (Tolhurst et al., 2000a; Grabowski et al., 2010). In addition, no uniform standards exist to convert CSM data into erosion thresholds (Watts et al., 2003). Therefore, the values of critical shear stress estimated from CSM may not be quantitatively accurate. However, multiple former studies have shown that CSM is useful in comparing relative erosion thresholds over different types of beds (Tolhurst et al., 1999; Tolhurst et al., 2006). Other than CSM, erosion threshold of soil can be estimated using mainstream formulas based on sediment parameters (**Table 2**). Two different formulas were used to calculate the critical erosion thresholds of sediment on hummocky patches and surrounding tidal flat and we found that the calculated values from the formula are much lower than the measured value of CSM (**Table 2**). The deviation may be related to biological activities as neither of the two formulas taken into account the influence of biological activities on sediment strength. Previous studies have shown that biological activities, such as fecal particle production, and mucus production, can largely change the physical characteristics of surface sediments, thus increasing the erosion threshold of seabed sediment by more than 10 times (Widdows et al., 1998). The maximum values of bed shear stress measured by CSM in other tidal flat areas reach more than 5 N/m^2 (**Table 2**), which are also related to biological activities. Without accounting for biological effects, the erosion thresholds calculated from formulas are much less than the measured bed shear stress caused by wave-current interactions. We infer that the accurate critical erosion shear stress of cohesive sediments with active biological activities can only be obtained by field measurements, therefore, the results from CSM observation are more reliable. Previous studies show that the critical erosion threshold of substrate sediments in the salt marsh zone of this

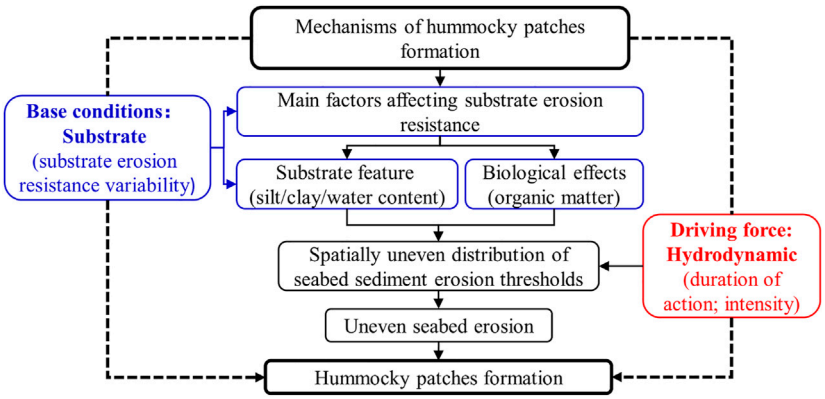

FIGURE 11 | Conceptual model of hummocky patches formation mechanism.

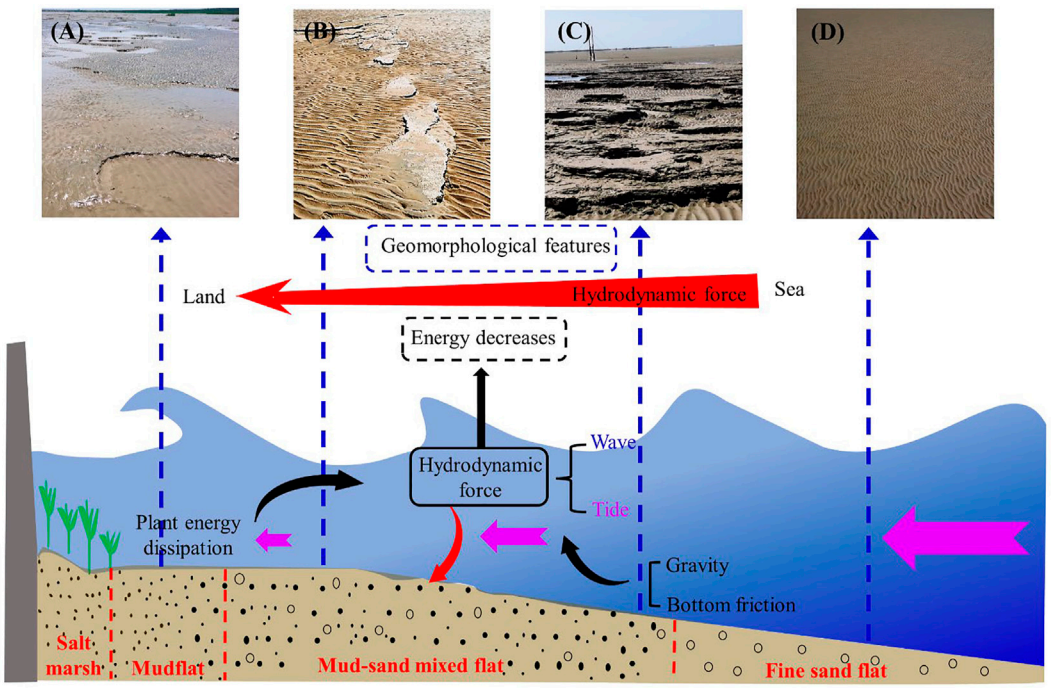

FIGURE 12 | Conceptual model of hummocky patches distribution mechanism. The hydrodynamic forces in the tidal flat are mainly tidal currents (pink arrow) and waves. The attenuation of hydrodynamic forces propagating ashore is represented by changes in the size of the tidal current arrow and the shape of the water surface wave. The hydrodynamic forces (red arrow) act on the flat surface and cause the zonation of the tidal flat (red font). **(A–D)** represent the geomorphological features of the hummocky patches distributed from land to sea in the tidal flat.

study area ranges from 0.3 to 0.4 N/m^2 based on CSM measurement (Chen et al., 2020), much smaller than our results, this may due to the dissipative and trapping effects of salt marsh that allow the settling of fine-grained sediments (sediment fraction is relatively homogeneous), resulting in a small critical erosion threshold.

In summary, the above results indicated that the uneven spatial distribution of erosion threshold caused by physical characteristics of sediments and biological activities provide the foundation of patches formation, while hydrodynamics is the crucial driving force in determining the development, distribution, and destruction of hummocky patches (**Figure 11**).

5.2 Distribution and Causes of Hummocky Patches

Hummocky patches mainly appear in the middle of intertidal zone (middle tidal zone, **Figure 12**), which is caused by two facts:

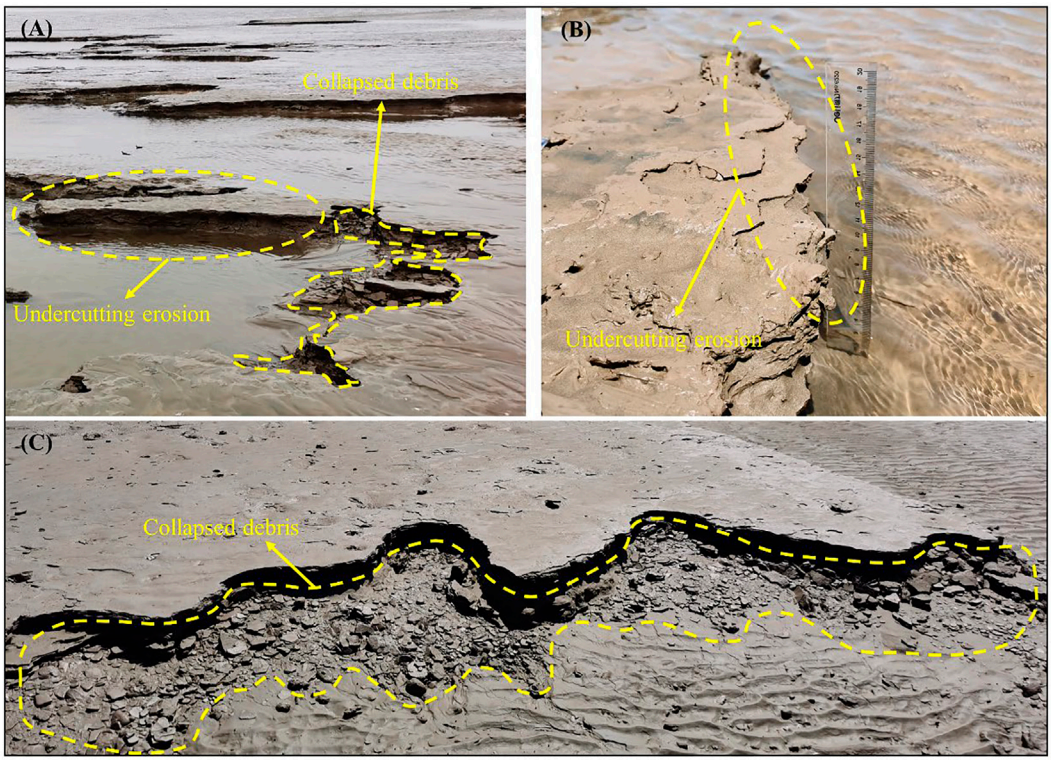

FIGURE 13 | Erosion and collapse phenomena appear during the development of hummocky patches. **A-C** are three well-developed patch units in the middle tidal zone, respectively. **A** clearly shows the developmental pattern of undercutting erosion and upper sediment debris collapse of the patch; **B,C** show the undercutting erosion and debris collapse stages of the patch during development, respectively.

1) Biological effects of the middle tidal zone favors the formation and development of hummocky patches. Organic matter produced by biological activities and EPS produced by decomposition highly increases the seabed resistance to erosion. 2) Hydrodynamics are the fundamental reason for the zonation of sediments on flat surfaces, which attenuates from low to high tidal flat (Shi et al., 2014). Accordingly, the contribution of suspended sediment to substrate increases. The surface sediment of the low tidal zone mainly come from bed loads, while the surface sediment of the high tidal zone mainly come from suspended sediment. The middle tide zone is a transitional area where substrate sediment consist of both suspended and bed loads including mud and sand (Yang et al., 2017). The uneven distribution of mud-sand mixed sediment increases soil density and strength, in favor to form hummocky patches. In the low tidal zone, hydrodynamic force is relatively strong where only coarse-grained sediment can be settled, resulting in comparatively uniform fine sand sediment on seabed. In addition, there are few biological activities in the low tidal zone of the intertidal flat. Therefore, the lower tidal flat cannot provide necessary conditions for the formation of hummocky patches (**Figure 12D**). In the upper part of the tidal flat (high tidal zone), biological activities in favor to form sediment with high resistance to erosion. However, due to the weak hydrodynamic condition, geomorphological features cannot be fully developed, so we observed pitches with a very small erosion depth (approximately 1 cm) in this zone (**Figure 12A**). Similarly, due to the attenuation of hydrodynamic intensity, the eroded landform cannot be fully developed on the shore side of the middle tidal flat (**Figure 12B**). Therefore, the lower part of middle tidal zone provides the best conditions for the formation of hummocky patches, where hummocky patches can be fully developed and the geomorphological features are remarkable (**Figure 12C**).

5.3 Development and Extinction of Hummocky Patches

The analysis of sediment from sediment cores shows that sediment properties of hummocky patches vary significantly downwards from the surface layer with a clear boundary at around 14 cm (**Figure 9**), consistent with the height of hummocky patches (14 cm). According to **Section 5.1**, four sedimentary parameters (σ, clay content, water content, and particle size distribution) are the most important factors affecting erosion resistance of sediments. The vertical variations of these parameters show that erosion resistance is gradually weakened downward (surface sediment is hardest and bottom sediment is the weakest), which determines the development pattern of hummocky patches. Sediment in the lowest part of hummocky patches will be eroded first, while surface sediment which are highly resistant to erosion, are stable

over time. This process leads to the hollowing structure of patches. With continuous hollowing of the bottom layer, the upper part of patches that are not easily eroded collapse, usually in the form of blocks, forming uneven surface on hummocky patches. These blocks are difficult to be transported and usually seen at the edge of patches (**Figures 13A-C**).

One thing worth noting is that there are some inconsistencies between our results and former studies. For example, it has been found that water content largely affects the mechanical properties of cohesive sediments, which is the primary cause for the changes in critical erosion shear stress. However, our results showed that those hummocky patches have a high erosion resistance (2–3 times) compared with the surrounding flat, mainly due to sediment composition and biological effects, while water content was similar between hummocky patches and surrounding flat. We infer that the comparative importance of water content in controlling erosion resistance reduces when there are large spatial variabilities in sediment property and biological activities. The evolution of hummocky patches is the result of long-term mutual coupling of sediment properties and hydrodynamics. During the 16-day observation, hummocky patches survived a spring tide and several wind events, with slight erosion and collapse incidents. Therefore, we did not observe the development and extinction processes of hummocky patches. We planned to investigate the evolution of hummocky patches under a longer time period and extreme dynamic conditions to quantitative evaluate sediment characteristics on critical erosion shear stress under different hydrodynamic conditions (especially extreme events) in our future work.

6 CONCLUSION

In this study, we observed a new mesoscale geomorphological unit on sand-mud mixed middle tidal flat zone, which we defined as hummocky patches. We investigated the formation, distribution, and development mechanisms of these hummocky patches from the perspective of sedimentary dynamics with field measurement data. We obtained the following conclusions:

1) The formation, distribution, and development of patches in the tidal flat are mainly influenced by the combination of hydrodynamics, sediment characteristics, and biological effects. The spatial variations in substrate sediment properties, including median grain size, mud content, water content, sorting coefficient, and organic matter content determine erosion threshold of sediment, providing the foundation for the formation of hummocky patches. Among these factors, organic matter content largely reflects the importance of biological activities while other factors are mainly controlled by the hydrodynamic condition of tidal flats. Hummocky patches are characterized with smaller median grain size with diverse sediment composition, higher mud and organic content, comparing to surrounding flat. All these features favor to form higher erosion threshold on hummocky patches. However, water content is similar between hummocky patches and surrounding flat, distinctive from other studies that water content largely controls sediment erosion thresholds on tidal flats. Our results shown that diverse sediment composition and biological activities are two main factors that also significantly affect sediment erosion thresholds, other than water content.
2) Hydrodynamic conditions drive the formation, distribution, and development of hummocky patches. Since the erosion threshold of seabed sediment varies spatially, sediment in areas with smaller erosion threshold are eroded first, while sediment in areas with larger erosion threshold are kept, forming hummocky patches. As soil erosion threshold increases downward due to soil consolidation, the vertical depth of hummocky patches is limited. The maximum depth of hummocky patches observed in this study was 20 cm. In general, the formation of hummocky patches requires a certain extent of hydrodynamic force and substrate soil with large cohesion. The gradual attenuation of hydrodynamic intensity shoreward with increased biological activities result in a higher degree of patch development and more distinguished geomorphic features in the middle tidal flat.
3) Sediment properties along vertical profile of hummocky patches are analyzed, showing a clear boundary at 14 cm from flat surface, which is defined as the depth of the hummocky patch. Mud content and sorting coefficient decreases from surface to bottom, while sediment median grain size and water content increase, indicating a decreasing trend of erosion threshold downward, which controls the extinction pattern of hummocky patches. Due to the small erosion threshold, bottom sediment of patches is weakest and eroded in the first place, while the upper part of the patches is stable over time. The gradual erosion of bottom sediment decreases supporting force for surface sediment on hummocky patches, finally leading to collapse of sediment from surface layer, forming sediment debris.

DATA AVAILABILITY STATEMENT

The original contributions presented in the study are included in the article/Supplementary Material, further inquiries can be directed to the corresponding authors.

AUTHOR CONTRIBUTIONS

The contributions made by each of the authors are listed as follows: 1) YW and FX put forward the idea, designed the experiments and funded the study. 2) SZ processed the main measurements/experiments data and completed the major sections of the manuscript. 3) YC helped making general changes and improvements to the article. 4) WY helped

providing partial data and processing data. 5) RL, ML, and BS reviewed this article and made suggestions to improve it.

FUNDING

This study was financially supported by the Jiangsu Special Program for Science and Technology Innovation (JSZRHYKJ202006), the Young Scientists Fund of National Natural Science Foundation of China (42006149), the Open Fund of East China Coastal Field Scientific Observation and Research Station, Ministry of Natural Resources (ORSECCZ2022205), the Program for Scientific Research Start-up Funds of Guangdong Ocean University under contract No. 060302112010, Urban Geological Survey Project of Lianyungang (20170821).

ACKNOWLEDGMENTS

We are also grateful to Dezhi Chen, Chao Gao, Yupeng Pan, Jing Tian, and Jianxiong Sun who participated in the field work.

REFERENCES

Allen, J. R. L. (1980). Sand Waves: a Model of Origin and Internal Structure. *Sediment. Geol.* 26 (4), 281–328. doi:10.1016/0037-0738(80)90022-6

Amos, C. L., Feeney, T., Sutherland, T. F., and Luternauer, J. L. (1997). The Stability of Fine-Grained Sediments from the Fraser River Delta. *Estuar. Coast. Shelf Sci.* 45 (4), 507–524. doi:10.1006/ecss.1996.0193

Amos, C., Bergamasco, A., Umgiesser, G., Cappucci, S., Cloutier, D., DeNat, L., et al. (2004). The Stability of Tidal Flats in Venice Lagoon—The Results of In-Situ Measurements Using Two Benthic, Annular Flumes. *J. Mar. Syst.* 51 (1-4), 211–241. doi:10.1016/j.jmarsys.2004.05.013

Besio, G., Blondeaux, P., and Vittori, G. (2006). On the Formation of Sand Waves and Sand Banks. *J. Fluid Mech.* 557, 1–27. doi:10.1017/s0022112006009256

Black, K. S., Sun, H., Craig, G., Paterson, D. M., Watson, J., and Tolhurst, T. (2001). Incipient Erosion of Biostabilized Sediments Examined Using Particle-Field Optical Holography. *Environ. Sci. Technol.* 35 (11), 2275–2281. doi:10.1021/es0014739

Black, K. S., Tolhurst, T. J., Paterson, D. M., and Hagerthey, S. E. (2002). Working with Natural Cohesive Sediments. *J. Hydraul. Eng.* 128 (1), 2–8. doi:10.1061/(asce)0733-9429(2002)128:1(2)

Blanton, J. O., Lin, G., and Elston, S. A. (2002). Tidal Current Asymmetry in Shallow Estuaries and Tidal Creeks. *Cont. Shelf Res.* 22 (11-13), 1731–1743. doi:10.1016/s0278-4343(02)00035-3

Boer, P. L. (1981). Mechanical Effects of Micro-organisms on Intertidal Bedform Migration*. *Sedimentology* 28 (1), 129–132. doi:10.1111/j.1365-3091.1981.tb01670.x

Brand, A., Lacy, J. R., Hsu, K., Hoover, D., Gladding, S., and Stacey, M. T. (2010). Wind-enhanced Resuspension in the Shallow Waters of South San Francisco Bay: Mechanisms and Potential Implications for Cohesive Sediment Transport. *J. Geophys. Res. Oceans* 115 (C11). doi:10.1029/2010jc006172

Chang, T. S., Joerdel, O., Flemming, B. W., and Bartholomä, A. (2006). The Role of Particle Aggregation/disaggregation in Muddy Sediment Dynamics and Seasonal Sediment Turnover in a Back-Barrier Tidal Basin, East Frisian Wadden Sea, Southern North Sea. *Mar. Geol.* 235 (1-4), 49–61. doi:10.1016/j.margeo.2006.10.004

Chen, Y., Thompson, C. E. L., and Collins, M. B. (2012). Saltmarsh Creek Bank Stability: Biostabilisation and Consolidation with Depth. *Cont. Shelf Res.* 35, 64–74. doi:10.1016/j.csr.2011.12.009

Chen, D., Wang, Y., Melville, B., Huang, H., and Zhang, W. (2018). Unified Formula for Critical Shear Stress for Erosion of Sand, Mud, and Sand-Mud Mixtures. *J. Hydraul. Eng.* 144 (8), 04018046. doi:10.1061/(asce)hy.1943-7900.0001489

Chen, D., Li, M., Zhang, Y., Zhang, L., Tang, J., Wu, H., et al. (2020). Effects of Diatoms on Erosion and Accretion Processes in Saltmarsh Inferred from Field Observations of Hydrodynamic and Sedimentary Processes. *Ecohydrology* 13 (8), e2246. doi:10.1002/eco.2246

Chenu, C., and Guérif, J. (1991). Mechanical Strength of Clay Minerals as Influenced by an Adsorbed Polysaccharide. *Soil Sci. Soc. Am. J.* 55 (4), 1076–1080. doi:10.2136/sssaj1991.03615995005500040030x

Dawkins, C. J. (1939). Tussock Formation by Schoenus Nigricans: the Action of Fire and Water Erosion. *J. Ecol.* 27 (1), 78–88. doi:10.2307/2256301

Defew, E. C., Tolhurst, T. J., and Paterson, D. M. (2002). Site-specific Features Influence Sediment Stability of Intertidal Flats. *Hydrol. Earth Syst. Sci.* 6 (6), 971–982. doi:10.5194/hess-6-971-2002

Dott, R. H., Jr, and Bourgeois, J. (1982). Hummocky Stratification: Significance of its Variable Bedding Sequences. *Geol. Soc. Am. Bull.* 93 (8), 663–680. doi:10.1130/0016-7606(1982)93<663:hssoiv>2.0.co;2

Edgar, L. A. (1982). Diatom Locomotion: a Consideration of Movement in a Highly Viscous Situation. *Br. Phycol. J.* 17 (3), 243–251. doi:10.1080/00071618200650261

French, J., Payo, A., Murray, B., Orford, J., Eliot, M., and Cowell, P. (2016). Appropriate Complexity for the Prediction of Coastal and Estuarine Geomorphic Behaviour at Decadal to Centennial Scales. *Geomorphology* 256, 3–16. doi:10.1016/j.geomorph.2015.10.005

Gao, S. (2009). Modeling the Preservation Potential of Tidal Flat Sedimentary Records, Jiangsu Coast, Eastern China. *Cont. Shelf Res.* 29 (16), 1927–1936. doi:10.1016/j.csr.2008.12.010

Gao, S. (2019). "Geomorphology and Sedimentology of Tidal Flats," in *Coastal Wetlands* (Elsevier), 359–381. doi:10.1016/b978-0-444-63893-9.00010-1

Gardel, A., Proisy, C., Lesourd, S., Philippe, S., Caillaud, J., Gontharet, S., et al. (2009). A Better Understanding of Mud Cracking Processes Gained from *In Situ* Measurements on an Intertidal Mudflat in French Guiana. *J. Coast. Res.* SI (56), 424–428. doi:10.2307/25737611

Gerbersdorf, S. U., Manz, W., and Paterson, D. M. (2008). The Engineering Potential of Natural Benthic Bacterial Assemblages in Terms of the Erosion Resistance of Sediments. *FEMS Microbiol. Ecol.* 66 (2), 282–294. doi:10.1111/j.1574-6941.2008.00586.x

Grab, S. (1997). Thermal Regime for a Thufa Apex and its Adjoining Depression, Mashai Valley, Lesotho. *Permafr. Periglac. Process.* 8 (4), 437–445. doi:10.1002/(sici)1099-1530(199710/12)8:4<437::aid-ppp264>3.0.co;2-o

Grabowski, R. C., Droppo, I. G., and Wharton, G. (2010). Estimation of Critical Shear Stress from Cohesive Strength Meter-Derived Erosion Thresholds. *Limnol. Ocean. Methods* 8 (12), 678–685. doi:10.4319/lom.2010.8.678

Grabowski, R. C., Droppo, I. G., and Wharton, G. (2011). Erodibility of Cohesive Sediment: The Importance of Sediment Properties. *Earth-Science Rev.* 105 (3-4), 101–120. doi:10.1016/j.earscirev.2011.01.008

Grant, J., Bathmann, U. V., and Mills, E. L. (1986). The Interaction between Benthic Diatom Films and Sediment Transport. *Estuar. Coast. Shelf Sci.* 23 (2), 225–238. doi:10.1016/0272-7714(86)90056-9

Green, M. O., and Coco, G. (2007). Sediment Transport on an Estuarine Intertidal Flat: Measurements and Conceptual Model of Waves, Rainfall and Exchanges with a Tidal Creek. *Estuar. Coast. Shelf Sci.* 72 (4), 553–569. doi:10.1016/j.ecss.2006.11.006

Guo, J. (2020). Empirical Model for Shields Diagram and its Applications. *J. Hydraul. Eng.* 146 (6), 04020038. doi:10.1061/(asce)hy.1943-7900.0001739

Harms, J. C. (1969). Hydraulic Significance of Some Sand Ripples. *Geol. Soc. Am. Bull.* 80 (3), 363–396. doi:10.1130/0016-7606(1969)80[363:hsossr]2.0.co;2

Hoagland, K. D., Rosowski, J. R., Gretz, M. R., and Roemer, S. C. (1993). Diatom Extracellular Polymeric Substances: Function, Fine Structure, Chemistry, and Physiology. *J. Phycol.* 29 (5), 537–566. doi:10.1111/j.0022-3646.1993.00537.x

Houwing, E.-J. (1999). Determination of the Critical Erosion Threshold of Cohesive Sediments on Intertidal Mudflats along the Dutch Wadden Sea Coast. *Estuar. Coast. Shelf Sci.* 49 (4), 545–555. doi:10.1006/ecss.1999.0518

Hughes, P. D. M., and Barber, K. E. (2004). Contrasting Pathways to Ombrotrophy in Three Raised Bogs from Ireland and Cumbria, England. *Holocene* 14 (1), 65–77. doi:10.1191/0959683604hl690rp

Jia, J., Wang, Y., Gao, S., Wang, A., and Li, Z. (2005). Interpretation of Bed Load Transport and Grain Size Trend Information in Dafeng Tidal Flat, Jiangsu Province. *Sci. Bull.* 50 (22), 2546–2554. doi:10.3321/j.issn:0023-074X.2005.22.017

Ke, X. (1993). The Ecological System and the Exploitation Mode of Tidal Flat-A Case Study of the Tidal Flat of Dafeng County, Jiangsu Province. *J. Nat. Resour.* 8 (02), 122–131.

Kirwan, M. L., and Megonigal, J. P. (2013). Tidal Wetland Stability in the Face of Human Impacts and Sea-Level Rise. *Nature* 504 (7478), 53–60. doi:10.1038/nature12856

Le Roux, J. P., and Rojas, E. M. (2007). Sediment Transport Patterns Determined from Grain Size Parameters: Overview and State of the Art. *Sediment. Geol.* 202 (3), 473–488. doi:10.1016/j.sedgeo.2007.03.014

Li, Z., Gao, S., and Chen, S. (2007). Characteristics of Tide Induced Bottom Boundary Layers over the Dafeng Intertidal Flats, Jiangsu Province, China. *Ocean. Eng.* 25, 212–219. doi:10.3969/j.issn.1005-9865.2007.03.008

Li, L., Wang, Y., and Liu, D. (2021). Phytoplankton Shifts in the Central Bohai Sea over the Last 250 Years Reflect Eutrophication and Input from the Yellow River. *Ecol. Indic.* 126, 107676. doi:10.1016/j.ecolind.2021.107676

Liu, H., He, Q., Wang, Y., and Zhai, X. (2006). OBS Situ Calibration Research in the Turbidity Maximum of the Changjiang Estuary,'China. *J. Sediment Res.* 0 (5), 52–58. doi:10.3321/j.issn:0468-155X.2006.05.009

Lundkvist, M., Grue, M., Friend, P. L., and Flindt, M. R. (2007). The Relative Contributions of Physical and Microbiological Factors to Cohesive Sediment Stability. *Cont. Shelf Res.* 27 (8), 1143–1152. doi:10.1016/j.csr.2006.01.021

Meckel, L. (1975). *Holocene Sand Bodies in the Colorado Delta Area*. northern Gulf of California: Houston Geological Society.

Meng, X.-m., Jia, Y.-g., Shan, H.-x., Yang, Z.-n., and Zheng, J.-w. (2012). An Experimental Study on Erodibility of Intertidal Sediments in the Yellow River Delta. *Int. J. Sediment Res.* 27 (2), 240–249. doi:10.1016/s1001-6279(12)60032-8

Morgan, R. P. C. (2009). *Soil Erosion and Conservation*. John Wiley & Sons.

Murray, A., Knaapen, M., Tal, M., and Kirwan, M. (2008). Biomorphodynamics: Physical-biological Feedbacks that Shape Landscapes. *Water Resour. Res.* 44 (11). doi:10.1029/2007wr006410

Panagiotopoulos, I., Voulgaris, G., and Collins, M. B. (1997). The Influence of Clay on the Threshold of Movement of Fine Sandy Beds. *Coast. Eng.* 32 (1), 19–43. doi:10.1016/s0378-3839(97)00013-6

Parchure, T. M., and Mehta, A. J. (1985). Erosion of Soft Cohesive Sediment Deposits. *J. hydraulic Eng.* 111 (10), 1308–1326. doi:10.1061/(asce)0733-9429(1985)111:10(1308)

Paterson, D. M., Tolhurst, T. J., Kelly, J. A., Honeywill, C., de Deckere, E. M. G. T., Huet, V., et al. (2000). Variations in Sediment Properties, Skeffling Mudflat, Humber Estuary, UK. *Cont. Shelf Res.* 20 (10), 1373–1396. doi:10.1016/S0278-4343(00)00028-5

Perkins, R. G., Paterson, D. M., Sun, H., Watson, J., and Player, M. A. (2004). Extracellular Polymeric Substances: Quantification and Use in Erosion Experiments. *Cont. Shelf Res.* 24 (15), 1623–1635. doi:10.1016/j.csr.2004.06.001

Pieterse, A., Puleo, J. A., and McKenna, T. E. (2016). Hydrodynamics and Sediment Suspension in Shallow Tidal Channels Intersecting a Tidal Flat. *Cont. Shelf Res.* 119, 40–55. doi:10.1016/j.csr.2016.03.012

Roberts, W., Le Hir, P., and Whitehouse, R. (2000). Investigation Using Simple Mathematical Models of the Effect of Tidal Currents and Waves on the Profile Shape of Intertidal Mudflats. *Cont. Shelf Res.* 20 (10-11), 1079–1097. doi:10.1016/s0278-4343(00)00013-3

Robinson, T. R., Davies, T. R. H., Reznichenko, N. V., and De Pascale, G. P. (2015). The Extremely Long-Runout Komansu Rock Avalanche in the Trans Alai Range, Pamir Mountains, Southern Kyrgyzstan. *Landslides* 12 (3), 523–535. doi:10.1007/s10346-014-0492-y

Rogers, J. J., and Head, W. B. (1961). Relationships between Porosity, Median Size, and Sorting Coefficients of Synthetic Sands. *J. Sediment. Res.* 31 (3), 467–470. doi:10.1306/74d70ba5-2b21-11d7-8648000102c1865d

Sanford, L. P. (2008). Modeling a Dynamically Varying Mixed Sediment Bed with Erosion, Deposition, Bioturbation, Consolidation, and Armoring. *Comput. Geosciences* 34 (10), 1263–1283. doi:10.1016/j.cageo.2008.02.011

Semeniuk, V. (1981). Long-term Erosion of the Tidal Flats King Sound, North Western Australia. *Mar. Geol.* 43 (1-2), 21–48. doi:10.1016/0025-3227(81)90127-4

Shi, B. W., Yang, S. L., Wang, Y. P., Yu, Q., and Li, M. L. (2014). Intratidal Erosion and Deposition Rates Inferred from Field Observations of Hydrodynamic and Sedimentary Processes: A Case Study of a Mudflat-Saltmarsh Transition at the Yangtze Delta Front. *Cont. Shelf Res.* 90, 109–116. doi:10.1016/j.csr.2014.01.019

Shi, B., Wang, Y. P., Wang, L. H., Li, P., Gao, J., Xing, F., et al. (2018). Great Differences in the Critical Erosion Threshold between Surface and Subsurface Sediments: A Field Investigation of an Intertidal Mudflat, Jiangsu, China. *Estuar. Coast. Shelf Sci.* 206, 76–86. doi:10.1016/j.ecss.2016.11.008

Soulsby, R., and Clarke, S. (2005). *Bed Shear-Stress under Combined Waves and Currents on Smooth and Rough Beds (TR 137)*.

Sumer, B. M., Whitehouse, R. J. S., and Tørum, A. (2001). Scour Around Coastal Structures: a Summary of Recent Research. *Coast. Eng.* 44 (2), 153–190. doi:10.1016/s0378-3839(01)00024-2

Syvitski, J. P. M., Vörösmarty, C. J., Kettner, A. J., and Green, P. (2005). Impact of Humans on the Flux of Terrestrial Sediment to the Global Coastal Ocean. *science* 308 (5720), 376–380. doi:10.1126/science.1109454

Takeuchi, S., and Tamaki, A. (2014). Assessment of Benthic Disturbance Associated with Stingray Foraging for Ghost Shrimp by Aerial Survey over an Intertidal Sandflat. *Cont. Shelf Res.* 84, 139–157. doi:10.1016/j.csr.2014.05.007

Taki, K. (2000). "Critical Shear Stress for Cohesive Sediment Transport," in *Proceedings in Marine Science* (Elsevier), 53–61. doi:10.1016/s1568-2692(00)80112-6

Teisson, C., Ockenden, M., Le Hir, P., Kranenburg, C., and Hamm, L. (1993). Cohesive Sediment Transport Processes. *Coast. Eng.* 21 (1-3), 129–162. doi:10.1016/0378-3839(93)90048-d

Tessler, Z. D., Vörösmarty, C. J., Grossberg, M., Gladkova, I., Aizenman, H., Syvitski, J. P. M., et al. (2015). Profiling Risk and Sustainability in Coastal Deltas of the World. *Science* 349 (6248), 638–643. doi:10.1126/science.aab3574

Tolhurst, T. J., Black, K. S., Shayler, S. A., Mather, S., Black, I., Baker, K., et al. (1999). Measuring the *In Situ* Erosion Shear Stress of Intertidal Sediments with the Cohesive Strength Meter (CSM). *Estuar. Coast. Shelf Sci.* 49 (2), 281–294. doi:10.1006/ecss.1999.0512

Tolhurst, T., Black, K., Paterson, D., Mitchener, H., Termaat, G., and Shayler, S. (2000a). A Comparison and Measurement Standardisation of Four *In Situ* Devices for Determining the Erosion Shear Stress of Intertidal Sediments. *Cont. Shelf Res.* 20 (10-11), 1397–1418. doi:10.1016/s0278-4343(00)00029-7

Tolhurst, T. J., Riethmüller, R., and Paterson, D. M. (2000b). *In Situ* versus Laboratory Analysis of Sediment Stability from Intertidal Mudflats. *Cont. shelf Res.* 20 (10-11), 1317–1334. doi:10.1016/s0278-4343(00)00025-x

Tolhurst, T. J., Gust, G., and Paterson, D. M. (2002). "The Influence of an Extracellular Polymeric Substance (EPS) on Cohesive Sediment Stability," in *Proceedings in Marine Science* (Elsevier), 409–425. doi:10.1016/s1568-2692(02)80030-4

Tolhurst, T. J., Defew, E. C., De Brouwer, J. F. C., Wolfstein, K., Stal, L. J., and Paterson, D. M. (2006). Small-scale Temporal and Spatial Variability in the Erosion Threshold and Properties of Cohesive Intertidal Sediments. *Cont. Shelf Res.* 26 (3), 351–362. doi:10.1016/j.csr.2005.11.007

Tucker, M. J., and Pitt, E. G. (2001). *Waves in Ocean Engineering*.

Underwood, G. J. C., and Paterson, D. M. (1993). Seasonal Changes in Diatom Biomass, Sediment Stability and Biogenic Stabilization in the Severn Estuary. *J. Mar. Biol. Ass.* 73 (4), 871–887. doi:10.1017/s0025315400034780

Van Ledden, M., Van Kesteren, W. G. M., and Winterwerp, J. C. (2004). A Conceptual Framework for the Erosion Behaviour of Sand-Mud Mixtures. *Cont. Shelf Res.* 24 (1), 1–11. doi:10.1016/j.csr.2003.09.002

Vardy, S., Saunders, J. E., Tolhurst, T. J., Davies, P. A., and Paterson, D. M. (2007). Calibration of the High-Pressure Cohesive Strength Meter (CSM). *Cont. Shelf Res.* 27 (8), 1190–1199. doi:10.1016/j.csr.2006.01.022

Walstra, D. J. R., Ruessink, B. G., Reniers, A. J. H. M., and Ranasinghe, R. (2015). Process-based Modeling of Kilometer-Scale Alongshore Sandbar Variability. *Earth Surf. Process. Landforms* 40 (8), 995–1005. doi:10.1002/esp.3676

Wang, Y., Gao, S., and Jia, J. (2006). High-resolution Data Collection for Analysis of Sediment Dynamic Processes Associated with Combined Current-Wave Action over Intertidal Flats. *Sci. Bull.* 51 (7), 866–877. doi:10.1007/s11434-006-0866-1

Wang, Y. P., Gao, S., Jia, J., Thompson, C. E. L., Gao, J., and Yang, Y. (2012). Sediment Transport over an Accretional Intertidal Flat with Influences of Reclamation, Jiangsu Coast, China. *Mar. Geol.* 291-294, 147–161. doi:10.1016/j.margeo.2011.01.004

Watts, C. W., Tolhurst, T. J., Black, K. S., and Whitmore, A. P. (2003). *In Situ* measurements of Erosion Shear Stress and Geotechnical Shear Strength of the Intertidal Sediments of the Experimental Managed Realignment Scheme at Tollesbury, Essex, UK. *Estuar. Coast. Shelf Sci.* 58 (3), 611–620. doi:10.1016/s0272-7714(03)00139-2

Weill, P., Mouazé, D., Tessier, B., and Brun-Cottan, J.-C. (2010). Hydrodynamic Behaviour of Coarse Bioclastic Sand from Shelly Cheniers. *Earth Surf. Process. Landforms* 35 (14), 1642–1654. doi:10.1002/esp.2004

Weill, P., Tessier, B., Mouazé, D., Bonnot-Courtois, C., and Norgeot, C. (2012). Shelly Cheniers on a Modern Macrotidal Flat (Mont-Saint-Michel Bay, France) - Internal Architecture Revealed by Ground-Penetrating Radar. *Sediment. Geol.* 279, 173–186. doi:10.1016/j.sedgeo.2010.12.002

Weimer, R. J., Howard, J. D., Lindsay, D. R., Scholle, P., and Spearing, D. (1982). "Tidal Flats and Associated Tidal Channels," in *Sandstone Depositional Environments* (Okla: American Association of Petroleum Geologists Tulsa), 191–245. doi:10.1306/m31424c9

Wiberg, P. L., Carr, J. A., Safak, I., and Anutaliya, A. (2015). Quantifying the Distribution and Influence of Non-uniform Bed Properties in Shallow Coastal Bays. *Limnol. Oceanogr. Methods* 13 (12), 746–762. doi:10.1002/lom3.10063

Widdows, J., Brinsley, M. D., Salkeld, P. N., and Elliott, M. (1998). Use of Annular Flumes to Determine the Influence of Current Velocity and Bivalves on Material Flux at the Sediment-Water Interface. *Estuaries* 21 (4), 552–559. doi:10.2307/1353294

Winterwerp, J. C., and Van Kesteren, W. G. (2004). *Introduction to the Physics of Cohesive Sediment Dynamics in the Marine Environment*. Elsevier.

Yang, Y., Gao, S., Zhou, L., Wang, Y., Li, G., Wang, Y., et al. (2017). Classifying the Sedimentary Environments of the Xincun Lagoon, Hainan Island, by System Cluster and Principal Component Analyses. *Acta Oceanol. Sin.* 36 (4), 64–71. doi:10.1007/s13131-016-0939-1

Zhang, C., Mengpiao, X. U., Zhou, Z., Gong, Z., Kang, Y., and Huan, L. I. (2018). Advances in Cross-Shore Profile Characteristics and Sediment Sorting Dynamics of Tidal Flats. *Adv. Water Sci.* 29, 269–282. doi:10.14042/j.cnki.32.1309.2018.02.015

Zhou, Z., Ye, Q., and Coco, G. (2016). A One-Dimensional Biomorphodynamic Model of Tidal Flats: Sediment Sorting, Marsh Distribution, and Carbon Accumulation under Sea Level Rise. *Adv. Water Resour.* 93, 288–302. doi:10.1016/j.advwatres.2015.10.011

Zhu, Q., Yang, S., and Ma, Y. (2014). Intra-tidal Sedimentary Processes Associated with Combined Wave-Current Action on an Exposed, Erosional Mudflat, Southeastern Yangtze River Delta, China. *Mar. Geol.* 347, 95–106. doi:10.1016/j.margeo.2013.11.005

Zhu, S., Hu, D., Zhang, H., Zeng, C., Li, Z., and Li, Z. (2019). Analysis of Short-Term Temporal and Spatial Changes and Sedimentary Dynamics at the Middle Section of Haikou Bay Beach. *Acta Trop. Oceanogr.* 38 (05), 77–85. doi:10.11978/2018120

Conflict of Interest: The authors declare that the research was conducted in the absence of any commercial or financial relationships that could be construed as a potential conflict of interest.

frontiers | Frontiers in Earth Science

ORIGINAL RESEARCH
published: 30 June 2022
doi: 10.3389/feart.2022.913022

Variations in the Suspended Sediment Concentration in Mountain-Type Rivers Flowing Into the Sea in the Past 60 years—Taking Nanliu River in Beibu Gulf as an Example

Shushi Li[1], Xialing Yang[2], Hu Huang[1], Xixing Liang[1], Riming Wang[1] and Bingbin Feng[2]*

[1]Guangxi Key Laboratory of Marine Environment Change and Disaster in Beibu Gulf (Beibu Gulf University), Qinzhou, China, [2]School of Geography and Planning, Nanning Normal University, Nanning, China

Suspended sediment in the water body of rivers flowing into the sea is of great significance to the accumulation process in river basins and change pattern of landforms. In particular, small and medium rivers entering the sea in mountainous areas exhibit the characteristics of both mountains and streams, and the suspended sediment concentration (SSC) greatly contributes to the formation and evolution of deltas. However, scholars rarely give attention to the factors influencing changes in the SSC in small- and medium-sized mountainous rivers, and few studies have examined SSC changes in small- and medium-sized mountainous rivers. Here, based on daily SSC and flow data obtained at the Bobai Station and Changle Station, the percentile method and regression analysis method are employed to analyse the changes in SSC from the Nanliu River to the Beibu Gulf and possible influencing factors. The main research results indicate that 1) the SSC in river water bodies from 1965 to 2020 generally reveals a downwards trend, with significant annual variations. Specifically, the overall trend can be divided into three stages: 1) the SSC is the highest from 1965 to 1971, and the mean yearly SSC reaches 0.25 kg/m^3; 2) the SSC is relatively high from 1972 to 2006, and the mean yearly SSC reaches 0.16 kg/m^3; and 3) the SSC is the lowest from 2007 to 2020, and the mean yearly SSC reaches 0.11 kg/m^3 2) High values of the SSC are mainly concentrated in the flood season, and low SSC values mostly occur in the dry season. The monthly average SSC in the flood season from April to September and the dry season from October to March exhibits the characteristics of a decrease in the flood season and an increase in the dry season. Moreover, the peak SSC value in the watershed obviously occurs out of sync with the peak flow value. Generally, the former precedes the latter. 3) The curve of the flow rate-sediment ratio is an irregular clockwise rhombus. Moreover, the impact of tropical cyclones, land cover changes, regional GDP per capita, and engineering construction are crucial reasons for the observed variations in the SSC in the Nanliu River Basin. In this paper, the obtained research results provide an important guiding significance for the planning and management of water and sediment resources in the Nanliu River and offer a reference for hydrological planning of other river basins discharging into the sea.

OPEN ACCESS

Edited by:
Xiaolei Liu,
Ocean University of China, China

Reviewed by:
Benwei Shi,
East China Normal University, China
Xiao Wu,
Ocean University of China, China

***Correspondence:**
Hu Huang
mrhuanghu@126.com

Specialty section:
This article was submitted to Hydrosphere, a section of the journal Frontiers in Earth Science

Received: *06 April 2022*
Accepted: *08 June 2022*
Published: *30 June 2022*

Citation:
Li S, Yang X, Huang H, Liang X, Wang R and Feng B (2022) Variations in the Suspended Sediment Concentration in Mountain-Type Rivers Flowing Into the Sea in the Past 60 years—Taking Nanliu River in Beibu Gulf as an Example. Front. Earth Sci. 10:913022. doi: 10.3389/feart.2022.913022

Keywords: suspended sediment concentration, tropical cyclone, human activities, nanliu river, beibu gulf

1 INTRODUCTION

The sediment transport process is highly important to socioeconomic development and the ecological environment in river basins. Suspended sediment in river water is transported to the ocean through rivers, and the main driving force is river flow (Matos et al., 2018; Wei et al., 2021). Sediment transport is very important among the processes on the Earth's surface, and sediment transport exerts a vital influence on the regulation of erosion-accretion phenomena and shaping of the landform pattern (Matos et al., 2018; Wei et al., 2021). Suspended sediment is the main component of the total sediment load, and sediment constitutes a natural part of the river environment and an indispensable part of the river system. Long-term deposition of suspended sediment plays a key role in the formation of the shallow sea continental shelf, evolution of the seabed topography, and estuary environment (Zuo et al., 2012; Zhang et al., 2014; Tang et al., 2019). However, in recent decades, horizontal transport of suspended sediment between the river and ocean has been greatly affected by human activities and climate change, which has caused changes in the transport volume and spatial distribution of sediment (Farnsworth and Milliman, 2003; Li et al., 2012; Wu et al., 2019; Huang et al., 2022a). Because of the continuous reduction of suspended sediment entering the sea, the ecological environment of the estuary has undergone tremendous changes, such as the retreat of coastlines, the reduction of wetland areas, and the impact of biological habitats (Coleman et al., 1998; Dai et al., 2013). Studies have demonstrated that tropical cyclones affect the spatial variation in the amount of suspended sediment (Huang et al., 2022b), leading to changes in the suspended sediment amount reaching the delta (Darby et al., 2016; Tang R. et al., 2021). Therefore, in recent years, researchers have given increasing attention to the long-term change trend and temporal and spatial changes in SSC from rivers to the ocean.

To date, a large number of studies have indicated that runoff and the SSC in many large rivers are regulated by human activities, especially the reconstruction of navigation channels, construction of dams and reservoirs, and soil and water conservation projects, which have caused the amount of suspended sediment in certain large rivers to drastically decrease (Yang et al., 2002; Walling and Fang, 2003; Yang S. L. et al., 2015; Dai et al., 2016). It has been confirmed that human activities are the main factor leading to a reduction in the SSC in rivers flowing to the sea (Dai et al., 2009; Wu et al., 2012). For example, after the completion of the Three Gorges Dam in the Yangtze River, the SSC in the estuary immediately dropped by 40.3%, and the sediment load in the Yangtze River estuary was drastically reduced, resulting in a sharp decline in the wetland area (Yang et al., 2005; Wang et al., 2015; Wei et al., 2021). An early study determined that the construction of the Xiaolangdi Reservoir in the middle and lower reaches of the Yellow River reduced the flow of sediment into the sea by more than 90% (Wang et al., 2010). Moreover, water and soil conservation projects and the Grain for Green project were initiated on the Loess Plateau in the 1970s, and water discharge and the daily SSC consequently declined significantly (Zhang et al., 2017). Not only are the variations in the SSC influenced by human activities (Yang et al., 2002; Chu et al., 2009), but also influenced by natural factors, such as tropical cyclones, rainfall seasonality, soil erosion, watershed size and topography, etc. (Montanher et al., 2018; Shams et al., 2020; Huang et al., 2022b). Therefore, scholars in the SSC-related research field have also studied other possible factors influencing the long-term variations in the SSC, and found that the changes of SSC is controlled by factors such as water flow direction, peak flow, rainfall intensity, and duration of extreme events (Nadal et al., 2007; Dan et al., 2020; Tang R. G. et al., 2021). In summary, researchers have conducted fruitful explorations of the possible factors influencing the variations in the SSC. However, most studies above have mainly concentrated on the impact of natural factors and human activities on the variations in the SSC in large rivers. Therefore, more attention should be given to SSC changes in small and medium mountain rivers flowing into the sea.

However, variations in the SSC influence the composition of local species, survival rate of organisms, estuarine delta marshes, and contents of nitrogen and phosphorus elements (Müller and Förstner, 1968; Yang et al., 2020; Li et al., 2021). Studies have demonstrated that the SSC is a significant nonbiological variable, and its changes can affect the life of benthic organisms (Tramblay et al., 2008; Shi et al., 2017). The SSC is related to the water temperature and salinity (Ramalingam and Chandra, 2019) and land-use change (Ferreira et al., 2020). Additionally, the SSC is also related to land reclamation (van Maren et al., 2016), reservoir storage (Yang Y. P. et al., 2015), and soil erosion (Syvitski et al., 2005). To date, although the study of the SSC has received extensive attention, the long-term and annual variations in the SSC should be further studied, especially in the mountainous Nanliu River.

The Nanliu River is located in the northern part of the Beibu Gulf. This river originates in the Darong Mountain and flows into Lianzhou Bay in Hepu County. The Nanliu is the single largest river in Guangxi flowing into the Beibu Gulf (**Figure 1**). The total drainage area reaches 9,700 km^2, and the river length is 287 km. This river is located in the southern subtropical maritime monsoon climate zone, with a mild climate and abundant rainfall, and the average annual rainfall reaches approximately 1736 mm (Li et al., 2016). The upper and middle reaches of the Nanliu River Basin are the Yulin Basin and Bobai Basin respectively, and the lower reaches include the Hepu Alluvial Plain and the Nanliu River Delta. The Nanliu River flows into the sea in a mountainous area. This river exhibits the highest long-term SSC among the various rivers flowing into the sea surrounding the Beibu Gulf. However, previous studies on the SSC have focused on large rivers,

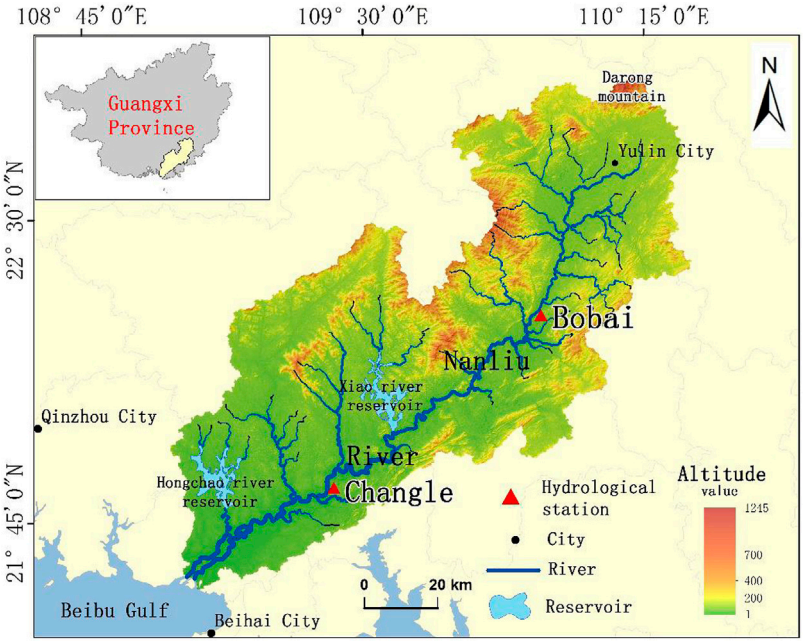

FIGURE 1 | Study area with the hydrological stations in the Nanliu River Basin.

such as the Yellow River (Wang et al., 2010), Amazon River (Montanher et al., 2018), Yangtze River (Chen et al., 2006), Rhine River (Asselman, 1999), and Mississippi River (Meade and Moody, 2010), in regard to the research area, but little attention has been given to the long-term sequential variations in the SSC in small and medium rivers and possible influencing factors. The variability and dynamics of the SSC in small and medium rivers thus remain unclear. Studying the change in the SSC in medium and small rivers can provide important information regarding engineering issues such as regional water conservancy design and river sediment control (Hsu and Cai, 2010). Therefore, it is of great practical significance to study small and medium rivers and provide them with hydrological management strategies. In this paper, the Nanliu River, a typical mountainous small to medium river flowing into the sea, is selected as the research object to study the variations in the SSC at various scales. The objectives of this paper are 1) to examine the overall features of the variations in the SSC in the Nanliu River in the past 60 years; 2) to analyse the main driving factors influencing changes in the SSC in the past 60 years.

2 MATERIALS AND METHODS

2.1 Materials

The Bobai Station is located in Chengxiang town, Bobai County, Yulin city, Guangxi, in the upper reaches of the Nanliu River. This station mainly controls the variations in water and sediment from the upstream region. The Changle Station is located in Changle town, Hepu County, Beihai city, Guangxi, in the lower reaches of the Nanliu River. This station mainly controls the variations in river flow and sediment volume in the middle and upper reaches of the river. These two stations are the most important hydrological stations in the Nanliu River. The data collected at these two stations can represent the flow and SSC in the Nanliu River. River flow and SSC data between 1965 and 2020 were obtained from the Pearl River Water Conservancy Commission of the Ministry of Water Resources of China, but some SSC data were missing, including data from 1967 to 1975 and 1985 to 2000. Precipitation data for the Nanliu River Basin between 1970 and 2020 were obtained from the China Meteorological Administration. The per capita GDP from 1989 to 2019 was retrieved from the Guangxi Statistical Yearbook of the various years. Additionally, the remote sensing image data mainly comes from the official website of the United States Geological Survey (https://earthexplorer.usgs.gov/bulk).

2.2 Methods

The percentile method is an important method to analyse the characteristics of long-series data. In this study, the percentile method was employed to analyse the changes in the SSC in the Nanliu River. With the use of percentiles, the daily SSC was divided into seven levels: 5, 10, 25, 50, 75, and 95%. The third level (25%) and fifth level (75%) of the daily SSC were selected as thresholds. The third level of 25% represents low-SSC events, while the fifth level of 75% represents high-SSC events. Moreover, to further analyse the changes in the daily SSC throughout the study year, the hydrological coefficient of variation (Cv) was calculated.

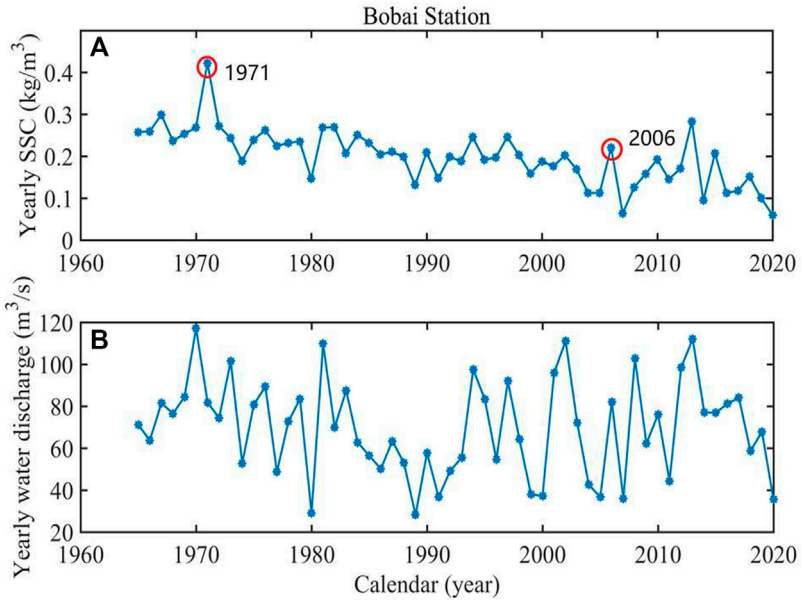

FIGURE 2 | Variation trends of the yearly SSC and yearly water discharge at the Bobai Station from 1965 to 2020 **(A)** variation in the average SSC; **(B)** variation in the water discharge.

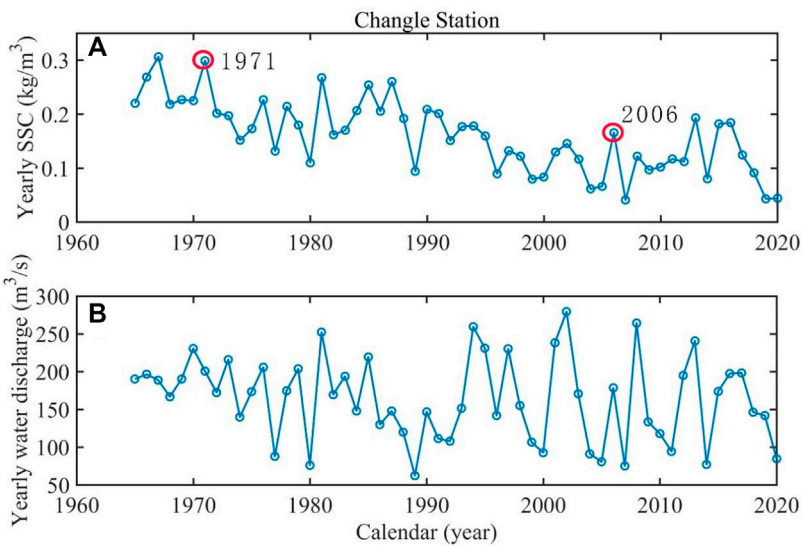

FIGURE 3 | Variation trend of the SSC and water discharge at the Changle Station from 1965 to 2020 **(A)** variation in the yearly SSC; **(B)** variation in the yearly water discharge.

To analyse the variations in the daily SSC, a combination of linear regression and power functions was applied to perform power regression of the daily water discharge and daily SSC data to obtain the sediment grade curve and constants a and b in the following form:

$$Q_{s=a}Q_w^b$$

where Q_S is the daily SSC, kg/m^3; Q_W is the water discharge rate, m^3/s; a is the slope of the equation; and b is the intercept of the curve (Guzman et al., 2013; Mouri et al., 2014; Dai et al., 2016).

To analyse the changes of building area in the Nanliu River Basin from 1988 to 2018, ENVI 5.3 was used to supervise and classify the remote sensing images, and the building area of the

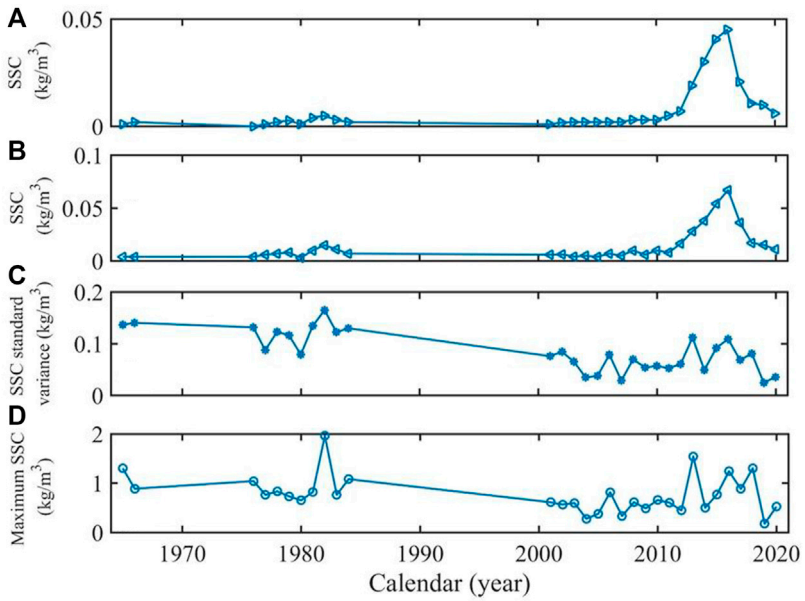

FIGURE 4 | Variation trend of the SSC in the Nanliu River water body from 1965 to 2020: SSC at the **(A)** third level and **(B)** fifth level **(C)** coefficient of variation, C_V; **(D)** maximum SSC.

Nanliu River Basin was extracted, and then the building area data of each year was obtained by calculation.

3 RESULTS

3.1 Annual Variation Characteristics of the SSC

Events with an annual average SSC higher than the fifth level at the Bobai Station mainly occurred before 1970, while events with a yearly average SSC lower than the third level mainly occurred after 2006 (**Figure 2A**). Events in which the yearly average SSC at the Changle Station was higher than the fifth level and lower than the third level occurred in 1971 and 2006, respectively (**Figure 3A**). Therefore, the annual average SSC in the Nanliu River Basin could be divided into three periods based on these two specific years of 1971 and 2006, namely, 1965–1971, 1972–2006, and 2007–2020. At the first stage, from 1965 to 1971, the annual average SSC was the highest, while at the second stage, from 1972 to 2006, the yearly average SSC was relatively high. Moreover, at the third stage, from 2007 to 2020, the annual average SSC was relatively low. The yearly mean SSC values during these three periods reached 0.25 kg/m^3, 0.16 kg/m^3 and 0.11 kg/m^3, respectively. The annual average SSC in the Nanliu River from 1965 to 2020 exhibited a downward trend in general.

The third-level change trend of the daily average SSC was basically consistent with the fifth-level change trend (**Figures 4A, B**). The third level of the daily SSC maintained a low average SSC from 1965 to 2010, which suggests that the proportion of low-to average-SSC events was high. Between 2011 and 2016, there occurred an upwards trend (**Figure 4A**). After 2016, a clear decreasing trend was observed. Furthermore, the hydrological coefficient and maximum average SSC exhibited a significant downwards trend (**Figures 4C, D**), indicating that the daily average SSC decreased in the past 60 years.

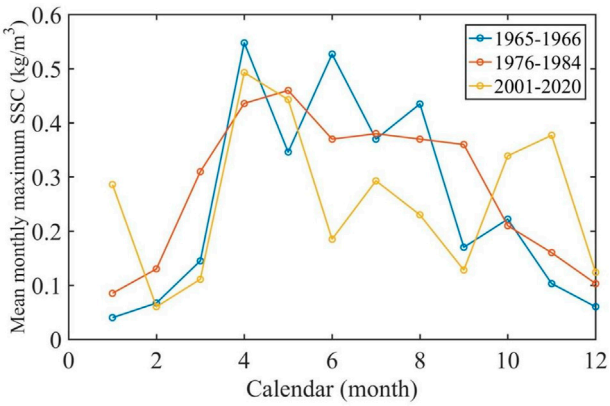

FIGURE 5 | Mean monthly maximum SSC at the three stages.

3.2 Frequency Distribution Characteristics of the SSC

Due to the lack of SSC data in certain years, the analysis was divided into three periods from 1965 to 1966, 1976 to 1984, and 2001 to 2020 based on the existing data. There occurred obvious differences in the monthly maximum SSC at the three stages, and the overall state fluctuated to varying degrees. According to the

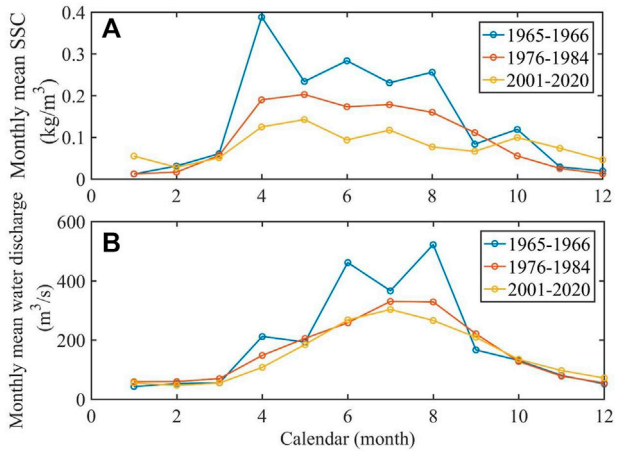

FIGURE 6 | Monthly mean SSC **(A)** and monthly mean water discharge **(B)** at the three stages.

seasonal difference in precipitation in the Nanliu River, April to September was categorized as the flood season, and October to December and January to March were categorized as the dry season. During the above three periods, low-value areas of the SSC mostly occurred in the dry season, and high-value sections were mainly distributed in the flood season. **Figure 5** shows that the mean monthly maximum SSC at the two stages of 1965–1966 and 1976–1984 indicated fluctuations of 0.04–0.56 kg/m^3 and 0.08–0.46 kg/m^3, respectively, and varied with the season. From 2001 to 2020, the mean monthly maximum SSC varied irregularly, fluctuating between 0.05 and 0.49 kg/m^3, with peaks in April, July, and November. During the above three periods, the mean monthly maximum SSC difference reached 0.53 kg/m^3, 0.36 kg/m^3, and 0.41 kg/m^3. The mean monthly maximum SSC from 1965 to 1966 varied the most, at 1.5 and 1.3 times that from 1976 to 1984 and 2001–2020, respectively (**Figure 5**). It should be noted that the maximum SSC in the dry season exhibited an upwards trend during the three periods, following 1965–1966<1976–1984<2001–2020, especially in January, March, November, and December. In contrast, the flood season exhibited a growth trend, following 1965–1966> 1976–1984> 2001–2020, especially in June and August.

Figure 6 shows that the monthly average SSC and monthly average flow significantly changed at the three stages. The monthly average SSC reached 0.24 kg/m^3 in the flood season between 1965 and 1966, and in the dry season, it reached 0.05 kg/m^3. The monthly average SSC was 0.17 kg/m^3 in the flood season from 1976 to 1984, and in the dry season, it reached 0.04 kg/m^3. The average monthly SSC values in the flood and dry seasons from 2001 to 2020 were 0.1 kg/m^3 and 0.06 kg/m^3, respectively. Among the three stages, the average monthly SSC was the highest in the dry season from 2001 to 2020, which was 0.01 kg/m^3 and 0.02 kg/m^3 higher than the monthly average SSC in the dry season from 1965 to 1966 and 1976 to 1984, respectively. From 1965 to 1966, the peak average SSC value reached 0.4 kg/m^3, which occurred in April, and the peak water discharge value occurred in August. Notably, the peak water discharge lagged behind the peak SSC by 4 months. The peak values of the monthly average SSC of 0.2 kg/m^3 and 0.15 kg/m^3 from 1976 to 1984 and 2001 to 2020, respectively, occurred in May. Therefore, the peak monthly average SSC sequentially decreased from 1965 to 1966, 1976 to 1984, and 2001 to 2020 (**Figure 6A**). The monthly average SSC reached 0.51 kg/m^3 in the flood season during these three periods, which is 0.36 kg/m^3 higher than the value of 0.15 kg/m^3 in the dry season. Moreover, the monthly average water discharge in the flood season reached 285 m^3/s, which is 212 m^3/s higher than that in the dry season. In addition, the monthly average SSC and monthly average flow during these three periods exhibited the characteristics of decreasing in the flood season and increasing in the dry season. Notably, the performance of the SSC in the flood season adhered to 1965–1966<1976–1984<2001–2020, and the performance of the SSC in the dry season followed 1965–1966>1976–1984>2001–2020, especially the flood season performance (**Figure 6B**). This phenomenon is similar to the change characteristics of the monthly maximum SSC (**Figure 5**).

At 0.01-kg/m^3 intervals, the frequency of the average daily SSC was analysed during the three periods. The results indicated that the frequency of daily average SSC values higher than 0.4 kg/m^3 exceeded 5% from 1965 to 1966, approached 5% from 1976 to 1984, and decreased to 2% from 2001 to 2002 (**Figure 7**). The frequency of values ≤0.1 kg/m^3 during these three periods accounted for 78, 85, and 92%, respectively, of the overall frequency. The daily average SSC within the interval of 0.2–0.4 kg/m^3 was very low, and there occurred almost no value from 2001 to 2020. The maximum frequency of the daily mean SSC was observed at 0.01 kg/m^3 from 1965 to 1966, and the frequency approached 40%. From 1976 to 1984 and 2001–2020, the maximum frequency occurred at 0.02 kg/m^3, and this frequency accounted for approximately 25% of the overall frequency. Furthermore, the proportion of 0.01 kg/m^3 successively decreased over the three periods, while the proportions of 0.02 and 0.03 kg/m^3 successively increased. From the above, the single-peak features of the daily average

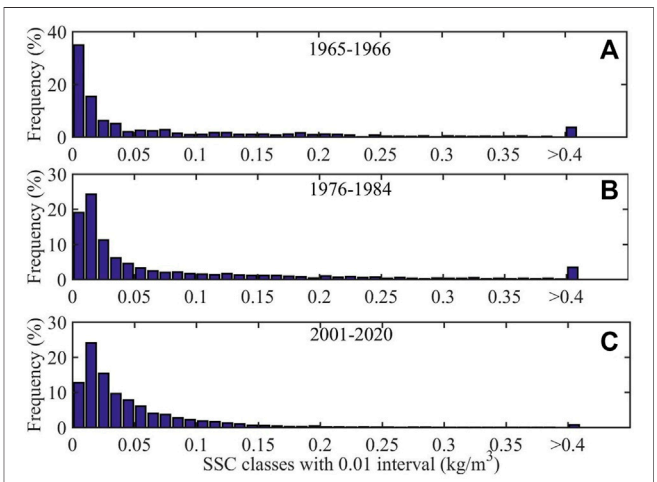

FIGURE 7 | Frequency of the daily SSC at the three stages **(A)** 1965–1966; **(B)** 1976–1984; **(C)** 2001–2020.

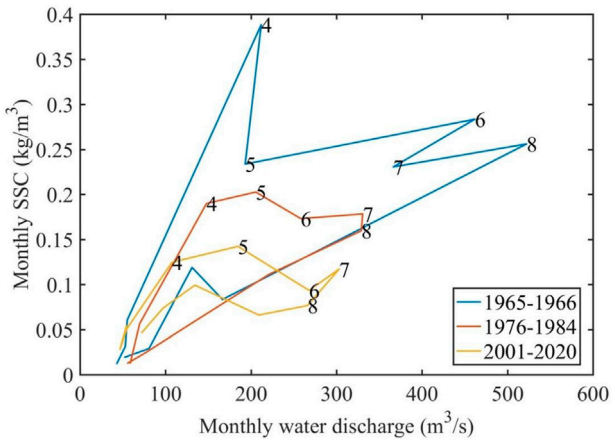

FIGURE 8 | Ratio curve of the monthly SSC and monthly water discharge (the number indicates the month).

SSC became increasingly distinct and tended to move backwards during the three periods.

3.3 Flow-Sediment Ratio Curve

The flow-sediment ratio curve reflects the different temporal and spatial variations in water and sediment (**Figure 8**). The SSC in the Nanliu River from 1965 to 1966 exhibited an increasing trend from January to April, with the highest peak in April and irregular fluctuations from April to August. Nevertheless, from August to December, the monthly average SSC gradually dropped to its lowest value. The area enclosed by the entire flow-sediment ratio curve resembled a clockwise irregular rhombus, which was the opposite to the counterclockwise rhombus revealed by the Yangtze River flow-sediment ratio curve (Dai et al., 2016). During the period from 1976 to 1984, the peak of the flow-sediment ratio curve was significantly reduced from 1965 to 1966, and the lowest peak occurred in May. The entire curve became relatively narrow, and the area enclosed by the curve was significantly smaller than that enclosed by the curve for the period from 1965 to 1966. Moreover, compared to the periods from 1965 to 1966 and 1976 to 1984, the flow-sediment curve was the narrowest from 2001 to 2020, indicating that the monthly average SSC changes were relatively limited. However, the flow-sediment curve for the two periods from 1976 to 1984 and 2001 to 2020 exhibited the same characteristics: the average SSC increased with increasing flow and time, and the average SSC occurred at the rising stage from January to May. This parameter reached its highest peak throughout the month (**Figure 8**). Therefore, there existed a positive correlation between the SSC and water discharge (Chu et al., 2009).

4 DISCUSSION

4.1 Relationship Between Rainfall and Flow

Rainfall is an important factor affecting river flow and SSC (Tang R. et al., 2021). **Figure 9** shows that the mean annual rainfall in the Nanliu River from 1960 to 2020 and the flow at the Bobai Station and Changle Station tended to change simultaneously, Changes in rainfall reflect trends in river flow. At the same time, it can be found from **Figure 9** that the rainfall of the Nanliu River during 1965–2020 reached a large value in 1981, 2002 and 2006, and the water discharge of Changle Station and Bobai Station also reached a large value. Rainfall is closely related to flow, rainfall and flow have a great impact on SSC (Moskalski and Torre, 2012). Furthermore, Comparing **Figure 9** with **Figure 2** and **Figure 3**, it can be found that the variation trends of rainfall, flow and SSC of Nanliu River are consistent, indicating that rainfall, flow and SSC are closely related. Further discussion on the relationship between rainfall and flow. In 1981, due to the superimposition effect of two

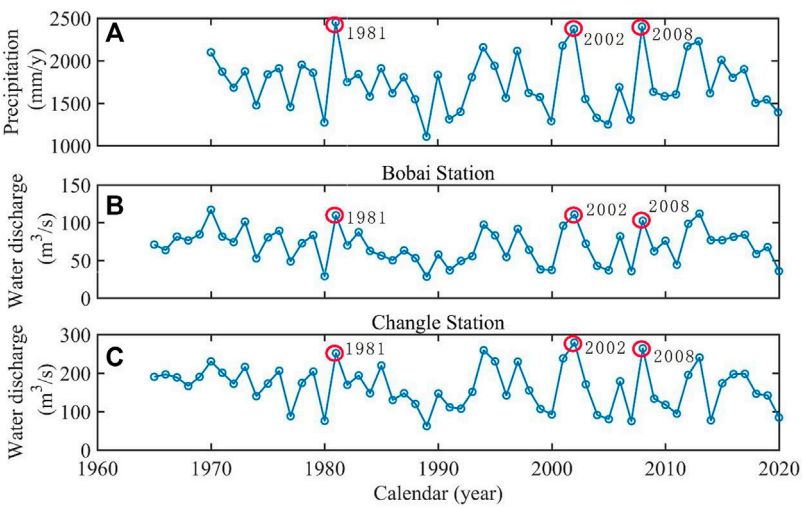

FIGURE 9 | Change trend of the precipitation and water discharge from 1965 to 2020 **(A)** yearly average precipitation; **(B)** yearly average water discharge at the Bobai station; **(C)** yearly average water discharge at the Changle station.

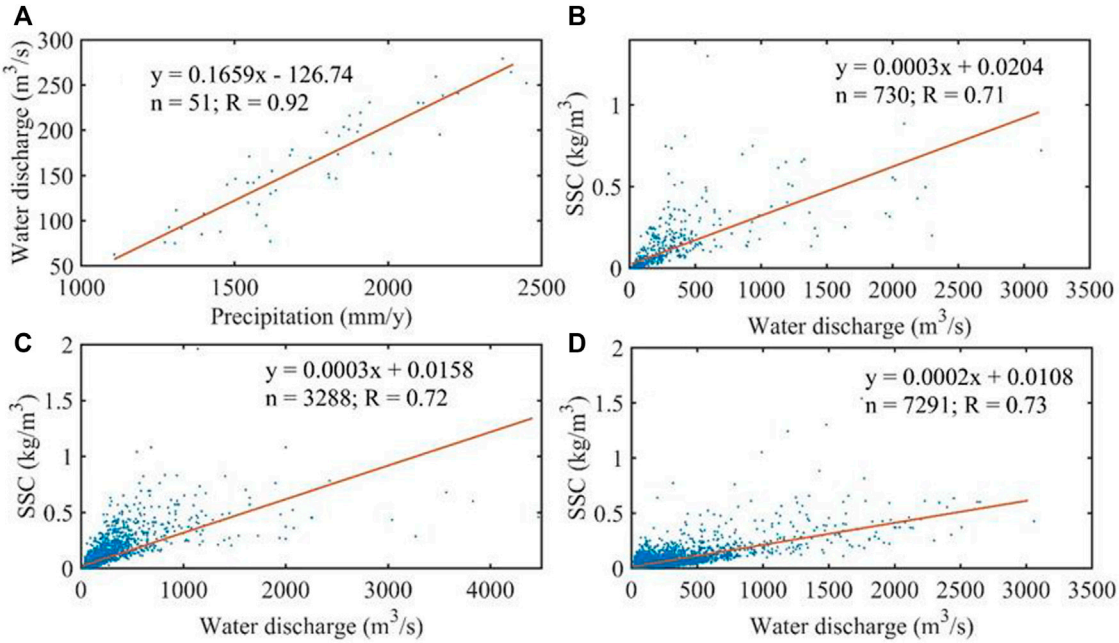

FIGURE 10 | Water discharge and precipitation from 1970 to 2020 **(A)**: SSC and water discharge **(B–D)** indicate 1965–1966, 1976–1984, and 2001–2020).

typhoons, i.e., Kaili and Linen, heavy rainfall occurred in the Nanliu River Basin, with a mean annual rainfall of approximately 2,452 mm. The Nanliu River experienced a significant increase in water discharge, and a once-in-a-year flood occurred. The peak water level reached as high as 18.18 m, and the peak discharge rate reached 3,630 m^3/s. In 2002, the average annual rainfall in the Nanliu River Basin reached 2,373 mm. There occurred a once-in-five-year flood in the Nanliu River, and the flood peak exhibited multipeak features. At this time, the flood peak water level reached 17.75 m, and the peak discharge reached 2,780 m^3/s, which accounted for 77% of that in 1981. Furthermore, in 2008, the basin was affected by Typhoon Hagupit, which occurred as a heavy rainstorm in southeastern Guangxi. The average annual rainfall in the Nanliu River Basin reached 2,400 mm, and an over-alert flood occurred in the upper reaches of the Nanliu River. Therefore, in the moderate-flood years of 1981, 2002, and 2008, the high precipitation intensity resulted in high water discharge at the Bobai Station and Changle Station (**Figures 9A–C**), indicating that precipitation was the principal source of water flow in the Nanliu River Basin.

4.2 Relationship Between the SSC and Flow

Rainfall and water discharge are the key factors influencing the changes in the sediment volume, and there exists a strong correlation among these three factors (Shams et al., 2020). The analysis revealed that there exists a significant positive correlation between the annual average water discharge and the annual average rainfall in the Nanliu River Basin (**Figure 10A**), indicating that the river basin flow mainly originates from precipitation, and the flow increases with the increase of rainfall (**Figure 9**). Studies have shown that rainfall erosion intensity affects the change of sediment volume, and there is a positive correlation between sediment volume and rainfall (Zhang et al., 2015; Shams et al., 2020). Then, correlation analysis between the daily average SSC and daily average water discharge during the three periods from 1965 to 1966, 1976 to 1984, and 2001 to 2020 demonstrated that there exists a positive correlation between these two parameters (**Figures 10B–D**), SSC changes with the water discharge (**Figures 2**, **3**), and the SSC and water discharge change synchronously. Flow is one of a primary controlling factors for the change of SSC, and SSC increases with the increase of flow (**Figure 8**) (Gong et al., 2011; Moskalski and Torre, 2012; Dai et al., 2016). To sum up, rainfall affects flow, which further affects SSC. It can be seen that rainfall is an indirect factor affecting the SSC, and flow is the most direct factor affecting the change of SSC.

The peak values of the SSC and water discharge in the watershed occurred obviously out of sync. Generally, the former preceded the latter. **Figures 2**, **3** show that the average annual precipitation was relatively low in 1980, and 1980 was a dry year, with a low average flow but high SSC value. The average annual rainfall in 2002 and 2006 was relatively high, which were flood years, with a relatively high average water discharge, but the SSC was low. Further analysis demonstrated that the peak values of the SSC and water discharge in 1980, 2002, and 2006 were delayed (**Figures 11A–C**, respectively). In 1980, the maximum daily average SSC value of 0.65 kg/m^3 occurred on July 20, and the maximum daily average water discharge occurred on August 23 (**Figure 11A**). In 2002, the highest daily average SSC (0.56 kg/m^3) occurred on June 4, and the highest daily average water discharge occurred on September 29 (**Figure 11B**). In 2006, the highest

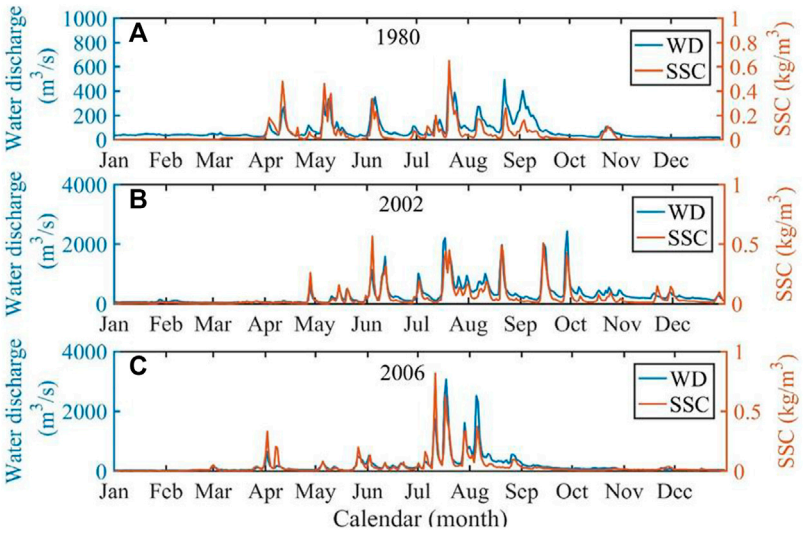

FIGURE 11 | Relationship between the SSC and water discharge **(A)** dry year of 1980; **(B)** flood year of 2002; **(C)** flood year of 2006.

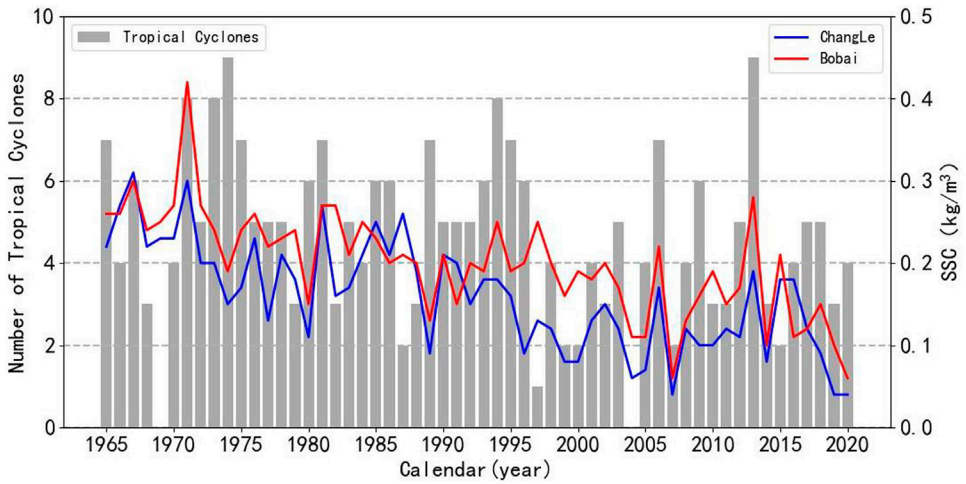

FIGURE 12 | Changes in the number of tropical cyclones and changes in the SSC from 1965–2020.

daily mean SSC (0.81 kg/m^3) occurred on July 11, and the highest daily mean water discharge occurred on July 18 (**Figure 11C**).

4.3 Relationship Between the SSC and Tropical Cyclones

Based on statistics, extreme weather events such as tropical cyclones exert an enormous impact on changes in the SSC in the Nanliu River. In years with more tropical cyclones, the yearly mean SSC was maintained at a relatively high level at the Changle and Bobai stations. (**Figure 12**). For example, from 1971 to 1974, the average SSC reached 0.21 kg/m^3 at the Changle station and reached up to 0.28 kg/m^3 at the Bobai station, which was higher than the multiyear average levels of 0.05 kg/m^3 and 0.08 kg/m^3, respectively. From 1995 to 1996, the average SSC reached 0.17 kg/m^3 at the Changle station and reached 0.22 kg/m^3 at the Bobai station, which remained higher than the mean level. In contrast, in 2004, without the influence of tropical cyclones, the average online concentration at these two stations remained low. Considering the above statistics, the Nanliu River Basin has been impacted by 260 tropical cyclones over the past 50 years, with an average of 4.6 cyclones per year. Tropical cyclones have become a vital factor impacting the changes in the SSC in the Nanliu River.

4.4 Impacts of Human Activities

Human activities can significantly affect the hydrological characteristics of rivers and changes along deltaic coasts (Yang

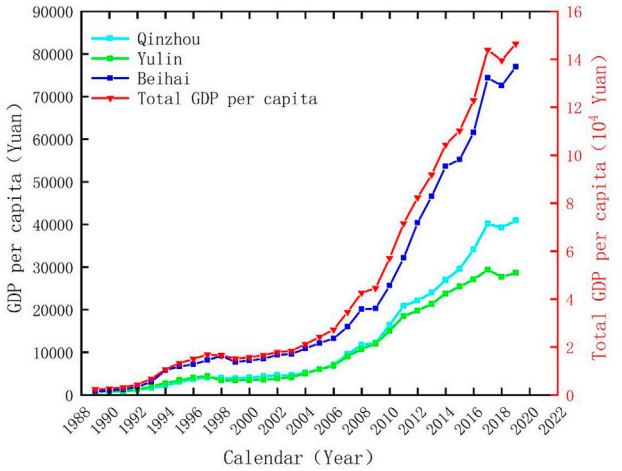

FIGURE 13 | Changes in the per capita GDP in the Nanliu River Basin from 1989–2019.

et al., 2002; Dai et al., 2011; Dai et al., 2014). The Nanliu River is located in the Beibu Gulf Economic Area, and the city is clustered around the Beibu Gulf. This region is affected by human activities such as urbanization and engineering construction. This paper analysed the impact on the SSC from the aspects of land cover change, per capita GDP, and water consumption.

4.4.1 Land Cover Change

Sediment transport depends on land cover and land use (Guzman et al., 2013). Based on the above aspects, the SSC in the Nanliu River exhibited a clear downwards trend, and the SSC revealed the characteristics of a phased decline during these three periods. This may be related to changes in land use, a significant factor reflecting the degree of anthropogenic activities. Deforestation in the basin is severe, and the forest coverage rate has declined, leading to substantial soil erosion. Choosing Lingshan County in the upper reaches of the Nanliu River as an example, the soil erosion area reached 3,120 hm^2 in 1974, increased to 5,500 hm^2 in 1980, and further increased to 2.141×10^5 hm^2 in 1987 (Li et al., 2016). Therefore, severe soil erosion caused relatively high SSC levels from 1972 to 2006, which is the second period.

Since 2000, the vegetation coverage in the Nanliu River Basin has started to increase, thanks to the large-scale artificial planting of eucalyptus forests. Simultaneously, In response to the problem of soil erosion, relevant departments have implemented corresponding measures. Governments at all levels in the basin area prioritized soil erosion control, extensively executed water and soil conservation laws and regulations, mobilized the masses to plant trees and build terraces, and achieved effective results. Governments at all levels increased funding to encourage people to engage in afforestation and fruit cultivation activities and prevent afforestation in mountains. Since 2016, the Yulin Municipal Government has carried out comprehensive work to improve the environment of the Nanliu River Basin. Therefore, effective results have been achieved in terms of forest protection, soil erosion has been effectively controlled, the river sediment load has been reduced, and the SSC has decreased, which represents the third period.

4.4.2 Economic and Social Development

By analysing the per capita GDP of the three cities of Qinzhou, Beihai, and Yulin in the Nanliu River Basin from 1989 to 2019, it was found that the per capita GDP of these three cities in the basin rapidly increased, revealing an upwards trend. From 1989 to 2006, the per capita GDP slowly rose. From 2007 to 2019, the per capita GDP rapidly increased (**Figure 13**). The GDP per capita of Qinzhou, Beihai, and Yulin in 2019 increased by 25, 24, and 14 times, respectively, over the 1993 levels, indicating that the economic development level in the Nanliu River Basin is continuously improving. With the improvement of economic level, the demand for construction land increases, which promotes the increase of building scale. It can be seen from **Figure 14** that the construction land area of Nanliu River increased significantly from 1988 to 2018. According to statistics, the construction area of Nanliu River Basin was 159 km^2 in 1988, and the construction area increased to 526 km^2 in 2018. In the past 30 years, the construction area increased by 367 km^2. River sediment and gravel are the main materials for construction (Chen et al., 2005), indicating that under the influence of the increase in demand for construction materials, sand mining activities increased to a certain extent, resulting in a decrease in river sediment. If the sediment transport is blocked by sand mining activities, the sediment carried by the water discharge will be reduced (Kondolf, 1997). To sum up, The economic development level and construction land of Nanliu River showed an upward trend in 1989–2019, But the SSC showed an overall downward trend (**Figure 2**; **Figure 3A**), indicating that there exists a connection among them. Therefore, sand mining activities caused by the improvement of economic development level may affect the reduction of river sediment to a certain extent, resulting in the decline of SSC.

4.4.3 Hydraulic Engineering

Studies have demonstrated that water conservancy projects such as dam regulation and reservoir construction projects are the main factors leading to reduction in the SSC in rivers flowing into the sea (Yang et al., 2005; Chu et al., 2009; Dai et al., 2016). The Nanliu River Basin contains two typical dams: Shahe Dam and Zongjiang Gate. Similarly, there are the Hongchaojiang Reservoir and Hepu Reservoir (Li et al., 2016). In 2002, Yulin city in the upper reaches and Hepu County in the lower reaches implemented embankments on both banks of the Nanliu River. Reconstruction and construction projects all control changes in the SSC along the Nanliu River. However, because most of these dams and reservoirs were built before 1965 in the basin, water and sediment observation data were lacking before 1965. At present, it is impossible to quantitatively evaluate the impact of dams and other hydraulic projects on the SSC. However, there is no doubt that the SSC has always been affected by human activities such as dam construction and reservoir repair activities.

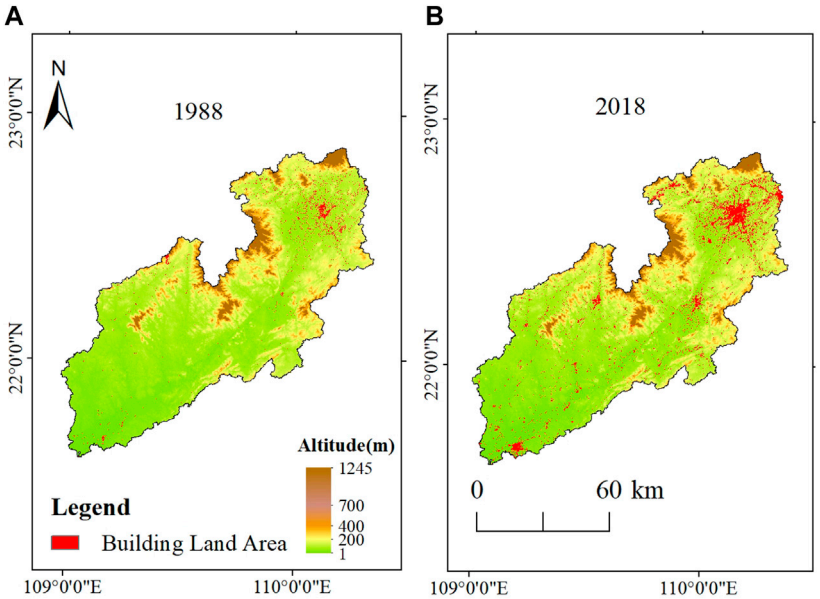

FIGURE 14 | Changes in nanliu river building land area: **(A)**1988; **(B)**2018.

5 CONCLUSION

As the largest river flowing into the Beibu Gulf along the coast of Guangxi, the Nanliu River plays a vital role in transporting suspended sediment from the river to the ocean. Here, analysis of the changes in the SSC provides a significant theoretical and practical significance in the Nanliu River. Therefore, we analysed SSC data for the Nanliu River in the past 60 years and obtained the following conclusions:

(1) The average SSC in the Nanliu River exhibited a downward trend from 1965 to 2020, and this period could be divided into three stages. The average SSC reached 0.25 kg/m^3 from 1965 to 1971, which was the highest average SSC value. From 1972 to 2006, the average value reached 0.16 kg/m^3, and the average SSC was relatively high. The average SSC was low from 2007 to 2020, with an average value of 0.11 kg/m^3.
(2) The average SSC in the Nanliu River revealed significant seasonal changes, and the observed seasonal oscillations also varied. High values of the SSC were mainly concentrated in the flood season, while low values were mostly distributed in the dry season. Moreover, the SCC during these three periods exhibited the characteristics of decreasing in the flood season and increasing in the dry season. Furthermore, the peak values of the SSC and water discharge in the watershed occurred obviously out of sync, and the former generally preceded the latter.
(3) In the past 60 years, the gradual and continuous decline in the SSC in the Nanliu River has been caused by human activities and climate change. This basin is relatively heavily affected by soil and water conservation projects, dam construction, reservoir water storage projects, and tropical cyclones. Between 1965 and 2020, the SSC was higher due to soil erosion. However, with the implementation of forest protection policies and construction of water conservancy projects, the SSC gradually decreased. Therefore, under the influence of human activities, the SSC in the Nanliu River may continue to decline in the future.

DATA AVAILABILITY STATEMENT

The data analyzed in this study is subject to the following licenses/restrictions: The data set is confidential. Requests to access these datasets should be directed to the corresponding author.

AUTHOR CONTRIBUTIONS

SL: Data Curation, Formal analysis, Project administration. XY: Writing—Original Draft, HH: Writing—Review and Editing. XL: Formal analysis, Visualization. RW: Field investigation and simulation test. BF: Field monitoring.

FUNDING

This study was supported by the National Science Foundation of Guangxi (2018JJD150005, 2019AC20109) and the National Science Foundation of China (NSFC) (41866001 and 41930537).

REFERENCES

Asselman, N. E. M. (1999). Suspended Sediment Dynamics in a Large Drainage Basin: the River Rhine. *Hydrol. Process.* 13, 1437–1450. doi:10.1002/(sici)1099-1085(199907)13:10<1437:aid-hyp821>3.0.co;2-j

Chen, X. Q., Zhang, E. F., Mu, H. Q., and Y, Z. (2005). A Preliminary Analysis of Human Impacts on Sediment Discharges from the Yangtze, China, into the Sea. *J. Coast. Res.* 21 (3), 515–521. doi:10.2112/03-0034.1

Chen, S.-L., Zhang, G.-A., Yang, S.-L., and Shi, J. Z. (2006). Temporal Variations of Fine Suspended Sediment Concentration in the Changjiang River Estuary and Adjacent Coastal Waters, China. *J. Hydrol.* 331, 137–145. doi:10.1016/j.jhydrol.2006.05.013

Chu, Z., Zhai, S., Zhang, J., and Ding, D. (2009). Filling of the Three Gorges Reservoir to the 135-m Level: Instant Effects on the Yangtze Discharge and Suspended Sediment Concentration Entering the Estuary. *J. Ocean. Univ. China* 8, 291–295. doi:10.1007/s11802-009-0291-6

Coleman, J. M., Roberts, H. H., and Stone, G. W. (1998). Mississippi River Delta: an Overview. *J. Coast. Res.* 14 (3), 698–716.

Dai, S. B., Yang, S. L., and Li, M. (2009). The Sharp Decrease in Suspended Sediment Supply from China's Rivers to the Sea: Anthropogenic and Natural Causes. *Hydrol. Sci. J.* 54, 135–146. doi:10.1623/hysj.54.1.135

Dai, Z., Du, J., Zhang, X., Su, N., and Li, J. (2011). Variation of Riverine Material Loads and Environmental Consequences on the Changjiang (Yangtze) Estuary in Recent Decades (1955-2008). *Environ. Sci. Technol.* 45, 223–227. doi:10.1021/es103026a

Dai, Z.-J., Chu, A., Li, W.-H., Li, J.-F., and Wu, H.-L. (2013). Has Suspended Sediment Concentration Near the Mouth Bar of the Yangtze (Changjiang) Estuary Been Declining in Recent Years? *J. Coast. Res.* 289 (4), 809–818. doi:10.2112/jcoastres-d-11-00200.1

Dai, Z., Liu, J. T., Wei, W., and Chen, J. (2014). Detection of the Three Gorges Dam Influence on the Changjiang (Yangtze River) Submerged Delta. *Sci. Rep.* 4, 6600. doi:10.1038/srep06600

Dai, Z., Fagherazzi, S., Mei, X., and Gao, J. (2016). Decline in Suspended Sediment Concentration Delivered by the Changjiang (Yangtze) River into the East China Sea between 1956 and 2013. *Geomorphology* 268, 123–132. doi:10.1016/j.geomorph.2016.06.009

Dan, S., Vandenabeele, S., Verwaest, T., and Montreuil, A.-L. (2020). Hydrodynamics versus Sediment Concentration at the Belgian Coast. *J. Coast. Res.* 95, 632–636. doi:10.2112/si95-123.1

Darby, S. E., Hackney, C. R., Leyland, J., Kummu, M., Lauri, H., Parsons, D. R., et al. (2016). Fluvial Sediment Supply to a Mega-Delta Reduced by Shifting Tropical-Cyclone Activity. *Nature* 539, 276–279. doi:10.1038/nature19809

Farnsworth, K. L., and Milliman, J. D. (2003). Effects of Climatic and Anthropogenic Change on Small Mountainous Rivers: the Salinas River Example. *Glob. Planet. Change* 39, 53–64. doi:10.1016/s0921-8181(03)00017-1

Ferreira, C. S. S., Walsh, R. P. D., Kalantari, Z., and Ferreira, A. J. D. (2020). Impact of Land-Use Changes on Spatiotemporal Suspended Sediment Dynamics within a Peri-Urban Catchment. *Water* 12, 665. doi:10.3390/w12030665

Gong, Z., Zhang, C. C., Zuo, C. B., and Wu, W. D. (2011). Sediment Transport Following Water Transfer from Yangtze River to Taihu Basin. *Water Sci. Eng.* 4 (04), 431–444. doi:10.3882/j.issn.1674-2370.2011.01.007

Guzman, C. D., Tilahun, S. A., Zegeye, A. D., and Steenhuis, T. S. (2013). Suspended Sediment Concentration-Discharge Relationships in the (Sub-) Humid Ethiopian Highlands. *Hydrol. Earth Syst. Sci.* 17, 1067–1077. doi:10.5194/hess-17-1067-2013

Hsu, Y.-S., and Cai, J.-F. (2010). Densimetric Monitoring Technique for Suspended-Sediment Concentrations. *J. Hydraul. Eng.* 136, 67–73. doi:10.1061/(asce)hy.1943-7900.0000132

Huang, Y.-G., Yang, H.-F., Jia, J.-J., Li, P., Zhang, W.-X., Wang, Y. P., et al. (2022). Declines in Suspended Sediment Concentration and Their Geomorphological and Biological Impacts in the Yangtze River Estuary and Adjacent Sea. *Estuar. Coast. Shelf Sci.* 265, 107708. doi:10.1016/j.ecss.2021.107708

Huang, Y.-G., Yang, H.-F., Wang, Y. P., Jia, J.-J., Wang, Z.-H., Zhu, Q., et al. (2022). Swell-driven Sediment Resuspension in the Yangtze Estuary during Tropical Cyclone Events. *Estuar. Coast. Shelf Sci.* 267, 107765. doi:10.1016/j.ecss.2022.107765

Kondolf, G. M. (1997). PROFILE: Hungry Water: Effects of Dams and Gravel Mining on River Channels. *Environ. Manag.* 21 (4), 533–551. doi:10.1007/s002679900048

Li, P., Yang, S. L., Milliman, J. D., Xu, K. H., Qin, W. H., Wu, C. S., et al. (2012). Spatial, Temporal, and Human-Induced Variations in Suspended Sediment Concentration in the Surface Waters of the Yangtze Estuary and Adjacent Coastal Areas. *Estuaries Coasts* 35 (5), 1316–1327. doi:10.1007/s12237-012-9523-x

Li, S. S., Dai, Z. J., Mei, X. F., Hu, H., Wei, W., and Gao, J. J. (2016). Dramatic Variations in Water Discharge and Sediment Load from Nanliu River (China) to the Beibu Gulf during 1960s–2013. *J. Quat. Int.* 440, 12–13. doi:10.1016/j.quaint.2016.02.065

Li, J., Chen, X., Townend, I., Shi, B., Du, J., Gao, J., et al. (2021). A Comparison Study on the Sediment Flocculation Process between a Bare Tidal Flat and a Clam Aquaculture Mudflat: The Important Role of Sediment Concentration and Biological Processes. *Mar. Geol.* 434, 106443. doi:10.1016/j.margeo.2021.106443

Matos, J. P., Hassan, M. A., Lu, X. X., and Franca, M. J. (2018). Probabilistic Prediction and Forecast of Daily Suspended Sediment Concentration on the Upper Yangtze River. *J. Geophys. Res. Earth Surf.* 123, 1982–2003. doi:10.1029/2017jf004240

Meade, R. H., and Moody, J. A. (2010). Causes for the Decline of Suspended Sediment Discharge in the Mississippi River System, 1940-2007. *Hydrol. Process.* 24, 35–49. doi:10.1002/hyp.7477

Montanher, O. C., Novo, E. M. L. d. M., and Souza Filho, E. E. d. (2018). Temporal Trend of the Suspended Sediment Transport of the Amazon River (1984-2016). *Hydrol. Sci. J.* 63, 1901–1912. doi:10.1080/02626667.2018.1546387

Moskalski, S., and Torre, R. (2012). Influences of Tides, Weather, and Discharge on Suspended Sediment Concentration. *Cont. Shelf Res.* 37, 36–45. doi:10.1016/j.csr.2012.01.015

Mouri, G., Ros, F. C., and Chalov, S. (2014). Characteristics of Suspended Sediment and River Discharge during the Beginning of Snowmelt in Volcanically Active Mountainous Environments. *Geomorphology* 213, 266–276. doi:10.1016/j.geomorph.2014.02.001

Müller, G., and Förstner, U. (1968). General Relationship between Suspended Sediment Concentration and Water Discharge in the Alpenrhein and Some Other Rivers. *Nature* 217 (5125), 244–245.

Nadal, E. R., Latron, J., Martí, B. C., and Regüés, D. (2007). Temporal Distribution of Suspended Sediment Transport in a Humid Mediterranean Badland Area: The Araguás Catchment, Central Pyrenees. *J. Geomorphol.* 97, 601–616. doi:10.1016/j.geomorph.2007.09.009

Ramalingam, S., and Chandra, V. (2019). Experimental Investigation of Water Temperature Influence on Suspended Sediment Concentration. *Environ. Process.* 6, 511–523. doi:10.1007/s40710-019-00371-0

Shams, S., Ratnayake, U., Abdul Rahman, E. K., and Alimin, A. A. (2020). Analysis of Sediment Load under Combined Effect of Rainfall and Flow. *IOP Conf. Ser. Earth Environ. Sci.* 476, 012111. doi:10.1088/1755-1315/476/1/012111

Shi, B. W., Yang, S. L., Wang, Y. P., Li, G. C., Li, M. L., Li, P., et al. (2017). Role of Wind in Erosion-Accretion Cycles on an Estuarine Mudflat. *J. Geophys. Res. Oceans* 122 (1), 193–206. doi:10.1002/2016jc011902

Syvitski, J. P. M., Vörösmarty, C. J., kettner, A. J., and Green, P. (2005). Impact of Humans on the Flux of Terrestrial Sediment to the Global Coastal Ocean. *Science* 308, 376–380. doi:10.1126/science.1109454

Tang, J., Wang, Y. P., Zhu, Q., Jia, J., Xiong, J., Cheng, P., et al. (2019). Winter Storms Induced High Suspended Sediment Concentration along the North Offshore Seabed of the Changjiang Estuary. *Estuar. Coast. Shelf Sci.* 228, 106351. doi:10.1016/j.ecss.2019.106351

Tang, R., Dai, Z., Zhou, X., and Li, S. (2021). Tropical Cyclone-Induced Water and Suspended Sediment Discharge Delivered by Mountainous Rivers into the Beibu Gulf, South china. *Geomorphology* 389, 107844. doi:10.1016/j.geomorph.2021.107844

Tang, R. G., Shen, F., Ge, J. Z., Yang, S. L., and Gao, W. L. (2021). Investigating Typhoon Impact on SSC through Hourly Satellite and Real-Time Field Observations: A Case Study of the Yangtze Estuary. *J. Cont. Shelf Res.* 224, 104475. doi:10.1016/j.csr.2021.104475

Tramblay, Y., St-Hilaire, A., and Ouarda, T. B. M. J. (2008). Frequency Analysis of Maximum Annual Suspended Sediment Concentrations in North America. *J. Water Energy Abstr.* 18, 12–13. doi:10.1623/hysj.53.1.236

van Maren, D. S., Oost, A. P., Wang, Z. B., and Vos, P. C. (2016). The Effect of Land Reclamations and Sediment Extraction on the Suspended Sediment Concentration in the Ems Estuary. *Mar. Geol.* 376, 147–157. doi:10.1016/j.margeo.2016.03.007

Walling, D. E., and Fang, D. (2003). Recent Trends in the Suspended Sediment Loads of the World's Rivers. *Glob. Planet. Change* 39, 111–126. doi:10.1016/s0921-8181(03)00020-1

Wang, H., Bi, N., Saito, Y., Wang, Y., Sun, X., Zhang, J., et al. (2010). Recent Changes in Sediment Delivery by the Huanghe (Yellow River) to the Sea: Causes and Environmental Implications in its Estuary. *J. Hydrol.* 391, 302–313. doi:10.1016/j.jhydrol.2010.07.030

Wang, C., Dai, S. B., Ran, L. S., Jiang, L., Li, W. T., and Mischke, S. (2015). Contribution of River Mouth Reach to Sediment Load of the Yangtze River. *Adv. Meteorol.* 2015, 1–9. doi:10.1155/2015/415058

Wei, L., Shen, F., He, Q., Cao, F., Zhao, H., and Li, M. (2021). Changes in Suspended Sediments in the Yangtze River Estuary from 1984 to 2020: Responses to Basin and Estuarine Engineering Constructions. *J. Sci. Total Environ.* 805, 150381. doi:10.1016/j.scitotenv.2021.150381

Wu, C. S., Yang, S. L., and Lei, Y.-p. (2012). Quantifying the Anthropogenic and Climatic Impacts on Water Discharge and Sediment Load in the Pearl River (Zhujiang),China (1954-2009). *J. Hydrol.* 452-453, 190–204. doi:10.1016/j.jhydrol.2012.05.064

Wu, C., Ji, C., Shi, B., Wang, Y., Gao, J., Yang, Y., et al. (2019). The Impact of Climate Change and Human Activities on Streamflow and Sediment Load in the Pearl River Basin. *Int. J. Sedim. Res.* 34, 307–321. doi:10.1016/j.ijsrc.2019.01.002

Yang, S.-l., Zhao, Q.-y., and Belkin, I. M. (2002). Temporal Variation in the Sediment Load of the Yangtze River and the Influences of Human Activities. *J. Hydrol.* 263, 56–71. doi:10.1016/s0022-1694(02)00028-8

Yang, S. L., Zhang, J., Zhu, J., Smith, J. P., Dai, S. B., Gao, A., et al. (2005). Impact of Dams on Yangtze River Sediment Supply to the Sea and Delta Intertidal Wetland Response. *J. Geophys. Res.* 110 (1-12), F03006. doi:10.1029/2004jf000271

Yang, S. L., Luo, X., Temmerman, S., Kirwan, M., Bouma, T., Xu, K., et al. (2020). Role of Delta-front Erosion in Sustaining Salt Marshes under Sea-level Rise and Fluvial Sediment Decline. *Limnol. Oceanogr.* 65 (9), 1990–2009. doi:10.1002/lno.11432

Yang, S. L., Xu, K. H., Milliman, J. D., Yang, H. F., and Wu, C. S. (2015). Decline of Yangtze River Water and Sediment Discharge: Impact from Natural and Anthropogenic Changes. *Sci. Rep.* 5, 12581. doi:10.1038/srep12581

Yang, Y.-P., Zhang, M.-J., Li, Y.-T., and Zhang, W. (2015). The Variations of Suspended Sediment Concentration in Yangtze River Estuary. *J. Hydrodyn.* 27, 845–856. doi:10.1016/s1001-6058(15)60547-9

Zhang, X., Hu, F., Zhang, J., and Tang, D. (2014). Northward Drift of Suspended Sediments in the Yangtze Estuary in Spring. *Int. J. Remote Sens.* 35, 4114–4126. doi:10.1080/01431161.2014.916455

Zhang, Y., Wang, P., Wu, B., and Hou, S. (2015). An Experimental Study of Fluvial Processes at Asymmetrical River Confluences with Hyperconcentrated Tributary Flows. *Geomorphology* 230, 26–36. doi:10.1016/j.geomorph.2014.11.001

Zhang, J., Zhang, X., Li, R., Chen, L., and Lin, P. (2017). Did Streamflow or Suspended Sediment Concentration Changes Reduce Sediment Load in the Middle Reaches of the Yellow River? *J. Hydrol.* 546, 357–369. doi:10.1016/j.jhydrol.2017.01.002

Zuo, S.-h., Zhang, N.-c., Li, B., and Chen, S.-l. (2012). A Study of Suspended Sediment Concentration in Yangshan Deep-Water Port in Shanghai, China. *Int. J. Sedim. Res.* 27, 50–60. doi:10.1016/s1001-6279(12)60015-8

Conflict of Interest: The authors declare that the research was conducted in the absence of any commercial or financial relationships that could be construed as a potential conflict of interest.

frontiers | Frontiers in Earth Science

ORIGINAL RESEARCH
published: 01 July 2022
doi: 10.3389/feart.2022.921995

Bottom Drag Variations Under Waves and Currents: A Case Study on a Muddy Deposit off the Shandong Peninsula

Fukang Qi[1], *Zhiqiang Liu*[1,2] *and Jingping Xu*[1,2]*

[1]Department of Ocean Science and Engineering, Southern University of Science and Technology, Shenzhen, China, [2]Southern Marine Science and Engineering Guangdong Laboratory (Guangzhou), Guangzhou, China

Bottom drag coefficient is one of the key parameters in quantifying shelf hydrodynamics and sediment transport processes. It varies markedly due to dynamic forcing and bed type differences, so a set of empirical values have been used for beds of coarse material where bedforms are often present. In comparison, dramatically fewer such rule-of-thumb values are available for muddy beds. Here, we present results of variations in bottom drag as calculated from *in situ* measurements by bottom-mounted tripods that were placed across the top of a muddy deposit during two different deployments, one in summer and another in winter. A tidal asymmetry of bottom drag was observed, most likely caused by variations of local bed roughness. For hydrodynamically smooth ($Re < 2.3 \times 10^5$) flows, computed values of bottom drag coefficient were fairly scattered but still showed an overall decreasing trend with an increase in Reynolds number. The bottom drag coefficient for hydrodynamically rough or transitional flow was typically constant, while the averaged drag coefficient over all observation periods was 1.7×10^{-3}. Smaller waves (bottom orbital velocity u_b <0.1 m/s) had a very limited impact on the bottom drag coefficient. However, with an increase in u_b, the wave–current interactions can decrease the time-averaged near-bed velocity and enhance turbulent kinetic energy, thus leading to an increase in the drag coefficient.

Keywords: continental shelf, drag coefficient, muddy deposit, tidal asymmetry, wave–current interaction

OPEN ACCESS

Edited by:
Ya Ping Wang,
East China Normal University, China

Reviewed by:
Qian Yu,
Nanjing University, China
Junbiao Tu,
Tongji University, China

***Correspondence:**
Jingping Xu
xujp@sustech.edu.cn

Specialty section:
This article was submitted to Geohazards and Georisks, a section of the journal Frontiers in Earth Science

Received: *17 April 2022*
Accepted: *12 May 2022*
Published: *01 July 2022*

Citation:
Qi F, Liu Z and Xu J (2022) Bottom Drag Variations Under Waves and Currents: A Case Study on a Muddy Deposit off the Shandong Peninsula. Front. Earth Sci. 10:921995. doi: 10.3389/feart.2022.921995

INTRODUCTION

Within the bottom boundary layer (BBL) on an oceanic shelf, bottom friction changes the velocity profile of the flow and the production/dissipation of turbulence, thus affecting the processes of physical, biological, chemical, and sediment transport (Trowbridge and Lentz, 2018). Among the numerous hydrodynamic and sediment dynamic models (Fringer et al., 2019), the current-related bed shear stress, τ_c, is commonly parameterized with the quadratic drag-law:

$$\tau_c = \rho C_D \bar{u}|\bar{u}|, \tag{1}$$

where ρ is the water density, $\bar{u}$ is the near-bed burst mean current velocity, and C_D is the bottom drag coefficient. In a current BBL (without waves and unstratified), the near-bed current velocity is usually represented by the logarithmic law of the wall (log-law):

$$\bar{u}(z) = \frac{u_{*c}}{\kappa} ln\left(\frac{z}{z_0}\right), \quad (2)$$

where u_{*c} ($\sqrt{\tau_c/\rho}$) is current-related frictional velocity, κ = 0.40 is the von Kármán constant, and z_0 is hydrodynamic roughness length, which is commonly a function of grain size, bedforms, and sediment motion (Xu and Wright, 1995; Trembanis et al., 2004). Combining **Eqs. 1**, **2**, we can deduce that the value C_D depends upon z_0 (e.g., Soulsby, 1997; Feddersen et al., 2003). Regions of sandy deposits with ripples or sand waves C_D could be well estimated by z_0 assuming the anisotropy of bedforms is appropriately quantified with sufficient spatiotemporal resolution (Scully et al., 2018). Unlike sandy deposits, sediments in muddy deposits usually exhibit cohesive properties that hinder the development of bedforms such as ripples (Baas et al., 2019). In the research practice of hydrodynamics, C_D is usually assumed to be a constant or a tuning parameter in the muddy areas (e.g., Harris and Wiberg, 2001; Magaldi et al., 2009). However, numerous observational studies have shown that C_D varies with waves, currents, biological conditions, and stratifications (e.g., Herrmann and Madsen, 2007; Safak, 2016; Xu et al., 2017; Egan et al., 2020a).

In the shallow water of continental shelves, the presence of surface waves (therefore wave-current interaction) impacts the hydrodynamics of the centimeter-scale wave BBL as well as the entire water column (Grant and Madsen, 1986). Wave actions change the velocity structure within the BBL and cause the flow to experience stronger drag (Grant and Madsen, 1979; Signell and List, 1997; Styles and Glenn, 2000; Nayak et al., 2015; Egan et al., 2019), but a recent study by Nelson and Fringer (2018) has shown that waves may lead to a decrease in drag on a smooth bed. Enhanced shear stress by energetic waves often leads to the resuspension of bed sediments (Brand et al., 2010; Egan et al., 2020b), which can further lead to stratification of suspended sediment and the drag-reduction effect on the flow (e.g., Wright et al., 1999; Peng et al., 2020). Therefore, the use of *in situ* data to obtain C_D a certain spatial and temporal resolution is of great importance for hydrodynamic and sediment dynamic studies.

Recent studies on sediment transport processes in the muddy areas of the East China Shelf Seas (ECSS) have often deployed numerical models such as the Regional Ocean Modeling System (e.g., Bian et al., 2013; Liu et al., 2015; Wang et al., 2019; Wang et al., 2020). The Regional Ocean Modeling System implements the simple quadratic drag-law approach for calculating BBL processes that require user input of the drag coefficient (Warner et al., 2008). This is often not an easy task because direct measurements of a drag coefficient are extremely scarce in the muddy areas of the ECSS due to a lack of *in situ* observations. Fan et al. (2019) derived the empirical relationship between C_D both currents and waves based on BBL observations at eight stations scattered over the ECSS, many of which are composed of the sandy sea bottom. To our knowledge, however, there has been no report on whether this empirical relationship also applies to coastal muddy areas of the ECSS.

In this study, a field campaign was conducted to measure the BBL dynamics across the top of a mud deposit off the Shandong Peninsula in the Yellow Sea of China. Reynolds stress, therefore C_D, can be estimated from those direct measurements of flows and turbulences. Our goal is to quantify the temporal and spatial variation C_D across the mud deposit, which is essential to interpreting the sediment transport and deposition patterns that shape the unique, elongated mud deposit. This paper is arranged as follows: This paper is arranged as follows: this *"Introduction"* is followed by *"Study Area"*. *"Materials and Methods"* describes the data and methods used in this study. The time series and tidally averages C_D are presented in *"Results"*. Detailed analyses on flood–ebb asymmetry C_D and the effect of waves are discussed in *"Discussion"*. *"Conclusion"* summarizes the findings in this research.

STUDY AREA

The scene of this study is around the depocenter of a muddy deposit in the coastal seas to the east of the Shandong Peninsula, China (**Figure 1A**). The water depths at the study stations are basically within 40 m, and their specific values are shown in **Table 1**. Previous sedimentary studies suggested that this muddy deposit was formed by sediments sourced from the Yellow River and transported by the Shandong Coastal Currents (SDCC), which flow out of the Bohai Sea to the Yellow Sea around the Shandong Peninsula (**Figure 1A**) (Alexander et al., 1991; Yang and Liu, 2007). Followed the Shepard scheme (Shepard, 1954), the surface sediment in the study area belongs to sandy silt with a mean grain size ranging from 5 to 6 ϕ (Yuan et al., 2020). Moreover, because the mud fraction is more than 10% (Yuan et al., 2020; Qi et al., 2022), the bed sediment may have significant cohesive properties (Bass et al., 2002; Van Rijn, 2007). In the Yellow Sea, the principal tidal constituent is M_2, followed by S_2 and K_1 (Teague et al., 1998). The hydrography of the Yellow Sea is also influenced by the seasonally varied East Asian Monsoon (Naimie et al., 2001). In summer, the southerly winds dominate the wind field, and in winter, strong northerly winds generally prevail over the Yellow Sea (Bian et al., 2013; Mo et al., 2016; Wang et al., 2020).

MATERIALS AND METHODS

Data Collection

Tripods were deployed at three stations on the Inner Shelf of the Shandong Peninsula during two 10-day field campaigns, one in summer (August 18–27, 2017), and another in winter (February 23–March 2, 2018) (**Figure 1B**). One more winter deployment (January 6–26, 2020) was conducted to make up for a fallen instrument at S2 during a previous deployment. Each tripod was equipped with an upward-looking Teledyne/RDI 600 kHz Acoustic Doppler Current Profiler (ADCP), a Nortek Vector Acoustic Doppler Velocimeter (ADV), a conductivity/temperature (CT) sensor, and a turbidity sensor (OBS or RBR-TU) (**Table 1**). The sampling period of each instrument is shown in **Table 1**. In addition, for winter observations at S2, turbidity sensors were placed at 0.45, 0.9, and 1.34 m above the bottom (mab) to record sediment concentrations within the bottom boundary layer (**Table 1**). CTD (SeaBird 19) packaged with Niskin bottles and a turbidity sensor was cast to collect water samples and profiles of temperature, salinity, and turbidity periodically from the watching boats that guarded each

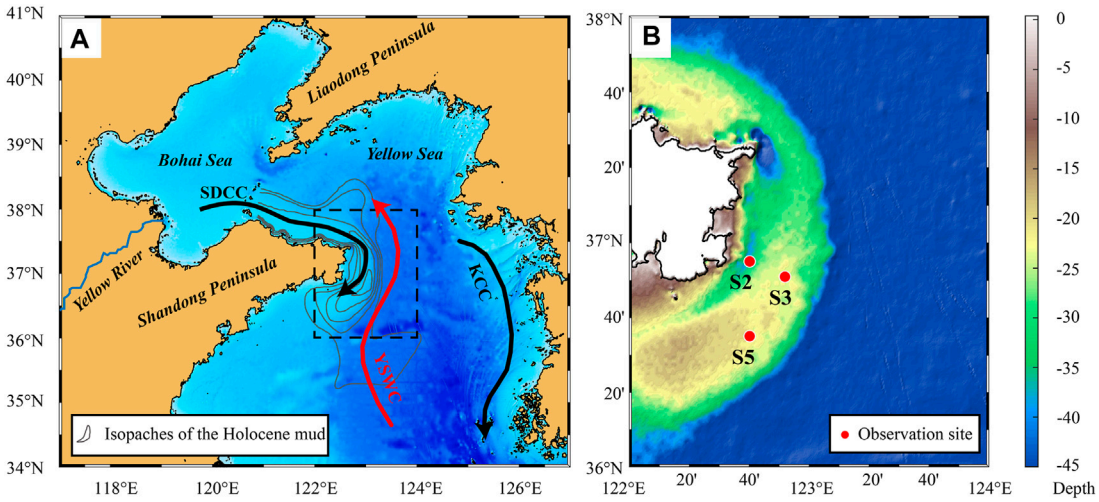

FIGURE 1 | (A) Topography and currents of the Bohai and Yellow seas. The isopaches of the muddy area were from Yang and Liu (2007), and the currents were based on Bian et al. (2013). These currents are the Shandong Coastal Current (SDCC), the Yellow Sea Warm Current (YSWC), and the Korea Coastal Current (KCC) **(B)** The location of the observation sites.

TABLE 1 | Mean water depth and settings of six observations.

Label	Depth (m)	Instruments	Mab	Sampling
S2 summer	40.1	ADCP	1.8	20 min (currents), 1 h (waves)
		ADV	0.67	1/32 s
		RBR-CT	1.1	3 s
		OBS	1.1	40 s
S3 summer	26.5	ADCP	1.5	10 min
		ADV	0.4	1/32 s
		RBR-CT	0.88	3 s
		OBS	0.88	1 min
S5 summer	23.3	ADCP	1.7	10 min
		ADV	0.48	1/32 s
		RBR-CT	1.15	3 s
		RBR-TU	1.15	3 s
S2 winter	38.9	ADCP	1.7	2 min (currents), 1 h (waves)
		ADV	0.6	1/32 s
		RBR-CT	0.83	10 s
		RBR-TU	0.45, 0.9, 1.34	3 s, 10 s, 3 s
S3 winter	26.6	ADCP	1.9	20 min (currents), 1 h (waves)
		ADV	0.88	1/32 s
		RBR-CT	1.16	10 s
		RBR-TU	1.16	10 s
S5 winter	23.3	ADCP	1.85	20 min (currents), 1 h (waves)
		ADV	0.84	1/32 s
		RBR-CT	1.2	10 s
		RBR-TU	1.2	10 s

Teledyne/RDI Acoustic Doppler Current Profiler (ADCP, 600 kHz); Nortek Vector Acoustic Doppler Velocimeter (ADV); Conductivity/temperature sensor (CT); Turbidity sensor (OBS or RBR-TU). Sites S2, S3, and S5 are mapped in ***Figure 1****.*

instrument against being damaged by trawling nets of passing fishing boats. These water samples were used to calibrate and convert the observed turbidities into suspended sediment concentrations (SSCs). Detailed processes of data quality assurance/quality control and calibration can be found in Qi et al. (2022).

Most ADCPs are equipped with a waving module that enables wave measurements (**Table 1**). In addition, hourly significant wave height and wave period data from the WaveWatch III Global Wave Model (WW3) at approximately 0.5° (~50 km) resolution (Tolman et al., 2014), is widely used in coastal studies (e.g., Duan et al., 2020; Silva et al., 2018), were downloaded. We compared the modeled and observed significant wave height (H_s) and peak wave period (T_p) at Site 3 (S3) in winter to verify the validity of the model, and the results

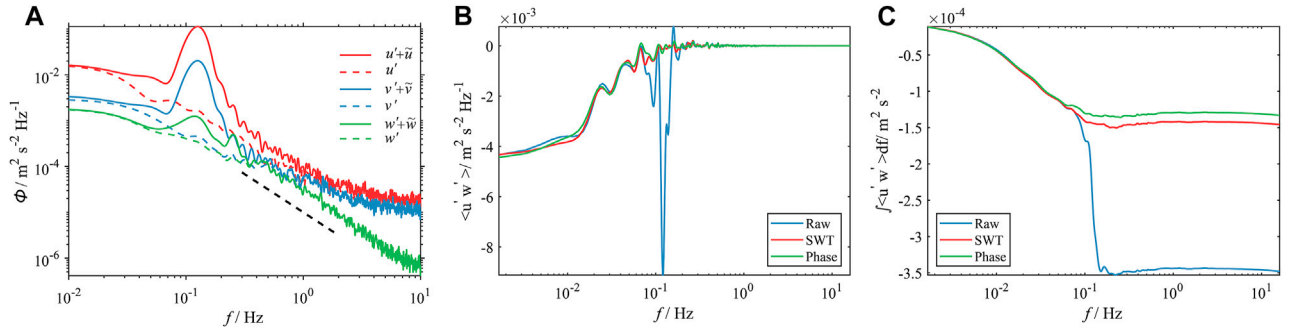

FIGURE 2 | (A) Power spectra of velocity fluctuation and turbulent fluctuation (u', v' and w') estimated by Phase method for burst 41 of S3 winter observation. **(B)** Cospectra and **(C)** accumulative cospectra of raw velocity fluctuation and turbulent fluctuations estimated by these two methods.

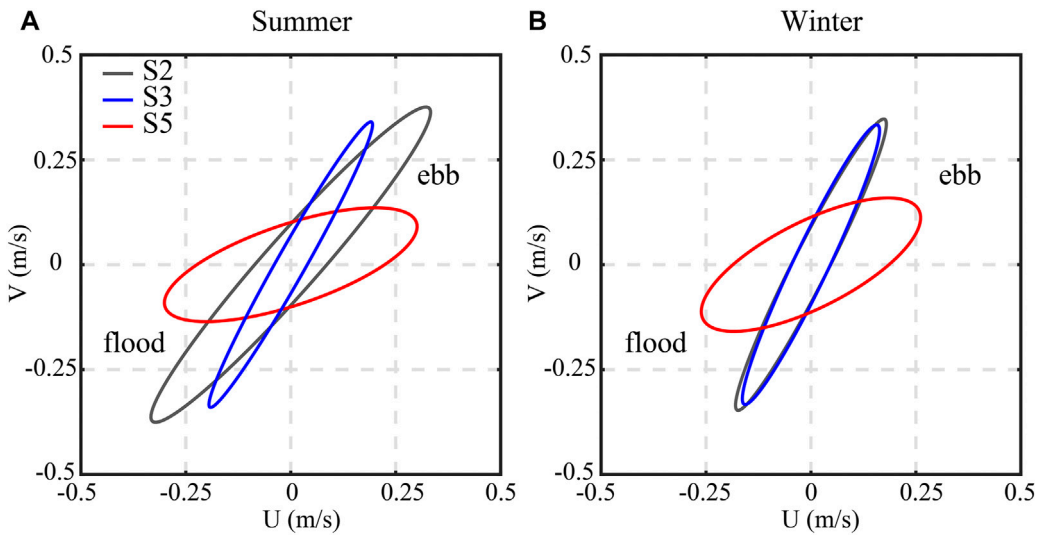

FIGURE 3 | Tidal ellipses of M_2 tidal components were calculated from the mean velocity at 1 mab in **(A)** summer and **(B)** winter for each of the three stations. The mean velocity was translated from ADV data by log law.

showed that both of them have a strong relationship, with a correlation coefficient R = 0.95 and 0.91, respectively (**Supplementary Figure S1**). Wind data were downloaded from the National Enters for Environmental Prediction Climate Forecast System Version 2 (NCEP/CFSv2) with a horizontal resolution of 0.205 ° × 0.204 ° (Saha et al., 2014).

Tidal Analysis and Wave Parameter Estimates

We used T_TIDE, a package of routines in MATLAB for harmonic analysis, to make a tidal prediction (Pawlowicz et al., 2002). In agreement with previous studies, the dominant tidal constituent was M_2, flowing southwest during flood tide and northeast during ebb tide.

The bottom wave orbital velocity, u_b, was estimated following Van Rijn (1993):

$$u_b = \frac{\pi H_s}{T_p \, shih\,(k \cdot h)}, \tag{3}$$

where H_s is the significant wave height, T_p is the peak wave period. k (= $2\pi/L$, where L is wavelength) is the wavenumber. Soulsby (2006) Newton–Raphson method was used to calculate wavenumbers, and the MATLAB function for this method could be found in Wiberg and Sherwood (2008). h is water depth.

Wave–Turbulence Decomposition and Turbulence Quantities

In a wavy aquatic environment, the ADV measured velocity components (u, v, and w) can be decomposed into the mean, wave, and turbulent fluctuation components. Before analysis, the horizontal velocities were rotated into a streamwise orthogonal coordinate system with u v components aligned with and

orthogonal to the direction of the mean flow. Take u as an example, $u = \bar{u} + \tilde{u} + u'$, where $\bar{u}$ the burst mean velocity averaged per 10 min, $\tilde{u}$ is the wave component and u_t' is the turbulent fluctuation. Assuming that waves and turbulence are uncorrelated (i.e., terms such as $\overline{u'\tilde{w}}$ vanish), the shear stress can be decomposed into turbulent and wave components:

$$\text{Total shear stress} = -\overline{u'w'} - \overline{\tilde{u}\tilde{w}}, \tag{4}$$

where $-\overline{u'w'}$ is the turbulent Reynolds stress and $-\overline{\tilde{u}\tilde{w}}$ is the wave momentum flux (wave stress). To obtain an accurate estimate of Reynolds stress, here we used the "Phase method" of Bricker and Monismith (2007) for the wave-turbulence decomposition (WTD). As shown in **Figure 2**, the Phase method can effectively remove the wave motions.

Following Feddersen and Williams (2007), we used the nondimensional integrated cospectrum (ogive) for controlling the quality of WTD and the Reynolds stress estimates. The ogive for $\overline{u'w'}$ is defined as

$$Og_{u'w'}(f) = \frac{\int^{f} Co_{u'w'}(\hat{f})d\hat{f}}{\langle u'w' \rangle}, \tag{5}$$

where $Co_{u'w'}$ is the $u'w'$ cospectrum. After removing the wave bias, the $Og(f)$ curves are expected to increase smoothly from 0 to 1 in the range $10^{-1} < 2\pi f z u < 10$ (Feddersen and Williams, 2007), similar to empirical curves proposed by Kaimal et al. (1972). Following Ruessink (2010), we applied the ogive acceptance range as: $-0.3 < Og(f) < 1.3$, where estimates outside of this range were eliminated. In addition, referring to Tu et al. (2021), we compared the observed ogive curves $\overline{u'w'}$ in the empirical form and rejected those that were not well fitted. The ogive test excluded 8.5–29.7% of the bursts from each deployment (**Supplementary Table S1**).

After obtaining the turbulent fluctuation in three directions, we calculated the Reynolds stress, turbulent kinetic energy (TKE), and turbulent energy dissipation rates (ε). The TKE was estimated as: $1/2\rho(\overline{u'^2} + \overline{v'^2} + \overline{w'^2})$. The inertial dissipation method was used to calculate the turbulent energy dissipation rates (Liu and Wei, 2007):

$$\varepsilon = 2\pi U^{-1}\alpha_3^{-3/2}\overline{\left[f^{5/2}\phi_{w'}^{3/2}(f)\right]}, \tag{6}$$

where U is the mean velocity of each burst, $\alpha_3 \approx 0.71$ is the Kolmogorov constant (Sreenivasan and Katepalli, 1995), f is the frequency of the inertial subrange, which is approximately 1–3 Hz here (**Figure 2**), and $\phi_{w_t'}$ is the frequency spectrum density of the w component over the inertial subrange.

Calculation of the Bottom Drag Coefficient

The Bottom drag coefficient was estimated following Egan et al. (2020a). As $\tau_c = -\rho\overline{u'w'}$, we rearranged **Eq. 1** and obtained

$$C_D = \frac{-\overline{u'w'}}{\bar{u}|\bar{u}|}. \tag{7}$$

The instantaneous C_D can be directly calculated by **Eq. 7**, and the C_D in a certain range of conditions (e.g., flood and ebb tide) can be estimated as the best-fit slope from a least-squares regression of the two terms on the right-hand side of **Eq. 7**. For the convenience of comparing C_D at different sites, we applied the log-law to deduce mean velocity at 1 mab ($\bar{u}_{100}$) during weak waves and unstratified periods. Based on **Eq. 2**, the mean current velocity at the reference height (1 mab) can be expressed as $\bar{u}_{100} = u(z) + (u_{*c}/\kappa)ln(1/z)$. C_{100} represents the drag coefficient calculated at 1 mab. As the calculation C_D is based on the assumption that the measuring volume is within the constant stress layer which is ~10–30% of the BBL thickness (δ) (Soulsby, 1997), we calculated δ using the equation (Soulsby, 1983): $\delta = 0.44u_{*c}/f$, where f is the Coriolis parameter, and retained data for δ greater than 10 m. The calculation results show that more than 99.8% of the bursts satisfy this condition.

Combining **Eqs. 1**, **2**, we can deduce the dependence of C_D on z_0:

$$C_D = \left[\frac{1}{\kappa}ln\left(\frac{z}{z_0}\right)\right]^{-2}. \tag{8}$$

RESULTS

Tides, Currents, Waves, and Winds

Figure 3 shows the tidal ellipses of M_2 tidal components in summer and winter for each of the three stations. According to the rotation rate of the tidal ellipse, tide currents in sites S2 and S3 were reversing currents, while the tide in Site 5 (S5) was rotary currents (**Figure 3**). The maximum tidal velocity had a certain difference for each site, and was generally satisfied: S2>S3>S5, where the maximum tidal velocity of S2 was approximately 0.5 m/s (**Figure 3**).

Figure 4 shows the magnitude of wave orbital velocities and wave directions. The maximum value of wave orbital velocity in summer was about 0.12 m/s (**Figure 4A**), and the average values were 0.01 m/s, 0.03 m/s, and 0.04 m/s at S2, S3, and S5, respectively. The wave propagation was mainly in the northwesterly direction in summer. It was not exactly matching with the direction of the instantaneous winds (**Figure 5A**) but was consistent with the trend of the prevailing southerly winds (Wu et al., 2019), indicating that the swell waves and background flow dominated the wave propagation.

The overall intensity of waves was significantly higher in winter than that in summer (**Figure 4**). The maximum value of wave orbital velocity in winter was about 0.37 m/s, and the average values at S2, S3, and S5 were 0.01 m/s, 0.05 m/s, and 0.06 m/s, respectively. The wave direction was modulated by the local wind field. During periods of weak wind (wind speed less than 10 m/s), the wind direction was not fixed and was dominated alternately by southwesterly and northeasterly winds (**Figure 5B**). Therefore, when the orbital velocity was smaller than 0.1 m/s, the wave propagation direction was mainly southwestward or northeastward (**Figure 4B**). However, the stronger wind events (wind speed greater than 10 m/s) that occurred during the observation period were dominated by northerly winds (**Figure 5B**). Therefore, the wave propagation direction was mainly southwesterly when the orbital velocity was greater than 0.1 m/s (**Figure 4B**). Wave orbital velocities were higher

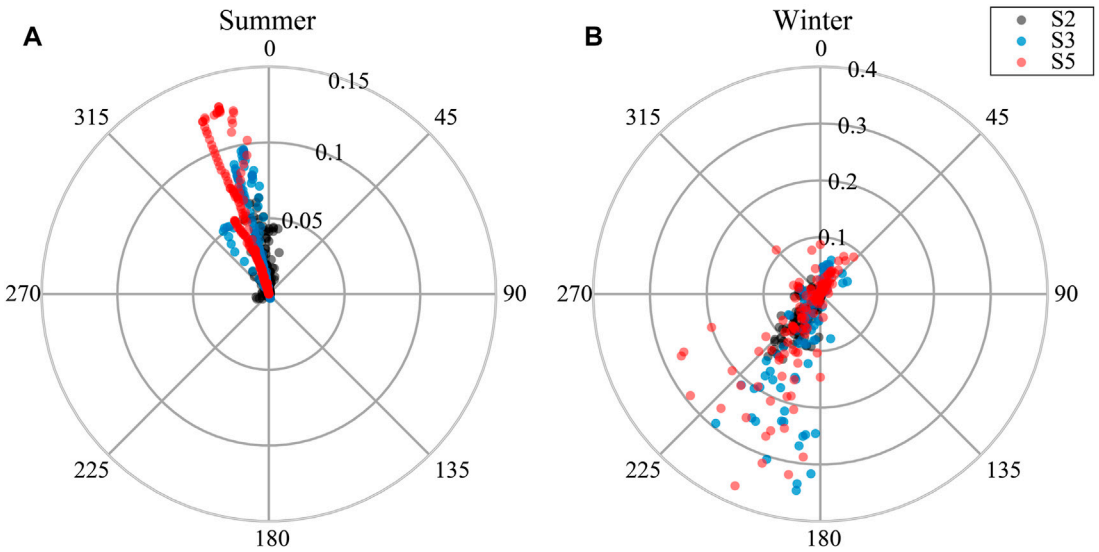

FIGURE 4 | Wave magnitude and direction for three stations (S2, S3, and S5) in **(A)** summer and **(B)** winter, with 0° corresponding to the northward propagating wave, and the radial axis representing the bottom wave-orbital velocity, u_b, in m/s.

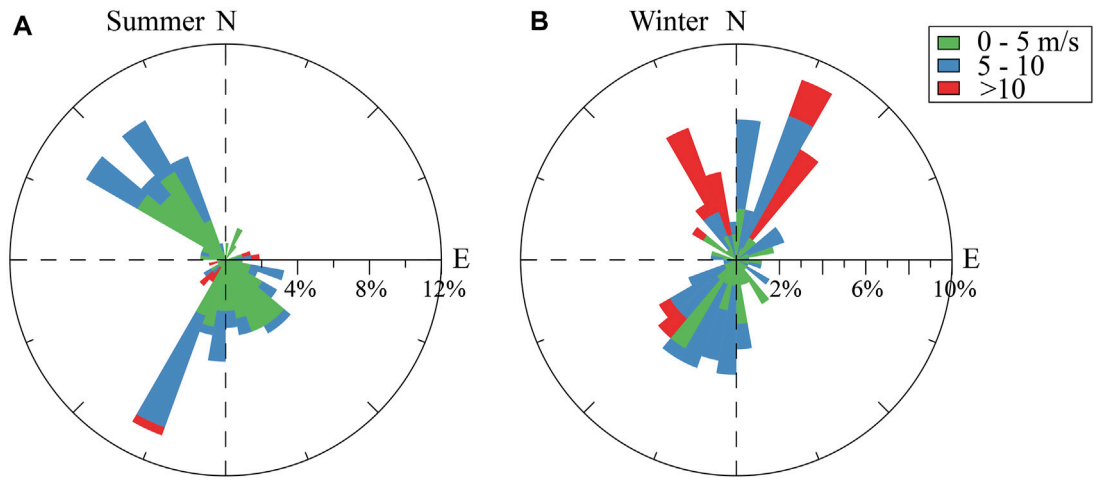

FIGURE 5 | Rose diagrams of hourly averaged wind frequencies during **(A)** summer and **(B)** winter observations at S3. The greyscale indicates the categories of wind speed (m/s).

at S3 and S5 than that at S2 because of the shallower water depth (**Table 1**). We used data in winter to discuss wave-current interactions in the rest of the article.

Bottom Drag Coefficient

First, we estimated time-series C_D values at the three stations during both summer and winter deployments. In summer, C_D varied from 5×10^{-4} to 10^{-2} at all stations, with most of it between 10^{-3} and 2×10^{-3} (**Figure 6**). In winter, C_D varied from 10^{-3} to 10^{-2} at S3 and S5, with most of it between 10^{-3} and 3×10^{-3} (**Figure 7**). At S2 in winter, the range C_D was the same as S3 and S5 before January 18. However, after 18 the maximum C_D extent to 10^{-1} (**Figure 8B**). From the time series data, we found that a sudden increase of the near-bottom SSC occurred around 08:00 on January 18 of the winter observation at S2 (**Figure 8C**). Thus, we divided the data into two periods: calm and event periods (**Figure 8**). The probable reason for this event will be discussed in the following part. Moreover, we found that C_D showed varying degrees of flood–ebb tidal asymmetry during the different observation periods. For example, at S3 in summer, the C_D values during ebb tides were larger than those during flood tides (**Figure 6D**). However, this relationship was not fixed between observations at different stations or even at the same station in different seasons. For example, station S2 had a larger

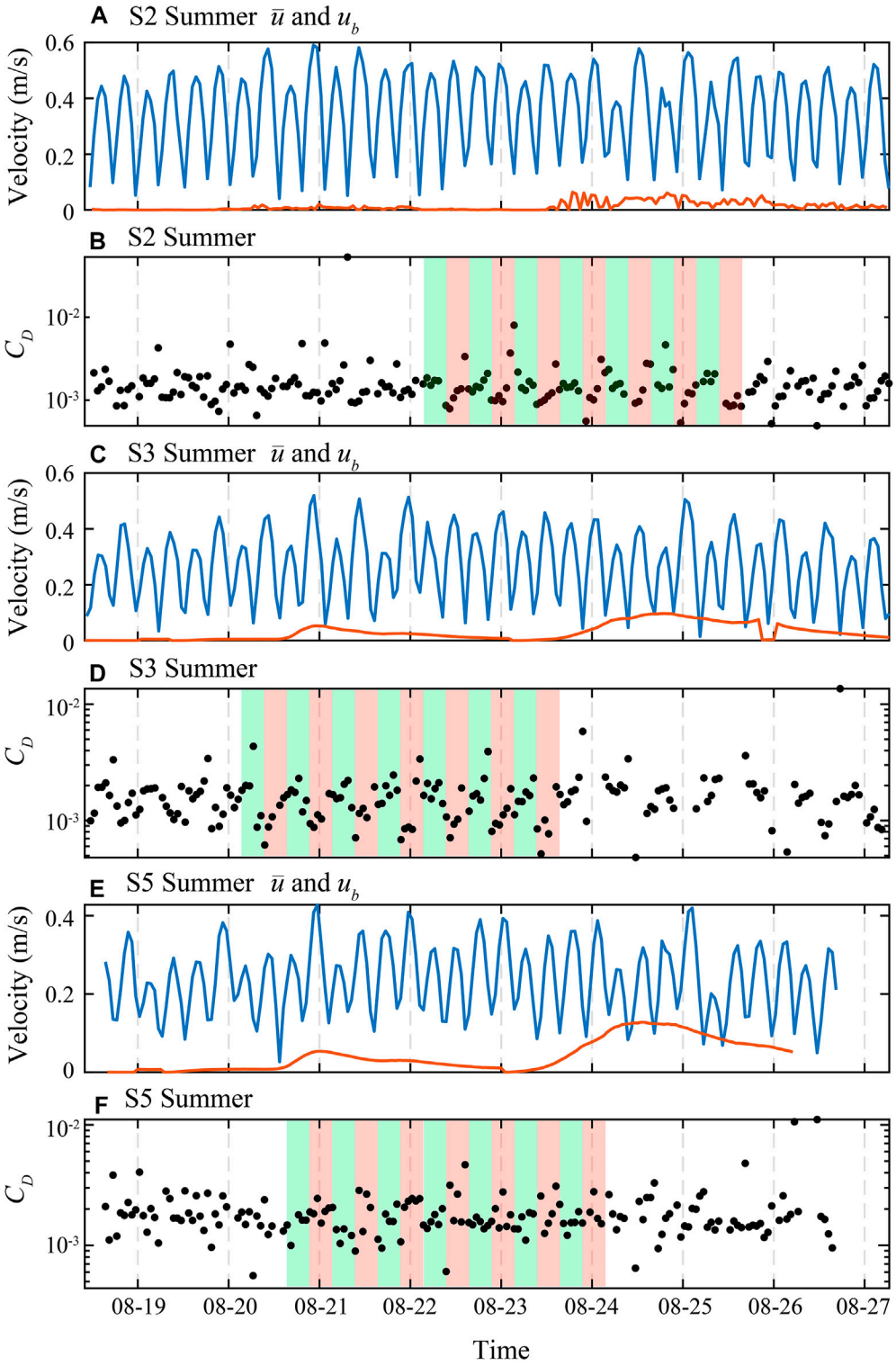

FIGURE 6 | Time series of **(A,C,E)** ADV's burst mean velocity ($\bar{u}$, blue line) and bottom wave orbital velocity (u_b, orange line) and **(B,D,F)** drag coefficient, C_D, estimated using ADV's burst mean velocity at S2, S3, and S5 in summer. Green and red shaded areas denote periods of ebb and flood tides, respectively.

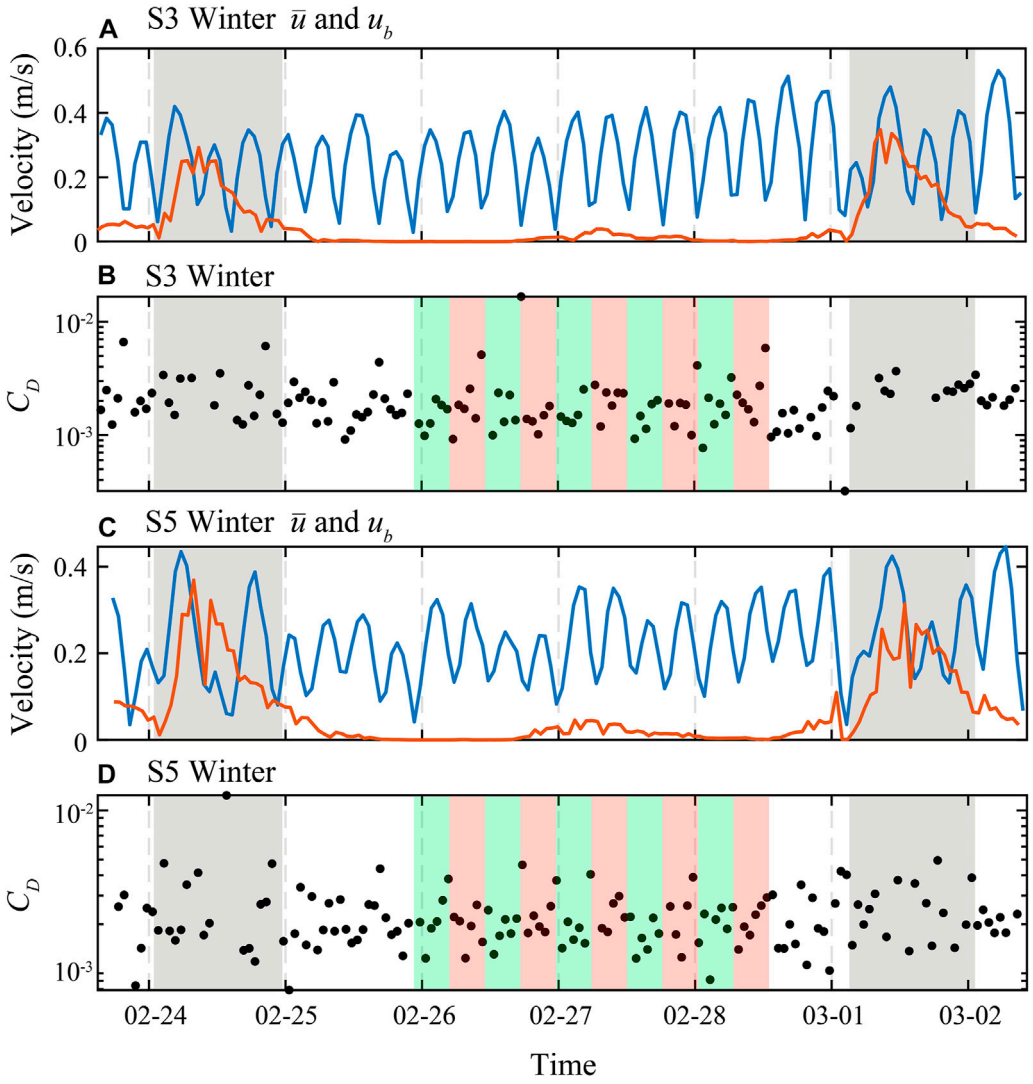

FIGURE 7 | Time series of **(A,C)** ADV's burst mean velocity ($\bar{u}$, blue line) and bottom wave orbital velocity (u_b, orange line) and **(B,D)** drag coefficient, C_D, estimated using ADV's burst mean velocity at S3 and S5 in winter. Green and red shaded areas denote periods of ebb and flood tides, respectively, and gray shaded areas denote periods of strong winds.

C_D ebb tide in summer (**Figure 6B**) and a larger C_D flood tide in winter (**Figure 8B**). Moreover, after the event, C_D increased significantly during flood tides, while the change C_D during ebb tides was relatively small (**Figure 8B**). In addition, the fluctuation C_D in summer followed the tidal cycle variation of flow velocity while the effect of waves was weak (**Figure 6**). But in winter, affected by stronger waves, C_D during the wind events were relatively larger than that during calm periods at all three stations (**Figures 7**,**8A**,**8B**).

To recognize the flood–ebb tidal asymmetry C_D and compare C_D at different sites, C_{100} flood or ebb tides at each station were estimated using least-squares regression (**Figure 9**). Note that only data during calm periods (with weak waves and no sediment stratification) are shown in **Figure 9** to ensure the feasibility of log law. Generally, C_{100} ranged from 0.0010 to 0.0020 (average, 0.0015 ± 0.0004) in summer and from 0.0013 to 0.0026 (average, 0.0019 ± 0.0005) in winter. There was little difference estimated C_D between summer and winter at S5. However, at S2 and S3, the C_D in winter was twice that in summer during the flood tide, while the estimated C_D did not show extensive differences during the ebbing tide in summer and winter. The R^2 of the fitted curves for each observation was above 0.71 except for the C_D S2 in winter. At S3 in summer and at S2 in winter, C_D a significant flood–ebb tidal asymmetry, and its controlling factors are discussed in **Section 5**.

DISCUSSION

Variation of C_D During an S2 Winter Event

During event periods, the SSC at 0.45 mab was significantly higher than that of 1.34 mab, which caused significant suspended

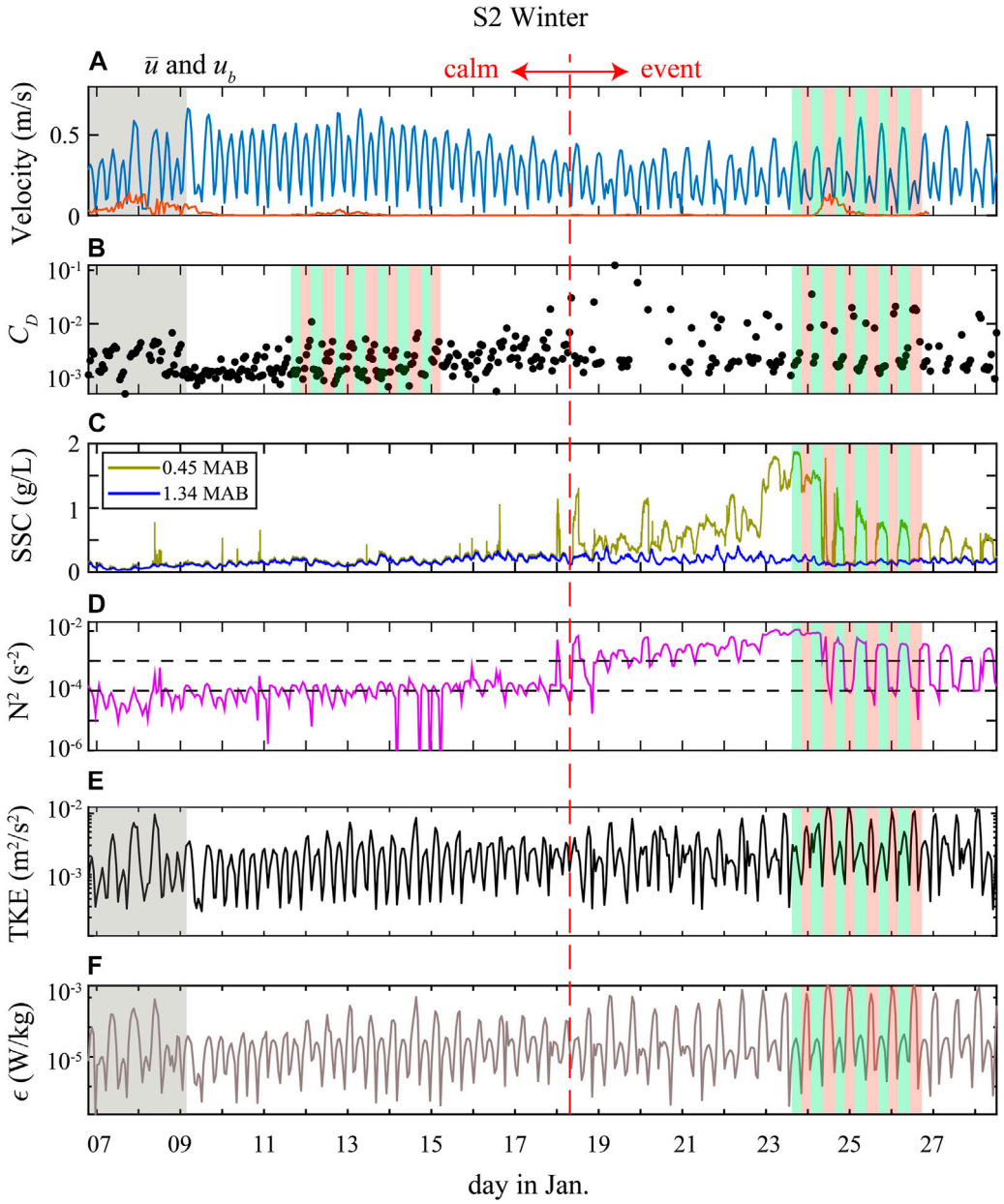

FIGURE 8 | Twenty-day time series during the winter deployment at S2 showing measurements of **(A)** ADV's burst mean velocity ($\bar{u}$, blue line) and bottom wave orbital velocity (u_b, orange line), **(B)** drag coefficient, C_D, estimated using ADV's burst mean velocity, **(C)** suspended sediment concentration (SSC) at 0.45 mab (yellow line) and 1.34 mab (blue line), **(D)** buoyancy frequency (N^2) and the black dashed line indicates N^2 is equal to 10^{-3} s^{-2}, and 10^{-4} s^{-2}, **(E)** turbulent kinetic energy (TKE) and **(F)** turbulence dissipation rates (ε). Green and red shaded areas denote periods of ebb and flood tides, respectively, and gray shaded areas denote periods of strong winds. The vertical red dashed line is the demarcation between the calm and event periods.

sediment stratification (**Figure 8C**). We used the buoyancy frequency squared, $N^2 = -\frac{g}{\rho_0}\frac{\partial \bar{\rho}}{\partial z}$, to quantify the magnitude of density stratification (**Figure 8D**). Jones and Monismith (2008) and MacVean and Lacy (2014) took $N^2 = 10^{-4}\,s^{-2}$ it as the threshold for sediment stratification. Also by comparing gradient Richardson numbers, Peters (1999) showed the critical N^2 of stratification probably be $10^{-3}\,s^{-2}$. In our study, N^2 fluctuated mainly around two typical values, i.e. about 10^{-4} during the calm period and exceeding 10^{-3} during a significant portion of the event period (**Figure 8D**). To facilitate the discussion of stratification, we took $N^2 = 10^{-3}\,s^{-2}$ it as the threshold for sediment stratification. The results showed that sediment stratification mainly occurred during the ebb tides, especially after January 24, and SSC showed significant tidal asymmetry, i.e., the concentration was not stratified during the flood tides but stratified during the ebb tides. At the same time, the current velocity also showed asymmetry (**Figure 8A**). During the calm period (except for January 9 when S2 was affected by

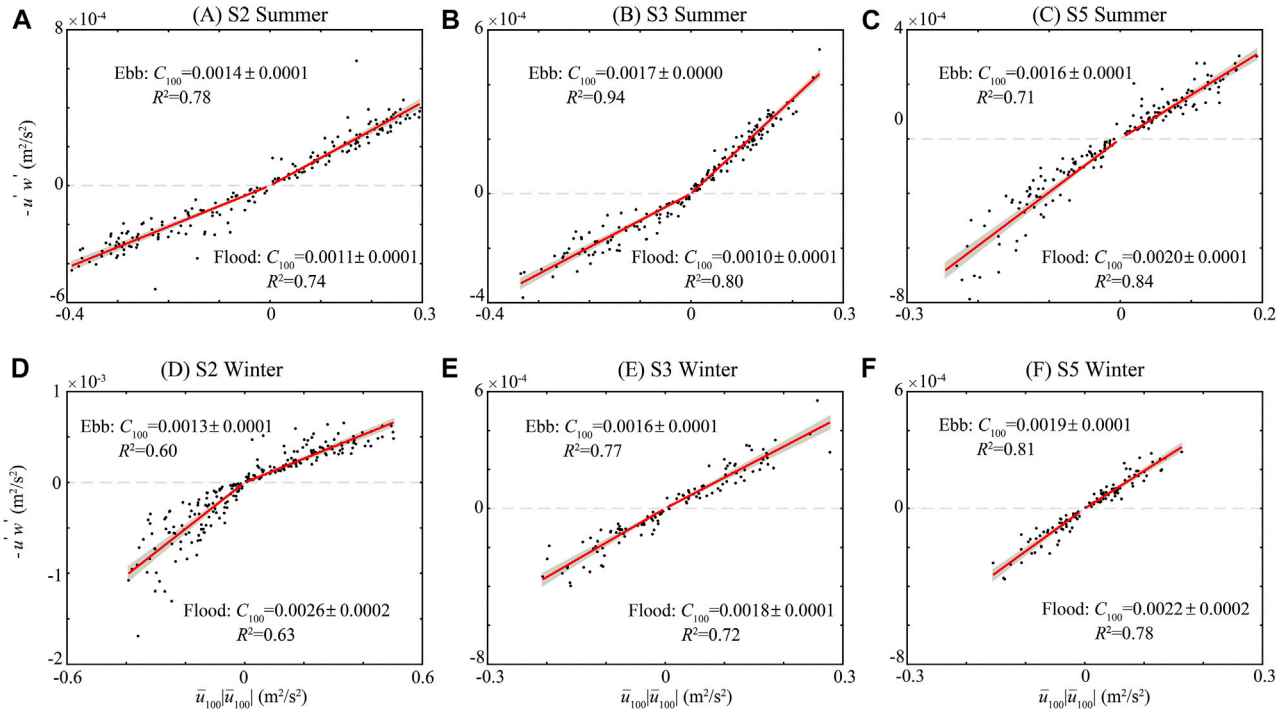

FIGURE 9 | Correlation between measured turbulent Reynolds stress, $-\overline{u'w'}$, and the sign-preserving squared mean velocity at 1 mab, $\bar{u}_{100}|\bar{u}_{100}|$, for the **(A,B,C)** summer and **(D,E,F)** winter. Note that only data during calm periods (with weak waves and no sediment stratification) are shown to ensure the feasibility of log law. The best fit lines are shown in red, with the slopes indicating the drag coefficient, C_{100}, for ebb tides (top) and flood tides (bottom). The 95% confidence intervals (gray shaded areas) and R^2 are shown for each regression.

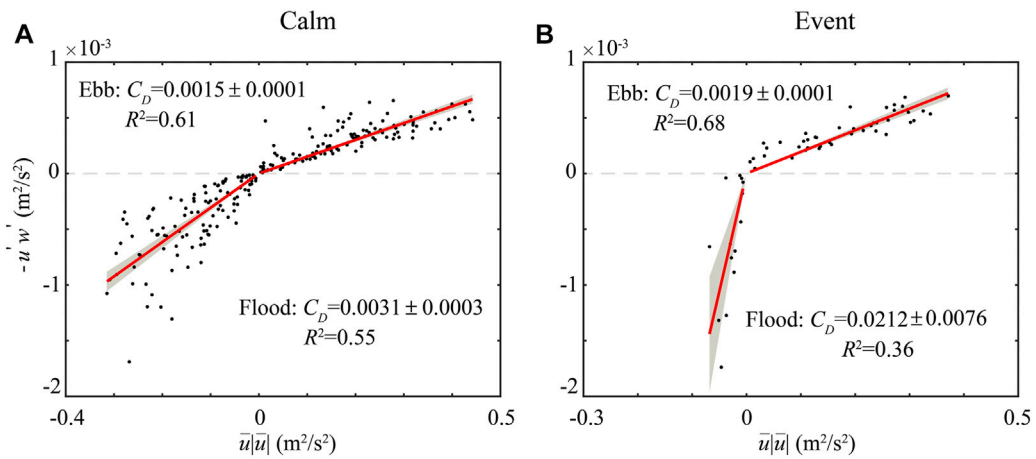

FIGURE 10 | Correlation between measured turbulent Reynolds stress, $-\overline{u'w'}$, and the sign-preserving squared ADV's burst mean velocity, $\bar{u}|\bar{u}|$ at S2 during winter observation. **(A)** Calm period with time before January 18, **(B)** event period after 12:00 on January 24.

strong winds), the current velocities of flood and ebb tides were similar. In contrast, during the event period, the velocity of the flood tides was significantly smaller than that of the ebb tides (**Figure 8A**).

Figure 10 shows the estimated C_D for two periods. Possibly due to enhanced noise contamination in the water column (Ruessink, 2010; Tu et al., 2021), there were few valid Reynolds stress estimates at the beginning of the event period and we only plotted data after 12:00 on January 24 (**Figure 10B**). For ebb tides, stronger stratification was observed during the event period. Previous studies have shown that sediment stratification could suppress turbulence and reduce the bottom

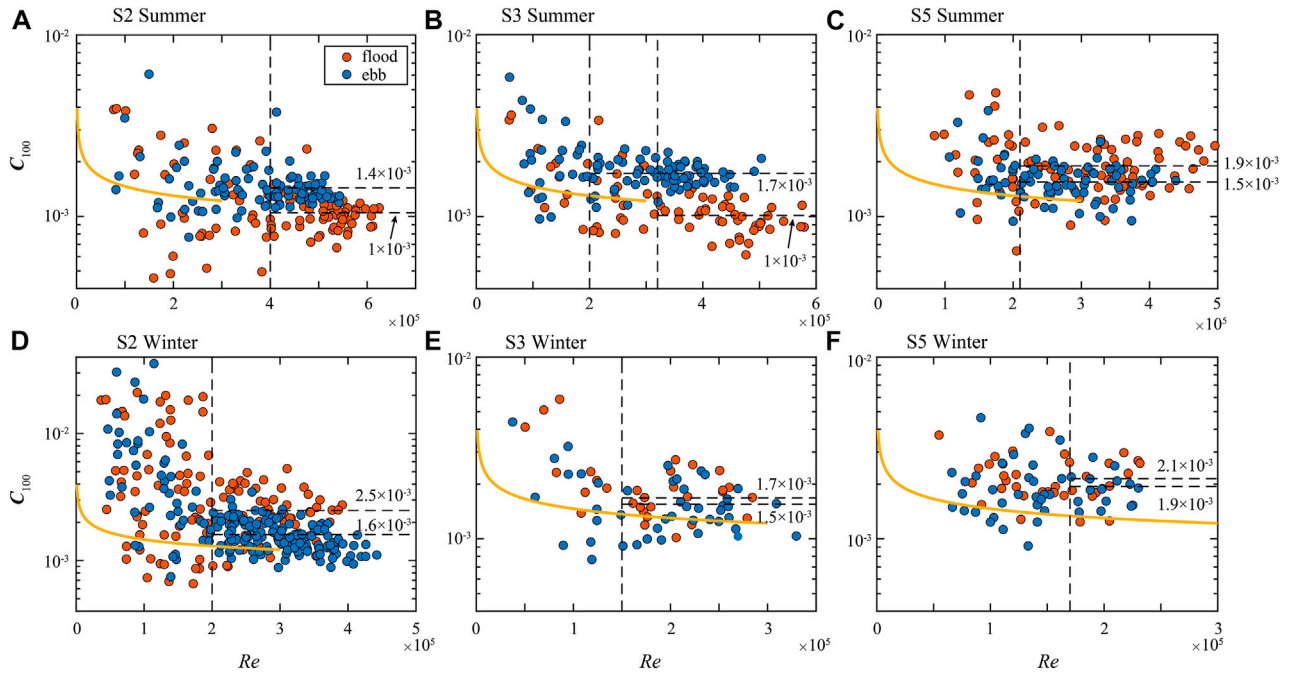

FIGURE 11 | Scatter plots of drag coefficient estimated at 1 mab, C_{100}, versus the Reynolds number (*Re*) for the **(A,B,C)** summer and **(D,E,F)** winter. The orange scatters represent the flood tide, and the blue scatters represent the ebb tide. The vertical dashed lines are the boundary between regions of relatively large and small dispersion. The horizontal dashed lines are the mean value of C_D the right-hand side of the boundary. The yellow lines are the empirical relationship under the assumptions for smooth flow.

drag (Adams and Weatherly, 1981; Tu et al., 2019; Wu et al., 2022). However, when comparing data from before and after the event, estimations C_D were generally the same during ebb tides (**Figure 10**). In addition, TKE and turbulent dissipation rates were also not controlled by stratification even from January 23 to 24, when sediment stratification was more significant and continuous (**Figures 8E,F**), but followed the asymmetry of the flood and ebb tides (**Figure 8A**). For flood tides, the C_D value during the event period was generally seven times larger than that during the calm period. These results suggest that the effect of stratification on C_D was relatively small and the variation of bed configurations, which increased upstream during flood tides, could be the main reason for the variation C_D. Because the study area was located in a shipping channel with shipping vessels moored for shelter and fishing vessels actively trawling, the actual cause of the bed roughness change remains difficult to determine.

Flood–Ebb Asymmetry of C_D

The variation of C_D could be affected by different factors, such as tidal currents (Wright, 1989; Xu et al., 2017), accelerating/decelerating flow (Soulsby and Dyer, 1981; Wright, 1989), waves (Safak, 2016), stratification (Peng et al., 2020), local bathymetry (Fong et al., 2009), upstream/downstream roughness (Scully et al., 2018), benthic biology (Egan et al., 2020a), and water depth (Wang et al., 2014). These factors can lead to asymmetry C_D by influencing mean current velocity or turbulence. First, changes in water depth between flood and ebb tides were relatively small and not sufficient to alter C_D, and we did not find sufficient substrate organisms to alter drag in several box samples. In addition, we did not observe near-bottom density stratification including temperature, salinity, and SSC in either CTD casts or bottom observations, except for the S2 winter (**Figure 8C**), for which there is still asymmetry C_D in the calm period without sediment stratification (**Figure 10A**). Moreover, it is difficult to explain the asymmetry with seasonal variation based on the wind and wave data. For example, the mean wavelength (L) at S5 during strong wind periods was estimated as 65 m; therefore, the wave base ($L/2$) was significantly larger than the water depth. However, C_D had no significant flood–ebb asymmetry at S5. For S2 and S3, the direction of flood tide coincided with the prevailing winter wind direction and was opposed to the prevailing summer wind, but the current experienced stronger drag during flood tides in winter than in summer, which is contrary to our general understanding. Furthermore, the acceleration/deceleration scale of the flow could be characterized by the time derivative of shear velocity (Soulsby and Dyer, 1981; Wilkinson, 1986). As each flood or ebb tide contains an accelerating and decelerating stage, acceleration and deceleration will only affect the fluctuations within a flood or ebb tide and cannot explain the flood–ebb asymmetry. By comparing phase-averaged tidal height (data not shown), we observed no significant seasonal differences, which indicates the variation in tidal forcing is small between winter and summer (Egan et al., 2020a).

Combined with the above analysis, variation in the tidal asymmetry C_D was most likely caused by the difference

TABLE 2 | The mean value of z_0 for hydrodynamic rough flow for flood and ebb tides in summer and winter.

	Summer			Winter		
	S2	S3	S5	S2	S3	S5
Flood	4.3e–6	3.5e–6	1.0e–4	3.2e–4	6.2e–5	1.7e–4
Ebb	2.6e–5	6.5e–5	3.9e–5	4.6e–5	3.7e–5	1.1e–4

between upstream and downstream roughness. In order to estimate upstream and downstream roughness, we should first determine the hydrodynamic roughness regimes. Generally, the flow regime in the boundary layer can be classified into smooth, transitional, and rough conditions. Hydrodynamically smooth flow, z_0 reflects only the thickness of the laminar sublayer and is not determined by bed configurations (Chriss and Caldwell, 1982; 1984). Meanwhile, experimental and observational evidence has shown that hydrodynamically rough flow, z_0 and C_D are no longer dependent on flow conditions but are related to bed configurations (Sternberg, 1970; Green and Mccave, 1995). Here, we used the Reynolds number (Re) as a criterion for distinguishing the flow conditions:

$$Re = \frac{u_r z_r}{\upsilon}, \tag{9}$$

where u_r is the velocity at the reference height z_r (= 1 m), and υ is the molecular kinematic viscosity taken as 0.01 cm^2/s in summer (20°C, 32 ‰) and 0.016 cm^2/s in winter (4°C, 32 ‰) (Soulsby, 1997). **Figure 11** shows the estimates C_D as a function of Re. Generally, the dispersion C_D decreased with increase Re. Following Sternberg (1968), using the criterion that C_D is generally a constant, we visually estimated the threshold of hydrodynamically smooth flow (vertical dashed lines in **Figure 11**). The mean value of critical Re was about 2.3×10^5. Unsurprisingly, as Re was less than the threshold (i.e., smooth flow), C_D decreased with increase Re, which is consistent with previous findings (Sherwood et al., 2006; Safak, 2016). We substituted the empirical formula z_0 for smooth flow ($z_0 = 0.11\upsilon/u_*$) (Sternberg, 1968, 1970; Chriss and Caldwell, 1984; Soulsby, 1997) into the log-law and plotted this relationship in **Figure 11** (yellow lines) for comparison. When Re was slightly larger than the threshold, C_D fluctuated around the empirical relationship but did not follow the empirical relationship exactly, which may reflect the characteristics of transitional flow. Because z_0 is a constant for rough flow, we found the estimation z_0 by substituting the mean values of C_D **Eq. 8** (**Table 2**). This shows that the larger the tidal asymmetry C_D, the greater the difference in upstream and downstream roughness, which suggests that varying upstream and downstream roughness is the main reason for the flood–ebb asymmetry of C_D.

Bottom Drag Enhanced by Waves

In addition to the change in roughness, the bottom drag experienced by currents could be enhanced by waves, which do affect the flood–ebb asymmetry C_D. We removed the data during strong waves ($u_b > 0.1$ m/s) in winter (red dots in **Figure 12**) and refitted the data to obtain C_D. After refitting the data of S3, the tidal asymmetry was reduced and the difference C_D between the flood and ebb tides changed from 5×10^{-4} to 2×10^{-4} (**Figure 12B**). After refitting the data of S5, the fitted R^2 during flood tides changed from 0.66 to 0.76 (**Figure 12C**). These findings indicated that stronger waves can have a significant effect on bottom drag at S3 and S5, leading to a bias in the C_D estimates. Because relatively few data are available for strong waves, the re-estimated C_D did not change significantly at S2 (**Figure 12A**).

To quantify the effect of waves, we used a one-dimensional time-dependent model, referred to as the Grant-Madsen (GM) model, that incorporates the combined effects of a steady current in the presence of oscillatory waves (Grant and Madsen, 1979). In the GM model, the friction velocity combined waves and currents (u_{*cw}) is given by

$$u_{*cw} = u_{*w}\left[1 + 2\left(u_{*c}/u_{*w}\right)^2 \cos\phi + \left(u_{*c}/u_{*w}\right)^4\right]^{1/4}, \tag{10}$$

where ϕ is the angle between currents and the direction of wave propagation. In addition, u_{*w} is the friction velocity associated with the wave-related bed shear stress (τ_w) given as

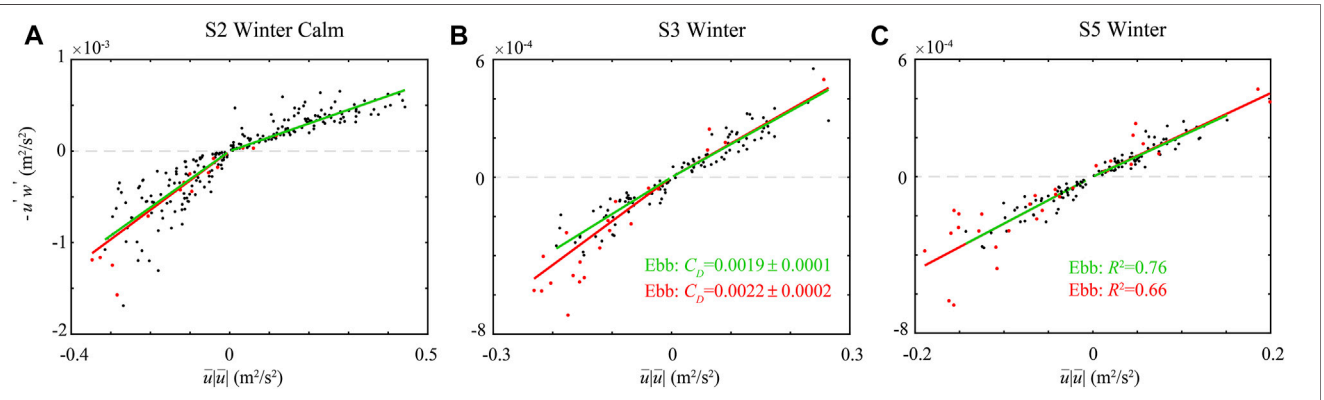

FIGURE 12 | Correlation between measured turbulent Reynolds stress, $-\overline{u'w'}$, and the sign-preserving squared ADV's burst mean velocity, $\overline{u}|\overline{u}|$, for the **(A)** S2 calm period, **(B)** S3, and **(C)** S5 in winter without the strong wave observations (red dots). The best fit lines without the strong wave observations (red dots) are shown in green and the best fit lines of all data are shown in red, with the slopes indicating the drag coefficients, C_D, for ebb tide (top) and flood tide (bottom).

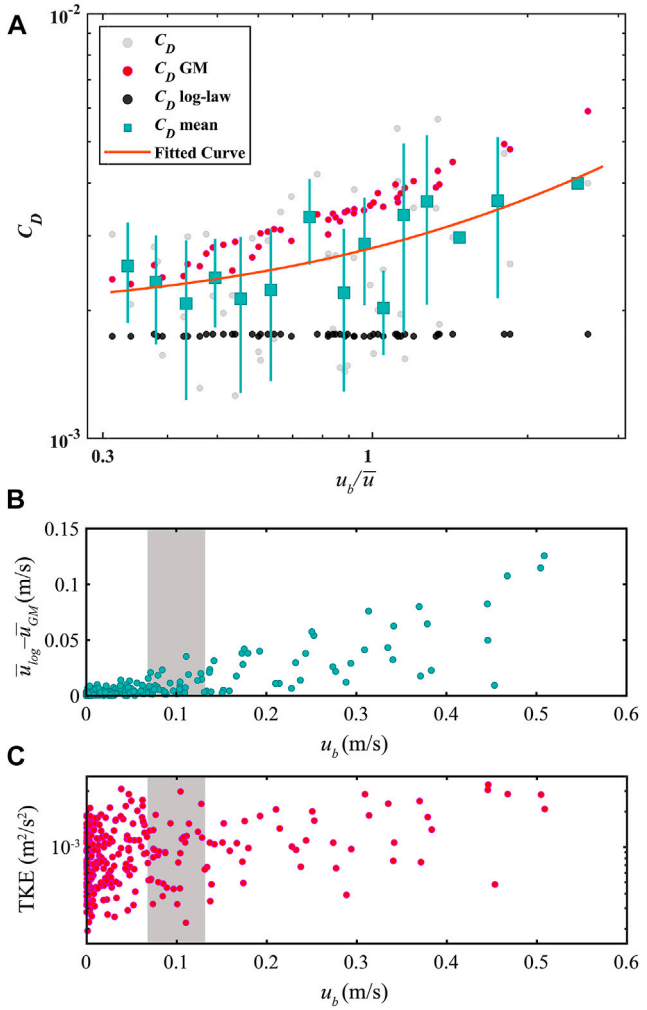

FIGURE 13 | (A) Scatter plots of C_D verses u_b / $\bar{u}$ when u_b > 0.1 m/s for S3 and S5 in winter. Gray dots indicate directly observed C_D, red dots indicate C_D calculated by the Grant-Madsen model, black dots indicate C_D calculated by log-law, blue squares are the bin averages of observed C_D, and vertical lines indicate standard deviation. The best fine line observed C_D is shown in orange. **(B)** The difference $\bar{u}$ calculated by the log-law velocity profile ($\bar{u}_{law}$) and the Grant-Madsen model ($\bar{u}_{GM}$) and **(C)** turbulent kinetic energy (TKE) as a function of u_b.

$$u_{*w}^2 = \frac{\tau_w}{\rho_0} = \frac{\kappa u_{*cw} u_b}{\sqrt{\left[\log\left(\frac{\kappa u_{*cw}}{z_0 \omega}\right) - 1.15\right]^2 + \left(\frac{\pi}{2}\right)^2}}, \tag{11}$$

where ω (= $2\pi/T_p$) is the wave frequency. Here, we assumed z_0 = 2×10^{-5} m, which is generally consistent with the value reported for other sites dominated by silt (Soulsby, 1983; Brand et al., 2010) and is in general agreement with our estimate in **Table 2**. In the region aforementionedthe wave-current boundary layer ($z > \delta_{cw} = \kappa u_{*cw}/\omega$), the effect of the wave-current interaction is to increase the roughness experienced by the current so that the log-law becomes

$$U(z) = \frac{u_{*c}}{\kappa}\left(\frac{u_{*c}}{u_{*cw}}\log\frac{\delta_{cw}}{z_0} + \log\frac{z}{\delta_{cw}}\right). \tag{12}$$

Based on the observed data, we calculated the $u_{*c-\mathrm{GM}}$ by solving **Eqs. 10–12** iteratively. By comparison, we found that $u_{*c-\mathrm{GM}}$ was in good agreement with the results calculated by observed data ($u_{*c-\mathrm{ADV}}$) (**Supplementary Figure S2**).

Figure 13A shows the estimates C_D as a function of the ratio of bottom wave orbital velocity to mean current velocity ($u_b/\bar{u}$) during strong waves, which is a common parameter used to quantify the effect of waves (Safak, 2016). The results show that C_D increased with the increase $u_b/\bar{u}$, which is similar to the findings of Safak (2016) and Fan et al. (2019) in muddy environments. In our study, the fitted equation between C_D and $u_b/\bar{u}$ was $C_D = 0.00087\frac{u_b}{\bar{u}} + 0.00194$, $R^2 = 0.61$ (orange line in **Figure 13A**). Although bin average C_D is somewhat scattered, the R^2 is pretty good. The constant term in the fitted equation was approximately equal to the average C_D during the winter S3 and S5 observations (**Figures 11E,F**). Moreover, GM-model results (red dots in **Figure 13A**) are in good agreement with the trend of the fitted curve of observed values (orange line in **Figure 13A**). However, when we used the log-law, which does not consider wave-current interactions, the calculation C_D remained almost unchanged (black dots in **Figure 13A**). It indicates that although our observations are not within the wave's bottom boundary layer, the effect of the wave is still significant. On the one hand, waves can modify the current structure within the bottom boundary layer. We obtained the difference $\bar{u}$ calculated by log-law ($\bar{u}_{log}$) and GM-model ($\bar{u}_{GM}$) (**Figure 13B**) and found that when $u_b > 0.1 \pm 0.03$ m/s, $\bar{u}_{log} - \bar{u}_{GM}$ tended to gradually increase. On the other hand, the wave effect could lead to an enhancement of the TKE (Perlin and Kit, 2002; Bricker et al., 2005). **Figure 13C** shows the variation of TKE, which is also bounded by $u_b = 0.1 \pm 0.03$ m/s. Therefore, we infer that in the study area, $u_b \approx 0.1$ m/s can be defined as an important threshold for determining whether the wave effect is significant in the bottom boundary layer. Note that although GM-model results have the right trend, there is no good agreement between it and the observed data, especially when $u_b/\bar{u}$ is large. It indicates that under wave-current conditions similar to those in this article, the fitted equation between C_D and $u_b/\bar{u}$ could give a more accurate estimate C_D.

CONCLUSION

In situ observations of currents, waves, and suspended sediment concentration at three stations on the muddy deposits off the Shandong Peninsula was conducted to investigate the variation of the bottom drag coefficient. Data collected in both summer and winter highlight the tidal variations and the effect of winter storm events. The results show that the estimated C_D was around 0.0015 in summer and 0.0019 in winter. A significant tidal asymmetry C_D was observed in both summer and winter. By analyzing the different influencing factors one by one, we conclude that this flood–ebb asymmetry was mainly caused by the variation of local roughness; the drag reduction caused by the suspended sediment stratification was limited. Variations C_D could be affected by different hydrodynamic flow regimes. For hydrodynamically smooth flow, the bottom drag coefficient was relatively dispersed and showed an overall decrease with increase *Re*.

For hydrodynamically rough or transitional flow, the bottom drag coefficient typically was a constant that varied from 1×10^{-3} to 2.5×10^{-3} over the different observation periods. On average, hydrodynamically smooth flow occurred when *Re* was less than 2.3×10^5. In addition, strong waves, during which the bottom drag generally increases with increasing wave forcing, can lead to bias in the C_D estimates. When $u_b > 0.1 \pm 0.03$ m/s, the current-only log-law is not valid in BBL while the GMmodel performs well in terms of trends. As the waves strengthen, TKE is also significantly enhanced. In general, we believe that $u_b \approx 0.1$ m/s is the critical value to determine whether the wave effect is important in the bottom boundary layer.

In this work, we provide an accurate estimate of C_D the study area, which would be useful to improve the hydrodynamic and sediment transport models in the muddy deposits of the East China Shelf Seas. Moreover, the threshold of u_b (≈ 0.1 m/s) has guiding significance for the study of sediment transport and erosion dynamics in the bottom boundary layer. These relationships between C_D waves or currents, though based on observations off the Shandong Peninsula, could provide a reference to related research in other muddy deposits over the continental shelf.

DATA AVAILABILITY STATEMENT

The original contributions presented in the study are included in the article/**Supplementary Material**; further inquiries can be directed to the corresponding author.

AUTHOR CONTRIBUTIONS

JX and ZL: conceptualization, methodology, and reviewing. FQ: conceptualization, methodology, data curation, analyses, and original draft preparation.

FUNDING

The authors gratefully acknowledge the financial support of the Key Special Project for Introduced Talents Team of the Southern Marine Science and Engineering Guangdong Laboratory (Guangzhou) (GML2019ZD0210), Guangdong Basic and Applied Basic Research Foundation (2021B1515120080) and the National Natural Science Foundation of China (NSFC, Grant No. 41530966).

ACKNOWLEDGMENTS

Special thanks go to Baoduo Wang, Meng Liu, Zhiwen Wang, and Xiaohang Liu for their support in fieldwork.

SUPPLEMENTARY MATERIAL

The Supplementary Material for this article can be found online at: https://www.frontiersin.org/articles/10.3389/feart.2022.921995/full#supplementary-material

REFERENCES

Adams, C. E., and Weatherly, G. L. (1981). Some Effects of Suspended Sediment Stratification on an Oceanic Bottom Boundary Layer. *J. Geophys. Res.* 86 (C5), 4161–4172. doi:10.1029/JC086iC05p04161

Alexander, C. R., DeMaster, D. J., and Nittrouer, C. A. (1991). Sediment Accumulation in a Modern Epicontinental-Shelf Setting: The Yellow Sea. *Mar. Geol.* 98 (1), 51–72. doi:10.1016/0025-3227(91)90035-3

Baas, J. H., Baker, M. L., Malarkey, J., Bass, S. J., Manning, A. J., Hope, J. A., et al. (2019). Integrating Field and Laboratory Approaches for Ripple Development in Mixed Sand-Clay-EPS. *Sedimentology* 66 (7), 2749–2768. doi:10.1111/sed.12611

Bass, S. J., Aldridge, J. N., McCave, I. N., and Vincent, C. E. (2002). Phase Relationships between Fine Sediment Suspensions and Tidal Currents in Coastal Seas. *J. Geophys. Res.* 107 (C10), 3146. doi:10.1029/2001jc001269

Bian, C., Jiang, W., and Greatbatch, R. J. (2013). An Exploratory Model Study of Sediment Transport Sources and Deposits in the Bohai Sea, Yellow Sea, and East China Sea. *J. Geophys. Res. Oceans* 118 (11), 5908–5923. doi:10.1002/2013JC009116

Brand, A., Lacy, J. R., Hsu, K., Hoover, D., Gladding, S., and Stacey, M. T. (2010). Wind-enhanced Resuspension in the Shallow Waters of South San Francisco Bay: Mechanisms and Potential Implications for Cohesive Sediment Transport. *J. Geophys. Res.* 115. doi:10.1029/2010JC006172

Bricker, J. D., Inagaki, S., and Monismith, S. G. (2005). Bed Drag Coefficient Variability under Wind Waves in a Tidal Estuary. *J. Hydraul. Eng.* 131 (6), 497–508. doi:10.1061/(asce)0733-9429(2005)131:6(497)

Bricker, J. D., and Monismith, S. G. (2007). Spectral Wave-Turbulence Decomposition. *J. Atmos. Ocean. Technol.* 24 (8), 1479–1487. doi:10.1175/JTECH2066.1

Chriss, T. M., and Caldwell, D. R. (1982). Evidence for the Influence of Form Drag on Bottom Boundary Layer Flow. *J. Geophys. Res.* 87 (C6), 4148. doi:10.1029/JC087iC06p04148

Chriss, T. M., and Caldwell, D. R. (1984). Universal Similarity and the Thickness of the Viscous Sublayer at the Ocean Floor. *J. Geophys. Res.* 89 (C4), 6403–6414. doi:10.1029/JC089iC04p06403

Duan, H., Xu, J., Wu, X., Wang, H., Liu, Z., and Wang, C. (2020). Periodic Oscillation of Sediment Transport Influenced by Winter Synoptic Events, Bohai Strait, China. *Water* 12 (4), 986. doi:10.3390/w12040986

Egan, G., Chang, G., Revelas, G., Monismith, S., and Fringer, O. (2020a). Bottom Drag Varies Seasonally with Biological Roughness. *Geophys. Res. Lett.* 47 (15). doi:10.1029/2020GL088425

Egan, G., Cowherd, M., Fringer, O., and Monismith, S. (2019). Observations of Near-Bed Shear Stress in a Shallow, Wave- and Current-Driven Flow. *J. Geophys. Res. Oceans* 124 (8), 6323–6344. doi:10.1029/2019JC015165

Egan, G., Manning, A. J., Chang, G., Fringer, O., and Monismith, S. (2020b). Sediment-Induced Stratification in an Estuarine Bottom Boundary Layer. *J. Geophys. Res. Oceans* 125 (8). doi:10.1029/2019JC016022

Fan, R., Zhao, L., Lu, Y., Nie, H., and Wei, H. (2019). Impacts of Currents and Waves on Bottom Drag Coefficient in the East China Shelf Seas. *J. Geophys. Res. Oceans* 124 (11), 7344–7354. doi:10.1029/2019JC015097

Feddersen, F., Gallagher, E. L., Guza, R. T., and Elgar, S. (2003). The Drag Coefficient, Bottom Roughness, and Wave-Breaking in the Nearshore. *Coast. Eng.* 48 (3), 189–195. doi:10.1016/s0378-3839(03)00026-7

Feddersen, F., and Williams, A. J. (2007). Direct Estimation of the Reynolds Stress Vertical Structure in the Nearshore. *J. Atmos. Ocean. Technol.* 24 (1), 102–116. doi:10.1175/JTECH1953.1

Fong, D. A., Monismith, S. G., Stacey, M. T., and Burau, J. R. (2009). Turbulent Stresses and Secondary Currents in a Tidal-Forced Channel with Significant Curvature and Asymmetric Bed Forms. *J. Hydraul. Eng.* 135 (3), 198–208. doi:10.1061/(asce)0733-9429(2009)135:3(198)

Francis P. Shepard, F. P. (1954). Nomenclature Based on Sand-Silt-Clay Ratios. *Sepm Jsr* Vol. 24 (3), 151–158. doi:10.1306/d4269774-2b26-11d7-8648000102c1865d

Fringer, O. B., Dawson, C. N., He, R., Ralston, D. K., and Zhang, Y. J. (2019). The Future of Coastal and Estuarine Modeling: Findings from a Workshop. *Ocean. Model.* 143, 101458. doi:10.1016/j.ocemod.2019.101458

Grant, W. D., and Madsen, O. S. (1979). Combined Wave and Current Interaction with a Rough Bottom. *J. Geophys. Res.* 84 (C4), 1797–1808. doi:10.1029/JC084iC04p01797

Grant, W. D., and Madsen, O. S. (1986). The Continental-Shelf Bottom Boundary Layer. *Annu. Rev. Fluid Mech.* 18 (1), 265–305. doi:10.1146/ANNUREV.FL.18.010186.001405

Green, M. O., and Mccave, I. N. (1995). Seabed Drag Coefficient under Tidal Currents in the Eastern Irish Sea. *J. Geophys. Res.* 100 (C8), 16057–16069. doi:10.1029/95JC01381

Harris, C. K., and Wiberg, P. L. (2001). A Two-Dimensional, Time-dependent Model of Suspended Sediment Transport and Bed Reworking for Continental Shelves. *Comput. Geosciences* 27 (6), 675–690. doi:10.1016/S0098-3004(00)00122-9

Herrmann, M. J., and Madsen, O. S. (2007). Effect of Stratification Due to Suspended Sand on Velocity and Concentration Distribution in Unidirectional Flows. *J. Geophys. Res.* 112 (C2). doi:10.1029/2006jc003569

Jones, N. L., and Monismith, S. G. (2008). Modeling the Influence of Wave-Enhanced Turbulence in a Shallow Tide- and Wind-Driven Water Column. *J. Geophys. Res.* 113, 1–13. doi:10.1029/2007JC004246

Kaimal, J. C., Wyngaard, J. C., Izumi, Y., and Coté, O. R. (1972). Spectral Characteristics of Surface-Layer Turbulence. *Q.J R. Met. Soc.* 98 (417), 563–589. doi:10.1002/QJ.49709841707

Liu, S., Qiao, L., Li, G., Li, J., Wang, N., and Yang, J. (2015). Distribution and Cross-Front Transport of Suspended Particulate Matter over the Inner Shelf of the East China Sea. *Cont. Shelf Res.* 107, 92–102. doi:10.1016/j.csr.2015.07.013

Liu, Z., and Wei, H. (2007). Estimation to the Turbulent Kinetic Energy Dissipation Rate and Bottom Shear Stress in the Tidal Bottom Boundary Layer of the Yellow Sea. *Progress in Natural Science* 17, 289–297. doi:10.1080/10020070612331343260

MacVean, L. J., and Lacy, J. R. (2014). Interactions between Waves, Sediment, and Turbulence on a Shallow Estuarine Mudflat. *J. Geophys. Res. Oceans* 119 (3), 1534–1553. doi:10.1002/2013JC009477

Magaldi, M. G., Özgökmen, T. M., Griffa, A., and Rixen, M. (2009). On the Response of a Turbulent Coastal Buoyant Current to Wind Events: the Case of the Western Adriatic Current. *Ocean. Dyn.* 60 (1), 93–122. doi:10.1007/s10236-009-0247-9

Mo, D., Hou, Y., Li, J., and Liu, Y. (2016). Study on the Storm Surges Induced by Cold Waves in the Northern East China Sea. *J. Mar. Syst.* 160, 26–39. doi:10.1016/j.jmarsys.2016.04.002

Naimie, C. E., Blain, C. A., and Lynch, D. R. (2001). Seasonal Mean Circulation in the Yellow Sea } a Model-Generated Climatology. *Cont. Shelf Res.* 21 (6), 667–695. doi:10.1016/S0278-4343(00)00102-3

Nayak, A. R., Li, C., Kiani, B. T., and Katz, J. (2015). On the Wave and Current Interaction with a Rippled Seabed in the Coastal Ocean Bottom Boundary Layer. *J. Geophys. Res. Oceans* 120 (7), 4595–4624. doi:10.1002/2014jc010606

Nelson, K. S., and Fringer, O. B. (2018). Sediment Dynamics in Wind Wave-Dominated Shallow-Water Environments. *J. Geophys. Res. Oceans* 123 (10), 6996–7015. doi:10.1029/2018jc013894

Pawlowicz, R., Beardsley, B., and Lentz, S. (2002). Classical Tidal Harmonic Analysis Including Error Estimates in MATLAB Using T_TIDE. *Comput. Geosciences* 28 (8), 929–937. doi:10.1016/S0098-3004(02)00013-4

Peng, Y., Yu, Q., Yang, Y., Wang, Y., Wang, Y. P., and Gao, S. (2020). Flow Structure Modification and Drag Reduction Induced by Sediment Stratification in Coastal Tidal Bottom Boundary Layers. *Estuar. Coast. Shelf Sci.* 241, 106829. doi:10.1016/j.ecss.2020.106829

Perlin, A., and Kit, E. (2002). Apparent Roughness in Wave-Current Flow: Implication for Coastal Studies. *J. Hydraul. Eng.* 128 (8), 729–741. doi:10.1061/(asce)0733-9429(2002)128:8(729)

Peters, H. (1999). Spatial and Temporal Variability of Turbulent Mixing in an Estuary. *J. Mar. Res.* 57 (6), 805–845. doi:10.1357/002224099321514060

Qi, F., Wu, X., Wang, Z., Wang, C., Duan, H., Liu, M., et al. (2022). Transport and Deposition Processes of the Sediment Depocenter off the Shandong Peninsula: An Observational Study. *Cont. Shelf Res.* 244, 104763. doi:10.1016/j.csr.2022.104763

Ruessink, B. G. (2010). Observations of Turbulence within a Natural Surf Zone. *J. Phys. Oceanogr.* 40 (12), 2696–2712. doi:10.1175/2010jpo4466.1

Safak, I. (2016). Variability of Bed Drag on Cohesive Beds under Wave Action. *Water* 8 (4), 131. doi:10.3390/w8040131

Saha, S., Moorthi, S., Wu, X., Wang, J., Nadiga, S., Tripp, P., et al. (2014). The NCEP Climate Forecast System Version 2. *J. Clim.* 27 (6), 2185–2208. doi:10.1175/JCLI-D-12-00823.1

Scully, M. E., Trowbridge, J. H., Sherwood, C. R., Jones, K. R., and Traykovski, P. (2018). Direct Measurements of Mean Reynolds Stress and Ripple Roughness in the Presence of Energetic Forcing by Surface Waves. *J. Geophys. Res. Oceans* 123 (4), 2494–2512. doi:10.1002/2017jc013252

Sherwood, C. R., Lacy, J. R., and Voulgaris, G. (2006). Shear Velocity Estimates on the Inner Shelf off Grays Harbor, Washington, USA. *Cont. Shelf Res.* 26 (17-18), 1995–2018. doi:10.1016/j.csr.2006.07.025

Signell, R. P., and List, J. H. (1997). Effect of Wave-Enhanced Bottom Friction on Storm-Driven Circulation in Massachusetts Bay. *J. Waterw. Port Coast. Ocean Eng.* 123 (5), 233–239. doi:10.1061/(asce)0733-950x(1997)123:5(233)

Soulsby, R. L. (1983). Chapter 5 the Bottom Boundary Layer of Shelf Seas. *Elsevier Oceanogr.* 35, 189–266. doi:10.1016/S0422-9894(08)70503-8

Soulsby, R. L., and Dyer, K. R. (1981). The Form of the Near-Bed Velocity Profile in a Tidally Accelerating Flow. *J. Geophys. Res.* 86 (C9), 8067–8074. doi:10.1029/JC086iC09p08067

Soulsby, R. L. (2006). *Simplified Calculation of Wave Orbital Velocities*. Wallingford: HR Wallingford Ltd.

Soulsby, R. L. (1997). *The Dynamics of Marine Sands: A Manual for Practical Applications*. London: Thomas Thelford.

Sreenivasan, K. R., and Katepalli, R. (1995). On the Universality of the Kolmogorov Constant. *Phys. Fluids* 7 (11), 2778–2784. doi:10.1063/1.868656

Sternberg, R. W. (1970). Field Measurements of the Hydrodynamic Roughness of the Deep-Sea Boundary. *Deep Sea Res. Oceanogr. Abstr.* 17 (3), 413–420. doi:10.1016/0011-7471(70)90056-2

Sternberg, R. W. (1968). Friction Factors in Tidal Channels with Differing Bed Roughness. *Mar. Geol.* 6 (3), 243–260. doi:10.1016/0025-3227(68)90033-9

Styles, R., and Glenn, S. M. (2000). Modeling Stratified Wave and Current Bottom Boundary Layers on the Continental Shelf. *J. Geophys. Res.* 105 (C10), 24119–24139. doi:10.1029/2000jc900115

Teague, W. J., Perkins, H. T., Hallock, Z. R., and Jacobs, G. A. (1998). Current and Tide Observations in the Southern Yellow Sea. *J. Geophys. Res.* 103 (C12), 27783–27793. doi:10.1029/98jc02672

Tolman, H. L., Accensi, M., Alves, H., Ardhuin, F., Bidlot, J., Booij, N., et al. (2014). *User Manual and System Documentation of WAVEWATCH III R Version 4.18*.

Trembanis, A. C., Wright, L. D., Friedrichs, C. T., Green, M. O., and Hume, T. (2004). The Effects of Spatially Complex Inner Shelf Roughness on Boundary Layer Turbulence and Current and Wave Friction: Tairua Embayment, New Zealand. *Cont. Shelf Res.* 24 (13-14), 1549–1571. doi:10.1016/j.csr.2004.04.006

Trowbridge, J. H., and Lentz, S. J. (2018). The Bottom Boundary Layer. *Annu. Rev. Mar. Sci.* 10, 397–420. doi:10.1146/annurev-marine-121916-063351

Tu, J., Fan, D., and Voulgaris, G. (2021). Field Observations of Turbulence, Sediment Suspension, and Transport under Breaking Tidal Bores. *Mar. Geol.* 437, 106498. doi:10.1016/j.margeo.2021.106498

Tu, J., Fan, D., Zhang, Y., and Voulgaris, G. (2019). Turbulence, Sediment-Induced Stratification, and Mixing under Macrotidal Estuarine Conditions (Qiantang Estuary, China). *J. Geophys. Res. Oceans* 124 (6), 4058–4077. doi:10.1029/2018jc014281

Van Rijn, L. C. (1993). *Principles of Sediment Transport in Rivers, Estuaries and Coastal Seas Part 1*. Amsterdam: Aqua Publications.

Van Rijn, L. C. (2007). Unified View of Sediment Transport by Currents and Waves. I: Initiation of Motion, Bed Roughness, and Bed-Load Transport. *J. Hydraul. Eng.* 133 (6), 649–667. doi:10.1061/(asce)0733-9429(2007)133:6(649)

Vieira da Silva, G., Toldo Jr., E. E., Klein, A. H. d. F., and Short, A. D. (2018). The Influence of Wave-, Wind- and Tide-Forced Currents on Headland Sand Bypassing - Study Case: Santa Catarina Island North Shore, Brazil. *Geomorphology* 312, 1–11. doi:10.1016/J.GEOMORPH.2018.03.026

Wang, A., Ralston, D. K., Bi, N., Cheng, Z., Wu, X., and Wang, H. (2019). Seasonal Variation in Sediment Transport and Deposition on a Muddy Clinoform in the Yellow Sea. *Cont. Shelf Res.* 179, 37–51. doi:10.1016/j.csr.2019.04.009

Wang, C., Liu, Z., Harris, C. K., Wu, X., Wang, H., Bian, C., et al. (2020). The Impact of Winter Storms on Sediment Transport through a Narrow Strait, Bohai, China. *J. Geophys. Res. Oceans* 125 (6), e2020JC016069. doi:10.1029/2020jc016069

Wang, D., Liu, Q., and Lv, X. (2014). A Study on Bottom Friction Coefficient in the Bohai, Yellow, and East China Sea. *Math. Problems Eng.* 2014, 1–7. doi:10.1155/2014/432529

Warner, J. C., Sherwood, C. R., Signell, R. P., Harris, C. K., and Arango, H. G. (2008). Development of a Three-Dimensional, Regional, Coupled Wave, Current, and Sediment-Transport Model. *Comput. Geosciences* 34 (10), 1284–1306. doi:10.1016/j.cageo.2008.02.012

Wiberg, P. L., and Sherwood, C. R. (2008). Calculating Wave-Generated Bottom Orbital Velocities from Surface-Wave Parameters. *Comput. Geosciences* 34 (10), 1243–1262. doi:10.1016/j.cageo.2008.02.010

Wilkinson, R. H. (1985). Variation of Roughness Length of a Mobile Sand Bed in a Tidal Flow. *Geo-Marine Lett.* 5 (4), 231–239. doi:10.1007/BF02233808

Wright, L. D. (1989). Benthic Boundary Layers of Estuarine and Coastal Environments. *Rev. Aquatic Sci.* 1, 75–95.

Wright, L. D., Kim, S. C., and Friedrichs, C. T. (1999). Across-shelf Variations in Bed Roughness, Bed Stress and Sediment Suspension on the Northern California Shelf. *Mar. Geol.* 154 (1), 99–115. doi:10.1016/S0025-3227(98)00106-6

Wu, H., Wang, Y. P., Gao, S., Xing, F., Tang, J., and Chen, D. (2022). Fluid Mud Dynamics in a Tide-Dominated Estuary: A Case Study from the Yangtze River. *Cont. Shelf Res.* 232, 104623. doi:10.1016/j.csr.2021.104623

Wu, X., Xu, J., Wu, H., Bi, N., Bian, C., Li, P., et al. (2019). Synoptic Variations of Residual Currents in the Huanghe (Yellow River)-Derived Distal Mud Patch off the Shandong Peninsula: Implications for Long-Term Sediment Transport. *Mar. Geol.* 417, 106014. doi:10.1016/j.margeo.2019.106014

Xu, J. P., and Wright, L. D. (1995). Tests of Bed Roughness Models Using Field Data from the Middle Atlantic Bight. *Cont. Shelf Res.* 15, 1409–1434. doi:10.1016/0278-4343(94)00083-Y

Xu, P., Mao, X., and Jiang, W. (2017). Estimation of the Bottom Stress and Bottom Drag Coefficient in a Highly Asymmetric Tidal Bay Using Three Independent Methods. *Cont. Shelf Res.* 140, 37–46. doi:10.1016/j.csr.2017.04.004

Yang, Z. S., and Liu, J. P. (2007). A Unique Yellow River-Derived Distal Subaqueous Delta in the Yellow Sea. *Mar. Geol.* 240 (1-4), 169–176. doi:10.1016/j.margeo.2007.02.008

Yuan, P., Wang, H., Wu, X., and Bi, N. (2020). Grain-Size Distribution of Surface Sediments in the Bohai Sea and the Northern Yellow Sea: Sediment Supply and Hydrodynamics. *J. Ocean. Univ. China* 19 (3), 589–600. doi:10.1007/s11802-020-4221-y

Conflict of Interest: The authors declare that the research was conducted in the absence of any commercial or financial relationships that could be construed as a potential conflict of interest.

Publisher's Note: All claims expressed in this article are solely those of the authors and do not necessarily represent those of their affiliated organizations, or those of the publisher, the editors, and the reviewers. Any product that may be evaluated in this article, or claim that may be made by its manufacturer, is not guaranteed or endorsed by the publisher.

frontiers | Frontiers in Earth Science

TYPE Original Research
PUBLISHED 12 August 2022
DOI 10.3389/feart.2022.932621

OPEN ACCESS

EDITED BY
Xiaolei Liu,
Ocean University of China, China

REVIEWED BY
Xianwei Zhang,
Institute of Rock and Soil Mechanics, (CAS), China
Zhang Bin,
China University of Geosciences, China

*CORRESPONDENCE
Bin Tang,
tangbin@glut.edu.cn
Yanxia Gong,
65185162@qq.com

SPECIALTY SECTION
This article was submitted to Geohazards and Georisks, a section of the journal Frontiers in Earth Science

RECEIVED 30 April 2022
ACCEPTED 14 July 2022
PUBLISHED 12 August 2022

CITATION
Tang B, Xie L, Wang W, Zhou B and Gong Y (2022), Unconfined compressive strength and pore structure evolution law of structural clay after disturbance.
Front. Earth Sci. 10:932621.
doi: 10.3389/feart.2022.932621

Unconfined compressive strength and pore structure evolution law of structural clay after disturbance

Bin Tang[1]*, Liang Xie[1,2], Wei Wang[1], Biaohe Zhou[1] and Yanxia Gong[3]*

[1]College of Civil Engineering and Architectural, Guilin University of Technology, Guilin, China, [2]Wuhan Surveying-Geotechnical Research Institute Co., Ltd. of MCC, Wuhan, China, [3]Department of Civil Engineering, HuBei University of Technology Engineering and Technology College, Wuhan, China

The clay in the Zhanjiang Formation has thixotropic properties, which has greatly influenced the foundation engineering in the Zhanjiang area. The evolution law of macroscopic strength and clay microstructure during thixotropy can be used to explain the practical engineering problems caused by thixotropy. For undisturbed and reconstituted soil curing for a different period, unconfined compressive strength test, scanning electron microscopy, and mercury injection porosimetry test were carried out to obtain the unconfined compressive strength and pore structure evolution law in the thixotropic process. The results indicate that the Zhanjiang Formation structural clay is very sensitive to disturbance and its unconfined compressive strength decreases from 180.29 to 11.73 kPa after the natural structure is completely destructed. After 300 d of curing, the unconfined compressive strength of clay increased from 11.73 to 53.43 kPa because of thixotropy, which increased by 3.55 times. The stacking flaky flocculation structure of the undisturbed soil is destructed by reconstituting, turning to flaky flocculation structure, and the large pores are homogenized, the small pores develop into medium pores, and there is a decrease in soil strength. In the process of thixotropy, the soil particles gradually coagulate and form an aggregates flocculation structure, and the strength of clay increases with the increase in the degree of cementation. Based on the results, the thixotropic pattern of clay was established and its thixotropic mechanism was explained.

KEYWORDS

thixotropy of clay, strength timeliness, unconfined compressive strength test, scanning electron microscopy test, mercury injection porosimetry test

1 Introduction

Clay thixotropy of refers to a phenomenon in which the original soil structure is destructed when the soil is disturbed, and its mechanical strength decreases dramatically. After disturbance, part of the mechanical strength gradually recovers with time (Boswell, 1948; Skemption and Northey, 1952; Mitchell, 1961; Mewis, 1979; Barnes, 1997; Díaz-Rodríguez and

Santamarina, 1999; Tang et al., 2021a). Shahriar and Jadid (2018) and Shahriar et al. (2018) studied the change rule of mechanical properties of reconstituted clays with specific water content over time, finding that the shear strength and yield stress of reconstituted clays increased significantly after 90 d compared to the initial moment. According to Kamil and Aljorany's (2019) study on the thixotropy of 180 soil samples, the strength of the soil decreased by 45% following reconstitution, and after 25 weeks of standing, the strength of the soil recovered to the strength of the undisturbed soil caused by the thixotropic effect. Under the influence of thixotropy, the strength and deformation characteristics of soil show strong time dependence (Ruge et al., 2019; Alam et al., 2021; Tang et al., 2021b). The study of thixotropic soil behavior can provide a basis for selecting parameters of reliability design of foundation engineering under long-term load.

Studies on the thixotropy of clay have achieved a lot in terms of macroscopic mechanical properties (Rinaldi and Clariá, 2016; Yang and Andersen, 2016; Larson and Wei, 2019; Ren et al., 2021; Yang et al., 2021; Zhou et al., 2021), but there is still no unified understanding of the action mechanism of the clay thixotropy. According to the study of Huo et al. (2016), the particles of clay are usually charged, and the electrostatic interaction between the particles causes the particles to flocculate, forming the first-order flocculation structure, and cementing between the flocculants to form the second order or even higher-order flocculation structure. The process of disturbance will destruct the flocculation structure of the clay. In the thixotropic process, the clay particles follow the minimum energy principle to re-flocculate and re-cement, forming a new stable structure, and the strength of the clay gradually increases. At the same time, because of the disturbance process, the part of particle protrusion may be peeled off, reducing the interlocking between particles, and the strength of this part of loss is difficult to recover. In general, the strength of the reconstituted soil is difficult to recover to the strength of the undisturbed soil in a short time. According to the research on the thixotropy mechanism of clay of Zhang et al. (2014) and Zhang X. W. et al. (2017), the microstructure of clay undergoes a process of destruction and reorganization in the thixotropy process, during which the force field between the particles causes the particles to condense and form aggregates. Landrou et al. (2018) studied the influence of inorganic dispersants on the thixotropic behavior of tight clay and pointed out that the rearrangement of clay particles and the interaction between the charge on the surface of the particles were the root of the thixotropic clay behavior. The stable lap modes of particles were only vertical and parallel, and the probability of reaching stability in the intermediate state was very small. The change of electrolyte concentration can alter the stable lapping pattern of clay particles from vertical to parallel to form a more stable structure (Chen et al., 2020). Peng et al. (2021) believed that the evolution of clay structure may be caused by various microscale particle rearrangements, including clay particle reorientation, aggregation, and flocculation, which are controlled by interparticle forces. To understand the nature of the clay thixotropic behavior, these studies laid a solid foundation. However, the thixotropic mechanism of clay is very complex, and the micro-macro evolution law of soil structure and strength characteristics during the disturbance and static process has not been fully elaborated. There are still some contradictions between many phenomena and theoretical description, and there is a lack of close relation between the micro theory and macro phenomenon, which needs to be further explored and verified.

FIGURE 1
Exposure profile of soil layer.

The clay thixotropy has a great influence on engineering practice (Kul'chitskii, 1975; Lutenegger, 2017). Engineering problems such as the strength growth of filling soil (Tsugawa et al., 2017), the bearing capacity of pile foundation in clay layer (Shen et al., 2005; Abu-Farsakh et al., 2015; Karlsson et al., 2019; Gong et al., 2020), and the time effect of anchoring force of anchor bolt (Zhang N et al., 2017) are closely related to the thixotropy of soil. These phenomena can be explained by the influence of thixotropy on clay strength, but the mechanism of thixotropy of clay has not been fully revealed. It can be seen from the existing research results that the thixotropy of clay stems from the evolution of its microstructure, and the thixotropy mechanism of clay can be revealed by studying the change rules of the internal structure and pores in the process of thixotropy. In this study, the clay in the Zhanjiang Formation in China was taken as the research object, and the strength, microstructure, and porosity of samples vary with time were studied. The tests included unconfined compressive strength (UCS) test, scanning electron microscopy (SEM), and mercury injection porosimetry (MIP). According to the test results, the laws of mechanical properties change, microstructure evolution, and pore evolution of the samples during thixotropy were obtained, and the thixotropic pattern of the clay in the Zhanjiang Formation was established to explain its thixotropy mechanism.

2 Unconfined compressive strength test

Undisturbed soil was obtained from the Baosteel Zhanjiang iron and steel base in the Donghai Island, Zhanjiang City,

FIGURE 2
Soil sample.

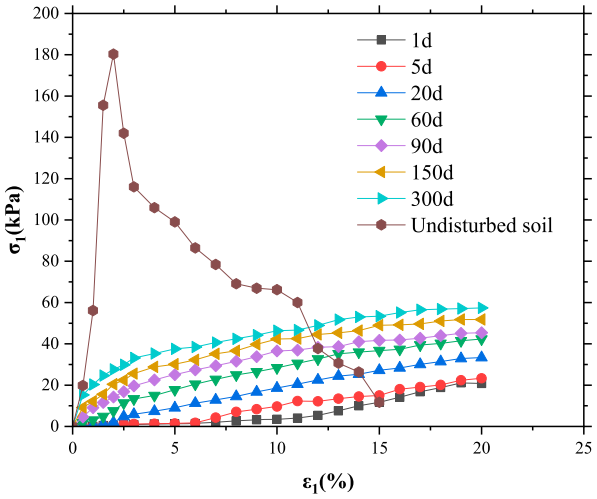

FIGURE 3
Relation curve between axial stress and axial strain.

Guangdong Province, China. This region is located in the southern tip of the Chinese mainland and the southwest of Guangdong Province, and in the low latitude area south of the Tropic of Cancer. It has a subtropical monsoon climate, with an annual average temperature of 23.5°C and an annual average rainfall of 1,556 mm. The geological age of the sampled soil layer is early Pleistocene. The exposed section of the soil layer is presented in Figure 1.

The soil sample is gray clay with clear bedding, as shown in Figure 2.

The natural moisture content of the soil sample is 40.7%, the natural density is 1.81 g/cm^3, and the specific gravity of soil particles is 2.71.

The undisturbed soil samples used in the test are cylindrical with a diameter of 39.1 mm and a height of 80 mm. During the preparation of undisturbed samples, wire saws were used to cut the soil samples into cuboids slightly larger than the specified size, and then soil sharpeners were used to carefully cut the cuboids into cylindrical shapes with a diameter of 39.1 mm. The unearthed samples were taken, and both ends of the soil samples were cut flat to a length of 80 mm to obtain undisturbed soil samples. During the preparation of reconstituted samples, the soil samples were naturally air-dried and then ground up, and then passed through a sieve of 2 mm. The soil samples with particle size <2 mm were put into fresh-keeping bags for sealing and reserve. At the same time, the air-dried moisture content of the soil samples was tested. The quality of distilled water needed to be added was calculated considering the natural moisture content and air-dried moisture content of soil samples. The distilled water needed for weighing was added into a sprayer, the soil sample was sprayed with the sprayer, and the soil sample was stirred at the same time to make the distilled water spray even. The soil sample with the prepared moisture content was put into a fresh-keeping bag and sealed for 24 h. Next, it was determined whether the moisture content of the soil sample was the target moisture content, and the error was controlled within ±1%. The prepared soil sample was placed into a fresh bag and sealed, and then put in a moisturizing tank for later use. The quality of a soil sample was calculated according to the natural density of the soil and the size of the sample. During sample preparation, 1/4 of the sample mass required was weighed, loaded into the sampler with a jack pressure to 1/4 of the sample height, unloading pressure, scraping in the stratified position. Next, 1/4 of the sample mass required was continued to be weighed and then loaded into the sampler. The above operations were repeated to prepare a cylindrical reconstituted sample with a diameter of 39.1 mm and a height of 80 mm. The sample was wrapped with cling film and put into the prepared PVC pipe. The lid was then closed, wrapped with adhesive tape, and sealed. Studies show that soil strength recovery is fast in the early stage, slow down in the middle stage, and tends to be stable in the late stage (Feng et al., 2004; Zhang X. W et al., 2017), so the curing time is 1, 5, 20, 60, 90, 150, and 300 d. UCS test was carried out on each curing sample, and the relation curve between axial stress and axial strain was obtained. The test method was in accordance with the relevant provisions of Article 20 of "Standard for Geotechnical Test Methods" in China (GB/T50123-2019). The relation curve between axial stress and axial strain of sample was obtained, as shown in Figure 3.

As can be seen from Figure 3, after the stress of the undisturbed soil sample reaches the peak, the stress greatly decreases with the increase of strain, there is an obvious strain softening phenomenon, and the soil structure is strong. For the undisturbed soil sample, because of the uneven internal structural strength, when the stress reaches the peak (180.29 kPa), the part of the small structural strength will break first, and the stress will begin to decrease. With the increase of strain, the damage of this structure will continue

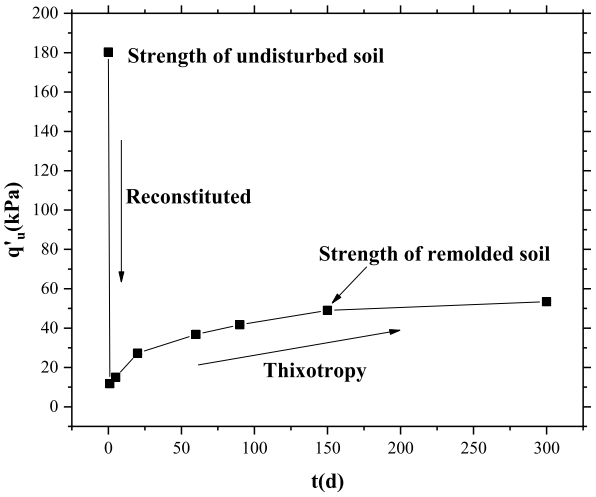

FIGURE 4
Relation curve between unconfined compressive strength and curring time.

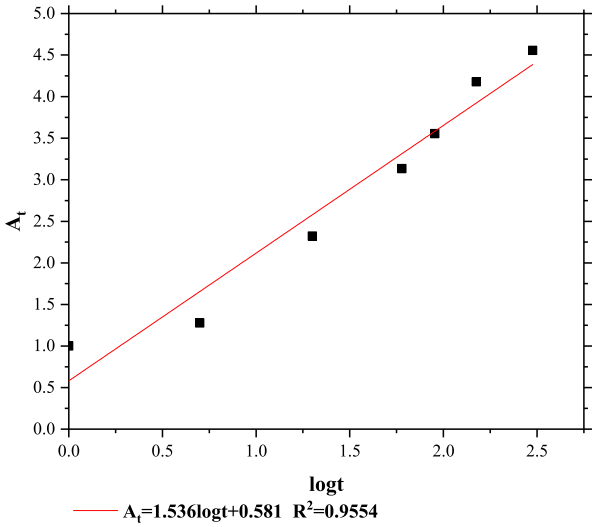

FIGURE 5
Correlation between the thixotropic strength ratio and curing time.

to accumulate and finally form a complete failure surface. When the strain reaches 10%, the stress continues to decrease because of the sliding of the failure surface. The $\sigma_1 - \varepsilon_1$ relation curve of reconstituted soil has no peak value, but gradually increases with the increase of curing time, indicating that the strength of reconstituted soil increases with the increase of curing time, and thixotropy is obvious. After reconstituting, the structure of the soil is completely destructed. After curing, the structure of the soil is restored to some extent, and its strength increases accordingly. For the undisturbed soil sample, the peak stress is taken as the UCS of the sample (180.29 kPa). For reconstituted soil samples, because their stress-strain relation does not have a peak value, we take the stress when the sample produces 15% axial strain as its UCS. At this time, the sample has undergone a large deformation, and it can be considered that the failure has occurred. The UCS of the samples at curing time of 1, 5, 20, 60, 90, 150 and 300 d were 11.73, 14.99, 27.24, 36.75, 41.70, 49.00 and 53.43kPa, respectively. The relation between UCS and curing time was established, as shown in Figure 4.

As can be seen from Figure 4, the mechanical properties of soil samples changed greatly before and after reconstituting, and the UCS of soil samples decreased significantly after reconstituting, from 180.29 to 11.73 kPa. Structural clay forms a stable structure in the deposition process, such as cementation between particles, which is destructed after disturbance. Therefore, the strength of reconstituted soil is lower than that of the undisturbed soil. Gong et al. (2000) also obtained the same view in his study. After curing, the soil forms a new structure, and its strength gradually recovers. The strength of soil increases rapidly in the period of 0–90 d, and tends to be stable after 90 d. After 300 d of curing, the UCS of clay increased from 11.73 to 53.43 kPa by 3.55 times. Zhang et al. (2014) and Zhang X. W. et al. (2017) conducted UCS tests on clay samples with different curing times and used the thixotropic strength ratio to measure the thixotropy of clay. However, the thixotropic strength ratio of clay varies with curing time and is not unique, so it is difficult to evaluate the thixotropic of different soil samples with different curing times. According to the data in Figure 4, the thixotropic strength ratio A_t corresponding to each curing time was obtained from the ratio of the strength of each curing time to the strength of curing for 1 d, and the relation between the thixotropic strength ratio A_t, and the logarithm of curing time $log_{10}t$ was established for linear fitting, as shown in Figure 5.

It can be seen from Figure 5 that the thixotropic strength ratio of soil increases with the increase of curing time, and there is a linear relation between the thixotropic strength ratio and the logarithm of curing time:

$$A_t = a\log_{10}t + b,$$

where b is a dimensionless regression parameter. Furthermore, a is the thixotropic recovery coefficient and is the slope of the curve of $A_t - log_{10}t$ relation, and it represents the change of thixotropic strength ratio A_t caused by each change of curing time by a logarithmic cycle (10 times), without dimension. a indicates the degree of soil thixotropy. The larger the a, the stronger the thixotropy of soil, and vice versa.

3 Scanning electron microscopy test

To explore the evolution law of microstructure of clay in the thixotropic process, SEM was carried out on the undisturbed soil samples and reconstituted soil samples cured for 1, 5, 20, 60, 90,

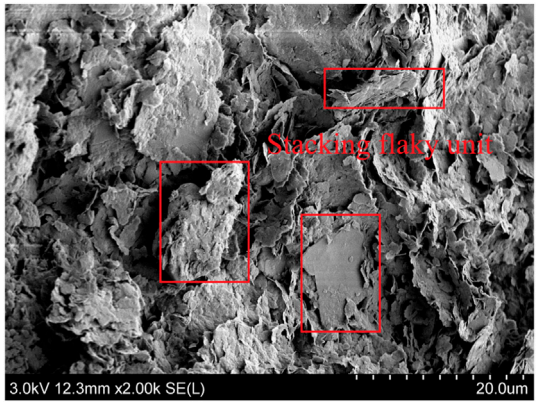

FIGURE 6
Scanning electron microscopy (SEM) photographs of undisturbed soil.

150, and 300 d. The size of the undisturbed soil sample was 10 mm × 10 mm × 10 mm. Refer to the method in Section 2 for preparation and curing of reconstituted soil. Since the reconstituted soil sample is soft, too small volume would produce large deformation during sample cutting, so the size of reconstituted soil sample was 20 mm × 20 mm × 20 mm. During the test, the sample with the corresponding specifications was cut with a thin blade and put into liquid nitrogen (boiling point −196°C) to freeze for 15–25 min, and then the frozen soil sample was placed into the freeze-drying machine. The frozen soil sample was vacuumed at −50°C for more than 24 h, so that the soil sample was dry and not easy to deform. An appropriate amount of conductive adhesive was taken to glue the sample to the sample column, and the sample was put into the vacuum sputtering coating machine for surface plating of the Au-Pd alloy film to obtain high-resolution image. After the coating was completed, the scanning electron microscope test was conducted to obtain the sample SEM images, as shown in Figures 6 and 7.

As can be seen from Figure 6, the undisturbed soil in the Zhanjiang Formation is a stacking flaky flocculation structure, and the structural units of soil are mainly stacking flaky units. Stacking flaky units are formed by the cementation of single-flake soil particles by stacking face to face, and the polyporous and non-directional flocculation structure is formed by edge-to-edge lap, corner-to-surface lap, and surface-to-surface lap among stacking flaky units, which makes soil more sensitive to disturbance and has a strong structure. As can be seen from Figure 7A, after reconstituting, the stacking flaky flocculation structure of the soil sample was destructed and turned into a loose flaky flocculation structure. The structural units of soil are dominated by single-flake soil particle units. The single-flake soil particles contact each other by the way of surface–surface, edge–surface, and point–surface. The pores between the soil particles increase, the dispersion degree increases, the degree of cementation between the particles is low, and the stability is poor. It can be seen from Figures 7A–C that in the first 20 d of curing time, the structural units of soil were dominated by single-flake soil particle units. The ability of single-flake soil particle units to resist external loads is weaker than that of stacking flaky units, and the macroscopic strength of reconstituted soil is significantly lower than that of undisturbed soil. As can be seen from Figures 7D,E, when curing time is 60 d and 90 d, some flake particles polymerize and form aggregates, and the structural units are in the mixing state of single-flake soil particles and aggregates, forming a single-flake particle–aggregate flocculation structure. When the flaky particles overlap with the surface of the aggregates, the pores between the soil particles are reduced, and the degree of cementation is improved. Compared with single-flake particles, aggregates have stronger resistance to external load, and the mixing state of single-flake particles and aggregates improves the soil strength to some extent. It can be seen from Figures 7F,G that when the curing time is 150 d and 300 d, the structural units are dominated by aggregates, forming an aggregated flocculation structure. The degree of cementation is obviously improved, and the strength of soil is further improved by surface-to-surface lapping of aggregates. Zhang et al. (2014) and Zhang X. W. et al. (2017) conducted SEM tests on clay samples with different curing times and summarized the change rule of particle lap mode in clay thixotropic process. In this study, the variation law of structural units in the thixotropic process is discussed from another angle, and the thixotropic pattern of clay is established. Based on the above analysis results, in the whole process, the unit of soil structure has experienced the change processes of stacking the flaky unit, single-flake particle unit, single-flake particle–aggregate unit, and aggregate unit. At a macroscopic level, the strength of undisturbed soil is higher than that of reconstituted soil, and the strength of reconstituted soil decreases obviously. After curing the reconstituted samples, the strength of the soil gradually increases. The structural characteristics and change process of the sample at different times are presented in Figure 8.

4 Mercury injection porosimetry test

To explore the evolution law of internal pores of clay in the thixotropic process, MIP test were carried out on the undisturbed soil sample and the reconstituted soil samples curing for 1, 5, 20, 60, 90, 150 and 300 d. Refer to the method in Section 2 for preparation and curing of reconstituted soil. For sample specification and freeze-drying method, refer to method 3. The test instrument adopts automatic mercury injection meter. During the test, the sample is loaded into the sample tube (dilatometer) for low pressure analysis and

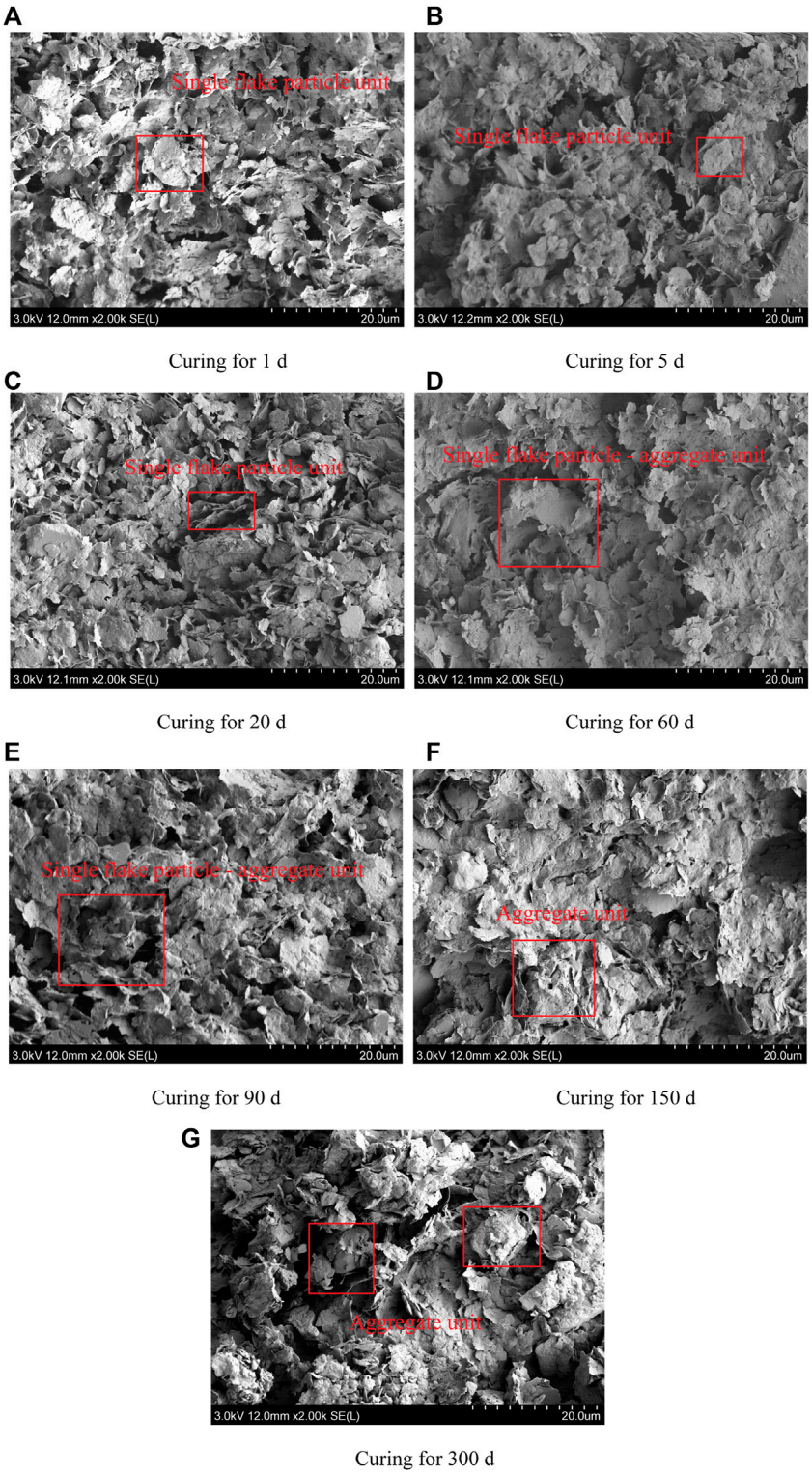

FIGURE 7
SEM photographs of reconstituted soil samples with different curing time.

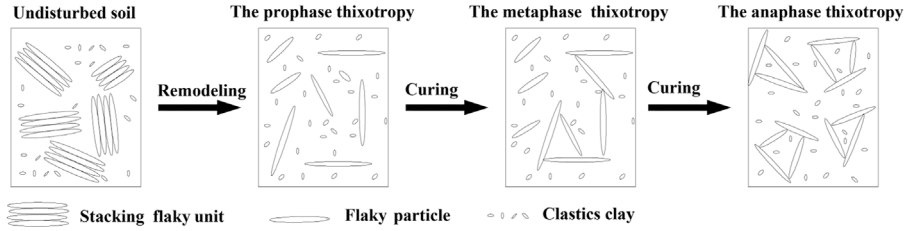

FIGURE 8
Thixotropic pattern of structural clay.

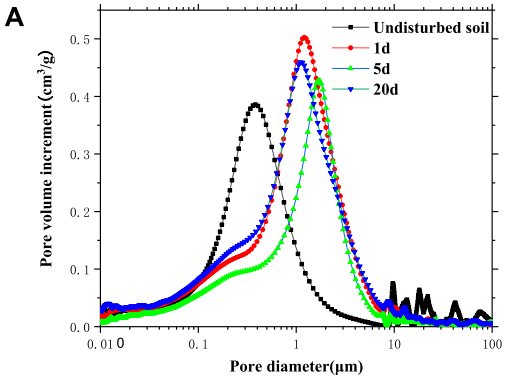

Pore distribution curves of undisturbed soil sample and reconstituted soil samples of prophase thixotropy

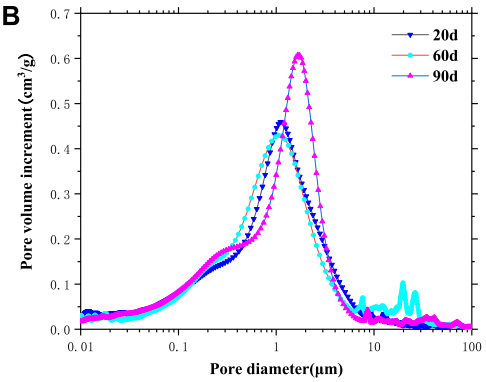

Pore distribution curve of reconstituted soil samples of metaphase thixotropy

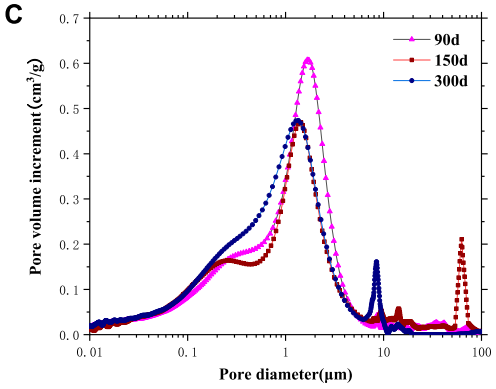

Pore distribution curve of reconstituted soil samples of anaphase thixotropy

FIGURE 9
Pore distribution curves of samples during thixotropy.

then transferred to the high-pressure station for high-pressure analysis to obtain the pore distribution curve of the sample. To observe the variation rule of sample pores during thixotropy more clearly, curing ages were divided into three groups: prophase thixotropy (the first 20 d), metaphase thixotropy (20–90 d) and anaphase thixotropy (90–300 d), as shown in Figure 9.

It can be seen from Figure 9A that the pore distribution curve of the undisturbed soil sample is characterized by one main peak and multiple sub-peaks. The pore diameter distribution range of

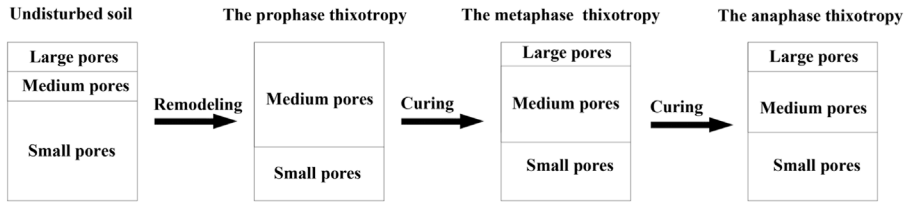

FIGURE 10
Schematic diagram of pore distribution changes.

the main peak of the curve of the undisturbed soil sample is 0.1–1.1μm, and the distribution range of the sub-peaks is 10.0–100.0 μm. The pore distribution curve of reconstituted soil samples in the prophase thixotropy is characterized by one main peak, and the sub-peaks are not obvious. The pore diameter of the main peak of the curve of reconstituted soil sample ranges from 0.1 to 5.0 μm. The pores with pore diameter <1.0 μm are defined as small pores, those with pore diameter >1.0 μm and <10.0 μm are defined as medium pores, and those with pore diameter >10.0 μm are defined as large pores. It should be noted that the small, medium, and large pores defined here are relative to each other to facilitate the clarification of the evolution law of pores. The pore diameter distribution range of the main peak of the sample curve before and after reconstituting changed from 0.1-1.1μm to 0.1–5.0μm, indicating that the pore distribution curve of the sample shifted to the right after reconstituting, and part of the original small pores developed into medium pores. Before reconstituting, the pore distribution curve of the sample has an obvious sub-peak, and after reconstituting, the sub-peak is weakened, indicating that the large pores in the undisturbed soil sample are homogenized into medium pores by reconstituting. As can be seen from Figure 9B, the pore diameter distribution range of the main peak of the reconstituted soil sample curve at the metaphase thixotropy ranges from 0.1 to 4.0μm, and the curve of the reconstituted soil sample shows an obvious sub-peak, indicating that with the increase of curing time, part of the medium pores re-develop into small and large pores. As shown in Figure 9C, the pore diameter of the main peak of the reconstituted soil sample in the anaphase thixotropy is in the range of 0.05–0.11 μm compared with that in the metaphase thixotropy, and the obvious sub-peak appears on the right side of the curve, indicating that the small pores and large pores are developed further in the anaphase thixotropy. Zhang et al. (2014) and Zhang X. W. et al. (2017) conducted mercury injection tests on clay samples with different curing times and simply summarized the variation rule of pore distribution in the clay thixotropic process. In this study, the variation law of the main peak and sub-peaks of the pore distribution curve, the movement of the pore distribution curve, and the variation of the proportion of different pores during the thixotropic process of clay are discussed further. To more directly represent the change rule of pores in the thixotropy process, the pore distribution change process in Figure 9 is represented by a schematic diagram, as shown in Figure 10. The area in the diagram represents the proportion of pores at all levels.

5 Conclusion

In this study, the UCS and pore structure evolution law of clay during the thixotropic process of 300 d were examined, and the following conclusions were obtained:

1) The Zhanjiang Formation structural clay is very sensitive to disturbance. After the complete destruction of natural structure, the UCS of clay decreases from 180.29 to 11.73 kPa. After 300 d of curing, the UCS of the clay increased from 11.73 kPa to 53.43 kPa because of thixotropy, which increased by 3.55 times.
2) There is a linear relation between the thixotropic strength ratio and the logarithmic value of curing time during the thixotropic process of Zhanjiang Formation structural clays, and the slope can be used to reflect the thixotropy strength. The higher the slope, the stronger the thixotropy, and vice versa.
3) The natural structural units of the Zhanjiang Formation structural clay are stacking flaky units. After reconstituting, the structural units become single-flake particle units. With the extension of curing time, the structural units gradually evolve into single-flake particle– aggregate units, and the aggregate units are formed following 300 d of thixotropy.
4) The large pores of undisturbed soil are homogenized, and the small pores develop into medium pores by reconstituting. In the prophase thixotropy, the pores are mainly medium and small. In the metaphase thixotropy, the macropores begin to develop. In the anaphase thixotropy, some medium pores develop into small and large pores.
5) The fundamental reason for the change of macroscopic strength of clay in the thixotropic process are the changes in the cementation degree between clay particles and pore

distribution. When the natural clay structure is destructed, with the extension of standing time, the reconstituted soil will gradually form a new stable structure, but the recovery of structure is limited, and in a short time, the strength of the reconstituted soil is difficult to regain the strength of the undisturbed soil.

6) Our study provides data support for revealing the thixotropic mechanism of clay, but the time scale of the study is limited, and further research is required to fully explain the thixotropic behavior of clay.

Data availability statement

The original contributions presented in the study are included in the article/supplementary material. Further inquiries can be directed to the corresponding author.

Author contributions

BT, LX and YG contributed to conception and design of the study. WW organized the database. LX performed the statistical analysis. BZ wrote the first draft of the manuscript. All authors contributed to manuscript revision, read, and approved the submitted version.

Funding

This work was supported by the Guangxi Natural Science Foundation (2020GXNSFAA297199), the National Natural Science Foundation of China (41867035), and the project of Guangxi Key Laboratory of Geotechnical Mechanics and Engineering (2016-A-01). The authors gratefully acknowledge the financial support.

Conflict of interest

LX was employed by Wuhan Surveying-Geotechnical Research Institute Co., Ltd. of MCC. The remaining authors declare that the research was conducted in the absence of any commercial or financial relationships that could be construed as a potential conflict of interest.

Publisher's note

References

Abu-Farsakh, M., Rosti, F., and Souri, A. (2015). Evaluating pile installation and subsequent thixotropic and consolidation effects on setup by numerical simulation for full-scale pile load tests. *Can. Geotech. J.* 52 (11), 1734–1746. doi:10.1139/cgj-2014-0470

Alam, M., Shahriar, A. R., Islam, M. S., Islam, N., and Abedin, M. (2021). Experimental investigation on the strength and deformation aspects of thixotropic aging in reconstituted clays. *Geotech. Geol. Eng. (Dordr).* 39 (3), 2471–2486. doi:10.1007/s10706-020-01639-1

Barnes, H. A. (1997). Thixotropy—A review. *J. Newt. fluid Mech.* 70 (1-2), 1–33. doi:10.1016/S0377-0257(97)00004-9

Boswell, P. G. H. (1948). A preliminary examination of the thixotropy of some sedimentary rocks. *Q. J. Geol. Soc.* 104 (1-4), 499–526. doi:10.1144/GSL.JGS.1948.104.01-04.23

Chen, B., Shu, Q.-F., and Deng, R.-S. (2020). Microscopic interpretation of time-depending strength of clay considering plate-shaped particle interactions. *Chin. J. Geotechnical Eng.* 43 (02), 271–280. doi:10.11779/CJGE202102007

Díaz-Rodríguez, J. A., and Santamarina, J. C. (1999). "Thixotropy: the case of Mexico city soils," in XI panamerican conference on soil mechanics and geotechnical engineering, , Brazil, 441–448. doi:10.13140/2.1.3191.4883

Feng, X-L., Zhou, S-W., Lin, L., Liu, T., and Wu, S-Q. (2004). The thixotropy of silt in huanghe delta. *Periodical Ocean Univ. China* 34 (6), 1053–1056. doi:10.16441/j.cnki.hdxb.2004.06.02

Gong, W., Li, L., Zhang, S., and Li, J. (2020). Long-term setup of a displacement pile in clay: an analytical framework. *Ocean. Eng.* 218, 108143. doi:10.1016/j.oceaneng.2020.108143

Gong, X-N., Xiong, C-X., Xiang, K-X., and Hou, Y-F. (2000). The formation of clay structure and its influence on mechanical characteristics of clay. *J. Hydraulic Eng.* (10), 43–47. doi:10.13243/j.cnki.slxb.2000.10.007

Huo, H-F., Qi, L., Lei, H-Y., and Yu, G. (2016). Analysis and experimental study on thixotropy of Tianjin soft clay. *Chin. J. Rock Mech. Eng.* 35 (3), 631–637. doi:10.13722/j.cnki.jrme.2015.0435

Kamil, A. S., and Aljorany, A. N. (2019). Thixotropic hardening of fao clay. *J. Eng.* 25 (5), 68–78. doi:10.31026/j.eng.2019.05.05

Karlsson, M., Yannie, J., and Dijkstra, J. (2019). Modeling aging of displacement piles in natural soft clay. *J. Geotech. Geoenviron. Eng.* 145 (10), 04019070. doi:10.1061/(ASCE)GT.1943-5606.0002110

Kul'chitskii, G. B. (1975). Thixotropy of soils of the middle Ob region and its consideration when constructing pile foundations. *Soil Mech. Found. Eng.* 12 (3), 168–170. doi:10.1007/BF01707641

Landrou, G., Brumaud, C., Plötze, M. L., Winnefeld, F., and Habert, G. (2018). A fresh look at dense clay paste: deflocculation and thixotropy mechanisms. *Colloids Surfaces A Physicochem. Eng. Aspects* 539, 252–260. doi:10.1016/j.colsurfa.2017.12.029

Larson, R. G., and Wei, Y. (2019). A review of thixotropy and its rheological modeling. *J. Rheology* 63 (3), 477–501. doi:10.1122/1.5055031

Lutenegger, A. J. (2017). "Aged undrained shear strength of remolded clays," in Offshore Site Investigation Geotechnics 8th International Conference Proceeding, London, September 12–14, 2017 (Society for Underwater Technology), 378–383. doi:10.3723/OSIG17.378

Mewis, J. (1979). Thixotropy-a general review. *J. Newt. Fluid Mech.* 6 (1), 1–20. doi:10.1016/0377-0257(79)87001-9

Mitchell, J. K. (1961). Fundamental aspects of thixotropy in soils. *Trans. Am. Soc. Civ. Eng.* 126 (1), 1586–1620. doi:10.1061/TACEAT.0008103

Peng, J., Luo, S., Wang, D., Ren, Y., Fan, L., DeGroot, D. J., et al. (2021). Quantitative evaluation of thixotropy-governed microfabric evolution in soft clays. *Appl. Clay Sci.* 210, 106157. doi:10.1016/j.clay.2021.106157

Ren, Y., Yang, S., Andersen, K. H., Yang, Q., and Wang, Y. (2021). Thixotropy of soft clay: a review. *Eng. Geol.* 287, 106097. doi:10.1016/j.enggeo.2021.106097

Rinaldi, V. A., and Clariá, J. J., Jr (2016). Time dependent stress–strain behavior of bentonite slurries; effect of thixotropy. *Powder Technol.* 291, 311–321. doi:10.1016/j.powtec.2015.12.036

Ruge, J. C., Molina-Gómez, F., and Rojas, J. P. (2019). Thixotropic behaviour study of clayey soils from the lacustrine deposits of Bogotá high plateau. *J. Phys. Conf. Ser.* 1386, 012050. IOP Publishing. doi:10.1088/1742-6596/1386/1/012050

Shahriar, A. R., Abedin, M. Z., and Jadid, R. (2018). Thixotropic aging and its effect on 1-D compression behavior of soft reconstituted clays. *Appl. Clay Sci.* 153, 217–227. doi:10.1016/j.clay.2017.12.029

Shahriar, A. R., and Jadid, R. (2018). An experimental investigation on the effect of thixotropic aging on primary and secondary compression of reconstituted dredged clays. *Appl. Clay Sci.* 162, 524–533. doi:10.1016/j.clay.2018.05.023

Shen, S. L., Jiang, Y. Q., Cai, F. X., and Xu, Y. S. (2005). Mechanisms of property changes of soft clays around deep mixing column. *Chin. J. Rock Mech. Eng.* 24 (23), 4320–4327. CNKI:SUN:YSLX.0.2005-23-021.

Skemption, A. W., and Northey, R. D. (1952). The sensitivity of clays. *Geotechnique* 3 (1), 30–53. doi:10.1680/geot.1952.3.1.30

Tang, B., Zhou, B., Xie, L., and Yin, J. (2021b). Evaluation method for thixotropy of clay subjected to unconfined compressive test. *Front. Earth Sci. (Lausanne).* 9, 683454. doi:10.3389/feart.2021.683454

Tang, B., Zhou, B., Xie, L., Yin, J., Zhao, S., Wang, Z., et al. (2021a). Strength recovery model of clay during thixotropy. *Adv. Civ. Eng.* 2021, 1–11. doi:10.1155/2021/8825107

Tsugawa, J. K., Pereira, K. F., and Boscov, M. E. (2017). Thixotropy of sludge from the Cubatão water treatment plant, Brazil. *Geotech. Front.* 2017, 842–851. doi:10.1061/9780784480472.090

Yang, S., and Andersen, K. H. (2016). Thixotropy of marine clays. *Geotech. Test. J.* 39 (2), 20150020. doi:10.1520/GTJ20150020

Yang, S., Ren, Y., and Andersen, K. H. (2021). Effects of thixotropy and reconsolidation on the undrained shear characteristics of remoulded marine clays. *Ocean. Eng.* 239, 109888. doi:10.1016/j.oceaneng.2021.109888

Zhang, N., Wu, H. N., Shen, J. S. L., Hino, T., and Yin, Z. Y. (2017). Evaluation of the uplift behavior of plate anchor in structured marine clay. *Mar. Georesources Geotechnol.* 35 (6), 758–768. doi:10.1080/1064119X.2016.1240273

Zhang, X.-w., Ling-wei, K., Li, J., and Ai-wu, Y. (2014). Microscopic mechanism of strength increase of clay during thixotropic process. *Chin. J. Geotechnical Eng.* 36 (08), 1407–1413. doi:10.11779/CJGE201408005

Zhang, X. W., Kong, L. W., Yang, A. W., and Sayem, H. M. (2017). Thixotropic mechanism of clay: a microstructural investigation. *Soils Found.* 57 (1), 23–35. doi:10.1016/j.sandf.2017.01.002

Zhou, B., Tang, B., and Kang, J. (2021). A constitutive model of clay considering structural failure. *Front. Mat.* 8, 697181. doi:10.3389/fmats.2021.697181

frontiers | Frontiers in Earth Science

TYPE Original Research
PUBLISHED 19 August 2022
DOI 10.3389/feart.2022.931472

OPEN ACCESS

EDITED BY
Paul Liu,
North Carolina State University,
United States

REVIEWED BY
Marcos Eduardo Cordeiro Bernardes,
Federal University of Southern Bahia,
Brazil
Junbiao Tu,
Tongji University, China

*CORRESPONDENCE
Li Li,
lilizju@zju.edu.cn
Yuezhang Xia,
yzxia@zju.edu.cn

SPECIALTY SECTION
This article was submitted to Geohazards and Georisks, a section of the journal Frontiers in Earth Science

RECEIVED 29 April 2022
ACCEPTED 14 July 2022
PUBLISHED 19 August 2022

CITATION
Li L, Xu J, Ren Y, Wang XH and Xia Y (2022), Effects of wave-current interactions on sediment dynamics in Hangzhou Bay during Typhoon Mitag. *Front. Earth Sci.* 10:931472. doi: 10.3389/feart.2022.931472

Effects of wave-current interactions on sediment dynamics in Hangzhou Bay during Typhoon Mitag

Li Li[1]*, Jiayang Xu[1], Yihan Ren[1], Xiao Hua Wang[2] and Yuezhang Xia[1]*

[1]Ocean College, Zhejiang University, Zhoushan, China, [2]The Sino-Australian Research Consortium for Coastal Management, School of Science, University of New South Wales at Canberra, Canberra, ACT, Australia

The hydrodynamics and sediment characteristics of muddy estuaries and coasts during typhoons are closely related to the geomorphic evolution, ecological environment, and economic development of coastal zones. Taking the macro-tidal turbid Hangzhou Bay (HZB) as an example, the sediment characteristics and effects of wave-current interactions on sediment dynamics during Typhoon Mitag were studied using a fully-calibrated numerical model. The model considered tide-wave sediment interactions and the reconstructed typhoon wind field. Net sediment fluxes were controlled by residual currents and suspended sediment concentration (SSC). The combined interactions of currents and waves led to a high SSC during the typhoon. Under calm weather conditions, the impact of wave-current interactions (wave dissipation, form drag, wave radiation stress, mean current advection and refraction) was small, except for the combined bottom stresses. The combined bottom stress was the primary wave-current interaction that changed sediment resuspension and increased SSC, particularly in shallow waters or during storms. The advection term, which played an essential role in reducing SSC in HZB, mainly affected SSC by increasing the velocity. The wave dissipation term enhanced vertical mixing, which involved the vertical exchange of suspended sediment and currents. In the shallow waters of the southern bay, the wave dissipation term mostly led to decreased bottom stresses, increased currents, decreased SSC, and increased SSC in deep waters. The effects of form drag, wave radiation stress, and refraction terms on the suspended sediment dynamics were relatively small. These findings provide a theoretical foundation for the study of dynamic geomorphology in macro-tidal estuaries.

KEYWORDS

ssc, sediment dynamics, wave-current interactions, Typhoon Mitag, Hangzhou Bay

Highlights

1 A numerical model coupling tides, waves, storm surges, reconstructed winds, and sediments was used and calibrated to study the effects of wave-current interactions on sediment dynamics in Hangzhou Bay during Typhoon Mitag.
2 Wave-current interactions during the typhoon changed the hydro and sediment dynamics in Hangzhou Bay, mainly through combined wave-current bottom stress, which changed sediment resuspension and, therefore, affected SSC.
3 Compared to during calm weather, lateral circulation at the Andong tidal flat was reversed during Typhoon Mitag, and sediment flux subsequently changed, controlled by the friction term and vertical profile of SSC.

1 Introduction

The dynamic characteristics of estuarine and coastal sediments are closely related to geomorphological evolution, the ecological environment, and marine and coastal economic development. The dynamic processes of estuaries, particularly currents and waves, are closely related to sediment resuspension processes. The hydrodynamics of estuaries and coasts are influenced by various factors, for example, tides, wind stress, river flow, and horizontal density gradients associated with ocean circulation (Soulsby, 1997). In the East China Sea, tides are the dominant forces in the area, and tidal energy accounts for 80% or more of the total energy in this ocean dynamics (Wang, 2014). Waves occur intermittently, and typically, the period of wind waves in estuaries and coasts is between 0.5–5 s. The period of surge waves may exceed 20 s (Shi et al., 2006). The nonlinear coupling of waves and currents is important in shallow seas because it drives sediments, shapes coastal geomorphology, and even causes greater erosion and siltation (Wang, 2014). Fast-varying strong turbulence near the bottom can also have important effects on sediment processes, such as flocculation, sedimentation, and the resuspension of sediments (Yuan et al., 2009; Yang et al., 2016). Therefore, studying hydrodynamic and sediment characteristics and mechanisms during typhoons is critical in estuarine sediment dynamics (Jiang et al., 2014).

Bed shear stress is an important parameter for discussing sediment resuspension (Zhu, 2017), and bed shear stress is difficult to directly measure (Grant and Madsen, 1979). Widely used theories for calculating flow-induced shear stress τ_c include the logarithmic distribution of current velocity, turbulent kinetic energy, and Reynolds stress, and there can be a 19% difference between different methods (Kim et al., 2000). Wave-induced shear stress τ_w is usually calculated based on linear wave theory (Green and Coco, 2007). Comparative studies on bed shear stress under the combined action of waves and currents have been conducted worldwide. Yang (2016) measured sediment resuspension in a radial sand ridge and Yangzi shoal in Jiangsu Province, China. The results showed that flow-induced shear stress was substantially larger than wave-induced shear stress in this tidal-dominated environment. For shallow water areas, such as tidal flats, wave motion is more likely to penetrate down to the seabed, and the effect of waves on sediment resuspension cannot be ignored, particularly during storms (Green and Coco, 2014). Many studies have shown that orbital motion, even under very small waves (<0.2 m), can lead to the resuspension of intertidal sediments (Dyer et al., 2000; Uncles and Stephens, 2010; Green, 2011). Christie et al. (1999) found that in the intertidal zone of the Humber Estuary in the UK, sediment resuspension was dominated by flow-induced shear stress during calm weather, while wave was dominant during storms, and the suspended sediment concentration (SSC) increased substantially. Xu et al. (2021) conducted continuous observations of sediment dynamics in the near-bottom layer of the southern channel of the Yangtze Estuary during Typhoon Rann. The results showed that the waves contributed significantly to increasing the shear stress in the bottom bed during the typhoon, SSC in the near-bottom layer of the south channel could reach 10 kg/m^3, and a fluid mud layer with a thickness of more than 1.15 m occurred.

In most coastal areas, waves and currents play an extremely important role in sediment dynamics. Wave-current interactions are complex and are not only a linear sum of their individual behaviors. Wave-current interactions mainly include wave-induced currents (including coastal current and bottom return flows), wave refraction (flow changes wavelength and phase velocity), and wave-current interactions in the boundary layer, leading to the nonlinear enhancement of sub-bed shear stress (Soulsby et al., 1993). Green et al. (1997) provided evidence for the effect of wave-current interactions on the intertidal zone based on seabed hydraulic roughness z_0. When waves are negligible, z_0 remains constant during the tidal cycle and when waves are present, z_0 changes immediately and increases markedly. Bricker et al. (2005) discussed wave-current coupling in terms of additional drag on the mean fluvial flow in the presence of waves. Talke and Stacey (2003) found a significant increase in the bottom bed shear stress and associated drag coefficient in the intertidal zone of San Francisco Bay in the presence of waves, which they attributed to wave-current coupling. D'Alpaos et al. (2013) analyzed the statistical characteristics of resuspension events caused by the total bed shear stress τ_{cw} in Venice Slipper Lake with exponentially distributed intervals. The effect of the non-linear interaction between waves and currents is defined as τ_{cw}-(τ_c+τ_w), which is approximately 10% of the total bottom shear stresses.

The suspended sediment flux at any given location can be defined as the integral of the product of SSC and horizontal current velocity over the water depth (Green and Coco, 2014). In general, tidal currents lift and transport sediment so that sediment transport essentially follows the tidal direction. However, the direction of long-period net suspended sediment

transport may differ substantially from the direction of the residual flow because the suspended sediment transport rate is nonlinearly related to current velocity and the effect of wave mixing is considered (Soulsby, 1997).

In the intertidal zones of estuaries and coasts, the mean suspended sediment transport direction of the tidal cycle under calm weather conditions is usually landward because of tidal asymmetry, subsidence lag effect, and scour lag effect (Green and Coco, 2014). Van Straaten and Kuenen (1957) and Postma (1961) elaborated on the settling time lag and scouring time lag and their resulting siltation of fine-grained sediments. Dronkers (1986) further refined this theory. Settling time lag is the lag between the time when advection decreases to the velocity at which a sediment particle is no longer suspended, and the time required for that particle to be finally deposited on the seabed. If the tidal velocity decreases shoreward, the settling time delay will lead to a net transport of sediment to the shore. The scour lag effect is similarly defined and depends on the difference between transport and erosion velocities. Dyer et al. (2000) observed a net landward transport of fine-grained sediment during calm weather in contrast to an ebb tide dominant tide, which they attributed to a lag mechanism. Pritchard (2005) confirmed that for fine-grained sediment, the settling time lag generally leads to landward transport, while the scouring time lag plays a weak but detectable role in enhancing landward net transport.

Several studies have measured and assessed the importance of waves in suspended sediment transport. Christie and Dyer (1998) concluded that wave transport (oscillating flux) is two orders of magnitude smaller than tidal transport (mean flux), and that the direction of wave transport is random. Green and MacDonald (2001) found that wave-induced suspended sediment flux is smaller than tidal transport flux, and decreases rapidly with increasing height above the bottom bed. On average, the direction of wave-induced suspended sediment flux is opposite to the direction of the tides. Wave orbital velocity and wave-induced bottom turbulence can have opposite effects on the direction of net transport. When sedimentation is delayed by additional wave-induced mixing, the settling time lag is prolonged and net landward suspended sediment transport is reduced (Shi and Chen, 1996).

Field data have shown that net landward suspended sediment transport under calm weather conditions can be reversed by waves (Christie and Dyer, 1998; Dyer et al., 2000; Andersen and Pejrup, 2001). This is typically attributed to the offsetting effect of waves on the settling time lag, where waves can prevent suspended sediment settling. Waves may also interact with baroclinic processes to affect net suspended sediment transport. For example, Ralston and Stacey (2007) conducted field observations of tidal flats in San Francisco Bay, where baroclinic dynamics associated with salinity fronts dominated sediment transport. During the storm, increased freshwater input and resuspension of sediment under wave influence resulted in a net suspended sediment transport in the offshore direction.

Hangzhou Bay (HZB) is located south of the Changjiang River Estuary. It is a macro-tidal turbid bay with a water area of approximately 4,800 km^2 and an average water depth of approximately 8–10 m. The northern side of HZB is a deep water tidal channel, while most of the southern shore is muddy tidal flat with an average water depth of less than 4 m (Hu et al., 2019). The bay is affected by its funnel-shaped coastline and sill-shaped bar. It has a macro-tidal range and strong tides, with annual averaged tidal range of 5.61 m (Jin and Sun, 1992; Xie et al., 2008). In addition, the seawater is highly turbid, and SSC is high (He et al., 2013; Hu et al., 2019). The bay is known for its tidal bores and has one of the highest SSCs in the world, with an average sand content of 1–3 kg/m^3 below Ganpu and a SSC of 10.6 kg/m^3 at the top of the bay during spring tides (Pan et al., 2013). HZB has strong tides and relatively weak runoffs, and the turbulence at the bottom layer because of friction is sufficient to agitate all the water (Ji and Lu, 2008), which is a typical strongly mixed estuary. Many studies, for example, Pan et al. (2013) and Zhang et al. (2017) have demonstrated that after the arrival of the tidal bore, the flow changed dramatically, and SSC increased significantly in the near-bottom layer. Wang and Eisma (1990) studied sand transport in northern tidal flats and showed clear seasonality in the hydro-sediment dynamics. The wave direction is southeast in the wet season and is northeast-northwest in the dry season. Sediment mainly comes from the Changjiang River, with a small amount from the Qianjiang River, and the sediment supply is largest in winter. Shi (2001) analyzed sediment data observed in the deep-water channel of the bay and found a stratified structure of near-bottom sediment, with low SSC near the surface layer, high SSC in the lower middle layer, and a fluid mud layer near the bed. Xie et al. (2013) established a two-dimensional suspended sediment numerical model based on Delft3D. They reproduced three high and two low turbidity zones in HZB, and concluded that sediment transport is controlled by tidal asymmetry patterns. Using field data in the upper HZB, Tu and Fan (2017) confirmed that the flood tides is abnormally accelerated in the first 10 minutes, tidal asymmetry is significant, and near-bottom turbulence generation and dissipation are in local equilibrium. Tu et al. (2019) further analyzed the data and found that the sediment concentration gradient changed flow structure.

Hangzhou Bay is a funnel shaped bay located on the coast of the East China Sea and is significantly affected by typhoons. According to statistical data, the East China Sea is affected by an average of four typhoons per year (Lu et al., 2018). The effects of storm events on estuarine hydrodynamic and sediment characteristics vary depending on the storm and estuary types (Williams, 2009; Leonardi et al., 2018). During Typhoon Chan-hom, the storm surge in HZB was mainly influenced by wind field and air pressure (Tang, 2018), sediment dynamics were most influenced by wave-current coupling (Yu, 2020), and the

near-bottom sediment resuspension process in the tidal area was mainly influenced by turbulence and waves (Li et al., 2022a).

In this study, the macro-tidal of HZB was selected to investigate suspended sediment dynamics under wave-current interactions during calm and extreme weather conditions. A three-dimensional wave-current-sediment coupling model was used and calibrated to study the multi-temporal scale hydrodynamic and physical sediment characteristics, focusing on determining the relative contribution and role of each wave-current coupling mechanism to the suspended sediment dynamics. The methodology is described in Section 2. The results are described in Section 3, and the mechanisms are discussed in Section 4. Section 5 summarizes the conclusions of this study.

2 Methodology

2.1 Wave-current coupling hydrodynamic model

The hydrodynamic model is based on the finite-volume coastal ocean model (FVCOM) (Chen et al., 2006) and coupled with the wave interaction process proposed by Mellor et al. (2008). The model uses unstructured triangular grid coordinates in the horizontal direction and sigma coordinates in the vertical direction. The model uses the finite volume method, which combines the advantages of a finite-element method for geometric flexibility and a finite-difference method for simple discrete computation. Dry and wet grid treatment method was used to determine the dry and wet states of the tidal flats. The vertical direction of the model uses sigma coordinates, as follows:

$$\varsigma = \frac{z-\xi}{D} \tag{1}$$

where z is the Cartesian vertical coordinate (positive upward), ξ is the free water surface, D is the total water depth, and ς is -1 and 0 at the seabed and surface, respectively.

In sigma coordinates, the continuity and momentum equations in the horizontal direction are

$$\frac{\partial \xi}{\partial t} + \frac{\partial uD}{\partial x} + \frac{\partial vD}{\partial y} + \frac{\partial \omega}{\partial \varsigma} = 0 \tag{2}$$

$$\frac{\partial uD}{\partial t} + \frac{\partial u^2 D}{\partial x} + \frac{\partial uvD}{\partial y} + \frac{\partial u\omega}{\partial \varsigma} - fvD = -gD\frac{\partial \xi}{\partial x} - \frac{gD}{\rho_0}\left[\frac{\partial}{\partial x}\left(D\int_{\varsigma}\rho d\varsigma'\right) + \zeta\rho\frac{\partial D}{\partial x}\right] + DF_u + \frac{1}{D}\frac{\partial\left(\tau_{tx}+\tau_{px}\right)}{\partial \varsigma} + R_x \tag{3}$$

$$\frac{\partial vD}{\partial t} + \frac{\partial uvD}{\partial x} + \frac{\partial v^2 D}{\partial y} + \frac{\partial v\omega}{\partial \varsigma} + fuD = -gD\frac{\partial \xi}{\partial y} - \frac{gD}{\rho_0}\left[\frac{\partial}{\partial y}\left(D\int_{\varsigma}\rho d\varsigma'\right) + \zeta\rho\frac{\partial D}{\partial y}\right] + DF_v + \frac{1}{D}\frac{\partial\left(\tau_{ty}+\tau_{py}\right)}{\partial \varsigma} + R_y \tag{4}$$

where x and y are the eastward and northward components of the coordinates, respectively, u and v are the velocity components in the x and y directions, respectively, ω is the vertical velocity, ρ is the density of the water column, f *is* the Coriolis parameter, g is the gravitational acceleration, and F_u and F_v are horizontal momentum diffusion terms. τ_{tx} and τ_{ty} are the components of the viscous part of the wind-stress turbulence. The model employs the Smagorinsky turbulence closure scheme (Smagorinsky, 1963) and the Mellor-Yamada level 2.5 turbulence closure scheme (Mellor and Yamada, 1982).

The form drag (τ_{px}, τ_{py}) and wave radiation stress (R_x, R_y) because of wave action are calculated as follows:

$$\begin{cases} \tau_{px} = \dfrac{\cosh\left[2kD\left(1+\varsigma\right)\right]}{2\pi\sinh\left(2kD\right)}\displaystyle\int_0^{2\pi} P_{w_0}\sin\phi\frac{\partial a\cos\phi}{\partial x}d\theta \\ \tau_{py} = \dfrac{\cosh\left[2kD\left(1+\varsigma\right)\right]}{2\pi\sinh\left(2kD\right)}\displaystyle\int_0^{2\pi} P_{w_0}\sin\phi\frac{\partial a\cos\phi}{\partial y}d\theta \end{cases} \tag{5}$$

$$\begin{cases} R_x = -D\left[\dfrac{\partial S_{xx}}{\partial x}+\dfrac{\partial S_{xy}}{\partial y}\right] + \varsigma\left[\dfrac{\partial D}{\partial x}\dfrac{\partial S_{xx}}{\partial \varsigma}+\dfrac{\partial D}{\partial y}\dfrac{\partial S_{xy}}{\partial \varsigma}\right] \\ R_y = -D\left[\dfrac{\partial S_{yx}}{\partial x}+\dfrac{\partial S_{yy}}{\partial y}\right] + \varsigma\left[\dfrac{\partial D}{\partial x}\dfrac{\partial S_{yx}}{\partial \varsigma}+\dfrac{\partial D}{\partial y}\dfrac{\partial S_{yy}}{\partial \varsigma}\right] \end{cases} \tag{6}$$

$$\begin{cases} S_{xx} = E_T\dfrac{k\{\cosh\left[2kD\left(1+\varsigma\right)\right]+1\}}{\sinh 2kD}\cos^2\theta - E_T\dfrac{k\{\cosh\left[2kD\left(1+\varsigma\right)\right]+1\}}{\sinh 2kD} + E_D \\ S_{yy} = E_T\dfrac{k\{\cosh\left[2kD\left(1+\varsigma\right)\right]+1\}}{\sinh 2kD}\sin^2\theta - E_T\dfrac{k\{\cosh\left[2kD\left(1+\varsigma\right)\right]+1\}}{\sinh 2kD} + E_D \\ S_{xy} = S_{yx} = E_T\dfrac{k\{\cosh\left[2kD\left(1+\varsigma\right)\right]+1\}}{\sinh 2kD}\sin\theta\cos\theta \end{cases} \tag{7}$$

where a is the amplitude, ϕ is the phase, P_{w_0} is the surface wind pressure, E_T is the total wave energy, E_D is the modified delta function, $E_D = 0$ when ς is not equal to 0, and $\int_{-1}^{0} E_D D d\varsigma = \frac{E_T}{2}$.

The wave energy density $E_\theta = \int_0^\infty E_{\sigma,\theta}d\sigma$ (where θ is the wave direction and σ is the wave frequency) is obtained by solving the wave energy equation as follows:

$$\frac{\partial E_\theta}{\partial t} + \frac{\partial}{\partial x_\alpha}\left[\left(\bar{c}_{g\alpha}+\bar{u}_{A\alpha}\right)E_\theta\right] + \frac{\partial}{\partial\theta}\left(\bar{c}_\theta E_\theta\right) + \int_{-1}^{0}\bar{S}_{\alpha\beta}\frac{\partial U_\alpha}{\partial x_\beta}Dd\varsigma = S_{\theta in} - S_{\theta Sdis} - S_{\theta Bdis} \tag{8}$$

where x_α is the horizontal coordinate, $x_1 = x$, $x_2 = y$ and α and β contain the implicit summation. The first two terms on the left-hand side of Eq. 8 determine the wave energy propagation in time and horizontal space, respectively, the third term is the refraction term, which reflects the change of wave energy propagation direction, the fourth term indicates the energy exchange with the mean velocity energy equation, and $S_{\alpha\beta}$ is the wave radiation stress term. The right side of Eq. 8 represents the wave energy term and wave dissipation term of the surface and bottom layers, respectively. The upper horizontal line represents the spectral average. For example, the spectral average wave group velocity expression is:

$$\bar{c}_{g\alpha} = \frac{\int_0^\infty c_{g\alpha} E_{\sigma,\theta} d\sigma}{\int_0^\infty E_{\sigma,\theta} d\sigma} \tag{9}$$

where $c_{g\alpha}$ is the component of the wave group velocity c_g in the α direction and $u_{A\alpha}$ is the component of the Doppler velocity u_A in the α direction.

$$u_{A\alpha} = kD \int_{-1}^{0} U_\alpha \left\{ \frac{\cosh[2kD(1+\varsigma)]}{\sinh(2kD)} + \frac{\sinh[2kD(1+\varsigma)]}{\sinh^2(kD)} \right\} d\varsigma \tag{10}$$

where k is the wave number, U_α is the component of the current velocity in the α direction plus the component of the Stokes drift velocity in the α direction, and c_θ is the wave energy refraction velocity defined as follows:

$$\begin{aligned} c_\theta = {} & \frac{g}{2c\cosh^2(kD)} \left(\sin\theta \frac{\partial D}{\partial x} - \cos\theta \frac{\partial D}{\partial y} \right) \\ & + \frac{k_\alpha}{k} \left(\sin\theta \frac{\partial u_{A\alpha}}{\partial x} - \cos\theta \frac{\partial u_{A\alpha}}{\partial y} \right) \end{aligned} \tag{11}$$

where c is the phase velocity of wave propagation.

Based on the spinlessness of the wave number, the wave frequency σ_θ at the angle θ can be solved using the following equation:

$$\begin{aligned} \frac{\partial \sigma_\theta}{\partial t} + \left(\bar{c}_{g\alpha} + \bar{u}_{A\alpha} \right) \frac{\partial \sigma_\theta}{\partial x_\alpha} = {} & -\frac{\partial \sigma_\theta}{\partial k} \left(\frac{k_\alpha k_\beta}{k} \frac{\partial \bar{u}_{A\alpha}}{\partial x_\beta} \right) + \frac{\partial \sigma_\theta}{\partial D} \left(\frac{\partial D}{\partial t} \right. \\ & \left. + \bar{u}_{A\alpha} \frac{\partial D}{\partial x_\alpha} \right) + \mathfrak{R} \end{aligned} \tag{12}$$

where $\frac{\partial \sigma_\theta}{\partial k} = \bar{c}_g$, $\frac{\partial \sigma_\theta}{\partial D} = (n-12)\frac{\sigma_\theta}{D}$, $n = 0.5 + \frac{kD}{\sinh 2kD}$. $\mathfrak{R}$ is the additional source term and the wind-driven region ($f_{spr} > 0$) is:

$$\mathfrak{R} = \sigma_p \left(\sigma_p - \sigma_\theta \right) f_{spr}^{0.5} \tag{13}$$

where σ_p is the peak frequency and $f_{spr} = \frac{S_{\theta in}}{\int_{-0.5\pi}^{0.5\pi} S_{\theta in} d\theta}$ is the diffusion function.

Wave-current coupling mainly includes combined wave-current bottom stress, wave dissipation, vertical transfer of wave-generated pressure to the mean momentum equation (also known as form drag), radiation stress, Stokes drift velocity, mean current advection of wave energy, and refraction (Mellor et al., 2008; Mellor, 2015). Wave-current coupling has received extensive domestic and international research, but almost all the studies have focused on only one or several wave-current coupling terms rather than their combined effects (Gao et al., 2018). Most studies use one-way coupling between the current and wave modules because two-way coupling has low computational efficiency. Taking POM as an example, coupling the SWAN model requires 86 times more computational time (Mellor et al., 2008). Therefore, Mellor et al. (2008) developed a more computationally efficient wave model (Mellor-Donelan-Oey wave model) (shoni2. princeton.edu/ftp/glm/). The model parameterizes the spectrum shape and treats wave energy as a function of wave propagation direction, horizontal coordinates, and time. In addition, wave frequency depends on the direction and is not an independent variable. Compared with the third-generation wave model, this model is relatively simple, with higher computational efficiency and better accuracy (Sheng and Liu, 2011).

2.2 Estuarine sediment model

The sediment model considers water-sediment density coupling, flocculation-sedimentation process, and fluid mud bottom boundary layer properties (Wang, 2002; Li et al., 2017; Li et al., 2018; Ye et al., 2019). Suspended sediment is calculated using the following concentration dispersion equation (Warner et al., 2008):

$$\begin{aligned} & \frac{\partial C}{\partial t} + \frac{\partial (uC)}{\partial x} + \frac{\partial (vC)}{\partial y} + \frac{\partial [(w - w_s)C]}{\partial z} \\ & = \frac{\partial}{\partial x} \left(A_H \frac{\partial C}{\partial x} \right) + \frac{\partial}{\partial y} \left(A_H \frac{\partial C}{\partial y} \right) + \frac{\partial}{\partial z} \left(K_h \frac{\partial C}{\partial z} \right) \end{aligned} \tag{14}$$

where C and w are the SSC and sink velocity, respectively and A_H and K_h are the horizontal and vertical vortex viscosity coefficients, respectively.

The model surface and bottom suspended sediment flux boundary conditions are defined separately as follows:

$$\begin{cases} K_h \dfrac{\partial C}{\partial z} = 0, \; z = \xi \\ K_h \dfrac{\partial C}{\partial z} = E - D, \; z = -H \end{cases} \tag{15}$$

where E is the sediment resuspension flux, $D = C_b w_b$ is the bottommost sediment deposition flux, C_b is the bottommost SSC, w_b is the bottommost suspended sediment sink rate, and H is the height of the seafloor to mean sea level.

The sediment resuspension flux, E, was calculated according to Van Prooijen and Winterwerp (2010):

$$\begin{cases} 0 & \tau_b < 0.52\tau_{ce} \\ E_0(1-P_b)\left[-0.144\left(\frac{\tau_b}{\tau_{ce}}\right)^3 + 0.904\left(\frac{\tau_b}{\tau_{ce}}\right)^2 - 0.823\frac{\tau_b}{\tau_{ce}} + 0.204 \right] & 0.52\tau_{ce} < \tau_b \le 1.70\tau_{ce} \\ E_0(1-P_b)\left(\frac{\tau_b}{\tau_{ce}} - 1\right) & \tau_b > 1.70\tau_{ce} \end{cases} \tag{16}$$

where E_0 is the sediment erosion rate, P_b is the porosity, τ_b is the bottom bed shear stress, the maximum instantaneous

value under wave-flow coupling is the vector sum of the time-averaged flow shear stress τ_c, and the maximum wave shear stress τ_{wm}; τ_{ce} is the critical starting stress of the sediment. When E is greater than D, the bottom bed erodes and the total thickness decreases. When E *is* less than D, the bottom bed is deposited, and the total thickness increases.

The model allows SSC to affect water density, and therefore, water circulation, based on the high turbidity of HZB. Winterwerp (2001) calculated seawater density ρ when considering the contribution of suspended sediment through a volumetric relationship.

$$\rho = \rho_w + \left(1 - \frac{\rho_w}{\rho_s}\right)C \tag{17}$$

where ρ_w is the density of seawater when water-sand density coupling is not considered and ρ_s is the sediment density.

Shi (2001) analyzed the sediment data of HZB and found that the near-bottom sediment had a stratified structure of a low-concentration suspended sediment layer, high-concentration suspended sediment layer, and fluid mud layer, in order from top to bottom. The rheological and consolidation characteristics of the fluid mud layer significantly influence the bottom boundary layer. The flux Richardson number R_f in the turbulence closure equation is introduced into the bottom friction coefficient C_d calculation equation to generalize the effect of the fluid mud layer on the bottom boundary layer (Wang, 2002; Wang et al., 2005):

$$C_d = \frac{\kappa^2}{\left(1 + AR_f\right)^2\left[\ln\left(\frac{h}{z_0}+1\right) - 1\right]^2} \tag{18}$$

where A = 5.5 is the empirical coefficient, κ is the Karmen constant, h is the water depth, and z_0 is the bottom roughness height; R_f is given by

$$R_f = -\frac{g}{\rho}\frac{\partial\rho}{\partial z}\frac{K_h}{K_m\left[(\partial u/\partial z)^2 + (\partial v/\partial z)^2\right]} \tag{19}$$

where K_m is the vertical eddy viscosity coefficient.

The sediments in HZB waters are dominated by fine-grained and clayey silt (Pang et al., 2015; Chen et al., 2018), which are highly susceptible to flocculation in a high turbidity water environment (Tang, 2007). The physical properties of sediment particles, such as particle size, density, and sink rate, change with flocculation. The model is based on the sediment flocculation method proposed by Cao and Wang (1994):

$$w_s = w_{s0}\frac{1 + c_2 C^{m_2}}{1 + c_1 u^{m_1}} \times k_s \tag{20}$$

where w_{s0} is the settling velocity of a single sediment particle calculated using Stokes' sink velocity formula, u is the current velocity, and k_s, c_1, c_2, m_1 and m_2 are empirical parameters.

Wind field data are particularly important during typhoons. To obtain more accurate wind fields, the rotational and moving wind fields of Typhoon Mitag were superimposed with the National Centers for Environmental Prediction (NCEP) wind field to reconstruct wind data. The Holland-Miyazaki model performed well and was used to reconstruct the wind field data in this study (Miyazaki et al., 1962; Holland, 1980; Ren, 2022).

2.3 Model configurations

The model domain encompassed a large area to ensure model stability during typhoons (Figure 1). The grid had 107,898 cells and 57,354 nodes. The resolution at the ocean open boundary was approximately 30 km and was refined to 150–800 m to fit the complex coastlines and bathymetry inside the bay. The grid resolution was higher than 100 m in the southern tidal flat of HZB. Eleven vertical layers are employed in the vertical direction (ζ = 0.0, −0.02, −0.08, −0.18, −0.32, −0.5, −0.68, −0.82, −0.92, −0.98, and −1.0). The model was calculated with a time step of 0.5 s for the outer mode and 5 s for the inner mode. Dry and wet module calculations were initiated with a critical minimum water depth of 0.05 m. The shoreline data of the model were obtained from the data provided by the National Oceanic and Atmospheric Administration (NOAA) (https://ngdc.noaa.gov). The shoreline data for Hangzhou Bay were corrected using 2019 annual Landsat satellite maps (http://www.gscloud.cn). The bathymetry data used were ETOP1 and were provided by NOAA. Topographic data with a resolution of $1' \times 1'$ were supplemented by high-resolution measured data and nautical chart data for key study areas.

The model's time period was from 20 February to 31 March 2013 (calm weather condition), and from 20 September to 15 October 2019 (Typhoon Mitag). The first 6 days were used for spin-up, and the subsequent results were used for the analysis. The model was cold-started, with initial tide level, current velocity, and SSC set to 0, and temperature and salinity set to 18°C and 27 psu, respectively (Chen et al., 2017). The model was driven by tides, runoff, and wind. The time series of tidal levels generated by the TPXO7.2 global tidal model was used at the ocean open boundary. The hourly tidal levels consisted of four diurnal tides (K_1, O_1, P_1, and Q_1), four semi-diurnal tides (M_2, S_2, N_2, and K_2), three shallow-water tides (M_4, MS_4, and MN_4), and two long-period tides (M_f and M_m). HZB is influenced by the Changjiang and Qianjiang rivers (Shou et al., 2009), and therefore, the model includes the effects of these two rivers. River discharge and sediment load data were obtained from the 2019 China River Sediment Bulletin (http://www.mwr. gov. cn/sj). The wind data under calm weather were at 10 m above sea level obtained from NCEP (https://rda.ucar.edu/datasets/ds084.1) with a temporal resolution of 6 h and a spatial resolution of approximately 0.2°. The Holland-Miyazaki method was used to re-construct the wind field data in this study (Li et al., 2022b). After sensitivity analysis (Ye, 2019), the main parameters of the model are shown in Table 1.

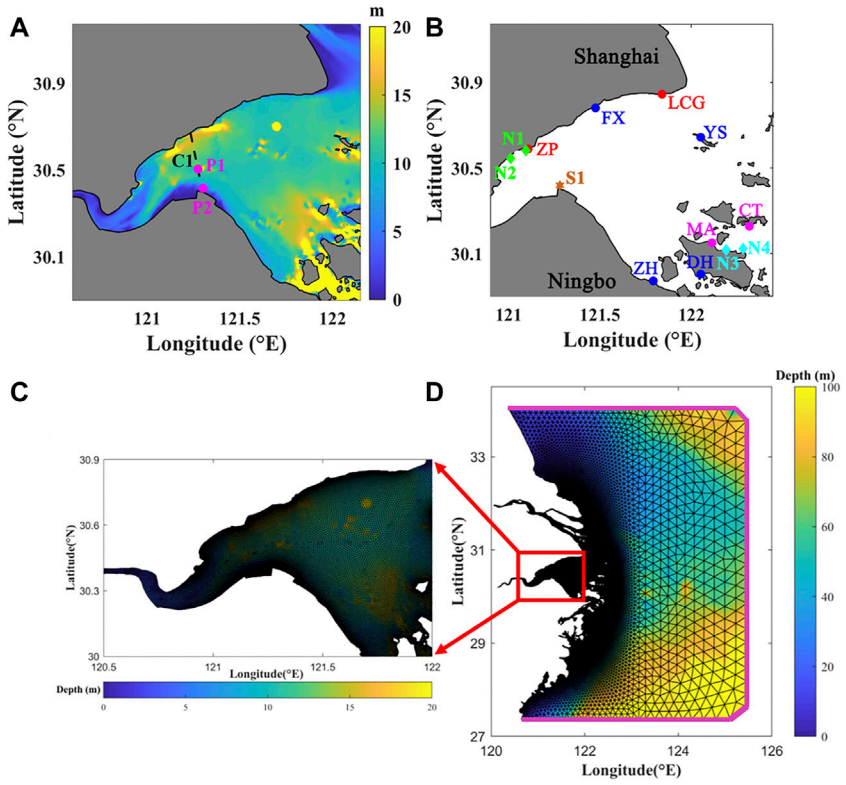

FIGURE 1
(A) Map of Hangzhou Bay. The color indicates water depth. **(B)** Field stations. LCG is Luchaogang, ZP is Zhapu, GP is Ganpu, MA is Maao, CT is Changtu, FX is Fengxian, YS is Yangshan, ZH is Zhenhai, and DH is Dinghai. Circles indicate tidal stations and diamonds indicate current and SSC stations. **(C)** Grids of Hangzhou Bay. **(D)** Grids of study area. Pink lines represent the oceanic boundaries.

TABLE 1 Main parameters of the model.

Model parameters	Parameter value
Number of nodes, meshes, sigma layers	57354, 107898, 11
Median sediment particle size	0.008 mm
Sediment porosity	0.5
Initial sub-bed layers and thickness	Four layers, 1 m per layer
Parameters of the sink velocity equation (Eq. 19): k_s, c_1, c_2, m_1, and m_2	1.30, 0.06, 4.60, 0.75, 0.90
Submarine roughness height	0.005–0.5 mm
Critical starting stress	0.1 N/m^2
Sediment erosion rate	0.00005–0.0006 kg/m/s^2

2.4 Numerical tests

The wave-current interaction mainly includes combined wave-current bottom stress, wave dissipation, form drag, radiation stress, Stokes drift velocity, mean current advection of wave energy, and refraction (Mellor et al., 2008; Mellor, 2015; Gao et al., 2018). To quantify the effects of the wave-current coupling mechanism on the characteristics of suspended sediment during calm weather and Typhoon Mitag, seven numerical conditions were designed to evaluate the contribution of different wave-current coupling terms (Table 2).

Test 1 was the reference model, which included all wave-current coupling effects. In Test 2, the combined wave-current bottom stress was replaced by the current-induced bottom stress, and the effect of wave-current bottom stress was removed. In Tests 3–7, the effects of wave dissipation, form drag, radiation stress, mean current advection of wave energy, and refraction terms were removed from the model. Separating the Stokes drift velocity from the current velocity at the equation level is difficult and unnecessary (Mellor, 2005). Therefore, the contribution of Stokes drift velocity is not discussed in this study.

Station P2 is located at the edge of the shallow shore of HZB, close to observation point S1, and is subject to significant wave-current interactions. Station P2 is used to illustrate the effects of wave-current coupling on suspended sediment dynamics during calm weather and during Typhoon Mitag. This paper will focus on the analysis of calm weather (three tidal cycles) and Typhoon Mitag (three tidal cycles) in Section 4. Under calm weather

TABLE 2 Numerical experiments.

Tests	Descriptions
Test 1	Control conditions including all wave interactions
Test 2	The combined wave-current bottom stress in Test 1 is changed to only current-induced bottom stress
Test 3	Removal of wave dissipation in Test 1
Test 4	Removal of form drag in Test 1 (Eq. 5)
Test 5	Removal of radiation stress in Test 1 (Eq. 6)
Test 6	Removal of mean current advection of wave energy in Test 1 (second term on the left side of Eq. 8)
Test 7	Removal of mean current refraction of wave energy in Test 1 (third term on the left side of Eq. 8)

conditions, the waves inside HZB were generally weak. However, during the typhoon, typhoon waves could propagate from the East China Sea into Hangzhou Bay, accompanied by a significant increase in both the significant wave height and wave orbital velocity within HZB.

2.5 Model validation

2.5.1 Calm weather

To ensure the accuracy and reliability of the established three-dimensional wave-current-sediment coupled model in HZB, the results were validated from multiple spatial and temporal perspectives using actual measurement data. The correlation coefficient (*CC*) and model evaluation coefficient (*SS*) were introduced to quantify the validation results (Murphy, 1992):

$$CC = \frac{1}{N}\sum_{i=1}^{N}\frac{(m_i - \bar{m})(o_i - \bar{o})}{S_m S_o} \tag{21}$$

$$SS = 1 - \frac{\sum_{i=1}^{N}(m_i - o_i)^2}{\sum_{i=1}^{N}(o_i - \bar{o})^2} \tag{22}$$

where m_i and o_i are the calculated and measured values of the model, respectively, $\bar{m}$ and $\bar{o}$ are the averages of the calculated and measured values of the model, respectively, S_m and S_o are the standard deviations of the calculated and measured values of the model, respectively, and *CC* is a parameter to study the degree of linear correlation between the variables. The closer it is to 1, the greater the correlation between the calculated and measured values, and the more accurate the model. When SS is greater than 0.50–0.65, the model is highly reliable. When it is less than 0.50–0.65, the model is less reliable (Allen et al., 2007).

The hydrodynamics model was validated from multiple spatial and temporal perspectives under calm weather conditions based on measured data from 2010, 2013, and 2014 (Figure 2A). The *CC* values for the four tidal elevation stations were 0.98, 0.98, 0.97, and 0.98, respectively. The *SS* values were 0.94, 0.94, 0.94, and 0.98, respectively. The current velocity and direction were verified using field data at stations N1–N4 during the neap and spring tides (Figure 2B). The average *CC* values at the four stations were 0.93, 0.94, 0.90, and 0.94, and the average *SS* values were 0.92, 0.91, 0.84, and 0.93, respectively. The average *CC* values for the current direction were 0.92, 0.91, 0.93, and 0.94, and the average SS values for the current direction were 0.90, 0.88, 0.93, and 0.92, respectively.

The harmonic constants of the M_2, S_2, K_1, O_1, M_4, and MS_4 tidal components (Pawlowicz et al., 2002) from September 2010 (An, 2016) were also validated (Ren, 2022). The absolute values of the amplitude differences of the M_2, S_2, K_1, O_1, M_4, and MS_4 were 0.02, 0.03, 0.03, 0.03, 0.02, and 0.01 m, respectively. The absolute values of the phase differences were 9.2°, 9.9°, 10.8°, 14.5°, 10.3°, and 11.8°, respectively.

The sediment model was validated based on measured vertical SSC data from the N1 and N2 stations in Zhapu (Figure 2C). The average *CC* values were 0.55 and 0.49, respectively, and the average SS values were 0.47 and 0.45, respectively.

2.5.2 Typhoon Mitag

The model was validated during Typhoon Mitag using water levels, current velocity, and significant wave heights (Figure 3). The simulated significant wave height was lower than the measured value, with a *CC* value of 0.93 and an SS value of 0.86. The CC values of current velocity and direction were 0.79 and 0.66, and SS values were 0.63 and 0.39, respectively. The simulated results of SSC were similar to the measured values, with a *CC* value of 0.70 and an *SS* value of 0.47. The validation of the significant wave heights had a *CC* value of 0.95 and an *SS* value of 0.91 (Figure 3F). The model was also validated using sea surface level, current, and significant wave height data during Typhoon Chan-hom at the bay mouth (Yangshan Harbour) (He et al., 2020; Yu, 2020).

3 Results

3.1 Asymmetric sediment dynamics during calm weather

The distribution of SSC in the HZB changes periodically with the tidal cycle (Figure 4A). During the spring tides, the shallow water of the southern shore is well mixed, and the SSC in the

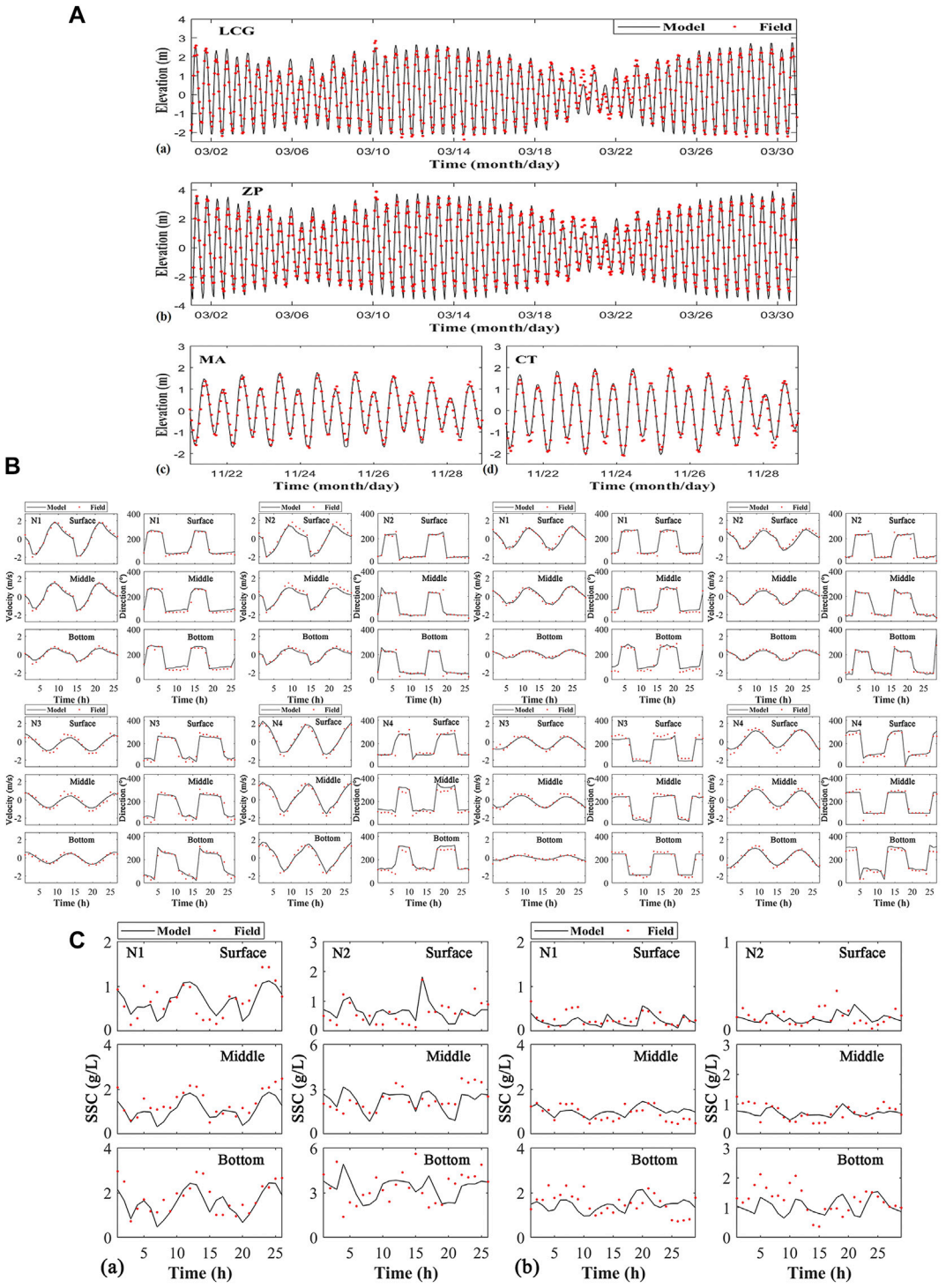

FIGURE 2
Model validation of **(A)** sea surface level (a,b) 2013, (c,b) 2014; **(B)** currents during spring tides and neap tides, N1 N2 were measured in 2013 and N3 N4 were measured in 2014; **(C)** SSC (a) spring tides and (b) neap tides in 2013.

surface and bottom layers are both at a high level. The SSC near the bottom layer exceeds 6 kg/m^3 during the flood tides. The surface SSC on the northern side of HZB is relatively low. SSC gradually decreases with decreased current velocity during high water and low water. The significant reduction in hydrodynamic forces during neap tides causes a decrease in sediment

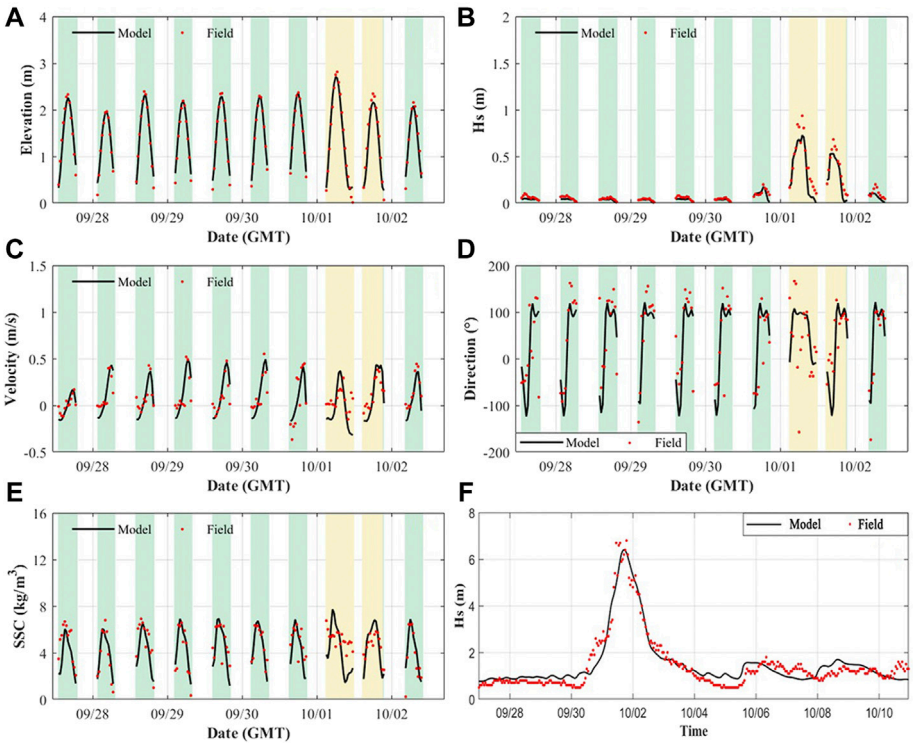

FIGURE 3
Model validation of sea surface level, currents, significant wave height, and SSC. **(A–E)** Station S1 in the Andong Shoal **(F)** near Zhoushan Islands. The green background represents the probes were underwater, and the yellow background represents that the speeds of local wind were larger than 10 m/s.

resuspension, and both the surface and bottom SSC are smaller than those during spring tides.

The tidal averaged sediment fluxes near the surface and bottom layers of HZB in 1 month are shown in Figure 4B. The net sediment flux at the head and mouth of the bay are large (approximately 0.5 kg/m/s^2) because of the large residual flow and high SSC (Figure 4A). The surface sediment flux is mostly smaller than that near the bottom level. Suspended sediment moves into the bay along the northern coast and out of the bay along the southern coast.

The net sediment transport near the Andong (AD) tidal flat (C1 section) is northward near the surface and southward near the bottom. Near the AD tidal flat (Figure 5), during the spring tides, the maximum value of the along-estuarine suspended sediment flux during the flood tide is close to 4 kg/m^2/s. Laterally, the peak sediment flux (0.8 kg/m^2/s) occurs near the bottom layer of the northern bank (Figure 5). This is because the SSC in the near-bottom layer is higher (Figure 4A). The maximum value of the along-estuarine sediment flux during the ebb tide is similar to that during the flood tide, except that the value is smaller (more than 2 kg/m^2/s). The maximum value of lateral suspended sediment flux is located in the bottom layer near the southern bank, which is approximately 0.7 kg/m/s^2. During neap tides, as the current velocity and SSC decrease, the characteristics of the along-estuarine and lateral suspended sediment fluxes are similar to those during spring tides, but the magnitudes are smaller.

Figures 5E,J show the along-estuarine and lateral sediment fluxes averaged over 1 month. The along-estuarine sediment fluxes indicate an alternative pattern of seaward and landward directions. Near the tidal flats and in the middle part of the tidal channel, net sediment fluxes are mainly seaward. Near the northern bank and approximately 20–25 km from the northern bank, sediment fluxes are mainly landward. Lateral net sediment fluxes are northward near the surface layer and southward near the bottom.

3.2 Asymmetric sediment dynamics during Typhoon Mitag

Figures 6A,B show the distributions of the surface and bottom SSC during Typhoon Mitag. During the typhoon, the wave height and wave orbital velocity in HZB gradually increase from the bay mouth to the bay head. The increased bottom stress leads to increased SSC. The tidal effect is stronger at the time of

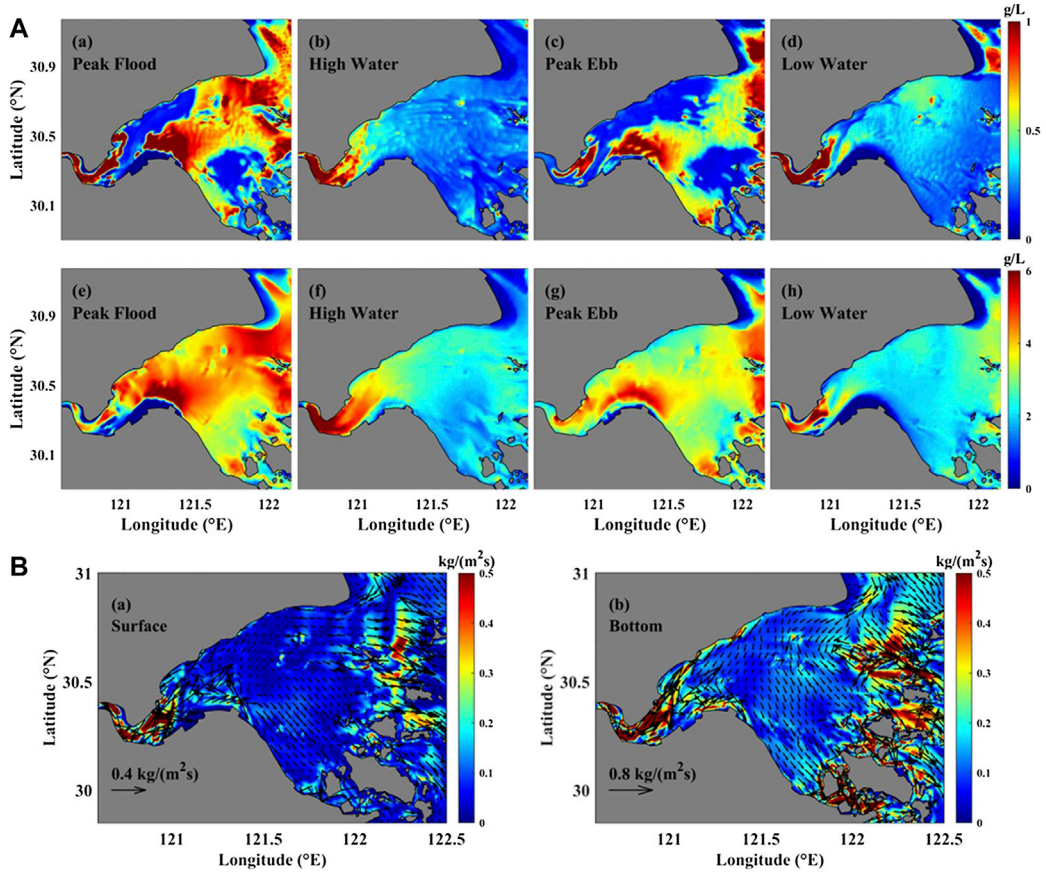

FIGURE 4
(A) Surface (a–d) and bottom (e–h) SSC during spring tides. **(B)** Cumulative (a) surface and (b) bottom net suspended sediment fluxes in 1 month (1–30 March 2013, GMT).

peak floods and peak ebbs, and the combined effect of currents and waves causes a higher SSC. In shallow water areas near the southern shore of the bay, the combined effect of the current-wave induces strong mixing, and the surface and bottom SSC values are large, with the maximum bottom SSC exceeding 6 kg/m^3. The high-turbidity area gradually expands to the northern bank and the head of the bay, and the maximum bottom SSC at the top of the bay during the storm exceeds 8 kg/m^3. The bottom SSC is less affected by the storm near the northern bank because of the presence of deep water, and the increase is less than 0.8 kg/m^3 (Figures 6B,D).

Typhoon Mitag strengthens the asymmetry of the flow field characteristics, and the surface currents are mainly controlled by winds (Figures 6E–H). The surface currents are enhanced by the typhoon (by ~0.2 m/s) during the flood tide (GMT 10-3–3:00) and are weakened during the typhoon departure period (GMT 10-1-15:00–18:00), depending on the directions of the tidal currents and winds. The surface currents increase because of the southward rotating wind field in the bay, moving mainly towards the south coast at the peak wind moment (GMT 10-1-12:00). The increased bottom currents are similar to, but smaller than, the increased surface currents.

The average along-estuarine and lateral suspended sediment fluxes during flood and ebb tides during the storm were studied in Section C1 (Figure 7). During flood tides, the average SSC in the near-bottom layer is approximately 4 kg/m^3 at 10–30 km from the northern bank, and the relative increase is more than 0.4 kg/m^3. The average suspended sediment flux in the landward direction is more than 4 kg/(m^{2}s), and the relative increase compared to the tidal drive is more than 1 kg/(m^{2}s). The northward and southward net suspended sediment fluxes near the surface level along the northern bank are enhanced by the typhoon, with an increase of more than 40%. During ebb tides, SSC and sediment fluxes are significantly weaker than during flood tides, and the average SSC near the bottom layer is approximately 3 kg/m^3. The suspended sediment moves out of the bay through two channels near the southern and northern bank (LS and LN in Figure 1), and the flux increases by more than 0.5 kg/(m^{2}s). Laterally, the southward net suspended sediment flux in the near-surface layer increases by approximately 0.4 kg/

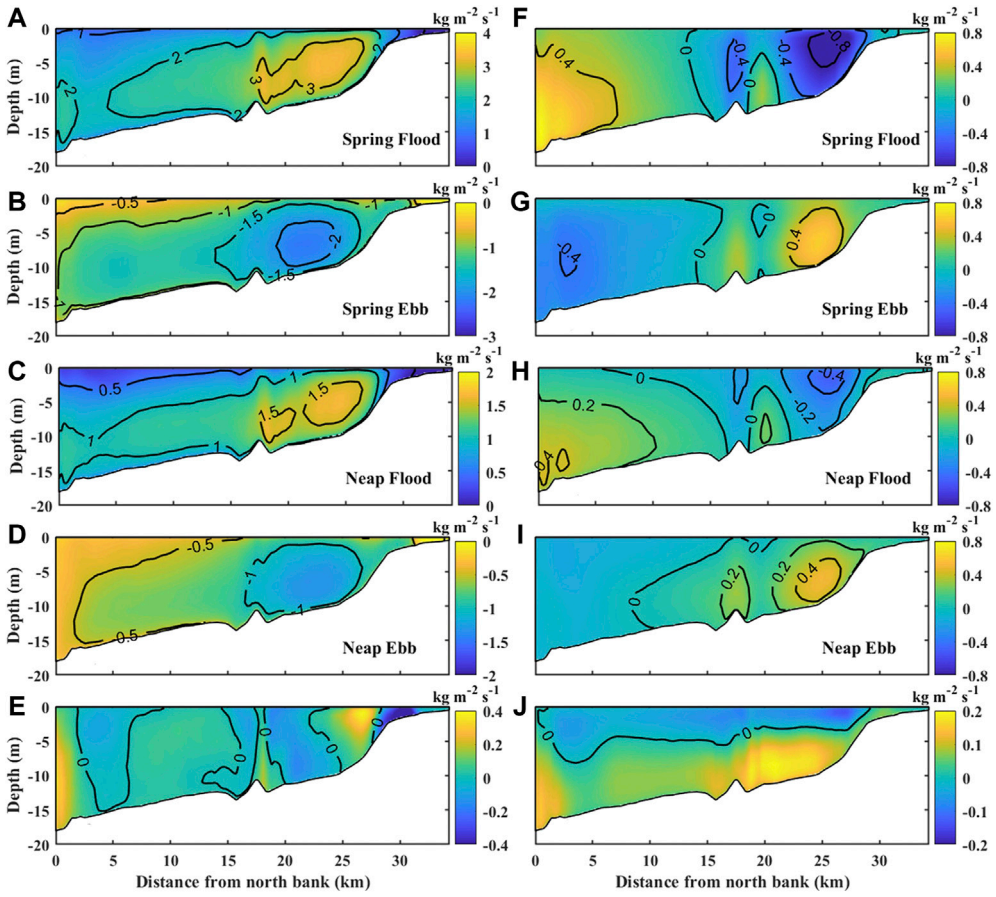

FIGURE 5
The distribution of sediment flux in the C1 section during the spring-flood tide **(A)** along-estuarine and **(F)** lateral. **(B,G)**, **(C,H)**, **(D,I)** are the same as **(A,F)**, and the times are for spring-ebb tide, neap-flood tide, and neap-ebb tide, respectively. **(E,J)** are the averaged along-estuarine and lateral sediment fluxes in 1 month, respectively. Positive values indicate landward or southern direction.

(m^2s), and the northward net suspended sediment flux in the near-bottom layer near the northern bank increases by approximately 0.2 kg/(m^2s).

Lateral sediment flux (Figures 7D,F) is reversed during Typhoon Mitag, with southward surface sediment flux and northward bottom sediment flux compared with that during calm weather (Figures 5F,G).

3.3 Mechanism of lateral circulation and sediment fluxes

3.3.1 Calm weather

During calm weather conditions (Ren, 2022), the lateral circulation at section C1 is towards the northern/southern bank at the surface/bottom layer (Figure 8A). Based on the analysis of the lateral circulation mechanism (Figure 9) (Kalkwijk and Booij, 1986; Xiao et al., 2019; Ren, 2022), convection, centrifugal force, and friction dominate lateral circulation. Convection and centrifugal force are of equal strength and in opposite directions in the surface and bottom layers. The friction effect is stronger in the bottom layer. Combined with the characteristics of high SSC in the bottom layer and low SSC in the surface layer (Figure 4), the net flux of sediment shows southward characteristics in the bottom layer and northward characteristics in the surface layer. The net sediment fluxes are towards the southern shoal.

3.3.2 Typhoon Mitag

The moments with peak surges during flooding (GMT 10-1-1: 00–6:00) and ebbing (GMT 10-1-19:00–10-2-2:00) tides are selected to illustrate the along-estuarine and lateral currents during typhoons at AD (section C1, Figures 8Ba–d,a'–d'). During flood tides, the along-estuarine currents in the northern tidal channel is approximately 1.5 m/s. The increase of velocity exceeds 0.2 m/s, with a larger increase occurring near the southern bank. Lateral currents are southward in the surface level near the northern bank

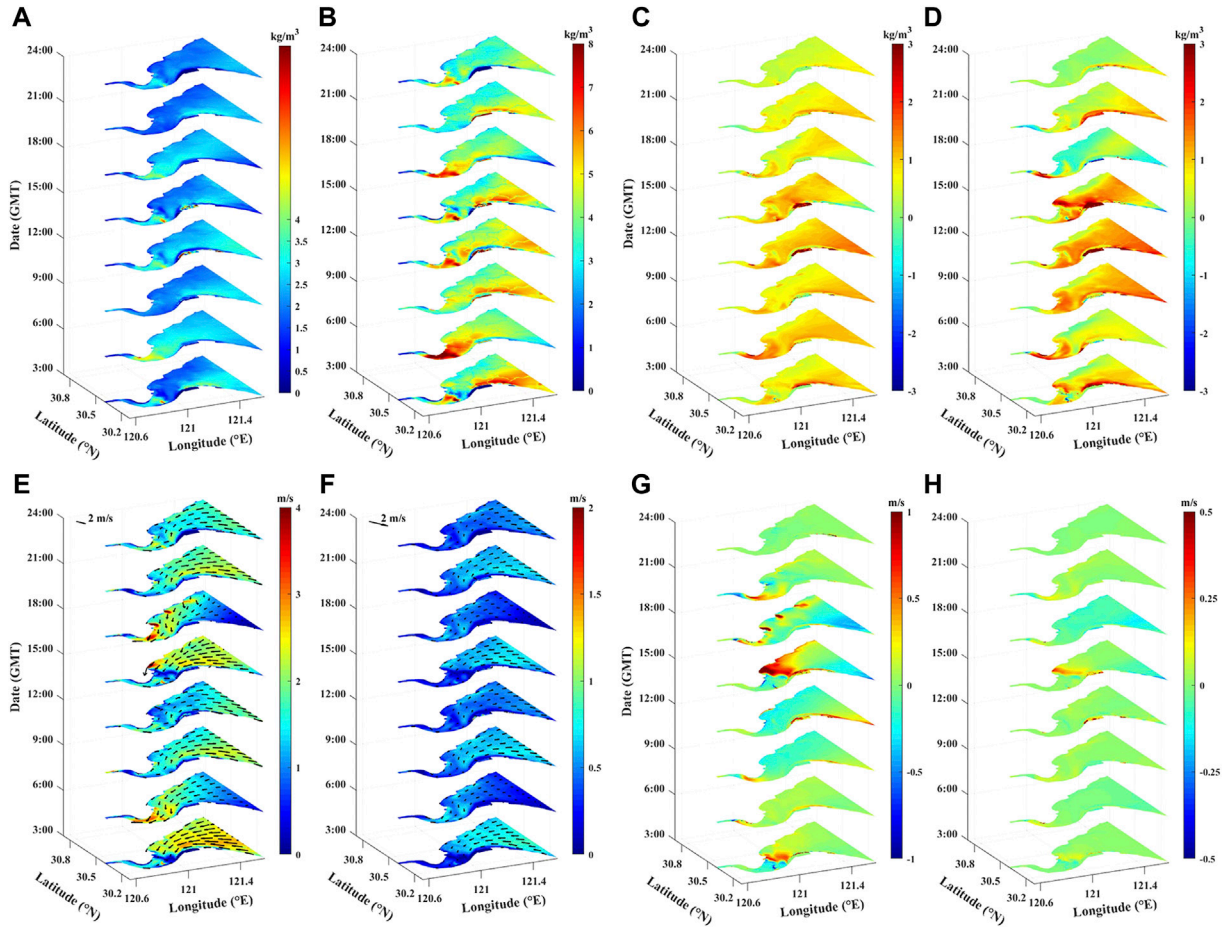

FIGURE 6
Distribution of SSC. **(A)** Surface layer and **(B)** bottom layer. **(C,D)** are the same as **(A,B)** except for difference in SSC between the test with Typhoon Mitag and the test with only tidal forcing (GMT 1 October 2019, 3:00–24:00). **(E–H)** are the same as **(A–D)** except for currents.

and northward in the bottom level near the northern bank, and velocity exceeds 0.4 m/s (with an increase of less than 0.2 m/s during the typhoon). During ebb tides, waters flow out of the bay through the two tidal channels, with a vertical-averaged along-estuarine current speed of approximately 1–1.5 m/s, which is slightly higher than that during calm weather. The lateral current was southward near the surface level near the southern bank and northward near the bottom level near the northern bank. The magnitude of the southward current is increased by 0.2 m/s.

During the typhoon, the friction term dominated lateral circulation (Figures 10E,F), and changed the lateral circulation direction at section C1. The strong wave and current interaction impacts wave dissipation, form drag and advection, and changes the vertical profile of eddy viscosity (K_m). Subsequently, the friction term was affected. During flood tides, the friction term was enhanced by the typhoon by 90% near the bottom level (Figure 10E), while it was reduced by 86% near the bottom level during ebb tides (Figure 10F). During ebb tides, the effect of the friction term occurs southward near the surface and northward near the bottom level.

Lateral circulation in the curvature was enhanced during Typhoon Mitag, and sediment flux was subsequently changed, controlled by the friction term and vertical profile of SSC.

4 Discussion

Wave-current coupling is critical to estuarine hydrodynamics and sediment processes, especially during storms (Graber et al., 1989; Dufois et al., 2014) and is an important research element in marine engineering and coastal dynamic geomorphology. Waves contribute substantially to sediment dynamics during typhoons in HZB, but have a small effect during calm weather conditions. Typhoon Mitag was used as an example to study the effect of wave-current interactions on sediment dynamics during extreme weather conditions.

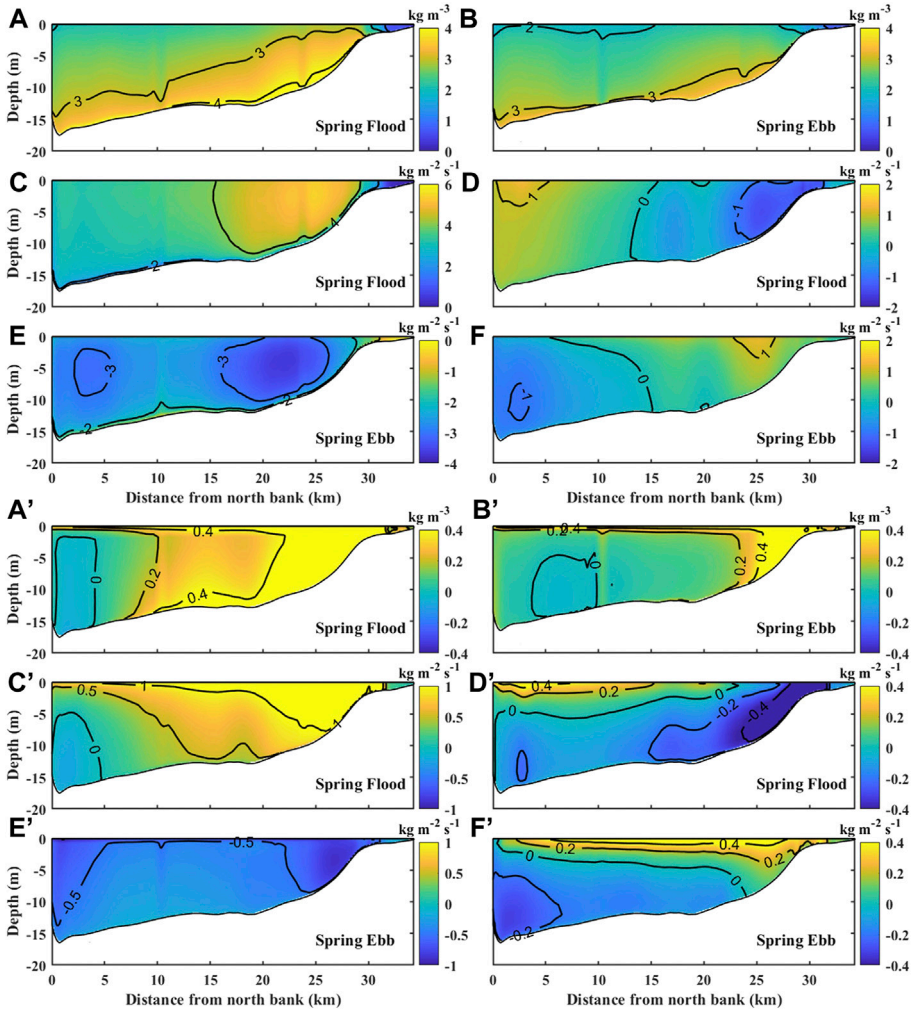

FIGURE 7
SSC at section C1 during spring **(A)** flood tide and **(B)** ebb tide. Along-estuarine and lateral sediment fluxes in section C1 **(C,D)** during spring-flood tide. **(E,F)** are the same as **(C,D)** except for the spring-ebb tide. Positive values indicate landward or southward direction. Difference of SSC at section C1 during spring flood **(A')** and ebb **(B')** tides between the test with Typhoon Mitag and the test with only tidal forcing. Difference of sediment flux at section C1 during spring-flood tides between the test with Typhoon Mitag and the test with only tidal forcing: **(C')** along-estuarine and **(D')** lateral. **(E',F')** are the same as **(C',D')** except for the spring ebb tide.

4.1 Tide-surge interaction

During typhoons, the strong tides in Hangzhou Bay interact nonlinearly with surges:

$$\eta_N = \eta_{T+S} - \eta_T - \eta_S \tag{23}$$

where η_T is astronomical tidal level (only tidal forcing), η_S is the water level during storms (only wind forcing); η_{T+S} is the total water level; η_N is the water level owing to the nonlinear interaction of tides and surges.

Figures 11A–E shows the trends of total water level, total surge, storm surge, nonlinear surge and significant wave height in Hangzhou Bay during thw Typhoon Mitag. The typhoon occurred during spring tides in the bay. At 18:00 (GMT), the significant wave height at the mouth and the middle of the bay exceeded 2 m (Figure 11E). The total water level showed semi-diurnal tides frequency variation and peaked (over 3 m) at 06:00 (GMT) on 1 October (Figure 11A). The surge occurred at the mouth of Hangzhou Bay and then propagated upstream to the bay head (Figure 11B). Owing to the effect of funnel-shaped geomorphology, the peak of surge gradually increased from the bay mouth towards the bay head. The trend of the non-linear surge was similar to that of the total surge (Figure 11D), with a gradual increase from the mouth to the top of the bay. The peak of non-linear surge occurred later than the peak of total surge (Figure 11C), corresponding to a period of greater total water level.

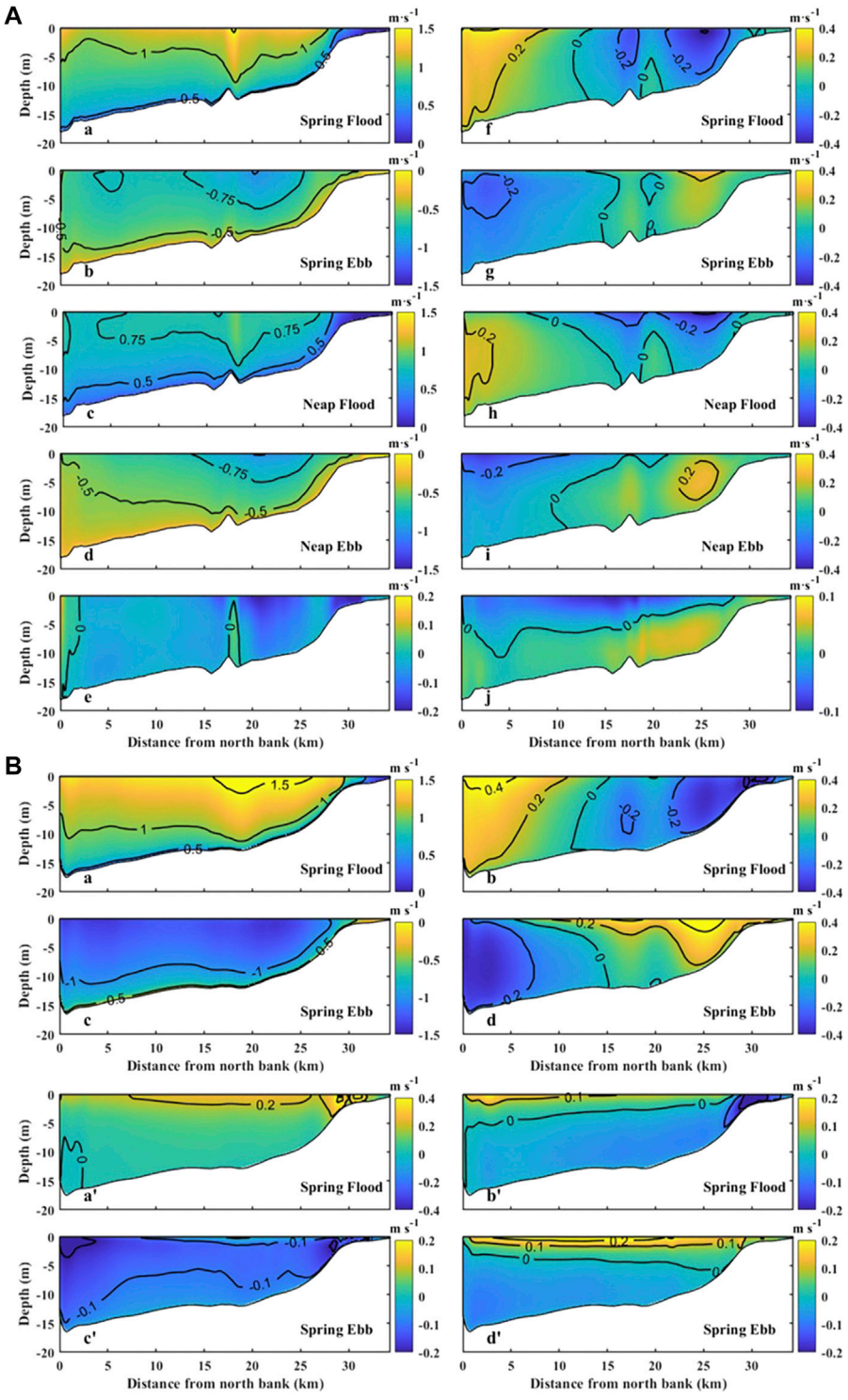

FIGURE 8
(A) Along-estuarine (left column) and lateral currents (right column) in section C1 (calm weather, 1–30 March 2013, GMT) (a,f) are for spring flood tide. (b,g) are for the spring ebb tide. (c,h) are for neap flood tide. (d,i) are for the neap ebb tide. (e,j) are for the averaged along-estuarine and lateral currents in 1 month. **(B)** Along-estuarine and lateral currents in section C1 (Typhoon Mitag). (a,b) are for spring flood tide and (c,d) is the same as (a,b) except for the spring ebb tide. Positive values indicate landward or southward direction. (a′–d′) are the same as (a–d) except for the differences of spring flood currents at section C1 between the test with Typhoon Mitag and the test with only tidal forcing.

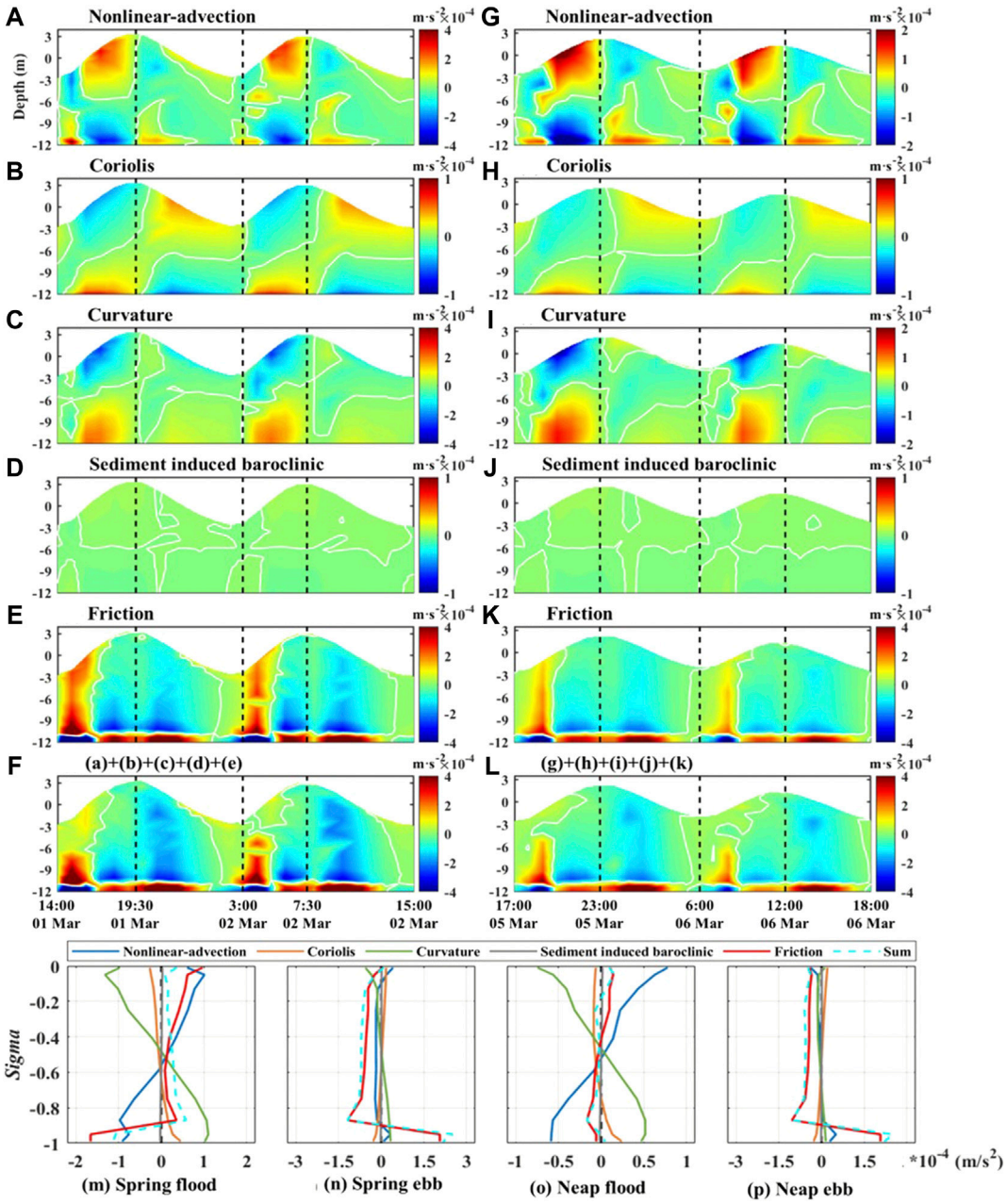

FIGURE 9
Times series of momentum terms in the main tidal channel at station P (calm weather) during **(A–F)** spring tides and **(G–L)** neap tides: vertical deviation from depth-averaged terms in lateral momentum Eq. 16. Vertical profile of the principal momentum terms in Eq. 16 at station P during **(M)** spring flood and **(N)** spring ebb tides. **(O–P)** Depict the same as **(M–N)** except for neap tides. Positive values indicate southward directions.

4.2 Combined wave-current bottom stress

The combined wave-current bottom stress is the vector sum of the time-averaged instantaneous current-induced bottom stress and wave-caused maximum bottom stress (Gao et al., 2018). The combined bottom stress of wave-current influences SSC through its effect on the resuspension process. The 50 h mean values before (calm weather condition) and during the typhoon (extreme weather condition) were used to illustrate the results in the discussion section.

During calm weather, the combined current-wave shear stress is only significantly different in shallow water compared to the current-induced shear stress condition, with little effect in

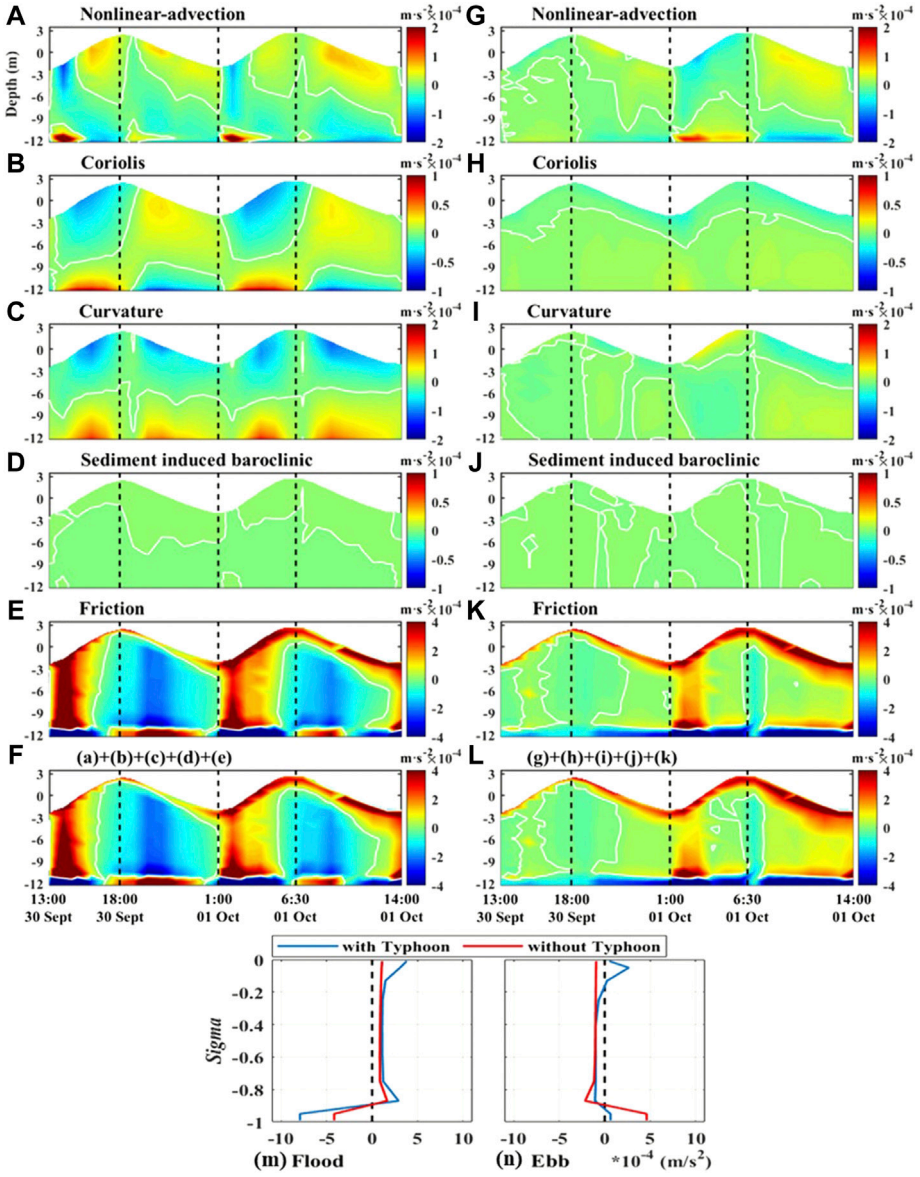

FIGURE 10
Times series in the main tidal channel at station P (during Typhoon Mitag) during **(A–F)** spring tides and **(G–L)** neap tides: vertical deviation from depth-averaged terms in lateral momentum (Eq. 16). Vertical profile of the principal momentum terms in Eq. 16 at station P during **(M)** flood and **(N)** ebb tides during the typhoon. Positive values indicate southward directions.

deeper water on the north shore. This is because wave-induced bottom stress is proportional to the square of the wave orbital velocity, which is more prominent in shallow water. The 50-h mean near-bottom SSC difference has the same distribution pattern, with an increase of more than 0.2 kg/m^3 in shallow water.

During the typhoon (Figure 12), the effect of the combined wave-current bottom stress (Figure 12A'–F') is more significant, with a large increase in significant wave height and wave orbital velocity. The 50-h mean bottom stress difference in shallow water exceeds 0.8 N/m^2, and the mean near-bottom SSC difference is greater than 1 kg/m^3 (Figures 12A–F).

Figure 13A shows the differences in bottom bed shear stress, SSC, K_m, and current velocity between Tests 1 and 2 at station P2 during calm weather and Typhoon Mitag. Compared with current-induced shear stress, the combined wave-current bottom stress under calm weather conditions is elevated, with values not exceeding 0.02 N/m^2. The difference in SSC is also not significant, and the difference exceeds 0.1 kg/m^3 only at 12:00 on 27 September.

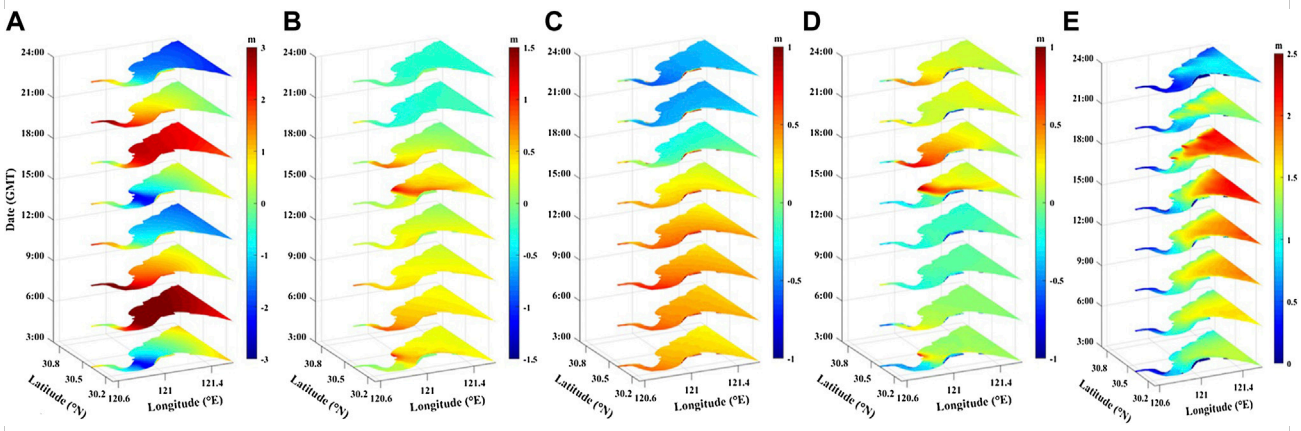

FIGURE 11
(A) Total water level, **(B)** total surge, **(C)** storm surge and **(D)** nonlinear surge **(E)** Hs (GMT 2019-10-01, 3:00–24:00).

The difference in bottom stress between Tests 1 and 2 at station P2 is more than 2.4 N/m^2. The difference in near-bottom SSC exceeds 2 kg/m^3 at 2:00, 8:00, and 20:00 on October 1, which is similar to the distribution pattern of bottom stress. The increase in SSC decreases from the bottom layer to the surface layer. In addition, the difference between the vertical eddy viscosity coefficient and current velocity between Tests one and two at station P2 is not significant, even during the storm. In summary, combined wave-current bottom stress can significantly affect the sediment resuspension process and consequently, SSC, particularly in shallow water or during storms.

4.3 Wave dissipation

Wave dissipation is an energy sink in the wave-energy equation (Eq. 8). However, wave dissipation at the surface and bottom is a source term in the vertical turbulence energy equation (a diffusion boundary condition). Therefore, wave dissipation can enhance vertical mixing. Enhanced vertical mixing not only acts on the vertical exchange of suspended sediment but also affects the flow and, therefore, the advection and resuspension processes of suspended sediment.

Under calm weather conditions, the effect of wave dissipation on suspended sediments in HZB is negligible (Figures 13Ba–d). During Typhoon Mitag, the difference in bottom stress between Tests 1 and 3 (Figure 13Be) and the difference in SSC in the near-bottom layer (Figures 13Bf) show spatial variability. In the shallow waters of southern HZB, wave dissipation mostly leads to decreased bottom stress and near-bottom SSC. In contrast, in deep tidal channels, bottom stress and near-bottom SSC mainly increase, and the difference in near-bottom SSC can reach 0.07–0.08 kg/m^3. Focusing on station P2, surface dissipation significantly enhances vertical mixing during the typhoon, whereas bottom dissipation has little effect on vertical mixing (Figure 13Bg).

On 1 October, station P2 experienced two events with significant wave-dissipation effects at 09:00 (peak ebb) and 16:00 (peak flood). During this period, bottom stress decreases by more than 0.5 N/m^2 (Figure 13Bg), current velocity increases by more than 0.3 m/s (Figure 13Bh), and vertical SSC decreases by approximately 1 kg/m^3.

In summary, the wave dissipation term is a source of the energy equation of vertical turbulence, which enhances vertical mixing. Enhanced vertical mixing not only affects the vertical exchange of suspended sediment but also influences the flow, which in turn affects the advection and resuspension processes of sediment. The wave dissipation term has a substantial effect in the bay only during typhoons, and its effect is related to water depth and tidal phases. In shallow waters, bottom stress and SSC are reduced, while current velocity is increased.

4.4 Form drag

The effect of wind stress can be divided into a turbulent viscous component (surface friction) and a pressure component (form drag). Form drag is related to the horizontal gradient of wave pressure because of wave-induced water level rise (Eq. 5). Wind pressure acts on the water column as form drag, therefore, entering the momentum equation and vertical turbulence closure equation (Mellor, 2005).

Similar to wave dissipation, the differences in form drag are almost 0 under calm weather conditions (Figure 13Ce), with almost no effect on the sediment dynamics in the bay (Figures 13Ca–d). During the typhoon, form drag mainly affects the

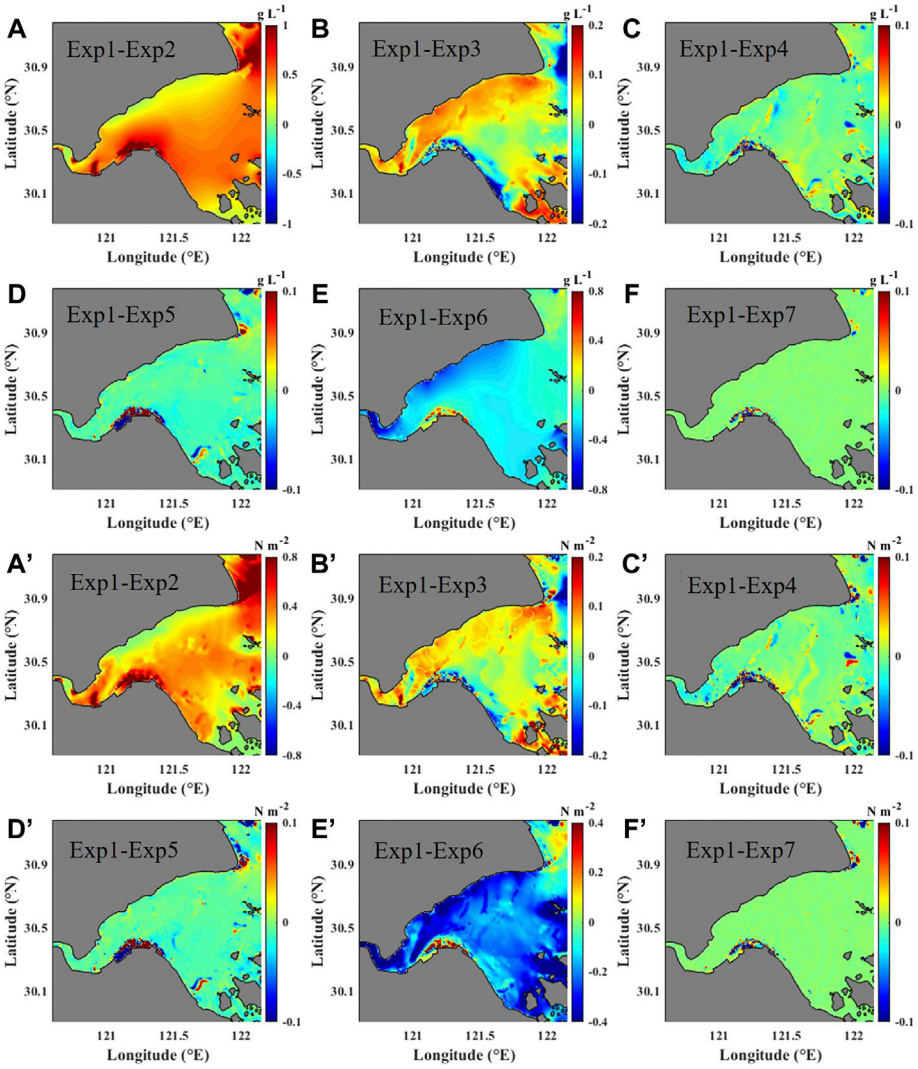

FIGURE 12
Differences of 50 h averaged **(A–F)** near-bottom SSC and **(A′–F′)** bottom stress during the Typhoon Mitag.

vertical mixing of each sigma layer in the vertical direction. However, the deviation is small, and the average K_m value of P2 differs by 7% at sigma = 0.5. Compared with Test 3, the form drag of Test one increases significantly in the surface layer and decreases with depth during Typhoon Mitag (Figure 13Cj), while enhancing vertical mixing in the upper layers of the water column (Figure 13Ch). The difference between the current velocity and bottom stress fluctuates and mainly decreases. The effect of form drag on SSC is relatively complex (Figure 13Cg). SSC in the middle and upper layers increases by more than 0.1 kg/m^3 at 13:00 on 1 October, which may be related to the enhanced vertical eddy viscosity coefficient. As the difference between the current velocity and bottom stress decreases, the difference between SSC at 15:00 on 1 October and 2:00 on 2 October is approximately 0.2 kg/m^3.

In general, form drag affects suspended sediment mainly by influencing K_m and has a significant effect only during storms in the bay, which is weaker than the combined bottom stress and wave dissipation.

4.5 Wave radiation stress

Wave radiation stress can be described as the energy exchange during the wave-current interaction, which is a wave residual momentum flow (Zou, 2005). Longuet-Higgins and Stewart (1962) defined radiation stress as the difference between the time-averaged value of the total momentum flow acting on a unit area of the water column and the hydrostatic pressure in the absence of waves. When a wave breaks, wave

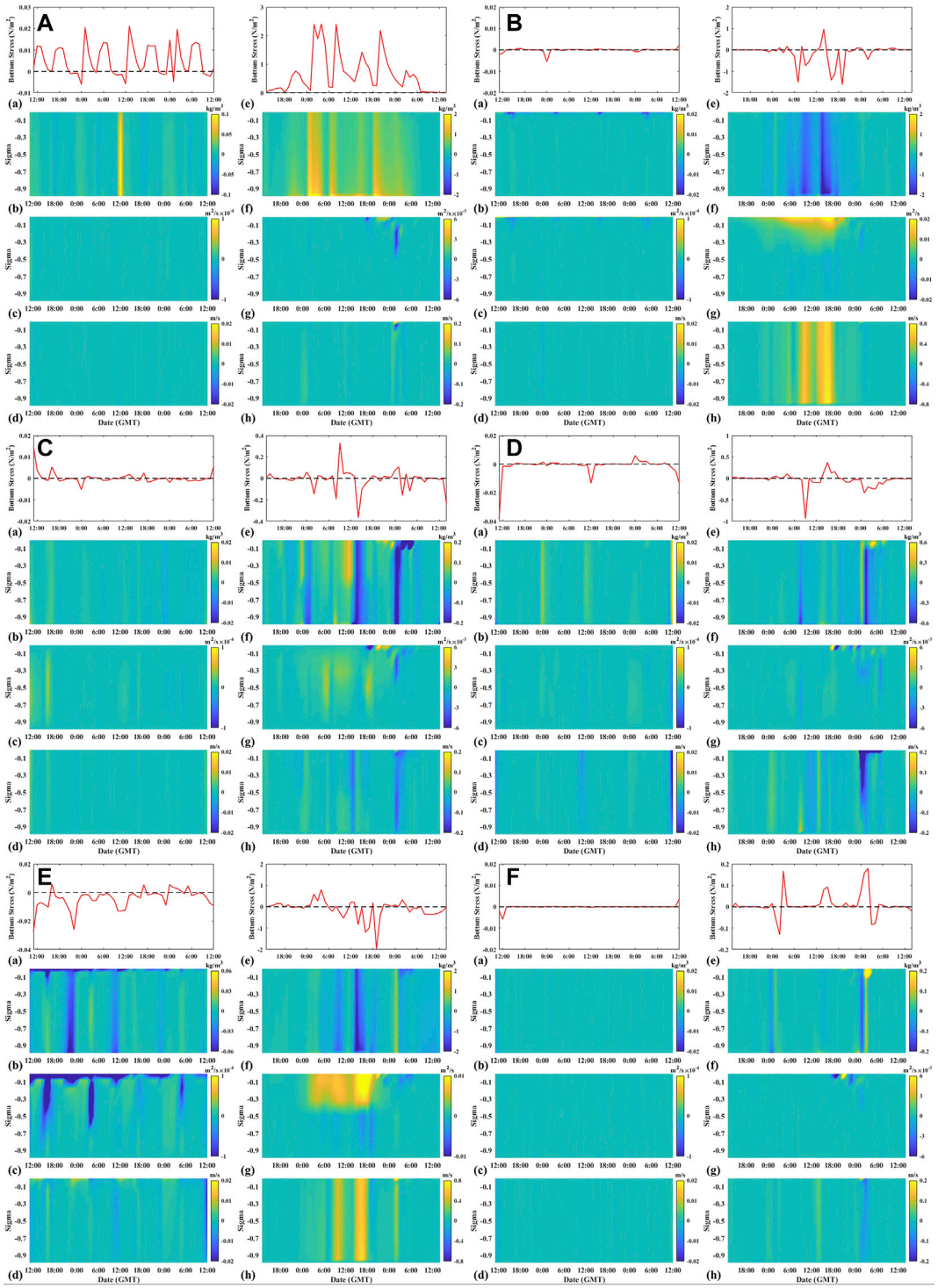

FIGURE 13
Differences between **(A)** Test 1 and Test 2, **(B)** Test 1 and Test 3, **(C)** Test 1 and Test 4, **(D)** Test 1 and Test 5, **(E)** Test 1 and Test 6, and **(F)** Test 1 and Test 7. (a) bottom bed shear stress, (b) SSC, (c) K_m and (d) current velocity during calm weather (averaged in 50 h before the typhoon) at station P2. (e–h) are the same as (a–d) except for Typhoon Mitag (averaged in 50 h during the typhoon).

height and momentum are subsequently reduced, and the reduced momentum is converted into a force acting on the surrounding fluid. Conversely, to maintain wave momentum, the surrounding fluid also exerts forces on the wave (Mu, 2020).

Under calm weather conditions, the effect of wave radiation stress on hydro and sediment dynamics in the bay is almost negligible, except for small shallow areas (Figures 13Da–d). During Typhoon Mitag, the wave radiation stress reduced SSC in most of the bay (approximately 0.01 kg/m^3), and it increased SSC in the shallow waters of the southern bay (approximately 0.3 kg/m^3) (Figure 13Dd). Wave radiation stress affects advective transport and subsequently changes SSC by changing the current velocity, for example, at 2:00 on 2 October. Changes in current velocity near the bottom also led to changes in bottom stress, with a maximum reduction of 0.94 N/m^2, at 9:00 on 1 October (Figure 13De). This, in turn, led to a significant decrease in SSC, with a decrease of more than 0.4 kg/m^3 in the middle and lower layers.

In summary, radiation stress affects advection by changing current velocity, and the change in bottom velocity also changes bottom stress, which in turn affects the resuspension process. Both processes have a negligible effect outside the shallow area of the bay and are weaker than the combined wave-current bottom stress and wave dissipation.

4.6 Mean current advection and refraction of wave energy

Flow can affect the propagation of wave energy through the advection term (second term on the left side of Eq. 8) and the refraction term (third term on the left side of Eq. 8). Both mechanisms provide feedback from the wave to the flow, which in turn affects SSC. If these two terms are omitted from the wave model, the effect of waves on the current changes.

Under calm weather conditions, the mean current advection of wave energy mainly reduces the surface vertical eddy viscosity coefficient (Figure 13Ec), which in turn affects SSC (Figure 13Eb). Large differences were observed during the typhoons. The mean current advection of wave energy generally reduces the near-bottom SSC in the bay, especially at the top of the bay and near the northern bank (Figure 13Ee). SSC in the shallow waters of the southern bay increases slightly, and its distribution pattern is consistent with that of the bottom stress difference (Figure 13Ee). At station P2, the difference in current velocity during the typhoon (Figure 13Eh) correlates with the difference in SSC (Figure 13Ef).

Two significant increases in current velocity difference were experienced at 10:00 and 15:00 on 1 October. Advective transport was affected, which in turn led to a decrease in SSC exceeding 1 kg/m^3. The change in the near-bottom current velocity also changed the bottom stress, with a maximum decrease of approximately 2 N/m^2 at 19:00 on 1 October (Figure 13Ee). The K_m values near the surface level (sigma > −0.45) increased significantly during the typhoon and decreased slightly near the bottom level (sigma < −0.45). The effect of wave energy mean flow refraction is small during both calm weather and Typhoon Mitag (Figure 13Eg).

The effect of the mean current refraction of wave energy is also small during both calm weather and Typhoon Mitag (Figure 13Ff). At 2:00 on 2 October, SSC at station P2 decreased by more than 0.15 kg/m^3. At 4:00 on 2 October, surface SSC increased by approximately 0.3 kg/m^3.

Generally, the advection term is the second most important term following the combined wave-current bottom stress, and works to reduce SSC. The refraction term is the weakest term among the six mechanisms.

5 Conclusion

This study uses the macro-tidal turbid HZB as an example to investigate sediment dynamics and the physical mechanism of wave-current interaction on sediment dynamics during Typhoon Mitag. The main conclusions are as follows.

(1) A numerical model coupled tide-wave-surge-sediment is established and fully validated in the HZB. The wave-current coupling process of the model fully considers combined wave-current bottom stress, wave dissipation, form drag, radiation stress, Stokes drift velocity, mean current advection of wave energy, and refraction. The sediment model coupled water-sediment density and considered the flocculation-settlement process and fluid mud bottom boundary layer characteristics. The surge model considered reconstructing and verifying the rotating and moving wind fields of typhoons using the Holland-Miyazaki model. The model results are thoroughly validated using field data of water levels, currents, significant wave heights, and SSC data during calm and extreme weather conditions.
(2) Hydro and sediment dynamics in HZB are spatially and temporally asymmetric and are controlled by different mechanisms, depending on water depth and tidal phases. The typhoon changed the asymmetrical characteristics of hydro and sediment dynamics in HZB. The increased bottom currents caused by typhoons are similar to, but smaller than, the increased surface currents. The combined interactions of currents and waves led to more sediment resuspension during the typhoon. The lateral circulation in the curvature was reversed during Typhoon Mitag, and the sediment flux subsequently changed, controlled by the friction term and vertical profile of SSC.
(3) The combined bottom stresses were the main wave-current interactions leading to increased SSC in HZB, which

significantly affected sediment resuspension and, therefore, affected SSC. Under calm weather conditions, except for the combined wave-current bottom stress, the effects of the other terms were minor. The combined bottom stress is the most critical wave-current interaction mechanism that increases SSC, which significantly affects sediment resuspension and SSC, especially in shallow waters or during storms. The advection term plays an essential role in reducing SSC by increasing current velocity and influencing advection transport. The wave dissipation term enhances vertical mixing. The enhancement of vertical mixing acts on the vertical exchange of suspended sediment, which affects flow, and further affects the advection and resuspension process. In the shallow waters of the southern bay, wave dissipation mostly leads to lower bottom stress, increased current velocity, and reduced SSC. In the deep tidal channels, SSC primarily increases. Form drag mainly influences the vertical eddy viscosity coefficient. Wave radiation stress affects advective transport by changing current velocity and then changes the bottom stress, which in turn affects the resuspension process. The effects of form drag and wave radiation terms are insignificant, and the effect of the refraction term is the smallest, even during storms.

Data availability statement

The original contributions presented in the study are included in the article/supplementary material, further inquiries can be directed to the corresponding authors.

Author contributions

LL, XW, and YX: manuscript writing, data analysis, methodology, and modelling. JX and YR: material collection, modelling, and data analysis.

Funding

This research was supported by the National Natural Science Foundation of China (41976157 and 42076177), and the Science Technology Department of Zhejiang Province (2020C03012, 2022C03044, and 2021C03180).

Conflict of interest

The authors declare that the research was conducted in the absence of any commercial or financial relationships that could be construed as a potential conflict of interest.

Publisher's note

All claims expressed in this article are solely those of the authors and do not necessarily represent those of their affiliated organizations, or those of the publisher, the editors and the reviewers. Any product that may be evaluated in this article, or claim that may be made by its manufacturer, is not guaranteed or endorsed by the publisher.

References

Allen, J. I., Somerfield, P. J., and Gilbert, F. J. (2007). Quantifying uncertainty in high-resolution coupled hydrodynamic-ecosystem models. *J. Mar. Syst.* 64 (1-4), 3–14. doi:10.1016/j.jmarsys.2006.02.010

An, B. C. (2016). *Numerical studies and application of tidal dynamics based on FVCOM in Hangzhou Bay and adjacent seas*. Shanghai: Shanghai Ocean University.

Andersen, T. J., and Pejrup, M. (2001). Suspended sediment transport on a temperate, microtidal mudflat, the Danish Wadden Sea. *Mar. Geol.* 173 (1-4), 69–85. doi:10.1016/s0025-3227(00)00164-x

Bricker, J. D., Inagaki, S., and Monismith, S. G. (2005). Bed drag coefficient variability under wind waves in a tidal estuary. *J. Hydraul. Eng.* 131 (6), 497–508. doi:10.1061/(asce)0733-9429(2005)131:6(497)

Cao, Z. D., and Wang, Y. H. (1994). *Numerical simulation of hydrodynamic sediment*. Tianjin: Tianjin University Press.

Chen, C. S., Beardsley, R. C., and Cowles, G. (2006). *An unstructured grid, finite-volume coastal ocean model: FVCOM user manual*. second edition. Oceanography. doi:10.5670/oceanog.2006.92

Chen, M., Yu, C. G., Hou, W. F., Xu, Y. J., Zheng, J., Deng, X. Y., et al. (2017). Study on distribution characteristics of temperature and salinity in spring and autumn in zhoushan coastal fishing ground. *J. Zhejiang Ocean Univ. Nat. Sci.* 36 (06), 495–502. doi:10.3969/j.issn.1008-830X.2017.06.005

Chen, Y., Cai, T., Chang, Y., Huang, S., and Xia, T. (2018). "Comparison of flow and energy reduction by representative intertidal plants, Southeast China," in The 28th International Ocean and Polar Engineering Conference, Sapporo, Japan, June 2018.

Christie, M. C., and Dyer, K. R. (1998). Measurements of the turbid tidal edge over the Skeffling mudflats. *Geol. Soc. Lond. Spec. Publ.* 139 (1), 45–55. doi:10.1144/gsl.sp.1998.139.01.04

Christie, M. C., Dyer, K. R., and Turner, P. (1999). Sediment flux and bed level measurements from a macro tidal mudflat. *Estuar. Coast. Shelf Sci.* 49 (5), 667–688. doi:10.1006/ecss.1999.0525

D'Alpaos, A., Carniello, L., and Rinaldo, A. (2013). Statistical mechanics of wind wave-induced erosion in shallow tidal basins: Inferences from the Venice Lagoon. *Geophys. Res. Lett.* 40 (13), 3402–3407. doi:10.1002/grl.50666

Dronkers, J. (1986). Tidal asymmetry and estuarine morphology. *Neth. J. Sea Res.* 20 (2-3), 117–131. doi:10.1016/0077-7579(86)90036-0

Dufois, F., Verney, R., Le Hir, P., Dumas, F., and Charmasson, S. (2014). Impact of winter storms on sediment erosion in the rhone river prodelta and fate of sediment in the gulf of lions (north western mediterranean sea). *Cont. Shelf Res.* 72, 57–72. doi:10.1016/j.csr.2013.11.004

Dyer, K. R., Christie, M. C., Feates, N., Fennessy, M. J., Pejrup, M., Van der Lee, W., et al. (2000). An investigation into processes influencing the morphodynamics of an intertidal mudflat, the dollard estuary, The Netherlands: I. Hydrodynamics and suspended sediment. *Estuar. Coast. Shelf Sci.* 50 (5), 607–625. doi:10.1006/ecss.1999.0596

Gao, G. D., Wang, X. H., Song, D., Bao, X., Yin, B. S., Yang, D. Z., et al. (2018). Effects of wave–current interactions on suspended-sediment dynamics during strong wave events in Jiaozhou Bay, Qingdao, China. *J. Phys. Oceanogr.* 48 (5), 1053–1078. doi:10.1175/jpo-d-17-0259.1

Graber, H. C., Beardsley, R. C., and Grant, W. D. (1989). Storm-generated surface waves and sediment resuspension in the East China and Yellow Seas. *J. Phys. Oceanogr.* 19 (8), 1039–1059. doi:10.1175/1520-0485(1989)019<1039:sgswas>2.0.co;2

Grant, W. D., and Madsen, O. S. (1979). Combined wave and current interaction with a rough bottom. *J. Geophys. Res.* 84 (C4), 1797–1808. doi:10.1029/jc084ic04p01797

Green, M. O., Black, K. P., and Amos, C. L. (1997). Control of estuarine sediment dynamics by interactions between currents and waves at several scales. *Mar. Geol.* 144 (1-3), 97–116. doi:10.1016/s0025-3227(97)00065-0

Green, M. O., and Coco, G. (2014). Review of wave-driven sediment resuspension and transport in estuaries. *Rev. Geophys.* 52 (1), 77–117. doi:10.1002/2013rg000437

Green, M. O., and Coco, G. (2007). Sediment transport on an estuarine intertidal flat: Measurements and conceptual model of waves, rainfall and exchanges with a tidal creek. *Estuar. Coast. Shelf Sci.* 72 (4), 553–569. doi:10.1016/j.ecss.2006.11.006

Green, M. O., and MacDonald, I. T. (2001). Processes driving estuary infilling by marine sands on an embayed coast. *Mar. Geol.* 178 (1-4), 11–37. doi:10.1016/s0025-3227(01)00188-8

Green, M. O. (2011). Very small waves and associated sediment resuspension on an estuarine intertidal flat. *Estuar. Coast. shelf Sci.* 93 (4), 449–459. doi:10.1016/j.ecss.2011.05.021

He, X., Bai, Y., Pan, D., Huang, N. L., Dong, X., Chen, J. S., et al. (2013). Using geostationary satellite ocean color data to map the diurnal dynamics of suspended particulate matter in coastal waters. *Remote Sens. Environ.* 133, 225–239. doi:10.1016/j.rse.2013.01.023

He, Z. G., Tang, Y. L., Xia, Y. Z., Chen, B. D., Xu, J., Yu, Z. Z., et al. (2020). Interaction impacts of tides, waves and winds on storm surge in a channel-island system: Observational and numerical study in yangshan harbor. *Ocean. Dyn.* 70 (3), 307–325. doi:10.1007/s10236-019-01328-5

Holland, G. J. (1980). An analytic model of the wind and pressure profiles in hurricanes. *Mon. Weather Rev.* 108 (8), 1212–1218. doi:10.1175/1520-0493(1980)108<1212:aamotw>2.0.co;2

Hu, Y. K., Yu, Z. F., Zhou, B., Li, Y., Yin, S. J., He, X. Q., et al. (2019). Tidal-driven variation of suspended sediment in Hangzhou Bay based on GOCI data. *Int. J. Appl. Earth Observation Geoinformation* 82, 101920. doi:10.1016/j.jag.2019.101920

Ji, R. Y., and Lu, Y. J. (2008). Advances in hydrodynamic and sedimentary processes of macro tidal estuary. *Hydro-Science Eng.* 3, 64–69. doi:10.16198/j.cnki.1009-640x.2008.03.011

Jiang, C. B., Wu, Z. Y., Chen, J., and Liu, J. (2014). Review of sediment transport and beach profile changes under storm surge. *J. Changsha Univ. Sci. Technol. Nat. Sci.* 11, 1–9. doi:10.3969/j.issn.1672-9331.2014.01.001

Jin, Y. H., and Sun, Z. L. (1992). Mixing characteristics of salt water and fresh water in Chinese estuaries. *Acta Geogr. Sin.* 47 (2), 165–173.

Kalkwijk, J. P. T., and Booij, R. (1986). Adaptation of secondary flow in nearly-horizontal flow. *J. Hydraul. Res.* 24 (1), 19–37. doi:10.1080/00221688609499330

Kim, S. C., Friedrichs, C. T., Maa, J. Y., and Wright, L. D. (2000). Estimating bottom stress in tidal boundary layer from acoustic Doppler velocimeter data. *J. Hydraul. Eng.* 126 (6), 399–406. doi:10.1061/(asce)0733-9429(2000)126:6(399)

Leonardi, N., Carnacina, I., Donatelli, C., Ganju, N. K., Plater, A. J., Schuerch, M., et al. (2018). Dynamic interactions between coastal storms and salt marshes: A review. *Geomorphology* 301, 92–107. doi:10.1016/j.geomorph.2017.11.001

Li, L., Guan, W. B., He, Z. G., Yao, Y. M., and Xia, Y. Z. (2017). Responses of water environment to tidal flat reduction in xiangshan bay: Part II locally re-suspended sediment dynamics. *Estuar. Coast. Shelf Sci.* 198, 114–127. doi:10.1016/j.ecss.2017.08.042

Li, L., Guan, W. B., Hu, J. Y., Cheng, P., and Wang, X. H. (2018). Responses of water environment to tidal flat reduction in xiangshan bay: Part I hydrodynamics. *Estuar. Coast. Shelf Sci.* 206, 14–26. doi:10.1016/j.ecss.2017.11.003

Li, L., Li, Z., He, Z., Yu, Z., and Ren, Y. (2022a). Investigation of storm tides induced by super typhoon in macro-tidal Hangzhou bay. *Front. Mar. Sci.* 9, 890285. doi:10.3389/fmars.2022.890285

Li, L., Ren, Y. H., Wang, X. H., and Xia, Y. Z. (2022b). Sediment dynamics on a tidal flat in macro-tidal Hangzhou bay during typhoon Mitag. *Cont. Shelf Res.* 237, 104684. doi:10.1016/j.csr.2022.104684

Longuet-Higgins, M. S., and Stewart, R. W. (1962). Radiation stress and mass transport in gravity waves, with application to 'surf beats. *J. Fluid Mech.* 13 (4), 481–504. doi:10.1017/s0022112062000877

Lu, J., Jiang, J., Li, A., and Ma, X. (2018). Impact of typhoon chan-hom on the marine environment and sediment dynamics on the inner shelf of the east China sea: *In-situ* seafloor observations. *Mar. Geol.* 406, 72–83. doi:10.1016/j.margeo.2018.09.009

Mellor, G. (2015). A combined derivation of the integrated and vertically resolved, coupled wave–current equations. *J. Phys. Oceanogr.* 45 (6), 1453–1463. doi:10.1175/jpo-d-14-0112.1

Mellor, G. L., Donelan, M. A., and Oey, L. Y. (2008). A surface wave model for coupling with numerical ocean circulation models. *J. Atmos. Ocean. Technol.* 25 (10), 1785–1807. doi:10.1175/2008jtecho573.1

Mellor, G. L., and Yamada, T. (1982). Development of a turbulence closure model for geophysical fluid problems. *Rev. Geophys.* 20 (4), 851–875. doi:10.1029/rg020i004p00851

Mellor, G. (2005). Some consequences of the three-dimensional current and surface wave equations. *J. Phys. Oceanogr.* 35 (11), 2291–2298. doi:10.1175/jpo2794.1

Miyazaki, M., Ueno, T., and Unoki, S. (1962). Theoretical investigations of typhoon surges along the Japanese coast. *Oceanogr. Mag.* 13 (2), 103–117.

Mu, H. R. (2020). *Study on the radiation stress of waves over two-dimensional variable bathymetry*. Dalian: Dalian University of Techonology.

Murphy, A. H. (1992). Climatology, persistence, and their linear combination as standards of reference in skill scores. *Weather Forecast.* 7 (4), 692–698. doi:10.1175/1520-0434(1992)007<0692:cpatlc>2.0.co;2

Pan, C. H., Zeng, J., Tang, Z. W., and Shi, Y. B. (2013). A study of sediment characteristics and riverbed erosion/deposition in Qiantang estuary. *Hydro-Science Eng.* (01), 1–7. doi:10.3969/j.issn.1009-640X.2013.01.001

Pang, H. J., Lou, Z. H., Jin, A. M., Yan, K. K., Jiang, Y., Yang, X. H., et al. (2015). Contamination, distribution, and sources of heavy metals in the sediments of Andong tidal flat, Hangzhou bay, China. *Cont. Shelf Res.* 110, 72–84. doi:10.1016/j.csr.2015.10.002

Pawlowicz, R., Beardsley, B., and Lentz, S. (2002). Classical tidal harmonic analysis including error estimates in MATLAB using T_TIDE. *Comput. Geosciences* 28 (8), 929–937. doi:10.1016/s0098-3004(02)00013-4

Postma, H. (1961). Transport and accumulation of suspended matter in the Dutch Wadden Sea. *Neth. J. Sea Res.* 1 (1-2), 148–190. doi:10.1016/0077-7579(61)90004-7

Pritchard, D. (2005). Suspended sediment transport along an idealised tidal embayment: Settling lag, residual transport and the interpretation of tidal signals. *Ocean. Dyn.* 55 (2), 124–136. doi:10.1007/s10236-005-0004-7

Ralston, D. K., and Stacey, M. T. (2007). Tidal and meteorological forcing of sediment transport in tributary mudflat channels. *Cont. Shelf Res.* 27 (10-11), 1510–1527. doi:10.1016/j.csr.2007.01.010

Ren, Y. (2022). *Characteristics and mechanism of suspended sediment in Hangzhou bay considering wave-current interaction*. Zhoushan: Zhejiang University.

Sheng, Y. P., and Liu, T. (2011). Three-dimensional simulation of wave-induced circulation: Comparison of three radiation stress formulations. *J. Geophys. Res.* 116 (C5), C05021. doi:10.1029/2010jc006765

Shi, J. Z., Luther, M. E., and Meyers, S. (2006). Modelling of wind wave-induced bottom processes during the slack water periods in Tampa Bay, Florida. *Int. J. Numer. Methods Fluids* 52 (11), 1277–1292. doi:10.1002/fld.1377

Shi, Z., and Chen, J. Y. (1996). Morphodynamics and sediment dynamics on intertidal mudflats in China (1961–1994). *Cont. Shelf Res.* 16 (15), 1909–1926. doi:10.1016/0278-4343(95)00059-3

Shi, Z. (2001). Observations on fluid mud in the deep water channel of Hangzhou Bay. *Mar. Sci. Bull.* 20 (06), 40–50. doi:10.3969/j.issn.1001-6392.2001.06.006

Shou, W. W., Wu, J. Z., Hu, R. J., and Zhu, L. H. (2009). 3-D hydrodynamic numerical modelling around the sea area of zhoushan islands. *Mar. Geol. Lett.* 25 (11), 1–9. doi:10.3969/j.issn.1009-2722.2009.11.001

Smagorinsky, J. (1963). General circulation experiments with the primitive equations: I. The basic experiment. *Mon. Weather Rev.* 91 (3), 99–164. doi:10.1175/1520-0493(1963)091<0099:gcewtp>2.3.co;2

Soulsby, R. L. (1997). Dynamics of marine sands: A manual for practical applications. *Oceanogr. Lit. Rev.* 9 (44), 947.

Soulsby, R. L., Hamm, L., Klopman, G., Myrhaug, D., Simons, R. R., Thomas, G. P., et al. (1993). Wave-current interaction within and outside the bottom boundary layer. *Coast. Eng.* 21 (1-3), 41–69. doi:10.1016/0378-3839(93)90045-a

Talke, S. A., and Stacey, M. T. (2003). The influence of oceanic swell on flows over an estuarine intertidal mudflat in San Francisco Bay. *Estuar. Coast. Shelf Sci.* 58 (3), 541–554. doi:10.1016/s0272-7714(03)00132-x

Tang, J. H. (2007). *Characteristics of fine cohesive sediment's flocculation in the Changjiang estuary and its adjacent sea area*. Shanghai: East China Normal University.

Tang, Y. L. (2018). *Numerical simulation of characteristics of storm tide in Yangshan Harbor based on tide-surge-wave model*. Zhoushan: Zhejiang University.

Tu, J., and Fan, D. (2017). Flow and turbulence structure in a hypertidal estuary with the world's biggest tidal bore. *J. Geophys. Res. Oceans* 122 (4), 3417–3433. doi:10.1002/2016jc012120

Tu, J., Fan, D., Zhang, Y., and Voulgaris, G. (2019). Turbulence, sediment-induced stratification, and mixing under macrotidal estuarine conditions (Qiantang Estuary, China). *J. Geophys. Res. Oceans* 124 (6), 4058–4077. doi:10.1029/2018jc014281

Uncles, R. J., and Stephens, J. A. (2010). Turbidity and sediment transport in a muddy sub-estuary. *Estuar. Coast. Shelf Sci.* 87 (2), 213–224. doi:10.1016/j.ecss.2009.03.041

Van Prooijen, B. C., and Winterwerp, J. C. (2010). A stochastic formulation for erosion of cohesive sediments. *J. Geophys. Res.* 115 (C1), C01005. doi:10.1029/2008jc005189

Van Straaten, L. M. J. U., and Kuenen, P. H. (1957). Accumulation of fine grained sediments in the Dutch Wadden Sea. *Geol. Mijnb.* 19, 329–354.

Wang, B. C., and Eisma, D. (1990). Supply and deposition of sediment along the north bank of Hangzhou Bay, China. *Neth. J. sea Res.* 25 (3), 377–390. doi:10.1016/0077-7579(90)90045-i

Wang, X. H., Byun, D. S., Wang, X. L., and Cho, Y. K. (2005). Modelling tidal currents in a sediment stratified idealized estuary. *Cont. shelf Res.* 25 (5-6), 655–665. doi:10.1016/j.csr.2004.10.013

Wang, X. H. (2002). Tide-induced sediment resuspension and the bottom boundary layer in an idealized estuary with a muddy bed. *J. Phys. Oceanogr.* 32 (11), 3113–3131. doi:10.1175/1520-0485(2002)032<3113:tisrat>2.0.co;2

Wang, Y. N. (2014). *Three-dimensional numerical simulation of tidal flow and sediment movement near shore*. Taiyuan: Taiyuan University of Technology.

Warner, J. C., Sherwood, C. R., Signell, R. P., Harris, C. K., and Arango, H. G. (2008). Development of a three-dimensional, regional, coupled wave, current, and sediment-transport model. *Comput. geosciences* 34 (10), 1284–1306. doi:10.1016/j.cageo.2008.02.012

Williams, H. F. (2009). Stratigraphy, sedimentology, and microfossil content of Hurricane Rita storm surge deposits in southwest Louisiana. *J. Coast. Res.* 25 (4), 1041–1051. doi:10.2112/08-1038.1

Winterwerp, J. C. (2001). Stratification effects by cohesive and noncohesive sediment. *J. Geophys. Res.* 106 (C10), 22559–22574. doi:10.1029/2000jc000435

Xiao, Z., Wang, X. H., Roughan, M., and Harrison, D. (2019). Numerical modelling of the sydney Harbour estuary, new south wales: Lateral circulation and asymmetric vertical mixing. *Estuar. Coast. Shelf Sci.* 217, 132–147. doi:10.1016/j.ecss.2018.11.004

Xie, D. F., Shu, G. A. O., Wang, Z. B., and Pan, C. H. (2013). Numerical modeling of tidal currents, sediment transport and morphological evolution in Hangzhou Bay, China. *Int. J. Sediment Res.* 28 (3), 316–328. doi:10.1016/s1001-6279(13)60042-6

Xie, M. X., Zhang, W., and Xie, H. J. (2008). Simplification method in numerical modeling of bridge pier group. *Chin. J. Hydrodynamics* 23 (4), 464–471.

Xu, S., Li, Z. H., Wang, Y. P., and Jia, J. J. (2021). Near-bottom sediment dynamical processes in the South Passage of the Yangtze Estuary during typhoon season. *J. Sediment Res.* 46 (04), 48–53. doi:10.16239/j.cnki.0468-155x.2021.04.008

Yang, Y., Wang, Y. P., Gao, S., Wang, X. H., Shi, B. W., Zhou, L., et al. (2016). Sediment resuspension in tidally dominated coastal environments: New insights into the threshold for initial movement. *Ocean. Dyn.* 66 (3), 401–417. doi:10.1007/s10236-016-0930-6

Ye, T. Y., Li, L., Wang, Y. X., He, Z. G., and Xia, Y. Z. (2019). Impacts of tidal flat reduction on suspended sediment dynamics in Hangzhou bay. *J. Tianjin Univ. Sci. Technol.* 52 (04), 392–403. doi:10.11784/tdxbz201804092

Ye, T. Y. (2019). *The multi-scale variations of suspended sediment dynamics in Hangzhou Bay and its interaction with tidal flat variations*. Zhoushan: Zhejiang University.

Yu, Z. Z. (2020). *Hydrodynamics and sediment transport during typhoon in Hangzhou Bay*. Zhoushan: Zhejiang University.

Yuan, Y., Wei, H., Zhao, L., and Cao, Y. (2009). Implications of intermittent turbulent bursts for sediment resuspension in a coastal bottom boundary layer: A field study in the Western yellow sea, China. *Mar. Geol.* 263 (1-4), 87–96. doi:10.1016/j.margeo.2009.03.023

Zhang, W., He, Z. G., Tan, L. M., Gao, G., He, H. Z., Hu, P., et al. (2017). Dynamic characteristics of Qiantang tidal bore based on field observations at a fixed location. *Chin. J. Hydrodynamics* 32 (02), 253–259. doi:10.16076/j.cnki.cjhd.2017.02.016

Zhu, Q. (2017). *Sediment dynamics on intertidal mudflats: A study based on* in situ *measurements and numerical modelling*. Shanghai: East China Normal University.

Zou, Z. L. (2005). *Water wave theories and their applications*. Beijing: Science Press.

frontiers | Frontiers in Earth Science

TYPE Original Research
PUBLISHED 29 August 2022
DOI 10.3389/feart.2022.932149

OPEN ACCESS

EDITED BY
Xiaolei Liu,
Ocean University of China, China

REVIEWED BY
Wenfei Ni,
Pacific Northwest National Laboratory, United States
Yuan-Pin Chang,
National Sun Yat-sen University, Taiwan

*CORRESPONDENCE
Li Li,
lilizju@zju.edu.cn
Zhiguo He,
hezhiguo@zju.edu.cn

SPECIALTY SECTION
This article was submitted to Geohazards and Georisks, a section of the journal Frontiers in Earth Science

RECEIVED 29 April 2022
ACCEPTED 27 July 2022
PUBLISHED 29 August 2022

CITATION
Li L, Shen F, He Z and Yu Z (2022), Suspended sediment dynamics in macrotidal turbid Hangzhou Bay during Typhoon Chan-hom.
Front. Earth Sci. 10:932149.
doi: 10.3389/feart.2022.932149

Suspended sediment dynamics in macrotidal turbid Hangzhou Bay during Typhoon Chan-hom

Li Li[1,2]*, Fangzhou Shen[1], Zhiguo He[1,2]* and Zhuzhu Yu[1]

[1]Ocean College, Zhejiang University, Zhoushan, China, [2]The Engineering Research Center of Oceanic Sensing Technology and Equipment, Ministry of Education, Hangzhou, China

Typhoons are extreme weather events that cause serious social and economic losses in coastal and estuarine areas worldwide. Understanding the impact of typhoons on sediment dynamics is essential for protecting coastal areas from these marine disasters. Hangzhou Bay is macro-tidal, turbid, and frequently affected by strong typhoons. In this study, we established and validated a three-dimensional model coupling waves, current, and sediment to investigate the sediment dynamics in Hangzhou Bay during Typhoon Chan-hom. The results showed that high suspended sediment concentration (SSC) areas during the typhoon were mainly located at the bay head and near the southern shore near the Andong tidal flat. The maximum bottom SSC was at least twice that near the surface. The peak bottom SSC values at the peak flood (6 g/L) were larger than those at the peak ebb (5 g/L) owing to the stronger current velocity at peak flood. The SSC near the northern shore was larger at the peak flood than at other times, and the SSC was high at the southern shore at peak ebb at the cross-section near the Andong tidal flat. The typhoon impacted SSC by changing the bottom stress. SSC was most influenced by wave action, followed by wind stress action, and was least influenced by air pressure action, which contributed 71.3%, 69.9%, and 1.8% to the bottom stress, respectively. Our findings are scientifically important for research on geomorphological evolution and are practically meaningful for coastal management.

KEYWORDS

sediment dynamics, ssc, wind, air pressure, wave, Typhoon Chan-hom, Hangzhou Bay

Highlights

1) We built and validated a numerical model coupling tides, waves, surges, and sediments to study sediment dynamics during Typhoon Chan-hom in Hangzhou Bay.
2) Suspended sediment concentration (SSC) during storm tides was double that during calm weather, and peak SSC and sediment fluxes occurred near the bay head and southern shore.
3) The large bottom stress caused by strong waves and winds, combined with strong advection changed the SSC and sediment fluxes in the bay during the storm tides.

4) Wave, wind stress, and air pressure contributed 71.3%, 69.9%, and 1.8% to the bottom stress, respectively and subsequently changed the SSC in HZB.

1 Introduction

Typhoons are extreme weather events that cause serious social and economic losses in coastal and estuarine areas worldwide (Peduzzi et al., 2012; Walsh et al., 2016; Cong et al., 2021). Owing to strong sea–air interactions, typhoons have remarkable effects on water level rise (Wang et al., 2020), tidal range changes (Pan et al., 2021; Wang et al., 2021), water circulation structure (Wu et al., 2016), sediment transport (Liu et al., 2011), and sea bed evolution (van Rijn, 2011; Xu, 2019). In particular, the transport, deposition, and burial of sediments on a continental shelf can lead to severe erosion near the track, the offshore movement of sand ridges, and deposition of layers of up to 25 cm during a storm (Allison et al., 2005; Goff et al., 2010; Li et al., 2015; Zang et al., 2018; Li H. et al., 2019).

Coastal and estuarine hydro-sediment dynamics are considerably affected by typhoons. *In situ* time-series observations in the northern South China Sea confirmed that typhoon events can intermittently block coastal upwelling (Zheng et al., 2018). Coastal topography and hydrological data from the northern coast of Hangzhou Bay before and after Typhoon Metsa revealed the response of the coast to the typhoon, including the advance and retreat of the shoreline and the washout of the topography of the silty coast (Dai et al., 2009). Remote sensing is one of the main methods used to obtain the suspended sediment concentration (SSC) (Li, 1987). Another method used for investigating the impact of typhoons is the rapid inversion and correction of the spatial and temporal SSC distribution in a sea area using remote sensing data (Liu et al., 2013; Wang et al., 2014; Jiang et al., 2015), the availability and quality of satellite data are affected by the thick clouds and water vapor in the air during typhoons (Wang et al., 2018a; Tang et al., 2021). *In situ* and satellite observations are the most direct methods used to obtain SSCs; however, they provide only local descriptions and cannot synchronously measure SSCs (Green et al., 1995; Williams and Rose, 2001; Aagaard et al., 2012; Wang et al., 2018b). Therefore, numerical models have become an important for analyzing sediment dynamics during typhoons. Numerical models have been combined with empirical data to study sediment transport and tidal flat siltation during typhoons in different regions (van Rijn, 2011; Oberle et al., 2014; Palinkas et al., 2014; Huang, 2017; Xu, 2019), showing that storm surges and wind-generated currents are the main forces driving sediment transport. Wind currents, combined with tidal currents, increase current velocities and accelerate sediment transport, and waves are the dominant factor affecting suspended sediment (Jiang et al., 2014). For example, when the water depth is less than 30 m, 49% of the sediment is mobilized in shelf areas (Oberle et al., 2014). Enhanced wave–current dynamics and increased bed shear stress during typhoons are the main reasons for the sharp increase in SSC; sediment is exchanged between channels and shoals during a typhoon, which affects the SSC distribution for up to 1 month (Tang et al., 2021).

Hangzhou Bay (Figure 1) is one of the most turbid estuaries in the world, with a multiyear average suspended particle concentration of 1.58 g/L in the tidal flats of the bay (Liu, 2013). It is a typical well mixed estuary. Tidal current is strong. Waves and runoff are relatively weak. The turbulence generated by bottom friction is enough to stir the entire water column (Ji and Lu, 2007). The suspended sediment concentration of Qiantang River discharges is lower than 0.25 g/L (Pan et al., 2013), and the particle sizes of suspended sediment and bed load are about 0.023 and 0.055 mm. The sediment supply is mainly from the Yangtze River (Wang and Esima, 1990). The large amount of sediment brought by the flood current accumulates as sandbar, and there are many obvious scour channels and sand ridges in the estuary (Ji and Lu, 2007). Reclamation and other marine engineering changed the estuarine bathymetry. Researchers have focused on setting parameters of suspended cohesive sediments (Wang et al., 2018a), the effect of waves on the sediment flushing process (Lu et al., 2019), the variation in near-bottom flow velocity for different wind directions, and sediment erosion rate under with wind directions and speeds (Shi et al., 2008). The spring-neap tides control SSC distribution and variation in shallow coastal areas. The increased turbulence energy during the typhoon affects the vertical mixing depth, thereby increasing the SSC on the surface (Li and Li, 2016). Wang et al. (2020) used the finite-volume coastal ocean model (FVCOM) to reappear tidal flooding in the south Yangtze coastal plain during the middle Holocene during sea level rise and storm surges (Huang et al., 2021). Model results showed that typhoons also induce larger tidal bores in Hangzhou Bay (Wang et al., 2021). The East China Sea is affected by an average of four typhoons per year (Lu et al., 2019). Extreme weather results in a large amount of sediment transport in estuaries within a short time, thus changing the topography (Xu, 2019). The effects of typhoon events on sediment in estuaries are related to estuary types (Leonardi et al., 2018). Hangzhou Bay is a macrotidal turbid bay with funnel-shaped geomorphology, which is frequently impacted by typhoons. Therefore, we want to investigate the sediment characteristics and mechanism during typhoons.

In this study, we established and validated a three-dimensional wave-current-sediment coupling model of Hangzhou Bay to simulate the sediment dynamics in Hangzhou Bay during Typhoon Chan-hom in 2015. We studied the effects of typhoon on SSC contribution and sediment transport in Hangzhou Bay, analyzed the influence of wind stress, atmospheric pressure and waves on the distribution of suspended sediment in Hangzhou Bay, and

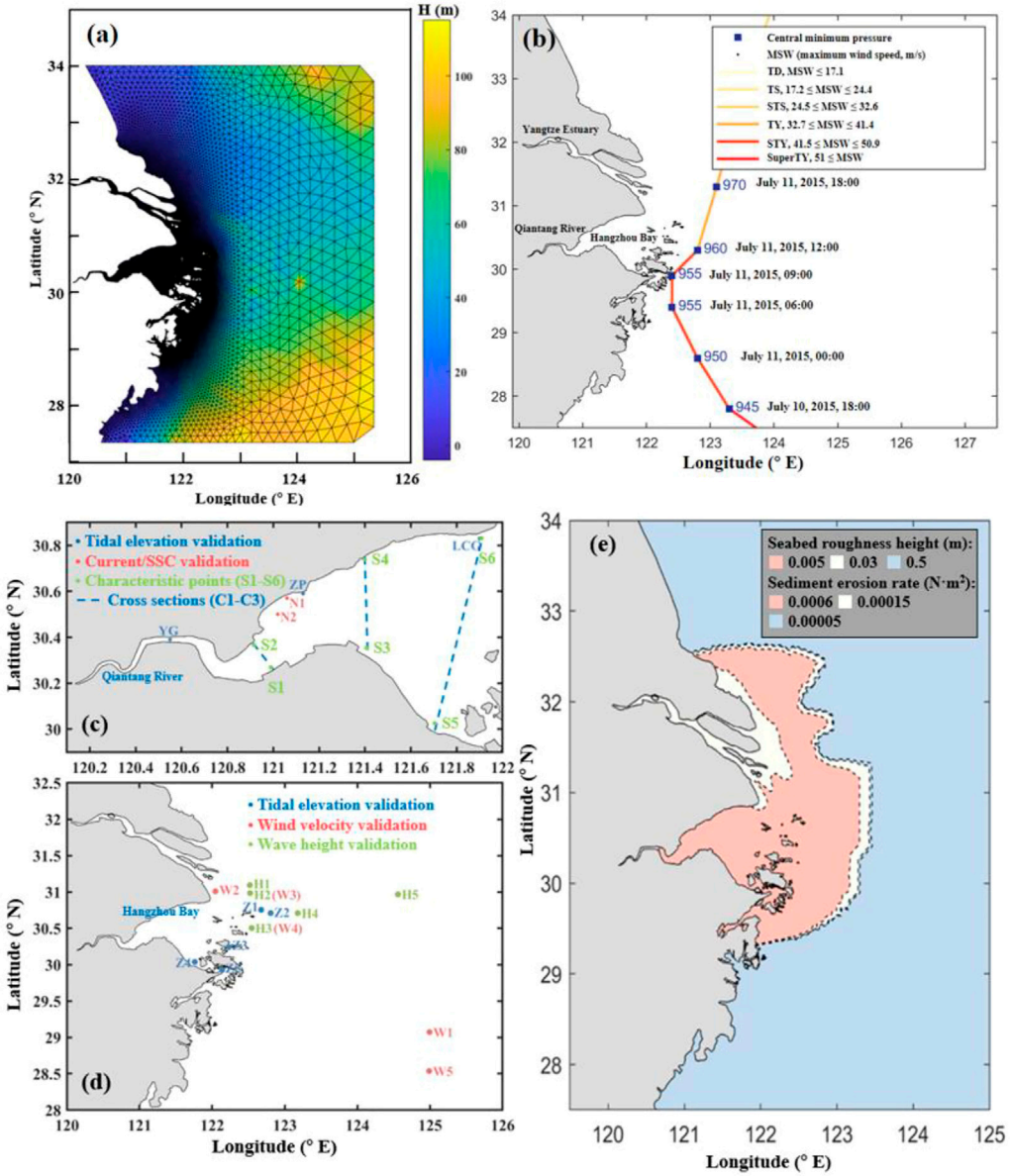

FIGURE 1
(A) Model domain. **(B)** Information of the Typhoon Chan-hom. **(C)** and **(D)** Field stations for model validation. **(E)** Settings for bottom friction.

calculated the bottom stress to analyze the influence mechanism of different factors on the SSC distribution.

2 Methodology

2.1 Model development

2.1.1 Tide-wave model

We used an unstructured grid FVCOM (Chen et al., 2003; Chen et al., 2006) to investigate the impact of typhoons on sediment transport in Hangzhou Bay. We discretized the FVCOM with an unstructured triangular mesh in the horizontal direction and a generalized terrain-following coordinate system in the vertical direction. The finite-volume method ensured the volume and mass conservation of the model. In the model, we adopted the Mellor and Yamada level 2.5 (MY-2.5) turbulence closure scheme to close the equation (Mellor and Yamada, 1982). We used FVCOM-SWAVE to simulate the generation and propagation of the typhoons and waves. This model is based on the third-generation wave model, SWAN, which is based on the Eulerian formulation of the discrete

spectral balance of action density (Booij et al., 1999). The equations governing the model are as follows:

$$\frac{\partial Du}{\partial x}+\frac{\partial Dv}{\partial y}+\frac{\partial w}{\partial \sigma}+\frac{\partial \zeta}{\partial t}=0$$

$$\frac{\partial uD}{\partial t}+\frac{\partial u^2D}{\partial x}+\frac{\partial uvD}{\partial y}+\frac{\partial uw}{\partial \sigma}-fvD = -gD\left[\frac{\partial(\zeta)}{\partial x}+\frac{1}{\rho_0}\left(\frac{\partial}{\partial x}\left(D\int_{\sigma}^{0}\rho d\sigma\right)+\sigma\rho\frac{\partial D}{\partial x}\right)\right]-D\frac{\partial(P_{atm})}{\partial x}+\frac{1}{D}\frac{\partial \tau_x}{\partial \sigma}+DF_u+R_x$$

$$\frac{\partial vD}{\partial t}+\frac{\partial uvD}{\partial x}+\frac{\partial v^2D}{\partial y}+\frac{\partial vw}{\partial \sigma}+fuD = -gD\left[\frac{\partial(\zeta)}{\partial y}+\frac{1}{\rho_0}\left(\frac{\partial}{\partial y}\left(D\int_{\sigma}^{0}\rho d\sigma\right)+\sigma\rho\frac{\partial D}{\partial y}\right)\right]-D\frac{\partial(P_{atm})}{\partial y}+\frac{1}{D}\frac{\partial \tau_y}{\partial \sigma}+DF_v+R_y$$

where x, y, and σ are the east, north, and vertical coordinates in the σ coordinate system, respectively; t is the time; u, v, and w are the velocity components in the three directions, respectively; $D = h + \zeta$ is the total water depth; f is the Coriolis force parameter; ρ is the sea water density; P_{atm} is atmospheric pressure; g is the gravitational acceleration; K_m is the vertical eddy viscosity coefficient; K_h is the vertical thermal vortex friction coefficient; τ_x and τ_y represent the turbulent stress term; R_x and R_y represent the wave radiation stress terms.

2.1.2 Sediment model

The sediment model in FVCOM (Wang, 2002; Ye, 2019) further considers the influence of sediment on water density, the influence of floating mud on bottom friction, and the flocculation and sedimentation processes.

1) The suspended sediment boundary conditions are described as follows:

$$K_H\frac{\partial C}{\partial z}=0, z=\zeta$$

$$K_H\frac{\partial C}{\partial z}=E-D, z=-H$$

where E is the sediment resuspension flux and D is the bottom sediment deposition flux.

$$D=C_b\omega_b$$

where C_b is the bottom SSC and ω_b is the bottom sediment settling velocity.

$$E\begin{cases}0, \tau_b<0.52\tau_{ce}\\ E_0(1-P_b)\left(\frac{\tau_b}{\tau_{ce}}-1\right), \tau_b>1.70\tau_{ce}\\ E_b(1-P_b)\left[-0.144\left(\frac{\tau_b}{\tau_{ce}}\right)^3+0.904\left(\frac{\tau_b}{\tau_{ce}}\right)^2-0.823\frac{\tau_b}{\tau_{ce}}+0.204\right], 0.52\tau_{ce}<\tau_b<1.70\tau_{ce}\end{cases}$$

where E_0 is the sediment erosion rate, P_b is the porosity, τ_b is the bottom shear stress, and τ_{ce} is the critical shear stress (Van Prooijen and Winterwerp, 2010).

$$\tau_b=\rho C_d|u_b|u_b$$

where u_b denotes the bottom velocity, ρ denotes the water density, and C_d denotes the bottom friction coefficient.

$$C_d=\frac{\kappa^2}{(\ln(h/z_0+1)-1)^2}$$

where κ =0.4 is the von Karman constant, h is the water depth, and z_0 is the roughness height (Koutitas, 1988).

2) Water-sediment density coupling. The high SSC affects the vertical distribution of water density in Hangzhou Bay. The influence of SSC on water density reflects the influence of sediments on water stratification.

$$\rho=\rho_w+\left(1-\frac{\rho_w}{\rho_s}\right)C$$

where ρ_w is the water density without sediment and ρ_s is the sediment density (Winterwerp, 2001).

3) Effect of mud. Mud often occurs in Hangzhou Bay when the water flow velocity is low owing to the high sediment content. The rheological and consolidation characteristics of mud have a substantial effect on the bottom boundary layer. Referring to Wang et al. (2005), we introduced the flux Richardson number in the turbulent closed equation into the friction coefficient equation to reduce C_d to reflect the drag reduction effect of mud on the bottom boundary layer.

$$C_d=\frac{\kappa^2}{\left(1+AR_f\right)^2(\ln(h/z_0+1)-1)^2}$$

where A=5.5 is the empirical parameter; R_f is the Richardson number, which is related to the vertical density gradient.

$$R_f=-\frac{g}{\rho}\frac{\partial \rho}{\partial z}\frac{K_h}{K_m\left[(\partial u/\partial z)^2+(\partial v/\partial z)^2\right]}$$

where K_m is the vertical eddy viscosity coefficient.

4) Flocculation sedimentation. Fine sediment is easily flocculated at a high SSC. Sediment settles in the form of flocs, which is different from a single particle. Shi et al. (2008) found that, by comparing various flocculation settlement formulas, the suspended sediment flocculation settlement formula proposed by Cao and Wang (1994) is the most suitable for numerically simulating suspended sediment near the Yangtze River estuary. Therefore, we used the settling velocity formula proposed by Cao and Wang (1994) for the sediment model,

$$w_s = w_{s0}\frac{1 + c_2 C^{m2}}{1 + c_1 U^{m1}} \times k_s$$

where w_{s0} is the settling velocity of a single particle; U is the current velocity; and c_1, c_2, $m1$, $m2$, and k_s are empirical parameters.

5) Thickness of erosion and deposition. We used the following relationship (Harris and Wiberg, 1997) to represent the active-layer thickness of the bottom sediment:

$$z_a = \max\left[k_1\left(\tau_{sf} - \tau_{ce}\right)\rho_0, 0\right] + k_2 D_{50}$$

where τ_{sf} is the maximum surface friction stress produced by wave–flow interaction, τ_{ce} is the critical stress, D_{50} is the median grain size of surface sediment, z_a is the active layer thickness, and k_1 = 0.007 and k_2 = 6.0 are the empirical parameters.

2.1.3 Wind data reconstruction

We used the Fujita–Takahashi formula (Wang et al., 1991) and reanalyzed ECMWF wind field data to reconstruct the pressure and wind fields for the wave–current–sediment coupling model. Fujita-Takahashi pressure field formula:

$$P(r) = P_\infty - \frac{P_\infty - P_0}{\sqrt{1 + 2(r/R)^2}} \quad 0 \le r \le 2R$$

$$P(r) = P_\infty - \frac{P_\infty - P_0}{1 + r/R} \quad 2R \le r \le \infty$$

where P_∞ is the typhoon peripheral pressure (P_∞ = 1013.2 MPa), P_0 is the typhoon center pressure, r is the distance from the point to the center of the typhoon, and R is the maximum wind radius.

After we constructed the pressure field, we used the gradient wind formula to calculate the corresponding wind field distribution according to the pressure distribution. The gradient wind formula is:

$$V_g = -\frac{1}{2}fr + \left[\left(\frac{1}{2}fr\right)^2 + \frac{r}{\rho_a}\frac{\partial P}{\partial r}\right]^{1/2}$$

where f Coriolis force parameter and ρ_a is the air density.

Selecting the maximum wind radius R is key to calculating the typhoon field in a typhoon simulation. We adopted the empirical formula (Li, 1987) in this study for calculation, and verified and adjusted the formula according to the measured wave data:

$$R = 28.52\tanh\left[0.0873(\phi - 28)\right] + 12.22/\exp\left[(1013.2 - P_0) \times /33.86\right] + 0.2V_c + 37.22$$

where ϕ and V_c are the latitude and velocity of the typhoon center, respectively.

Finally, we superimposed the gradient wind field and ECWMF background wind field with a certain weight to construct a new synthetic wind field:

$$W(r) = EW(r)_{ECMWF} + (1 - E)V_g(r)$$

where $W(r)$ is the synthetic wind field, $W(r)_{ECMWF}$ is the ECMWF background wind field, and E is the superimposed weight coefficient.

$$E = \frac{C^4}{1 + C^4}$$

$$C = \frac{r}{nR_{\max}}$$

where n = 9 is the same as in (Liu et al., 2013).

The velocity components of the synthetic wind field are

$$u = -W(r)\sin\theta; \quad v = W(r)\cos\theta$$

where u is the east–west directional velocity component, v is the south–north directional.velocity component, and θ is the angle between the line of the calculation point and.

typhoon center and the direction due east.

We selected the field wind data at five stations (W1 were selected W5) to validate the reconstructed wind fields. The field data period ranged from July 1 to 15, 2015, including July 10 to 12, when Hangzhou Bay was affected by Typhoon Chan-hom (Figure 1B). Few wind field data during typhoons are available, whereas the reconstructed wind field data effectively increased the accuracy of the wind speed prediction during typhoons, the values of which were closer to the field data (Figure 2). The reconstructed wind field data more accurately fit the trajectory and center of the typhoon (Figure 3). The modified wind field data have a higher temporal resolution (1 h) during typhoons than the ECMWF data (6 h).

2.2 Model domain and configurations

We used an unstructured triangular mesh for the model domain covering the Yangtze River estuary, Hangzhou Bay, Zhoushan Archipelago, and most of the East China Sea (120°–125.5° E, 27.5°–34° N), with 60,441 nodes and 114,211 cells. We varied the horizontal resolution of the mesh from 100 to 200 m in Hangzhou Bay and the Zhoushan Archipelago to approximately 30 km at the open boundary to consider both calculation efficiency and accuracy. We vertically divided the water column into 11 uniform sigma layers. To refine the study area with notable changes in water and sediment elements, we set the proportion of each layer to the total water depth to 0.0, −0.02, −0.08, −0.18, −0.32, −0.5, −0.68, −0.82, −0.92, −0.98, and −1.0. We obtained eight major astronomical tidal constituents (K1, O1, P1, Q1, M2, S2, N2, and K2) from TPXO8 for tidal forcing (Egbert and Erofeeva, 2002). We set the initial temperature and salinity to 20°C and 30‰, respectively, because of the short-term nature of

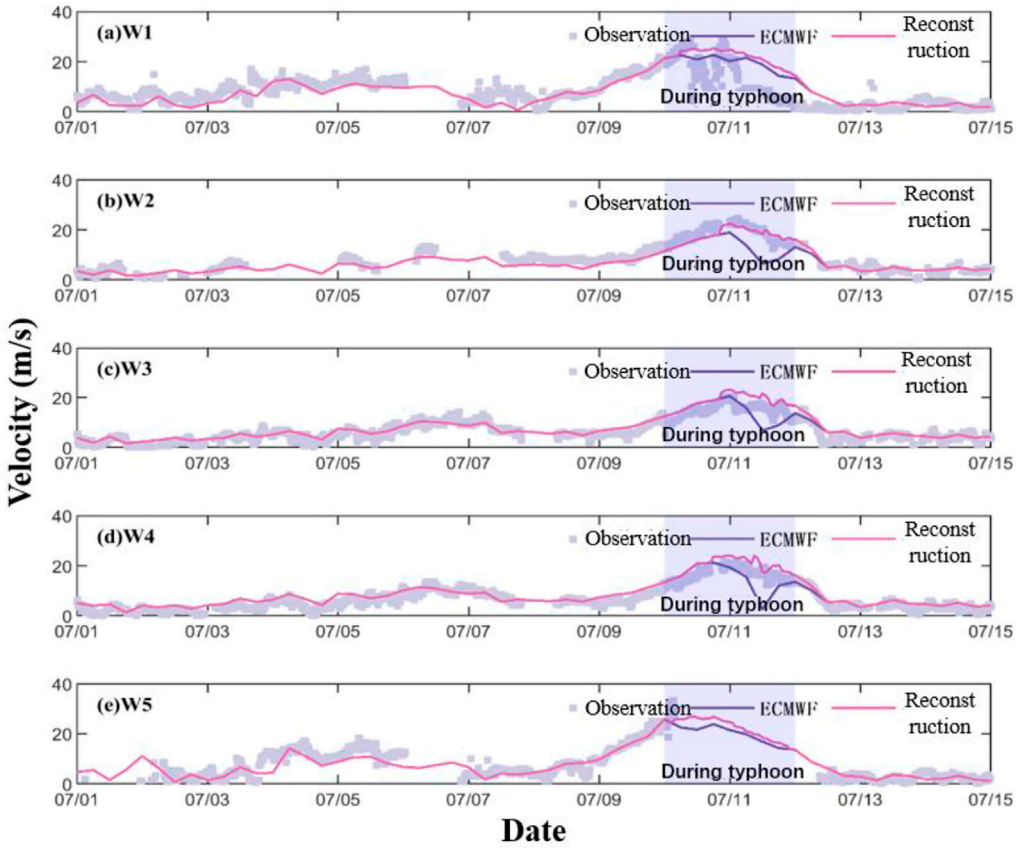

FIGURE 2
Synthetic wind field data (purple lines) vs. ECMWF wind field data (blue lines) vs. observational data (gray dots) at the five stations W1 to W5.

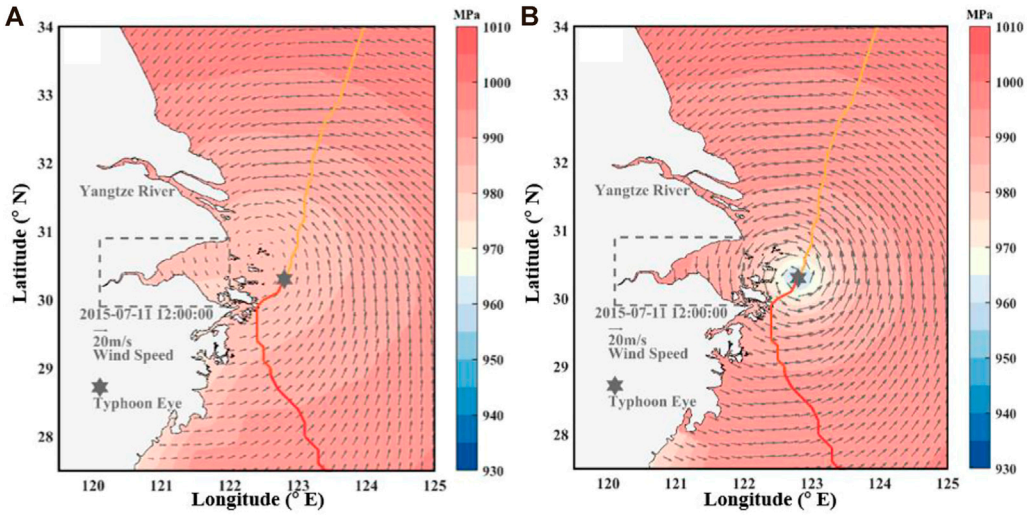

FIGURE 3
Comparison of **(A)** ECMWF and **(B)** synthetic wind field distribution (11 July 2015, 12:00:00).

TABLE 1 Main parameters of the sediment and wave models.

Parameters	Value
Wave spectral resolution	20×30
Wave frequency	0.04–0.4 Hz
Median particle size	0.008 mm
Porosity	0.5
Critical shear stress for erosion	0.1 N m^2
Seabed roughness height	0.005 (red area), 0.03 (white area), 0.5 (blue area) in Figure 1E
Sediment erosion rate	0.0006 (red area), 0.00015 (white area), 0.00005 (blue area) in Figure 1E

the simulation. We considered only viscous sand for the sediment. We set the median particle size and critical shear stress for erosion to 0.008 mm and 0.1 Nm^2, respectively (Pan et al., 2013). Because of the difference of the particle size of the bottom sediment (Pan et al., 2013; Zhang et al., 2013) and the influence of the floating mud in the simulation area, Hangzhou Bay, we then determined the initial sediment erosion rate (E_0) and seabed roughness height (Z_0) by region (Ye, 2019) (Figure 1 and Table 1).

2.3 Model validation

We divided the validation of the model into two parts: validation of tidal currents and SSC during calm weather (March 1 to 31, 2013) and validation of tidal currents and wave heights during a typhoon (June 28 to 15 July 2015). We validated the model using multiple observational datasets, including the tidal elevation at seven stations (YG, ZP, and LCG, March 1 to 31, 2013; Z1, Z2, Z3, Z4, and Z5, June 28 to 15 July 2015); currents and SSC at two stations (N1 and N2) from March 1 to 31, 2013; substantial wave heights at five stations (H1, H2, H3, H4, and H5) and wind velocities at five stations (W1, W2, W3, W4, and W5) during Typhoon Chan-hom. The measured data were provided by Shanghai Typhoon Research Institute. The measured data used in this paper were provided by the Shanghai Meteorological Service, the Center for Numerical Prediction and Innovation, and the Zhejiang Marine Monitoring and Forecasting Center (He et al., 2020).

We used the correlation coefficients (*CC*) and model evaluation coefficient (*Skill*) (Murphy, 1992) to evaluate the credibility and accuracy of the model.

$$CC = \frac{1}{N}\sum_{i=1}^{N}\frac{(m_i - \bar{m})(O_i - \bar{O})}{S_m S_o}$$

$$Skill = 1 - \frac{\sum_{i=1}^{N}(m_i - O_i)^2}{\sum_{i=1}^{N}(O_i - \bar{O})^2}$$

TABLE 2 Model validation.

Tidal elevation

Station	Z1	Z2	Z3	Z4	Z5
Skill	0.98	0.98	0.97	0.97	0.98
CC	0.97	0.98	0.96	0.97	0.96

Current velocity and direction

Station	Currents	*Skill*	*CC*
H4	Velocity	0.88	0.81
	Direction	0.82	0.67

Waves

Station	H1	H2	H3	H4	H5
Skill	0.97	0.96	0.97	0.97	0.95
CC	0.95	0.93	0.96	0.96	0.94

SSC

Tide	Station	Layers	*Skill*	*CC*
Neap	N1	Surface	0.52	0.49
		Middle	0.67	0.49
		Bottom	0.64	0.38
	N2	Surface	0.42	0.10
		Middle	0.63	0.49
		Bottom	0.86	0.79
Spring	N1	Surface	0.42	0.18
		Middle	0.80	0.52
		Bottom	0.53	0.21
	N2	Surface	0.57	0.28
		Middle	0.58	0.33
		Bottom	0.77	0.63

where m_i and O_i are the simulated and observed data, respectively; $\bar{m}$ and $\bar{O}$ are the average values of the simulated and observed data, respectively; and S_m and S_o are the standard deviations of the simulated and observed data, respectively. A model has high credibility when *Skill* > 0.5 (Murphy, 1992; Allen et al., 2007).

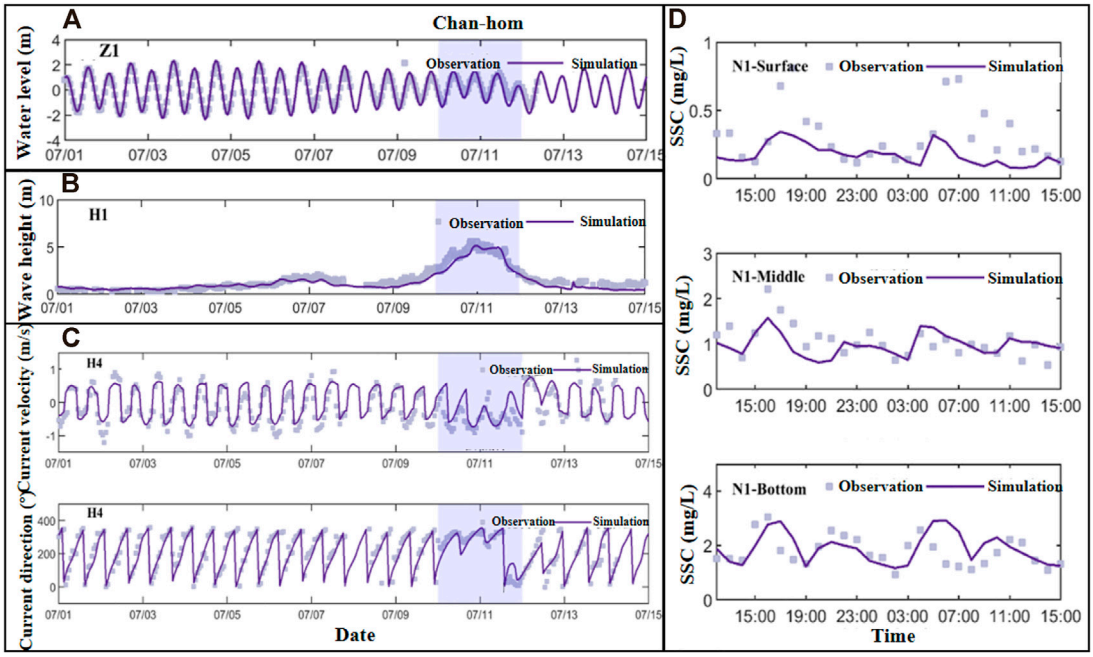

FIGURE 4
Model validation for **(A)** sea surface level, **(B)** significant wave height, **(C)** current magnitude and direction, and **(D)** suspended sediment concentration.

2.3.1 Tides and currents

The simulated tidal elevation was in good agreement with observational data. The *Skill* and *CC* of LCG and ZP were above 0.96. Station YG is vulnerable to tidal surges because it is located upstream of the Qiantang River estuary. Therefore, the *Skill* and *CC* at this station were relatively low, 0.84 and 0.70, respectively (Ye, 2019).

We used observational tidal elevation data at five stations (Z1, Z2, Z3, Z4, and Z5, which are the blue points in Figure 1E) to validate the tide elevation during Typhoon Chan-hom. The values of *Skill* and *CC* in Table 2 and Figure 4 show that the simulated values and observational data of tidal elevation fit well at all five stations.

We obtained the current velocity data from two stations (N1 and N2, which are red points in Figure 1E). We obtained high quality validation results for current velocity and direction for each layer at N1 and N2 stations. The *CC* and *Skill* of each layer of current velocity during the neap tide (12:00 on March 6 to 16:00 7 March 2013) were above 0.9. The minimum *CC* of each layer in the current direction was 0.78 and *Skill* was greater than 0.84. The simulation results were relatively poor during spring tide (8: 00 March 12 to 9:00 13 March 2013), and the minimum *Skill* and *CC* were 0.82 and 0.66, respectively (Ye, 2019).

We obtained current data on typhoon weather from station H4. The *Skill* and *CC* of the current velocity were 0.88 and 0.81, respectively; those of the current direction were 0.82 and 0.67, respectively. In general, the results of the current validation were good.

2.3.2 Waves and SSC

The *Skill* of the substantial wave heights was higher than 0.95, and the *CC* was higher than 0.93. Overall, the simulated wave height values matched the observational data well, so we found that the model was able to accurately simulate the process of wave generation and extinction during typhoons, laying a suitable foundation for analyzing the effect and influence of waves.

The SSC validation results at stations N1 and N2 were consistent with the vertical distribution of the actual SSC. The model accurately reflected the trend in the variation in SSC over time. The *Skill* of SSC in the surface layer were lower than those in the other two layers. When the SSC was large, the simulated surface SSC at N1 (Figure 4) was smaller than the measured data. The N1 station is nearshore. The instantaneous SSC at station N1 is subject to various factors, which would impact the model validation. Moreover, we ignore wave-current interaction and wind during calm weather, which may result in low surface SSC. In general, the quality of the results of SSC validation were not as high as those of hydrodynamic validation. The simulation results met the reliability requirement that the *Skill* value be greater than 0.5. Therefore, based on the model results, we studied the sediment dynamic characteristics during a

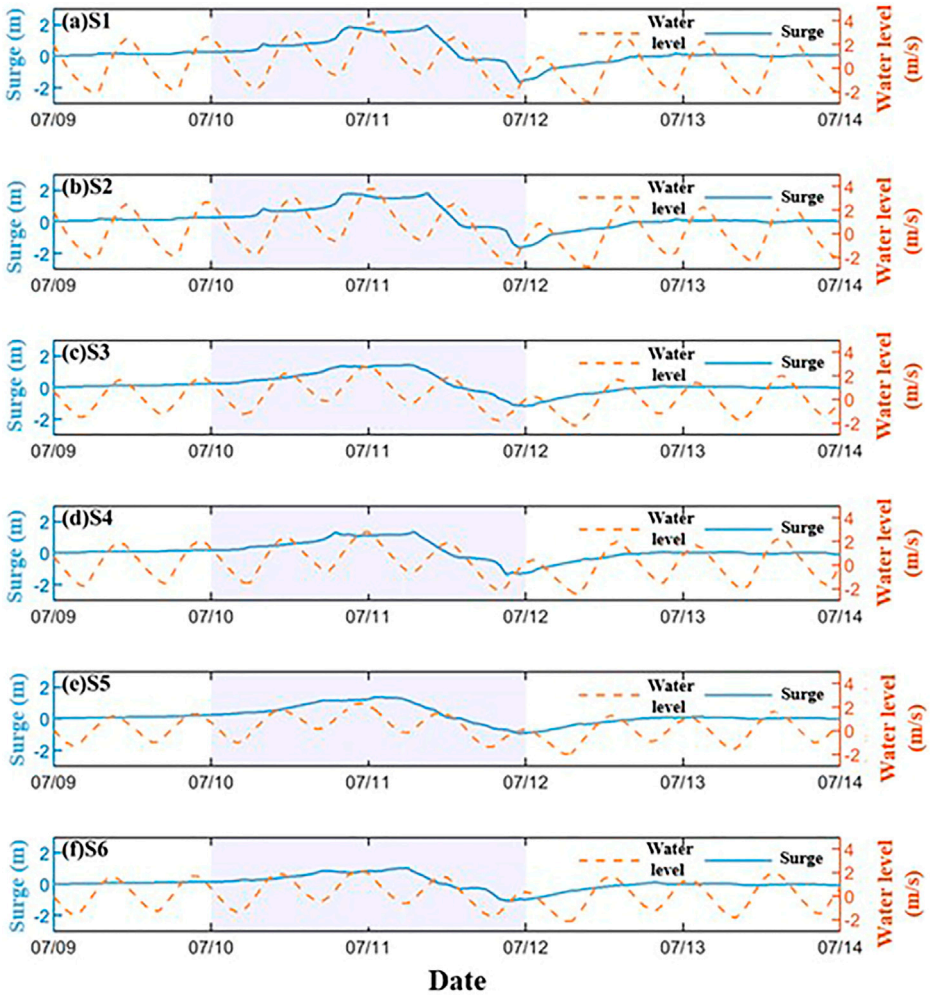

FIGURE 5
Comparison between surge and water level from July 9 to 14 July 2015 at stations **(A–F)** stations S1 to S6, respectively. Surge is the water level difference between Case0 and Case4.

typhoon in Hangzhou Bay. More information about the model validation was provided by Yu (2020) and He et al. (2020).

2.4 Sediment flux

Sediment flux is one of the main parameters used to study sediment transport. We believe that sediment is mainly transported by current. So, we use the current velocity and SSC of each layer to calculate sediment flux at different locations in the paper, and then we integrate it over time to get the net flux.

$$SedFlux = \sum_{T}\sum_{i=1}^{N} v_i \cdot SSC_i$$

where v_i and SSC_i are the current velocity of each layer; T is the integral time.

3 Results

We analyzed the surge characteristics and SSC in Hangzhou Bay before and after the typhoon based on the results of the model. To facilitate the analysis, we selected six characteristic points (S1–S6) and three cross-sections (C1–C3) in Hangzhou Bay, and divided the bay into three parts: the top (TB), center (CB), and mouth (MB) of the bay.

3.1 Surge

The maximum water levels (4.03, 3.98, 2.93, 2.96, 2.44, 2.33 m at S1 to S6, respectively) all occurred during high slack water. We found that the difference in water levels between the northern and southern shores in the same section was small. Similarly, the

maximum surge values at S1 to S6 were 2.04, 1.95, 1.55, 1.42, 1.50, and 1.10 m, respectively. The surges on the southern shore were larger than those on the northern shore. The surges in the MB were smaller than those in the CB and TB. From the MB to TB, the maximum surge occurred approximately 2 h later. As the typhoon approached, the peak surge advanced from the MB to the TB (Figure 5).

With the gradual approach of the typhoon, the water level at MB was the first to increase. Subsequently, the surge propagated to the CB and TB. The maximum sea surface levels at the MB and CB were 2.5 and 3.5 m, respectively. At 1:00 on 11 July 2015, the sea surface level at the TB was 4.0 m at C1. Similarly, the maximum surge advanced from the MB to the TB, with the maximum surge of approximately 1.2 m at C3 in the MB and up to 1.5 m at C2 in the CB, and finally reached a maximum of 3.0 m in the TB at 00:00 on 11 July 2015. The typhoon affected the surge to a lesser extent, which was always smaller in the MB because the MB is wide and deep, so the geomorphology had a lesser effect here than at the TB. The bay is sheltered from the impact of typhoons by the Zhoushan Islands. The maximum surge was mainly related to the distance between typhoon and Hangzhou Bay. The maximum water level was predominantly influenced by the tidal level. The time of the maximum tidal level at each point was later than the time of the maximum surge. So, the surge increased before the water level and the maximum surge occurred earlier than the maximum water level. More information about the sea surface level, surge, currents, and waves was provided by Yu (2020) and Li et al. (2022).

3.2 SSC

As the typhoon approached, the SSC increased in most areas of the bay (Figures 6A,B). In the southern part of the MB, the SSC at the surface and bottom layers was always approximately 1 g/L. The high-SSC area in the middle of the MB gradually expanded northward. Finally, the surface and bottom SSC in the northern part of the MB reached 5 and 10 g/L, respectively. Similar to the MB, the SSC in the CB extended from the southern shore to the north. The surface and bottom SSC increased from 2.5 to 4.5 and 5–12 g/L, respectively. The cross-section of the TB was narrow, so the SSC substantially changed under the influence of the typhoon. During the typhoon, the SSC throughout the water column in the TB increased, with the surface and bottom SSC reaching 5.5 and 14 g/L, respectively.

Comparing the surface and the bottom SSC distribution on 10 July 2015 at 23:00, when the typhoon had the strongest impact on the SSC in Hangzhou Bay, we found that the temporal and spatial SSC distributions in the surface water layer were basically the same as in the bottom layer, but the SSC in the surface layer was only approximately 30% of that in the bottom layer (Figures 6C,D). The high SSC in Hangzhou Bay was mainly distributed in the shoal and northern-central parts of the MB. The SSC in Hangzhou Bay was relatively low before and after typhoon, and typhoon increased it. Before the typhoon, the area with high SSC was distributed in the TB and northern shore of the bay. After typhoon, the area with high SSC in the bay moved to the southern shore (Figure 7).

In the ebb and flood periods, the difference in the vertical SSC in each section was large, and the bottom SSC was more than 10 times larger than at the surface (Figure 8), which may cause turbidity currents near bottom. The minimum SSC occurred owing to the low water velocity during high and low water. The water in section C1 was shallow and narrow. Therefore, the peak SSC in section C1 was larger than that in sections C2 and C3. The SSC near the southern shore was larger than that near the northern shore in section C2 at peak ebb and peak flood. The SSC of C3 section was higher near the northern shore than near the southern shore at the peak flood tide, and reversed at the peak ebb tides because the northern and southern shores were the main flood and ebb tidal channels, respectively.

3.3 Sediment flux

We calculated the net sediment fluxes during the foreruner, main shock, and aftershock periods, and the results are shown in Figure 9. In the foreruner period, suspended sediment was transported into the bay mainly through the middle and northern parts of the MB from the open sea, and the SSC was generally small. The SSC of the southern shore of the CB was relatively large. During the mainshock of the typhoon, large amounts of suspended sediment were transported from the middle and northern parts of the MB to the bay, most of which was transported to the southern shore of Hangzhou Bay and the Zhoushan Islands. A small portion was transported to the bay, reaching the CB and even the TB. The SSC on the southern shore of the CB was large (80–100 kg/m^3). During the aftershock period, the SSC net flux differed from that in the previous two periods. Overall, suspended sediment was transported from within the bay to the open sea. The sediment flux on the southern shore of the MB was large. Hence, during the typhoon, the transport of suspended sediment in Hangzhou Bay was similar to that during the main shock period. Suspended sediment was transported through the middle and northern parts of the MB from the open sea to the bay. Most of the sediment was transported to the southern shore of the MB and the Zhoushan Islands, and a small portion was transported upstream. The sediment flux on the southern shore of the CB was large. Therefore, the typhoon led to a substantial increase in the SSC on the southern shore of the CB and MB and the Zhoushan Islands.

4 Discussion

During typhoons, SSC is affected by many factors such as wind stress, atmospheric pressure, and waves. To examine the impact of

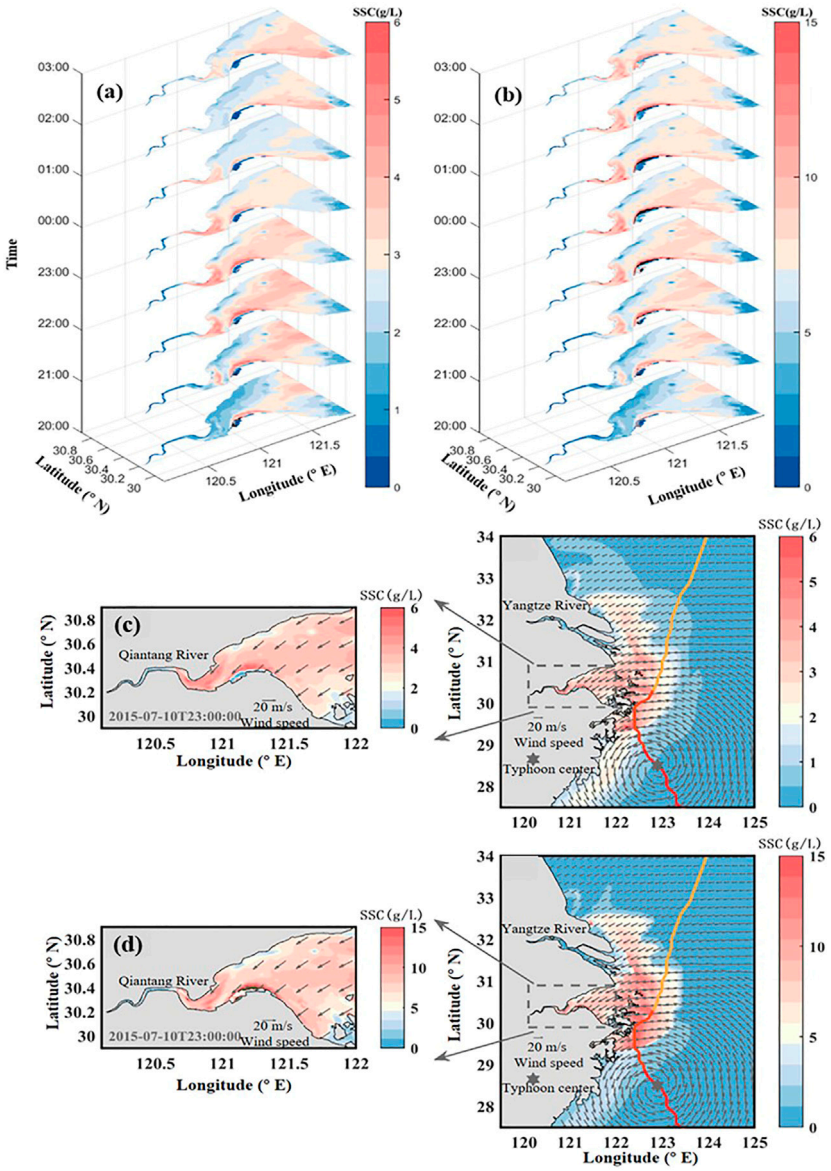

FIGURE 6
Time-series of SSC distribution in the surface and bottom layer (20:00 on 10 July 2015 to 03:00 11 July 2015): **(A)** surface and **(B)** bottom layers. SSC distribution in the **(C)** surface and **(D)** bottom layers at 23:00 on 10 July 2015. The vector indicates wind.

various factors on the change in SSC, we conducted various numerical tests in this study, as shown in Table 3. We analyzed the effects of various factors on the SSC during a typhoon by comparing the test results under different driving forces. Case 0 was the control group. In the Case 1, we turned off all the wind field input. During the typhoon, atmospheric pressure changes greatly over the sea, so we turned off the atmospheric pressure field input in the Case 2 to study its influence on the SSC. In the Case 3, we turned off the wave model. For the Case 1–3, the tidal forcing still existed (the water level on the open boundary). In the Case 4, we only considered the effect of tide on the SSC, that is, we only gave the tidal forcing to the model. In the Case 5, we canceled the tidal forcing on the open boundary (there were no water level change on the open boundary). In all cases, we didn't consider the current input on the open boundary.

4.1 Correlation of bottom stress and SSC

Before Typhoon Chan-hom, current-induced bottom stress was dominant, and the wave-induced bottom stress was close to zero during calm weather (Figure 10). The difference between surface

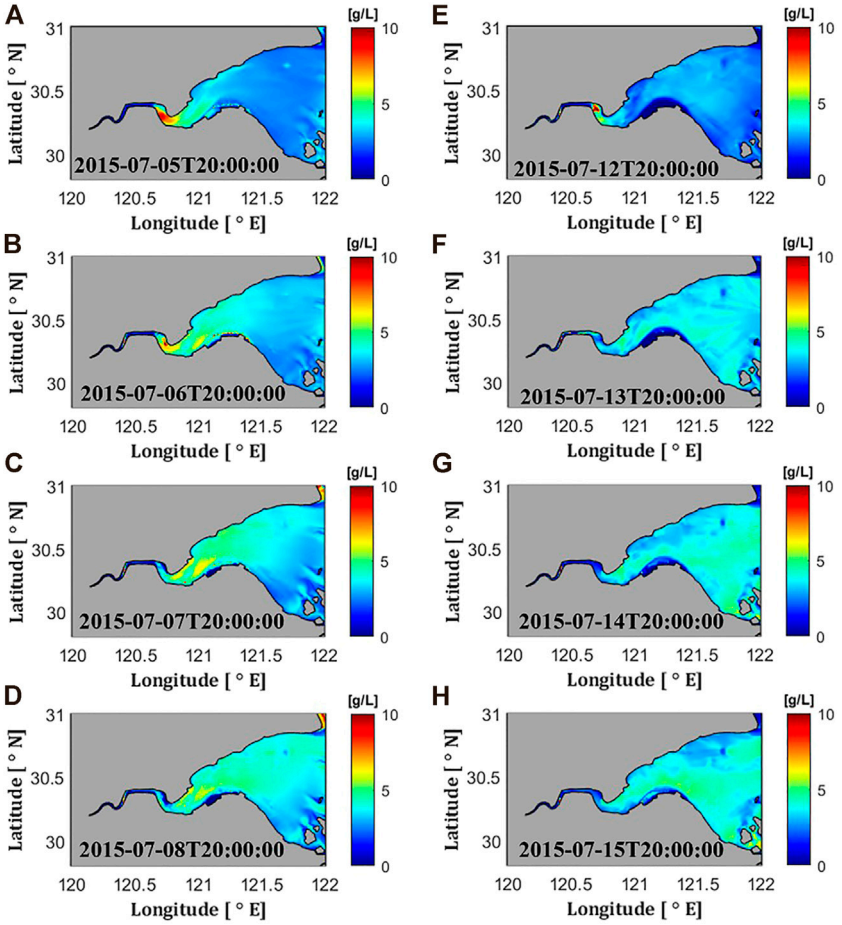

FIGURE 7
Bottom SSC condition in the calm period before typhoon **(A–D)** and after typhoon **(E–H)**.

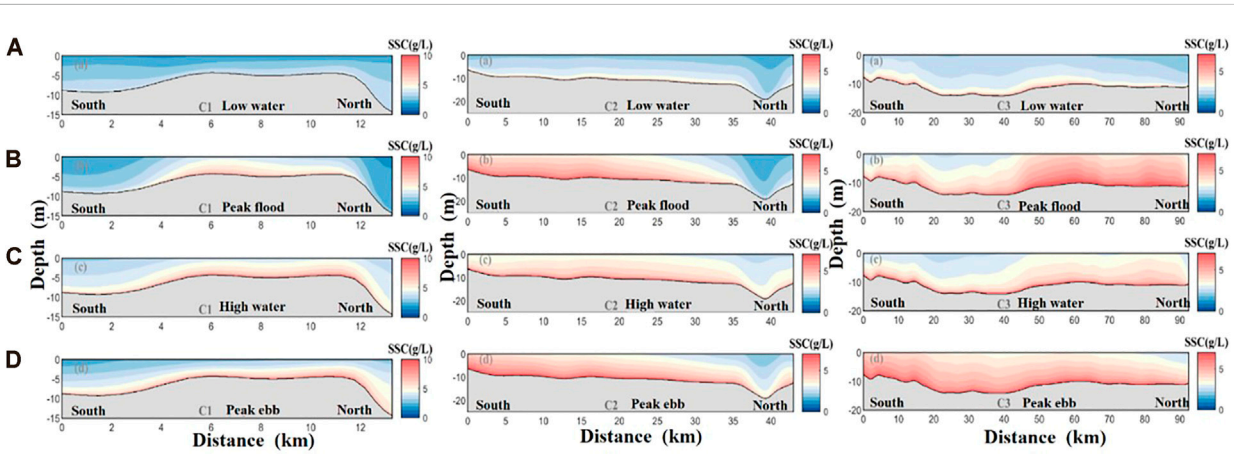

FIGURE 8
Vertical SSC distribution at C1, C2, and C3 cross-sections: **(A)** low water, **(B)** peak flood, **(C)** high water, and **(D)** peak ebb.

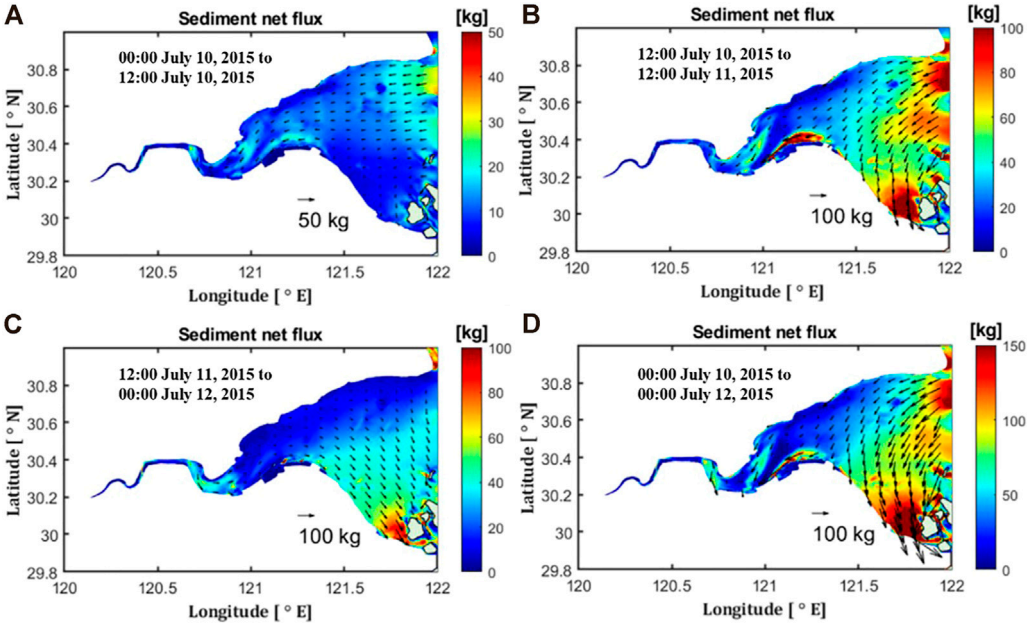

FIGURE 9
Net sediment flux during Typhoon Chan-hom: **(A)** forerunner, **(B)** main shock, **(C)** aftershock, and **(D)** whole typhoon periods.

TABLE 3 Forcings considered in the numeric tests.

Forcing	Case 0	Case 1	Case 2	Case 3	Case 4	Case 5
Wind	√	×	√	√	×	√
Wave	√	√	√	×	×	√
Atmospheric pressure	√	√	×	√	×	√
Tide	√	√	√	√	√	×
Sediment	√	√	√	√	√	√
Wave	√	√	√	×	×	√

SSC and bottom SSC was significantly smaller than that during typhoon. However, the bottom SSC substantially increased during the typhoon, and the maximum bottom SSC was 10 g/L among the six stations. The surface SSC simultaneously increased by less than 5 g/L. Therefore, the difference between the surface and bottom SSC increased because waves had a considerable impact on the bottom SSC during the typhoon. During the typhoon, wave-induced bottom stress remarkably increased from 5 to 10 Pa. The current velocity and current-induced bottom stress simultaneously slightly increased. We found modest difference between the current-induced bottom stress during calm (0–1 Pa) and typhoon weather (2 Pa). Therefore, the increase in the bottom stress under the combined action of waves and current substantially increased the bottom SSC. The surface SSC was impacted by the suspension of sediment, so the surface SSC also increased with bottom SSC.

When the typhoon center was located southeast of Hangzhou Bay (11 July 2015 at 01:00), the SSC reached its maximum and an ebb current was present in Hangzhou Bay (Figure 11). The current velocity on the southern shore was higher than that on the northern shore, and the current velocity at MB was higher than that at TB. Therefore, the current-induced bottom stresses on the south and north shores were 2 and 0.5 Pa, respectively. The current-induced bottom stresses at MB were 0.5–2 Pa, and no more than 0.5 Pa at TB. In the Qiantang River, the current-induced bottom stress was 4 Pa because the waterway was narrow.

The wave-induced bottom stress during the typhoon was similar to that under the combined effect of waves and currents; therefore, waves had the dominant influence on bottom stress during the typhoon (Figures 11C,E). The magnitude of wave-induced bottom stress is mainly determined by the bottom roughness, wave height, and water depth. In this study, the

TABLE 4 Characteristic SSC caused by wind stress.

Station	Max. Surface SSC for case 0 (g/L)	Surface max. SSC (g/L)					
		Wind stress		Air pressure		Wave	
		SSC (g/L)	Ratio (%)	SSC (g/L)	Ratio (%)	SSC (g/L)	Ratio (%)
S1	3.11	1.68	53.82	0.02	0.69	1.95	62.79
S2	3.34	1.55	46.26	0.05	1.64	1.98	59.31
S3	4.33	2.90	66.90	0.11	2.60	3.90	89.95
S4	2.54	1.53	60.39	0.06	2.18	2.04	80.44
S5	4.17	3.31	79.45	0.06	1.48	3.61	86.56
S6	2.92	1.72	58.77	0.05	1.81	2.12	72.61
Station	Max. bottom SSC for Case 0 (g/L)	Bottom max. SSC (g/L)					
		Wind stress		Air pressure		Wave	
		SSC (g/L)	Ratio (%)	SSC (g/L)	Ratio (%)	SSC (g/L)	Ratio (%)
S1	7.00	4.88	69.48	0.10	1.41	4.38	62.45
S2	5.9	2.88	48.36	0.07	1.23	3.13	52.58
S3	10.55	8.78	83.27	0.21	2.03	8.64	81.93
S4	5.84	3.90	66.86	0.11	1.84	4.75	81.32
S5	8.41	6.69	79.47	0.20	2.42	6.22	73.96
S6	6.88	4.97	72.16	0.14	1.98	5.20	75.68

wave-induced bottom stress was low in the open sea, and the maximum was less than 5 Pa because of the high waves and water depth. The wave-induced bottom stress in Hangzhou Bay was restricted by three factors. High bottom stress was mainly distributed in the middle of the MB owing to the large wave height, the Andong shoal (the southern shore of the CB), and the Qiantang River above the TB because of the shallow water. The stress at the Andong Shoal was 10 Pa.

4.2 Influence of wind on SSC

The stress produced by the action of the wind enhanced the lifting of the bottom sediment, mainly by intensifying wave action (Figure 12I-I'). The surface SSC synchronized the variation of bottom SSC with approximately half of the magnitude. In calm weather, the wind is weak and has less influence on the SSC. The surface SSC caused by wind stress (dark blue line) was close to zero, and the bottom SSC (light blue line) was less undulating. During the typhoon, the SSC changed significantly owing to the increase in wind velocity.

The surface SSC and bottom SSC caused by wind stress both increased, with the latter increasing more. This is because the increase in wind force acted directly on the waves and currents, increasing the bottom stress and, thus, the bottom SSC.

Because S3 was located on the Andong Shoal, the SSC at this station was the highest, with a surface and bottom SSC of 4.3 and 10.5 g/L, respectively. The surface and bottom SSC caused by wind stress was 2.9 and 8.78 g/L, respectively. Both Cases 0 and 1 showed that the maximum SSC occurred approximately 00:00 on 11 July 2015. The maximum surface SSC caused by wind stress at stations S1–S6 were 53.8%, 46.3%, 66.9%, 60.4%, 79.5%, and 58.8% of the maximum total surface SSC value, respectively, with a mean value of 60.93%. The ratios of the bottom layer were 69.5%, 48.4%, 83.3%, 66.9%, 79.5%, 72.2%, respectively, with a mean value of 69.9% (Table 4), indicating that the wind stress had a slightly stronger effect on SSC in the bottom layer that in the surface layer.

The bottom stress caused by wind was close to 0 Pa during calm weather. The wind-induced bottom stress was consistent with the increase in the wind-speed curve. The bottom stress at S1–S6 reached a maximum at approximately 00:00 on July 11, which were 3.8, 1.7, 9.7, 2.7, 6.9, and 4.6 Pa, respectively. The maximum wind-induced bottom stresses at S1–S6 were 89.8%, 63.9%, 99.7%, 85%, 98.6%, and 75.2% of the maximum bottom stress in Case 0, respectively, with a mean value of 85.4%. This indicated that wind had a strong effect on bottom stress through wave action and, thus, on the resuspension of sediment.

4.3 Influence of air pressure on SSC

The effect of air pressure on the SSC was explored by comparing the results of Cases 0 and 2 (Figure 12II-II'). Compared with the effect of wind stress on SSC, the effect of

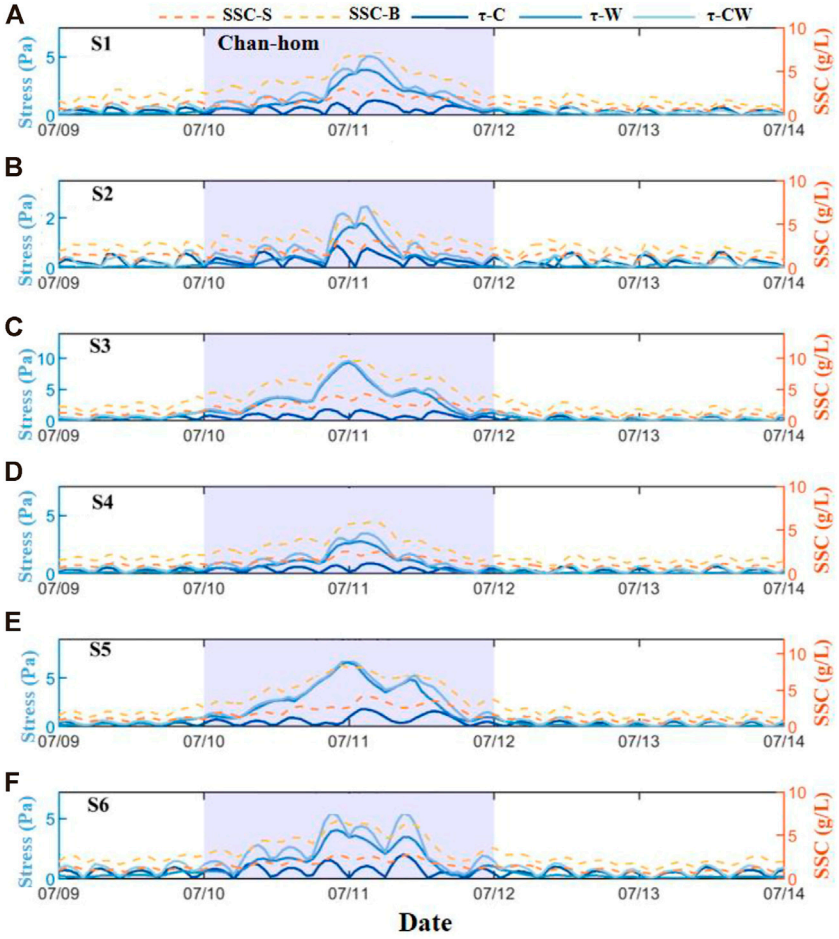

FIGURE 10
Comparison between SSC and bottom stress from July 9 to 14 July 2015 at stations **(A–F)** stations S1 to S6, respectively. SSC-S, surface SSC; SSC-B, bottom SSC; τ-C, current-induced bottom stress; τ-W, wave-induced bottom stress; τ-CW, combined wave- and current-induced bottom stress.

air pressure on SSC was small. The SSC values in the surface and bottom layers owing to air pressure were close to 0. During the typhoon, with the fluctuation in air pressure, the value of the bottom SSC increased slightly, with a small amplitude, within 0.1 g/L.

At stations S1-S6, the ratios of the surface maximum SSC caused by air pressure to the total surface maximum SSC were 0.7%, 1.6%, 2.6%, 2.2%, 1.5%, and 1.8%, respectively, and the mean value was 1.7%. In the bottom layer, the ratios were 1.4%, 1.2%, 2%, 1.8%, 2.4%, 2%, and the mean value was 1.8%, respectively (Table 4). The maximum SSC caused by air pressure variation occurred at station S3. The value was 0.1 g/L in the surface layer and 0.2 g/L in the bottom layer.

During the typhoon, the air pressure decreased significantly, but the bottom stress caused by the air pressure variation was always close to 0, indicating that the influence of air pressure on the bottom stress was far less than that of the wind stress.

4.4 Influence of wave on SSC

Waves have a strong sand-lifting effect, and the presence of waves significantly changes the bottom stress, thus affecting the SSC distribution. The results of SSC in cases 0 and 3 were compared and analyzed to determine the effect of the wave effect on SSC (Figure 12III-III').

In calm weather, the SSC in the surface and bottom layers caused by wave action was similar at different stations, all below 0.5 g/L. During the typhoon, the wave action increased and the SSC increased significantly. The surface SSC increased to 4 g/L and the bottom SSC increased to approximately 3 g/L and 8 g/L, respectively, at different stations. The latter is larger than the former.

The SSC caused by wave action at S3 and S5 reached the maximum at 23:00 on 10 July 2015; the increase in the bottom SSC was 8.6 and 6.2 g/L, respectively. The maximum wave-induced SSC was reached at 00:00 on July 11 at S1, S2, S4, and S6, where the increase in surface SSC

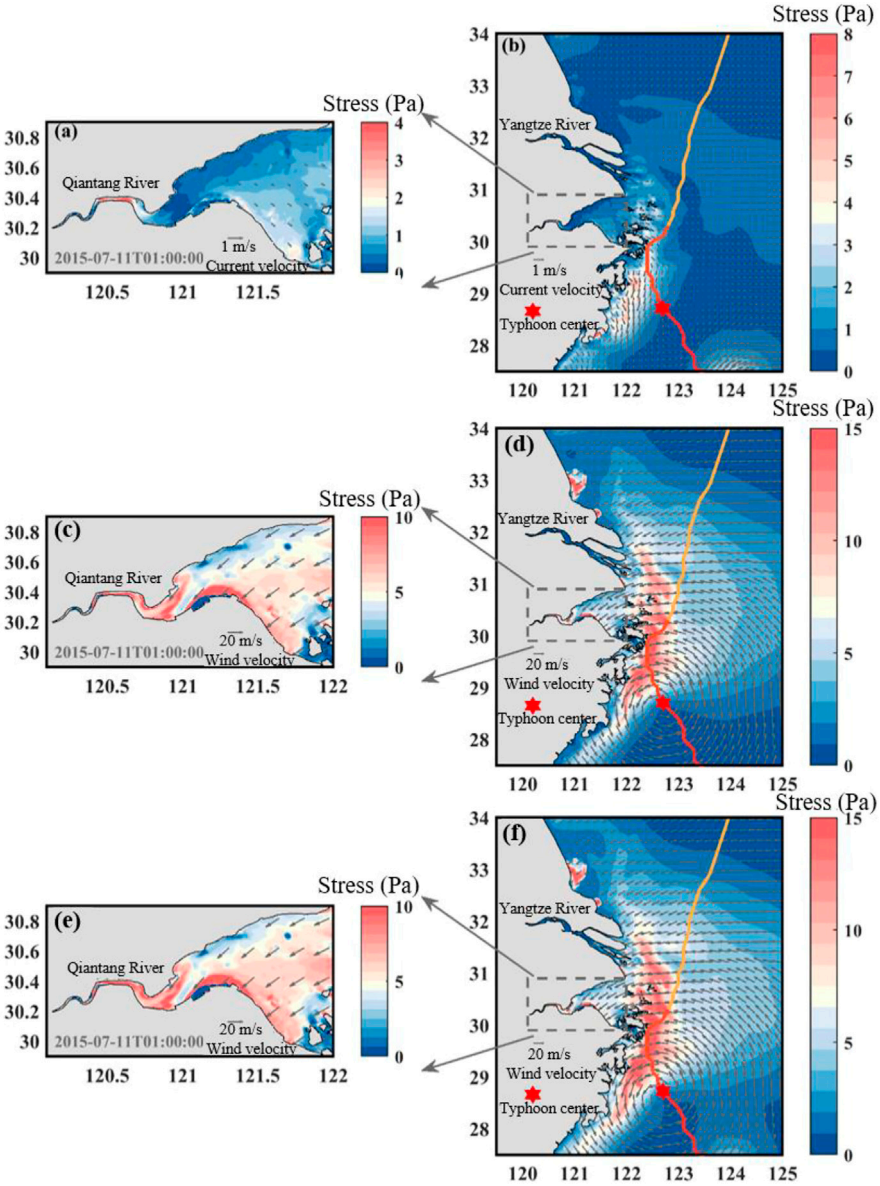

FIGURE 11
Bottom stress induced by **(A,B)** currents (arrow indicates bottom current velocity), **(C,D)** waves (arrow indicates wind velocity), and **(E,F)** combined action of currents and waves (arrow indicates wind velocity) at 01:00 on 11 July 2015 (the red and orange gradient line indicates typhoon path, the red six-pointed star indicates typhoon center).

was 2, 2, 2, and 2.1 g/L and the increase in bottom SSC was 4.4, 3.1, 4.8, and 5.2 g/L, respectively. The peak surface SSC caused by wave action at S1–S6 was 62.8%, 59.3%, 90%, 80.4%, 86.6%, and 72.6% of the maximum surface SSC of Case 0, respectively, with a mean value of 75.3%. The maximum bottom SSC caused by wave action was 62.5%, 52.6%, 81.9%, 81.3%, 74%, and 75.7% of that in Case 0 at S1–S6, respectively, and the mean value was 71.32% (Table 4).

The change in the bottom stress curve positively correlated with the change in large wave height. The larger the wave height, the higher the bottom stress. The magnitude of the bottom stress was also influenced by the water depth when the wave heights were similar. So, the bottom stress at S3, where the water was shallowest, was 8.8 Pa, whereas the maximum value of bottom stress at S2, where the water was deepest, was only 2.6 Pa. The bottom stress at S1 to S6 under wave action was 3.8, 2.6, 8.78, 3, 5.8, and 4.3 Pa, respectively; the maximum bottom stresses, under full driving action, were 90.4%, 94.9%, 90.4%, 93.1%, 82.6%, and 71%, respectively, and the mean value was 87.1%.

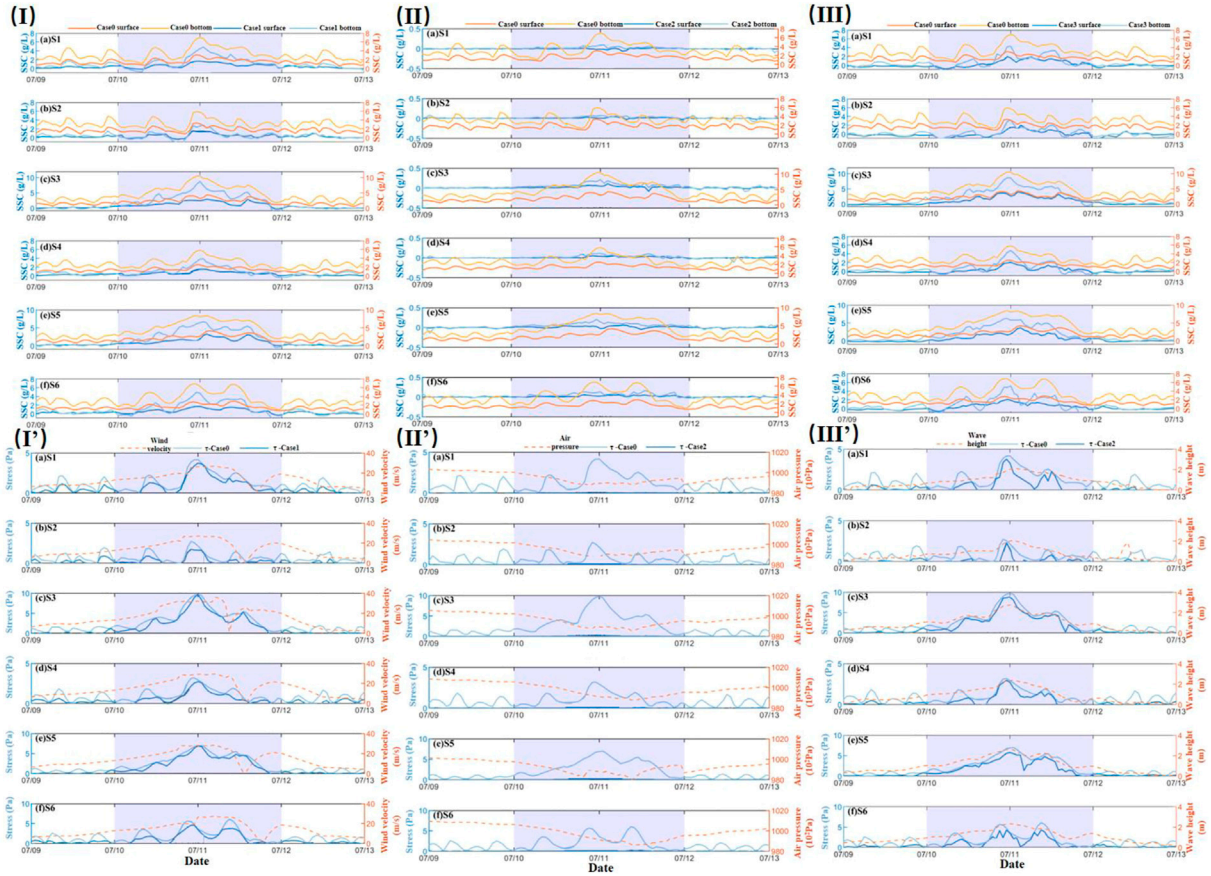

FIGURE 12
(I-I') Comparison of SSC and bottom stress curves of Cases 0 and 1 (July 9–13, 2015). **(II-II', III-III')** The same as **(I-I')**, but for Cases 0 and 2, and 0 and 3, respectively.

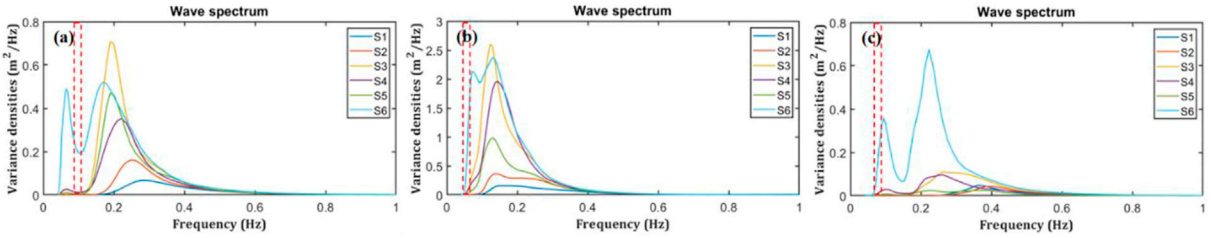

FIGURE 13
Separation of wind-wave and swell of S1-S6 of Hangzhou Bay at different time [**(A)**: 07/10 00:00; **(B)** 07/11 00:00; **(C)** 07/12 00:00; red dotted box: S1-S6 separation frequency range].

4.5 Influence of the tide-wave-wind interactions on SSC

The bottom stress increased under the combined action of waves and currents, which led to an increase in sediment resuspension. The surface SSC increased under the action of the suspension and diffusion of sediment.

Comparing Cases 0 and 1, we determined the influence of the wind waves and velocity increase on SSC. The surface and bottom SSC accounted for 60.9% and 69.9% (average value of

six stations) of the SSC in Case 0, respectively. Comparing Cases 0 and 3, we determined the effects of wind waves and swells on the SSC. The surface and bottom SSC accounted for 75.3% and 71.3% (average value of six stations) of the SSC in Case 0, respectively. We found that the influence of wind waves on SSC overlapped when we compared the two groups.

So, we wanted to consider the contribution of wind waves and swells to SSC. By using PM (Pierson-Moskowitz) method (Li Y. et al., 2019), the calculated separation frequency separated the one-dimensional wave spectra of the station S1-S6. The proportion of wind waves and swells of these stations in Hangzhou Bay during the typhoon Chan-hom was obtained (Figure 13). During the typhoon, wind waves played a dominated role (~100%) because the terrain blocked the propagation of swells into the bay. However, the wave spectrum of the station S6 showed obvious double peaks in the forerunner and aftershock period of typhoon, indicating that swells also occupied a certain proportion at these time (~10%), because it is closer to the open sea. Hence, we believed that the influence of wave on SSC in Hangzhou Bay was almost all influenced by wind waves (75.3% and 71.3%) and accordingly, swells had almost no influence on SSC. Then, compared the contribution of waves and winds, the wind-induced velocity reduced the SSC at these six stations. This phenomenon was obvious in the surface layer (14.4%) and slight in the bottom layer (1.4%).

Comparing Case 0 and 4, we determined the influence of the tidal level and tidal current on SSC. The surface and bottom SSC accounted for 37.0% and 20.3% (average value of six stations) of the SSC in Case 0, respectively. The total influence of tide, wave (almost wind wave), wind-induced current and air pressure were 99.6% (surface) and 92.0% (bottom), respectively. Hence the contribution of the interaction of tide, wave and wind-induced current on SSC were less than 10%.

5 Conclusion

Based on the three-dimensional numerical model of ocean dynamics (FVCOM) and considering the extreme weather conditions produced by Typhoon Chan-hom, we established and validated a three-dimensional wave–current–sediment coupled numerical model in Hangzhou Bay. We investigated the characteristics of suspended sediments, and examined the dynamic changes in the characteristics of sediment in Hangzhou Bay. Our main conclusions are as follows:

1) The sediment content in Hangzhou Bay was high during the typhoon, and SSC was substantially affected by waves. The high-SSC area in Hangzhou Bay was mainly concentrated at the MB and south shore of the CB. As the typhoon gradually approached, the surface and bottom SSC in the northern part of the MB reached 5 and 10 g/L, respectively. It increased from 2.5 to 4.5 g/L and 5–12 g/L at the CB, respectively, and reached 5.5 and 14 g/L at the TB, respectively. The maximum bottom SSC was at least twice the maximum surface SSC. A larger increase in bottom stress and SSC occurred at the southern shore of the CB and Qiantang River.
2) The typhoon affected the current velocity and SSC in the bay. The flow velocity at peak flood was higher than that at peak ebb; therefore, the maximum bottom SSC at peak flood (6 g/L) was higher than that at the peak ebb (5 g/L). The SSC at low and high water levels was the lowest. The maximum SSC at C1 was larger than those in C2 and C3. The SSC on the northern shore was substantially higher at peak flood and that on the south shore at peak ebb at C3. The SSC on the south shore was considerably larger than that in the north at these two times at C3 because of the shallow water.
3) During the typhoon, suspended sediment was transported through the middle and north of the MB from the sea to the bay, most of which was transported to the south shore of the MB and the Zhoushan Islands, the rest of which was transported upstream. Areas with a high SSC net flux included the southern shore of the MB and the CB, where siltation occurred.
4) SSC and bottom stress were most influenced by wave action, followed by wind stress action, and least influenced by air pressure action. The maximum SSC contributed by the waves to the peak SSC in Case 0 was 75.3% in the surface layer and 71.3% in the bottom layer; the contribution under the wind stress action was 60.9% in the surface layer and 69.9% in the bottom layer; the contribution of air pressure action was 1.7% and 1.8% in the surface and bottom layers, respectively.

Data availability statement

The original contributions presented in the study are included in the article/supplementary material, further inquiries can be directed to the corresponding authors.

Author contributions

LL and ZH: manuscript writing, data analysis; methodology; modelling. FS and ZY: material collection; modelling; data analysis.

Funding

This study was partially supported by the National Key Research and Development Program of China (2021YFE0206200), the National Natural Science Foundation of China (41976157,

42076177), the Science Technology Department of Zhejiang Province (2021C03180, 2020C03012, 2022C03044).

Conflict of interest

The authors declare that the research was conducted in the absence of any commercial or financial relationships that could be construed as a potential conflict of interest.

Publisher's note

All claims expressed in this article are solely those of the authors and do not necessarily represent those of their affiliated organizations, or those of the publisher, the editors and the reviewers. Any product that may be evaluated in this article, or claim that may be made by its manufacturer, is not guaranteed or endorsed by the publisher.

References

Aagaard, T., Hughes, M., Baldock, T., Greenwood, B., Kroon, A., and Power, H. (2012). Sediment transport processes and morphodynamics on a reflective beach under storm and non-storm conditions. *Mar. Geol.* 326, 154–165. doi:10.1016/j.margeo.2012.09.004

Allen, J. I., Somerfield, P. J., and Gilbert, F. J. (2007). Quantifying uncertainty in high-resolution coupled hydrodynamic-ecosystem models. *J. Mar. Syst.* 64 (1-4), 3–14. doi:10.1016/j.jmarsys.2006.02.010

Allison, M. A., Sheremet, A., Goni, M. A., and Stone, G. W. (2005). Storm layer deposition on the Mississippi-Atchafalaya subaqueous delta generated by Hurricane Lili in 2002. *Cont. Shelf Res.* 25 (18), 2213–2232. doi:10.1016/j.csr.2005.08.023

Booij, N., Ris, R. C., and Holthuijsen, L. H. (1999). A third-generation wave model for coastal regions - 1. Model description and validation. *J. Geophys. Res.* 104 (C4), 7649–7666. doi:10.1029/98jc02622

Cao, Z., and Wang, Y. (1994). *Numerical simulation of hydrodynamic and sediment dynamics*. Tianjing, China: Tianjin University Press.

Chen, C. S., Beardsley, R. C., Cowles, G., Qi, J., Lai, Z., Gao, G., et al. (2006). *An unstructured grid, finite-volume coastal ocean model: FVCOM user manual*. Boston: Smast/Umassd.

Chen, C. S., Liu, H. D., and Beardsley, R. C. (2003). An unstructured grid, finite-volume, three-dimensional, primitive equations ocean model: Application to coastal ocean and estuaries. *J. Atmos. Ocean. Technol.* 20 (1), 159–186. doi:10.1175/1520-0426(2003)020<0159:Augfvt>2.0.Co;2

Cong, S., Wu, X., Ge, J., Bi, N., Li, Y., Lu, J., et al. (2021). Impact of Typhoon Chan-hom on sediment dynamics and morphological changes on the East China Sea inner shelf. *Mar. Geol.* 440, 106578. doi:10.1016/j.margeo.2021.106578

Dai, Z., Zhang, X., Yan, H., Li, J., and Hun, C. (2009). Morphodynamic behavior of the mud coast in response to typhoon action. *Ocean Eng.* 27 (2), 63–69. 95. Retrieved from <Go to ISI>://CSCD:3538044. doi:10.16483/j.issn.1005-9865.2009.02.004

Goff, J. A., Allison, M. A., and Gulick, S. P. S. (2010). Offshore transport of sediment during cyclonic storms: Hurricane ike (2008), Texas gulf coast, USA. *Geology* 38 (4), 351–354. doi:10.1130/g30632.1

Green, M. O., Vincent, C. E., McCave, I. N., Dickson, R. R., Rees, J. M., and Pearson, N. D. (1995). Storm sediment transport - observations from the British North-sea shelf. *Cont. Shelf Res.* 15 (8), 889–912. doi:10.1016/0278-4343(95)80001-t

Harris, C. K., and Wiberg, P. L. (1997). Approaches to quantifying long-term continental shelf sediment transport with an example from the Northern California stress mid-shelf site. *Cont. Shelf Res.* 17 (11), 1389–1418. doi:10.1016/s0278-4343(97)00017-4

He, Z. G., Tang, Y. L., Xia, Y. Z., Chen, B. D., Xu, J., Yu, Z. H., et al. (2020). Interaction impacts of tides, waves and winds on storm surge in a channel-island system: Observational and numerical study in yangshan harbor. *Ocean. Dyn.* 70 (3), 307–325. doi:10.1007/s10236-019-01328-5

Huang, J., Li, Y., Ding, F., Zheng, T., Meadows, M. E., and Wang, Z. (2021). Sedimentary records of mid-Holocene coastal flooding at a Neolithic site on the southeast plain of Hangzhou Bay, east China. *Mar. Geol.* 431, 106380. doi:10.1016/j.margeo.2020.106380

Huang, S. (2017). *Investigation on storm surge and erosion-deposition in Zhejiang coastal waters*. Hangzhou, China: Zhejiang University. (Doctor)Available from Cnki.

Ji, R., and Lu, Y. (2007). Advances in hydrodynamic and sedimentary processes of macrotidal estuary. *Hydro-Sci. Eng.* 3, 64–74. doi:10.16198/j.cnki.1009-640x

Jiang, B., Zhang, x., Huang, D., Du, Y., Yang, D., and Yao, L. (2015). Retrieving high concentration of suspended sediments based on GOGI: An example of cosatal water around Hangzhou Bay, China. *J. Zhejiang Univ. Sci. Ed.* 42 (02), 213–220. Available at: https://kns.cnki.net/kcms/detail/33.1246.n.20150325.1529.007.html.

Jiang, C., Wu, Z., Chen, J., and Liu, J. (2014). Review of sediment transport and beach profile changes under storm surge. *J. Changsha Univ. Sci. Technol. Nat. Sci.* 11 (01), 1–9.

Koutitas, C. G. (1988). *Mathematucal models in coastal engineering*. London: Pentech Press.

Leonardi, N., Carnacina, I., Donatell, C., Ganju, N., Plater, A., Schuerch, M., et al. (2018). Dynamic interactions between coastal storms and salt marshes: A review. *Geomorphology* 301, 91–107. doi:10.1016/j.geomorph.2017.11.001

Li, H., Li, Y., Zheng, B., Zhong, G., Zhang, H., Wang, H., et al. (2019a). Typhoon Soudelor (2015) induced offshore movement of sand dunes and geomorphological change: Fujian coast, China. *Water* 11 (6), 1191. doi:10.3390/w11061191

Li, J. (1987). Monitoring the suspended sediment content in Hangzhou Bay by using AVHRR data of NOAA satellite. *Acta Oceanol. Sin. Chin. version)* (01), 132–135.

Li, L., Li, Z., He, Z., Yu, Z., and Ren, Y. (2022). Investigation of a storm tides induced by super typhoon in macro-tidal Hangzhou Bay. *Front. Mar. Sci.*

Li, Y., Li, H., Qiao, L., Xu, Y., Yin, X., and He, J. (2015). Storm deposition layer on the Fujian coast generated by Typhoon Saola (2012). *Sci. Rep.* 5, 14904. doi:10.1038/srep14904

Li, Y., and Li, X. (2016). Remote sensing observations and numerical studies of a super typhoon-induced suspended sediment concentration variation in the East China Sea. *Ocean. Model.* 104, 187–202. doi:10.1016/j.ocemod.2016.06.010

Li, Y., Tao, A., Li, X., Zheng, X., and Yin, S. (2019b). Study on separation method of wind-wave and swell in the Taiwan Strait. *Haiyang Xuebao* 41 (11), 25–34.

Liu, G., Zhong, Q., Ye, Y. l., Wang, H. b., Hu, L. j., Qin, Z. k., et al. (2013). Expression of beclin 1 in bladder cancer and its clinical significance. *Int. J. Biol. Markers* 41 (02), 56–62. doi:10.5301/JBM.2012.9769

Liu, J., Cai, S., and Wang, S. (2011). Observations of strong near-bottom current after the passage of typhoon pabuk in the south China sea. *J. Mar. Syst.* 87 (1), 102–108. doi:10.1016/j.jmarsys.2011.02.023

Liu, M., Shen, F., Ge, J., and Sun, Y. (2013). Diurnal variation of suspended sediment concentration in Hangzhou Bay from geostationary satellite observation and its hydrodynamic analysis. *J. Sediment Res.* (01), 7–13. doi:10.16239/j.cnki.0468-155x.2013.01.003

Lu, H., Gu, F., Chen, X., and Qi, D. (2019). Effect of sea waves on sediment transport in the sea waters surrounding Zhoushan Islands, China. *Periodical Ocean Univ. China* 49 (08), 1–9. doi:10.16441/j.cnki.hdxb.20180116

Mellor, G. L., and Yamada, T. (1982). Development of a turbulence closure-model for geophysical fluid problems. *Rev. Geophys.* 20 (4), 851–875. doi:10.1029/RG020i004p00851

Murphy, A. H. (1992). Climatology, persistence, and their linear combination as standards of reference in skill scores. *Weather Forecast.* 7 (4), 692–698. doi:10.1175/1520-0434(1992)007<0692:cpatlc>2.0.co;2

Oberle, F. K. J., Storlazzi, C. D., and Hanebuth, T. J. J. (2014). Wave-driven sediment mobilization on a storm-controlled continental shelf (Northwest Iberia). *J. Mar. Syst.* 139, 362–372. doi:10.1016/j.jmarsys.2014.07.018

Palinkas, C. M., Halka, J. P., Li, M., Sanford, L. P., and Cheng, P. (2014). Sediment deposition from tropical storms in the upper Chesapeake Bay: Field observations and model simulations. *Cont. Shelf Res.* 86, 6–16. doi:10.1016/j.csr.2013.09.012

Pan, C., Zeng, J., Tang, Z., and Shi, Y. (2013). A study of sediment chatacteristics and riverbed erosion/deposition in Qiantang estuary. *Hydro-Sci. Eng.* 1, 1–7. doi:10.16198/j.cnki.1009-640x.2013.01.009

Pan, C., Zheng, J., Zeng, J., and Cheng, G. (2021). Analysis of annual maximum tidal range in Hangzhou Bay. *Chin. J. Hydrodynomics* 36 (2), 201–209. Retrieved from <Go to ISI>://CSCD:7010568. doi:10.16076/j.cnki.cjhd.2021.02.006

Peduzzi, P., Chatenoux, B., Dao, H., De Bono, A., Herold, C., Kossin, J., et al. (2012). Global trends in tropical cyclone risk. *Nat. Clim. Chang.* 2 (4), 289–294. doi:10.1038/nclimate1410

Shi, J. Z., Gu, W., and Wang, D. (2008). Wind wave-forced fine sediment erosion during the slack water periods in Hangzhou Bay, China. *Environ. Geol.* 55 (3), 629–638. doi:10.1007/s00254-007-1013-2

Tang, R., Shen, F., Ge, J., Yang, S., and Gao, W. (2021). Investigating typhoon impact on SSC through hourly satellite and real-time field observations: A case study of the Yangtze estuary. *Cont. Shelf Res.* 224, 104475. doi:10.1016/j.csr.2021.104475

Van Prooijen, B. C., and Winterwerp, J. C. (2010). A stochastic formulation for erosion of cohesive sediments. *J. Geophys. Res.* 115, C01005. doi:10.1029/2008jc005189

van Rijn, L. C. (2011). Coastal erosion and control. *Ocean Coast. Manag.* 54 (12), 867–887. doi:10.1016/j.ocecoaman.2011.05.004

Walsh, K. J. E., McBride, J. L., Klotzbach, P. J., Balachandran, S., Camargo, S. J., Holland, G., et al. (2016). Tropical cyclones and climate change. *WIREs Clim. Change* 7 (1), 65–89. doi:10.1002/wcc.371

Wang, B. C., and Esima, D. (1990). Supply and deposition of sediment along the north bank of Hangzhou Bay, China. *Netherlands J. Sea Res.* 25 (3), 377–390. doi:10.1016/0077-7579(90)90045-I

Wang, D., Cao, A., Zhang, J., Fan, D., Liu, Y., and Zhang, Y. (2018a). A three-dimensional cohesive sediment transport model with data assimilation: Model development, sensitivity analysis and parameter estimation. *Estuar. Coast. Shelf Sci.* 206, 87–100. doi:10.1016/j.ecss.2016.08.027

Wang, D., Zhang, J., He, X., Chu, D., Lv, X., Wang, Y. P., et al. (2018b). Parameter estimation for a cohesive sediment transport model by assimilating satellite observations in the Hangzhou Bay: Temporal variations and spatial distributions. *Ocean. Model.* 121, 34–48. doi:10.1016/j.ocemod.2017.11.007

Wang, F., Wang, S., Wang, X., Song, L., Xu, Q., and Zheng, H. (2014). Remote sensing inversion and dynamic analysis of suspended sediment in Hangzhou Bay. *J. Central China Normal Univ. Nat. Sci.* 48 (01), 112–116+135. doi:10.19603/j.cnki.1000-1190.2014.01.023

Wang, Q., Pan, C., and Pan, D. (2021). Numerical study of the effect of typhoon Yagi on the Qiantang River tidal bore. *Regional Stud. Mar. Sci.* 44, 101780. doi:10.1016/j.rsma.2021.101780

Wang, S., Ge, J., Kilbourne, K. H., and Wang, Z. (2020). Numerical simulation of mid-Holocene tidal regime and storm-tide inundation in the south Yangtze coastal plain, East China. *Mar. Geol.* 423, 106134. doi:10.1016/j.margeo.2020.106134

Wang, X. H., Byun, D. S., Wang, X. L., and Cho, Y. K. (2005). Modelling tidal currents in a sediment stratified idealized estuary. *Cont. Shelf Res.* 25 (5-6), 655–665. doi:10.1016/j.csr.2004.10.013

Wang, X. H. (2002). Tide-induced sediment resuspension and the bottom boundary layer in an idealized estuary with a muddy bed. *J. Phys. Oceanogr.* 32 (11), 3113–3131. doi:10.1175/1520-0485(2002)032<3113:Tisrat>2.0.Co;2

Wang, X., Yin, Q., and Zhang, B. (1991). Research and application of typhoon storm surge forecast model in China Sea. *Adv. Water Sci.* (01), 1–10.

Williams, J. J., and Rose, C. P. (2001). Measured and predicted rates of sediment transport in storm conditions. *Mar. Geol.* 179 (1-2), 121–133. doi:10.1016/s0025-3227(01)00191-8

Winterwerp, J. C. (2001). Stratification effects by cohesive and noncohesive sediment. *J. Geophys. Res.* 106 (C10), 22559–22574. doi:10.1029/2000jc000435

Wu, X., Wang, H., Bi, N., Song, Z., Zang, Z., and Kineke, G. C. (2016). Bio-physical changes in the coastal ocean triggered by typhoon: A case of typhoon meari in summer 2011. *Estuar. Coast. Shelf Sci.* 183, 413–421. doi:10.1016/j.ecss.2016.04.014

Xu, L. (2019). *Fully coupled numerical modeling of sediment transport and bed change under currents and waves influences (Master)*. Hangzhou, China: Zhejiang University. Available from Cnki.

Ye, T. (2019). *The multi-scale variations of suspended sediment dynamics in Hangzhou Bay and its interaction with tidal flat variations. (Master)*. Hangzhou, China: Zhejiang University. Available from Cnki.

Yu, Z. (2020). *Hydrodynamics and sediment transport during typhoon in the Hangzhou Bay. (Master)*. Hangzhou, China: Zhejiang University. Available from Cnki.

Zang, Z., Xue, Z. G., Bao, S., Chen, Q., Walker, N. D., Haag, A. S., et al. (2018). Numerical study of sediment dynamics during hurricane Gustav. *Ocean. Model.* 126, 29–42. doi:10.1016/j.ocemod.2018.04.002

Zhang, W., Zhang, X., Jing, H., Feng, X., Yao, X., Gao, W., et al. (2013). Dynamic sedimentary environment and the provenance characteristics in Yangtze River Estuary-Hangzhou Bay and its adjacent waters. *Acta Geogr. Sin.* 68 (05), 640–650.

Zheng, B., Li, Y., Li, J., Shu, F., and He, J. (2018). Impact of tropical cyclones on the evolution of the monsoon-driven upwelling system in the coastal waters of the northern South China Sea. *Ocean. Dyn.* 68 (2), 223–237. doi:10.1007/s10236-017-1126-4

frontiers | Frontiers in Earth Science

TYPE Original Research
PUBLISHED 01 September 2022
DOI 10.3389/feart.2022.981606

OPEN ACCESS

EDITED BY
Chong Xu,
National Institute of Natural Hazards, China

REVIEWED BY
Min Zhang,
Shanghai Normal University, China
Shenliang Chen,
East China Normal University, China
Hualong Luan,
Changjiang River Scientific Research Institute (CRSRI), China

*CORRESPONDENCE
Cong Lin,
lcnju1994@163.com
Ya Ping Wang,
ypwang@nju.edu.cn

SPECIALTY SECTION
This article was submitted to Geohazards and Georisks, a section of the journal Frontiers in Earth Science

RECEIVED 29 June 2022
ACCEPTED 05 August 2022
PUBLISHED 01 September 2022

CITATION
Lu T, Lin C, Wang YP, Wu H, Zhou M, Chen Y and Shen Y (2022), Mapping the most heavily reclaimed shorelines of the Yangtze River delta urban agglomerations.
Front. Earth Sci. 10:981606.
doi: 10.3389/feart.2022.981606

Mapping the most heavily reclaimed shorelines of the Yangtze River delta urban agglomerations

Ting Lu[1,2], Cong Lin[1,3]*, Ya Ping Wang[2,4]*, Hao Wu[2], Mengxiao Zhou[1], Yu Chen[5] and Yu Shen[1]

[1]Nanjing Research Institute of Surveying, Mapping and Geotechnical Investigation, Co., LTD, Nanjing, China, [2]Ministry of Education Key Laboratory for Coast and Island Development, School of Geography and Ocean Science, Nanjing University, Nanjing, China, [3]State Key Laboratory of Information Engineering in Surveying, Mapping and Remote Sensing (LIESMARS), Wuhan University, Wuhan, China, [4]State Key Laboratory of Estuarine and Coastal Research, School of Marine Sciences, East China Normal University, Shanghai, China, [5]School of Environment and Spatial Informatics, China University of Mining and Technology, Xuzhou, China

Objectively understanding the characteristics and evolution of coastal geomorphology, and predicting the growth potential of intertidal flats are the prerequisites for the effective conservation and development of shoreline resources. However, the vulnerability of shorelines in the long term and large space scale needs to be assessed since human intervention in recent decades has intensified the double oppression of river delta system transformation and land reclamation. The Yangtze River Delta Urban Agglomerations (YRDUA) is a highly developed global economy, therefore, the YRDUA with the most intense reclamation, and their dynamic shoreline changes before and after the sharply decreasing sediment supply were detected based on 4,596 remote sensing images and corresponding hydrodynamic data. We found that the sediment replenishment from the radial sand ridges on the middle Jiangsu Coast made the shoreline expansion rate reach 4–5 times that of other Jiangsu coasts. Specifically, a close correlation between the shoreline accretion rate and the amount of sediment supply was found on the eastern Chongming Wetland. Generally, there were still sufficient sediments on the Yangtze River Estuary and Hangzhou Bay interface to support the shoreline expansion despite the upstream sediment reduction. The longshore sediment transport from the delta-front erosion and the land reclamation including vegetation ecological responses were the main factors promoting the shoreline advance. Human interventions, dominated mainly by reclamation, formed positive feedback with local hydrodynamic processes and promoted continuous shoreline accretion. This study focused on the external and internal drivers and their interactions of long-term shoreline evolution with very intensive human activities, which can provide the decision-making reference for the regional coastal zone management and conservation.

KEYWORDS

shoreline change, Yangtze River Delta Urban Agglomerations (YRDUA), sediment supply, land reclamation, Google Earth Engine

1 Introduction

Shorelines, as well as the new reserved land brought about by the shoreline expansion, are the most valuable natural resource in the land-ocean interaction areas (Temmerman et al., 2013). As the value provider for ecosystem services (Chen et al., 2020), they could ensure the land demand for increased human survival and development space, provide habitat for fish, birds and benthic organisms, and serve as the buffer zone and natural barrier against marine disasters such as storm surges (Allen, 2000; Costanza, 2006). Therefore, investigating the changes in the key areas of shoreline expansion is necessary for coastal zone environmental planning and ecological conservation (Wang et al., 2012; Addo, 2013; Li et al., 2014).

Coastal wetlands within the shoreline are facing non-ignorable challenges under the threat of the worldwide reduced river sediment supply due to upstream dam constructions (Syvitski et al., 2009), such as the Nile (Stanley and Warne, 1993), Colorado (Carriquiry et al., 2001), Mississippi (Blum and Roberts, 2009), and Yellow River (Wang et al., 2010). However, an opposite view was that the vulnerability of coastal wetlands was overestimated contributing to the combination of higher tidal inundation and developing salt marshes capturing fine-grained sediments (Foster et al., 2013; Kirwan et al., 2016; Langston et al., 2020). Moreover, a new insight has been proposed in some recent findings that even with a sharp decrease in upstream sediment supply, coastal wetlands still tend to expand seaward under conditions of local suspended sediment concentrations (SSC) remained unchanged caused by the offshore budget (Long et al., 2021; Lou et al., 2022). The hydrodynamic environment in estuaries and coasts determines the direction and destination of suspended sediment transport (Wang et al., 2013; Xiong et al., 2017; Li et al., 2018). Hence, the physical processes of local hydrodynamic-sediment coupling and the corresponding biological responses affect the seaward/landward trend of coastal wetlands and, therefore, shoreline changes (Chen et al., 2020).

The human intervention caused mainly by land reclamation is the prominent feature of the shoreline changes in economically developed regions (Wu et al., 2016; Du et al., 2019). Economic development, population growth, and regional natural characteristics are attention-getting factors contributing to sequential coastal reclamations (Wu et al., 2016). The abundant sediment supply from the Yangtze River (YZR) has aggravated coastal erosion/deposition and benefited the reclamation (Gao et al., 2013). Meanwhile, continuing reclamation depends largely on sediment accumulation rates on tidal flats (Du et al., 2019). The internal salt marsh systems attenuate hydrodynamics and reduce erosion, with more significant accumulation rates than bare flats. Thus, regions with vegetation cultivation, such as salt marshes, become the main reclamation targets (Chen et al., 2020). Therefore, an urgent requirement for the rational use of new land is to better understand the coastal hydrodynamic-sediment coupling process and ecological response under the influence of anthropogenic activities at spatial and temporal scales.

On account of the time-consuming field observations and computationally expensive limitations of morphodynamic models, investigating shoreline changes relies on massive spatio-temporal data accumulated by advanced remote sensing technology (Li et al., 2016). The development of geospatial information cloud computing platforms, especially Google Earth Engine (GEE), has dramatically improved the ability of spatio-temporal large-scale expression (Tamiminia et al., 2020). Medium-resolution and multi-temporal images, such as the Landsat data, are widely used in the aspect of shoreline change analysis (Pardo-Pascual et al., 2012; Addo, 2013; Li et al., 2014), providing convenience for the detection of large-spatial scales and long-time scales.

Furthermore, the present studies have focused mainly on the dynamic shoreline changes, but few have systematically revealed the controlling factors of the temporal and spatial changes from the perspective of the natural geographical characteristics and the forcing of anthropogenic interventions, and the Yangtze River Delta Urban Agglomerations (YRDUA) is a highly developed global economy under the double oppression of the delta system transformation due to the dam construction and land reclamation behavior for economic growth. In this study, Landsat images in long sequences of several decades and local hydrodynamic-sediment data were collected, and images were processed on the GEE platform to obtain the spatial-temporal distribution of coastal surface water variations, quantify shoreline forward/backward rates, and discuss the natural or anthropogenic sources affecting shoreline changes. The present study has a certain value for coastal vulnerability assessment and wetland management.

2 Study area

The YRDUA is north of Yancheng, Jiangsu Province, and south of Taizhou, Zhejiang Province (Figure 1A). It connects the Abandoned Yellow River Delta, Jiangsu Coast, Yangtze River Estuary (YRE), Hangzhou Bay (HZB), and Zhejiang Coast (Figure 1B). As a semi-enclosed embayment, the Jiangsu Coast is adjacent to the South Yellow Sea (Dong et al., 2011), with an average tidal range reaching 3.68 m (Chen et al., 2020). The YRE is located downstream of the YZR (Figure 1B), with an

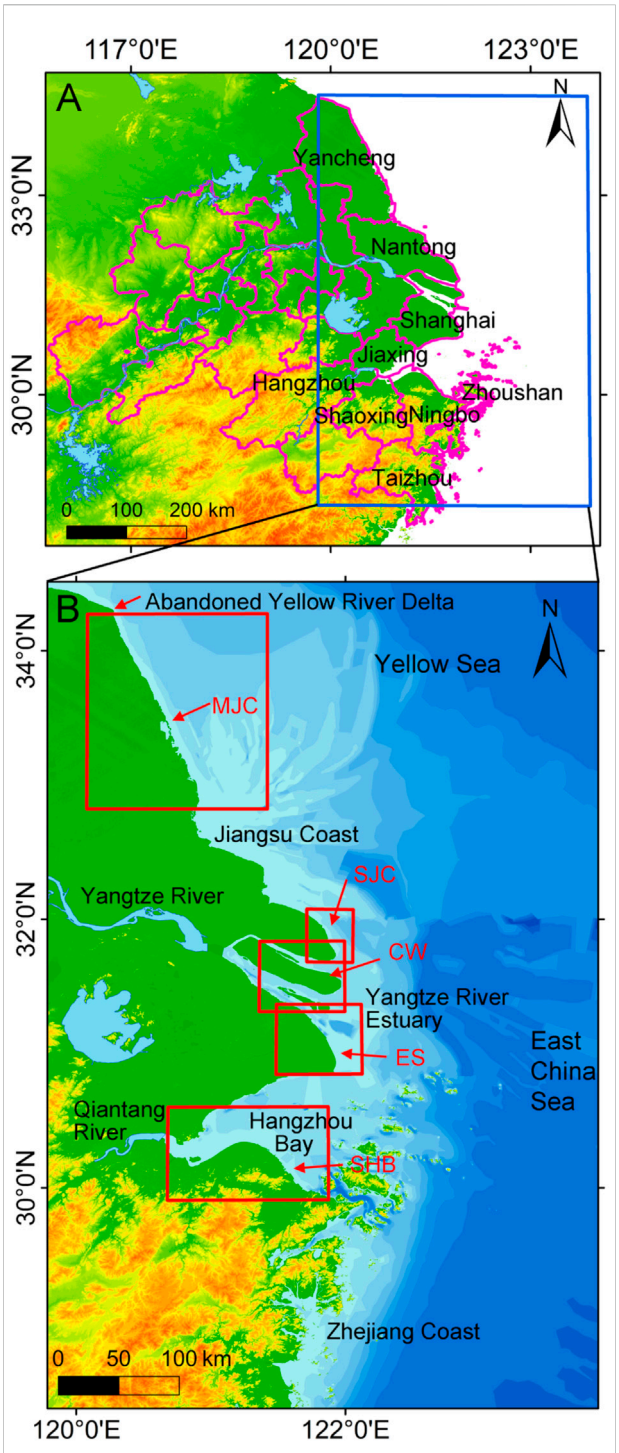

FIGURE 1
Study area and typical shoreline change areas. **(A)** The geographical location of the YRDUA, and the labeled are coastal cities including Yancheng, Nantong, Shanghai, Jiaxing, Hangzhou, Shaoxing, Ningbo, Zhoushan, and Taizhou. **(B)** The schematic diagrams of typical shoreline change areas are marked by red wireframes (MJC: middle Jiangsu Coast; SJC: southern Jiangsu Coast; CW: Chongming Wetland; ES: eastern Shanghai; SHB: southern Hangzhou Bay).

average tidal range of 2.67 m (Dai et al., 2013). The HZB is located downstream of the Qiantang River (QTR) (Figure 1B), and the tidal ranges of the north and south bank are 2–4 m and 1–2 m respectively due to the terrain obstruction of islands (Xie et al., 2017).

The sediments are dominated by fine-grained mud and silt from the Jiangsu Coast to the HZB, presenting complex underwater geomorphological features. Offshore on the middle Jiangsu Coast (MJC), radial sand ridges diverge in the adjacent waters (Xing et al., 2012; Xiong et al., 2017), with approximately a length of 90 km from the east to the west and a width of 200 km from the northwest to the southeast (Liu et al., 1989; Wang et al., 2012), which is the largest sand ridges on the Chinese continental shelf (Xu et al., 2016; Chen et al., 2020). Located in the YRE, the estuarine turbidity maximum with a length of about 25–46 km from the northwest to the southeast and a width of about 90 km from the north to the south, is formed by the accumulation of fine-grained sediments within the water column (Li and Zhang, 1998; Lu et al., 2020). The HZB shows a significant turbid water state on the suspension of extremely high concentrations (Shi, 2011; He et al., 2016), with 70% of the fine-grained particles coming from the YZR sediment transport (He et al., 2016).

As the shoreline advances bring potential land resources, the reclamation since 1949 has altered hydrodynamics and resulted in considerable reductions of tidal flats within shorelines (Wang et al., 2012). Typical native and introduced vegetation communities are distributed over the salt marshes, and the introduced *Spartina* species are outcompeting the native species (Wang et al., 2012; Li et al., 2014), becoming the potential primary target of land reclamations.

3 Materials and methods

3.1 Data sources

The Landsat series provide global-scale optical satellite images with the longest time series remote sensing data, and we used the atmospheric-corrected Landsat Surface Reflectance products based on the GEE platform to calculate coastal surface water variations each year (Chen et al., 2017; Wang et al., 2020; Long et al., 2022). We selected a total of 4,596 images with less than 30% cloud coverage, including Landsat 5 TM, Landsat 7 ETM+ and Landsat 8 OLI (Table 1).

In order to improve the accuracy of surface water extraction in remote sensing images, we also used relevant public data stored on the GEE platform (Figure 2), including: 1) Digital Elevation Model (DEM) reflecting elevation and slope information, and chose a data-complete V4 version with a spatial resolution of 90 m (Farr et al., 2007) (Figure 2A); 2)

TABLE 1 Statistical information for the Landsat data collections.

Year	Sensors	Image count				
		Spring	Summer	Autumn	Winter	Yearly
1986	TM	17	12	15	24	68
1987	TM	8	12	32	26	78
1988	TM	16	21	38	25	100
1989	TM	13	15	25	17	70
1990	TM	23	26	14	11	74
1991	TM	17	32	37	20	106
1992	TM	35	30	32	29	126
1993	TM	19	15	15	27	76
1994	TM	24	19	25	14	82
1995	TM	24	19	21	29	93
1996	TM	16	8	20	28	72
1997	TM	26	22	33	24	105
1998	TM	10	23	24	23	80
1999	TM\ETM+	12	14	34	43	103
2000	TM\ETM+	57	52	50	46	205
2001	TM\ETM+	66	52	76	33	227
2002	TM\ETM+	32	51	75	57	215
2003	TM\ETM+	24	28	61	67	180
2004	TM\ETM+	46	51	57	57	211
2005	TM\ETM+	48	38	72	43	201
2006	TM\ETM+	52	31	66	32	181
2007	TM\ETM+	51	32	26	49	158
2008	TM\ETM+	54	40	48	54	196
2009	TM\ETM+	56	39	52	32	179
2010	TM\ETM+	40	40	55	66	201
2011	TM\ETM+	57	28	42	41	168
2012	ETM+	37	10	37	14	98
2013	OLI	18	22	26	18	84
2014	OLI	21	16	39	45	121
2015	OLI	22	14	29	13	78
2016	OLI	23	31	17	37	108
2017	OLI	28	31	30	30	119
2018	OLI	28	34	31	29	122
2019	OLI	29	28	40	27	124
2020	OLI	28	15	28	25	96
2021	OLI	19	15	29	28	91

MERIT Hydro global hydrological dataset containing Height Above the Nearest Drainage (HAND) with a spatial resolution of 3 arcseconds (Nobre et al., 2011; Dai et al., 2019) (Figure 2B); 3) Global Human Settlement Layer (GHSL) containing built-up region data in 1975, 1990, 2000, and 2014 with a spatial resolution of 30 m (Pesaresi et al., 2016) (Figure 2C).

We collected relevant hydrodynamic and sediment transport data to analyze natural factors of shoreline changes. The annual suspended sediment load (SSD) at Datong Station, the most downstream hydrological station of the YZR, was obtained from the Changjiang Water Resource Committee and the China River Sediment Bulletin, and data at the representative hydrological station of the QTR was from the China River Sediment Bulletin. The wave direction and wave period data were from the European Centre for Medium-Range Weather Forecasts (ECMWF) (https://apps.ecmwf.int/datasets/data/interim-full-daily/levtype=sfc/).

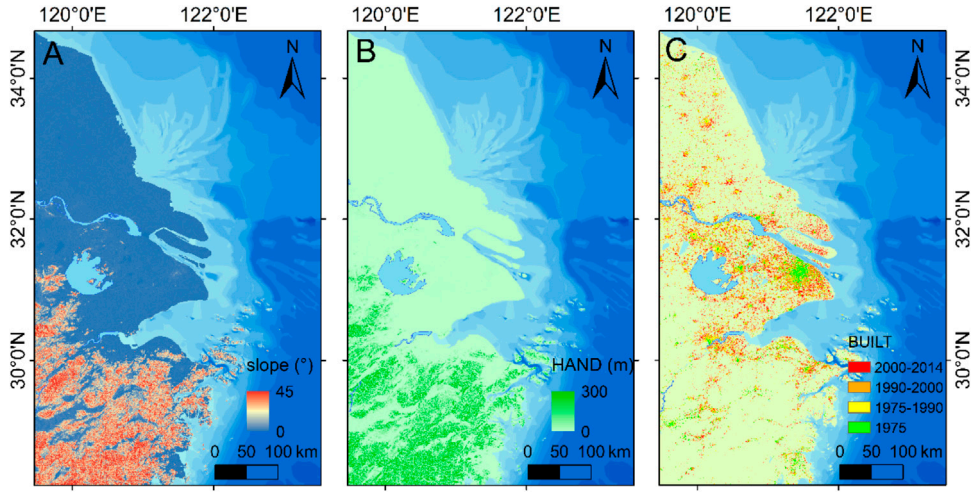

FIGURE 2
Datasets of the study area for multi-level surface water extraction post-processing rules. **(A)** The slope map; **(B)** the Height Above the Nearest Drainage (HAND) map; **(C)** the built-up map in different years.

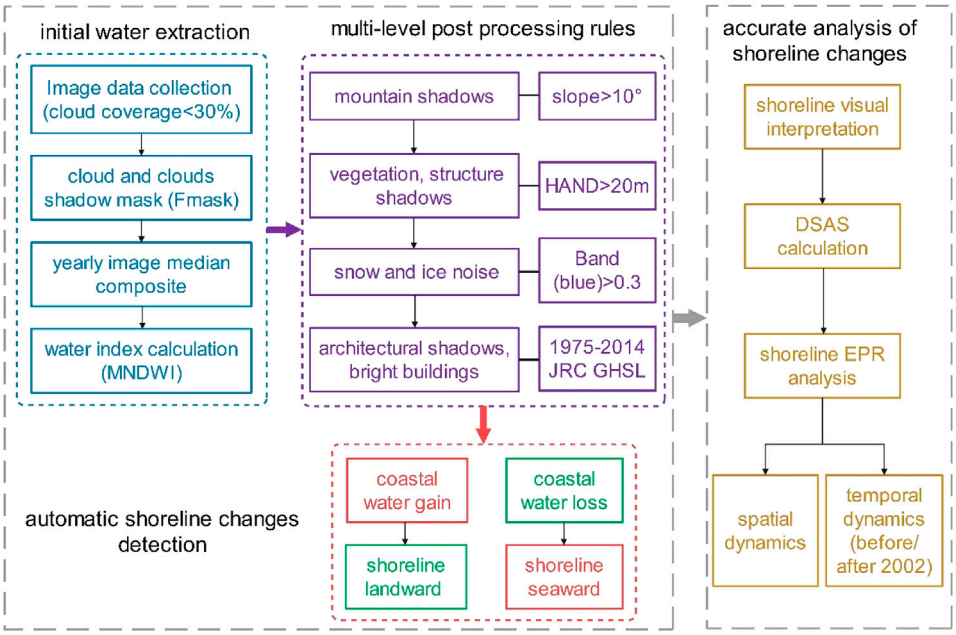

FIGURE 3
Workflow of the automatic shoreline change extraction and accurate analysis. We conducted the automatically coastal surface water extraction method (including the initial water extraction and then multi-level post-processing rules) to detect shoreline change areas and analyze shoreline change trends. Then, we obtained accurate shorelines by artificial visual interpretation based on the shoreline change areas detection by the automatically coastal surface water extraction method.

3.2 Methods

3.2.1 Image processing

As procedures shown in the workflow (Figure 3), the preparation and processing of the image data include: 1) the images with less than 30% cloud coverage screening; 2) the cloud and cloud shadow masking using the Fmask algorithm for filtered (Zhu and Woodcock, 2012); 3) the yearly image median composite. The purpose of the image median composite was to make up for some of the data gaps caused by single-period image clouds and cloud shadow masks.

We indirectly described the shoreline changes by the automatically coastal surface water extraction method (Figure 3). The shoreline retreated landward when the coastal water increased and accreted seaward when it decreased. We used the improved normalized water index (MNDWI) to conduct the water extraction (Xu, 2006).

$$MNDWI = (\rho_{GREEN} - \rho_{SWIR})/(\rho_{GREEN} - \rho_{SWIR}) \quad (1)$$

where ρ_{GREEN}, ρ_{SWIR} were the reflectance in the green and SWIR bands, respectively.

The water index method can efficiently extract the surface water at large spatial scales, but this method is susceptible to low-reflectance features such as terrain and building shadows and high-reflective features such as snow and bright buildings. Therefore, we have constructed multi-level water extraction post-processing rules for the removal of major noises from initial water extractions, which applied to all flat areas, not just this study (Figure 3): 1) based on the slope information (Slope > 10°) to mask obvious undulating regions of terrain to solve the mis-extraction of mountain shadows (Lu et al., 2016); 2) based on the Height Above the Nearest Drainage (HAND > 20 m) to remove the effects of other shadows such as vegetation, structures, etc. (Tsyganskaya et al., 2018); 3) based on the Blue-band surface reflectivity greater than 0.3 masking to remove the effects of snow and ice noise (Yang et al., 2020); 4) based on the 1975–2014 JRC GHSL global human settlement data masking urban built-up regions to prevent architectural shadows and bright building mis-extraction in the city (Pesaresi et al., 2016).

3.2.2 Analysis of shoreline changes

By conducting initial water extraction and multi-level post-processing rules, the spatial/temporal variations of coastal water increases/decreases within the interannual period were obtained, and thus the landward/seaward trends of shoreline changes were indirectly obtained (Figure 3).

In order to quantify the shoreline trend in more detail (Figure 3), we used the digital shoreline analysis system (DSAS), an extension software for ArcGIS that allows shoreline change rate statistics to detect the seaward/landward trend in the region where shorelines have changed for decades (Thieler et al., 2009). We calculated the end-point rate (EPR) to quantify the interannual shoreline seaward/landward rate according to dividing the shoreline travel distance by the time elapsed from shoreline movement (Thieler et al., 2009; Long et al., 2021).

$$EPR = (D_{new} - D_{old})/(Y_{new} - Y_{old}) \quad (2)$$

where, D_{new}, D_{old} were the distance between the shoreline and the baseline of the latest year and the oldest year, respectively, and the Y_{new}, Y_{old} were the latest and oldest years, respectively.

We accurately characterized shoreline changes: 1) at large spatial scales, since the YRDUA has undergone large-scale land reclamation on account of emerging economies, and 2) on temporal scales before and after 2002, since the YRDUA is a typical case under the oppression of the delta system transformation due to the Three Gorges Dam construction in 2002 (Figure 3).

4 Results

4.1 Temporal and spatial coastal surface water variations

The temporal and spatial coastal surface water increases/decreases every 1 year and every 5 years were presented in Figures 4–6. Generally, coastal surface water variations and shoreline changes mainly occurred in the following typical regions: the MJC; SJC; CW; ES, and SHB. The decreasing trend of coastal surface water was more common than the increasing trend to a large extent, indicating that most shorelines were pushed seaward and the new land was expanded contributing mainly to the land reclamation in recent decades (Figures 4A,B).

The dynamic process of coastal surface water variations in key shoreline change areas was depicted in Figures 5, 6. Salt pans and aquaculture bases were distributed on the Jiangsu Coast (Figures 5A,B,D,E). Both the water gains and losses of each year showed fluctuation characteristics during the whole period (Figures 5C,F). Meanwhile, the total water change areas, including the sum of water gains/losses of every 5 years remained almost unchanged after 1996 on the Jiangsu Coast (including the MJC and SJC). The decreasing area of water losses when the increasing area of water gains, and vice versa (Figures 5C,F).

The coastal surface water on the YRE-HZB interface (including the CW, ES, and SHB) showed different change patterns from the Jiangsu Coast (Figures 6A–I). Generally, the coastal water experienced massive degradation. There was almost no peak of water gains, but significant peaks of water losses every 5 years, and the time of the most water losses on the CW, ES, and SHB were in 1996, from 1996 to 2006 and in 2001 (Figures

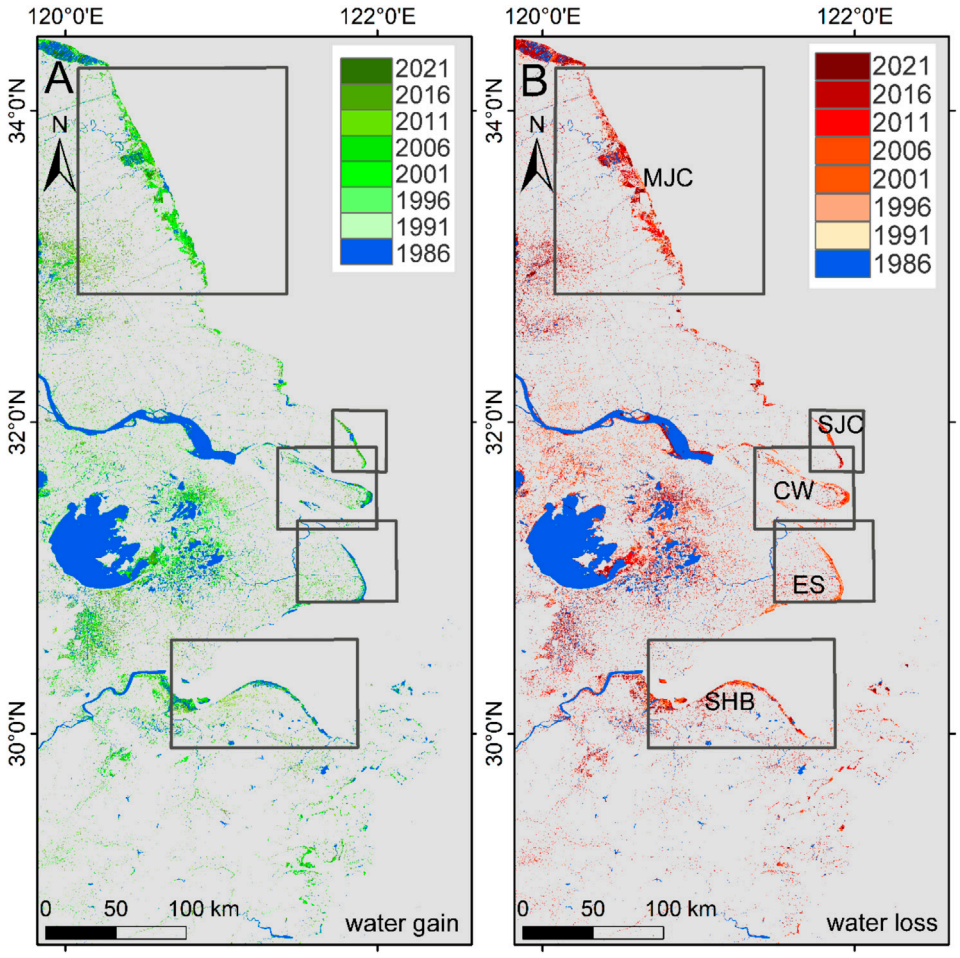

FIGURE 4
Spatial variations of the coastal surface water in the study area, and the schematic diagrams of typical shoreline change areas [including the middle Jiangsu Coast (MJC), southern Jiangsu Coast (SJC), Chongming Wetland (CW), eastern Shanghai (ES), and southern Hangzhou Bay (SHB)] are marked by dark gray wireframes. The MJC and SJC are on the Jiangsu Coast, and the CW, ES, and SHB are on the Yangtze River Estuary (YRE) and Hangzhou Bay (HZB) interface. **(A)** Gains; **(B)** losses of the total surface water area from 1986 to 2021. Blue areas show the extent of the coastal surface water in the initial year 1986, and the amount of water gain/losses in each period are represented by green/red gradient areas.

6C,F,I). Generally, the variation range of coastal wetland areas gradually decreased on the YRE-HZB interface (Figures 6C,F,I). The yearly water gains were close to water losses on the CW after 2015 (Figure 6C), indicating that the shoreline accretion rate has slowed down. Nevertheless, the yearly water losses were still greater than water gains on the SHB after 2015 (Figure 6I), which revealed that the SHB shoreline was still expanding seaward.

4.2 Shoreline changes

4.2.1 Changes in the total area

The accurate depictions of shoreline changes were shown in Figures 7, 8, indicating that the shoreline pushed seaward in the YRDUA during recent decades. For the temporal variations before (BD) and after the dam construction in 2002 (AD), the most shoreline seaward trend on the MJC and eastern CW was during BD (Figures 7A–E, 8A–E). Conversely, the more significant shoreline accretion on the SJC, ES, and inner SHB was during AD (Figures 7F–J, 8F–O).

More specifically, the shoreline expansion rate on the MJC near the radial sand ridges, northern MJC part and SJC were 213.4 m/yr, 50.8 m/yr, and 42.0 m/yr, respectively (Figures 7B,G), indicating that the accretion rate with the radial sand ridge sediment supply was 4–5 times that of other Jiangsu coasts. Comparatively, the CW accretion rates in the eastern and western parts were 157.1 m/yr and 82.5 m/yr, respectively, and the south and north of the ES were 98.7 m/yr and 22.5 m/yr, respectively (Figures 8B,G). In the outer and inner SHB, the average accretion rates were 88.9 m/yr and 154.8 m/yr,

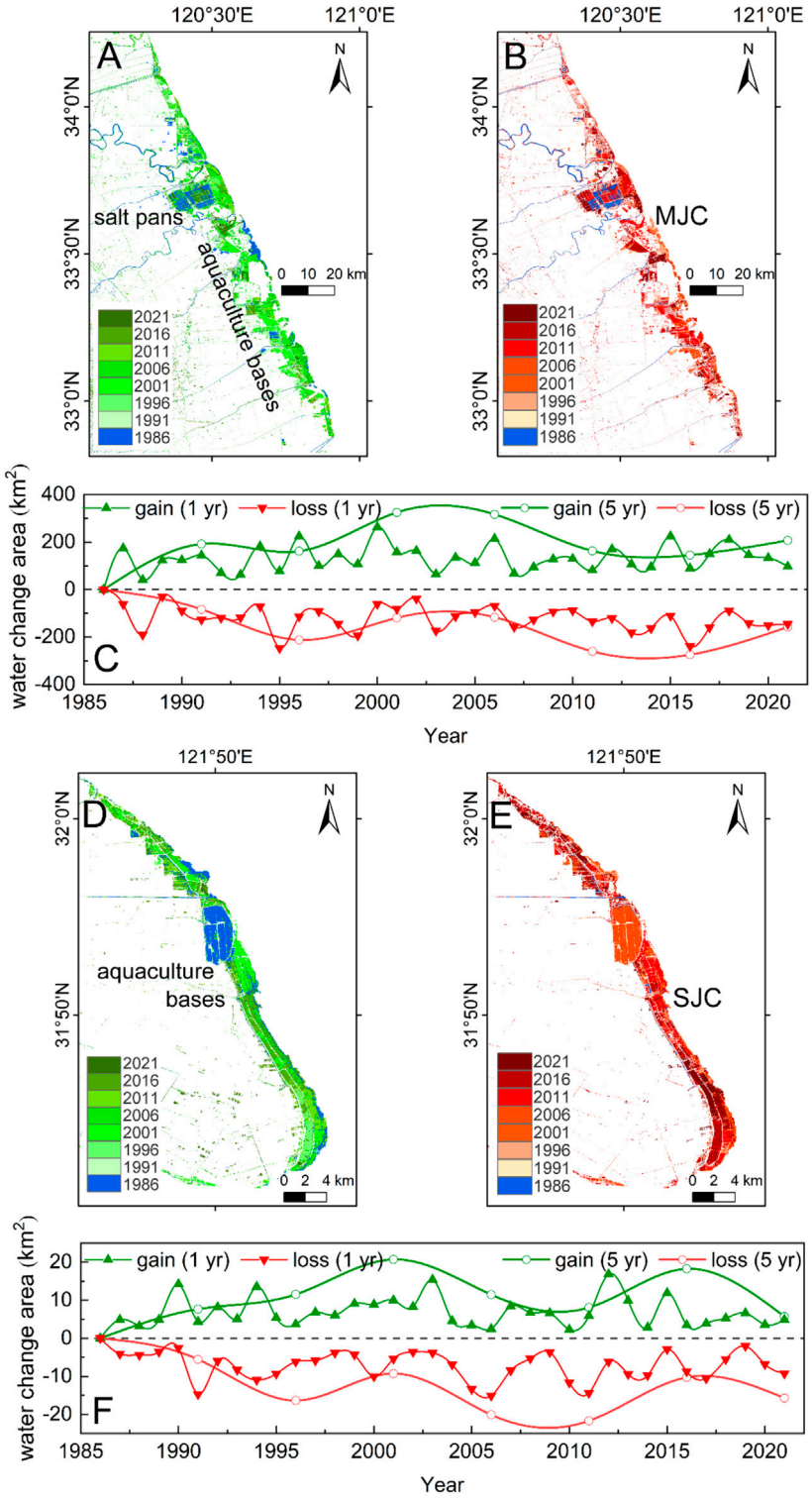

FIGURE 5
Spatial variations of the coastal surface water on the Jiangsu Coast. **(A)** Gains; **(B)** losses; **(C)** water change areas on the middle Jiangsu Coast (MJC); **(D)** gains; **(E)** losses; **(F)** water change areas on the southern Jiangsu Coast (SJC) from 1986 to 2021. Blue areas **(A,B,D,E)** show the extent of the coastal surface water in the initial year 1986. The amount of water gains **(A,D)** and water losses **(B,E)** in each period are represented by green/red gradient areas. Green/red dot lines **(C,F)** indicate the water gain/loss trend divided by every 1 year (triangular solid dot lines) and every 5 years (circular hollow dot lines).

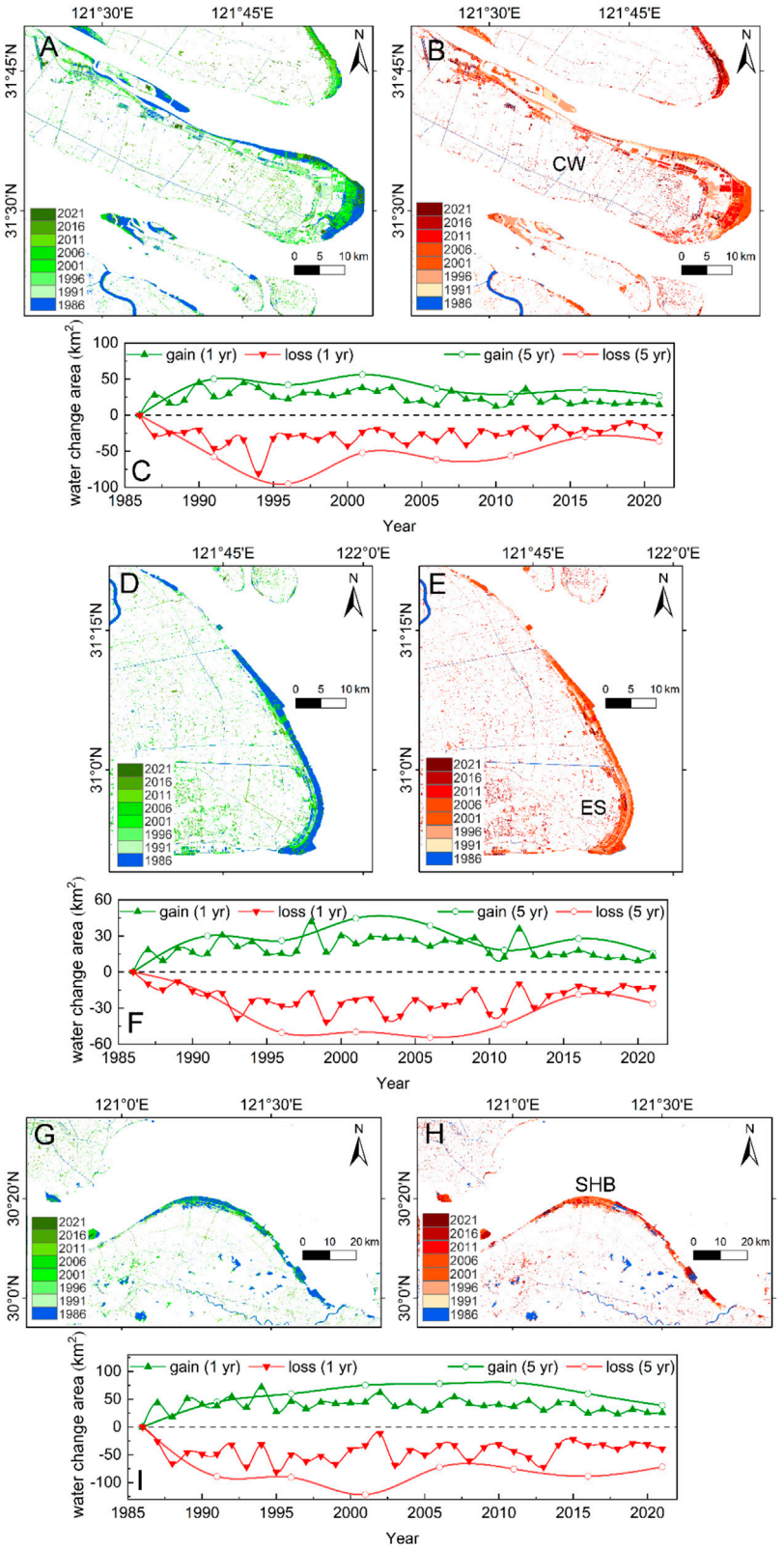

FIGURE 6
Spatial variations of the coastal surface water on the Yangtze River Estuary (YRE) and Hangzhou Bay (HZB) interface. **(A)** Gains; **(B)** losses; **(C)** water change areas on the Chongming Wetland (CW); **(D)** gains; **(E)** losses; **(F)** water change areas on the eastern Shanghai (ES); **(G)** gains; **(H)** losses; **(I)** water change areas on the southern Hangzhou Bay (SHB) from 1986 to 2021. Blue areas **(A,B,D,E,G,H)** show the extent of the coastal surface water in the initial year 1986. The amount of water gains **(A,D,G)** and water losses **(B,E,H)** in each period are represented by green/red gradient areas. Green/red dot lines **(C,F,I)** indicate the water gain/loss trend divided by every 1 year (triangular solid dot lines) and every 5 years (circular hollow dot lines).

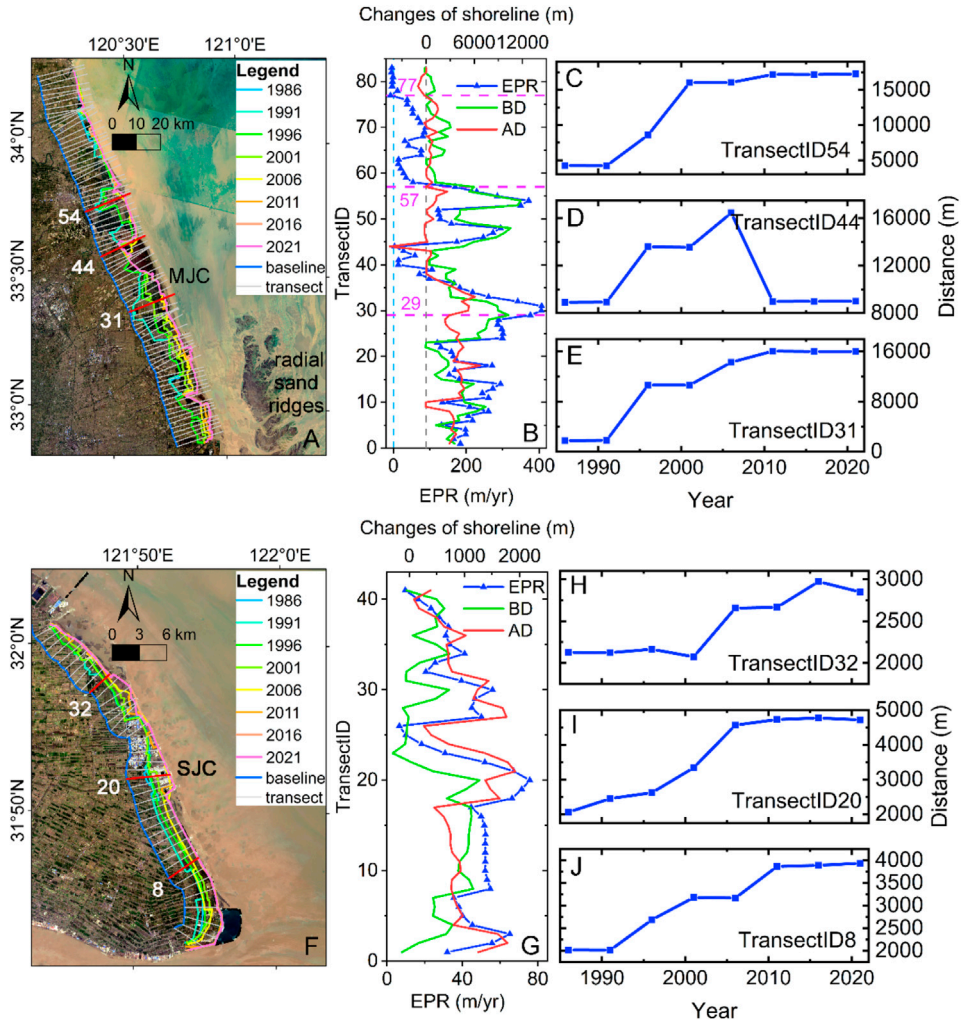

FIGURE 7
Shoreline changes on the Jiangsu Coast. Shorelines on the **(A)** middle Jiangsu Coast (MJC), and the MJC is adjacent to radial sand ridges; **(F)** southern Jiangsu Coast (SJC). End-point rate (EPR) of the shoreline (the blue triangle dot-dash line) and the shoreline change distance before the dam construction in 2002 (during BD, the green line) and after the dam construction in 2002 (during AD, the red line) on the **(B)** MJC; **(G)** SJC. Variations in distance from **(C–E)** Transect54, 44, 31 [marked in **(A)**] to the baseline [the dark blue line in **(A)**] **(H–J)** Transect32, 20, 8 [marked in **(F)**] to the baseline [the dark blue line in **(F)**]. The transect was generated equidistant from the baseline, and each transect was perpendicular to the baseline.

respectively (Figure 8L), which revealed that the seaward rate of the inner bay was about 2 times that of the outer bay.

4.2.2 Temporal variations in different regions

For the temporal variations, notably, the MJC shoreline accretion trend was hindered and even landward in the northern Transect77 during AD (Figures 7A,B). The CW shoreline expansion trend was hindered during AD (Figure 8A), and the rates in the most significant accretion eastern part (Transect9 to Transect18) during BD and AD were 302.6 m/yr and 48.0 m/yr, respectively (Figure 8B). However, the SHB shorelines moved continuously seaward (Figure 8K), and the shoreline accretion rates on the inner western part of Transect42 during BD and AD were 104.9 m/yr, 192.2 m/yr, respectively (Figure 8L). Meanwhile, the SHB accretion rate during BD was more significant on the inner Transect78 (Figure 8L).

4.2.3 Spatial patterns in different regions

For the spatial variations, on the Jiangsu Coast, the maximum rate was 406.9 m/yr in Transect31 and the seaward distance from 1991 to 1996 accounted for 62% of the total expansion distance (Figures 7B,E). The smallest rate was in Transect44 with advancing seaward but retreating landward rapidly (Figures

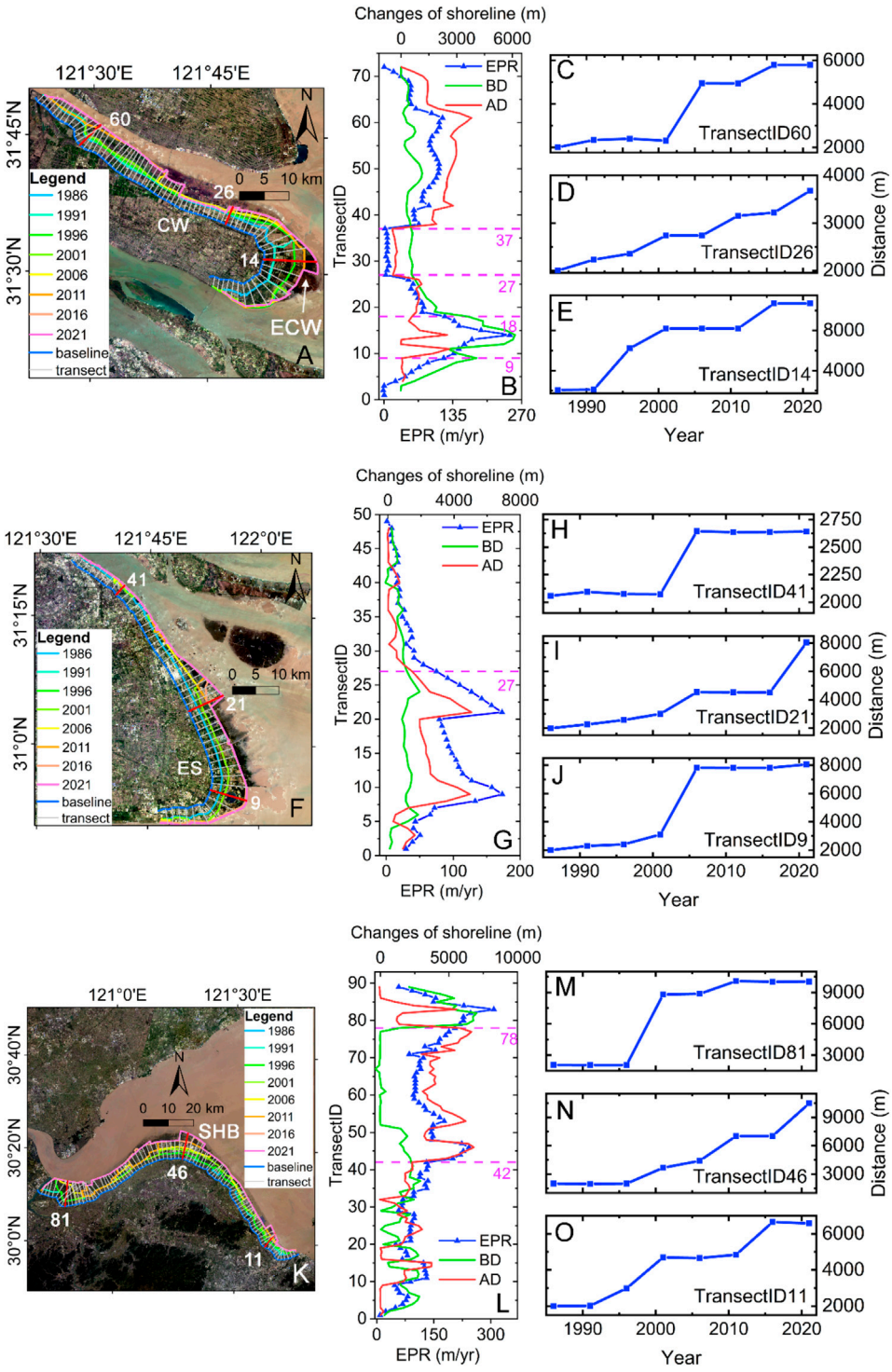

FIGURE 8
Shoreline changes on the Yangtze River Estuary [YRE, including the Chongming Wetland (CW) and the eastern Shanghai (ES)] and Hangzhou Bay (HZB) interface. Shorelines on the **(A)** CW (ECW: eastern Chongming Wetland); **(F)** ES; **(K)** southern HZB (SHB). End-point rate (EPR) of the shoreline (the blue triangle dot-dash line) and shoreline change distance before the dam construction in 2002 (during BD, the green line) and after the dam construction in 2002 (during AD, the red line) on the **(B)** CW; **(G)** ES; **(I)** SHB. Variations in distance from **(C–E)** Transect60, 26, 14 [marked in **(A)**] to the baseline [the dark blue line in **(A)**]; **(H–J)** Transect41, 21, 9 [marked in **(F)**] to the baseline [the dark blue line in **(F)**]; **(M–O)** Transect81, 46, 11 [marked in **(K)**] to the baseline [the dark blue line in **(K)**]. Transect was generated equidistant from the baseline, and each transect was perpendicular to the baseline.

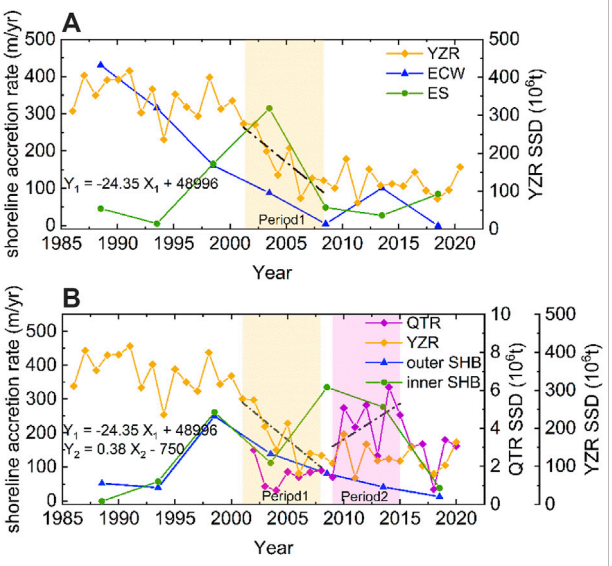

FIGURE 9
The relationship between shoreline accretion rate and suspended sediment load (SSD). **(A)** SSD at Datong station of the Yangtze River (YZR), and its impact on the Eastern Chongming Wetland [ECW, Transect9-Transect18 of the Chongming Wetland (CW)] and Eastern Shanghai (ES, Transect1-Transect27); **(B)** SSD of the Yangtze River (YZR) and Qiantang River (QTR), and their impacts on the outer and inner southern Hangzhou Bay (SHB). The YZR SSD was sharply reduced with a rate of −24.35 Mt/yr in Period1 and the QTR SSD was slightly increased with a rate of 0.38 Mt/yr in Period2.

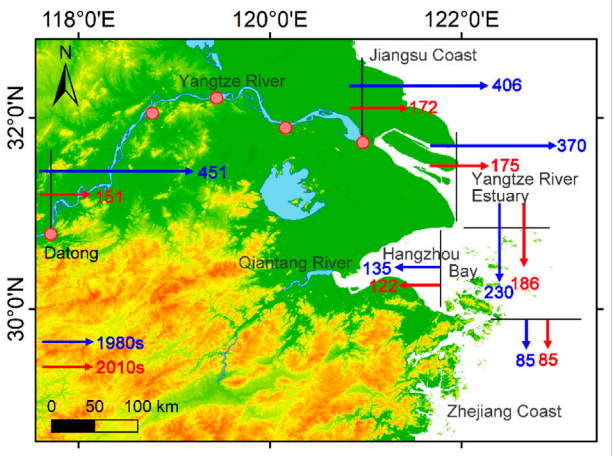

FIGURE 10
Sediment flux model on the Yangtze River Estuary (YRE) and Hangzhou Bay (HZB) interface from Xie et al. (2017). Blue lines show the sediment flux in the 1980s and red lines show the result in the 2010s, which could be associated with shoreline changes from remote sensing data. The unit of the sediment flux is Mt/year.

7B,D). In Transect54, the main expansion occurred from 1991 to 2001 (Figures 7B,C). Therefore, the shoreline of the Jiangsu Coast (including the MJC and SJC) gradually expanded from 1991 to 2006, whereas changed little after 2011 (Figures 7C–J).

On the YRE-HZB interface, most CW shoreline expansions occurred from 1991 to 2001 with the maximum rate (Figure 8E), and 70% occurred from 2001 to 2006 in Transect60 (Figure 8C). On the ES, the shoreline pushed 4,718 m seaward from 2001 to 2006 in Transect9 and accreted 3,529 m seaward from 2016 to 2021 in Transect21 (Figures 8I,J). In particular, the SHB shoreline experienced two expansions in Transect11 (Figure 8O) and gradually pushed seaward after 1996 in Transect46 (Figure 8N). Generally, there was a shoreline accretion trend after 2011.

5 Discussion

5.1 Impacts of natural hydrodynamic-sediment coupling environments

5.1.1 Sediment supply and interface exchange

Estuarine sediment supply from upstream rivers provides adequate sediment sources for the coastal zone (Long et al., 2022), enhancing the possibility of shoreline seaward progradation. The sediments carried by the YZR were served as the most crucial element of the HZB (He et al., 2016). There was a sharp decrease in the SSD of the YZR during the following 5 years after the Three Gorges Dam construction in 2002 (Figure 9) (Gao and Wang, 2008; Yang et al., 2018; Lu et al., 2020). Comparatively, the QTR was 2 orders of magnitude smaller than the YZR and had a weak impact on geomorphological changes and shoreline expansions (Figure 9B).

We compared the relationship between the shoreline change and the sediment supply carried by the YZR and QTR (Figures 9A,B), suggesting a very close positive correlation between the 5-year averaged shoreline change of the ECW and the amount of SSD at Datong Station (Figure 9A). Nevertheless, the correlation did not exist on the ES and SHB (Figures 9A,B), and the increase of coastal deposition contributed to the land enclosure caused by human reclamations might be a crucial contributor (van der Wal et al., 2002; Xie et al., 2017). The relationship on the ECW could be described as: $y = 1.195 \times x - 121.07$ ($R^2 = 0.83$), where x was the median value between the minimum and maximum SSD limits during the corresponding period, and y was the averaged shoreline accretion rate. Dividing time periods by flood and drought years with 2 to 5 years, a positive correlation was also demonstrated and the statistical correlation coefficient R^2 was 0.62 before 2010 (Li et al., 2014). However, the ECW shoreline has been continuously expanding seaward after 2010 although the YZR SSD was only 36% of that before the dam construction (Figures 8A–E, 9A), mainly on account of the longshore sediment replenished by the delta-front erosion (Fagherazzi et al., 2020; Lou et al., 2022).

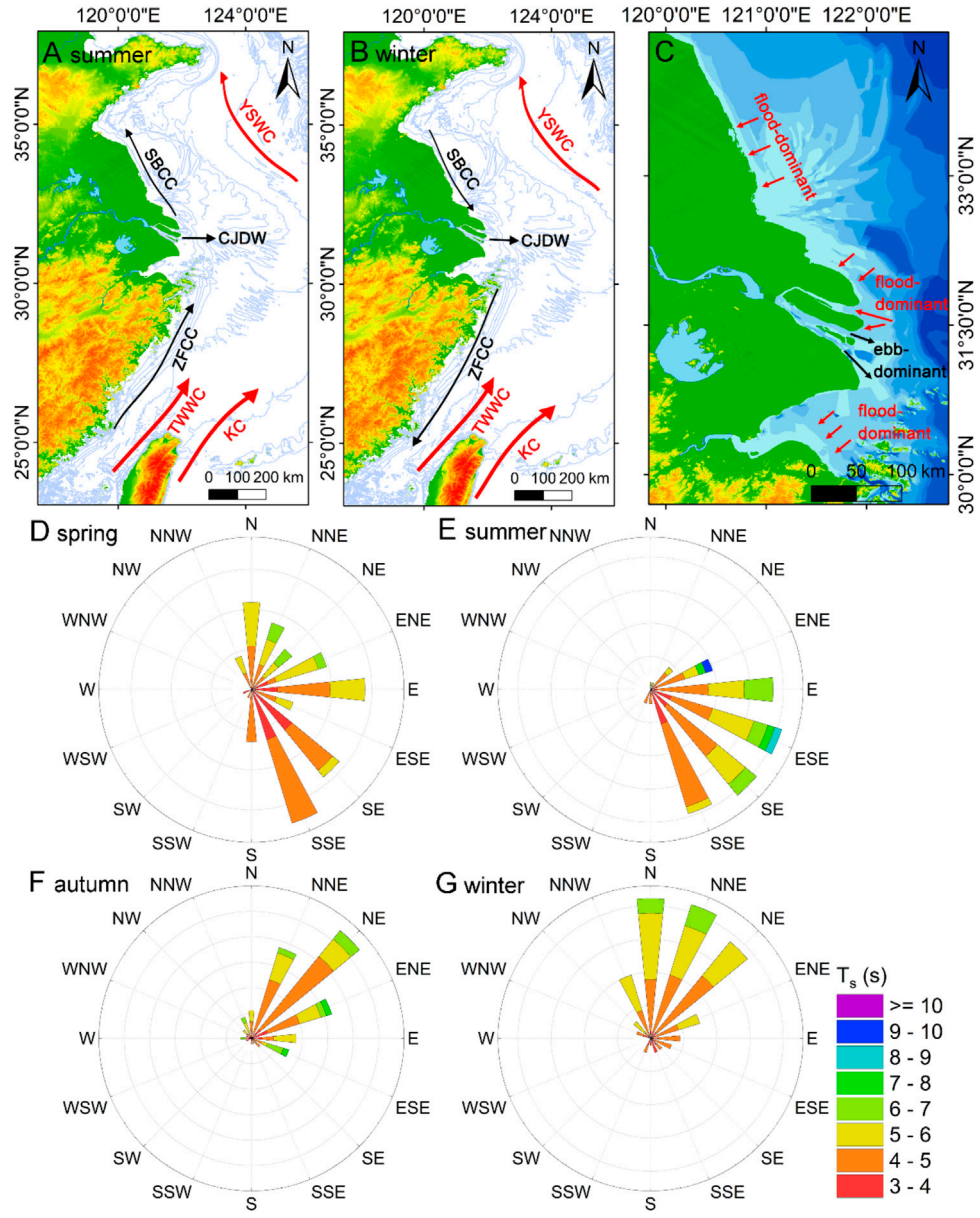

FIGURE 11
The tide and wave characteristics. Circulation systems in **(A)** summer; **(B)** winter (YSWC: The Yellow Sea Warm Current; SBCC: The Subei Coastal Current; CJDW: The Changjiang Diluted Water; ZFCC: Zhejiang-Fujian Coastal Current; TWWC: Taiwan Warm Current; and KC: Kuroshio Current); **(C)** division of flood-/ebb-dominant currents in typical areas with shoreline changes; **(D–G)** the seasonal wave direction and wave period (T_s) distributions, where spring is from March to May, summer is from June to August, autumn is from September to November, and winter is from December to February.

Based on the sediment budget scheme of the YRE and HZB interface exchange proposed by Xie et al. (2017), the SSD from the YRE to the eastern HZB decreased by 140 Mt/yr (230–370) and increased by 11 Mt/yr (186–175), respectively (Figure 10), indicating the sediment compensation from the outer YRE. The sediment transported to HZB decreased by only 13 Mt/yr (122–135) and the SSD on the YRE and eastern HZB interface decreased by 44 Mt/yr (186–230), while on the eastern HZB and Zhejiang Coast interface remained unchanged (85–85) (Figure 10). Our result revealed that there was a significant shoreline accretion trend of the inner HZB after 2006 despite the SSD reduction (Figures 8K–O, 9B). Therefore, it can be inferred that the erosion response of the SSD reduction mainly occurred outside the HZB, while the sediment was

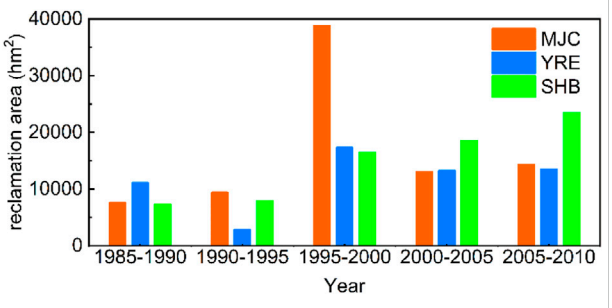

FIGURE 12
The reclamation area trend in the most heavily reclaimed middle Jiangsu Coast (MJC), Yangtze River Estuary [YRE, including the Chongming Wetland (CW) and the eastern Shanghai (ES)], and southern Hangzhou Bay (SHB) from 1985 to 2010.

compensated inside the HZB supplied by local reclamation activities (Xie et al., 2017).

5.1.2 Tide- and wave-induced sediment transport

The suspended sediment transport process is one of the major forces driving the present-day coastal geomorphology and shoreline evolution (Xing et al., 2012; Xiong et al., 2017). The northerly wind in winter carried sediments to transport along the southward SBCC (Ren, 1986; Zhu et al., 1986; Yuan and Hsueh, 2010), while some residual sediments carried by the YZR entered HZB southward (He et al., 2016) (Figures 11A,B).

The tide was demonstrated as the dominant factor influencing suspended sediment distribution (Xing et al., 2012). Most of the Jiangsu Coast was dominated by the flood-dominant tidal asymmetry (Figure 11C), and was contributed to the net landward sediment replenished by the offshore radial sand ridges (Dronkers, 1986; Wang et al., 2012). The northern channel of the ECW was flood-dominant due to the weak runoff and strong tide (Chen and Chen, 2003) (Figure 11C), and the shoreline accretion of the northeastern and eastern parts was mainly supplied by the longshore sediment transport. In contrast, the southern shore was ebb-dominant (Lou et al., 2022). Thus, the ECW shoreline expansion was mainly in the northeastern and eastern parts (Figures 8A–E). The SHB was flood-dominant (Figure 11C), and the sediment resuspension and transport caused by strong tidal currents were the main contributors to maintaining high concentrations in the HZB (Shi, 2011).

Additionally, the evident seasonal waves contributed to the seasonality of sediment concentration (Du et al., 2019). The wave direction was south or southeast in spring and summer and north or northeast in autumn and winter (Figures 11D–G), and the wave height in autumn and winter was much more significant than that in spring and summer under normal conditions (Dong et al., 2011). Generally, waves enhanced the sediment resuspension and favored the nearshore sediment erosion/deposition.

5.2 Impacts of human intervention dominated by reclamations

5.2.1 The reclamation impact on calm weather conditions

The intensive reclamations including coastal engineering constructions and vegetation planting in the YRDUA (accounted for 39.7% in China from 1985 to 2010) were mainly constructed in muddy estuaries and coasts (Wu et al., 2016), promoting shoreline progradation. Generally, the reclamation was the most intensive from 1995 to 2000 in the YRE and increased continuously on the SHB (Figure 12).

Continuous reclamation largely depends on the sediment accumulation rate in coastal zones (Du et al., 2019). Meanwhile, reclamation interrupts tidal currents, and limits sediment-carrying capacities, eventually transforming sediment transport patterns and promoting erosion and deposition (Wang et al., 2012). The SHB shoreline seaward trend was on account of the anthropogenic reclamation intervention with the increased sediment resuspension induced by the seabed erosion (He et al., 2013; Liu and Wu, 2015; Xie et al., 2017). However, the SSD transported to the SHB has decreased by 13 Mt/yr (122–135) although the continued erosion of the outer HZB replenished suspended sediments (Figure 10) (Xie et al., 2013). Therefore, the geomorphology and shoreline changes within the SHB require decades of long-term scale modelings (Xie et al., 2017).

Vegetation planting is a typical anthropogenic process affecting coastal wetland expansions and shoreline changes (Zhang et al., 2020). *Spartina alterniflora* was introduced to resist coastal erosion and promote deposition and sedimentation on the Jiangsu Coast in 1979 and ECW in 1995, respectively (Yuan et al., 2011; Du et al., 2019). In the salt marsh ecosystem, the introduced *S. alterniflora* species has a strong expansion rate and can occupy a lower ecological niche compared with native species (Zhang et al., 2004; Huang and Zhang, 2007; Zhu et al., 2012). Native and introduced vegetations increased the deposition rate by 2–3 times compared with bare flats (Wang et al., 2005), and this ecological response explained the internal mechanisms of salt marshes and bare flats (Lou et al., 2022), enhancing shoreline progradation process when bare flats migrate seaward.

5.2.2 The reclamation impact on coastal flood risks

The tidal flat reclamation is demonstrated to profoundly enhance the hydrodynamic processes, and thus, contribute to the increase in wave heights (Loder et al., 2009; Liu et al., 2019; Zhang et al., 2021). For coasts with fast shoreline accretion rates, reclamations have a suppressed and weakened impact on the

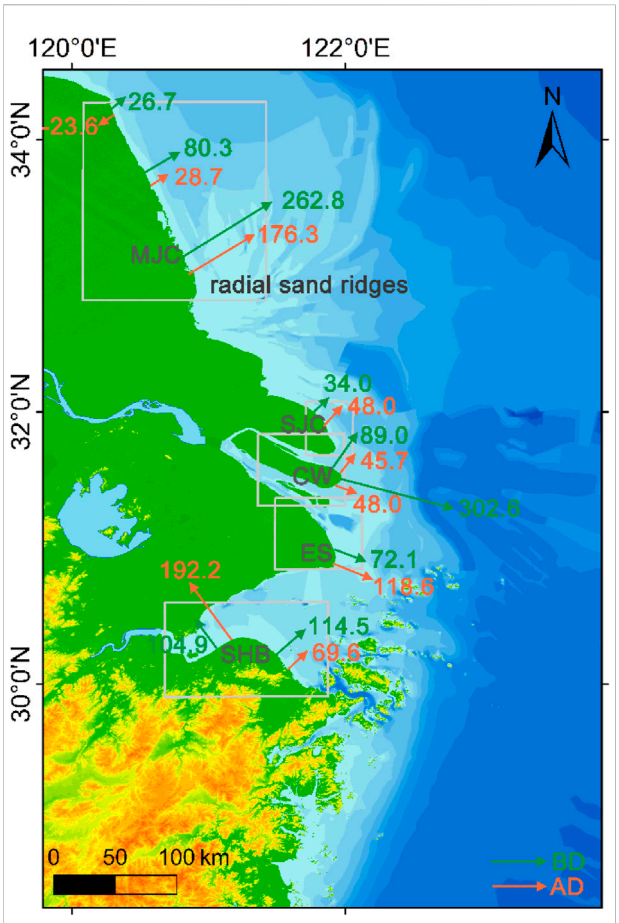

FIGURE 13
Spatial patterns of shoreline changes before the dam construction in 2002 (during BD, the green line) and after the dam construction in 2002 (during AD, the orange line). The schematic diagrams of typical areas with shoreline changes [including the middle Jiangsu Coast (MJC) with the adjacent radial sand ridges, southern Jiangsu Coast (SJC), Chongming Wetland (CW), eastern Shanghai (ES), and southern Hangzhou Bay (SHB)] are marked by gray wireframes. The unit of shoreline change rate is m/year. The seaward direction is positive and the landward direction is negative.

potential nearshore waves and coastal flood risks (Zhang et al., 2018). For vegetation planting of saltmarshes on the intertidal flat, the vegetation induced increasing bottom friction and drag force and remarkable feature of the wave attenuation (Vuik et al., 2016; Du et al., 2019). The wide and shallow tidal flat before the reclamation could efficiently reduce the wave height by the rate of 35% with the wind speed of 20 m/s and the wind angle normal to the shoreline. Therefore, the reclamation has occupied the wide intertidal flat and its internal saltmarsh, and coastal wetlands become less resistant to wind and waves during storm surges conditions (Zhang et al., 2021).

The intertidal flat and coastal wetland conservation will be highlighted due to the reclamation *via* human intervention under the global trend of sea-level rise and increasing extreme events (Kirwan et al., 2016). In response to the more frequent coastal flood hazards due to tidal flat losses, a nature-based solution considering physical environments such as sediment availability (including the sediment supply and transport) and ecological values such as vegetation consolidation is more attractive rather than the straightforward seawall heightening approach (Zhang et al., 2021).

5.3 Dynamic spatial patterns of shoreline changes

The key areas of shoreline changes showed different spatial distribution patterns during BD and AD (Figure 13). Generally, the shoreline accretion and progradation occurred widely during BD and AD except for some slight erosion with -23.6 m/yr near the Abandoned Yellow River Delta during AD (Figures 1, 13). Specifically, the MJC shoreline during BD was in a state of increasing seaward accretion rate from the northern to the southern part, while during AD was transformed from slight erosion and decrement to significant deposition and progradation. The eastern part of the ECW during BD experienced an extremely rapid progradation rate of 302.6 m/yr, but during AD the accretion rate was similar to the SJC and the northern ECW, which was only 16% of before. Both shorelines of the ES and the inner SHB were in a much greater expansion state during AD than BD despite the sediment supply reduction. However, the outer SHB progradation trend was hindered during AD (Figure 13). Since the shoreline was distinguished by coastal deposits or vegetations, our ECW shoreline accretion rate statistics of 45.7–48.0 m/yr during AD were similar to the salt marsh expansion rate of 39.5–60.6 m/yr proposed by Lou et al. (2022).

The dynamic spatial patterns have summarized and predicted the YRDUA shoreline changes in the future. Generally, the shorelines are unlikely to maintain the same seaward advance rate as before since the oppression of upstream sediment reduction induced delta system transformation, but keep pushing seaward compensated by the sediment transport from the delta-front erosion or radial sand ridges supplement. However, the intensive land reclamation has promoted the shoreline progradation more rapidly during AD on the ES and inner SHB (Figure 13), and has remained existing coastal water losses and shoreline accretion after 2015 (Figures 6, 8). The future geomorphic evolution still needs to be investigated, simulated and predicted on a longer time scale as the change of land reclamation intensity supported by government policies or economic growth, and the outer sea gradually reaching its seabed erosion critical threshold oppressed by the delta system transformation.

6 Conclusion

As a representative region oppressed by the sediment supply reduction and reclamation activities, the YRDUA shorelines have undergone dynamic changes. Remote sensing technology was proposed to evaluate the vulnerability of coastal wetlands at a large spatial scale and long-term scale. We investigated the coastal surface water variations from remote sensing images, distinguished the dynamic shoreline changes temporally, and discussed the internal and external driving forces of shoreline changes.

The total shoreline progradation increased incrementally in the YRDUA. The shoreline expansion rate adjacent to the radial sand ridges was 4–5 times that of other coastal areas in Jiangsu, but the shoreline on the northern MJC has experienced slight erosions. Specifically, there was a positive correlation between the shoreline accretion rate and the amount of sediment supply on the ECW. However, the sediment supply was still sufficient to support the shoreline expansion on the coasts of the YRE-HZB interface on the premise of the upstream sediment reduction, although the accretion rate has slowed down. The ES and inner SHB were exceptions, as accretion rates have been expedited even after 2015, mainly for the extremely intensive land reclamation activities.

Human interventions, dominated mainly by land reclamations (including the external coastal engineering constructions and internal ecological vegetation planting), affected intertidal flat mechanisms and shoreline changes. The continuous reclamation in recent decades was determined by sediment accumulation rates to some extent. On the one hand, under the background of the delta system transformation with upstream sediment decline, the hydrodynamic-sediment coupling process caused by waves and currents formed different seaward expansion degrees and provided sufficient sediments for the reclamation on inner coasts. On the other hand, anthropogenic reclamation enhanced hydrodynamic morphology and increased coastal flood hazard risks due to tidal flat losses. A nature-based solution considering the sediment availability and ecological value is more attractive for coastal wetland conservation.

Data availability statement

The original contributions presented in the study are included in the article/supplementary material, further inquiries can be directed to the corresponding authors.

Author contributions

CL and YW put forward the idea, designed the experiments and funded the study. TL processed the main measurements/experiments data and completed the major sections of the manuscript. HW and YC helped making general changes and improvements to the article. MZ helped processing partial data. YS reviewed this article and made suggestions to improve it. All authors contributed to manuscript revision, read, and approved the submitted version.

Funding

Financial support was provided by the Research Project of Nanjing Research Institute of Surveying, Mapping and Geotechnical Investigation, Co., Ltd. (2021RD02), the Innovation Program of Shanghai Municipal Education Commission (2019-01-07-00-05-E00027) and the National Natural Science Foundation of China (U2240220).

Acknowledgments

We thank Xiangyu Nie, Shibing Zhu, and Junhao Fu for their assistance in providing suggestions and checking out the manuscript.

Conflict of interest

Authors TL, CL, MZ, and YS were employed by Nanjing Research Institute of Surveying, Mapping and Geotechnical Investigation Co., LTD.

The remaining authors declare that the research was conducted in the absence of any commercial or financial relationships that could be construed as a potential conflict of interest.

The authors declare that this study also received funding from Geotechnical Investigation, Co., Ltd. The funder was not involved in the study design, collection, analysis, interpretation of data, the writing of this article or the decision to submit it for publication.

Publisher's note

References

Addo, K. A. (2013). Shoreline morphological changes and the human factor. Case study of Accra Ghana. *J. Coast. Conserv.* 17 (1), 85–91. doi:10.1007/s11852-012-0220-5

Allen, J. R. L. (2000). Morphodynamics of holocene salt marshes: A review sketch from the atlantic and southern north sea coasts of europe. *Quat. Sci. Rev.* 19 (12), 1155–1231. doi:10.1016/S0277-3791(99)00034-7

Blum, M. D., and Roberts, H. H. (2009). Drowning of the Mississippi Delta due to insufficient sediment supply and global sea-level rise. *Nat. Geosci.* 2 (7), 488–491. doi:10.1038/ngeo553

Carriquiry, J. D., Sánchez, A., and Camacho-Ibar, V. F. (2001). Sedimentation in the northern Gulf of California after cessation of the Colorado River discharge. *Sediment. Geol.* 144 (1-2), 37–62. doi:10.1016/s0037-0738(01)00134-8

Chen, B., Xiao, X., Li, X., Pan, L., Doughty, R., Ma, J., et al. (2017). A mangrove forest map of China in 2015: Analysis of time series Landsat 7/8 and Sentinel-1A imagery in Google Earth Engine cloud computing platform. *ISPRS J. Photogrammetry Remote Sens.* 131, 104–120. doi:10.1016/j.isprsjprs.2017.07.011

Chen, D., Li, M., Zhang, Y., Zhang, L., Tang, J., Wu, H., et al. (2020). Effects of diatoms on erosion and accretion processes in saltmarsh inferred from field observations of hydrodynamic and sedimentary processes. *Ecohydrology* 13 (8), 1–15. doi:10.1002/eco.2246

Chen, J., and Chen, S. (2003). The changes of ecologic environment in Yangtze River estuary and some suggestions for estuary regulation. *Water Resour. Hydropower* 34 (01), 19–25. (in Chinese with English Abstract).

Costanza, R., Mooney, H. A., Capistrano, D., Carpenter, S. R., Chopra, K., Cropper, A., et al. (2006). Nature: The many benefits of ecosystem services. *Nature* 443, 749. doi:10.1038/443749a

Dai, Y., Daiki, I., Jeison, S., and Pavelsky, T. M. (2019). MERIT Hydro: A high-resolution global hydrography map based on latest topography dataset. *Water Resour. Res.* 55 (6), 5053–5073. doi:10.1029/2019WR024873

Dai, Z., Liu, J. T., Fu, G., and Xie, H. (2013). A thirteen-year record of bathymetric changes in the North Passage, Changjiang (Yangtze) estuary. *Geomorphology* 187 (4), 101–107. doi:10.1016/j.geomorph.2013.01.004

Dong, L. X., Guan, W. B., Chen, Q., Li, X. H., Liu, X. H., and Zeng, X. M. (2011). Sediment transport in the Yellow Sea and east China sea. *Estuar. Coast. Shelf Sci.* 93 (3), 248–258. doi:10.1016/j.ecss.2011.04.003

Dronkers, J. (1986). Tidal asymmetry and estuarine morphology. *Neth. J. Sea Res.* 20 (2-3), 117–131. doi:10.1016/0077-7579(86)90036-0

Du, J., Shi, B., Li, J., and Wang, Y. P. (2019). "Muddy coast off Jiangsu, China: Physical, ecological, and anthropogenic processes," in *Sediment dynamics of Chinese muddy coasts and estuaries*, 25–49.

Fagherazzi, S., Mariotti, G., Leonardi, N., Canestrelli, A., and Kearney, W. S. (2020). Salt marsh dynamics in a period of accelerated sea level rise. *JGR. Earth Surf.* 125, e2019JF005200. doi:10.1029/2019JF005200

Farr, T. G., Rosen, P. A., Caro, E., Crippen, R., Duren, R., Hensley, S., et al. (2007). The shuttle radar topography mission. *Rev. Geophys.* 45 (2), RG2004. doi:10.1029/2005rg000183

Foster, N. M., Hudson, M. D., Bray, S., and Nicholls, R. J. (2013). Intertidal mudflat and saltmarsh conservation and sustainable use in the UK: A review. *J. Environ. Manag.* 126, 96–104. doi:10.1016/j.jenvman.2013.04.015

Gao, S., and Wang, Y. P. (2008). Changes in material fluxes from the Changjiang River and their implications on the adjoining continental shelf ecosystem. *Cont. Shelf Res.* 28 (12), 1490–1500. doi:10.1016/j.csr.2007.02.010

Gao, Y., Wang, H., Su, F., and Liu, G. (2013). Spatial and temporal of continental coastalline of China in recent three decades. *Acta Oceanol. Sin.* 35 (6), 31–42. (in Chinese with English Abstract).

He, X., Bai, Y., Pan, D., Huang, N., Dong, X., Chen, J., et al. (2013). Using geostationary satellite ocean color data to map the diurnal dynamics of suspended particulate matter in coastal waters. *Remote Sens. Environ.* 133, 225–239. doi:10.1016/j.rse.2013.01.023

He, Z., Huangfu, K., Yuan, Y., Song, D., and Li, L. (2016). Variations of temperature, salinity and current in the southern tidal passage of the Hangzhou Bay, China. *Acta Oceanol. Sin.* 35 (3), 30–37. doi:10.1007/s13131-016-0819-8

Huang, H. M., and Zhang, L. Q. (2007). The spatio-temporal dynamics of salt marsh vegetation for chongming dongtan national nature reserve, Shanghai. *Acta Ecol. Sin.* 27 (10), 4166–4172. (in Chinese with English Abstract).

Kirwan, M. L., Temmerman, S., Skeehan, E. E., Guntenspergen, G. R., and Fagherazzi, S. (2016). Overestimation of marsh vulnerability to sea level rise. *Nat. Clim. Chang.* 6 (3), 253–260. doi:10.1038/nclimate2909

Langston, A. K., Vinent, O. D., Herbert, E. R., and Kirwan, M. L. (2020). Modeling long-term salt marsh response to sea level rise in the sediment-deficient Plum Island Estuary, MA. *Limnol. Oceanogr.* 65, 2142–2157. doi:10.1002/lno.11444

Li, J., and Zhang, C. (1998). Sediment resuspension and implications for turbidity maximum in the Changjiang Estuary. *Mar. Geol.* 148 (3-4), 117–124. doi:10.1016/S0025-3227(98)00003-6

Li, S., Dragicevic, S., Castro, F. A., Sester, M., Winter, S., Coltekin, A., et al. (2016). Geospatial big data handling theory and methods: A review and research challenges. *ISPRS J. Photogrammetry Remote Sens.* 115, 119–133. doi:10.1016/j.isprsjprs.2015.10.012

Li, X., Zhou, Y., Zhang, L., and Kuang, R. (2014). Shoreline change of chongming dongtan and response to River Sediment load: A remote sensing assessment. *J. Hydrology* 511, 432–442. doi:10.1016/j.jhydrol.2014.02.013

Li, Y., Jia, J., Zhu, Q., Cheng, P., Gao, S., and Wang, Y. P. (2018). Differentiating the effects of advection and resuspension on suspended sediment concentrations in a turbid estuary. *Mar. Geol.* 403, 179–190. doi:10.1016/j.margeo.2018.06.001

Liu, G. S., and Wu, X. G. (2015). Study on dynamics geomorphology evolution of Huibieyang zone in recent ten years. *J. Sediment Res.* 3, 42–48. (in Chinese with English Abstract).

Liu, X., Wang, Y., Costanza, R., Kubiszewski, I., Xu, N., Yuan, M., et al. (2019). The value of China's coastal wetlands and seawalls for storm protection. *Ecosyst. Serv.* 36, 100905. doi:10.1016/j.ecoser.2019.100905

Liu, Z., Huang, Y., and Zhang, Q. (1989). Tidal current ridges in the southwestern Yellow Sea. *J. Sediment. Res.* 59 (3), 432–437. doi:10.1306/212F8FB7-2B24-11D7-8648000102C1865D

Loder, N. M., Irish, J. L., Cialone, M. A., and Wamsley, T. V. (2009). Sensitivity of hurricane surge to morphological parameters of coastal wetlands. *Estuar. Coast. Shelf Sci.* 84 (4), 625–636. doi:10.1016/j.ecss.2009.07.036

Long, C., Dai, Z., Wang, R., Lou, Y., Zhou, X., Li, S., et al. (2022). Dynamic changes in mangroves of the largest delta in northern Beibu Gulf, China: Reasons and causes. *For. Ecol. Manag.* 504, 119855–119866. doi:10.1016/j.foreco.2021.119855

Long, C., Dai, Z., Zhou, X., Mei, X., and Mai Van, C. (2021). Mapping mangrove forests in the red river delta, vietnam. *For. Ecol. Manag.* 483, 118910–118923. doi:10.1016/j.foreco.2020.118910

Lou, Y., Dai, Z., Long, C., Dong, H., Wei, W., and Ge, Z. (2022). Image-based machine learning for monitoring the dynamics of the largest salt marsh in the Yangtze River Delta. *J. Hydrology* 608, 127681–127694. doi:10.1016/j.jhydrol.2022.127681

Lu, S., Jia, L., Zhang, L., Wei, Y., Baig, M. H. A., Zhai, Z., et al. (2016). Lake water surface mapping in the Tibetan Plateau using the MODIS MOD09Q1 product. *Remote Sens. Lett.* 8 (3), 224–233. doi:10.1080/2150704x.2016.1260178

Lu, T., Wu, H., Zhang, F., Li, J., Zhou, L., Jia, J., et al. (2020). Constraints of salinity- and sediment-induced stratification on the turbidity maximum in a tidal estuary. *Geo-Mar. Lett.* 40 (5), 765–779. doi:10.1007/s00367-020-00670-8

Nobre, A. D., Cuartas, L. A., Hodnett, M., Rennó, C. D., Rodrigues, G., Silveira, A., et al. (2011). Height above the nearest drainage – A hydrologically relevant new terrain model. *J. Hydrology* 404 (1-2), 13–29. doi:10.1016/j.jhydrol.2011.03.051

Pardo-Pascual, J. E., Almonacid-Caballer, J., Ruiz, L. A., and Palomar-Vázquez, J. (2012). Automatic extraction of shorelines from Landsat TM and ETM+ multi-temporal images with subpixel precision. *Remote Sens. Environ.* 123, 1–11. doi:10.1016/j.rse.2012.02.024

Ren, M. e. (1986). *Comprehensive investigation of the coastal zone and tidal land resources of Jiangsu Province*. Beijing: Ocean Press.

Pesaresi, M., Ehrlich, D., Ferri, S., Florczyk, A., Freire, A., Stamatia, H., et al. (2016). *Operating procedure for the production of the Global Human Settlement Layer from Landsat data of the epochs 1975, 1990, 2000, and 2014*. European Commission: JRC Technical Reports, 1–62.

Shi, J. Z. (2011). Tide-induced fine sediment resuspension in the well-mixed Hangzhou bay, east China sea, China. *Earth Environ. Sci. Trans. R. Soc. Edinb.* 102 (1), 25–34. doi:10.1017/s1755691011010061

Stanley, D. J., and Warne, A. G. (1993). Nile delta: Recent geological evolution and human impact. *Science* 260 (5108), 628–634. doi:10.1126/science.260.5108.628

Syvitski, J. P. M., Kettner, A. J., Overeem, I., Hutton, E. W. H., Hannon, M. T., Brakenridge, G. R., et al. (2009). Sinking deltas due to human activities. *Nat. Geosci.* 2 (10), 681–686. doi:10.1038/ngeo629

Tamiminia, H., Salehi, B., Mahdianpari, M., Quackenbush, L., and Brisco, B. (2020). Google Earth engine for geo-big data applications: A meta-analysis and

systematic review. *ISPRS J. Photogrammetry Remote Sens.* 164, 152–170. doi:10.1016/j.isprsjprs.2020.04.001

Temmerman, S., Meire, P., Bouma, T. J., Herman, P. M., Ysebaert, T., and De Vriend, H. J. (2013). Ecosystem-based coastal defence in the face of global change. *Nature* 504 (7478), 79–83. doi:10.1038/nature12859

Thieler, E. R., Himmelstoss, E. A., Zichichi, J. L., and Ergul, A. (2009). *The digital shoreline analysis system (DSAS) version 4.0 - an ArcGIS extension for calculating shoreline change.* doi:10.3133/ofr20081278

Tsyganskaya, V., Martinis, S., Marzahn, P., and Ludwig, R. (2018). SAR-Based detection of flooded vegetation – A review of characteristics and approaches. *Int. J. Remote Sens.* 39 (8), 2255–2293. doi:10.1080/01431161.2017.1420938

van der Wal, D., Pye, K., and Neal, A. (2002). Long-term morphological change in the ribble estuary, northwest england. *Mar. Geol.* 189 (3-4), 249–266. doi:10.1016/S0025-3227(02)00476-0

Vuik, V., Jonkman, S. N., Borsje, B. W., and Suzuki, T. (2016). Nature-based flood protection: The efficiency of vegetated foreshores for reducing wave loads on coastal dikes. *Coast. Eng.* 116, 42–56. doi:10.1016/j.coastaleng.2016.06.001

Wang, A., Gao, S., Jia, J., and Pan, S. (2005). Contemporary sedimentation rates on salt marshes at wanggang, Jiangsu, China. *Acta Geogr. Sin.* 60 (1), 61–70. (in Chinese with English Abstract).

Wang, H., Bi, N., Saito, Y., Wang, Y., Sun, X., Zhang, J., et al. (2010). Recent changes in sediment delivery by the Huanghe (Yellow River) to the sea: Causes and environmental implications in its estuary. *J. Hydrology* 391 (3-4), 302–313. doi:10.1016/j.jhydrol.2010.07.030

Wang, X., Xiao, X., Zou, Z., Hou, L., Li, B., Dong, J., et al. (2020). Mapping coastal wetlands of China using time series Landsat images in 2018 and Google Earth Engine. *ISPRS J. Photogrammetry Remote Sens.* 163, 312–326. doi:10.1016/j.isprsjprs.2020.03.014

Wang, Y. P., Gao, S., Jia, J., Thompson, C. E. L., Gao, J., and Yang, Y. (2012). Sediment transport over an accretional intertidal flat with influences of reclamation, Jiangsu coast, China. *Mar. Geol.* 291-294, 147–161. doi:10.1016/j.margeo.2011.01.004

Wang, Y. P., Voulgaris, G., Li, Y., Yang, Y., Gao, J., Chen, J., et al. (2013). Sediment resuspension, flocculation, and settling in a macrotidal estuary. *J. Geophys. Res. Oceans* 118 (10), 5591–5608. doi:10.1002/jgrc.20340

Wu, W. T., Tian, B., Zhou, Y. X., Shu, M. Y., Qi, X. Y., and Xu, W. (2016). The trends of coastal reclamation in China in the past three decades. *Acta Ecol. Sin.* 36 (16), 5007–5016. (in Chinese with English Abstract).

Xie, D., Gao, S., Wang, Z., and Pan, C. (2013). Numerical modeling of tidal currents, sediment transport and morphological evolution in Hangzhou Bay, China. *Int. J. Sediment Res.* 28 (3), 316–328. doi:10.1016/s1001-6279(13)60042-6

Xie, D., Pan, C., Wu, X., Gao, S., and Wang, Z. (2017). The variations of sediment transport patterns in the outer Changjiang Estuary and Hangzhou Bay over the last 30 years. *J. Geophys. Res. Oceans* 122 (4), 2999–3020. doi:10.1002/2016jc012264

Xing, F., Wang, Y. P., and Wang, H. V. (2012). Tidal hydrodynamics and fine-grained sediment transport on the radial sand ridge system in the southern Yellow Sea. *Mar. Geol.* 291-294, 192–210. doi:10.1016/j.margeo.2011.06.006

Xiong, J., Wang, X. H., Wang, Y. P., Chen, J., Shi, B., Gao, J., et al. (2017). Mechanisms of maintaining high suspended sediment concentration over tide-dominated offshore shoals in the southern Yellow Sea. *Estuar. Coast. Shelf Sci.* 191, 221–233. doi:10.1016/j.ecss.2017.04.023

Xu, F., Tao, J., Zhou, Z., Coco, G., and Zhang, C. (2016). Mechanisms underlying the regional morphological differences between the northern and southern radial sand ridges along the Jiangsu Coast, China. *Mar. Geol.* 371, 1–17. doi:10.1016/j.margeo.2015.10.019

Xu, H. (2006). Modification of normalised difference water index (NDWI) to enhance open water features in remotely sensed imagery. *Int. J. Remote Sens.* 27 (14), 3025–3033. doi:10.1080/01431160600589179

Yang, H. F., Yang, S. L., Xu, K. H., Milliman, J. D., Wang, H., Yang, Z., et al. (2018). Human impacts on sediment in the Yangtze River: A review and new perspectives. *Glob. Planet. Change* 162, 8–17. doi:10.1016/j.gloplacha.2018.01.001

Yang, X., Qin, Q., Yésou, H., Ledauphin, T., Zhu, Z., Grussenmeyer, P., et al. (2020). Monthly estimation of the surface water extent in France at a 10-m resolution using Sentinel-2 data. *Remote Sens. Environ.* 244, 111803. doi:10.1016/j.rse.2020.111803

Yuan, D., and Hsueh, Y. (2010). Dynamics of the cross-shelf circulation in the Yellow and east China seas in winter. *Deep Sea Res. Part II Top. Stud. Oceanogr.* 57 (19-20), 1745–1761. doi:10.1016/j.dsr2.2010.04.002

Yuan, L., Zhang, L., Xiao, D., and Huang, H. (2011). The application of cutting plus waterlogging to control Spartina alterniflora on saltmarshes in the Yangtze Estuary, China. *Estuar. Coast. Shelf Sci.* 92 (1), 103–110. doi:10.1016/j.ecss.2010.12.019

Zhang, M., Dai, Z., Bouma, T. J., Bricker, J., Townend, I., Wen, J., et al. (2021). Tidal-flat reclamation aggravates potential risk from storm impacts. *Coast. Eng.* 166, 103868. doi:10.1016/j.coastaleng.2021.103868

Zhang, R. S., Shen, Y. M., Lu, L. Y., Yan, S. G., Wang, Y. H., Li, J. L., et al. (2004). Formation of Spartina alterniflora salt marshes on the coast of Jiangsu Province, China. *Ecol. Eng.* 23 (2), 95–105. doi:10.1016/j.ecoleng.2004.07.007

Zhang, X., Xiao, X., Wang, X., Xu, X., Li, B., Wang, J., et al. (2020). Quantifying expansion and removal of Spartina alterniflora on Chongming island, China, using time series Landsat images during 1995-2018. *Remote Sens. Environ.* 247 (15), 111916. doi:10.1016/j.rse.2020.111916

Zhang, X., Zhang, Y., Zhu, L., Chi, W., Yang, Z., Wang, B., et al. (2018). Spatial-temporal evolution of the eastern Nanhui mudflat in the Changjiang (Yangtze River) Estuary under intensified human activities. *Geomorphology* 309, 38–50. doi:10.1016/j.geomorph.2018.02.023

Zhu, D., Ke, X., and Gao, S. (1986). Tidal flat sedimentation of Jiangsu coast. *J. Oceanogr. Huanghai Bohai seas* 4 (3), 19–27. (in Chinese with English Abstract).

Zhu, Z., and Woodcock, C. E. (2012). Object-based cloud and cloud shadow detection in Landsat imagery. *Remote Sens. Environ.* 118, 83–94. doi:10.1016/j.rse.2011.10.028

Zhu, Z., Zhang, L., Wang, N., Schwarz, C., and Ysebaert, T. (2012). Interactions between the range expansion of saltmarsh vegetation and hydrodynamic regimes in the Yangtze Estuary, China. *Estuar. Coast. Shelf Sci.* 96, 273–279. doi:10.1016/j.ecss.2011.11.027

frontiers | Frontiers in Earth Science

TYPE Original Research
PUBLISHED 09 September 2022
DOI 10.3389/feart.2022.975220

OPEN ACCESS

EDITED BY
Xiaolei Liu,
Ocean University of China, China

REVIEWED BY
Peter Feldens,
Leibniz Institute for Baltic Sea Research (LG), Germany
Bimlesh Kumar,
Indian Institute of Technology Guwahati, India

*CORRESPONDENCE
Jingping Xu,
xujp@sustech.edu.cn

SPECIALTY SECTION
This article was submitted to Geohazards and Georisks, a section of the journal Frontiers in Earth Science

RECEIVED 22 June 2022
ACCEPTED 26 August 2022
PUBLISHED 09 September 2022

CITATION
Yang Y, Liu M, Xu J and Xu W (2022), Migrating sandwaves riding on relict dunes of Taiwan shoal, northern South China Sea.
Front. Earth Sci. 10:975220.
doi: 10.3389/feart.2022.975220

Migrating sandwaves riding on relict dunes of Taiwan shoal, northern South China Sea

Yuping Yang[1], Meng Liu[1], Jingping Xu[1,2]* and Weikun Xu[3]

[1]Department of Ocean Science and Engineering, Southern University of Science and Technology, Shenzhen, China, [2]Southern Marine Science and Engineering Guangdong Laboratory (Guangzhou), Guangzhou, China, [3]National Deep Sea Center, Qingdao, China

Sandwaves, a ubiquitous bedform commonly found in most coastal seas and sometimes in deep waters of continental slopes and submarine canyons, are often the subject of marine hazard studies because their frequent migration can pose potential threats to pipelines or other engineering structures in the ocean. Analyses of high-resolution bathymetric data collected along a 136-km multibeam bathymetric survey line demonstrate the co-existence of three different sizes of sandwaves: giant, primary dunes (~10-15 m in height, up to 2,000 m in length); small, secondary sandwaves (~1 m in height, ~50 m in length) riding on the stoss side of the primary dunes; and mid-size dunes (~5-10 m in height, ~100-500 m in length) found in the trough of primary dunes. While the tidal current-driven, secondary sandwaves are migrating, the primary and mid-size dunes are immobile. Empirical model results suggest that the primary dunes are relict dunes that were most likely formed in geologic past when sea level was higher or the seabed elevation was lower, but water depth is probably not the only factor in limiting the formation of the primary dunes.

KEYWORDS

sandwaves, relict dunes, migration, Taiwan shoal, south China sea

Introduction

Sandwaves, also known as dunes, are both a sediment transport mechanism and a dynamic morphologic feature in subaqueous environments that are commonly found in submarine canyons and continental shelves around the world (Flemming, 1980; Ashley, 1990; Wynn and Stow, 2002). The rhythmic bed forms develop because of seabed deformation in response to various dynamic forces, such as tidal currents (Off, 1963; Stride et al., 1982; Amos and King, 1984; Besio et al., 2004) or storm waves (Bao et al., 2020). The size, shape, and distribution of sandwaves are determined by factors such as topography, sediment grain size, sediment supply, as well as global variations in climate and sea level (Rubin and McCulloch, 1980; Viana et al., 1998; Francken et al., 2004; Bartholdy et al., 2005). Kubo et al. (2004) and other researchers also pointed out that local topographic constraints (i.e., narrow channels and depressions) play a key role in accelerating bottom currents that promote the formation of giant sandwaves (Barrie et al., 2009; Rovere et al., 2019). Migrating giant sandwaves often become potential hazards to coastal engineering structures: destabilizing underwater drilling platforms,

causing pipeline overhang and even creating fractures (Belde et al., 2017). Sandwave mobility (e.g., Ferret et al., 2010; Damen et al., 2018) or sediment transport (Dalrymple, 1984; Vandenberg, 1987; Hoekstra et al., 2004; Xu et al., 2008) are typically the focus of studies on sandwave migrations. The direction of sandwave migration can be determined by the geometrical asymmetry of sandwaves that normally have a steeper, shorter lee side (downstream) and a gentler, longer stoss side (upstream) (McCave, 1971; Bartholdy et al., 2002; Wynn and Stow, 2002; Zhou et al., 2018). The degree of sandwave asymmetry can be parameterized to help estimate the migration direction and rates (Knaapen, 2005; Xu et al., 2008). Observational studies indicate that giant sandwaves migrate slower than smaller ones because more sediment must be mobilized in larger sandwaves (i.e., Whitmeyer and FitzGerald, 2008). In addition, details of small scale, high resolution investigations (e.g., the relations between waves and wave-generated sand ripples and their migrations) have been obtained by video imaging analyses as well as numerical and physical modeling techniques (Xu, 2005; Li et al., 2011).

Since the first report of the phenomenon in the 1970s (Boggs, 1974), sandwaves have been intensively studied in the Taiwan Shoal, especially over the past 20 years (Cai et al., 2003; Kai-guo et al., 2009; Bao et al., 2014; Zhou et al., 2018; Zhou et al., 2020; Zhou et al., 2022). Synthetic-aperture radar (SAR) imagery provided a regional glimpse of the size and orientation of sandwaves in the Taiwan Shoal, with sandwave lengths between 500-5,000 m and heights between 2-6 m respectively (Huang et al., 2008). High-resolution multibeam images have enabled scientists to catalogue the various morphological types of sandwaves: giant sandwaves of ~1,200 m in length and ~15 m in height and small sandwaves of ~50 m in length and ~1.5 m in height (Zhou et al., 2018; Zhou et al., 2020). Hydrodynamic measurements, such as the acoustic Doppler current profiler (ADCP), have helped to establish empirical relationships between wave/current forces and the size/migration rate of sandwaves (Zhou et al., 2018; Bao et al., 2020). For reasons that are not specified in the literature, all previous multibeam surveys were collected along track lines (NW-SE) in small oblique angles to the dominant orientation of the sandwave crests. The cross-section bathymetric profile of sandwaves is the most important parameter in characterizing the static shape as well as the dynamic migration and transport of sandwaves. As a result, multibeam data from track lines that is perpendicular to the overall crest orientation would clearly be more ideal.

This study analyzes a dataset from a high-resolution multibeam survey collected on a research vessel heading southwest across the Taiwan Shoal, a track line that is almost perpendicular to the crest of the sandwaves. This allows us to more accurately 1) characterize the geometries and migration patterns of the sandwaves, 2) estimate the developmental conditions (for example, the flow velocity and water depth) of those sandwaves of different shapes and sizes.

Geologic and hydrodynamic settings

Taiwan Strait is a narrow channel between the southeastern portion of mainland China and the island of Taiwan. The strait has an average width of 180 km, an average length of 360 km, and an average water depth of 60 m (Hu et al., 2013; Shen et al., 2021). The Taiwan Shoal (Figure 1) is an area of ~13,000 km^2 at the southwest corner of the strait, where average water depth is only 20 m (Zhou et al., 2018). Influenced by East Asian monsoons, the average wave height in the strait is about 2 m with a period of 4-5 s in winter, but only 1-1.25 m with a period of 4-5 s in summer (Zhou et al., 2020). When typhoons and tropical storms, which

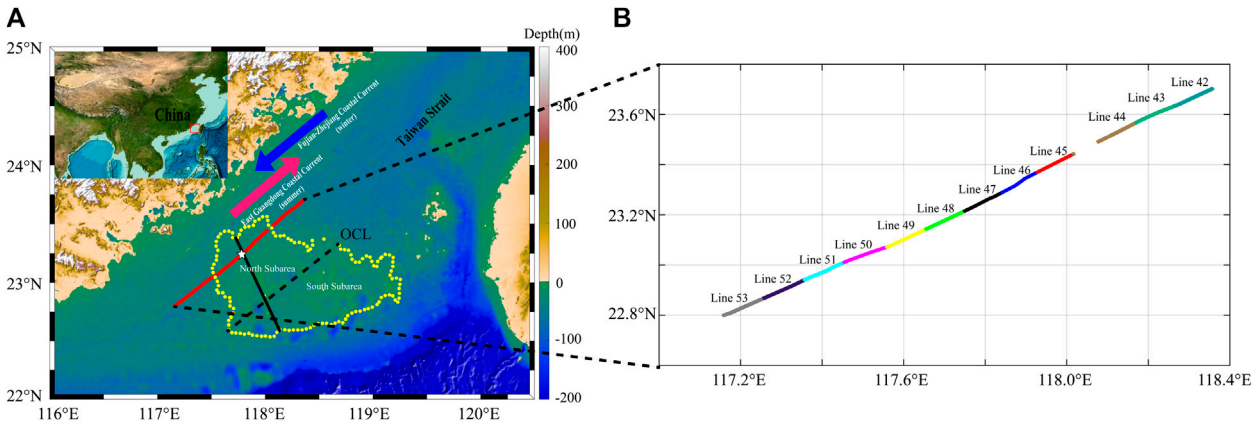

FIGURE 1
(A) A regional map showing the Taiwan Shoal (yellow dotted line), the two main coastal currents in the strait (thick red and blue arrows), the vessel's path (red solid line, heading southwest), Zhou et al., 2018's multibeam survey track (solid black line) and their arbitrary Orientation Changing Limit (dashed black line). The white pentagram at the crossing (117.7757°E 23.2510°N) for the two survey lines is the location whose current velocity and direction data were used in the numerical modelling. **(B)** Close up of the multibeam survey data in this study. For the ease of plotting and presentations, the track line is divided into 12 sections, Line 42-53.

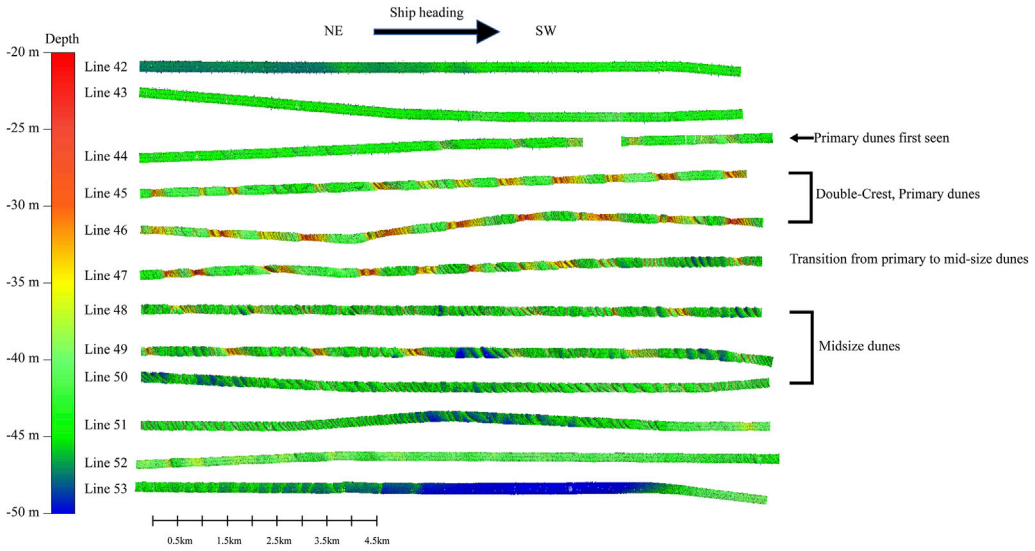

FIGURE 2
The overall morphological characteristics of dunes from the multibeam survey lines. The smaller secondary sandwaves are too small to be clearly identified.

on average, occur six times a year, pass through the strait, wave heights can reach as high as 6 m (Zhou et al., 2020; Zhou et al., 2022). Tides in the strait are dominated by the semidiurnal M_2, with an average current speed of about 0.46 m/s (Wang et al., 2003; Du et al., 2010; Zhou et al., 2018). The East Guangdong Coastal Current primarily occurs in summer and flows northeast along the coast at an average speed of 0.20-0.75 m/s. The Fujian-Zhejiang Coastal Current occurs mainly in winter and flows southwest at an average speed of 0.15-0.25 m/s (Hong et al., 2009; Zhou et al., 2022). The shoal, especially the sandwave field, is composed of well sorted, rounded medium-coarse sands of mean grain size of 0.50 ~ 0.58 mm (Zhou et al., 2020). Borehole data suggests that the deposits of the giant sandwaves are relics from the Pleistocene and early Holocene (Wang et al., 2014) that consist of a great number of shell fragments, beach rock masses, and basalt gravels (Cai et al., 2003). Based on the orientation changing limit (OCL) of the sandwave field, Zhou et al. (2018) divided the Taiwan Shoal into two subareas (Figure 1): the north subarea in which sandwaves are primarily oriented NW-SE and the south subarea where the orientation is mainly W–E and NE–SW.

Data collection

The high-resolution multibeam data used in this study was collected by a ship of opportunity, the R/V Shenhaiyihao, which happened to pass through the Taiwan Shoal on her way to another field experiment site in the South China Sea. For nearly 5.5 h on 30th September 2020, this vessel travelled at a speed of 13 knots heading southwest (Figure 1). The multibeam bathymetric data was acquired using the EM 712 multibeam echo sounder (MBES) with a maximum of 1,600 soundings being conducted per ping over a swath width of 140 and in a range of 40–100 kHz, which allowed a maximum speed of 14 knots to measure profiles of the dunes. The system can accommodate an acquisition depth between 3–3,500 m below its transducers, depending on the array size.

The raw multibeam bathymetric data was first processed using sound velocity calibration, tide correction, data cleaning, and data quality control via the Qimera software (version 1.0.4.93). A Digital Bathymetric Model (DBM) with along-track resolution of 1.2 m in horizontal and 1 cm in depth, both maximum possible for a cruising speed of 13 knots, was constructed. The 136 km long, 150-200 m wide swath of sandwaves bathymetry were divided into a dozen 12 km sections (Lines 42–53) to facilitate the ensuring data analyses. One key different between the multibeam data from previous studies and this one is the orientation of the track lines. Track lines perpendicular to the crest of the sandwaves have clear advantages in more accurately measuring the bedform parameters such as periods and heights.

Results

Size and shapes of sandwaves

High-resolution DBM revealed the details of the morphological variation along the 136-km track line across

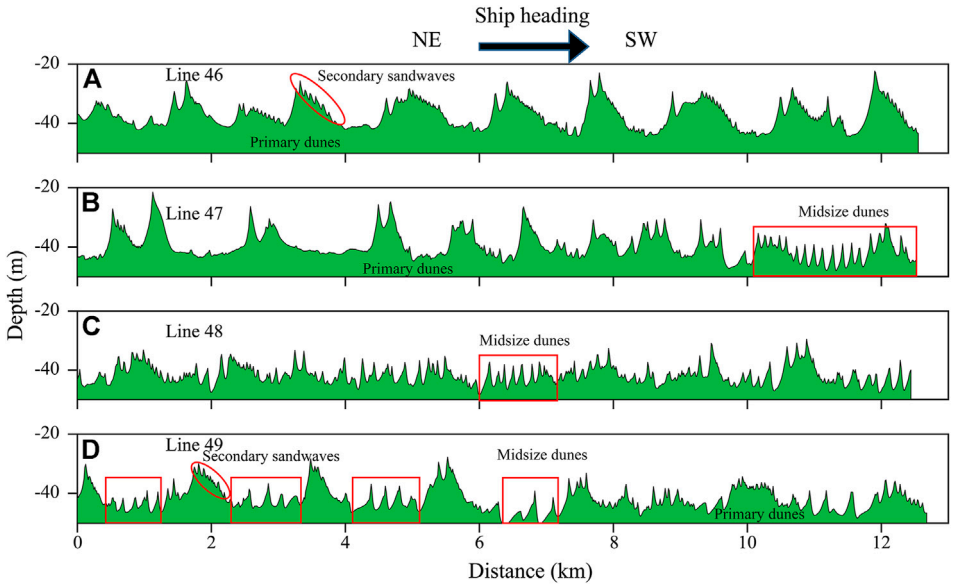

FIGURE 3
The morphological profile of sandwaves in Lines 46, 47, 48, and 49. **(A)** Line 46 contains mainly the primary (giant) dunes, with secondary (small) sandwaves riding on the stoss side of the primary. **(B)** Line 47 depicts the transition from primary to the midsize dunes that tend to reside in the troughs of the primary. **(C)** Line 48 is dominated by the midsize dunes such that primary dunes are hardly identifiable. **(D)** Line 49 has the primary dunes returned but also clearly shows the midsize dunes in the troughs and the secondary sandwaves on the stoss side of the primary dunes.

TABLE 1 The statistics of the sandwave parameters.

	Sample size	Wave height (m)			Wave length (m)		
		Max	Mean	Standard deviation	Max	Mean	Standard deviation
Primary dunes	13	14.7	12.0	1.5	2,000	800	240.9
Midsize dunes	46	9.7	6.3	1.3	500	290	82.3
Secondary sandwaves	132	1.5	1.2	0.1	50	45	28.8

the Taiwan Shoal (Figure 2). Based on the wave height and length, the recorded sandwaves are arbitrarily divided into three classes: The giant sandwaves of 10 m high and 1,000 m long are hereafter called *primary dunes*. The much smaller sandwaves of ~1 m high and <100 m long are called *secondary sandwaves*. Anything in between are hereafter called *midsize dunes*. Figure 2 clearly shows that primary dunes first appear in Line 44, and gradually change from single crest to double-crest in Line 45-46. Their sizes decrease to midsize dunes in Line47 and continued in Line 48-50 before gradually tapering off in Line 51.

Figure 3 plots the details bathymetrical profiles of several lines. Line 46 (Figure 3A) shows the presence of both the primary dunes and secondary sandwaves. The primary giant dunes are of ~10-15 m in wave height and up to 2,000 m in wave length. Some of them have the typical double-crest shape described in earlier studies (Zhou et al., 2020). The much smaller secondary sandwaves (~1 m in height, ~50 m in length) are found to develop on the stoss side of the primary dunes. The asymmetry of both the primary dunes and secondary sandwaves indicates that both of them were likely formed by flows moving upcoast (against the ship heading).

The primary dunes' shape and size changed markedly in Line 47 (Figure 3B), with much longer wave length, less asymmetry, and lack of secondary sandwaves on their stoss side. Near the end of this line, the midsize dunes become more populated, present both in the trough and on the crest of the primary dunes, with 5-10 m height and 150 m wave length.

The dominance of midsize dunes continued in Line 48 (Figure 3C) with dune heights of ~5-10 m and dune lengths of ~120 m. The shape of the primary dunes can still be vaguely

TABLE 2 The detailed information about filters.

	Cutoff frequency (m^{-1})	Filters
Primary dunes	1/800	Lowpass
Midsize dunes	Upper:1/50	Bandpass
	Lower:1/800	
Secondary sandwaves	1/50	Highpass

seen but far less clear than in Line 46 or Line 47. Secondary sandwaves are also seen on the stoss side of a few primary dunes.

Line 49 (Figure 3D) show cases a 'family portrait' of the three types of sandwaves, with the midsize dunes in the troughs of the primary dunes and the secondary sandwaves on the stoss side of primary dunes. Here the average wave height and length for the three classes of sandwaves are (12.0 m, 800 m) for the primary dunes, (6.3 m, 290 m) for the midsize dunes, and (1.2 m, 45 m) for the secondary sandwaves.

Table 1 lists the size parameter statistics estimated from the 4 lines in Figure 3. Filters were applied to the raw bathymetric profile data in order to separate the three different sandwave sizes and detailed information about filters is shown in the Table 2. Overall the statistical values in Table 1 are comparable to those in previous studies such as Zhou et al., 2018, 2020. For instance, the size of the primary dune class in this study is equivalent to the Double-crested (Dc-type) and the Single-crested (Sc-type) sandwaves (8-16 m in height, 1,000-2000 m in length) in Zhou et al., 2020. In the small area where the multibeam track lines from this study and Zhou et al., 2020 cross (Figure 1), manually measured sandwave parameters resulted in an average of 14 m in wave height and 510 m in wave length. While the mean wave heights from the two studies are about the same, the wave length in the present study is clearly shorter. This is perhaps, at least in part, due to the fact that the track line in this study is neary at a right angle with the crest lines of the sandwaves. Therefore, the wave length values from the present study is deemed more accurate.

The directions of the sandwave migration

The asymmetry of sandwaves profiles can be used to determine their migration direction because sandwaves tend to migrate towards the steeper (lee) side (McCave, 1971; Bartholdy et al., 2002; Zhou et al., 2018). Quantitative methods such as "asymmetry index" (Xu et al., 2008) were used in several studies with favorable results (Zhou et al., 2018). It starts with calculating the first derivative (namely dη/dx, the gradient) (Figure 4B) of the sandwave profiles (Figure 4A). The amplitude n (with signs) and the zero-crossing length l of the dη/dx waveform is then measured (Figure 4C). The "asymmetry index" is the sum of the n/l pairs for each sandwave (Figure 4D). A positive asymmetry index means that the sandwave migrates to the left, and a negative asymmetry index represents migration to the right.

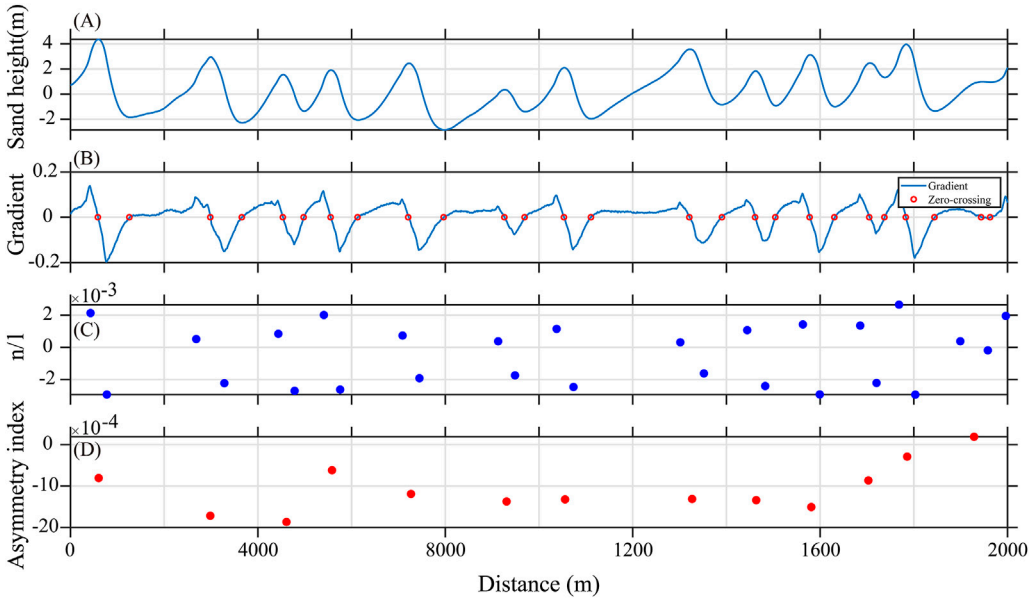

FIGURE 4
Correlation of sandwave migration direction with wave asymmetry. **(A)** a train of asymmetrical sandwaves from Line50. **(B)** the first derivative (gradient) of η. **(C)** the ratio of n/l (height/wavelength). **(D)** The asymmetry index is the sum of the n/l pair for each individual sandwave. This result (negative index) show that sandwave migrated to the right.

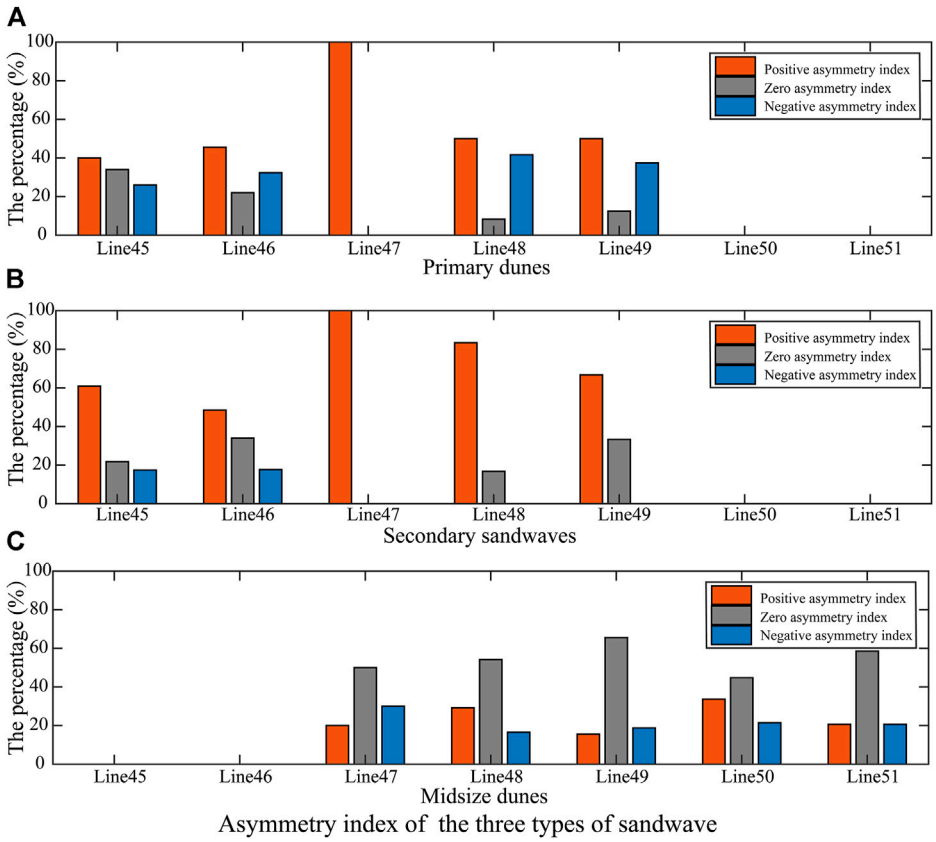

FIGURE 5
Histogram of frequency distribution of the asymmetry index (AI) of **(A)** primary dunes, **(B)** secondary sandwaves and **(C)** midsize dunes on each of the 7 sections of the survey line. The red represents the positive asymmetry index and blue represents the negative asymmetry index. The neutral index, in grey color, is defined as values between $-\frac{1}{2}\frac{(AI_{max}-AI_{min})}{10}$ to $\frac{1}{2}\frac{(AI_{max}-AI_{min})}{10}$.

This method is used to compute the asymmetry index for all three sandwave classes in Lines 45 to 51 (Figure 5). Here a positive value of the asymmetry index represents upcoast migrating sandwaves (towards the northeast) and vice versa.

Figure 5 plots the histograms of asymmetry index (AI) for all three classes of sandwaves found in each of the 7 sections (Line 45-51). The neutral index values represent sandwaves of nearly symmetrical, which is defined here to include index values between $-\frac{1}{2}\frac{(AI_{max}-AI_{min})}{10}$ to $\frac{1}{2}\frac{(AI_{max}-AI_{min})}{10}$. For the primary dunes, there are more positive index than negative in all sections, but the positive dominance appears to have declined towards Southwest (Figure 5A). The secondary sandwaves are overwhelmingly positive index (Figure 5B). The midsize dunes, however, are less asymmetrical than either the primary dunes or secondary sandwaves. Except for Line 50, there are more neutral index than either positive or negative values (Figure 5C).

The asymmetry statistics appear to correlate well with the line drawings of the bed surface: the primary dunes and secondary sandwaves, mostly observed inside the Taiwan Shoal boundary (Figure 1), showed a tendency of upcoast migration (toward northeast). The midsize dunes in the trough of the primary dunes within the shoal boundary are predominantly neutral, while the midsize dunes outside the shoal (e.g., Line 50) are downcoast-migrating dominant. (Figure 6).

Discussion

Required flow velocity and water depth for the development of the observed sandwaves in Taiwan Shoal

Subaqueous bedforms (ripples, sandwaves and dunes) are generally treated as cyclic depositional and erosional features formed mainly during the bedload transport process that are controlled by flow velocity, grain size, and water depth (Rubin and McCulloch, 1980; Flemming, 2000; Xu et al., 2008). An empirical relationship proposed by Yalin, 1964 is often used to calculate the bedform parameters:

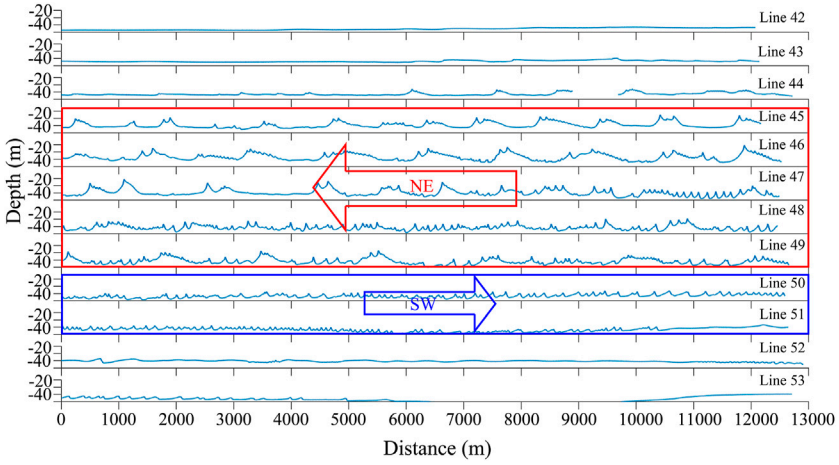

FIGURE 6
Overall sandwave migration patterns from profiles of survey lines. Lines in the red box are sandwaves primarily migrating upcoast (toward northeast); lines in the bule box are midsize sandwave migrating downcoast (toward southwest).

$$\eta/h = 1/6(\tau - \tau_c)/\tau \quad (1)$$

where η is bedform wave height, τ and τ_c are bed shear stress and critical shear stress respectively. The Yalin, 1964 formula was derived from a wide range of experimental data from both laboratory flumes and rivers. Those experimental data were collected in a wide ranges of sediment grain-size (0.085–2.45 mm) and water depth (1.32 cm–28 m). The surface sediments on the Taiwan Shoal are primarily composed of sands with a median grain size (D_{50}) of ~0.5 mm and a sort coefficient ranging from 0.42 to 1.3 (Zhou et al., 2020). While the grain size is well within the range of the data from the Yalin, 1964 formula was developed, the average water depth, 42 m, of dune field in this study is ~20 m deeper than the maximum water depth in Yalin's experiments.

The critical shear stress τ_c for non-viscous particles can be calculated using the empirical formulas (Soulsby, 1997):

$$\tau_c = g(\rho_s - \rho)D\theta_c \quad (2)$$

$$\theta_c = \frac{0.3}{1 + 1.2D_*} + 0.055\left[1 - \exp(-0.020D_*)\right] \quad (3)$$

where D is grain size diameter, ρ and ρ_s are respectively the density of water and sand grains, g the acceleration of gravity (9.8 m/s^2), and

$$D_* = \left[g(\rho_s/\rho - 1)/\nu^2\right]^{1/3}D \quad (4)$$

is the dimensionless grain size. Here ν is the kinematic viscosity of water.

The bed shear stress can be estimated via a simple quadratic equation (e.g., Huntley et al., 1994)

$$\tau = \rho C_D U_{c100}^2 \quad (5)$$

in which ρ (=1,026 kg/m^3) is the density of seawater, C_D is the drag coefficient with a nominal value 2×10^{-3} (Huntley et al., 1994; Green and McCave, 1995; Xu et al., 2008), and U_{c100} is the current speed at 1 m above the seabed. These empirical formulas assume that grains of sand are of uniform size.

Grain size analysis from 98 bed samples collected in Taiwan Shoal showed that the shoal is primarily composed of sand with a median grain size of ~0.5 mm (Zhou et al., 2020). The critical shear stress τ_c for this type of sand is ~2.5 dyne/cm^2. Assuming a mean water depth of 45 m and bedform height of 12 m, 5 m, 1 m, for the primary dunes, midsize dunes, and secondary sandwaves respectively, the flow velocity required for the development of the three classes of sandwaves can be estimated (Table 3). For dunes whose height is greater than around 8 m, the quadratic Eq. 5 resulted in velocities of imaginary values, namely, this equation has no solution, indicating that they cannot be formed in water depth of 45 m or less. For the midsize dunes and the secondary sandwaves, the required minimum velocity are about 0.8 and 0.4 m/s, respectively. In fact, we tested using 3 different coefficient parameters for the Yalin equation (Table 4) for sensitivity investigation. With the actual water depth and sandwave height in the Taiwan Shoal, we found that the calculated current velocities from using the different coefficients varied very little (Table 4). Thus, the coefficient of 1/6 for the Yalin equation can effectively calculate the required flow velocity for the development of the observed sandwaves in Taiwan Shoal.

The same equations can also be used to estimate the minimum water depth required for the certain size of dunes to fully develop when the flow velocity is known. For the primary

TABLE 3 Estimated flow velocity required for the development of the three sizes of sandwave observed in this study.

Sandwave Types	Wave Height (m)		Velocity Required for Sandwaves Development (m/s) D_{50}=0.5 mm, Water Depth = 45 m	
	Max	Mean	Max	Mean
Primary dunes	14.7	12.0	——	——
Midsize dunes	9.7	6.3	——	0.77
Secondary sandwaves	1.5	1.2	0.39	0.38

TABLE 4 Different coefficient parameters of the Yalin, 1964 equation to estimated flow velocity required for the development of the secondary sandwaves.

Sandwave Types	Yalin, 1964 equation	Wave Height (m)		Velocity Required for Sandwaves Development (m/s) D_{50}=0.5 mm, Water Depth = 45 m	
	Coefficient	Max	Mean	Max	Mean
Secondary sandwaves	1/6	1.5	1.2	0.39	0.38
Secondary sandwaves	1/3	1.5	1.2	0.37	0.36
Secondary sandwaves	1/10	1.5	1.2	0.42	0.40

dunes of mean height of 12 m, for example, the minimum water depth for such dunes to form under flow velocity of 1, 2, and 3 m/s are respectively 82, 74, and 73 m. The tidal currents in Taiwan Strait are often greater than 1 m/s (Wang, 2004), especially during typhoons or storms, so the magnitude of flow velocity used in the above estimation is realistic. But the derived water depths are much greater than the current average water depth of the Taiwan Shoal, which is roughly 20 m at present time (Liu et al., 1998; Zhou et al., 2018). We could argue that the primary dunes of this study must have been formed in geologic past when the strait was much deeper, but published literatures showed that the highest sea level in the Holocene (~7,000 years ago) was only 2-5 meters greater than today's sea level (Chen and Liu, 1996; Liu et al., 2004). Adding these numbers to the today's water depth today only comes to less than half of the water depth (~70 m) required for the primary dunes to form according to the empirical formula. This discrepancy suggests that water depth is perhaps not the most important factor in limiting the formation of those large size primary dunes. Large submarine dunes like those on the Norwegian shelf (up to 4 m in height and 500 m in wavelengths) were formed by wave and current reworking of glacial and glaciomarine deposits during the eustatic sea level rise after the last glaciation (Bøe et al., 2009). Similarly, super large dunes (up to 36 m in height) found on the Irish shelf (Van Landeghem et al., 2009) were also formed on the shelf during the sea level rise (Scourse and Austin, 2002). It was postulated that these large dunes may have developed in marine transgression after the last glacial maximum, i.e., in much shallower water than the water depths of present day, from 80 to 100 m (Van Landeghem et al., 2009) to more than 200 m (Bøe et al., 2009).

Dynamic secondary sandwaves riding on static primary dunes

Figure 7 shows one of several sections where smaller secondary sandwaves developed on one side of the much larger primary dunes (Figure 7A). According to the arguments in Section 5.1, the hydraulic conditions of present day are not adequate for the development of the primary dunes in the Taiwan Shoal. Because of this, we might also argue, the primary dunes should also be immobile. This is supported by previous studies (Zhou et al., 2022) whose three multibeam surveys revealed very low mobility of the primary dunes (called giant sandwaves in

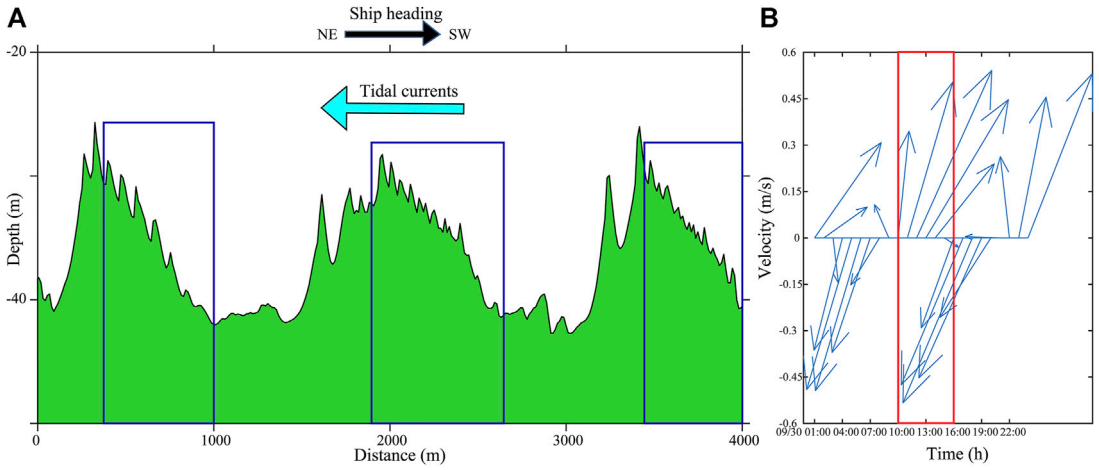

FIGURE 7
(A) A part of the multibeam bathymetric profile of Line 46 depicting the much smaller secondary sandwaves riding on the side of primary dunes. Both the ship heading and the direction of tidal current are also shown. **(B)** A time-series vector plot of the tidal flow generated using the TPXO data (https://tpxows.azurewebsites.net) for the position shown in Figure 1 (117.7757°E, 23.2510°N). The multibeam survey was collected in the time window (between the two red vertical lines) during which tidal currents flowed toward upcoast (toward northeast).

their studies). Those same studies also showed that the smaller secondary sandwaves were very active with much strong mobility. For instance, Ernstsen et al. (2006) showed that superimposed dunes (equivalent to the secondary sandwaves here) migrated 0.51–1.82 m during the tidal cycle. Zhou et al. (2022) showed a longterm average of migration rate of 5 m/year. Because tide is the primary force driving the formation and migration of sandwaves, it is natural to relate the mobility of those secondary sandwaves to tidal currents. Ernstsen et al. (2006) showed that during a tidal cycle, the asymmetry of the sandwaves changes from one tidal phase to the next, while the much larger primary dunes remain unchanged throughout the whole tidal cycle. Asymmetry index (Figure 5) can be used to describe the direction of sandwave migration. The overwhelming positive asymmetry index for the secondary sandwaves are primarily due to the fact that they were in the process of migrating upcoast during the survey when the tidal current was flowing upcoast. For the primary dunes, the value of asymmetry index can only indicate the migration direction at the time of their forming because they are at present immobile. For the same reason, the dominance of "zero asymmetry index" for the mid-size dunes suggest that they are either immobile like the primary dunes, or have a net migration of nearly zero.

Today's hydraulic conditions in the strait can generate those secondary sandwaves (see Table 3), and it is therefore reasonable to state that the secondary sandwaves, such as those shown in Figure 7, change their asymmetry with the reversing tidal currents. A multibeam bathymetric data taken during at least two opposite tidal phases would prove it. Additionally, some erosion on the top of the primary dunes is likely to occur during storm weather (Bao et al., 2020) even though they are generally immobile. Quantification of such changes requires further investigations.

Conclusion

A 136 km swath of high-resolution multibeam bathymetry, collected along a track line nearly perpendicular to the sandwave crests, allowed us to closely examine the dynamic and morphological characteristics of sandwaves in the Taiwan Shoal. The following conclusions have been drawn:

1) Three sizes of sandwaves co-exist on the Taiwan Shoal: primary dunes (~10-15 m in height, up to 2,000 m in length); small, secondary sandwaves (~1 m in height, ~50 m in length), and midsize dunes (~5-10 m in height, ~100-500 m in length). Small secondary sandwaves often ride on the stoss side of the primary dunes whereas midsize dunes are often in the troughs of primary dunes.
2) Both primary and midsize dunes are probably immobile under present tidal flow conditions, even though asymmetry index suggests that they could have migrated in opposite directions. Multibeam data collected during both flooding and ebbing phases are required to further prove the arguments that the secondary sandwaves' asymmetry is correlated to tidal currents.
3) The present water depth in Taiwan Shoal is too shallow for the primary dunes to develop. It is likely that these primary dunes were formed in geologic past when sea level was higher

or the seabed elevation was lower, but water depth is probably not the only factor in limiting the formation of the primary dunes.

Data availability statement

The datasets used in the article would be made accessible by contacting the corresponding author through email and describing the intended purpose of usage.

Author contributions

JX: Conceptualization, Methodology and Reviewing. YY: Conceptualization, Methodology, Analyses, Original draft preparation. ML: Methodology and Analyses. WX: Data collection and curation.

Funding

This study was supported by the Key Special Project for Introduced Talents Team of Southern Marine Science and Engineering Guangdong Laboratory (Guangzhou) (GML2019ZD0210) and the National Natural Science Foundation of China (41720104001). We would like to thank everyone who contributed to the field observations in the Taiwan Shoal. We would also like to thank Dr. Simin Gao for editing the English language draft of this manuscript.

Conflict of interest

The authors declare that the research was conducted in the absence of any commercial or financial relationships that could be construed as a potential conflict of interest.

Publisher's note

All claims expressed in this article are solely those of the authors and do not necessarily represent those of their affiliated organizations, or those of the publisher, the editors and the reviewers. Any product that may be evaluated in this article, or claim that may be made by its manufacturer, is not guaranteed or endorsed by the publisher.

References

Amos, C.L., and King, E.L. (1984). Bedforms of the Canadian eastern seaboard: A comparison with global occurrences. *Mar. Geol.* 57 (1-4), 167–208. doi:10.1016/0025-3227(84)90199-3

Ashley, G.M. (1990). Classification of large-scale subaqueous bedforms-a new look at an old problem- SEPM Bedforms and Bedding Structure Research Symposium. *J. Sediment. Petrology* 60 (1), 160–172.

Bao, J.J., Cai, F., Ren, J.Y., Zheng, Y.L., Wu, C.Q., Lu, H.Q., et al. (2014). Morphological characteristics of sand waves in the middle taiwan shoal based on multi-beam data analysis. *Acta Geol. Sin. - Engl. Ed.* 88 (5), 1499–1512. doi:10.1111/1755-6724.12314

Bao, J.J., Cai, F., Shi, F.Y., Wu, C.Q., Zheng, Y.L., Lu, H.Q., et al. (2020). Morphodynamic response of sand waves in the Taiwan Shoal to a passing tropical storm. *Mar. Geol.* 426, 106196. doi:10.1016/j.margeo.2020.106196

Barrie, J.V., Conway, K.W., Picard, K., and Greene, H.G. (2009). Large-scale sedimentary bedforms and sediment dynamics on a glaciated tectonic continental shelf: Examples from the Pacific margin of Canada. *Cont. Shelf Res.* 29 (5-6), 796–806. doi:10.1016/j.csr.2008.12.007

Bartholdy, J., Bartholomae, A., and Flemming, B.W. (2002). Grain-size control of large compound flow-transverse bedforms in a tidal inlet of the Danish Wadden Sea. *Mar. Geol.* 188 (3-4), 391–413. doi:10.1016/s0025-3227(02)00419-x

Bartholdy, J., Flemming, B.W., Bartholoma, A., and Ernstsen, V.B. (2005). Flow and grain size control of depth-independent simple subaqueous dunes. *J. Geophys. Res.* 110 (4). doi:10.1029/2004jf000183

Belde, J., Reuning, L., and Back, S. (2017). Bottom currents and sediment waves on a shallow carbonate shelf, Northern Carnarvon Basin, Australia. *Cont. Shelf Res.* 138, 142–153. doi:10.1016/j.csr.2017.03.007

Besio, G., Blondeaux, P., Brocchini, M., and Vittori, G. (2004). On the modeling of sand wave migration. *J. Geophys. Res.* 109, C04018. doi:10.1029/2002jc001622

Bøe, R., Bellec, V.K., Dolan, M.F.J., Buhl-Mortensen, P., Buhl-Mortensen, L., Slagstad, D., et al. (2009). Giant sandwaves in the hola glacial trough off vesterålen, north Norway. *Mar. Geol.* 267 (1-2), 36–54. doi:10.1016/j.margeo.2009.09.008

Boggs, S. (1974). Sand-wave fields in Taiwan Strait. *Geol.* 2, 251–253. doi:10.1130/0091-7613(1974)2<251:sfits>2.0.co;2

Cai, A.Z., Zhu, Z.N., Li, Y.M., and Cai, Y. (2003). Sedimentary environment in the taiwan shoal. *Mar. Georesources Geotechnol.* 21 (3-4), 201–211. doi:10.1080/02640410310000710 29

Chen, Y.G., and Liu, T.K. (1996). Sea level changes in the last several thousand years, Penghu Islands, Taiwan Strait. *Quat. Res.* 45 (3), 254–262. doi:10.1006/qres.1996.0026

Dalrymple, R.W. (1984). Morphology and internal structure of sandwaves in the Bay of Fundy. *Sedimentology* 31 (3), 365–382. doi:10.1111/j.1365-3091.1984.tb00865.x

Damen, J.M., van Dijk, T., and Hulscher, S. (2018). Spatially varying environmental properties controlling observed sand wave morphology. *J. Geophys. Res. Earth Surf.* 123 (2), 262–280. doi:10.1002/2017jf004322

Du, X.Q., Gao, S., and Li, Y. (2010). Hydrodynamic processes and bedload transport associated with large-scale sandwaves in the Taiwan Strait. *J. Coast. Res.* 26 (4), 688–698. doi:10.2112/08-1113.1

Ernstsen, V.B., Noormets, R., Winter, C., Hebbeln, D., Bartholomä, A., Flemming, B.W., et al. (2006). Quantification of dune dynamics during a tidal cycle in an inlet channel of the Danish Wadden Sea. *Geo-Mar. Lett.* 26 (3), 151–163. doi:10.1007/s00367-006-0026-2

Ferret, Y., Le Bot, S., Tessier, B., Garlan, T., and Lafite, R. (2010). Migration and internal architecture of marine dunes in the eastern English channel over 14 and 56 year intervals: The influence of tides and decennial storms. *Earth Surf. Process. Landf.* 35 (12), 1480–1493. doi:10.1002/esp.2051

Flemming, B.W. (1980). Sand transport and bedform patterns on the continental shelf between Durban and Port Elizabeth (southeast African continental margin). *Sediment. Geol.* 26 (1-3), 179–205. doi:10.1016/0037-0738(80)90011-1

Flemming, B.W. (2000). "The role of grain size, water depth and flow velocity as scaling factors controlling the size of subaqueous dunes," in Marine Sandwave Dynamics, January 2000.

Francken, F., Wartel, S., Parker, R., and Taverniers, E. (2004). Factors influencing subaqueous dunes in the Scheldt Estuary. *Geo-Marine Lett.* 24 (1), 14–21. doi:10.1007/s00367-003-0154-x

Green, M.O., and McCave, I.N. (1995). Seabed drag coefficient under tidal currents in the eastern Irish Sea. *J. Geophys. Res.* 100 (C8), 16057–16069. doi:10.1029/95jc01381

Hoekstra, P., Bell, P., van Santen, P., Roode, N., Levoy, F., and Whitehouse, R. (2004). Bedform migration and bedload transport on an intertidal shoal. *Cont. Shelf Res.* 24 (11), 1249–1269. doi:10.1016/j.csr.2004.03.006

Hong, H., Zhang, C., Shang, S., Huang, B., Li, Y., Li, X., et al. (2009). Interannual variability of summer coastal upwelling in the Taiwan Strait. *Cont. Shelf Res.* 29 (2), 479–484. doi:10.1016/j.csr.2008.11.007

Hu, Y., Chen, J., Xu, J., Wang, L.M., Li, H.D., and Liu, H.S. (2013). Sand wave deposition in the taiwan shoal of China. *Acta Oceanol. Sin.* 32 (8), 26–34. doi:10.1007/s13131-013-0338-9

Huang, W., Fu, B., Yang, J., Zhang, H., Chen, P., Xiao, Q., et al. (2008). "SAR measurements of the taiwan shoal in China," in *Remote sensing of the ocean, sea ice, and large water regions 2008* (Bellingham, Washington, United States: International Society for Optics and Photonics), 71050O.()

Huntley, D.A., Nicholls, R.J., Liu, C.L., and Dyer, K.R. (1994). Measurements of the semi-diurnal drag coefficient over sand waves. *Cont. Shelf Res.* 14 (5), 437–456. doi:10.1016/0278-4343(94)90097-3

Kai-guo, F.A.N., Wei-gen, H., Ming-xia, H.E., and Bin, F.U. (2009). A review about shallow sea bottom topography mapping by SAR. *Prog. Geophys.* 24 (2), 714–720.

Knaapen, M.A.F. (2005). Sandwave migration predictor based on shape information. *J. Geophys. Res.* 110. doi:10.1029/2004jf000195

Kubo, Y., Soh, W., Machiyama, H., and Tokuyama, H. (2004). Bedforms produced by the kuroshio current passing over the northern izu ridge. *Geo-Marine Lett.* 24 (1), 1–7. doi:10.1007/s00367-003-0134-1

Li, Y., Lin, M.A., Jiang, W.B., and Fan, F.X. (2011). Process control of the sand wave migration in beibu gulf of the south China sea. *J. Hydrodyn.* 23 (4), 439–446. doi:10.1016/s1001-6058(10)60134-5

Liu, J.P., Milliman, J.D., Gao, S., and Cheng, P. (2004). Holocene development of the yellow river's subaqueous delta, north yellow sea. *Mar. Geol.* 209 (1-4), 45–67. doi:10.1016/j.margeo.2004.06.009

Liu, Z.X., Xia, D.X., Berne, S., Wang, K.Y., Marsset, T., Tang, Y.X., et al. (1998). Tidal deposition systems of China's continental shelf, with special reference to the eastern Bohai Sea (vol 145, pg 225, 1998). *Mar. Geol.* 148 (1-2), 115–115.

McCave, I.N. (1971). Sand waves in the north sea off the coast of holland. *Mar. Geol.* 10, 199–225. doi:10.1016/0025-3227(71)90063-6

Off, T. (1963). Rhythmic linear sand bodies caused by tidal currents. *Am. Assoc. Pet. Geol. Bull.* 47 (2), 324–341. doi:10.1306/BC743989-16BE-11D7-8645000102C1865D

Rovere, M., Pellegrini, C., Chiggiato, J., Campiani, E., and Trincardi, F. (2019). Impact of dense bottom water on a continental shelf: An example from the SW Adriatic margin. *Mar. Geol.* 408, 123–143. doi:10.1016/j.margeo.2018.12.002

Rubin, D.M., and McCulloch, D.S. (1980). Single and superimposed bedforms: A synthesis of san francisco bay and flume observations. *Sediment. Geol.* 26 (1-3), 207–231. doi:10.1016/0037-0738(80)90012-3

Scourse, J.D., and Austin, W.E.N. (2002). Quaternary shelf sea palaeoceanography: Recent developments in europe. *Mar. Geol.* 191, 87–94. doi:10.1016/s0025-3227(02)00526-1

Shen, X.T., Jian, X., Li, C., Liu, J.T., Chang, Y.P., Zhang, S., et al. (2021). Submarine topography-related spatial variability of the southern Taiwan Strait sands (East Asia). *Mar. Geol.* 436, 106495. doi:10.1016/j.margeo.2021.106495

Soulsby, R.L. (1997). *The dynamics of marine sands: A manual for practical applications*. London: Thomas Thelford.

Stride, A.H., Beldenson, R.H., and Kenyon, N.H. (1982). "Offshore tidal deposits: Sand sheet and sand bank facies," in *Offshore tidal sands processes and deposits* (London, United Kingdom: Chapman & Hall), 95–125.

Van Landeghem, K.J.J., Uehara, K., Wheeler, A.J., Mitchell, N.C., and Scourse, J.D. (2009). Post-glacial sediment dynamics in the Irish sea and sediment wave morphology: Datamodel comparisons. *Cont. Shelf Res.* 29 (14), 1723–1736. doi:10.1016/j.csr.2009.05.014

Vandenberg, J.H. (1987). Bedform migration and bed load transport in some rivers and tidal environments. *Sedimentology* 34 (4), 681–698. doi:10.1111/j.1365-3091.1987.tb00794.x

Viana, A.R., Faugeres, J.C., and Stow, D.A.V. (1998). Bottom-current-controlled sand deposits - a review of modern shallow- to deep-water environments. *Sediment. Geol.* 115 (1-4), 53–80. doi:10.1016/s0037-0738(97)00087-0

Wang, L.B., Chen, Z.X., Zhao, J.T., Bai, F.L., Hu, B.Q., et al. (2014). Late Pleistocene and Holocene stratigraphy and paleoenvironmental evolution in the western taiwan shoal. *Acta Sedimentol. Sin.* (in Chinese). doi:10.14027/j.cnki.cjxb.2014.06.011

Wang, Y.-H. (2004). Analysis of flow at the gate of Taiwan Strait. *J. Geophys. Res.* 109, C02025. doi:10.1029/2003jc001937

Wang, Y.H., Jan, S., and Wang, D.P. (2003). Transports and tidal current estimates in the Taiwan Strait from shipboard ADCP observations (1999-2001). *Estuar. Coast. Shelf Sci.* 57 (1-2), 193–199. doi:10.1016/s0272-7714(02)00344-x

Whitmeyer, S.J., and FitzGerald, D.M. (2008). Episodic dynamics of a sand wave field. *Mar. Geol.* 252 (1-2), 24–37. doi:10.1016/j.margeo.2008.03.009

Wynn, R.B., and Stow, D.A.V. (2002). Classification and characterisation of deep-water sediment waves. *Mar. Geol.* 192 (1-3), 7–22. doi:10.1016/s0025-3227(02)00547-9

Xu, J.P. (2005). Observations of plan-view sand ripple behavior and spectral wave climate on the inner shelf of San Pedro Bay, California. *Cont. Shelf Res.* 25 (3), 373–396. doi:10.1016/j.csr.2004.10.004

Xu, J.P., Wong, F.L., Kvitek, R., Smith, D.P., and Paull, C.K. (2008). Sandwave migration in monterey submarine canyon, central California. *Mar. Geol.* 248 (3-4), 193–212. doi:10.1016/j.margeo.2007.11.005

Yalin, M. S. (1964). Geometrical properties of sand wave. *J. Hydr. Div.* 90 (5), 105–119. doi:10.1061/jyceaj.0001097

Zhou, J.Q., Wu, Z.Y., Jin, X.L., Zhao, D.N., Cao, Z.Y., and Guan, W.B. (2018). Observations and analysis of giant sand wave fields on the Taiwan Banks, northern South China Sea. *Mar. Geol.* 406, 132–141. doi:10.1016/j.margeo.2018.09.015

Zhou, J.Q., Wu, Z.Y., Zhao, D.N., Guan, W.B., Cao, Z.Y., and Wang, M.W. (2022). Effect of topographic background on sand wave migration on the eastern Taiwan Banks. *Geomorphology* 398, 108030. doi:10.1016/j.geomorph.2021.108030

Zhou, J.Q., Wu, Z.Y., Zhao, D.N., Guan, W.B., Zhu, C., and Flemming, B. (2020). Giant sand waves on the Taiwan Banks, southern Taiwan Strait: Distribution, morphometric relationships, and hydrologic influence factors in a tide-dominated environment. *Mar. Geol.* 427, 106238. doi:10.1016/j.margeo.2020.106238

frontiers | Frontiers in Earth Science

TYPE Original Research
PUBLISHED 20 September 2022
DOI 10.3389/feart.2022.994258

OPEN ACCESS

EDITED BY
Ya Ping Wang,
East China Normal University, China

REVIEWED BY
Jianzhong Ge,
East China Normal University, China
Zhanhai Li,
East China Normal University, China

*CORRESPONDENCE
Longhai Zhu,
zhulonghai@ouc.edu.cn

SPECIALTY SECTION
This article was submitted to Geohazards and Georisks, a section of the journal Frontiers in Earth Science

RECEIVED 14 July 2022
ACCEPTED 22 August 2022
PUBLISHED 20 September 2022

CITATION
Xie B, Bao R, Yin D, Zhu L, Hu R, Cai W, Liu T, Lin C and Lu P (2022), The spatio-temporal distribution and transport of suspended sediment in Laizhou Bay: Insights from hydrological and sedimentological investigations. *Front. Earth Sci.* 10:994258. doi: 10.3389/feart.2022.994258

The spatio-temporal distribution and transport of suspended sediment in Laizhou Bay: Insights from hydrological and sedimentological investigations

Bo Xie[1], Rui Bao[2], Dongxiao Yin[3], Longhai Zhu[1,4]*, Rijun Hu[1,4], Weiwei Cai[5], Tao Liu[6], Chaoran Lin[1] and Pengfei Lu[1]

[1]College of Marine Geo-Science, Ocean University of China, Qingdao, China, [2]Frontiers Science Center for Deep Ocean Multispheres and Earth System, Key Laboratory of Marine Chemistry Theory and Technology, Ministry of Education, Ocean University of China, Qingdao, China, [3]Virginia Institute of Marine Science, Gloucester Point, VA, United States, [4]Key Lab of Submarine Geosciences and Prospecting Techniques, Ministry of Education, Qingdao, China, [5]Qingdao Boyan Marine Environment Technology Co., Qingdao, China, [6]School of Geography and Ocean Science, Ministry of Education Key Laboratory for Coast and Island Development, Nanjing University, Nanjing, China

Suspended sediment transport and deposition are crucial physical processes controlling the geomorphological evolution of estuaries and bays. Specially, under the context of worldwide coastal erosion, knowledge of the spatio-temporal distribution of suspended sediment concentration (SSC) and its associated sediment load have become increasingly important for bay management. However, our understanding of the mechanisms of suspended sediment dynamics continues to be hampered by the lack of high-resolution observations. Here, we present a study of the transport mechanisms and controlling factors of suspended sediment over Laizhou Bay. For this, we conducted continuous measurements of SSC, salinity, temperature, and flow velocity at nine stations throughout Laizhou Bay for one 25-h period during each of the spring and moderate tides. Based on these data, residual current, gradient Richardson numbers, and suspended sediment flux were calculated. Our results indicate that a strong current field occurs near the Yellow River mouth, corresponding to the zone with high SSC. The overall diffusion characteristics of suspended sediment are controlled by the tidal current field. Furthermore, our findings suggest that different degrees of stratification occur in the water column, which inhibit the effective vertical diffusion of suspended sediment; Higher water temperature was the main cause of stronger water column stratification of spring tide than moderate tide. Finally, our results reveal that the type of seabed sediment is an important factor controlling SSC by influencing resuspension flux. We conclude that the primary mechanisms controlling suspended sediment transport in Laizhou Bay are advection and tidal pumping, especially advection. Our research provides both a foundational reference for the sediment source-to-sink process from the Yellow River to the sea, as well as guideline implications for coastal engineering construction and channel dredging.

KEYWORDS

suspended sediment, spatio-temporal distribution, transport mechanisms, control factors, laizhou bay

1 Introduction

Quantifying suspended sediment load and understanding the physical mechanisms behind it is an important topic of sediment dynamics in estuarine and bay areas (Allen, 2008; Bianchi and Allison, 2009; Yin et al., 2013). Suspended sediment is a major carrier of heavy metals and organic matter, playing a significant role in environmental pollution (Oliveira et al., 2021). In addition, suspended sediment can strongly affect the primary productivity in the ocean by acting as the major carrier of nutrients, or via attenuating the degree of light penetration in the water column (Vonda et al., 2020). Moreover, cross-shore suspended sediment transport can be tied with beach morphodynamics (Pang et al., 2019). Thus, it is essential to quantify suspended sediment transport and reveal the controlling mechanisms behind it.

Being typically located in coastal regions, bay areas have some of the highest human development (Xu and Xu, 2013). Suspended sediment transport over bays not only affects seabed evolution and coastal erosion (Jillian et al., 2018), but also largely influences the delivery of nutrients and pollutants from the land to the ocean (Wang et al., 2014; Hu et al., 2016; Nour et al., 2022). Different bays have distinct geomorphic and topographic features, hydrodynamic conditions, and sediment types, as well as suspended sediment transport mechanisms (Fang et al., 2000; Tong et al., 2018; Bo Liu et al., 2020). Since the Anthropocene, human activity has largely transformed upstream rivers (Syvitski and Milliman, 2007)), exerting substantial effects on the patterns of suspended sediment transport in bays (Jillian et al., 2018). The Yellow River is well known for its high SSC (Milliman and Meade, 1983). The seasonal variation of sediment and seawater inflow from the Yellow River has an important effect on the suspended sediment transport pattern in Laizhou Bay (Liu et al., 2013). The mouth of the Yellow River is located at the intersection of the central shallow sea basin of the Bohai Sea and Laizhou Bay; further, the sediment transport from the Yellow River into the sea is the main source of sediment in Laizhou Bay (Qin et al., 1985; Liu et al., 2005; Shou et al., 2016; Bo Liu et al., 2020). Recent studies indicate that sediment input from the Yellow River has decreased considerably due to anthropogenic activities (Wu et al., 2017; Fu et al., 2021). High turbidity zones from the Yellow River estuary to the middle of Laizhou Bay are correlated with seabed sediment types. Fine-grained sediment area within the bay tend to cause high turbidity (Wang and Wang, 2005). Although there are abundant observational and numerical studies in parts of Laizhou Bay, especially at the Yellow River mouth, the physical condition of suspended sediment transport in Laizhou Bay as a whole needs further study.

Remote sensing is widely used to study the suspended sediment transport. Wang and Wang (2005) analyzed the transport path of suspended sediment in Laizhou Bay using Landsat imagery. Similarly, Bi et al. (2011) used Moderate Resolution Imaging Spectroradiometer (MODIS) data to study the seasonal changes in suspended sediment transport in the Yellow River. In addition, the sediments from the Yellow River are mainly transported outward along two pathways by combining the measured data (SSC) with MODIS images and ocean current data (Xingmin Liu et al., 2020). However, remote sensing cannot effectively monitor water below the surface layer; the bottom SSC tends to be larger than the surface SSC, especially when the water column is strongly stratified. Thus, continuous and synchronous investigations are important to understand the continuous variation characteristics and overall transport mechanism of suspended sediment in Laizhou Bay.

Previous research on the sediment dynamics of Laizhou Bay have focused more on the southwest and northeast parts of the bay, or on the Yellow River mouth during the summer and winter seasons (Wang and Wang, 2005; Li et al., 2015; Chao Jiang et al., 2017; Bo Liu et al., 2020). At spring, not only has the amount of water and sediment inflow into the Yellow River increased, and water column stratification in the Bohai Sea at April (Su, 2005; Liu and Pan, 2007), which have an impact on the suspended sediment transport. However, the transport patterns of suspended sediment in Laizhou Bay in the spring, which is the transitional period between winter and summer, remain unclear.

In this study, we conducted continuous measurements of SSC, salinity, temperature and flow velocity for one the tidal cycle (25-h period) at nine sampling stations across Laizhou Bay during each of the spring and moderate tides. The objectives of this study are twofold: 1) to explore the characteristics of spatio-temporal variation of SSC in Laizhou Bay during spring, as well as their primary controlling factors, and 2) to reveal the patterns and influencing factors of suspended sediment transport. Our findings shed light on the distribution characteristics and transport mechanisms of suspended sediment in Laizhou Bay in the spring, which can provide baseline knowledge for bay and estuary management.

2 Background of the study area

Laizhou Bay is one of three bays in the Bohai Sea (Figure 1), which is a semi-enclosed inland sea with a total area of about 77,000 km^2, an average water depth of approximately 18 m, shallower water along the coast, and deeper water in the central basin and Bohai Strait (Zhao et al., 2020). The landforms of eastern Laizhou Bay differ greatly from those of western Laizhou Bay. The coast of the eastern uplift area features a large expanse of typical

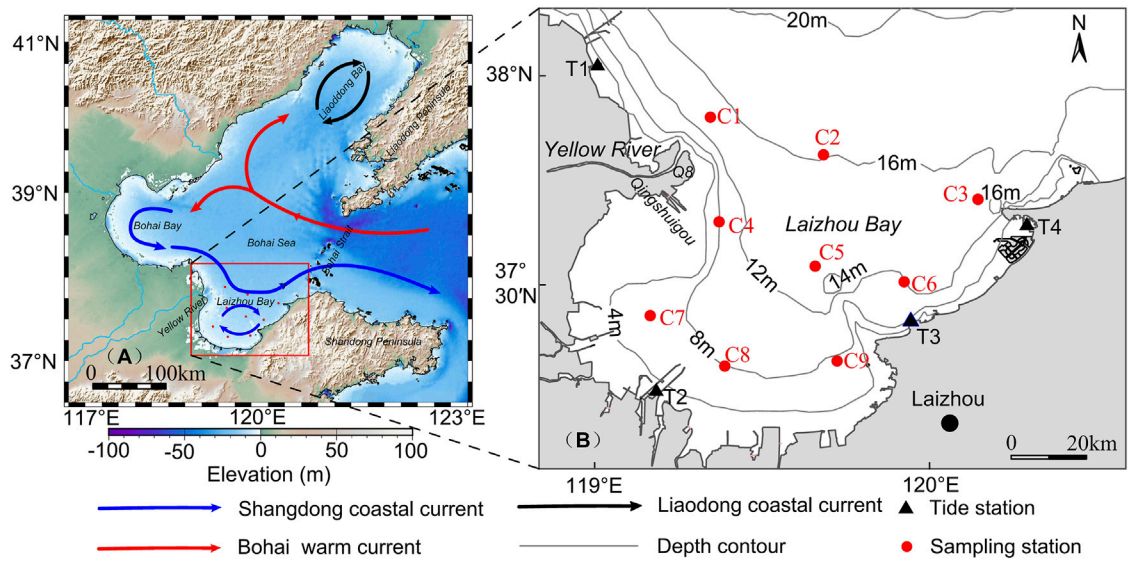

FIGURE 1
(A) Map of the study area (red open box) in the Bohai Sea. The elevation (+) over land and water depth (-) in the ocean are also shown (adapted from Fang et al. (2000)). Blue arrows represent the Shangdong coastal current. Red arrows represent the Bohai warm current. Black arrows represent the Liaodong coastal current **(B)** The red solid circle represents the sampling stations. The black solid triangles represent the tide stations. Gray lines represent isobaths.

sandy coast, mostly lagoons, low hills, sand bars, and sand spits. The topography in the western subsidence area is gentle, with a wide tidal flat, and the seabed sediment types are mainly silt, sandy silt, and silty sand (Zhao et al., 2020). Since the 1950's, the sediment discharge from the Yellow River have experienced stepwise downtrend, decreasing from 1.23 Gt/yr during the period of 1950–1968 to 0.15 Gt/yr during the period of 2000–2005 (Wang et al., 2007).

In terms of hydrodynamics, the tidal range increases as the water depth from the bay mouth to the bay head becomes shallower, with an average water depth of about 10 m, which is a typical shallow bay. The normal wave direction is primarily NE, and the secondary normal wave direction is NNE during winter, with an average wave height of approximately 0.6 m (Qin et al., 1985). The Bohai warm current, Shandong coastal current, and Liaodong coastal current are the main circulation systems in the Bohai Sea during winter, and the circulation does not change its main pattern in spring, in the main studying period of this work (Su, 2005). The circulation flows in from the north and out from the south of the Bohai Strait (Fang et al., 2000) (Figure 1A).

3 Materials and methods

3.1 Materials

The hydrological and sediment data were investigated by two field surveys, each over one tidal cycle (25 h), that included nine sample stations (C1–C9) and four tide stations (T1–T4), conducted in Laizhou Bay during the spring (May 27–28, 2020) and moderate tides (April 24–25, 2020) (Figure 1).

3.1.1 Current and tide

An Acoustic Doppler Current Profiler (ADCP) was mounted in the rear of a ship on the right side, and data were collected every 10 min. The DCX-22–2 Tidal Level Meter (Global Water) and HY1300 Digital Tidal Level Meter (Chengdu CSCC Electronic Technology Co., Ltd.) were used for tidal level observations, with a 1 s sampling interval.

3.1.2 Temperature and salinity

Water temperature (sampling frequency: 5 Hz, accuracy: ±0.005°C) and salinity (sampling frequency: 5 Hz, conductivity measurement accuracy: ±0.009 ms/cm) were measured using a conductivity-temperature-depth (CTD)-NV probe (Teledyne RD Instruments). CTD was devolved at a rate of 0.5 m/s.

3.1.3 Turbidity and SSC

Turbidity was measured using an AQUA logger® 310TY Turbidimeter (Aquatec Group Ltd., Basingstroke, United Kingdom; sampling frequency: 1 Hz, accuracy: ±0.01 NTU). At each station, SSC was measured via filtration weighing at the surface (approximately 1 m from the water surface), middle (0.5 H, H: water depth), and bottom (approximately 1 m from the sea floor) water samples with a volume of about 1,000 ml. SSC was measured by filtration

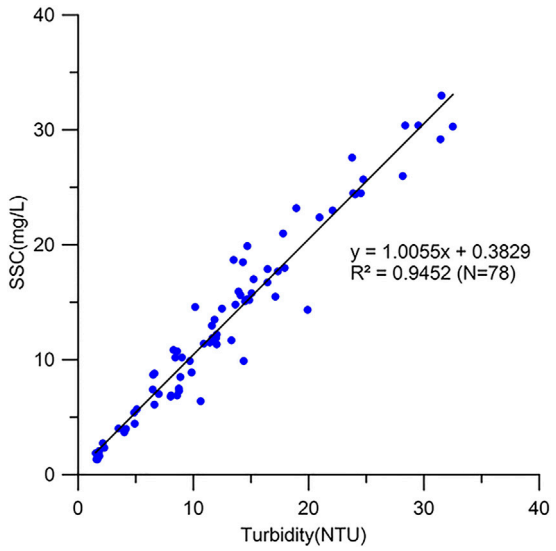

FIGURE 2
The relationship between SSC and turbidity.

weighing. A fiber acetate membrane with a pore size of 0.45 μm was used for extraction, which was then dried and weighed before the data were corrected using a double membrane. SSC was the ratio of sediment bulk density to water sample volume. To verify the accuracy of the SSC measurement, we analyzed the correlation between turbidity and measured SSC at the C2 station (Figure 2); the correlation coefficient was 0.945. Similarly, the correlation coefficient of other stations surpassed 0.82, which indicated that there was a strong corresponding relation between SSC and turbidity (Zhou et al., 2017).

3.2 Methods

3.2.1 Gradient richardson number (*Rig*)

At present, the gradient Richardson number (*Rig*) (Trowbridge, 1992) is one of the most commonly used characteristic parameters for describing the mixing degree (Tong et al., 2018; Meng et al., 2020; Xingmin Liu et al., 2020), and the it is calculated as follows:

$$Rig = -\frac{g}{\rho}\frac{\partial \rho}{\partial z}\left(\frac{\partial u}{\partial z}\right)^{-2} \tag{1}$$

where z denotes the height above the bed and u represents the flow velocity of the corresponding horizon. The *Rig* is compared with the critical value (when *Rig* reached 0.25, stratified mixing is in equilibrium state) to judge the mixing state of the water (Turner and Benton, 1974; Xu and Xu, 2013). When *Rig* was greater than 0.25, the water column was stratified and mixing was inhibited. In contrast, when *Rig* was less than 0.25, the stratification degree weakened and the mixing degree strengthened.

In Eq. 1, ρ is the water density, and can be calculated using the seawater state equation (Millero and Poisson, 1981):

$$\rho = \rho_0 + AS + BS^{3/2} + CS^2 \tag{2}$$

where ρ_0, A, B, and C are functions of water temperature (T), and S is water salinity.

3.2.2 Decomposition of suspended sediment flux

The flux decomposition method proposed was used to calculate suspended sediment transport flux. This method revealed the main contribution rate of different processes by comparing the values of decomposition terms (Dyer, 1997). This method was more mature in domestic and foreign application (Li et al., 2022), but the effect of wave action was not fully considered. This method was more suitable for analyzing seas with weak wave activity. It is known that Laizhou Bay is dominated by monsoon-formed waves and that weak southerly wind prevail at the end of spring (Qin et al., 1985). Therefore, this method was suitable for this research.

In accordance with the method proposed by Ingram (1981) and Uncles et al. (1985) to decompose the instantaneous material flux with relative water depth, the measured velocity (u) was decomposed into $u = \bar{u} + u' = \overline{u_0} + \overline{u_t} + u_0' + u_t'$, where $\overline{u_0}$ and $\overline{u_t}$ represent the mean velocity and oscillatory velocity of $\bar{u}$, respectively; u_0' and u_t' represent the mean velocity and oscillatory velocity of u', respectively. Similarly, SSC (c) were also decomposed, and water depth (h) can be expressed as $h = h_0 + h_t$, where $h_0$and h_t represent the mean depth and oscillatory depth during a tidal cycle. The formula of suspended sediment transport flux (F) in a tidal period (T_t) was calculated using Eq. 3. In this paper, the nomenclature of the parameters in the formulas is following the framework of the Lagrangian transport. Therefore, some parameters may be represented by symbols different from previous studies.

$$\begin{aligned} F &= \frac{1}{T_t}\int_0^{T_t}\int_0^{h} ucdz\,dt \\ &= \underbrace{\frac{h_0\overline{u_0}\,\overline{c_0}}{T_1}}_{} + \underbrace{\frac{\langle h_t\overline{u_t}\rangle\overline{c_0}}{T_2}}_{} + \underbrace{\frac{\langle h_t\overline{c_t}\rangle\overline{u_0}}{T_3}}_{} + \underbrace{\frac{\langle h_t\overline{u_t c_t}\rangle}{T_4}}_{} + \underbrace{\frac{h_0\overline{u_0'c_0'}}{T_5}}_{} \\ &\quad + \underbrace{\frac{\langle h_t u_0' c_t'\rangle}{T_6}}_{} + \underbrace{\frac{\langle h_t u_t' c_0'\rangle}{T_7}}_{} + \underbrace{\frac{\langle h_t u_t' c_t'\rangle}{T_8}}_{} \end{aligned} \tag{3}$$

where T_1 is the non-tidal flux called the Eulerian flux, T_2 is the Stokes drift flux, and $T_1 + T_2$ is the Lagrange flux, belonging to advection transport term. T_3 is the correlation between tidal and suspended sediment, T_4 is the correlation between suspended sediment and tidal current change, T_5 is the correlation term

between vertical velocity change, and SSC change is the sediment transport term generated by vertical net circulation; $T_3 + T_4 + T_5$ is collectively known as the tidal pumping contribution terms. T_6 is the tidally averaged vertical circulation, T_7 is derived from the change of the vertical distribution of SSC and velocity, and T_8 is the vertical tidal oscillation shear.

First of all, tidal current was decomposed along the *X*-axis (positive direction towards east) and the Y -axis (positive direction towards north). The magnitudes and directions of instantaneous tida1-averaged suspended sediment flux per unit width were computed according to the vector synthesis method.

4 Results

The study area included nine stations that were divided into three groups based on the geographical features in which they were located. Stations C1, C2, and C3 were in the bay mouth; stations C4, C5, and C6 were in the middle of the bay; and stations C7, C8, and C9 were in the head of the bay.

4.1 Variability of SSC

During the spring tide (Figures 3A,B), the horizontal SSC at each station ranged from 1.3 to 18.9 mg/L, and the average SSC was 9.1 mg/L. Overall, compared to SSC in winter, SSC was reduced by 3–4 times due to the large amount of resuspension sediment caused by strong wind in winter (Qiao et al., 2010; Bi et al., 2011). Figure 3A shows that surface SSC varied substantially. SSC levels were found to be high in western Laizhou Bay. The sea at the Yellow River mouth and in southeastern Laizhou Bay likewise showed high-SSC values in this high-SSC zone, but the sea near the abandoned Qingshuigou (QSG) delta had relatively low SSC values. This indicates that the causes of elevated SSC levels in both zones were different. Similarly, satellite remote sensing data revealed the above SSC distribution characteristics (Figure 3E). The surface SSC of the Yellow River mouth decreased rapidly near the shore (no more than 20 km from the mouth). In addition, this surface SSC extended to the southwest nearshore direction. There was a surface low SSC zone in the middle of Laizhou Bay, which is consistent with the previous studies using measured data (Qiao et al., 2010). The average SSC in eastern Laizhou Bay was between that of the west and middle of the bay. The bottom SSC distribution was similar to that of the surface SSC. However, the bottom SSC, located in the area near the Yellow River mouth, had the highest value. During moderate tide, the average SSC (10.1 mg/L) was higher than that of the spring tide (9.1 mg/L), and its coverage was also greater than that of the spring tide. The remaining characteristics were similar to those of the spring tide.

According to the geographical position of the stations, during the spring tide (Figures 4A–I), the SSC at the bay mouth ranged from 1.3 to 30.4 mg/L, with an average SSC of 5.8 mg/L. The SSC at the C1 station near the Yellow River mouth was higher than that at other stations. In the middle of bay, the SSC ranged from 4.8 to 52.5 mg/L, with an average of 8.8 mg/L. The highest SSC value was recorded at the C4 station. At the head of bay, the SSC varied from 4.9 to 57.1 mg/L, and the average SSC reached 14.1 mg/L. The highest SSC zone was recorded at the C7 station. Vertically, the surface SSC was lower than the bottom SSC. For example, the surface SSC at C8 was only 2.4 mg/L, whereas the bottom SSC was 29.2 mg/L. During the moderate tide (Figure 4K–R), the surface SSC ranged between 0.9 and 85.6 mg/L at each station, with an average SSC of 13.4 mg/L. SSC distribution characteristics from the bay mouth to its head were similar to those observed during spring tide, and SSC decreased vertically from surface to bottom. Overall, the SSC in spring was high in western Laizhou Bay and low in eastern Laizhou Bay, high at the head of the bay and low at the bay mouth, and high at the bottom and low at the surface. The average SSC of the spring tide was slightly lower than that of the moderate tide. In the tidal cycle, there were 2–4 times of high SSC field, which generally appeared around the peak of flow velocity; the low SSC field appeared during slack waters period (Figures 4, 6).

4.2 Tidal current and residual current variability

In the study area, the discriminant index (K, K is the ratio of the sum value of the major half axis of the tidal current ellipse of K_1 and O_1 to the value of the major half axis of the tidal current ellipse of M_2) of tidal properties was greater than 0.5 and less than 2, which belonged to the irregular semi-diurnal tidal sea area. Reciprocating current was the main form of tidal current movement, which is consistent with previous studies (Huang et al., 1999). It showed the vertical average tidal current at each station in the spring (Figure 5A) and moderate (Figure 5B) tides. The spring and moderate tide flow directions were similar. The flow direction was essentially the same along the coast, whereas the far coast had rotating current characteristics (Figure 5). In addition to the bay mouth, the terrain gradually widened and began to exhibit a rotating current, and the main direction of flood and ebb tides changed with the coastal trend of the Shandong Peninsula. Furthermore, the flood and ebb tide flow directions were almost symmetric, which was consistent with round-trip flow characteristics. However, the flow direction at the C9 station exhibited some rotating flow features, which were assumed to be produced by the lifting of the convex bank based on the water depth topography (Figure 1). As seen C1 station in Figure 5, there was a high-velocity field in northwestern Laizhou Bay, followed by the middle and eastern Laizhou Bay. This was

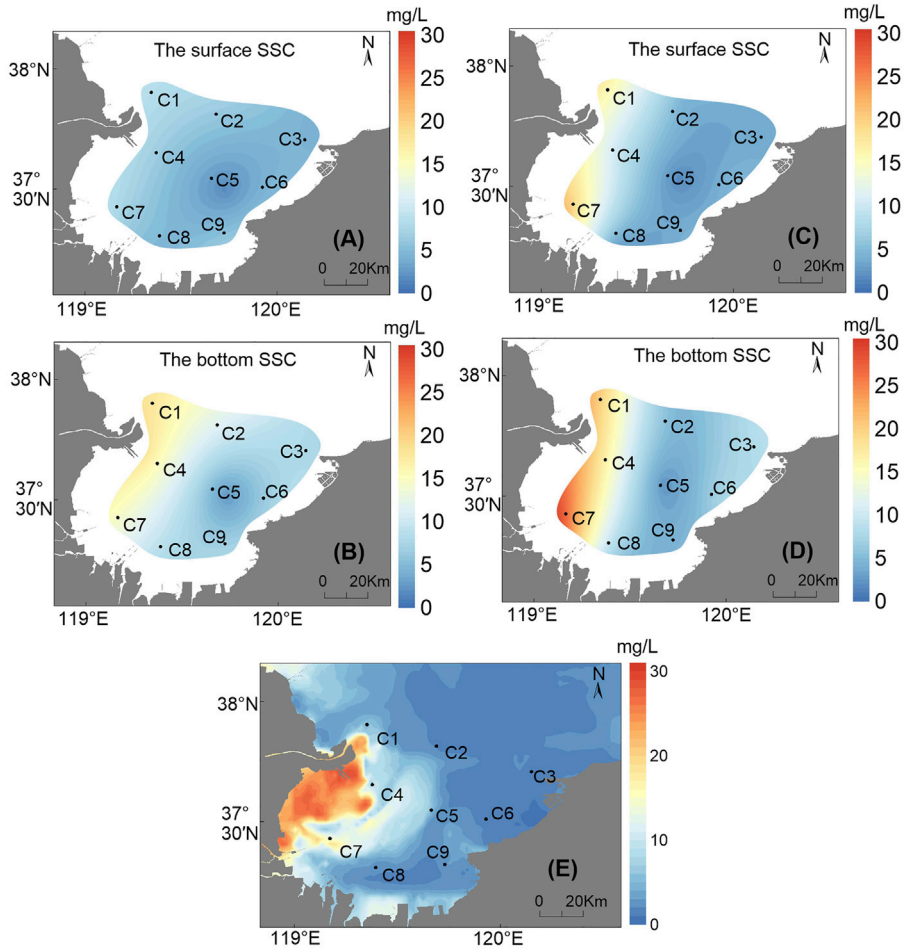

FIGURE 3
Horizontal distribution of the surface SSC **(A)** and the bottom SSC **(B)** during the spring tide (May 24–25, 2020); horizontal distribution of the surface SSC **(C)** and the bottom SSC **(D)** during the moderate tide (April 27–28, 2020). **(E)** Geostationary Ocean Color Imager (GOCI) satellite image of SSC on 23 May 2020.

comparable to the horizontal distribution of SSC analyzed above (Figure 3E).

To further study the distribution characteristics of flow velocity, the vertical flow velocity profiles were analyzed for the spring (Figure 6A) and moderate tides (Figure 6B). There were 3–4 flow velocity peaks in a tidal cycle, which was consistent with characteristics of semi-diurnal tide. These peak values occurred at the flood tide and ebb tide, and the average flow velocity of the flood tide (37.8 cm/s) was slightly higher than that of the ebb tide (37.2 cm/s). Both the spring (93.7 cm/s) and moderate tides (83.0 cm/s) had the highest flow velocity at the C1 station in the area near the Yellow River mouth. The flow velocity decreased gradually from the surface layer to the bottom layer. Furthermore, when the surface flow velocity increased, the bottom flow velocity did increase gradually, albeit with a delay. An asymmetry in the flow velocity and duration between flood and ebb tides was observed during a tidal cycle. In terms of flow velocity, the average flow velocity (36.23 cm/s) of the flood tide was slightly lower than the average flow velocity (40.14 cm/s) of the ebb tide, which might be attributable to topographical influence of the Yellow River Delta (Li, 1990). In addition, flood tide lasted around 1–2 h longer than the ebb tide. Overall, due to the topography of the Yellow River Delta, a strong current field was formed in northwestern Laizhou Bay. There were weak current fields in southeastern Laizhou Bay (Figure 5). The maximum and average surface flow velocity at each station were greater than those at the bottom (Figure 6), and the average ratio of surface flow velocity to bottom flow velocity is 2.65.

Residual current was obtained by separating the periodic tidal current from the measured data. The residual current can indicate the movement and exchange of water (Zhao et al., 1995), which is a critical aspect of further research on suspended sediment transport in shallow continental shelfs. In this study,

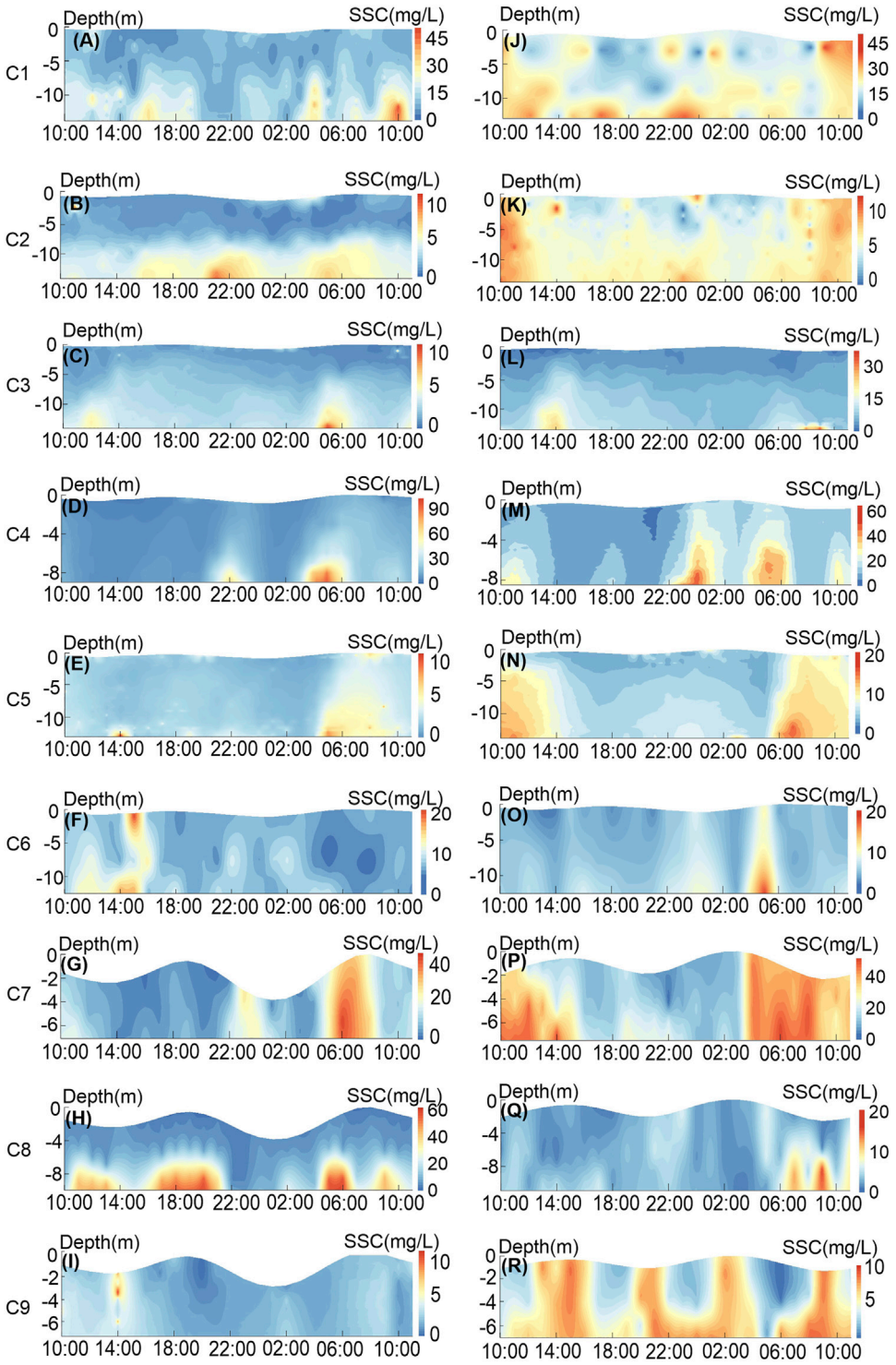

FIGURE 4
Time series of SSC profiles at various stations during the spring **(A–I)** and moderate **(J–R)** tides.

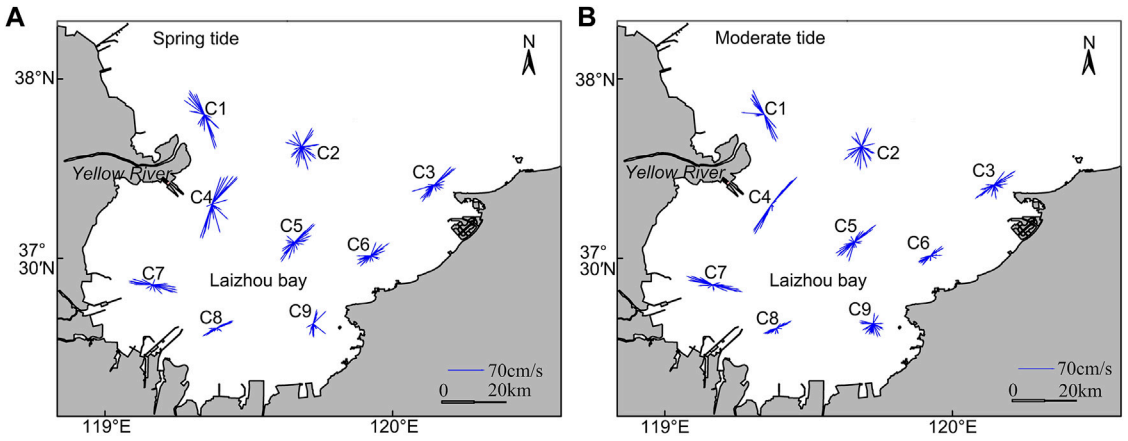

FIGURE 5
Vertical average tidal current at each station during the spring **(A)** and moderate **(B)** tides.

tide-induced residual current was calculated using tidal harmonic analysis through the program 'T_TIDE' package (Table 1). During the spring tide, the residual current velocity in Laizhou Bay ranged between 0.5 and 8.3 cm/s. The C5 station had the lowest bottom residual current velocity, with a flow direction of 151.0°. The surface residual current velocity was the largest at the C3 station, with a flow direction of 91.0°. The residual current velocity was 0.6–10.9 cm/s during the moderate tide period. The bottom residual current velocity was the lowest at the C7 station, and its direction was 231.1°. The C9 station had the greatest bottom residual current velocity. Overall, the residual current velocity was high near the surface and gradually decreased from the surface to the bottom. This was similar to the variation in tidal current velocity. It should be noted that the flow directions of surface and bottom residual currents were not consistent.

4.3 Water temperature and salinity variability

The average temperature increased from the bay mouth to the head of the bay over the whole tidal cycle of the spring and moderate tides (Figures 7A,E). Notably, there was a low salinity zone near southern Laizhou Bay, which may reflect the influence of small local rivers (Qiao et al., 2010). During the spring and moderate tides, surface temperature was generally higher than bottom temperature, while the water salinity variation was the opposite (Figures 7C,D,G,H). The largest water temperature difference was recorded during spring tide at the C1 station in the head of the bay, with a difference of 2.5°C. The maximum salinity difference was 2.0 psu at the C1 station near the Yellow River mouth. In addition, the temperature difference value showed an increasing trend from the head of the bay to the bay mouth (Figures 7B,F), which was similar to the change of water depth. In particular, the increase in solar thermal radiation at noon further increased the temperature difference between surface and bottom water (Simpson and Dickey, 1981). Based on Figures 9A,C,E,G, we found that the average water temperature progressively increased from the mouth to the head of the bay, while the average salinity gradually decreased. Due to the input of other rivers at the head of the bay and the diluted water of the Yellow River (Qiao et al., 2010), the average salinity from the Yellow River mouth to southwestern Laizhou Bay did not exceed 29 psu.

4.4 Mixing degree variability

To better characterize the variation of the water mixing degree in Laizhou Bay, representative stations were selected and *Rig* was used to describe the stratification mixing degree of the water structure. This study set the ordinate to Q (Q = In (Rig/0.25)). When Q was greater than 0, the stratification of the water column was high; the greater the value was, the stronger the stratification of the water column was. When Q was less than 0, the vertical mixing degree of the water column increased.

Except for the near bottom, the zone of positive value spanned the bulk of the spring tide (Figures 8A–D), indicating that the stratification degree was high. The C3 station had the largest stratification zone (less than 0), followed by the C4 and C5 stations, and the C9 station had the smallest, which was associated with the low average salinity and shallow water depth of the head of the bay (Chen et al., 2015). The high value zone was mostly concentrated at about 14:00, which is thought to be caused by solar thermal radiation, and the temperature

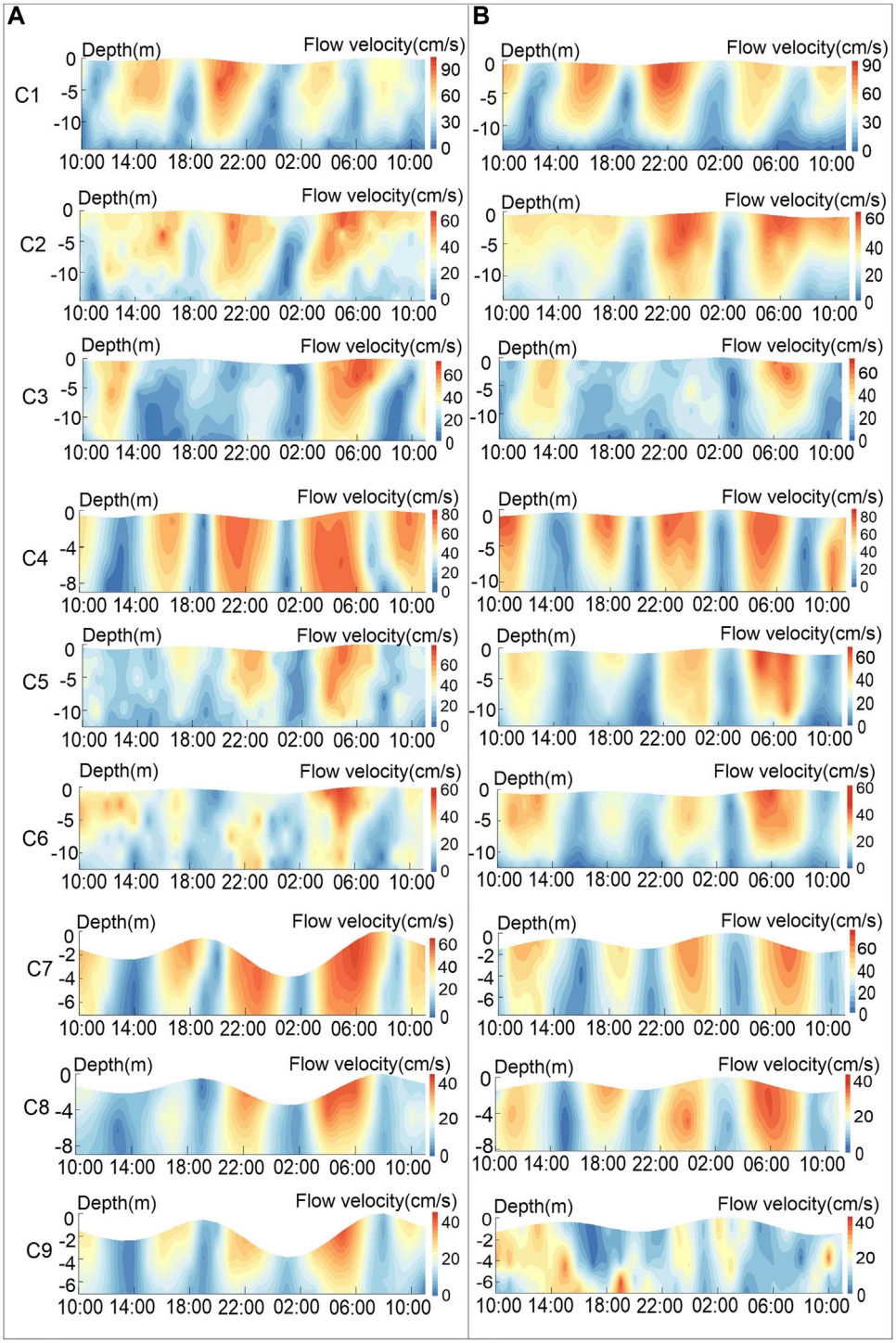

FIGURE 6
Flow velocity profiles at various stations for the spring **(A)** and moderate **(B)** tides.

difference between the surface and bottom was intensified, promoting water stratification. During the moderate tide, water column stratification was weaker than that of spring tide, substantially. According to Eq. 1, the temperature gradient, salinity gradient, and water depth were proportional to the stratification degree and inversely

TABLE 1 Residual current at each station in the spring and moderate tides (velocity: cm/s, direction: degrees).

Tide	Station	Surface		Bottom	
		Velocity	Direction	Velocity	Direction
Spring tide	C1	4.4	201.0	2.7	233.6
	C2	3.3	82.7	1.7	114.0
	C3	8.3	91.0	2.4	275.4
	C4	7.0	127.5	9.0	165.9
	C5	5.6	100.8	0.5	151.0
	C6	3.9	43.0	2.0	267.6
	C7	1.5	46.4	1.2	180.5
	C8	2.7	53.2	2.0	129.4
	C9	2.5	69.4	2.4	115.6
Moderate tide	C1	3.6	66.7	0.6	230.4
	C2	4.8	91.5	0.8	234.3
	C3	6.8	82.3	4.7	191.2
	C4	4.9	130.1	4.9	194.1
	C5	3.3	16.5	2.5	237.9
	C6	3.2	168.6	2.6	244.9
	C7	3.8	17.4	0.2	231.1
	C8	2.6	63.7	2.4	162.6
	C9	1.9	155.3	2.1	137.0

proportional to the flow velocity gradient. Among them, the average water depth of the spring and the moderate tide was not much different (difference value was less than 0.5 m), and the flow velocity gradient during the spring tide was stronger than that of the moderate tide. In addition, during the short period between spring and moderate tides, the salinity gradient did not change much (Figures 7D,H). According to the Global Weather Network (www.tianqi.com), the average air temperature in Laizhou Bay in April and May 2020 was 13.0 and 19.5°C, respectively. In addition, Figures 7B,F showed that the water temperature difference value (1.2 °C) of the spring tide was larger than that of the moderate tide (0.7°C). Thus, the water temperature was the main cause of high stratification degree. Moreover, Q also decreased substantially during the moderate tide (Figures 9A–D). From the analysis of horizontal distribution, the stratification degree at the C5 station in the middle of Laizhou Bay was the most considerable, which may be related to the substantial depth and low flow velocity, which was conducive to stratification. However, due to shallow water depth and tidal waves deformation in coastal waters, water column stratification could not be easily established.

This study utilized the vertical gradient method for expression to further analyze the depth at which thermocline occurred (Jiang et al., 2016). According to that method, the water column with a temperature gradient greater than or equal to 0.2 C/m in shallow water (depth of less than 200 m) is defined as thermocline. The upper limit depth is the depth of the upper water column reaching the critical value of the temperature gradient, and the lower limit depth is the depth of the lower water column. In this study, typical C3–C5, and C9 stations were selected for simultaneous analysis (April and May 2020, 14:00), and the results are shown in Figures 8C, D, G, H and Figures 9C, D, G, H. The thermocline thickness varied between 2.0 and 4.5 m and the depth of the lower thermocline was about 2.0–4.5 m.

4.5 Suspended sediment flux

The suspended sediment fluxes (F) at each station were calculated for the spring and moderate tides (Table 2). The suspended sediment flux of the spring and moderate tides at each station ranged from 0.57 to 9.38 g s^{-1}·m^{-1} and 1.30–13.62 g s^{-1}·m^{-1}, respectively. Furthermore, the F of these stations were oriented towards land. The direction of the highest suspended sediment flux was 184.41° during the moderate tide at the C4 station, and the direction of the minimum suspended sediment flux was 171.64° in spring tide

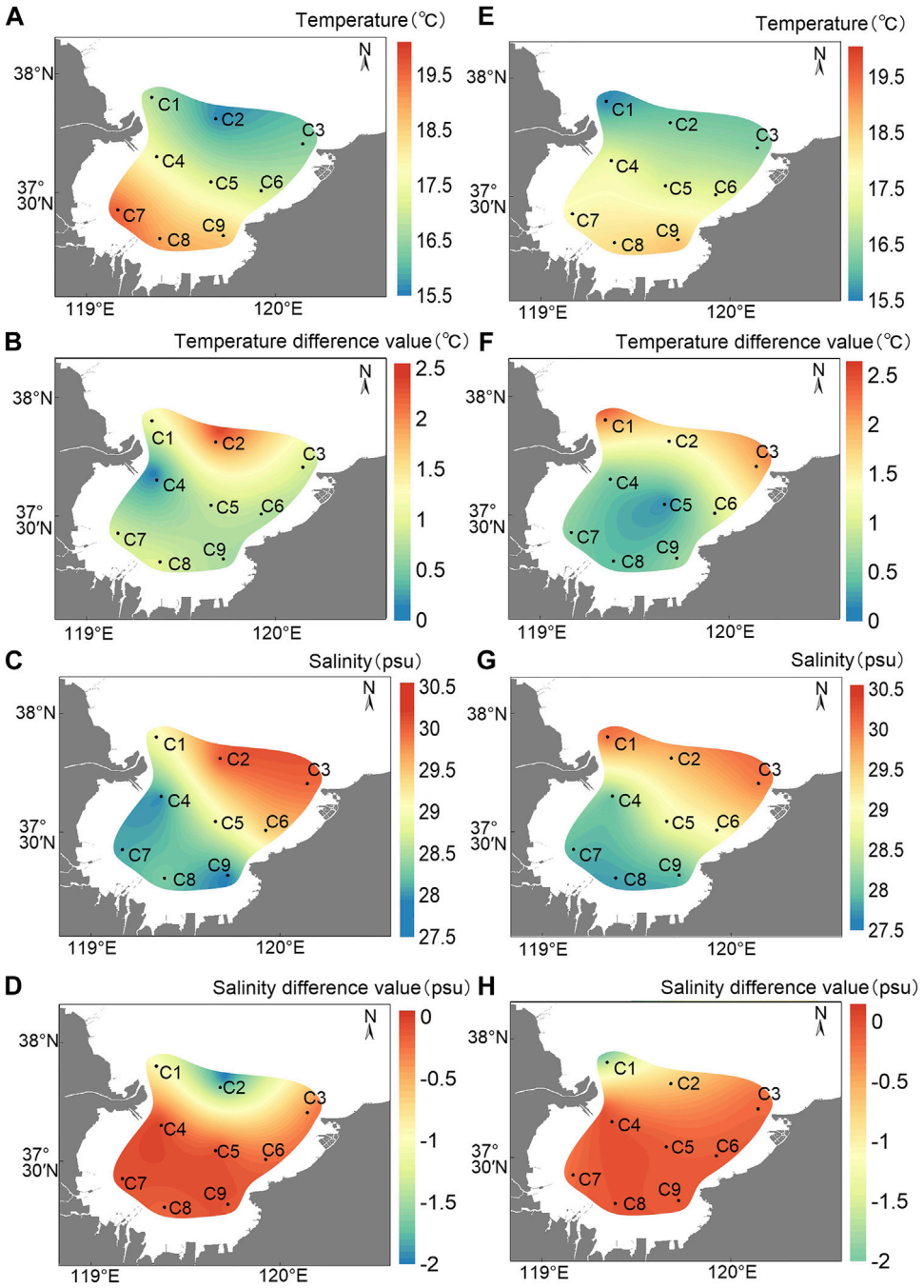

FIGURE 7
Contour of average temperature **(A)** and salinity **(C)** during the spring tide; surface minus bottom temperature **(B)** and salinity **(D)** difference during the spring tide; contour of average temperature **(E)** and salinity **(G)** during the moderate tide; surface minus bottom temperature **(F)** and salinity **(H)** difference during the moderate tide.

at the C8 station. The flux of suspended sediment transport generated by $T_6 + T_7 + T_8$ accounted for an average of only 1.73% of suspended sediment flux, therefore its contribution to the suspended sediment flux was negligible. $T_1 + T_2$ were the dominant elements (the average ratio of $T_1 + T_2$ to F reaches 1.01), and $T_3 + T_4 + T_5$ increased their proportion from the bay mouth to the head of the bay. During moderate tide (Table 2), average suspended sediment flux

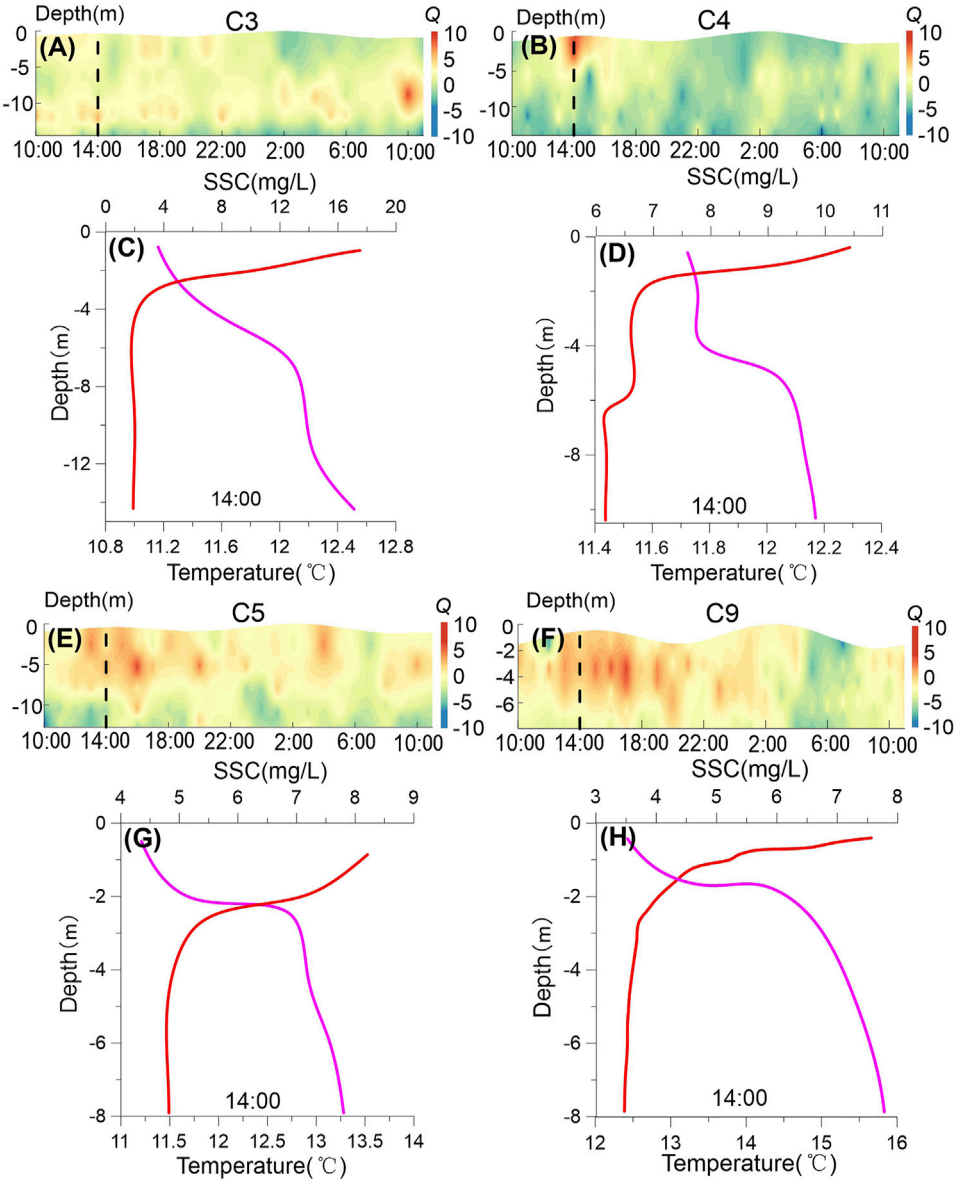

FIGURE 8
The time series diagrams of Q (Q = ln (Rig/0.25)) during the spring tide **(A,B,E,F)**, the vertical sections of temperature (red line) and SSC (fuchsia line) at typical stations at 14:00 in May 2020 **(C,D,G,H)**.

of moderate tide (4.15 g s^{-1} m^{-1}) was higher to those of the spring tide (3.87 g s^{-1} m^{-1}). Overall, according to the results of Table 2, the transport items of T_1, T_2, and $T_3 + T_4 + T_5$ constitute the main part of the suspended sediment flux in Laizhou Bay, accounting for 0.68–1.49, 0.02–0.65, 0.01–0.54 respectively with F, of which T_1 is the main transport term. The suspended sediment flux generated in western Laizhou Bay was considerably higher, followed by that in the middle of Laizhou Bay, and was lowest in eastern Laizhou Bay (except for the C9 station). The Lagrange transport term ($T_1 + T_2$) had the highest proportion and played the most important function, followed by the tidal pumping transport term ($T_3 + T_4 + T_5$).

5 Discussion

5.1 Controlling factors of SSC variations

SSC is influenced by many factors related to runoff, seabed sediment, tide, tidal current, wave, and wind-ocean current (Guo et al., 2017; Qiu et al., 2017; Bo Liu et al., 2020). In

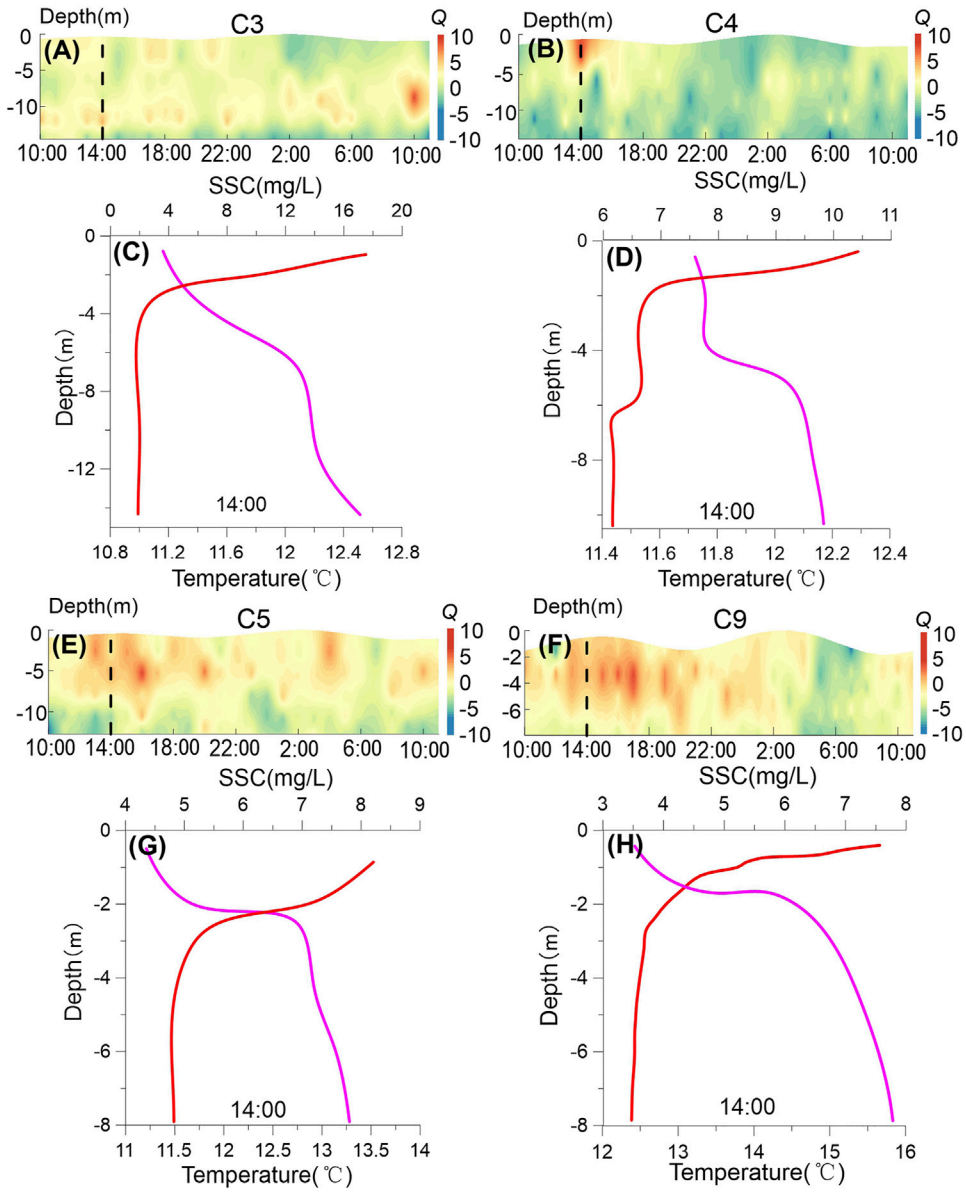

FIGURE 9
The time series diagrams of *Q* (*Q* = ln (*Rig*/0.25)) during the moderate tide **(A,B,E,F)**, the vertical sections of temperature (red line) and SSC (fuchsia line) at 14:00 in April 2020 **(C,D,G,H)**.

addition, the inflow of the material of the Yellow River brings complicated changes to the study of suspended sediment transport in Laizhou Bay. Not only do sediment particles and colloids from the Yellow River (Hill et al., 2009; Geyer and Maccready, 2014) have an important impact on deposition and transport of suspended sediment in Laizhou Bay, but the inflow of a large amount of diluted water into the bay would affect water density and circulation of Laizhou Bay, thereby changing the water structure (Leblond et al., 1986). We will discuss the primary controlling factors of SSC and suspended sediment transport mechanisms in Laizhou Bay from the following perspectives.

5.1.1 Influences of tidal current on the SSC

Under normal weather and tidal conditions, tidal current is an important dynamic source of suspended sediment transport in a semi-enclosed sea (Du et al., 2012; Bo Liu et al., 2020). We analyzed and described the relationship between flow velocity

TABLE 2 The sediment transport flux at various stations during the spring and moderate tides (items without parentheses are sediment transport flux ($g \cdot s^{-1} \cdot m^{-1}$), and items in parentheses are suspended sediment transport direction (degrees)).

Tide	Station	T_1	T_2	$T_1 + T_2$	$T_3 + T_4 + T_5$	$T_6 + T_7 + T_8$	F
Spring tide	C1	8.59	0.37	8.75	1.39	0.04	7.72
		(225.67)	(161.1)	(203.48)	(344.96)	(330.71)	(210.25)
	C2	8.18	0.16	8.2	1.05	0.02	7.61
		(237.23)	(155.06)	(236.11)	(10.23)	(239.61)	(242.49)
	C3	0.85	0.06	0.82	0.24	0.02	0.57
		(159.54)	(40.25)	(155.75)	(6.05)	(205.57)	(217.04)
	C4	10.78	0.59	10.42	2.12	0.13	9.38
		(143.45)	(14.89)	(140.92)	(31.35)	(180.43)	(129.97)
	C5	0.47	0.1	0.41	0.06	0.02	0.38
		(173.44)	(44.61)	(162.69)	(304.87)	(196.03)	(171.64)
	C6	0.66	0.26	0.54	0.13	0.01	0.59
		(265.43)	(63.19)	(217.75)	(211.18)	(168.61)	(214.84)
	C7	1.41	2.25	2.15	1.87	0.03	3.45
		(252.07)	(139.58)	(176.98)	(115.13)	(280.64)	(149.49)
	C8	0.53	0.19	0.53	0.34	0.06	0.89
		(160.77)	(62.6)	(140.3)	(144.68)	(240.93)	(147.73)
	C9	5.19	0.22	4.98	0.55	0.19	4.66
		(155.65)	(339.12)	(155.5)	(351.68)	(192.54)	(153.51)
Moderate tide	C1	9.05	0.76	8.46	0.94	0.08	7.54
		(196.74)	(339.09)	(199.88)	(345.78)	(349.02)	(202.81)
	C2	3.03	0.15	3.05	0.13	0.01	2.95
		(158.92)	(242.39)	(161.72)	(288.88)	(3.01)	(163.41)
	C3	2.11	0.24	2.21	1.07	0.04	2.34
		(152.7)	(222.53)	(158.48)	(252.26)	(10.99)	(184.99)
	C4	14.97	0.58	14.42	0.92	0.02	13.62
		(183.27)	(19.23)	(182.64)	(335.26)	(130.69)	(184.41)
	C5	0.88	0.2	1.08	0.25	0.01	1.30
		(243.7)	(241.21)	(243.24)	(213.16)	(36.99)	(237.65)
	C6	0.80	0.14	0.89	0.06	0.01	0.94
		(266.17)	(353.45)	(253.64)	(208.87)	(180.73)	(219.08)
	C7	3.02	2.02	5.00	0.58	0.05	4.43
		(131.67)	(117.85)	(126.14)	(165.28)	(158.04)	(124.58)
	C8	0.74	0.04	0.75	0.02	0.00	0.73
		(169.77)	(254.23)	(172.68)	(40.04)	(29.33)	(172.02)
	C9	3.19	0.44	3.62	0.04	0.02	3.58
		(237.47)	(227.2)	(236.22)	(48.66)	(335.08)	(236.64)

and SSC at the following nine stations (C1–C9) in spring and moderate tides, as shown in Figures 4, 6, respectively. Theoretically, there were two important sources of suspended sediment for a given station, local resuspension and advection transportation (Yu et al., 2012; Xiong et al., 2017). The horizontal advection of the SSC gradient resulted in SSC tidal variations (Ni et al., 2014). It is known that the combined effects of suspended sediment particle size and tidal current can cause sediment resuspension time lag on the inland shelf and influence cross-shore SSC distribution (Niedoroda et al., 1995; Guillén et al., 2002). In addition, as seen in Figure 3E, coarse-grained Yellow River sediment was rapidly deposited near the Yellow River delta, while fine-grained sediment was transported to the southern and northern Yellow River mouth, influenced by the isobaric-parallel tidal current (Qiao et al., 2010). As seen in Figures 3A,C, 4, the distribution of the surface SSC corresponded well with the tidal

current field. Through remote sensing images, Li et al. (2001) found that the current field and distribution of suspended sediment in the Yellow River mouth was controlled by the interaction between the river and the tidal current, rather than by waves. Similarly, Chao Jiang et al. (2017) and Bo Liu et al. (2020) observed this characteristic in southwestern and northeastern Laizhou Bay.

As the main current movement in the Bohai Sea, tidal current is the main driving force of sediment transport in Laizhou Bay (Qin et al., 1985). There were strong and weak tidal current fields in Laizhou Bay. The high-velocity field was located outside the Yellow River mouth and the weak-velocity field was located in southeast Laizhou Bay (Figure 5). The flow velocity was the highest outside the Yellow River mouth, and showed a tongue-like decreasing trend to the north and south. The velocity decreases rapidly towards the mouth (Figure 5). High surface SSC in Laizhou Bay mainly existed in the spatial velocity the high-velocity field, and surface SSC decreased as the flow velocity decreased. The suspended sediment from the Yellow River mouth firstly diffused southward and southeastward (towards the head of Laizhou Bay). However, the influence scope of suspended sediment is generally located in the shallow coastal sea withing isobaths of about 15 m (Figure 3). The existence of the high-velocity field controlled the outer boundary of the diffusion of suspended sediment into Laizhou Bay. The SSC in the middle and eastern Laizhou Bay was relatively low. Therefore, there was a strong correspondence between the high SSC zone in Laizhou Bay and the high-velocity field outside the Yellow River mouth (Figures 3, 5). The diffusion of such surface suspended sediment in Laizhou Bay is roughly consistent with the distribution of low-salt sea area near the Yellow River mouth (Figures 3A,C, 7C,G). In addition, not only the formation of the low SSC field in eastern Laizhou Bay corresponds to the weak tidal current (Figures 3, 5), but may be also related to the lack of suspended sediment sources (Chen et al., 2015).

Aside from advection transport, another factor that contributed to SSC variation was local resuspension. In addition to the sediment types, external variables such as waves and tidal currents also had an impact on the local resuspension (Sarik and Charitha, 2020). Near-bed turbulence was the primary factor affecting sediment resuspension in calm weather conditions as well as sediment characteristics (particle size, etc.), and was very common in estuarine and coastal environments (Fettweis et al., 2006; Jiang et al., 2020). The sediment lifting of the tidal current was controlled by the diffusion of the turbulence, which relates to its flow velocity, motion viscosity coefficient of the water column, and the roughness of the seabed. The SSC varied periodically due to the alternation of the flood and ebb tides and the fluctuating flow velocity. Although the flow velocity also increased, it did not reach the peak value rapidly or correspondingly, but lagged behind the peak of the flow velocity (Figures 4, 6). Rather, the resuspension and diffusion of suspended sediment required a time process. The lag time varied according to the different sea areas and seasons (Yuan et al., 2011), which is consistent with previous research on bays and shallow seas (Rui Jiang et al., 2017; Bo Liu et al., 2020; Meng et al., 2020).

Notably, not all the flow velocity peak produced the SSC peak, which suggests that under the same conditions, the bottom flow velocity was critical for sediment resuspension (Scully and Friedrichs, 2003). For example, the C5 station reached the peak of surface flow velocity at approximately 16:00 (Figure 6A), but the bottom flow velocity did not increase considerably, resulting in no considerable increase of SSC (Figure 4E). At approximately 05:00, the bottom flow velocity increased considerably, which resulted in high SSC. It can be considered that tidal current not only influenced horizontal distribution of SSC, but influenced vertical distribution of SSC.

5.1.2 Relationship between water stratification and SSC

Water mixing affects not only the tidal current field, but is also closely related to the vertical diffusion of SSC (Li et al., 2013b; Li, 2018; Tong et al., 2018; Yang et al., 2021; Li et al., 2022). In this study, water column stratification hindered the vertical diffusion of suspended sediment. Figures 5, 6 show that the bottom SSC at the C3, C4, and C5 stations were much higher than surface SSC, mainly because seabed sediment had entered the water column. Since the degree of diffusion was inhibited by the stratification, the suspended sediment could not spread effectively in the vertical direction, resulting in a large difference in the surface and bottom SSC. Bi et al. (2010) studied sediment transport into the Yellow River in the summer and winter, and found that the water column was highly stratified in the summer, and that the gradient of vertical SSC was considerable, which is consistent with our observations. In windy weather conditions during the winter, the stratification of the water column was broken, and the surface SSC was similar to the bottom (Bi et al., 2021).

In addition, Scully and Friedrichs (2003) discovered that sediment resuspension in the substrate depended on the critical shear stress, which was less affected by lamination. However, after the sediment entered the water column, its resuspension height and duration in the water column were determined by the turbulence diffusion coefficient at this depth, which was greatly impacted by lamination. The degree of influence was inversely proportional to the stratification height from the seafloor, which was proportional to stratification strength (Scully and Friedrichs, 2003; Courtney et al., 2022). According to Figure 6A, during the spring tide at 19:30–22:00 (from low tide to high tide), although the highest near-bed flow velocity exceeded 40 cm/s at flood tide, the SSC did not increase considerably. The bottom SSC reached a peak rapidly only at the time of rest (22:00) when the strength of stratification was the weakest (Q less than 0). Although we are

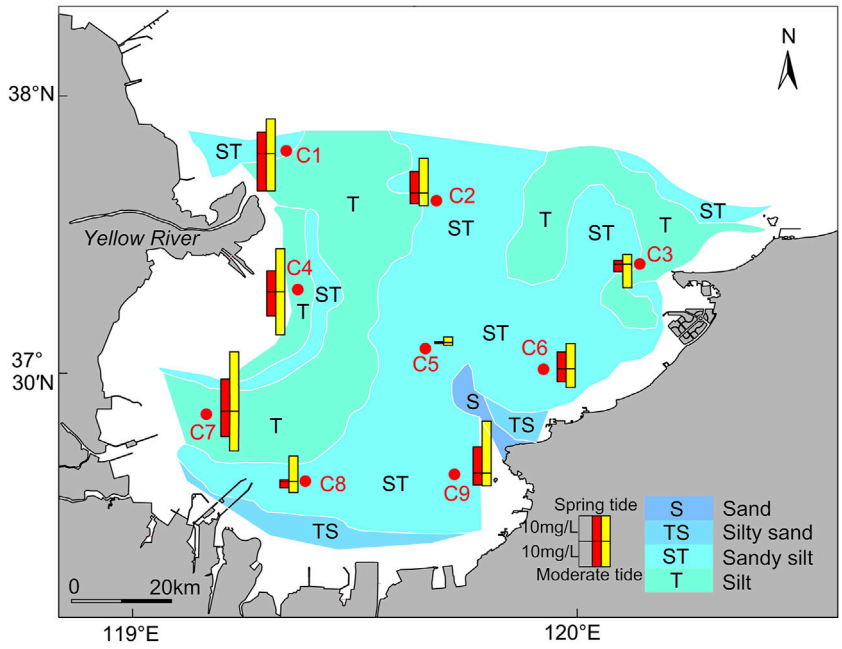

FIGURE 10
Distribution of seabed sediment types (adapted from Qiao et al. (2010)) and distribution of the surface (red rectangle) and bottom SSC (yellow rectangle).

not directly observing near-bed turbulence, the study shown that water column stratification inhibited the intensity of turbulent mixing near the bottom layer (Scully and Friedrichs, 2003; Yuan et al., 2011). When the stratification weakened, water turbulence diffusion strengthened, and the sediment rapidly diffused to a higher elevation. Most Q was less than 0 (except for around 14:00) at the C4 station (Figures 8D, 9D) in particular, indicating that vertical mixing was dominant during this period. Furthermore, the difference between surface and bottom SSC also decreased, and suspended sediment particles could be effectively diffused vertically.

Moreover, water mixing plays the important role for vertical diffusion of suspended sediment and local resuspension by influencing the turbulence efficiency. When stratification exists in the water column, turbulence is inhibited by that stratification. Sediment resuspension is largely controlled by near-bed turbulence (Ali and Dey, 2016). By observing the flow velocity variations at the C5 station around 04:00–06:00 (flood tide) during the spring tide (Figure 6A), we found that when the near-bottom flow velocity gradually increased at 04:00, the bottom SSC rose suddenly at about 05:00. Although both the bottom flow velocity and the corresponding SSC began to decrease after that, the surface flow velocity reached a maximum value at around 05:30. This suggested that when the bottom flow velocity increased, the seabed sediment resuspended and formed a high SSC zone in the bottom layer, and a large vertical SSC gradient formed in the water column. As shown in Figure 8E, the Q value at the C5 station decreased around 05:30–06:00, indicating that the degree of stratification was decreasing. The continuous vertical diffusion of suspended sediment to the surface water column over time could also verify that the degree of stratification weakened at 05:30–06:00 at the C5 station. In general, tidal current is the main driving force for sediment resuspension under normal weather. In other words, water column stratification reduced the sediment resuspension by inhibiting near-bed turbulence, and then affected vertical SSC.

In summary, water column stratification influenced the vertical SSC variation by hindering the vertical diffusion of suspended sediment and affecting the sediment resuspension, thereby forming a layer with high SSC at the bottom (Stretch et al., 2010). In addition, under normal weather, the weak stratification during moderate tidal was explained why, in normal weather, the average SSC of the middle tide was higher than that of the spring tide, even though flow velocity during spring tide was higher than that of moderate tide (Figure 3).

5.1.3 Effect of seabed sediment on distribution of suspended sediment

The seabed sediment types also have a considerable influence on the distribution characteristics of SSC, mainly because fine-grained sediment is one of the important components of suspended sediment in water column (Qiao et al., 2010; Wang

et al., 2020). In addition, seabed sediment was a key element in the formation of resuspension. Many recent studies have focused on the effect of resuspension on suspended sediment transport, particularly in explaining seasonal sediment transport patterns in the Bohai, Yellow, and East China Seas (Gong et al., 2021). Thus, the analysis of seabed sediment types was one of the major methods for studying the suspended sediment distribution in Laizhou Bay. Wang and Wang (2005) found that the high turbidity zone around the Yellow River mouth was closely related to the types of seabed sediment in Laizhou Bay, as shown in Figures 3, 10. Furthermore, monsoon and wave action have been found to play an important role in seabed sediment resuspension in the Bohai Sea (Qin et al., 1985; Qiao et al., 2010; Bi et al., 2021). However, a more complete explanation of the resuspension process necessitates a closer study during calmer weather.

Laizhou Bay can be divided into four regions based on the spatial distribution of seabed sediment types: western, eastern, central, and southern. The western section was primarily silty sand, whereas the central section was mostly coarse silty sand. The Yellow River continues to be the primary source of sediment (Bi et al., 2010; Qiao et al., 2010). Furthermore, under the influence of tidal currents and waves, the original abandoned QSG delta changed from a sedimentary state to an erosion state and has evolved into a new sediment source (Bi et al., 2021). In addition, since the artificial implementation of water and sediment diversion, the sediment supply of the Yellow River has decreased substantially (Wang et al., 2017). To regulate the balance of water and sediment supply, the sediment of the lower reaches was naturally eroded (Bi et al., 2014). The seabed sediments found in the eastern and southern Laizhou Bay were mostly sandy silt. The primary source of sediment is coastal rivers (Liu et al., 2013; Chen et al., 2015). Furthermore, from the analysis of shoreline changes, the average shoreline erosion rate reached 3.92 m/year during 2006–2013 (Zhan et al., 2017). Thus, coastal erosion is also an important source of sediment in eastern and southern Laizhou Bay, whereas sediment sources tend to be complex and varied in the middle of Laizhou Bay (Qiao et al., 2010; Wang et al., 2010). Because of the weak hydrodynamics (Figures 5, 6) and the low influence by sediment from surrounding rivers and land the middle of Laizhou Bay, the seabed sediment type mainly is silty.

Seabed sediment at the C1 and C4 stations was mostly fine-grained silt or clay silt from the Yellow River, which was prone to resuspension (Wang and Wang, 2005; Zheng et al., 2015). At the C2 station, the seabed sediment type located in the middle and southern Laizhou Bay was mainly coarse silt, and the average flow velocity of the tidal current was relatively slow (28.45 cm/s) (Figure 6), corresponding to the low SSC zone (Figure 4). Combined with the variation characteristic of SSC mentioned above, the bottom sediment resuspension caused by tidal current played an important role for SSC in the water column. However, the proportion of sediment entering the water column under the influence of resuspension is unknown (Qiao et al., 2010). The sediment induced was resuspended and entered the water column as the flow velocity increased and the seabed sediment reached critical shear stress (Chen et al., 2015). Under the influence of water column stratification, suspended sediment cannot be effectively diffused vertically and the high value zone appeared about 1–2 h after peaks of flow velocity sharply. Following that, the flow velocity gradually decreased, resulting in the deposition of suspended sediment. The low SSC value zone developed approximately 2 h after the flood and ebb tides (Figure 5).

The seabed sediment types, strong tidal current zone, and high SSC zone exhibited a strong corresponding relationship in Laizhou Bay (Figures 3–5, 10). Previous studies suggested that under extreme storm surge weather, the maximum SSC in the southwest coastal area of Laizhou Bay may be increased tenfold (Liu et al., 2013). These results indicate that sediment resuspension is very important to the contribution of suspended sediment in Laizhou Bay. Moreover, the grain size of seabed sediment has been found to have a positive effect on resuspension (Wang and Wang, 2005). Under the same dynamic conditions, the seabed sediment (not including clay) with fine particles is more likely to be resuspended. However, the specific linking mechanism between seabed sediment and SSC in Laizhou Bay has remained unclear, as did the resuspension flux.

In order to specifically analyze the behavior of fine-grained sediment in different seabed sediment types, we further studied the sediment resuspension and deposition fluxes. According to the data, the median grain size (D_{50}) of seabed sediment in Laizhou Bay ranged from 0.12 to 0.77 mm (D_{50} of the C3, C6, C8, and C9 stations is from Zhao et al. (2021)). Empirical formulas proposed by Partheniades (1965) and Krone (1962) were used for the calculations, due to the wave effect being very weak (Wang et al., 2014). Further, due to the short interval between the two field survey phases, the median grain size of seabed sediment in the spring and middle tides remained unchanged. Thus, the changes in the spring and moderate tides were similar, and the sediment resuspension and deposition fluxes were selected for calculation during the spring tide.

$$\frac{\mathrm{d}M_{\mathrm{E}}}{\mathrm{d}t} = E\left(\frac{\tau_0}{\tau_{\mathrm{cr}}} - 1\right) \tag{4}$$

$$\tau_{cr} = g\theta_{cr}(\rho_s - \rho)D_{50} \tag{5}$$

$$\frac{\mathrm{d}M_D}{\mathrm{d}t} = C_b W_s\left(1 - \frac{\tau_0}{\tau_{\mathrm{cr}}}\right) \tag{6}$$

In these equations, M_E is the resuspension flux, E is the resuspension constant, τ_0 is the bottom shear stress, τ_{cr} is the critical shear stress, g is the acceleration of gravity, θ_{cr} is the Shields parameter, ρ_s is the sediment density (constant value of 2,650 kg/m^3), ρ is the water column density, D_{50} is the median

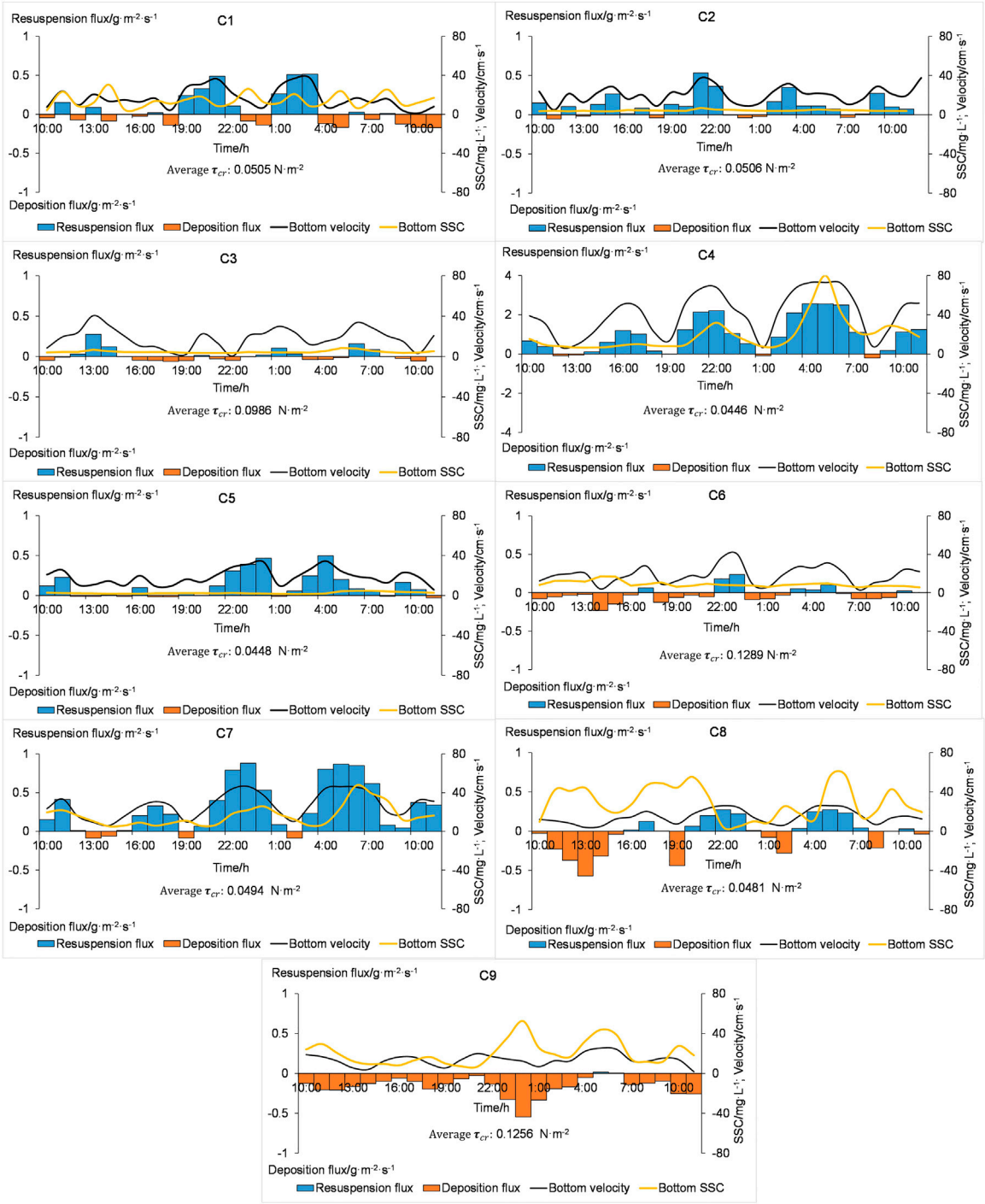

FIGURE 11
Resuspension flux (blue rectangle) and deposition (orange rectangle) flux at each station during the spring tide. Black line represents bottom flow velocity. Yellow line represents bottom SSC.

grain size of seabed sediment, M_D is the deposition fluxes, C_b is the near-bed SSC, and W_s is the settling velocity of suspended sediment.

In this paper, the settling velocity of suspended sediment was calculated using the modified Richardson formula (Huang, 1981):

$$W_s = W_0(1 - 8.9C_v) \quad (7)$$

Where W_0 is the settling velocity of single particle, C_v is the volume ratio of sand content. W_0 is calculated using semi-empirical formula (Camenen, 2007):

$$W_0 = \frac{v}{d}\left[\sqrt{\frac{1}{4}\left(\frac{A}{B}\right)^{2/m} + \left(\frac{4}{3}\frac{d_*}{B}\right)^{1/m}} - \frac{1}{2}\left(\frac{A}{B}\right)^{1/m}\right]^m \quad (8)$$

Where $d*$ is the dimensionless particle diameter; d is the particle diameter; v is the fluid viscosity constant (constant value of $1.007\times10^{-6}ms^2$), A, B, m are the coefficients in the resistance coefficient equation, and their values are based on previous studies (Hu, 2009), which are taken from 38, 3.55, and 1.12, respectively.

The results indicate that there was a large difference in the resuspension flux and deposition flux between various stations in Laizhou Bay (Figure 11), with a variation range of 0.01–2.60 g m^{-2} s^{-1}. Among these, the suspension flux at the C4 station located at the QSG sub-delta lobe was the largest, reaching 2.60 g m^{-2} s^{-1}. In addition to the influence of the elliptic high flow velocity field in the Yellow River mouth (Liu et al., 2005; Qiao et al., 2010), the bottom flow velocity increased, and fine-grained sediment also provided powerful conditions for the occurrence of resuspension. However, the deposition flux at the C4 station was far lower than the resuspension flux, indicating that the fine resuspension sediment particles did not settle *in situ*. Then fine resuspension sediment may be transported to the sea with a slow flow velocity of water, and then deposited. Notably, the resuspension and deposition fluxes at the C1 station near the Yellow River mouth were small (Figure 11). This may be related to the coarsening of grain size near the Yellow River mouth (Bi et al., 2014). Additionally, the water column was stratified due to Yellow River runoff, resulting in substantial differences in surface and bottom flow velocity (Figure 6). Thus, sediment resuspension was not strong at C1 station (Figure 11). Overall, due to the large particle size of seabed sediment in eastern Laizhou Bay, most of the suspended sediment was settled, with the exception of a small quantity of sediment resuspension when the flow velocity approached the flow velocity of initiation of sediment.

The seabed sediment type in the eastern Laizhou Bay was dominated by seasonal river sediment, which was mostly river of mountain stream, with coarse silt as the main sediment entering the sea (Chen et al., 2015). For example, at the C9 station during the spring tide (Figure 11), due to the coarse particle size of seabed sediment (71.95 μm) and low near-bed flow velocity (20.58 cm/s), the critical shear stress generated was not enough to cause sediment resuspension. Thus, there was almost no resuspension flux at C9 station, and the suspended sediments in the water column are basically in a settlement state. This also reflected that the SSC in the water column was not only affected by sediment resuspension, but also advection transport played an important role in maintaining the SSC. In eastern or southern Laizhou Bay, the coarse grain size of seabed sediment and the weak flow velocity were insufficient to produce sediment resuspension when the wave was weak (Figures 5A, 11). However, in western Laizhou Bay, especially near the abandoned QSG delta (C4 station) and southwestern Laizhou Bay (C7 station), the variation of resuspension flux had a strong correspondence with the variation of bottom SSC (Figure 11), indicating that the suspended sediment generated by resuspension may be the main source of the bottom suspended sediment. Therefore, the seabed sediment types are an important factor controlling variation of SSC by influencing resuspension flux.

On this basis, the seabed sediment types had an important control role in the distribution of SSC. The particle size of the seabed sediment would directly affect the strength of the resuspension. The fine-grained seabed sediment was conducive to the generation of resuspension and bottom high SSC. This was critical because the sediment transport occurred primarily through the bottom high SSC layer (Li et al., 2013a; Lu et al., 2018). However, it can also be related to maintaining the suspension duration of fine-grained sediment in the water column to be carried by the tidal current (Hu, 1984; Gao and Jia, 2002).

5.2 Suspended sediment transport mechanisms in Laizhou Bay

Eq. 3 reveals that the net suspended sediment flux is a function of flow velocity, tidal duration, SSC, and depth. Accordingly, the suspended sediment flux is controlled by these factors. The above results indicate that not only did the horizontal and vertical variation of SSC and flow velocity have a great difference, but they also showed asymmetries with tidal duration (Figures 3, 4, 6). There were considerable differences between tidal duration and suspended sediment transport characteristics from other seas, such as Hangzhou Bay, Funing Bay and the south side of the Yangtze River estuary (Wang et al., 2006; Ni et al., 2012; Wang et al., 2014; Meng et al., 2020). Due to the different characteristics of suspended sediment and tidal current in Laizhou Bay, the suspended sediment transport mechanisms were not identical. The suspended sediment transport in western Laizhou Bay was mainly affected by the high-velocity field near the Yellow River mouth. The Yellow River is the second largest sediment-laden river in the world, transporting as much as 1.1 Gt/year of sediment to the ocean (Milliman and Meade, 1983). In addition, the abandoned QSG delta was in a state of severe erosion and had become a new source of sediment (Bi et al., 2021). It has been shown that seabed sediment can re-enter and diffuse into water column under the action of current and waves, combined with the high flow velocity zone near the Yellow River mouth (Figure 5; Liu

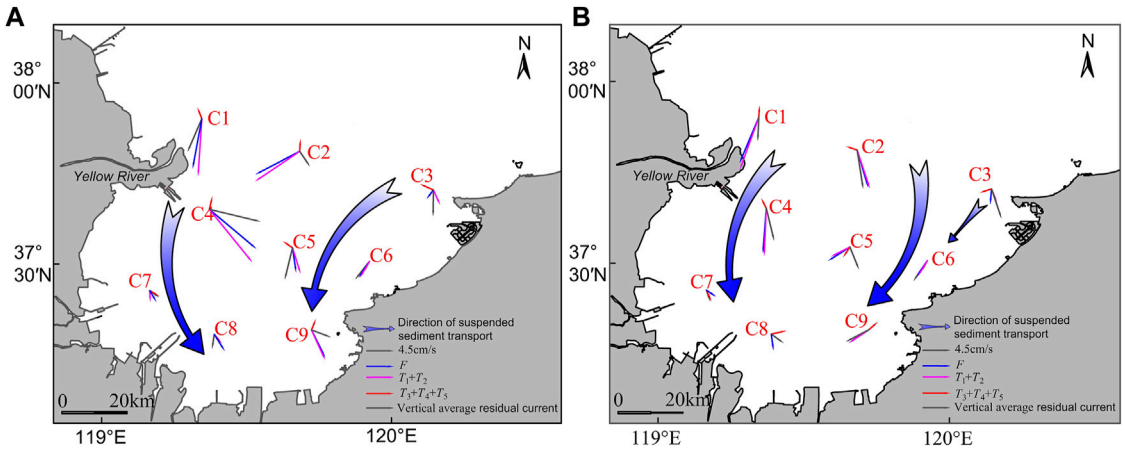

FIGURE 12
Vector diagrams of F (blue arrow), vertical average residual current, $T_1 + T_2$ (gray arrow) and $T_3 + T_4 + T_5$ (red arrow) during the spring **(A)** and moderate **(B)** tides (F of the C6–C8 stations increased to twice the original; $T_3 + T_4 + T_5$ of the C6–C8 stations increased to 6 times the original; and $T_3 + T_4 + T_5$ of the C1–C5 and C9 stations increased to 3 times of original). Gradient blue arrow represents the direction of suspended sediment transport.

et al., 2013), the combined factors of which lead to relatively high suspended sediment flux in western Laizhou Bay. Due to the relatively singular source of sediment (Qin et al., 1985; Zhan et al., 2017), the overall net suspended sediment flux in eastern and southern Laizhou Bay was small (Table 2), which was owing to the coarse particle size of seabed sediment and the weak resuspension effect. $T_1 + T_2$ was related to the residual current, and has a linear relationship with the average SSC and water depth of the local tidal period. The high flow velocity field in northwest Laizhou Bay and the influence of the average SSC makes advective sediment transport dominant in Laizhou Bay. In previous studies, researchers studied the suspended sediment transport mechanism in southwestern and eastern Laizhou Bay in autumn and winter, and the results suggested that $T_1 + T_2$ contributed more than 90% to F. The research results were consistent with the research results of our study. However, F was larger than that in our study, which may be due to the production of a large amount of resuspension sediment under the combined action of strong wind, current, and water temperature, which generated a large amount of resuspension (Bi et al., 2010; Liu et al., 2013).

Tidal pumping is one of the important mechanisms for suspended sediment transport (Jay and Smith, 1990), especially in estuaries with tidal asymmetry. The sediment exchange and lag effect at the bottom of the water column caused the SSC at the flood and ebb tide to be asymmetrical and there was a certain phase difference with the duration and flow velocity (Figures 4, 6), so that suspended sediment flux of the flood and ebb tide during the tidal cycle cannot cancel each other, resulting in the net suspended sediment flux. However, from the mouth to the head of the bay, the process of tidal pumping transport showed a different pattern. For example, at spring tide C4 station, there was different correlation between vertical average velocity and vertical average SSC during ebb and flood tides (Figures 4, 6). This meaned that during the ebb tide, flow velocity was faster than that of high tide, resulting in a higher resuspension flux during the ebb tide. Thus, this led to asymmetries in the SSC and leaded to seaward tidal pumping flux. However, as the sediment from the Yellow Sea was transported to the southern Laizhou Bay during flood tide, the landward advection flux was larger. Therefore, the direction of net suspended sediment transport was generally landward (Figure 12). At C7 station located at the head of the bay, the average flow velocity of flood tide (32.46 cm/s) was greater than that of ebb tide (29.08 cm/s), and the SSC of flood tide was higher than that of ebb tide, so the transport direction of tide pumping was consistent with that of flood tide. During the moderate tide, due to the low flow velocity, the sediment resuspension effect is weakened, which is reflected in the resuspension flux (Figure 12). Therefore, the ratio of the average tidal pumping flux to suspended sediment flux during the moderate tide (12.48%) was considerably lower than that of the spring tide (26.50%).

Residual current also has an important impact on sediment transport in the Bohai Sea (Zhao et al., 1995). The residual current can indicate the direction of suspended sediment transport to some extent (Chen et al., 2015). Generally, in the sea area dominated by the power of the tidal current, the direction of water movement is similar to that of suspended sediment transportation. Thus, residual current direction can basically indicate the net suspended sediment transport direction (Zhao et al., 1995; Bo Liu et al., 2020). Notably, the directions of residual current and suspended sediment transport at some

stations were quite different (Figure 12). In Laizhou Bay, current is more affected by wind (Su, 2005). In spring, Laizhou Bay has changed from the northerly wind to the weak southerly wind. The surface water column was affected by the southern wind, and the overall net surface water was moved to the sea, while net bottom water was carried to the land (Table 1). Further, the activity of bottom water is also a key factor affecting suspended sediment transport (Courtney et al., 2022). This also explains the reason why surface suspended sediment transport was small despite of large residual current value. Thus, the F was moving towards the direction of flood tide (inside the bay). The trend of suspended sediment transport was similar in spring tide and moderate tide. Thus, it is indicated that the tidal-induced residual current controlled the southward transport of suspended sediment when monsoon winds were weak.

In summary, combined with Figure 12, we can obtain the following preliminary understanding: horizontal advection was one of the main transport mechanisms of suspended sediment in Laizhou Bay, followed by tidal pumping. In addition, the result of Q indicates that the overall vertical mixing was weak in spring, and the water column stratification was relatively strong (Figures 8, 9). The suspended sediment transport was mainly caused by advection transport and the re-distribution of resuspension sediment at the bottom under the action of tidal current. The suspended sediment in Laizhou Bay presented a trend of migration from offshore to inland. From the combined analysis of Figures 3, 12, we speculate that the suspended sediment migrated to the bay and was temporarily stored after the long-term movement, deposition, and re-movement cycle under the action of advection and tidal pumping. Under the long and continuous northward gale weather conditions in winter, a large amount of sediment will likely be suspended and transported to eastern Laizhou Bay, possibly through the Bohai Strait (Wang et al., 2011; Bo Liu et al., 2020). Bi et al. (2014) observed that the salinity of winter was lower than that in summer in the southern Bohai Strait, indicating that the diluted water of the Yellow River gathered in Laizhou Bay in spring and summer (this was consistent with our salinity observations), and that winter freshwater was transported along eastern Laizhou Bay by northwesterly winds to the southern Bohai Strait. Overall, it can be concluded that the main transport mechanism of suspended sediment in Laizhou Bay in spring is mainly horizontal advection and tidal pumping. Moreover, the tidal pumping during the spring tide was stronger than that during the moderate tide, as determined from the flow velocity, temperature, and SSC asymmetry between the flood and ebb tides. The tidal and residual current were the main driving forces for the transport of suspended sediment.

Although this study took into account the impact of various factors on SSC, there were several flaws that could be corrected in future studies to better depict the interplay between these factors. Although the resuspension flux and deposition flux of Laizhou Bay were calculated in spring, there is no further knowledge of their behavior during winter, when the resuspension effect is strong. Moreover, our study did not explore the effects of waves and monsoons. However, because of the shallow water of Laizhou Bay, the waves have a considerable impact on seabed sediment resuspension. Previous studies have shown the role of waves and monsoon effects on sediment transport patterns (Yang et al., 1992; Bi et al., 2011).

6 Conclusion

Hydrological and sedimentological data were investigated by two field surveys, each of one tidal cycle (25 h), across nine sample stations and four tide stations, conducted in Laizhou Bay during the spring (May 2020) and moderate tides (April 2020). The primary controlling factors and transport mechanisms of suspended sediment were analyzed based on the tidal current variation characteristics, mixing degree of water column, and distribution of seabed sediment types in Laizhou Bay during the spring. Our primary conclusions are as follows:

(1) Laizhou Bay had an irregular semi-diurnal tide which was dominated by recurrent movement. Northwestern Laizhou Bay had a strong current zone, and the head of the bay had a weak current zone. The vertical flow velocity gradually decreased from the surface to the bottom and the average ratio of surface flow velocity to bottom flow velocity is 2.65.
(2) Overall, the horizontal distribution of SSC indicated that a high SSC zone was mainly present in southwestern Laizhou Bay. The SSC high value region mainly appeared at the bottom. The average SSC of the spring tide was higher than that of the moderate tide. The SSC peaked about 1–2 h after the flow velocity peaked.
(3) The tidal current, mixing degree, and seabed sediment types were the dominant factors controlling the distribution of SSC in Laizhou Bay. The periodic tidal current influenced the vertical and upward periodic variation of SSC. The water column stratification was relatively strong, which inhibited the vertical diffusion of suspended sediment and resulted in the difference between surface and bottom SSC. Moreover, the contribution of fine sediment resuspension flux to SSC in western Laizhou Bay was higher than that in other parts of Laizhou Bay.
(4) According to the decomposition of suspended sediment flux, the Lagrange transport flux occupied the largest proportion and played a dominant role, followed by tidal pump transport. From the mouth of the bay to the top of the bay, the tidal pumping flux was transported in the direction of the dominant tide with different dominant tides. The ratio of the average tidal pumping flux to suspended sediment flux during the spring tide

(26.50%) was considerably higher than that of the moderate tide (12.48%).

Data availability statement

The original contributions presented in the study are included in the article/supplementary material, further inquiries can be directed to the corresponding author.

Author contributions

BX: Conceptualization, Investigation, Writing–original draft, Writing–review and editing. RB: Writing–review and editing. DY: Writing–review and editing. LZ: Project administration, Funding acquisition, Conceptualization, Writing–review and editing. RH: Methodology, Writing–review. CW: Investigation, Visualization. TL: Investigation, Visualization. CL: Visualization, Software, Methodology. PL: Methodology, Visualization, Software. All authors have read and agreed to the published version of the manuscript.

Funding

This study was financially supported by the Sub-project of Basic Condition Investigation and Evaluation of Bohai Region in Shandong (402001202000006_001), the National Natural Science Foundation of China (NSFC, No.41776059), and the National Natural Science Foundation of China (Grants, No.42076037).

Acknowledgments

Our deepest gratitude goes to the reviewers for their careful work and thoughtful suggestions that have helped improve this paper substantially. The authors thank the Ocean University of China and the Qingdao Boyan Marine Environment Technology Co. for their assistance with the laboratory analyses. We would like to thank Editage (https://www.editage.cn/) for English language editing.

Conflict of interest

Author WC was employed by Qingdao Boyan Marine Environment Technology Co., China.

The remaining authors declare that the research was conducted in the absence of any commercial or financial relationships that could be construed as a potential conflict of interest.

Publisher's note

All claims expressed in this article are solely those of the authors and do not necessarily represent those of their affiliated organizations, or those of the publisher, the editors and the reviewers. Any product that may be evaluated in this article, or claim that may be made by its manufacturer, is not guaranteed or endorsed by the publisher.

References

Ali, Z, S., and Dey, S. (2016). Hydrodynamics of sediment threshold. *Phys. Fluids (1994).* 28, 075103. doi:10.1063/1.4955103

Allen, P. A. (2008). From landscapes into geological history. *Nature* 451, 274–276. doi:10.1038/nature06586

Bi, N., Yang, Z., Wang, H., Fan, D., and Ji, Y. (2010). Dispersal characteristics of the Huanghe (Yellow River) water and sediment to the sea during Water-Sediment Regulation period of the Huanghe and its dynamic mechanism. *Mar. Geol. Qua. Geol.* 30 (2), 27–34. doi:10.3724/sp.j.1140.2010.02027

Bi, N., Yang, Z., Wang, H., Fan, D., Sun, X., and Lei, K. (2011). Seasonal variation of suspended-sediment transport through the southern Bohai Strait. *Estuar. Coast. Shelf Sci.* 93, 239–247. doi:10.1016/j.ecss.2011.03.007

Bi, N., Wang, H., and Yang, Z. (2014). Recent changes in the erosion–accretion patterns of the active Huanghe (Yellow River) delta lobe caused by human activities. *Cont. Shelf Res.* 90, 70–78. doi:10.1016/j.csr.2014.02.014

Bi, N., Wang, H., Wu, X., Saito, Y., Xu, C., and Yang, Z. (2021). Phase change in evolution of the modern huanghe (Yellow River) delta: Process, pattern, and mechanisms. *Mar. Geol.* 437, 106516. doi:10.1016/j.margeo.2021.106516

Bianchi, T. S., and Allison, M. A. (2009). Large-river delta-front estuaries as natural "recorders" of global environmental change. *Proc. Natl. Acad. Sci. U. S. A.* 106, 8085–8092. doi:10.1073/pnas.0812878106

Bo Liu, B., Hu, R., Yuan, X., Zhu, L., Jiang, S., Nan, V., et al. (2020). Spatiotemporal distribution pattern and transport mechanism of suspended sediments in Longkou offshore under the action of tidal current. *Mar. Geol. Qua. Geol.* 40 (4), 55–66. doi:10.16562/j.cnki.0256-1492.2019072301

Camenen, B. (2007). Simple and general formula for the settling velocity of particles. *J. Hydraul. Eng.* 133, 229–233. doi:10.1061/(asce)0733-9429(2007)133:2(229)

Chao Jiang, C., Pan, S., and Chen, S. (2017). Recent morphological changes of the Yellow River (Huanghe) submerged delta: Causes and environmental implications. *Geomorphology* 293, 93–107. doi:10.1016/j.geomorph.2017.04.036

Chen, B., Liu, J., and Gao, F. (2015). Suspended sediment transport mechanism in Laizhou Bay. *Adv. Water. Resour.* 26 (5), 857–866. doi:10.14042/j.cnki.32.1309.2015.06.012

Courtney, K. H., Jacob, T. W., Matthew, J. F., and Jessica, M. C. (2022). ADCP observations of currents and suspended sediment in the macrotidal gulf of martaban, Myanmar. *Front. Earth Sci. (Lausanne).* 10, 820326. doi:10.3389/feart.2022.820326

Du, J., Pei, Y., Gao, J., Yu, X., Wang, F., Fan, C., et al. (2012). The suspended sediment transport associated with low flow patterns in shallow waters: A case study from the tianjin subtidal area. *Acta. Oceanol. Sin.* 34, 136–144. doi:10.1007/s11783-011-0280-z

Dyer, B. (1997). Estuaries: A physical introduction. *Geogr. J.* 140, 316. doi:10.2307/1797104

Fang, Y., Fang, G., and Zhang, Q. (2000). Numerical simulation and dynamic study of the wintertime circulation of the Bohai Sea. *Chin. J. Oceanol.* 18, 1–9. doi:10.1007/bf02842535

Fettweis, M., Francken, F., Pison, V., and Van den Eynde, D. (2006). Suspended particulate matter dynamics and aggregate sizes in a high turbidity area. *Mar. Geol.* 235, 63–74. doi:10.1016/j.margeo.2006.10.005

Fu, Y., Chen, S., Ji, H., Fan, Y., and Peng, L. (2021). The modern Yellow River delta in transition: Causes and implications. *Mar. Geol.* 436, 106476. doi:10.1016/j.margeo.2021.106476

Gao, S., and Jia, J. (2002). Modeling suspended sediment distribution in continental shelf upwelling/downwelling settings. *Geo-Mar. Lett.* 22, 218–226. doi:10.1007/s00367-002-0116-8

Geyer, W. R., and Maccready, P. (2014). The estuarine circulation. *Annu. Rev. Fluid Mech.* 46, 175–197. doi:10.1146/annurev-fluid-010313-141302

Gong, Z., Ge, R., Feng, Q., Wei, J., Su, M., Jin, C., et al. (2021). Cohesive forces between sediment particles and its impact on incipient motion of sediment:a review. *Adv. Water. Sci.* 32, 801–812. doi:10.14042/j.cnki.32.1309.2021.05.015

Guillén, J., Jiménez, J. A., Palanques, A., Gracia, V., Puig, P., and Sánchez-Arcilla, A. (2002). Sediment resuspension across a microtidal, low-energy inner shelf. *Cont. Shelf Res.* 22, 305–325. doi:10.1016/s0278-4343(01)00059-0

Guo, K., Zou, T., Jiang, D., Tang, C., and Zhang, H. (2017). Variability of Yellow River turbid plume detected with satellite remote sensing during water-sediment regulation. *Cont. Shelf Res.* 135, 74–85. doi:10.1016/j.csr.2017.01.017

Hill, D. F., Ciavola, S. J., Etherington, L., and Klaar, M. (2009). Estimation of freshwater runoff into Glacier Bay, Alaska and incorporation into a tidal circulation model. *Estuar. Coast. Shelf Sci.* 82, 95–107. doi:10.1016/j.ecss.2008.12.019

Hu, D. (1984). Upwelling and sedimentation dynamics I. The role of upwelling in sedimentation in the huanghai Sea and east China sea-a description OF general features. *Chin. J. Oceanol. Limnol.* 2, 13–19. doi:10.1007/BF02888388

Hu, R. (2009). *Sediment transport and dynamic mechanism in the Zhoushan Archipelago sea area*. [dissertation thesis]. Shandong: Ocean University of China.

Hu, R., Ma, F., Wu, J., Zhang, W., Jiang, S., Xu, Y., et al. (2016). Sediment transport in the nearshore area of Phoenix Island. *J. Ocean. Univ. China* 15, 767–782. doi:10.1007/s11802-016-2967-z

Huang, D., Su, J., and Backhaus, J. O. (1999). Modelling the seasonal thermal stratification and baroclinic circulation in the Bohai Sea. *Cont. Shelf Res.* 47, 1485–1505. doi:10.1016/s0278-4343(99)00026-6

Huang, J. (1981). Experimental study of settling properties of cohesive sediment in still water. *Sediment. Res.* 2, 30–41. doi:10.16239/j.cnki.0468-155x.1981.02.003

Ingram, R. G. (1981). Characteristics of the great whale river plume. *J. Geophys. Res.* 86, 2017–2023. doi:10.1029/jc086ic03p02017

Jay, D. A., and Smith, J. D. (1990). Residual circulation in shallow estuaries. 1. Highly stratified, narrow estuaries. *J. Geophys. Res.* 95, 711–731. doi:10.1029/jc095ic01p00711

Jiang, W., Xin, B., Lou, W., and Lian, R. (2016). Comparisons of three thermocline detection methods. *Mar. Fornt.* 33, 41–49. doi:10.11737/j.issn.1003-0239.20l6.03

Jiang, M., Pang, C., Liu, Z., and Jiang, J. (2020). Sediment resuspension in winter in an exceptional low suspended sediment concentration area off Qinhuangdao in the Bohai Sea. *Estuar. Coast. Shelf Sci.* 245, 106859. doi:10.1016/j.ecss.2020.106859

Jillian, M. M., Samuel, Bentley, J., Zhang, K., Jeffrey, O., Ioannis, Y., et al. (2018). Mississippi River subaqueous delta is entering a stage of retrogradation. *Mar. Geol.* 400, 12–23. doi:10.1016/j.margeo.2018.03.001

Krone, B. R. (1962). *Flume studies of the transport of sediment in estuarial schoaling processes*. Berkeley: Hydraulic Engineering Laboratory and Sanitary Engeering Research Laboratory, University of California.

Leblond, P. H., Emery, W. J., and Nicol, T. A. (1986). A climatic model of runoff-driven coastal circulation. *Estuar. Coast. Shelf Sci.* 23, 59–79. doi:10.1016/0272-7714(86)90085-5

Li, G., Tang, Z., Yue, S., Zhuang, K., and Wei, H. (2001). Sedimentation in the shear front off the Yellow River mouth. *Cont. Shelf Res.* 21, 607–625. doi:10.1016/s0278-4343(00)00097-2

Li, X., Hu, G., and Shi, Z. (2013a). Mixing, stratification and tidal straining in dry season within the north passage of the south branch south channel of the Changjiang River estuary. *Port. Waterw. Engi.* 9, 79–88. doi:10.3969/j.issn.1002-4972.2013.09.018

Li, Y., Lei, Q., Wang, A., Yong, Z., Fang, J., and Jian, C. (2013b). Seasonal variation of water column structure and sediment transport in a mud depo-center off the Zhejiang-Fujian coast in China. *Ocean. Dyn.* 63, 679–690. doi:10.1007/s10236-013-0620-6

Li, S., Wang, H., Zhang, Y., Bi, N., Wu, X., and Hu, B. (2015). Variation in sediment load and grain-size under the influence of Water and Sediment Reguration Scheme (WSRS) of the Huanghe (yellow) river. *Mar. Geol. Front.* 31, 20–27. doi:10.16028/j.1009-2722.2015.07003

Li, Z., Jia, J., Wang, Y., and Zhang, G. (2022). Net suspended sediment transport modulated by multiple flood-ebb asymmetries in the progressive tidal wave dominated and partially stratified Changjiang Estuary. *Mar. Geol.* 443, 106702. doi:10.1016/j.margeo.2021.106702

Li, Z., Ruan, Y., Guo, Z. D., Cong, H., Zhang, K. Y., and Takemura, H. (1990). Function and localization of high and low affinity binding sites to muscarinic receptors in longitudinal and circular smooth muscles of human stomach. *Res. Commun. Chem. Pathol. Pharmacol.* 4, 31–42.

Li, X. (2018). *Suspended Sediment Transport in stratified waters: Field observation and numerical simulation of the Changjiang Estuary*. Shanghai: East. China. Norm. Univ.

Liu, H., and Pan, W. (2007). Numerical simulation of the seasonal variations of the stratification and tidal front in the Bohai Sea. *Adv. Water. Sci.* 3, 398–403. doi:10.3321/j.issn:1001-6791.2007.03.015

Liu, Y., Chen, S., and Li, J. (2005). Patterns of variations in the water and sediment fluxes from the Yellow River to the estuary. *B. Mar. Sci.* 24, 1–8. doi:10.3969/j.issn.1001-6392.2005.06.001

Liu, Y., Huang, H., and Yang, X. (2013). The transportation and deposition of suspended sediment and its dynamic mechanism analysis based on Landsat images in the Laizhou Bay. *Acta. Oceanol. Sin.* 35 (6), 43–53. doi:10.3969/j.issn.0253-4193.201

Lu, J., Jiang, J., Li, A., and Ma, X. (2018). Impact of typhoon chan-hom on the marine environment and sediment dynamics on the inner shelf of the east China sea: *In-situ* seafloor observations. *Mar. Geol.* 406, 72–83. doi:10.1016/j.margeo.2018.09.009

Meng, L., Hu, R., Li, Y., Yuan, X., Zhu, L., and Guo, J. (2020). Transport characteristics of suspended sediment in Funing Bay during spring tide in winte. *Mar. Geol. Quat. Geol.* 40, 61–73. doi:10.16562/j.cnki.0256-1492.2019111801

Millero, F. J., and Poisson, A. (1981). International one-atmosphere equation of state of seawater. *Deep Sea Res. Part A. Oceanogr. Res. Pap.* 28, 625–629. doi:10.1016/0198-0149(81)90122-9

Milliman, J. D., and Meade, R. H. (1983). World-wide delivery of river sediment to the oceans. *J. Geol.* 91, 1–21. doi:10.1086/628741

Ni, Z., Chen, H., Dong, L., Shi, Z., Wang, D., and Zhai, Q. (2012). Measurement and analysis of vertical mixing and stratification within the plume outside the changjiang River estuary. *J. Shanghai. J. Univ.* 46, 1862–1873. doi:10.16183/j.cnki.jsjtu.2012.11.030

Ni, W., Wang, Y., Zhou, X., Zhang, J., and Gao, J. (2014). Sediment dynamics in an offshore tidal channel in the southern Yellow Sea. *Int. J. Sediment Res.* 29, 246–259. doi:10.1016/s1001-6279(14)60040-8

Niedoroda, A. W., Reed, C. W., Swift, D. J. P., Arato, H., and Hoyanagi, K. (1995). Modeling shore-normal large-scale coastal evolution. *Mar. Geol.* 126, 181–199. doi:10.1016/0025-3227(95)98961-7

Nour, H. E., Helal, S. A., and Wahab, M. A. (2022). Contamination and health risk assessment of heavy metals in beach sediments of Red Sea and Gulf of Aqaba, Egypt. *Mar. Pollut. Bull.* 177, 113517. doi:10.1016/j.marpolbul.2022.113517

Oliveira, M. L. S., Dotto., G. L., Pinto., D., Alcindo, N., and Silva., L. F. O. (2021). Nanoparticles as vectors of other contaminants in estuarine suspended sediments: Natural and real conditions. *Mar. Pollut. Bull.* 168, 112429. doi:10.1016/j.marpolbul.2021.112429

Pang, W., Dai, Z., Ge, Z., Li, S., Mei, X., Gu, J., et al. (2019). Near-bed cross-shore suspended sediment transport over a meso-macro tidal beach under varied wave conditions. *Estuar. Coast. Shelf Sci.* 217, 69–80. doi:10.1016/j.ecss.2018.11.007

Partheniades, E. (1965). Erosion and deposition of cohesive soils. *J. Hydr. Div.* 91, 105–139. doi:10.1061/jyceaj.0001165

Qiao, S., Shi, X., Zhu, A., Liu, Y., Bi, N., Fang, X., et al. (2010). Distribution and transport of suspended sediments off the Yellow River (huanghe) mouth and the nearby Bohai Sea. *Estuar. Coast. Shelf Sci.* 86 (3), 337–344. doi:10.1016/j.ecss.2009.07.019

Qin, Y., Zhao, Y., and Zhao, S. (1985). *Geology of the Bohai Sea*. Beijing: Science Press, 1–232.

Qiu, Z. F., Xiao, C., Perrie, W., Sun, D., Wang, S., Shen, H., et al. (2017). Using Landsat 8 data to estimate suspended particulate matter in the Yellow River estuary. *J. Geophys. Res. Oceans* 122, 276–290. doi:10.1002/2016jc012412

Rui Jiang, R., Wu, J., Zhu, L., Hu, R., and Yue, N. (2017). The concentration changes and transport mechanism of suspended sediments in southwestern Laizhou Bay. *Mar. Geo. Front.* 33, 25–32. doi:10.16028/j.1009-2722.2017.09004

Sarik, S., and Charitha, P. (2020). Sediment resuspension due to near-bed turbulent coherent structures in the nearshore. *Cont. Shelf Res.* 194, 104048. doi:10.1016/j.csr.2020.104048

Scully, M. E., and Friedrichs, C. T. (2003). The influence of asymmetries in overlying stratifi-cation on near-bed turbulence and sediment suspension in a partially mixed estuary. *Ocean. Dyn.* 53, 208–219. doi:10.1007/s10236-003-0034-y

Shou, W., Zong, H., and Ding, P. (2016). Numerical study of the circulation influenced by runoff input in the Huanghe (Yellow) River Estuary and adjacent waters in summer. *Acta. Oceanol. Sin.* 38, 1–13. doi:10.3969/j.issn.0253-4193.2016.07.001

Simpson, J. J., and Dickey, T. D. (1981). The relationship between downward irradiance and upper ocean structure. *J. Phys. Oceanogr.* 11, 309–323. doi:10.1175/1520-0485(1981)011<0309:TRBDIA>2.0.CO;2

Stretch, D. D., Rottman, J. W., Venayagamoorthy, S. K., Nomura, K. K., and Rehmann, C. R. (2010). Mixing efficiency in decaying stably stratified turbulence. *Dyn. Atmos. Oceans* 49, 25–36. doi:10.1016/j.dynatmoce.2008.11.002

Su, J. (2005). *China Offshore Hydrology*. Beijing: China Ocean Press.

Syvitski, J., and Milliman, J. (2007). Geology, geography, and humans battle for dominance over the delivery of fluvial sediment to the coastal ocean. *J. Geol.* 115 (1), 1–19. doi:10.1086/509246

Tong, C., Li, L., Meng, Y., and Wang, B. (2018). Analysis of stratification-mixing mechanism during spring tide of dry season in the Modaomen waterway. *Hyd-Sci. Eng.* 1, 48–57. doi:10.16198/.enk.1009-640X.2018.01.008

Trowbridge, J. H. (1992). A simple description of the deepening and structure of a stably stratified flow driven by a surface stress. *J. Geophys. Res.* 97 (C10), 15529–15543. doi:10.1029/92JC01512

Turner, J. S., and Benton, E. R. (1974). Buoyancy effects in fluids. *Phys. Today.* 27, 52–53. doi:10.1063/1.3128495

Uncles, R. J., Elliott, R. C. A., and Weston, S. A. (1985). Dispersion of salt and suspended sediment in a partly mixed estuary. *Estuaries* 8, 256–269. doi:10.2307/1351486

Vonda, J. C., Jennifer, B., Valeria, M., James, J. B., Dianne, T., Malcolm, R. C., et al. (2020). Responses of a common New Zealand coastal sponge to elevated suspended sediments: Indications of resilience. *Mar. Environ. Res.* 155, 104886. doi:10.1016/j.marenvres.2020.104886

Wang, W., and Wang, H. (2005). Distribution of suspended matter and its relationship with sediment particle size in Laizhou Bay. *Chin. J. Oceanol. Limnol.* 36, 97–103. doi:10.3321/j.issn:0029-814X.2005.02.001

Wang, Y., Pan, S., Wang, H. V., Gao, J., Yang, S., Wang, A., et al. (2006). Measurements and analysis of water discharges and suspended sediment fluxes in changjiang estuary. *J. Geogr.* 01, 35–46. doi:10.11821/xb200601004

Wang, H., Yang, Z., Saito, Y., Liu, J. P., Sun, X., and Wang, Y. (2007). Stepwise decreases of the Huanghe (Yellow River) sediment load (1950–2005): Impacts of climate change and human activities. *Glob. Planet. Change.* 57, 331–354. doi:10.1016/j.gloplacha.2007.01.003

Wang, K., Shi, X., Cai, S., Qiao, S., and Jiang, X. (2010). Distribution and provenance of the seabed sediment of the Yellow River mouth and Laizhou Bay deduced from heavy minerals. *Mar. Geol. Quat. Geol.* 30, 1–8. doi:10.3724/SP.J.1140.2010.06001

Wang, H., Han, S., Guo, P., and Li, G. (2011). Transportation of sediment from Yellow River in Bohai Sea due to tidal currents. *J. Sediment. Res.* 1, 51–59. doi:10.16239/j.cnki.0468-155x.2011.01.008

Wang, H., Wang, A., Bi, N., Zeng, X., and Xiao, H. (2014). Seasonal distribution of suspended sediment in the Bohai Sea, China. *Cont. Shelf Res.* 90, 17–32. doi:10.1016/j.csr.2014.03.006

Wang, H., Wu, X., Bi, N., Li, S., Yuan, P., Wang, A., et al. (2017). Impacts of the dam-orientated water-sediment regulation scheme on the lower reaches and delta of the Yellow River (Huanghe): A review. *Glob. Planet. Change* 157, 93–113. doi:10.1016/j.gloplacha.2017.08.005

Wang, Y., Zhang, G., Zhou, S., and Meng, L. (2020). Study on critical shear stress of cohesionless uniform single sediment particle. *J. Sediment. Res.* 1, 1–6. doi:10.16239/j.cnki,0468,155x.2020.01.001

Wu, X., Bi, N., Xu, J., Nittrouer, J. A., Yang, Z., Saito, Y., et al. (2017). Stepwise morphological evolution of the active Yellow River (Huanghe) delta lobe (1976-2013): Dominant roles of riverine discharge and sediment grain size. *Geomorphology* 292, 115–127. doi:10.1016/j.geomorph.2017.04.042

Xingmin Liu, X., Qiao, L., Zhong, Y., Wan, X., Xue, W., and Liu, P. (2020). Pathways of suspended sediments transported from the Yellow River mouth to the Bohai Sea and Yellow Sea. *Estuar. Coast. Shelf Sci.* 236, 106639. doi:10.1016/j.ecss.2020.106639

Xiong, J., Wang, X., Wang, Y., Chen, J., Shi, B., Gao, J., et al. (2017). Mechanisms of maintaining high suspended sediment concentration over tide-dominated offshore shoals in the southern Yellow Sea. *Estuar. Coast. Shelf Sci.* 191, 221–233. doi:10.1016/j.ecss.2017.04.023

Xu, S., and Xu, Y. (2013). Review on water environment evolution and strategy after land reclamation. *Adv. Water. Sci.* 24, 138–145. doi:10.14042/j.cnki.32.1309.2013.01.016

Yang, Z., Guo, Z., Wang, Z., Xu, J., and Gao, W. (1992). Suspended sediments on the yellow and east China sea shelf and macropattern of their being transported to the eastern deeper sea. *Acta. Oceanol. Sin.* 14 (2), 81–90. doi:10.1007/BF02677081

Yang, G., Wang, X., Cheng, Z., Zhong, Y., and Thomas, O. (2021). Modelling study on estuarine circulation and its effect on the turbidity maximum zone in the Yalu River Estuary, China. *Estuar. Coast. Shelf Sci.* 263, 107634. doi:10.1016/j.ecss.2021.107634

Yin, D., Wu, J., Hu, R., and Zhu, L. (2013). Recent evolution and sediment transport patterns of the Dengzhou Shoal. *Mar. Geol. Front.* 29 (8), 25–32. doi:10.16028/j.1009-2722.2013.08.007

Yu, Q., Wang, Y., Flemming, B., and Gao, S. (2012). Tide-induced suspended sediment transport: Depth-averaged concentrations and horizontal residual fluxes. *Cont. Shelf Res.* 34, 53–63. doi:10.1016/j.csr.2011.11.015

Yuan, Y., Wang, W., Gao, H., and Guo, X. (2011). Resuspension and associated horizontal, settling fluxes of sediment in the weakly stratified Laizhou Bay mouth. *Oceanol. Limnol. Sin.* 42, 1–8. doi:10.11693/hyhz201101001001

Zhan, C., Yun, J., Wang, Q., Li, Z., and Zhou, D. (2017). Spatial and temporal dynamics of sandy coastal geomorphology in the east of Laizhou Bay over recent 60 years. *Acta. Oceanol. Sin.* 39, 90–100. doi:10.3969/j.issn.0253-4193.2017.09.009

Zhao, B., Zhuang, G., and Cao, D. (1995). Circulation, tidal residual currents and their effects on the sedimentation in the Bohai sea. *Oceanol. Limnol. Sin.* 26, 466–473. doi:10.3321/jissn:0029-814X.1995.05.003

Zhao, Y., Sun, S., You, L., Su, B., Ma, Y., Li, M., et al. (2020). Distribution characteristics of grain size and heavy metals of sediments in Laizhou Bay. *Mar. Sci.* 45, 43–50. doi:10.11759/hykx20200806004

Zheng, J., Jia, Y., Liu, X., Liu, B., Fu, T., and Zhang, L. (2015). Field measurement of sediment critical shear stress in the modern Yellow River Delta. *Acta. Oceanol. Sin.* 37, 86–98. doi:10.3969/j.issn.0253-4193.215

Zhou, Z., Bian, C., Wang, C., Jiang, W., and Bi, R. (2017). Quantitative assessment on multiple timescale features and dynamics of sea surface suspended sediment concentration using remote sensing data. *J. Geophys. Res. Oceans* 122, 8739–8752. doi:10.1002/2017jc013082

frontiers | Frontiers in Earth Science

TYPE Original Research
PUBLISHED 26 September 2022
DOI 10.3389/feart.2022.1010710

OPEN ACCESS

EDITED BY
Ya Ping Wang,
East China Normal University, China

REVIEWED BY
Chao Chen,
Zhejiang Ocean University, China
Ronald Steel,
University of Texas at Austin,
United States

*CORRESPONDENCE
Zhiguo He,
hezhiguo@zju.edu.cn
Yuezhang Xia,
yzxia@zju.edu.cn

SPECIALTY SECTION
This article was submitted to Geohazards and Georisks, a section of the journal Frontiers in Earth Science

RECEIVED 03 August 2022
ACCEPTED 06 September 2022
PUBLISHED 26 September 2022

CITATION
Wang S, He Z, Gu H and Xia Y (2022), The "two-step" yielding process of the natural mud under steady and oscillatory shear stress.
Front. Earth Sci. 10:1010710.
doi: 10.3389/feart.2022.1010710

The "two-step" yielding process of the natural mud under steady and oscillatory shear stress

Shaohua Wang, Zhiguo He*, Hengye Gu and Yuezhang Xia*

Ocean College, Zhejiang University, Zhoushan, China

The rheological properties of natural mud are closely related to nautical depth estimation, wave propagation, and morphology evolution of muddy coast. In this study, the rheological properties of the natural mud collected from Luxi Island and Zhoushan Island in China were investigated. Shear stresses in steady state or oscillatory state were imposed on mud samples directly to obtain the yielding process under tidal currents or waves. The results showed that both apparent viscosity and complex viscosity experienced two sharp declines with increasing shear stress, indicating a two-step yielding nature of natural mud. Two yield stresses, namely, static yield stress and fluidic yield stress correspond to the yielding processes of elasticity and viscosity breakdown, respectively. The static yield stress in the oscillatory shear stress tests was lower than that in the steady shear stress tests, and the fluidic yield stress of natural mud in oscillatory shear stress tests was higher than that in the steady shear stress tests. The above phenomenon was explained by the viscoelastic-oscillation theory. Furthermore, the experimental results indicated that the initial storage modulus had a closer connection to both yield stresses in comparison with mud density. This study not only provided a guideline for having a better understanding of the two-step yielding process of natural mud, but will also provide scientific support for the assessment of fluid-mud formation, sediment transport and morphology evolution, the interaction between waves or tidal currents and muddy seabed, and protection of seafloor infrastructures.

KEYWORDS

natural mud, rheological properties, yield stress, two-step yielding, storage modulus

Introduction

Muddy coasts are widespread in estuaries, regressive deltaic coasts, and open coast tidal flats, such as the Amazon Estuary, the Yellow River Estuary, and the Gulf of Mexico (Almashan and Dalrymple, 2015; Vanlede et al., 2019), and a quarter of China's coasts are muddy coasts (Pang et al., 2020). Natural mud compositions, such as clay minerals, saline water, organic contents, and some amounts of sand form the complex internal microstructures. The microstructures can be destroyed and reformed under large shear loads such as waves and tidal currents, causing mud fluidization and forming a fluid-mud layer at the seabed surface (Green and Coco, 2014; McAnally et al., 2016). The fluid mud is a high-concentration aqueous non-Newtonian fluid within a density range of

1,030–1,300 kg/m^3 and has high potential mobility, which can flow down slopes as a mudflow and accumulate at the bottom, reducing the nautical depth and impeding navigation (McAnally et al., 2007). In addition, the fluid mud can absorb a large amount of wave energy for its high viscosity when waves propagate over the muddy seabed, resulting in significant wave attenuation (Sheremet, 2003; Safak et al., 2017), which has been especially concerning for a long time; on the other hand, the fluid mud can reduce the vertical eddy viscosity and bottom drag coefficient in the bottom boundary layer (Xia and Zhu, 2010), which may have a significant effect on tidal dynamics and change the tidal characteristics such as tidal current amplitudes and phases (Wang, 2002; Wang et al., 2005). Moreover, the mudflow is not only an important sediment transport process in the ocean environment with a significant effect on the morphology evolution, but also poses a threat to seafloor infrastructures such as pipelines (Mehta et al., 2014; McAnally et al., 2016; Kirichek et al., 2020; Kameda and Yohei, 2021). Furthermore, the transport of polluted mud is a highly controversial issue in coastal environmental studies (McAnally et al., 2007; Song et al., 2018; Mirlean et al., 2020). Therefore, accurate knowledge of mud rheological behaviors plays a crucial role in coastal dynamics and is of great significance to engineering design and coastal hazards.

During past decades, numerous experimental results show that natural mud exhibits complex rheological behaviors (e.g., Jiang and Mehta, 1990; Van Kessel and Blom, 1998; Huang and Huhe, 2009; Yang et al., 2014; Xu and Huhe, 2016; Nie et al., 2018; Shakeel et al., 2020a), among which the yield stress, marking the transition from solid to fluidic behavior, is a critical parameter to estimate the incipient motion of cohesive sediments (McAnally et al., 2016; Wang and Sturm, 2016; Zhang and Yu, 2017; Kirichek et al., 2020). Yield stress can be determined indirectly and directly (Nguyen and Boger, 1992). In indirect methods, the yield stress is usually determined by extrapolating the measured flow curve to zero shear rate with the help of a rheological model. The commonly used rheological models are the Herschel–Bulkley model (Kameda and Yohei, 2021), the Bingham model (O'Brien and Julien, 1988; Bai et al., 2002), the dual Bingham model (Huang and Huhe, 2009), the dual Herschel–Bulkley model (Xu and Huhe, 2016), and the Casson model (Wang et al., 2022). Since the extrapolation of the measured flow curve is highly dependent on the selected rheological model, the great scatter of the yield stress determined from different rheological models can always be observed (Huang and Huhe, 2009; Messaoudi et al., 2018; Wang et al., 2022). The direct methods generally rely on some independent assessment of the critical shear stress at which the mud starts to flow according to the experimental data. For example, the yield stress can be determined from the sharp variation of apparent viscosity in shear stress sweep tests (Shakeel et al., 2020a). Therefore, direct methods may be a better choice to determine the yield stress of the natural mud.

The direct methods to determine the yield stress are usually conducted under steady and oscillatory shear loads, which are similar to shear loads such as tidal currents and waves imposed to the natural mud. In a coastal environment, natural mud is usually disturbed by tidal currents and waves, forced by these two different shear loads, and the yielding process of the natural mud may be different. In the past decades, a rich literature has been built up on the yielding process and rheological properties of natural mud under steady shear loads (Coussot and Piau, 1994; Bai et al., 2002; Messaoudi et al., 2018; Fonseca et al., 2019), while the natural mud in coastal areas is usually disturbed by oscillatory shear loads such as waves. The knowledge about the yield process of the natural mud under the oscillatory shear loads is still insufficient. Furthermore, the exterior shear loads imposed on the natural mud are usually assumed as shear stress rather than shear rate or shear strain, especially when researchers estimate incipient motion and the transportation of the natural mud and establish the numerical model (Zhang et al., 2017; Emami et al., 2020; Orseau et al., 2020). Additionally, attributing to the improvement of rheometer accuracy, the rheological behaviors of the natural mud in very low shear rate regions have been investigated; contrary to the single yielding behavior, a two-step yielding process for natural mud was observed by researchers (Nie et al., 2020; Shakeel et al., 2021). This two-step yielding phenomenon also has been reported for other soft materials in the previous literature (Koumakis and Petekidis, 2011; Ahuja et al., 2020a; Minami et al., 2020), which was attributed to the two different length levels of internal structures of materials. In addition, the two-step yielding feature relates to the two critical shear stresses when natural mud transits its state from solid to solid-fluidic state and from the solid-fluid state to the fluidic state. Based on the long-term average values of the shear stress from waves or currents in a muddy coast and the two yield stresses mentioned above, the state of natural mud can be determined and then the influence of the natural mud on wave attenuation and tidal dynamics can be estimated. Therefore, it is important to figure out the two-step yielding process of the natural mud when it was forced to shear stress directly and investigate the similarities and differences of the yielding process under steady and oscillatory shear stress.

In this study, the rheological properties of the natural mud collected from Luxi Island and Zhoushan Island in China are analyzed based on the experimental results. This study aims to deepen our understanding of the yielding process of the natural mud under steady and oscillatory shear stress and identify the similarities and differences between the yielding process under these two types of shear stress.

Materials and methods

Materials preparation

The natural mud samples used in this study were from Zhejiang Province in China, three of them were collected from Luxi Island

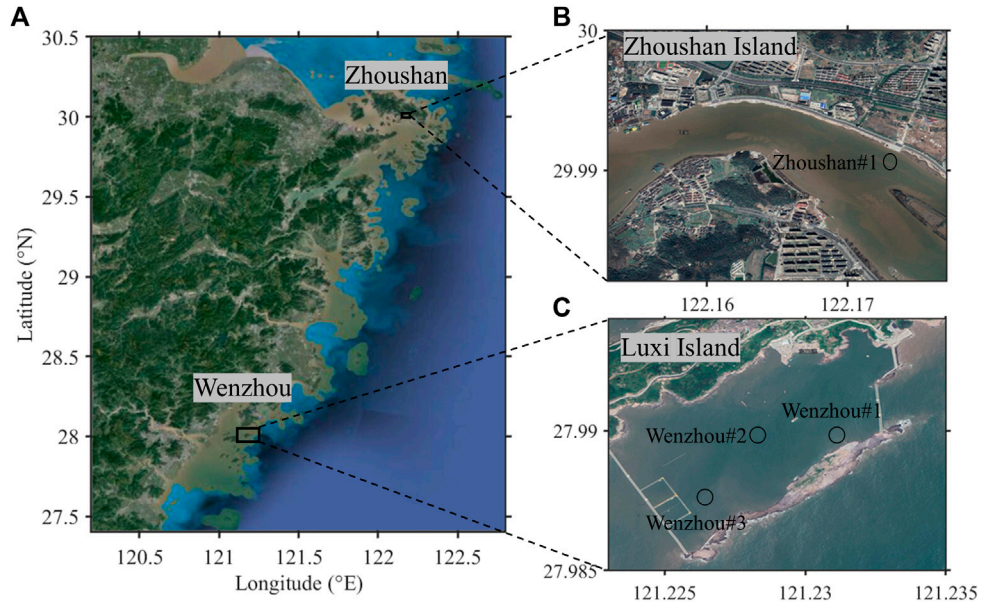

FIGURE 1
(A) Geographical location of Luxi Island and Zhoushan Island; **(B)** and **(C)** depict the selected location in Zhoushan Island and Luxi Island for collecting natural mud samples.

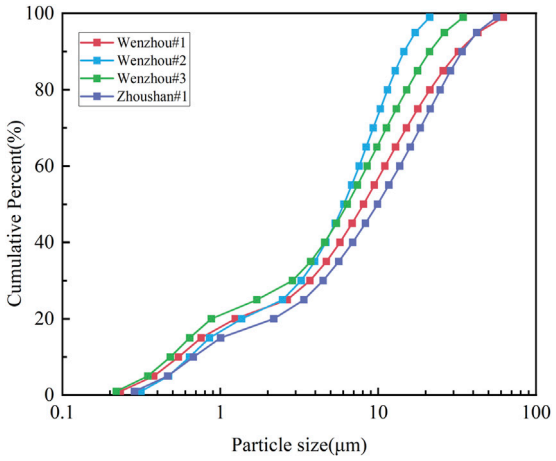

FIGURE 2
Particle distribution of the collected natural mud samples.

where the source of fine sediment is influenced by the Oujiang Estuary, and the other one from Zhoushan Island (Figure 1) where the source of fine sediment is influenced by the Yangtze Estuary and Hangzhou Bay. A gravity-based grab sampler was adopted in this study, which can be inserted into the seabed to collect the natural mud sample; after the collection, the mud samples were packed in different sealed containers to avoid evaporation of water.

Particle size distributions of the natural mud samples were determined using static light scattering methods (Malvern MasterSizer 3000), and the results are given in Figure 2. To determine the density of the mud samples, small amounts of each mud sample were dried at 105°C for 24 h in a drying box, and the corresponding water content of each mud sample was determined by calculating the weight difference between the mud sample before and after drying. The dry density of the mud samples was assumed to be 2,650 kg/m^3, based on the water content of each mud sample, and the bulk density of the mud samples was obtained. The characters of the four mud samples are summarized in Table 1.

Rheological measurements

The rotational rheometer DHR-I (TA Instruments, United States) equipped with a cone and plate geometry was adopted in this study to investigate the rheological response under steady and oscillatory shear stress, as this geometry can produce more constant shear loads on the natural mud samples and has successful application in previous studies (Huang and Huhe, 2009; Shakeel et al., 2020b; Knappe et al., 2020). The cone and plate geometry has a diameter of 40 mm with a 2° cone angle and a 0.048-mm gap between the cone and plate. The rheometer is characterized by high precision and accuracy, and its minimum torque in steady and oscillatory shear tests is 10 and 20 nNm,

10.3389/feart.2022.1010710

TABLE 1 Characters of the mud samples.

Sample ID	D_{25} (μm)	D_{50} (μm)	D_{75} (μm)	D_{99} (μm)	Water content (%)	Density (kg m^{-3})
Wenzhou#1	2.65	8.07	17.83	62.01	91.00	1,484
Wenzhou#2	2.48	6.06	10.31	21.2	118.05	1,400
Wenzhou#3	1.70	6.37	13.05	34.55	93.64	1,474
Zhoushan#1	3.38	9.90	21.35	56.3	62.88	1,619

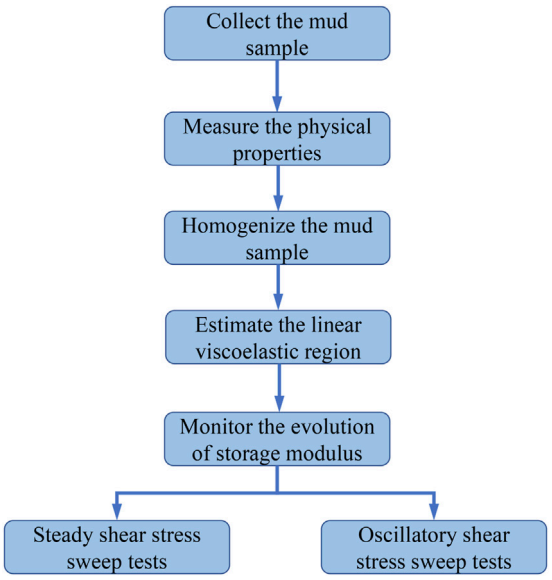

FIGURE 3
Technology flow of the experiments.

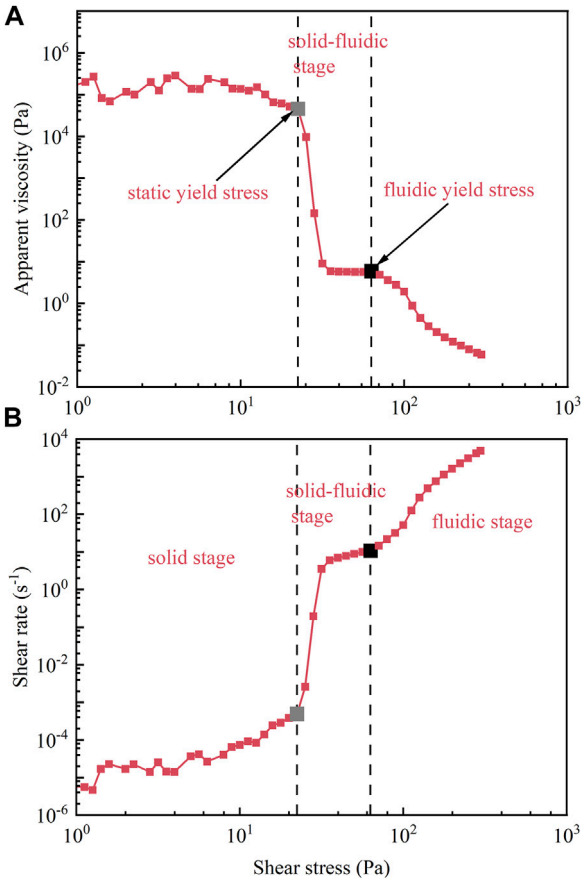

FIGURE 4
The apparent viscosity **(A)** and shear rate **(B)** evolution with increasing shear stress of the Wenzhou#1 mud sample. In the figure, the grey point and the black point represent the first yielding point and second yielding point of the Wenzhou#1 natural mud sample, respectively.

respectively. The temperature was maintained at 20°C during all the experiments using a Peltier controller system.

The experimental procedures in this study are organized as follows. First, each natural sample was homogenized by mild hand stirring before experiments to ensure the repeatability of the experiments. Second, the preliminary oscillatory amplitude sweep tests were performed to estimate the linear viscoelastic region of each natural mud sample, and the oscillatory shear stress logarithmically increased from 1 to 200 Pa at a constant frequency of 1 Hz. Based on the evolution of the storage modulus versus the oscillatory shear stress, the linear viscoelastic region can be determined (Figure 5). Third, the measurements of the rheological response of the natural mud under steady and oscillatory shear stress were performed. After attaining the measurement position, a waiting time was given to eliminate the disturbance created by the insertion of the bob; meanwhile, an oscillatory time sweep test in a linear viscoelastic regime was conducted to monitor the evolution of the storage modulus and the oscillatory shear stress was set to 1 Pa for all natural mud samples. When the increase of the storage modulus as a function of time was slight, the shear stress sweep tests and the oscillating amplitude sweep tests were performed.

In the shear stress sweep tests, the applied shear stress logarithmically increased from 1 to 300 Pa, and the corresponding motor displacement was recorded; thus, the shear rate and apparent viscosity can be determined. In the oscillatory amplitude sweep tests, the natural mud was applied to sinusoidal shear stress which increases logarithmically from 1 to 200 Pa at a constant frequency of 1 Hz, and the rheological parameters such as storage modulus (G') and loss modulus (G'') are obtained. To obtain adequate experimental data for analysis, twenty measuring points were set in each decade with a measuring time of 15 s for each point for both steady and oscillatory shear stress tests. The technology flow of the experiments is given in Figure 3.

Results and analysis

Steady shear stress tests

Figure 4 depicts the apparent viscosity and shear rate evolution with increasing shear stress of the Wenzhou#1 natural mud sample. It is noted that with increasing shear stress, the apparent viscosity experienced two sharp declines (Figure 4A), indicating that the yielding process of natural mud is not a single behavior as observed in previous studies (e.g., Coussot and Piau, 1994; Van Kessel and Blom, 1998; Bai et al., 2002; Kameda and Hirauchi, 2018) but a two-step yielding process which exists a transition state between solid state and fluidic state.

The yielding process of the Wenzhou#1 mud sample can be divided into three stages. In the initial stage, the apparent viscosity shows a slight variation with increasing shear stress until the imposed shear stress exceeds a critical value where the mud samples yield for the first time. In this stage, the natural mud behaves like a solid material for its large apparent viscosity. Subsequently, the apparent viscosity experienced a sharp decline with increasing shear stress where the apparent viscosity is reduced by five orders of magnitude in a very narrow range of shear stress, and meanwhile, the shear rate suddenly increases from 10^{-3} to 10 s^{-1}. After this sharp decline, the apparent viscosity reaches a plateau, and the shear rate experienced slow growth. In this stage, the natural mud exhibits both characteristics of solid and fluid. As the shear stress continues to increase, the apparent viscosity departed from the plateau and decreased again, and the apparent viscosity reduced from 5 to 0.05, indicating the natural mud yield again.

The two-step yielding process has been reported in glassy systems, colloidal gels, electro and magnetorheological fluids, and commercial formulations, indicating the presence of two characteristic forces between the interacting particles or two varying representative length scales (Altieri et al., 2018; Ahuja et al., 2020b; Minami et al., 2020; Moghimi and Petekidis, 2020). This two-step yielding behavior is consistent with the previous study conducted by Shakeel et al. (2020a), who investigated the rheological properties of the natural mud from the Port of Hamburg.

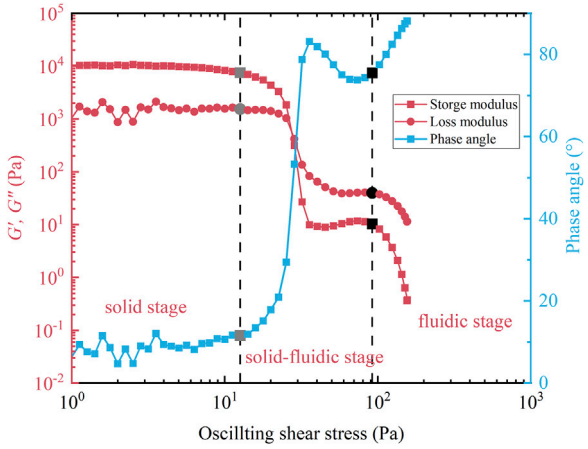

FIGURE 5
Results of amplitude sweep tests for Wenzhou#1 mud samples, the storage modulus G', the loss modulus G'', and phase angle evolution with increasing oscillatory shear stress. In the figure, the grey point and the black point represent the first yielding point and the second yielding point of the Wenzhou#1 natural mud sample, respectively.

Corresponding to the two-step yielding process, there are two yield stresses, namely, static yield stress (τ_s) and fluidic yield stress (τ_f) put forward by previous studies (Ahuja et al., 2020a; Shakeel et al., 2020b; Nie et al., 2020). These two yield stresses are critical stresses when the natural mud transitions from solid to solid-fluidic state and from the solid-fluid state to the fluidic state, which can be determined directly from the apparent viscosity curve based on two sharp declines. In Figure 4, the static yield stress and the fluidic yield stress of the Wenzhou#1 natural mud sample are marked as a grey point and a black point, respectively.

Oscillatory shear stress tests

The results of oscillatory amplitude sweep tests for the Wenzhou#1 natural mud sample are given in Figures 5, 6. From Figure 5, it is noted that both storage modulus G' and loss modulus G'' experience two sharp declines with the increasing oscillatory stress, which is familiar to the evolution of the apparent viscosity shown in Figure 4. The yielding process of natural mud under oscillatory shear stress can also be divided into three stages as steady shear stress tests. In the first stage, the storage modulus is one order magnitude larger than the loss modulus and their values are almost constant, indicating the solid nature of the mud sample and meaning that the internal microstructures of the mud sample are not destroyed by oscillatory shear stress in this time. Correspondingly, the

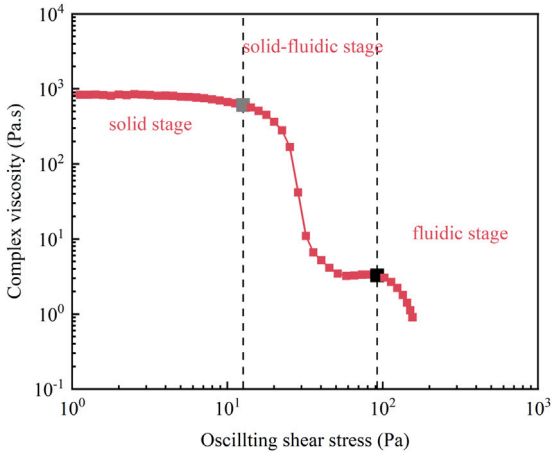

FIGURE 6
Results of amplitude sweep tests for Wenzhou#1 mud samples: the complex viscosity evolution with increasing oscillatory shear stress. In the figure, the grey point and the black point represent the first yielding point and the second yielding point of the Wenzhou#1 natural mud sample, respectively.

complex viscosity shows behavior similar to that of the storage modulus (Figure 6); its value remains unchanged in this region, and the small phase angle shown in Figure 5 also indicates the solid nature of the mud sample. At this time, the mud sample behaves as a linearly elastic solid (Yang and Yu, 2018; Shakeel et al., 2020a; Nie et al., 2020).

In the second stage, the storage modulus G', the loss modulus G'', and the complex viscosity experienced a sharp decline and subsequently reached a new state of equilibrium. During this time, the storage modulus decreases faster than the loss modulus and is lower than the loss modulus eventually (Figure 5), indicating that the elastic effect is weakened and the viscous effect dominates in this stage. In the meanwhile, the phase angle given in Figure 5 increases with the oscillatory shear stress and reached around 90° quickly; furthermore, the complex viscosity shown in Figure 6 decreased three orders in its magnitudes, indicating that the internal microstructures of the natural mud sample are gradually destroyed by the imposed oscillatory shear stress, meaning the natural mud yields for the first time and the mud samples experienced the transition from the solid state to the solid-fluidic state.

In the final stage, the natural mud yields again. After a transient equilibrium state, the storage modulus and the loss modulus declined again, and the decrease rate of the storage modulus was still larger than that of the loss modulus (Figure 5), meaning that the internal microstructures of the mud samples are destroyed more thoroughly. In addition, the increasing phase angle (Figure 5) and the decreasing complex viscosity (Figure 6) also implied the destroyed internal microstructures of the mud samples; at the end of the experiments, the mud sample behaves like fluids.

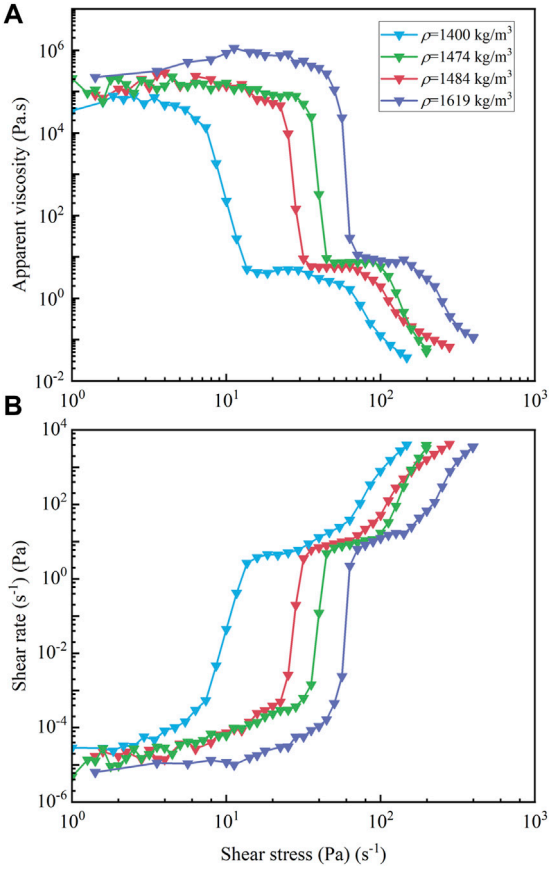

FIGURE 7
The apparent viscosity **(A)** and shear rate **(B)** evolution with increasing shear stress of the different mud samples.

Compared to Figure 4, it can be seen that under the oscillatory shear stress, the mud samples also show the "two-step" yielding feature, indicating that the two-step yielding process is the instinctive feature of the mud sample and irrelevant to the manner of the exposed loads. The "two-step" yielding feature closely relates to the variation of microstructures of the natural mud sample under external shear stress, and the linkages between the particles are gradually destroyed by the imposed loads, indicating the presence of two characteristic forces between the interacting particles or two varying representative length scales of the natural mud, which is similar to other materials in previous studies (Ahuja et al., 2020b; Moghimi and Petekidis, 2020).

Density effect on rheological properties

Figure 7 depicts the evolution of the flow curve and the apparent viscosity of the natural mud samples; it can be seen that all the mud samples show the two-step yielding feature, despite

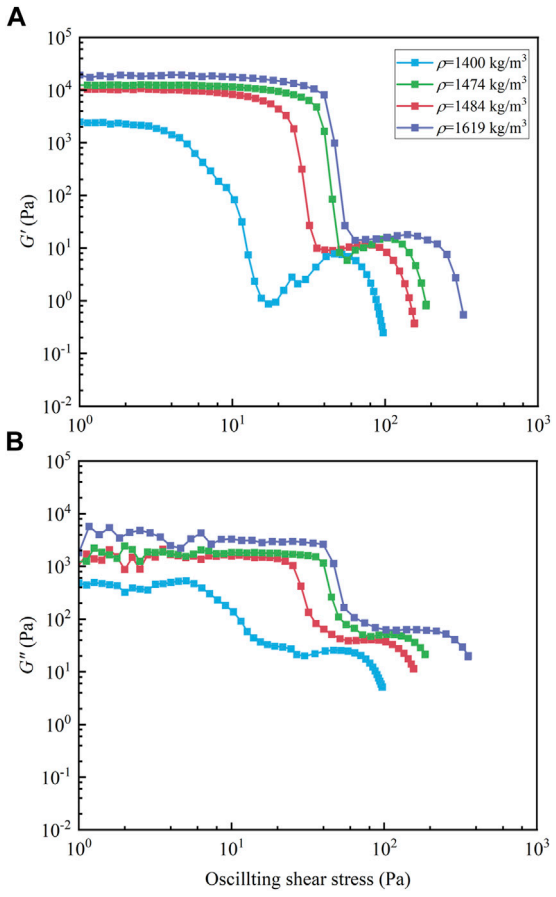

FIGURE 8
Results of oscillatory stress sweep tests for different mud samples: **(A)** the storage modulus G' and **(B)** the loss modulus G''.

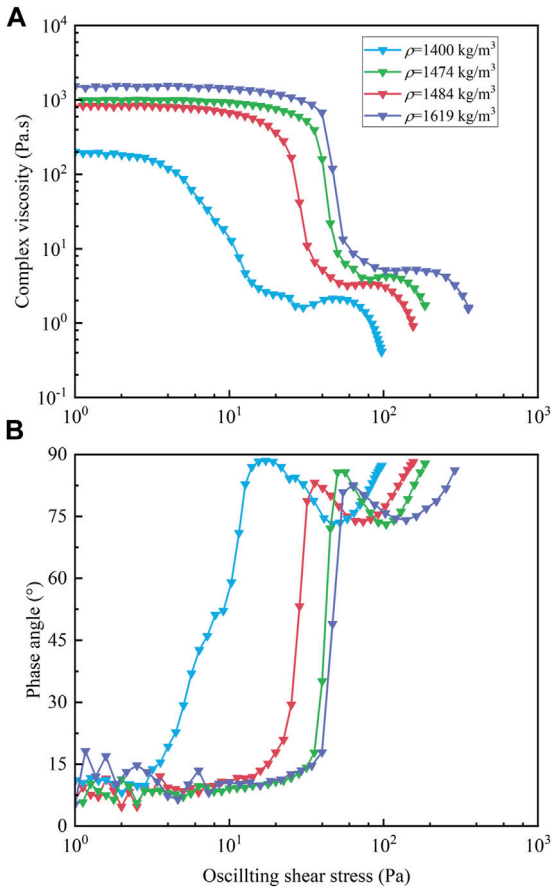

FIGURE 9
Results of oscillatory stress sweep tests for different mud samples: **(A)** the complex viscosity and **(B)** the phase angle evolution versus imposed oscillatory shear stress.

their different density and particle size distribution. In addition, it is worth noting that though the apparent viscosity of the natural mud samples is different from each other in the first stage, they nearly reached the same value in a plateau after the first yielding process. The yielding process of the natural mud is influenced by both density and particle size distribution. From Figure 7, it can be seen that the Zhoushan#1 mud sample (ρ=1619 kg/m^3) has the highest apparent viscosity and yield stress compared to other mud samples, which can be attributed to its relatively large density. However, the particle size distribution also affects the yielding process of the natural mud. For instance, the densities of Wenzhou#1 (ρ=1,484 kg/m^3) and Wenzhou#3 (ρ=1,474 kg/m^3) are almost equal, but the yield stress of Wenzhou#3 is obviously higher than that of Wenzhou#1, which may be attributed to the finer grained particles distribution of the Wenzhou#3, as the finer particles are more likely to form the internal bonds and destroying it requires higher shear stress.

The results of oscillatory shear stress sweep tests with different mud samples are shown in Figures 8, 9, indicating that all the mud samples show the similar "two-step" yielding feature independent of their density and particle size distribution. According to the picture, it can be seen that the Zhoushan#1 mud sample (ρ=1,619 kg/m^3) shows the maximum storage modulus and complex viscosity, which may be attributed to the maximum density in these mud samples; correspondingly, the Wenzhou#2 (ρ=1,400 kg/m^3) displays the minimum storage modulus and complex viscosity. By comparing the Wenzhou#1 (ρ=1,484 kg/m^3) and Wenzhou#3 (ρ=1,474 kg/m^3), it can be seen that despite the slightly higher density of the Wenzhou#1 mud sample, the Wenzhou#3 mud sample shows the higher storage modulus and complex viscosity and the higher static yield stress. The results of the Wenzhou#2 mud sample show a slight difference from the other mud samples: it shows the minimum storage modulus and complex viscosity. From the aforementioned, both density and particle size distribution can affect the rheology of the mud

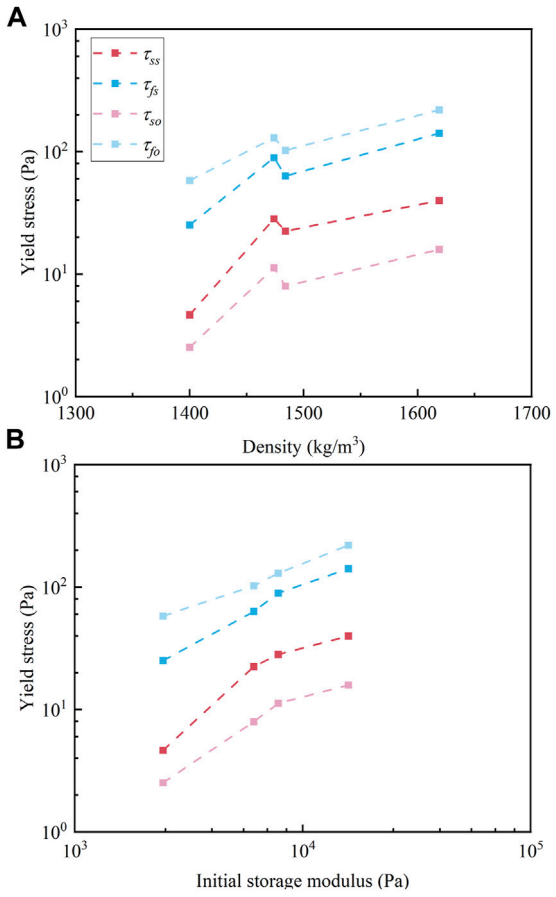

FIGURE 10
Plots of yield stress versus **(A)** density and **(B)** initial storage modulus. The first letter of subscript "*s*" and "*f*" of τ denote static and fluidic, respectively, and the second letter of subscript "*s*" and "*o*" represent steady and oscillatory, respectively.

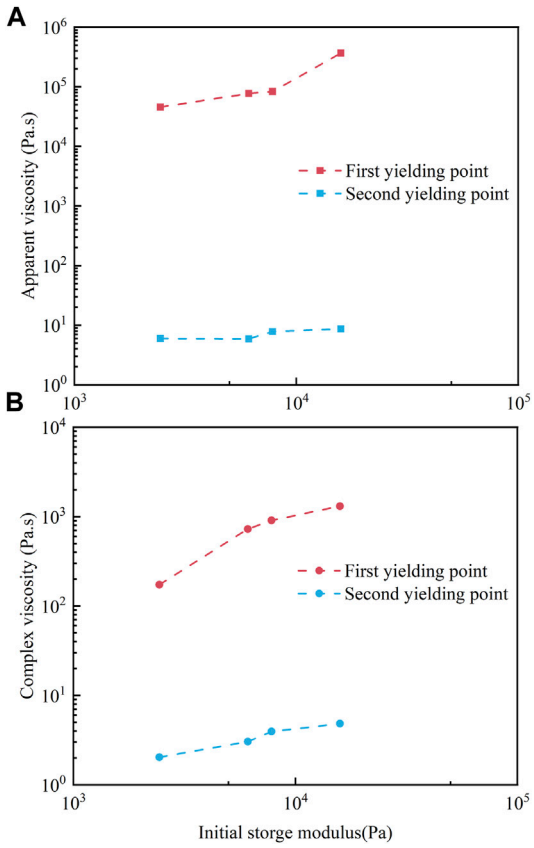

FIGURE 11
Variations of apparent viscosity **(A)** and complex viscosity **(B)** as functions of initial storage modulus.

samples; in the final analysis, all of them can have a significant effect on the internal structure of the mud samples.

The density affects the particle amounts per unit volume of the natural mud, and the linkages between different particles determine the state of the natural mud; if these linkages are undamaged, the natural mud behaves as a solid state; furthermore, if these linkages are partially destroyed, the natural mud presents a transition state, which shows the solid-fluidic character; ultimately, if all linkages are destroyed, the natural mud shows a fluid behavior. The more the amount of particles per unit volume of the natural mud, the larger the exposed loads needed to destroy the linkage between the particles; therefore, the Zhoushan#1 mud sample shows the largest storage modulus and the complex viscosity in Figure 8, and the Wenzhou#2 mud sample shows the lowest storage modulus and the complex viscosity. Similar to the density, the particle size distribution of the natural mud has a significant effect on the amounts per unit volume of the natural mud; when the density of the natural mud is determined, the smaller particle size means the more the amount of particles per unit volume of the natural mud, the more the linkages between these particles, so the transition from the solid state to the solid-fluid state needs the higher oscillatory stress of Wenzhou#3 compared to that of Wenzhou#1 shown in Figures 8, 9, despite the slightly higher density of the Wenzhou#1 mud sample.

Discussion

In this study, the natural mud was imposed on the shear stress in the experiments as the natural mud was subjected to the shear stress from exterior loads directly (Shakeel et al., 2020a); thus, the yield stress can be determined directly from the results without extra extrapolation. The experimental results presented show the "two-step" yielding feature of the mud samples; correspondingly, there are two yielding stresses that existed, consistent with the two-step yielding process. The first yielding stress, namely, static yield stress (τ_s), is the critical stress when the mud samples transform from the solid state

to the solid-fluidic state. Similarly, the second yield stress, namely, fluidic yield stress (τ_f), is the critical stress when the mud samples transform from the solid-fluid state to the fluidic state.

The density is a crucial parameter which has been adopted to predict the yield stress of natural mud in previous studies (e.g., Huang and Huhe, 2009; Mehta et al., 2014; Xu and Huhe, 2016); however, the other parameters such as temperature, pH, compositions, and particle size distribution also affect the value of the yield stress. Therefore, it is necessary to adopt a more suitable parameter to predict the yield stress. The value of yield stress reflects the ability to resist to flow of the natural mud, which usually relates to the internal microstructures of the natural mud. The initial storage modulus before shearing is an appropriate parameter to assess the structural level (Shakeel et al., 2020c), which may be a better choice to predict the yield stress of natural mud.

Figure 10 shows the static yield stress and the fluidic yield stress of the different mud samples versus density (Figure 10A) and initial modulus (Figure 10B); the initial storage modulus of each natural mud sample is obtained through the oscillatory time sweep within the linear viscoelastic regions before the steady and oscillatory shear stress tests. It is noted that both static yield stress and fluidic yield stress increase with initial storage modulus (Figure 10B), while the correlation between these two yield stresses and densities is not monotonous, indicating the initial storage modulus is a better choice to predict the yield stress of natural mud.

The exposed manner of exterior loads has a significant effect on the static yield stress and fluidic yield stress. Figure 10 presents the comparison of static yield stress and fluidic yield stress between two exposed exterior loads. For the static yield stress, it is noted that the results of the steady shear stress sweep tests are higher than those of the oscillatory shear stress sweep tests for all the mud samples, which indicates that the mud samples need higher loads to transform from solid to the solid-fluidic state when it is imposed to the static loads. On the contrary, for the static yield stress, the comparison shows that the steady shear stress sweep tests are lower than the oscillatory shear stress sweep tests for all the mud samples, which means that mud samples require higher shear stress to transform their state from the solid-fluidic state to the fluidic state when it is imposed to the oscillatory loads.

As a viscoelastic material, under the exterior loads, the shear force F of natural mud satisfies the following equation:

$$F_{s(o)} = \mathrm{m}\ddot{\gamma} + \mu\dot{\gamma} + k\gamma, \tag{1}$$

where m is the mass of the natural mud, γ is shear strain, $\dot{\gamma}$ is shear rate, $\ddot{\gamma}$ is derivative of $\dot{\gamma}$ and can be regarded as the acceleration, and the subscript s or o represents steady shear or oscillatory shear. Thus, on the right side of Eq. 1, the first term is the inertial force, the second term is the viscous force, and the third term is the elastic force. When the natural mud yields the first time, the elastic force is dominant; for the steady shear tests, inertial force and viscous force can be omitted, and the Eq. 1 can be rewritten as

$$k\gamma = F_s - \mathrm{m}\ddot{\gamma} - \mu\dot{\gamma} \approx F_s. \tag{2}$$

For the oscillatory shear test, as shown in Figure 5, the elastic force is dominant at this moment and the viscous force can be omitted; thus, Eq. 1 can be rewritten as

$$k\gamma = F_o - \mathrm{m}\ddot{\gamma}. \tag{3}$$

As a simple harmonic motion, Eq. 3 can be rewritten as

$$k\hat{\gamma}\cos(\omega t + \varphi) = \hat{F}_o\cos(\omega t + \varphi) + m\omega^2\hat{\gamma}\cos(\omega t + \varphi), \tag{4}$$

where superscript ˆ means the amplitude; thus

$$F_s = \hat{F}_o + m\omega^2\hat{\gamma} \Rightarrow F_s > F_o. \tag{5}$$

Equation 5 explains why static yield stress in steady shear tests is larger compared to that of oscillatory shear tests. Similarly, when the natural mud yields the second time, viscous force is dominant; for the steady shear tests, Eq. 1 can be rewritten as

$$\mu\dot{\gamma} = F_s - k\gamma - \mathrm{m}\ddot{\gamma} \approx F_s. \tag{6}$$

For the oscillatory shear test, as shown in Figure 5, viscous force is dominant at the moment, and Eq. 1 can be rewritten as

$$\mu\dot{\gamma} = F_o - \mathrm{m}\ddot{\gamma}. \tag{7}$$

As a simple harmonic motion, Eq. 7 can be rewritten as

$$\mu\hat{\dot{\gamma}}\cos(\omega t) = \hat{F}_o\cos(\omega t + \varphi) + m\omega^2\hat{\gamma}\cos(\omega t). \tag{8}$$

Using the complex variable method, Eq. 8 can be rewritten as

$$\mu\hat{\dot{\gamma}} = \frac{\hat{F}_o}{\sqrt{1 + \left(\frac{m\omega}{\mu}\right)^2}} = F_s \Rightarrow F_o > F_s. \tag{9}$$

Equation 9 explains why the fluidic yield stress in oscillatory shear tests is larger compared to that of steady shear tests.

Figures 11A,Bgive the apparent viscosity and the complex viscosity at the first and the second yielding point, respectively. Under steady shear stress, the apparent viscosity at the first yielding point increases with the initial storage modulus, whereas the variation of the apparent viscosity in the second yielding point is slight with the initial storage modulus. Furthermore, the apparent viscosity in the first yielding point is nearly three orders of magnitude higher than it is in the second yielding point. For the oscillatory shear stress test, the complex viscosity in these two yielding points are increasing with initial storage modulus, and the complex viscosity in the first yielding point is two orders of magnitude higher than it is in the second yielding point.

The natural soft mud on the coastal areas is usually disturbed by various exterior loads, such as currents, waves, tides, and storms. As aforementioned, the natural mud needs higher

exterior loads to fluidize when it is imposed on the oscillatory loads, meaning that currents, instead of waves, make the natural mud easier to be fluidic, and the mud needs higher exterior loads to fluidize when it is forced to the waves. The fluidization of natural mud is closely related to the fluid-mud formation; besides, the fluidic yield stress is found to be exponentially proportional to the critical Shields parameter of cohesive sediments (Wang and Sturm, 2016; Zhang and Yu, 2017). Due to the difference of yield stress of natural mud when it is imposed to waves or tidal currents, it is of great importance to consider the dominant hydrodynamic condition of a specific muddy coast when estimating the fluid-mud formation and the incipient motion of cohesive sediment.

Conclusion

In this study, the yielding process of four different natural mud samples collected from Zhejiang Province in China was investigated through a DHR-I rheometer with a cone-plate geometry. Both steady and oscillatory shear stresses were imposed on the natural mud samples directly, and a two-step yielding feature of the natural mud was observed. Based on the analysis of the experimental data, the main findings are summarized as follows:

1) The yielding process of natural mud is a two-step yielding behavior. Both results of steady and oscillatory shear stress tests show that the viscosity (apparent viscosity and complex viscosity) experienced two sharp declines, meaning the "two-step" yielding feature is the intrinsic character of the natural soft mud; consequently, the two-step yielding process of natural mud can be divided into three stages. In the solid stage, the elastic effect dominates and the natural mud behaves as a linearly elastic solid; with increasing shear stress, the elastic effect is weakened, and the viscous effect gradually dominates in the solid-fluidic stage and the fluidic stage, and natural mud behaves like fluids.
2) The initial storage modulus is a better parameter to predict the yield stress than the density of the natural mud. Compared to density, the initial storage modulus reflects the internal microstructures before steady and oscillatory shear stress tests. The experimental results show that both static yield stress and fluidic yield stress monotonically increase with initial storage modulus.
3) Both static yield stress and fluidic yield stress are susceptive to the imposed manner of the exterior loads. The static yield stress in the oscillatory shear tests is lower than that in the steady shear tests ($\tau_{so}<\tau_{ss}$), and the fluidic yield stress of natural mud in oscillatory shear tests is higher than that in the steady shear tests ($\tau_{fo}>\tau_{fs}$), which can be explained by introducing the viscoelastic-oscillation theory.

Data availability statement

The original contributions presented in the study are included in the article/Supplementary Material; further inquiries can be directed to the corresponding authors.

Author contributions

SW, HG, and YX conceived and designed the framework of this study. SW performed experiments, analyzed the experimental data, and drafted the original manuscript. ZH reviewed the manuscript and with constructive discussions. HG helped conduct the experiments and process data. YX reviewed the manuscript and funded this study.

Funding

The study was financially supported by the National Natural Science Foundation of China (42076177), the National Key Research and Development Program of China (2020YFD0900803), and the Talent Program of Zhejiang Province (2021R52049).

Conflict of interest

The authors declare that the research was conducted in the absence of any commercial or financial relationships that could be construed as a potential conflict of interest.

Publisher's note

References

Ahuja, A., Pappas, I., and Potanin, A. (2020a). Relation between structure and stability of toothpaste with two-step yielding. *Rheol. Acta* 59, 133–145. doi:10.1007/s00397-019-01183-7

Ahuja, A., Potanin, A., and Joshi, Y. M. (2020b). Two step yielding in soft materials. *Adv. Colloid Interface Sci.* 282, 102179. doi:10.1016/j.cis.2020.102179

Almashan, N., and Dalrymple, R. A. (2015). Damping of waves propagating over a muddy bottom in deep water: Experiment and theory. *Coast. Eng.* 105, 36–46. doi:10.1016/j.coastaleng.2015.08.008

Altieri, A., Urbani, P., and Zamponi, F. (2018). Microscopic theory of two-step yielding in attractive colloids. *Phys. Rev. Lett.* 121, 185503. doi:10.1103/PhysRevLett.121.185503

Bai, Y., Ng, C., Shen, H., and Wang, S. (2002). Rheological properties and incipient motion of cohesive sediment in the haihe estuary of China. *China Ocean. Eng.* 16, 483–498. doi:10.3321/j.issn:0890-5487.2002.04.005

Coussot, P., and Piau, J. M. (1994). On the behavior of fine mud suspensions. *Rheol. Acta* 33, 175–184. doi:10.1007/bf00437302

Emami, S., Mousavi, S., Hosseini, K., Fouladfar, H., and Mohammadian, M. (2020). Comparison of different turbulence models in predicting cohesive fluid mud gravity current propagation. *Int. J. Sediment Res.* 35, 504–515. doi:10.1016/j.ijsrc.2020.03.010

Fonseca, D. L., Marroig, P. C., Carneiro, J. C., Gallo, M. N., and Vinzón, S. B. (2019). Assessing rheological properties of fluid mud samples through tuning fork data. *Ocean. Dyn.* 69, 51–57. doi:10.1007/s10236-018-1226-9

Green, M. O., and Coco, G. (2014). Review of wave-driven sediment resuspension and transport in estuaries. *Rev. Geophys.* 52, 77–117. doi:10.1002/2013RG000437

Huang, Z., and Huhe, A. (2009). A laboratory study of rheological properties of mudflows in Hangzhou Bay, China. *Int. J. Sediment Res.* 24, 410–424. doi:10.1016/S1001-6279(10)60014-5

Jiang, F., and Mehta, A. J. (1990). Mudbanks of the southwest coast of India iv: Mud viscoelastic properties. *J. Coast. Res.* 11, 918–926.

Kameda, J., and Hirauchi, K. (2018). Rheological properties of composite serpentine-brucite suspensions: Implications for mudflow behavior on forearc seamounts. *Mar. Geol.* 403, 191–196. doi:10.1016/j.margeo.2018.06.004

Kameda, J., and Yohei, H. (2021). Influence of biopolymers on the rheological properties of seafloor sediments and the runout behavior of submarine debris flows. *Sci. Rep.* 11, 1493. doi:10.1038/s41598-021-81186-8

Kirichek, A., Shakeel, A., and Chassagne, C. (2020). Using *in situ* density and strength measurements for sediment maintenance in ports and waterways. *J. Soils Sediments* 20, 2546–2552. doi:10.1007/s11368-020-02581-8

Knappe, E., Manga, M., and Le Friant, A. (2020). Rheology of natural sediments and its influence on the settling of dropstones in hemipelagic marine sediment. *Earth Space Sci.* 7, e2019E–e2876E. doi:10.1029/2019EA000876

Koumakis, N., and Petekidis, G. (2011). Two step yielding in attractive colloids: Transition from gels to attractive glasses. *Soft Matter* 7, 2456. doi:10.1039/c0sm00957a

McAnally, W. H., Friedrichs, C., Hamilton, D., Hayter, E., Shrestha, P., Rodriguez, H., et al. (2007). Management of fluid mud in estuaries, bays, and lakes. I: Present state of understanding on character and behavior. *J. Hydraul. Eng.* 133, 9–22. doi:10.1061/(asce)0733-9429(2007)133:1(9)

McAnally, W. H., Kirby, R., Hodge, S. H., Welp, T. L., Greiser, N., Shrestha, P., et al. (2016). Nautical depth for U.S. Navigable waterways: A review. *J. Waterw. Port. Coast. Ocean. Eng.* 142, 4015014. doi:10.1061/(ASCE)WW.1943-5460.0000301

Mehta, A. J., Samsami, F., Khare, Y. P., and Sahin, C. (2014). Fluid mud properties in nautical depth estimation. *J. Waterw. Port. Coast. Ocean. Eng.* 140, 210–222. doi:10.1061/(ASCE)WW.1943-5460.0000228

Messaoudi, A., Bouzit, M., and Boualla, N. (2018). Physical and rheological properties of the chorfa dam mud: Dependency on solids concentration. *Appl. Water Sci.* 8, 178. doi:10.1007/s13201-018-0805-8

Minami, S., Watanabe, T., Sasaki, Y., Minato, H., Yamamoto, A., Suzuki, D., et al. (2020). Two-step yielding behavior of densely packed microgel mixtures with chemically dissimilar surfaces and largely different sizes. *Soft Matter* 16, 7400–7413. doi:10.1039/D0SM00366B

Mirlean, N., Calliari, L., and Johannesson, K. (2020). Dredging in an estuary causes contamination by fluid mud on a tourist ocean beach. Evidence via ree ratios. *Mar. Pollut. Bull.* 159, 111495. doi:10.1016/j.marpolbul.2020.111495

Moghimi, E., and Petekidis, G. (2020). Mechanisms of two-step yielding in attractive colloidal glasses. *J. Rheology* 64, 1209–1225. doi:10.1122/8.0000057

Nguyen, Q. D., and Boger, D. V. (1992). Measuring the flow properties of yield stress fluids. *Annu. Rev. Fluid Mech.* 24, 47–88. doi:10.1146/annurev.fl.24.010192.000403

Nie, S., Jiang, Q., Cui, L., and Zhang, C. (2020). Investigation on solid-liquid transition of soft mud under steady and oscillatory shear loads. *Sediment. Geol.* 397, 105570. doi:10.1016/j.sedgeo.2019.105570

Nie, S., Jiang, Q., Wang, L., Zhang, J., and Liu, P. (2018). A laboratory study of rheological properties of soft mud using a dynamic shear-controlled oscillatory viscometer. *J. Coast. Res.* 85, 1226–1230. doi:10.2112/SI85-246.1

O'Brien, J. S., and Julien, P. Y. (1988). Laboratory analysis of mudflow properties. *J. Hydraulic Eng.* 114114, 8778–8887. doi:10.1061/(ASCE)0733-9429

Orseau, S., Huybrechts, N., Tassi, P., Pham Van Bang, D., and Klein, F. (2020). Two-dimensional modeling of fine sediment transport with mixed sediment and consolidation: Application to the gironde estuary, France. *Int. J. Sediment Res.* 36, 736–746. doi:10.1016/j.ijsrc.2019.12.005

Pang, Q., Zhang, R., and Wen, C. (2020). Fluid mud induced by super typhoon and fluvial flood in a deep-dredged waterway of xiamen, China. *J. Waterw. Port. Coast. Ocean. Eng.* 146, 4020004. doi:10.1061/(ASCE)WW.1943-5460.0000567

Safak, I., Sheremet, A., Davis, J., and Kaihatu, J. M. (2017). Nonlinear wave dynamics in the presence of mud-induced dissipation on atchafalaya shelf, Louisiana, USA. *Coast. Eng.* 130, 52–64. doi:10.1016/j.coastaleng.2017.09.014

Shakeel, A., Kirichek, A., and Chassagne, C. (2020c). Effect of pre-shearing on the steady and dynamic rheological properties of mud sediments. *Mar. Petroleum Geol.* 116, 104338. doi:10.1016/j.marpetgeo.2020.104338

Shakeel, A., Kirichek, A., and Chassagne, C. (2020a). Rheological analysis of mud from Port of Hamburg, Germany. *J. Soils Sediments* 20, 2553–2562. doi:10.1007/s11368-019-02448-7

Shakeel, A., Kirichek, A., and Chassagne, C. (2020b). Yield stress measurements of mud sediments using different rheological methods and geometries: An evidence of two-step yielding. *Mar. Geol.* 427, 106247. doi:10.1016/j.margeo.2020.106247

Shakeel, A., MacIver, M. R., van Kan, P. J. M., Kirichek, A., and Chassagne, C. (2021). A rheological and microstructural study of two-step yielding in mud samples from a Port area. *Colloids Surfaces A Physicochem. Eng. Aspects* 624, 126827. doi:10.1016/j.colsurfa.2021.126827

Sheremet, A. (2003). Observations of nearshore wave dissipation over muddy sea beds. *J. Geophys. Res.* 108, 3357. doi:10.1029/2003JC001885

Song, J., Qu, B., Li, X., Yuan, H., Li, N., and Duan, L. (2018). Carbon sinks/sources in the Yellow and East China seas—air-sea interface exchange, dissolution in seawater, and burial in sediments. *Sci. China Earth Sci.* 61, 1583–1593. doi:10.1007/s11430-017-9213-6

Van Kessel, T., and Blom, C. (1998). Rheology of cohesive sediments: Comparison between a natural and an artificial mud. *J. Hydraulic Res.* 36, 591–612. doi:10.1080/00221689809498611

Vanlede, J., Dujardin, A., Fettweis, M., Van Hoestenberghe, T., and Martens, C. (2019). Mud dynamics in the Port of zeebrugge. *Ocean. Dyn.* 69, 1085–1099. doi:10.1007/s10236-019-01273-3

Wang, H., Zentar, R., and Wang, D. (2022). Rheological characterization of fine-grained sediments under steady and dynamic conditions. *Int. J. Geomech.* 22, 4021260. doi:10.1061/(ASCE)GM.1943-5622.0002243

Wang, X. H. (2002). Tide-induced sediment resuspension and the bottom boundary layer in an idealized estuary with a muddy bed. *J. Phys. Oceanogr.* 32, 3113–3131. doi:10.1175/1520-0485(2002)032<3113:TISRAT>2.0.CO;2

Wang, X. H., Byun, D. S., Wang, X. L., and Cho, Y. K. (2005). Modelling tidal currents in a sediment stratified idealized estuary. *Cont. Shelf Res.* 25, 655–665. doi:10.1016/j.csr.2004.10.013

Wang, Y., and Sturm, T. W. (2016). Effects of physical properties on erosional and yield strengths of fine-grained sediments. *J. Hydraul. Eng.* 142, 4016049. doi:10.1061/(ASCE)HY.1943-7900.0001193

Xia, Y., and Zhu, K. (2010). A study of wave attenuation over a maxwell model of a muddy bottom. *Wave Motion* 47, 601–615. doi:10.1016/j.wavemoti.2010.05.001

Xu, J., and Huhe, A. (2016). Rheological study of mudflows at lianyungang in China. *Int. J. Sediment Res.* 31, 71–78. doi:10.1016/j.ijsrc.2014.06.002

Yang, W., and Yu, G. (2018). Rheological response of natural soft coastal mud under oscillatory shear loadings. *J. Waterw. Port. Coast. Ocean. Eng.* 144, 5018005. doi:10.1061/(ASCE)WW.1943-5460.0000461

Yang, W., Yu, G., Tan, S. K., and Wang, H. (2014). Rheological properties of dense natural cohesive sediments subject to shear loadings. *Int. J. Sediment Res.* 29, 454–470. doi:10.1016/S1001-6279(14)60059-7

Zhang, M., and Yu, G. (2017). Critical conditions of incipient motion of cohesive sediments. *Water Resour. Res.* 53, 7798–7815. doi:10.1002/2017WR021066

Zhang, M., Yu, G., La Rovere, A., and Ranzi, R. (2017). Erodibility of fluidized cohesive sediments in unidirectional open flows. *Ocean. Eng.* 130, 523–530. doi:10.1016/j.oceaneng.2016.12.021

frontiers | Frontiers in Earth Science

TYPE Original Research
PUBLISHED 10 January 2023
DOI 10.3389/feart.2022.933031

OPEN ACCESS

EDITED BY
Ya Ping Wang,
East China Normal University, China

REVIEWED BY
Kiichiro Kawamura,
Yamaguchi University, Japan
Davide Tiranti,
Agenzia Regionale per la Protezione Ambientale del Piemonte (Arpa Piemonte), Italy

*CORRESPONDENCE
Hongxian Shan,
hongxian@ouc.edu.cn
Yonggang Jia,
yonggang@ouc.edu.cn

SPECIALTY SECTION
This article was submitted to Geohazards and Georisks, a section of the journal Frontiers in Earth Science

RECEIVED 30 April 2022
ACCEPTED 23 September 2022
PUBLISHED 10 January 2023

CITATION
Xue L, Liu H, Li Z, Sun Z, Shan H and Jia Y (2023), In situ observation of wave-induced deformation of submarine landslides in tidal channel areas. *Front. Earth Sci.* 10:933031. doi: 10.3389/feart.2022.933031

In situ observation of wave-induced deformation of submarine landslides in tidal channel areas

Liang Xue[1,2], Hanlu Liu[1,2], Zhenghui Li[1,2], Zhongqiang Sun[1,2], Hongxian Shan[1,2,3]* and Yonggang Jia[1,2,3]

[1]Shandong Provincial Key Laboratory of Marine Environment and Geological Engineering, Ocean University of China, Qingdao, China, [2]Laboratory for Marine Geology, Qingdao National Laboratory for Marine Science and Technology, Qingdao, China, [3]Key Laboratory of Marine Environment and Ecology, Ministry of Education, Ocean University of China, Qingdao, China

Landslides often occur in land slopes, estuaries, fjords, and intertidal zones in the marine environment, while landslides in tidal channels have not been systematically reported. The Zhoushan sea area is dotted with islands and crisscross tidal channels, which is a typical tidal channel development area. The data from the coastal zone and island survey, offshore engineering site selection, and environmental survey show that landslides are very common in tidal channel areas. The detailed study of this kind of landslide will enrich the research theory of submarine landslide and have important guiding significance for marine planning, development and site selection, and construction of coastal engineering in coastal areas. First, the submarine landslide in southwest of Zhujiajian Island in Zhoushan is investigated in this study. It is found that the sliding zone is parallel to the island coastline, with a length of about 250 m and an extension of 2 km, and the buried depth of the sliding surface is generally 8–10 m; then, through the self-developed seabed deformation observation system, combined with the hydrodynamic observation system, the landslide was observed *in situ* for 75 days. The observation results showed that the landslide slides at a constant speed along the sliding surface under the action of weight; the slides accelerate under the action of waves, and multiple sliding surfaces are generated in the landslide body at the same time. Finally, the genetic mechanism of submarine landslides in tidal channel areas is put forward.

KEYWORDS

submarine landslide, *in situ* observation, storm wave, seabed creep deformation, multistage sliding

Introduction

Marine resources are an important part of natural resources. The rational development of marine resources is related to the sustainable development of human society in the future. There are many kinds of marine geological disasters, and the laws of disaster occurrence and development are complex and difficult to predict (Liu et al., 2020). With the rapid development of science and technology in recent years, especially the continuous emergence of modern remote sensing technology, wireless communication technology, and various sensing technologies, the early identification, monitoring, and early warning of hidden dangers of geological disasters have become an important means of active prevention and control of geological disasters (Xu, 2020).

Seabed instability will lead to submarine landslide, collapse depression, and other geological disasters. Some scholars have proposed various seabed deformation and sliding modes such as translational, rotational, and slump based on the geophysical survey, indoor test, and other research methods (Xu, 2006; Yang and Chen, 1994; Chang, 2009), which pose a serious threat to the safety of submarine pipelines, platforms, and other engineering structures. The real mechanism of instability triggering of the *in situ* submarine slope is not caused by a single factor but more by very complex mutual coupling in different periods (Prior, 1986a; Yang and Chen, 1994; Wang, 2015). During the cyclic action of ocean dynamics (waves, tides, etc.) on the seabed, it will exert vertical pressure, tension, and horizontal shear force on sediments. Under the action of this cyclic load, pore water pressure accumulates in the sediment, and the strength of the sediment decreases. When the strength is not enough to resist the force of ocean power, the sediment will deform and slide at different scales, which may further lead to large-scale submarine landslides and harm to marine engineering (Sultan et al., 2007; Liu et al., 2015; Liu et al., 2016; Nian et al., 2016).

At present, the investigation and research of submarine landslides mainly rely on marine geophysical detection technologies such as side scan sonar and shallow formation profile technology. The occurrence process and triggering factors of landslides can only be known by speculation (Vanneste et al., 2014; Jia et al., 2017). In contrast, seabed *in situ* observation technology can obtain dynamic observation data with timeliness, which is more conducive to the study of the occurrence mechanism and evolution process of submarine landslides (Zhang et al., 2016). Prior and others used sediment dynamic observation devices to record acceleration and inclination changes and found the revival of submarine landslide induced by storm surge in the underwater delta of the Yellow River (Prior et al., 1989); Chadwick et al. (2012) and Wallace et al. (2016) used high-precision water pressure gauges to monitor seabed subsidence and uplift in the deep sea so as to predict the time of volcanic eruption and capture the process of tectonic movement; Blum et al. (2010) used the seabed acoustic measurement system to monitor the unstable slope of the seabed for the first time; Urlaub et al. (2018) used the acoustic measurement system and pressure gauge to capture the sliding deformation process of the flank of Etna volcano; and Wang successfully captured the seabed deformation process induced by storm surge in the underwater delta of the Yellow River using the submarine landslide monitoring system (SLM) and put forward the mechanism of wave induced seabed instability in the underwater delta of the Yellow River (Wang et al., 2018; Wang et al., 2020).

The Zhoushan archipelago is located in the northeast of Zhejiang Province. It is composed of more than 1,300 islands of different sizes. It is the largest archipelago in China and rich in fishery resources, with many deep-water ports and developed shipping channels. It is a key logistic transit base in the Yangtze River Delta and its surrounding areas and has an important strategic position. Submarine landslides of different sizes are widely developed in the Zhoushan sea area. Among them, there are many gorge tidal channels in the south of Zhoushan Islands. A large number of submarine landslides are developed in these channels. The vast majority of landslides are an overall failure, mainly slicing and sliding along the slope. Ye et al. (1996), Lai et al. (2000), and Lai and Ye (2011) concluded that the uneven distribution of erosion and deposition in the tidal channel leads to the continuous increase of the seabed slope, and finally, the overall sliding failure occurs under the action of gravity as the main driving force. Marine geological disasters represented by submarine landslides pose a great threat to the safety of offshore engineering facilities in the Zhoushan sea area. It is particularly important to explore the excitation mechanism and cause mechanism of submarine deformation disasters such as submarine landslides.

Based on the self-developed *in situ* observation system, this study carried out *in situ* observation for 75 days on the typically inclined seabed slope in the southwest of Zhujiajian Island, Zhoushan, and obtained the observation data of lateral deformation and deformation direction of sliding surface (Xue et al., 2020; Liang et al., 2021).

The Zhoushan archipelago is located in the south of the Yangtze River Estuary. As the largest estuary in China, a large amount of sediment carried by the Yangtze River is deposited near the Zhoushan archipelago during its southward migration. Therefore, this area is a typical distribution area of muddy coast. After preliminary field exploration, the sea area in the southwest of Zhujiajian Island is selected as the *in situ* long-term observation area. Zhujiajian Island is located in the southeast of the Zhoushan archipelago in Zhejiang Province, with a maximum length of 13 km in the North-South direction and 7 km in the East-West direction. It is the fifth largest island in the Zhoushan archipelago (Feng, 2012). The observation area is the submarine landslide area in the southwest of Zhujiajian Island in the Zhoushan archipelago (Figure 1A), which is located on the northeast slope of the tidal scouring trough and close to the

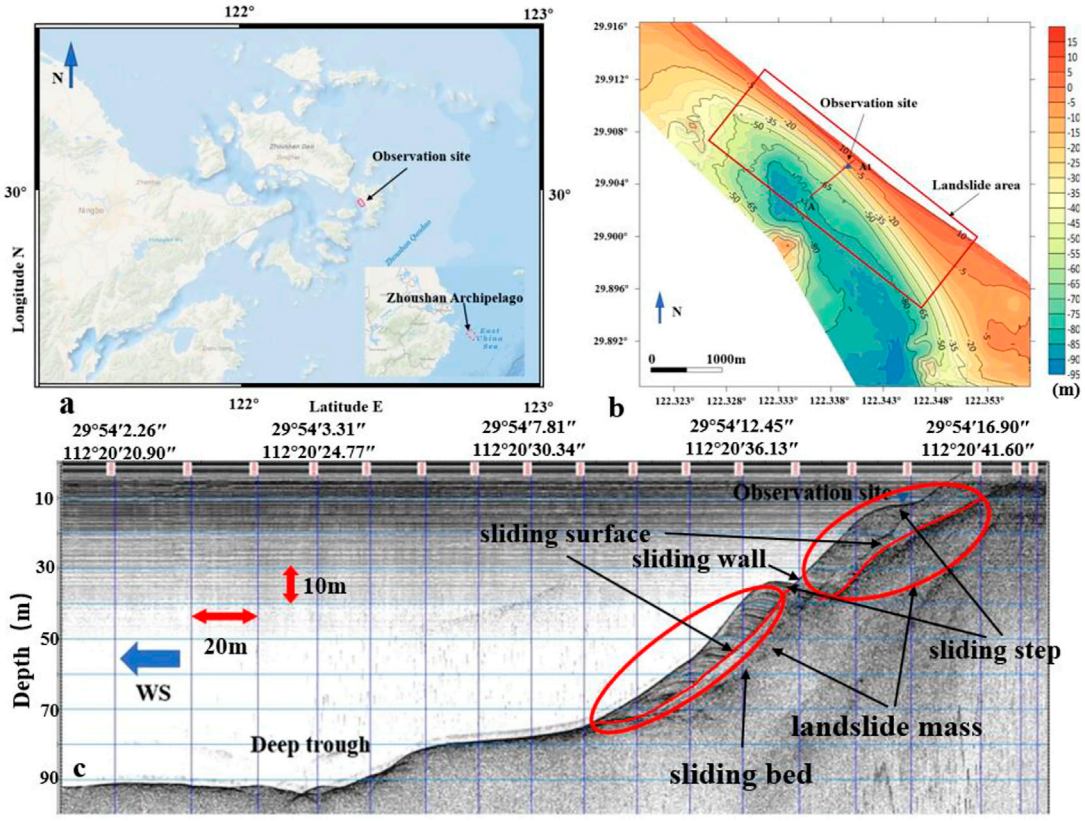

FIGURE 1
Geographical location map, water depth topographic map, and shallow stratum profile of the study area. **(A)** Shows the map of the Zhoushan archipelago, China, with the Zhujiajian study area marked with a red rectangle. **(B)** Shows the multibeam topographic map of study area with the observation site highlighted within the blue triangle. **(C)** Shows subbottom profiling of a scarp near the observation site denoted by a blue triangle.

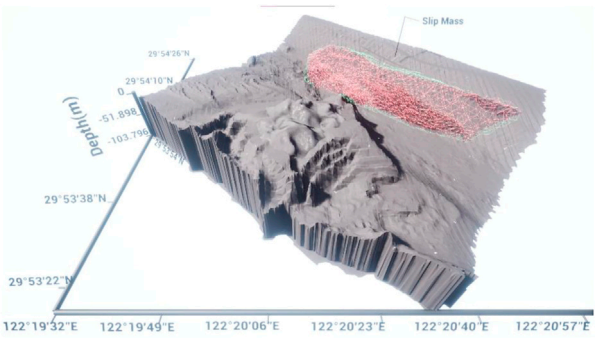

FIGURE 2
Schematic diagram of the Zhujiajian landslide.

Fulimen reclamation project of Zhujiajian Island. This area belongs to a typical tidal channel development area, with tidal channels crisscrossing and many landslides occurring (Liu et al., 2007). The tidal category of the observed sea area is the regular semidiurnal tide. The velocity of a rising tide is significantly faster than that of a falling tide, with an average tidal range of 2.5–2.8 m and a maximum tidal range of 4.79 m. Waves are mainly wind waves, and big waves are mostly caused by windy weather. The annual average wave height is 0.1 m, and the regular wave is southward (Chen et al., 1982; Zhang, 2013).

The water depth of the observation points selected in this study is about 10–12 m. The local terrain is flat, and the slope is small. There are steep slopes in the southwest, with an average slope of 8–9°, as shown in Figure 1B. Clear landslide mass, sliding surface, sliding bed, sliding wall, and sliding step can be seen from the records of the shallow stratum section. Irregular "feathery" bedding can be seen in the sliding body with the structural characteristics of a traction landslide (Figure 1C).

The boundary and shape of landslide mass in combination with multi-beam and shallow section data were drawn (Figure 2). The whole sliding zone is parallel to the island coastline, extending about 2 km and about 250 m in length. The water depth extends from about 5 m near the shore to about 70 m. The

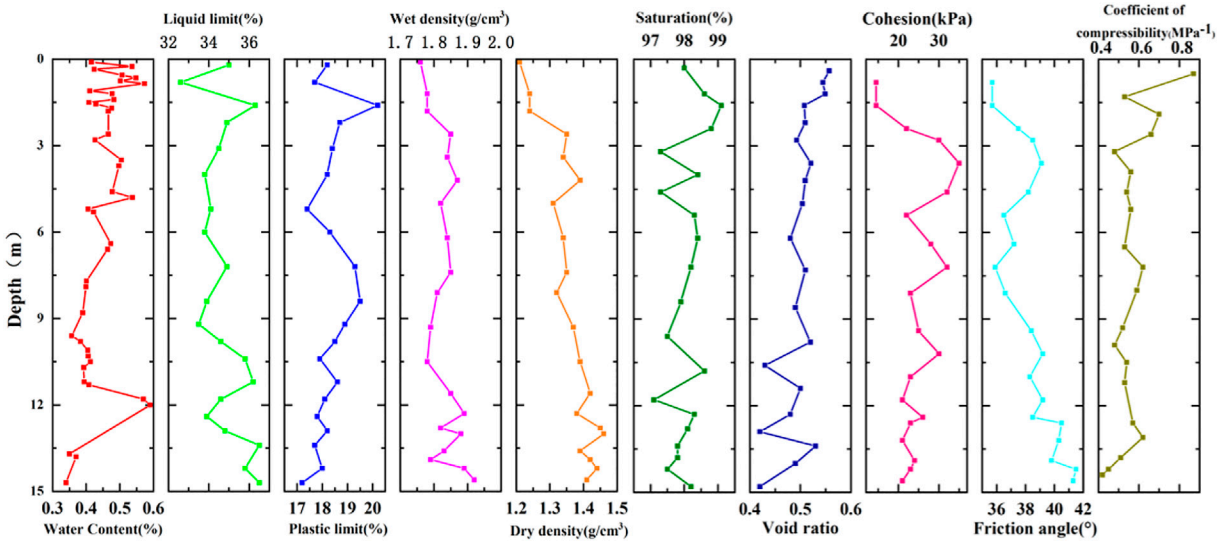

FIGURE 3
Physical and mechanical properties of seabed soils at a depth of 15 m.

buried depth of the sliding surface is generally 5–6 m, up to about 15 m.

A 15-m core sample extracted from the observation site showed mainly gray muddy clay and silty clay, with mud–sand interbedding, whose silt content >70% (Figure 3).

Materials and methods

Monitoring equipment

Seabed deformation and sliding are the most intuitive indices to reflect seabed stability. On the one hand, the observation data can help us analyze the deformation characteristics of preseabed geological disasters and provide strong evidence for the study of disaster mechanisms. On the other hand, they can provide early warning for marine engineering and ensure the safety of engineering and personnel. At home and abroad, most of the investigation and research on the deformation process of seabed sediments are geophysical investigation, sediment sampling, model test, numerical calculation, and other methods; therefore, it is difficult to obtain the field dynamic data of the deformation process of seabed sediments. Due to the complex engineering and dynamic geological process of the seabed, the implementation of *in situ* observation is difficult and the technical requirements for observation equipment are high. Therefore, the research on the deformation and sliding process of the seabed, especially the *in situ* observation method of the large-scale long-distance sliding migration process, is in the exploratory stage at home and abroad.

The *in situ* observation system of shallow water sediment deformation process applied in this paper consists of a deformation observation system and a supporting observation system. The deformation observation system is built with the array displacement meter as the core, which can realize the *in situ* real-time observation of the vertical deformation of seabed sediments and the lateral deformation process at different depths. The data acquisition and storage system can collect and store the lateral and vertical deformation data of seabed sediments obtained by the deformation observation system. The power supply system is composed of a high-capacity lithium battery pack and an underwater sealed cabin, which can provide long-term power supply for the deformation observation system and data transmission system. The supporting observation system is composed of a hydrodynamic condition observation system, which can carry out *in situ* long-term observation of marine dynamic conditions and seabed sediment deformation process at observation points at the same time so as to provide more comprehensive and timely data support for the analysis and discussion of the sediment deformation process.

The *in situ* seabed deformation observation system is composed of an array displacement meter, data acquisition, a storage system, and a power supply system (Figure 4A). The core component of deformation observation is the array displacement meter, which is composed of multiple rigid measurement units of equal lengths. The measurement units are connected in parallel, which can bend in any direction but resist torsional movement (Figure 4B). A high-precision MEMS accelerometer is integrated into the measurement unit to obtain the bending angle and

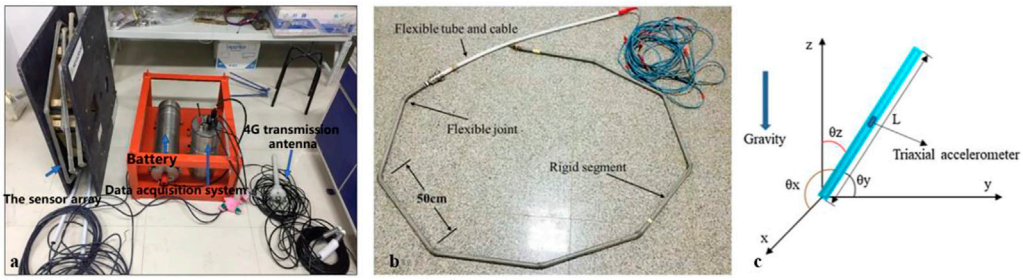

FIGURE 4
Seabed deformation observation system and working principle. **(A)** Shows the physical map of the seabed deformation observation system, **(B)** shows the physical map of sensor array, and **(C)** shows the sketch map of the single shape accel array segment.

direction of each observation node by sensing the change of acceleration field and then calculate the deformation of each observation unit by relying on the built-in microprocessor (Figure 4C). The rigid rods of array displacement sensors are connected together through nodes so that the *X*, *Y*, and *Z* coordinate systems of adjacent rods are associated so as to accumulate the spatial coordinate positions of each node point (Danisch et al., 2007). This method is based on the principle that the three-dimensional shape sensing system is constrained by degrees of freedom along the path and was originally applied to the optical fiber curvature sensor (Danisch et al., 1999). The calculation of the deformation of the array displacement sensor is divided into two steps. First, the original data is converted into triaxial acceleration (a triaxial component of gravity acceleration), and then a 3D displacement calculation is carried out.

The first step of the calculation is to analyze how the triaxial acceleration of each rod section is distributed in the gravity field to determine the initial space attitude of each segment in the static state. The relationship between angle and spatial attitude is calibrated by the array displacement sensor manufacturer before leaving the factory. The length of each segment is known (L = 50 cm); therefore, we can determine the coordinate value of the tail node of each rod segment ($L\cos\theta_x, L\cos\theta_y, L\cos\theta_z$). For the array displacement sensor of the whole multi-rod section, the coordinate value of the tail end of each rod section is calculated by accumulating the coordinate value of the previous rod section one by one ($\sum_{k=1}^{n} L\cos\theta_{xn}$; $\sum_{k=1}^{n} L\cos\theta_{yn}$; $\sum_{k=1}^{n} L\cos\theta_{zn}$). When the array displacement sensor deforms, the spatial attitude of each rod section will change. The displacement change of each node of the array displacement sensor can be obtained by calculating the difference between the corresponding coordinate value at this time and the initial coordinate value.

Taking the displacement change of each axis in section *n* as an example, the calculation formula is as follows:

$$\begin{aligned}\Delta x &= \sum_{k=1}^{n} L\cos\theta_{xnt_1} - \sum_{k=1}^{n} L\cos\theta_{xnt_0}\\ \Delta y &= \sum_{k=1}^{n} L\cos\theta_{ynt_1} - \sum_{k=1}^{n} L\cos\theta_{ynt_0}\\ \Delta z &= \sum_{k=1}^{n} L\cos\theta_{znt_1} - \sum_{k=1}^{n} L\cos\theta_{znt_0}\end{aligned} \quad (1)$$

where t_1 and t_0 represent the measurement cutoff time and the initial time, respectively, and the calculation results represent the displacement change of each axis between the two times.

In order to ensure the accuracy of the measurement, the first-rod segment (i.e., reference point) must be stationary. When the array displacement sensor is placed vertically in the seabed, the calculation is simplified by ignoring the coordinate value of the *Z*-axis, which is almost unchanged during horizontal deformation.

Since the calculation is gradually accumulated through the first-rod section, the corresponding error will also accumulate with the increase of the length of the array displacement sensor. The measurement accuracy of the sensor is 0.5 mm/32 m. The shorter the length, the higher the accuracy. The calculation formula is as follows:

$$\varepsilon = \sqrt{\frac{X}{32}} \cdot 0.5\text{mm} \quad (2)$$

where ε is the measurement error of the sensor and X is the distance from the node to the origin (fixed point).

Array displacement meter has the advantages of high precision, large range, high stability, and reusability and has achieved good results in the application of monitoring and early warning of landslides on land (Chen et al., 2015; Wei, 2015; Uhlemann et al., 2016).

Equipment emplacement

In this study, the array displacement sensor is vertically placed in the *in situ* seabed sediment, and the deformation of the sediment is quantified by the deformation of the sensor. The

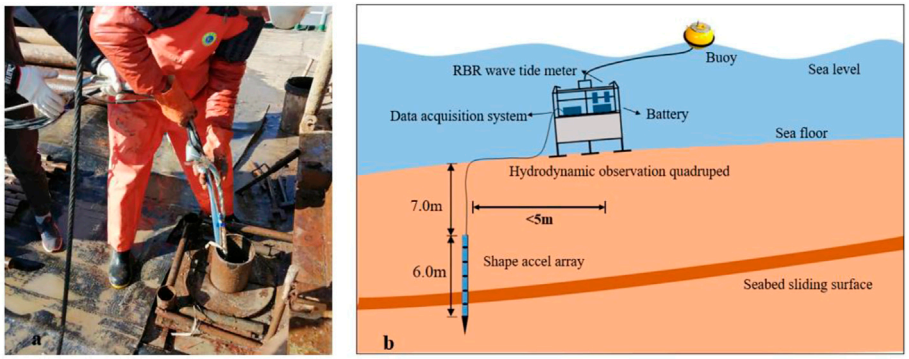

FIGURE 5
(A) Offshore drilling used to emplace the shape accel array. **(B)** Emplacement setup of the submarine landslide observation system, including the position of the shape accel array and hydrodynamic observation quadruped.

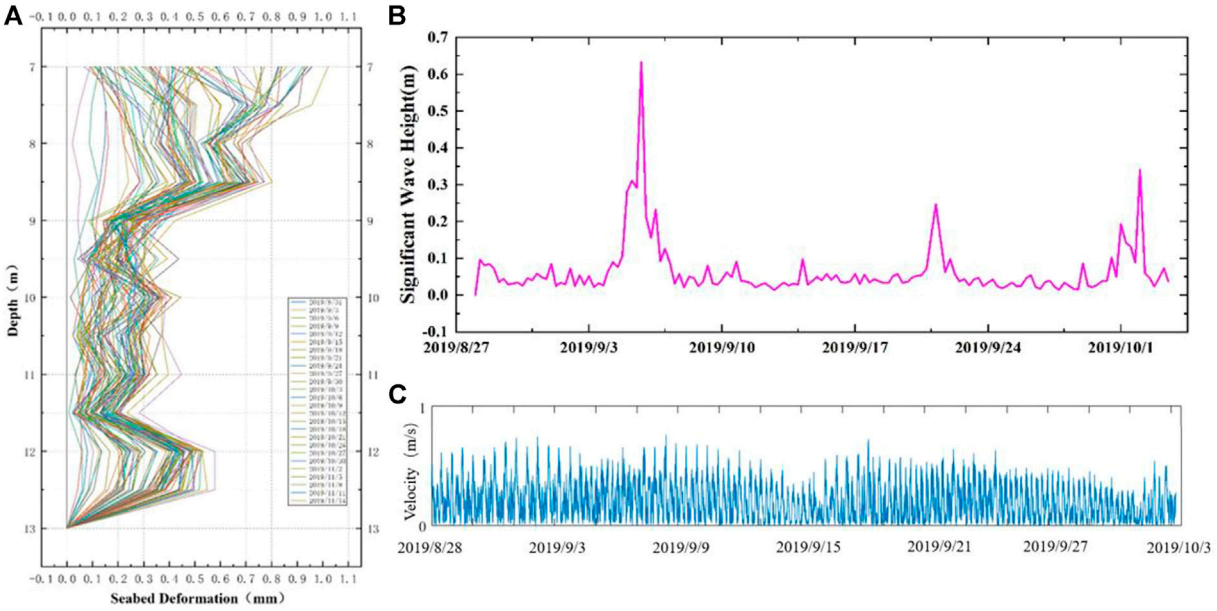

FIGURE 6
(A) Time series of cumulative horizontal deformation of the shape accel array, attached with the significant wave height **(B)** and the flow rate **(C)**.

French Institute for Marine Development (INFREMER) made the first attempt at its deployment method (Stegmann et al., 2012). The inclinometer probe developed by INFREMER is also composed of an array displacement sensor, and the layout method is a free-fall gravity penetration. The equipment is used for long-term *in situ* observation on the underwater slope of Nice, France. The landslide surface of the Zhujiajian sea area in the study area of *in situ* observation in this study is relatively deep and cannot penetrate to the specified depth; therefore, its layout method is not suitable. Therefore, in this study, the offshore drilling technology is used to implement the 13-m deep drilling, and the array displacement sensor is vertically buried on the seabed to make the sensor pass through the landslide surface with a fixed counterweight at the bottom making it relatively stationary during observation (Figure 5A). During the placement of the array displacement sensor, the casing pipe is placed while drilling to prevent the hole from collapsing. After the sensor is vertically placed in the hole, the fine sand is backfilled to maintain the vertical attitude of the sensor. At the same time, the rapid settlement of the fine

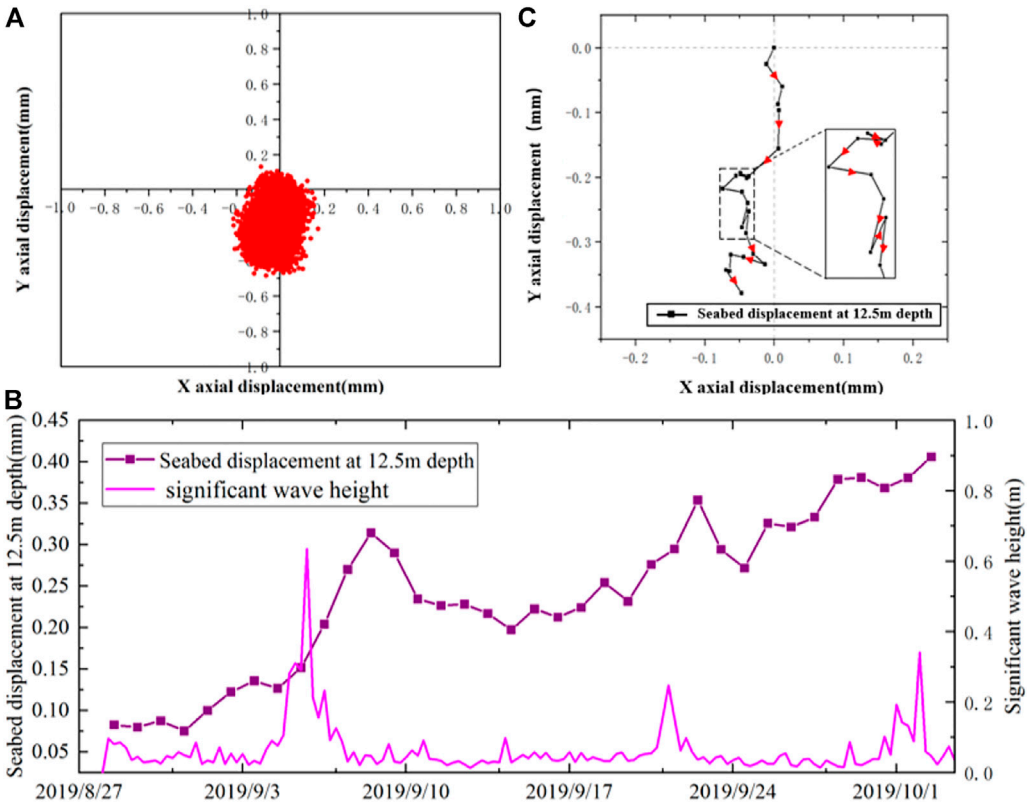

FIGURE 7
(A) Node location during observation at the depth of 12.5 m, **(B)** seabed displacement at 12.5 m depth and significant wave height during observation, and **(C)** deformation direction during storm event at the depth of 12.5 m.

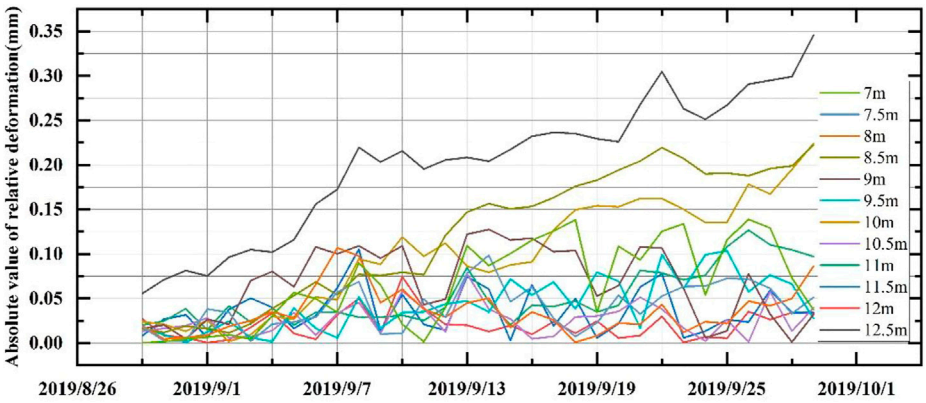

FIGURE 8
Absolute value of relative deformation during observation.

sand will leave the sensor in the hole, and the casing will not be brought out during the recovery process. The placement point of the array displacement sensor is about 5 m away from the quadruped (Figure 5B). The observation system was emplaced in the seabed on 28 August 2019 and recovered on 9 December 2019.

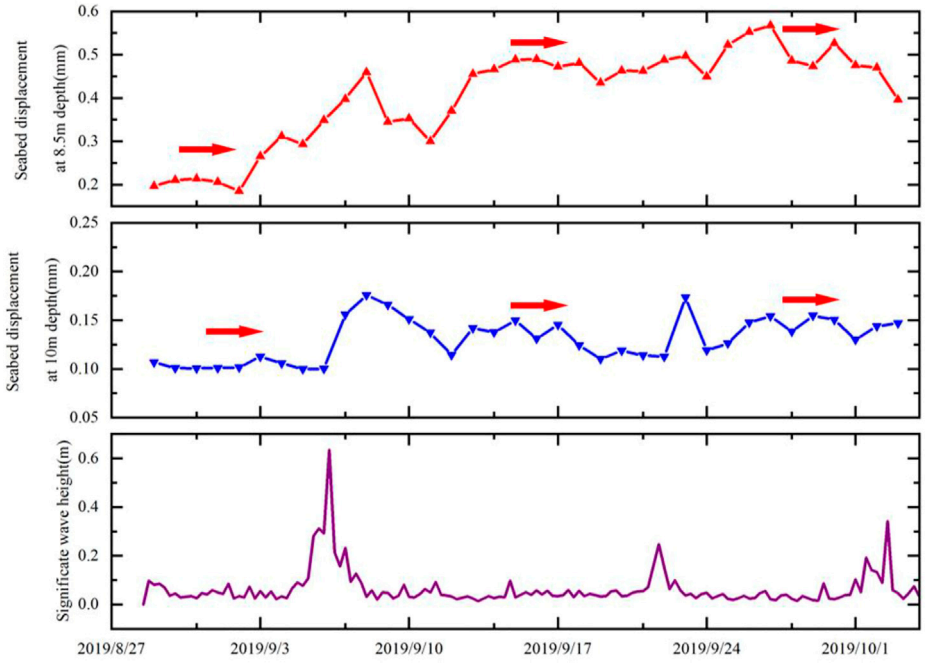

FIGURE 9
Seabed displacement at 8.5 m and 10 m depths and significant wave height during observation.

Observation results

The whole observation is in autumn and winter, during which storms occur frequently. The effective data are selected for analysis and statistics, and the results of *in situ* observation of environmental elements including significant wave height, average current velocity, and seabed deformation are obtained. We conduct statistical analysis on wave data, screen out the abnormal data in the later stage, and conduct statistical analysis with 36 days of low noise and high-quality data. The results show that during the observation period, the maximum deformation of the seabed is 1 mm (Figure 6A), which is greater than the measurement error of the sensor, which can reflect the deformation and sliding of the seabed. During the observation period, the average wave height of the observed sea area was about 0.1 m, during which three obvious storm events were experienced, and the significant wave height increased significantly (6 September with 0.65 m significant wave height; 20 September with 0.3 m significant wave height; 2 October with 0.35 m significant wave height) (Figure 6B). During most of the observation period, the measured velocity of the seabed current is less than 80 cm/s, and the bottom velocity does not change significantly during storm events (Figure 6C).

It can be seen from the aforementioned that the buried depth of the sliding surface of the Zhujiajian landslide is about 12.5 m, and the displacement sensor data at the depth of 12.5 m of the seabed is selected for analysis (Figure 7).

Figure 7A shows the process of the deformation direction at the depth of 12.5 m. The *X*-axis and *Y*-axis represent the two coordinate systems of the array displacement sensor on the horizontal plane, which can be understood as the top view of the sliding surface. The results show that the deformation direction is mainly distributed in the *Y*-axis direction. According to the layout of field equipment, the *Y*-axis direction corresponds to the inclination of the slope, indicating that the deformation direction of the sliding surface is mainly concentrated in the inclination direction.

The external forces causing the deformation and sliding of the seabed slope include the cyclic shear stress generated by the wave load in the sediment, the shear stress formed by the wave current on the seabed surface, and the sliding force caused by the component of gravity along the slope (Jia et al., 2011). Wave current coupling generates bottom flow in the seabed boundary layer, and the bottom shear stress caused is very small, which is only a few pascals even in storm events (Dufois et al., 2008; Wang et al., 2018), and has little effect on the deformation and sliding of sediments in a short time. In addition, no earthquake event occurred near the observation area during the observation period (China Seismic Network Center). The influence of seismic load is not considered in this study. Therefore, the external forces causing the deformation and sliding of seabed slope are mainly gravity and the cyclic shear stress generated by wave load in the sediment.

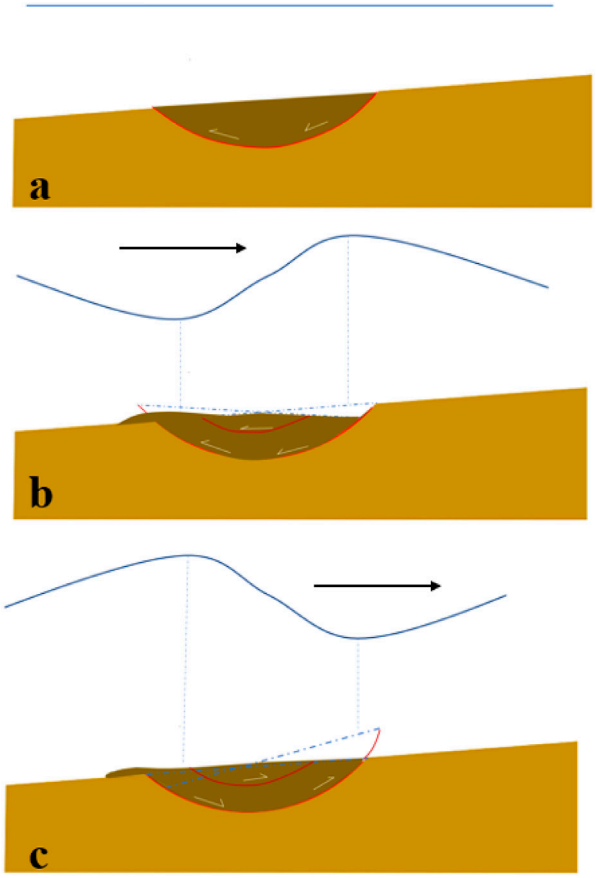

FIGURE 10
Schematic diagram of seabed deformation and sliding in the study area. **(A)** Shows that the seabed slides along the slope of the sliding surface under the action of gravity, **(B)** shows that the direction of shear stress formed by wave crest and wave trough is opposite to the wave direction, and the soil will oscillate clockwise, and **(C)** shows that the direction of shear stress formed by wave crest and wave trough is the same as that of the wave, and the soil will oscillate anticlockwise.

Comparing the deformation data at the sliding surface with the wave data (Figure 7B), it is found that the deformation at the sliding surface gradually increases. Under the calm sea condition, the deformation of the seabed soil at the sliding surface increases slowly, indicating that the landslide is in the limit equilibrium state and slowcreep slide occurs under the action of gravity. During the storm event, significant wave height reached 0.65 m on 6 September, the seabed deformation speed increased, and the same phenomenon occurred in the storm event on 20 September. Due to the hysteretic effect, the deformation slip caused by the storm event on 2 October is not shown. This indicates that the seabed creep slide speed increases under the cyclic shear stress generated by wave load in the seabed and with an obvious hysteretic effect.

The seabed generates horizontal cyclic shear stress under the alternating action of peak compressive stress and trough tensile stress (Liam Finn et al., 1983; de Groot et al., 2006), and cyclic oscillation movement will occur after the seabed sediments become unstable (Liu et al., 2013; Zhang et al., 2018a). According to the *in situ* observation results, the seabed deformation direction is along the negative direction of the *Y* axis, indicating that the seabed deformation is in a gradually progressive process as a whole; during this period, it is accompanied by reciprocating motion, corresponding to the cyclic oscillation deformation of seabed induced by the storm (Figure 7C).

It can be seen from Figure 6A that during the observation process, some nodes at the depth of 7–13 m were found to have larger deformation than adjacent nodes, and there may be some other sliding interfaces. The relative deformation of the sensor at each depth (the absolute opposite value of the deformation difference between the node and the previous node) was processed and analyzed, and the results as shown in Figure 8 were obtained. It was found that except for 12.5 landslide sliding surfaces, there are also obvious sliding interfaces at 8.5 m and 10 m depths. Combined with the borehole data, the corresponding mud–sand interbedding sediment at the depths of 8.5 m and 10 m are found. During the observation, the seabed deformation at 8.5 m and 10 m depths is noted, as shown in Figure 9.

The deformation at 8.5 m and 10 m depths does not change significantly during the observation. During the storm events on 6 September and 22 September, the deformation increased significantly and also had an obvious hysteretic effect; after the storm event, the seabed soil returned to a stable state. This shows that during the storm event, other sliding surfaces will be generated in the landslide mass, and multistage sliding will occur on the slope.

Discussion: Analysis of the submarine landslide deformation pattern

The initiation mechanism of wave-induced sediment instability and further seabed deformation sliding mainly includes liquefaction failure and shear failure (Rahman 1991; Rahman, 1997; Zhang et al., 2016). Simple shear failure is more likely to occur on the seabed of sediments with high clay content, while simple liquefaction failure analysis is mainly aimed at the seabed of cohesionless sediments (Rahman and Jabery 1986; Rahman 1991; Jeng 2001). The soil in the study area is fine, basically belonging to clayey silt or silty clay; therefore, mainly shear failure is seen.

The Zhujiajian landslide has obvious multistage sliding characteristics. In general, the multistage of landslide can be divided into two categories: one is caused by the difference in sliding speed of each part of landslide mass in the first sliding

of soil mass and the other is that a new landslide is generated on the basis of the previous landslide. According to the advancing direction of a landslide, it can be divided into traceability landslide and advancing landslide. The so-called traceable landslide means that the landslide mass has multiple landslides in turn toward the source, and the forward landslide means that the landslide mass follows the direction of the landslide. No matter which type, they all show multilevel step landforms on the section. It can be clearly seen from Figure 1A that two sliding steps can be seen in the main section. The sliding surface along the direction of the landslide is clearer and clearer each time, indicating that the damage develops along the direction of the landslide.

According to the monitoring data, the deformation pattern of the Zhujiajian landslide can be expressed as follows: on the inclined seabed, the slope will creep slide along the landslide tendency under the action of gravity to form an integral circular arc sliding (Figure 10A); under the action of waves, the wave crest and trough form shear stress on the seabed. With the alternating action of wave crest and trough, the seabed soil moves cyclically and the creep slide speed is accelerated. At the same time, there will also be a sliding surface at the position of sediment interbedding in the landslide body, and the soil at the sliding surface also moves cyclically (Figures 10B,C). When the wave action is strong enough, the landslide will have a multistage sliding phenomenon.

Conclusion

Based on the observation system independently developed and designed, this study carried out long-term *in situ* observation on the typically inclined seabed slope in the southwest of Zhujiajian Island, Zhoushan, and obtained hydrodynamic data such as lateral deformation size and direction at different depths of the seabed slope, wave height, and velocity. The following conclusion is obtained.

1. Under the action of weight, Zhujiajian landslide slides slowly and slides along the slope tendency, and the sliding rate is basically unchanged. In storm events, the slope slides accelerate, the sliding rate increases, and the seabed soil moves cyclically with the action of waves; after the storm event, the landslide returned to the original sliding rate.
2. Under calm sea conditions, the landslide is in an overall sliding state. During the storm event, a sliding surface is generated at the mud–sand interbedding sediment in the landslide body. After the storm event, the landslide still slides as a whole.

Data availability statement

The original contributions presented in the study are included in the article/supplementary material; further inquiries can be directed to the corresponding author.

Author contributions

LX: conceptualization, methodology, software, investigation, formal analysis, and writing—original draft; HL: data curation and writing—original draft; HS: visualization and investigation; YJ: resources and supervision; ZS: software and validation; and ZL: visualization and writing—review and editing.

Funding

This work was funded by the Key Project of NSFC-Shandong Joint Research Funding POW3C (U1906230), the National Natural Science Foundation of China (41877223), and Key Science and Technology Plan of Power China Huadong Engineering Corporation Limited (KY2018-ZD-01).

Acknowledgments

The authors deeply appreciate the help of Chunsheng Ji, Ziqi Peng, Tianyang Liang, Yankai Hou, and Naili Hu in carrying out the observations. They thank Peng, Miaojun Sun, and Weida Ni of Power China Huadong Engineering Corporation Limited for their support of the project. Comments from reviewers and the editor greatly improved the manuscript and are highly appreciated.

Conflict of interest

The authors declare that the research was conducted in the absence of any commercial or financial relationships that could be construed as a potential conflict of interest.

Publisher's note

References

Blum, J. A., Chadwell, C. D., and Driscoll, N. (2010). Assessing slope stability in the Santa Barbara Basin, California, using seafloor geodesy and CHIRP seismic data [J]. *Geophys. Res. Lett.* 37 (13), 438–454.

Chadwick, W. W., Dziak, R. P., Haxel, J. H., Embley, R. W., and Matsumoto, H. (2012). Submarine landslide triggered by volcanic eruption recorded by *in situ* hydrophone. *Geology* 40 (1), 51–54. doi:10.1130/g32495.1

Chang, F. (2009). *Study on submarine landslide in the Yellow River Estuary under wave action [D]*. Qingdao: Ocean University of China.

Chen, H., Li, Y., and Fang, R. (2015). Research on new technology of landslide deep displacement monitoring and early warning and prediction [J]. *J. rock Mech. Eng.* 34 (S2), 4063–4070.

Chen, H., Yan, Q., and Xiang, L. (1982). Modern coastal sedimentation of Zhujiajian island in Zhoushan [J]. *J. East China Normal Univ. Nat. Sci. Ed. [J]* (02), 77–91.

Danisch, L. A., Englehart, K., and Trivett, A. (1999). Spatially continuous six degree of freedom position and orientation sensor. *Sens. Rev.* 3541 (2), 106–112. doi:10.1108/02602289910266142

Danisch, L. A., Lowery-Simpson, M. S., and Abdoun, T. H. (2007). Shape-acceleration measurement device and method. *U.S. Pat. no.* 7296, 363.

De Groot, M. B., Bolton, M. D., Foray, P., Meijers, P., Palmer, A. C., Sandven, R., et al. (2006). Physics of liquefaction phenomena around marine structures. *J. Waterw. Port. Coast. Ocean. Eng.* 132 (4), 227–243. doi:10.1061/(asce)0733-950x(2006)132:4(227)

Dufois, F., Garreau, P., Hir, P. L., and Forget, P. (2008). Wave- and current-induced bottom shear stress distribution in the Gulf of Lions. *Cont. Shelf Res.* 28 (15), 1920–1934. doi:10.1016/j.csr.2008.03.028

Feng, S. (2012). *Characteristics and numerical simulation of tidal current and suspended sediment in winter in luotou waterway*. Hangzhou: Zhoushan [D] Zhejiang University.

Jeng, D. S. (2001). Mechanism of the wave-induced seabed instability in the vicinity of a breakwater: A review. *Ocean. Eng.* 28 (5), 537–570. doi:10.1016/s0029-8018(00)00013-5

Jia, Y., Shan, H., and Yang, X. (2011). *Sediment dynamics and geological hazards in the Yellow River estuary*. Beijing: M] Science Press.

Jia, Y., Wang, Z., and Liu, X. (2017). Research progress on field investigation and *in-situ* observation methods of submarine landslide [J]. *J. Ocean Univ. China (natural Sci. Ed.* 47 (10), 61–72.

Lai, X., and Ye, Y. (2011). *Study on submarine landslide types and sliding mechanism in tidal channel area off the coast of eastern Zhejiang [C].China Offshore Engineering Symposium*.

Lai, X., Ye, Y., and Xie, Q. C. (2000). Types and characteristics of underwater landslides in tidal channel area of eastern Zhejiang [J]. *Donghai Ocean.* 18 (004), 1–8.

Liam Finn, W. D., Siddharthan, R., and Martin, G. R. (1983). Response of seafloor to ocean waves. *J. Geotech. Engrg.* 109 (4), 556–572. doi:10.1061/(asce)0733-9410(1983)109:4(556)

Liu, B., Nian, T., Liu, M., Zheng, D., song, L., and Yin, P. (2016). Stability evaluation of submarine slope based on upper bound method of limit analysis [J]. *Acta Oceanogr. Sin.* 38 (7), 135–143.

Liu, X., Jia, Y., and Zheng, J. (2015). Field experimental study on excess pore pressure response of seabed sediments in the Yellow River Estuary caused by waves [J]. *Geotech. Mech.* 36 (11), 3055–3062.

Liu, X. L., Jia, Y. G., Zheng, J. W., Hou, W., Zhang, L., Zhang, L. P., et al. (2013). Experimental evidence of wave-induced inhomogeneity in the strength of silty seabed sediments: Y ellow River delta, China. *Ocean. Eng.* 59, 120–128. doi:10.1016/j.oceaneng.2012.12.003

Liu, X., Lu, Y., and Wang, Y. (2020). Exploration of marine resources and marine engineering geology:Summary on the 2nd international symposium on marine engineering geology[J]. *J. Eng. Geol.* 28 (1), 169–177. doi:10.13544/j.cnki.jeg.2019-493

Liu, Y., Xia, X., and Jia, J. (2007). Sediment dynamics and erosion and deposition evolution characteristics of the coastal slope of Zhoushan waidiaoshan [J]. *Ocean. Bull.* (06), 53–60.

Liang, T., Xue, L., Hou, Y., Zhang, H., and Shan, H. (2021). Research on deformation of submarine slope in Zhoushan Islands by *in-situ* observation. *E3S Web Conf.* 261, 03015. doi:10.1051/e3sconf/202126103015

Nian, T., Liu, M., Liu, B., Zheng, D., song, L., and Yin, P. (2016). Analysis of seabed stability of clayey slope under extreme wave conditions [J]. *Ocean. Eng.* 34 (4), 9–15.

Prior, D. B., Suhayda, J. N., Lu, N. Z., Bornhold, B. D., Keller, G. H., Wiseman, W. J., et al. (1989). Storm wave reactivation of a submarine landslide. *Nature* 341 (6237), 47–50. doi:10.1038/341047a0

Rahman, M. S. (1997). Instability and movement of oceanfloor sediments: A review. *Int. J. Offshore Polar Eng.* 7 (3), 220–225.

Rahman, M. S., and Jabery, W. Y. (1986). A simplified drained analysis for wave-induced liquefaction in ocean floor sands. *Soils Found.* 26 (1), 57–68. doi:10.3208/sandf1972.26.3_57

Rahman, M. S. (1991). Wave-induced instability of seabed: Mechanism and conditions. *Mar. Geotechnol.* 10, 277–299. doi:10.1080/10641199109379896

Stegmann, S., Sultan, N., Garziglia, S., Pelleau, P., Appriroual, R., Kopf, A., et al. (2012). "A long-term monitoring array for landslide precursors: A case study at the ligurian slope (western mediterranean sea)," in *Offshore technology conference*.

Sultan, N., V oisset, M., Marsset, B., Marsset, T., Cauquil, E., and Colliat, J. L. (2007). Potential role of compressional structures in generating submarine slope failures in the Niger Delta. *Mar. Geol.* 237 (3), 169–190. doi:10.1016/j.margeo.2006.11.002

Uhlemann, S., Smith, A., Chambers, J., Dixon, N., Dijkstra, T., Haslam, E., et al. (2016). Assessment of ground-based monitoring techniques applied to landslide investigations. *Geomorphology* 253, 438–451. doi:10.1016/j.geomorph.2015.10.027

Urlaub, M., Petersen, F., Gross, F., Bonforte, A., Puglisi, G., Guglielmino, F., et al. (2018). Gravitational collapse of Mount Etna's southeastern flank. *Sci. Adv.* 4 (10), eaat9700. doi:10.1126/sciadv.aat9700

Vanneste, M., Sultan, N., Garziglia, S., Forsberg, C. F., and L'Heureux, J. S. (2014). Seafloor instabilities and sediment deformation processes: The need for integrated, multi-disciplinary investigations. *Mar. Geol.* 352, 183–214. doi:10.1016/j.margeo.2014.01.005

Wallace, L. M., Webb, S. C., Ito, Y., Mochizuki, K., Hino, R., Henrys, S., et al. (2016). Slow slip near the trench at the Hikurangi subduction zone, New Zealand. *Science* 352 (6286), 701–704. doi:10.1126/science.aaf2349

Wang, Hu (2015). *Mechanism and evaluation method of seabed instability in the Yellow River Delta under wave action [D]*. Qingdao: Ocean University of China.

Wang, Z., Jia, Y., Liu, X., Wang, D., Shan, H., Guo, L., et al. (2018). *In situ* observation of storm-wave-induced seabed deformation with a submarine landslide monitoring system. *Bull. Eng. Geol. Environ.* 77 (3), 1091–1102. doi:10.1007/s10064-017-1130-4

Wang, Z., Sun, Y., Jia, Y., Shan, Z., Shan, H., Zhang, S., et al. (2020). Wave-induced seafloor instabilities in the subaqueous Yellow River delta—Initiation and process of sediment failure. *Landslides* 17 (8), 1849–1862. doi:10.1007/s10346-020-01399-2

Wei, Y. (2015). *SAA measurement technology and its application in slope monitoring [D]*. Nanjing: Nanjing University.

Xu, G. (2006). *Study on submarine sliding of silty soil gentle slope caused by waves – Taking the underwater delta of the Yellow River as an example [D]*. Qingdao: Ocean University of China.

Xu, Q. (2020). Understanding the landslide monitoring and early warning: Consideration to practical issues[J]. *J. Eng. Geol.* 28 (2), 360–374. doi:10.13544/j.cnki.jeg.2020-025

Xue, L., Jia, Y., Hou, Y., Liang, T., Shan, H., Shan, Z., et al. (2020). Stability of submarine landslides by *in situ* observation. *IOP Conf. Ser. Earth Environ. Sci.* 570, 062038. doi:10.1088/1755-1315/570/6/062038

Yang, Z., and Chen, W. (1994). Subaqueous landslide system of the Yellow River [J]. *Ocean Limnol.* 25 (6), 573–581.

Zhang, C. (2013). *Study on tidal current and sediment characteristics in the offshore area of Zhujiajian Island [D]*. Shanghai: East China Normal University.

Zhang, M., Huang, Y., and Bao, Y. (2016). The mechanism of shallow submarine landslides triggered by storm surge. *Nat. Hazards (Dordr).* 81 (2), 1373–1383. doi:10.1007/s11069-015-2112-0

Zhang, S., Jia, Y., Wang, Z., Wen, M., Lu, F., Zhang, Y., et al. (2018a). Wave flume experiments on the contribution of seabed fluidization to sediment resuspension. *Acta Oceanol. Sin.* 37 (3), 80–87. doi:10.1007/s13131-018-1143-2

Frontiers in Earth Science

Investigates the processes operating within the major spheres of our planet

Advances our understanding across the earth sciences, providing a theoretical background for better use of our planet's resources and equipping us to face major environmental challenges.

Discover the latest Research Topics

See more →

Frontiers

Avenue du Tribunal-Fédéral 34
1005 Lausanne, Switzerland
frontiersin.org

Contact us

+41 (0)21 510 17 00
frontiersin.org/about/contact